

Lecture Notes in Mechanical Engineering

Manvandra Kumar Singh
Rakesh Kumar Gautam *Editors*


Recent Trends in Design, Materials and Manufacturing

Selected Proceedings of ICRADMM 2020

 Springer


Lecture Notes in Mechanical Engineering

Series Editors

Francisco Cavas-Martínez , Departamento de Estructuras, Construcción y Expresión Gráfica Universidad Politécnica de Cartagena, Cartagena, Murcia, Spain

Fakher Chaari, National School of Engineers, University of Sfax, Sfax, Tunisia

Francesca di Mare, Institute of Energy Technology, Ruhr-Universität Bochum, Bochum, Nordrhein-Westfalen, Germany

Francesco Gherardini , Dipartimento di Ingegneria “Enzo Ferrari”, Università di Modena e Reggio Emilia, Modena, Italy

Mohamed Haddar, National School of Engineers of Sfax (ENIS), Sfax, Tunisia

Vitalii Ivanov, Department of Manufacturing Engineering, Machines and Tools, Sumy State University, Sumy, Ukraine

Young W. Kwon, Department of Manufacturing Engineering and Aerospace Engineering, Graduate School of Engineering and Applied Science, Monterey, CA, USA

Justyna Trojanowska, Poznan University of Technology, Poznan, Poland

Lecture Notes in Mechanical Engineering (LNME) publishes the latest developments in Mechanical Engineering—quickly, informally and with high quality. Original research reported in proceedings and post-proceedings represents the core of LNME. Volumes published in LNME embrace all aspects, subfields and new challenges of mechanical engineering. Topics in the series include:

- Engineering Design
- Machinery and Machine Elements
- Mechanical Structures and Stress Analysis
- Automotive Engineering
- Engine Technology
- Aerospace Technology and Astronautics
- Nanotechnology and Microengineering
- Control, Robotics, Mechatronics
- MEMS
- Theoretical and Applied Mechanics
- Dynamical Systems, Control
- Fluid Mechanics
- Engineering Thermodynamics, Heat and Mass Transfer
- Manufacturing
- Precision Engineering, Instrumentation, Measurement
- Materials Engineering
- Tribology and Surface Technology

To submit a proposal or request further information, please contact the Springer Editor of your location:

China: Ms. Ella Zhang at ella.zhang@springer.com

India: Priya Vyas at priya.vyas@springer.com

Rest of Asia, Australia, New Zealand: Swati Meherishi at swati.meherishi@springer.com

All other countries: Dr. Leontina Di Cecco at Leontina.dicecco@springer.com

To submit a proposal for a monograph, please check our Springer Tracts in Mechanical Engineering at <https://link.springer.com/bookseries/11693> or contact Leontina.dicecco@springer.com

Indexed by SCOPUS. All books published in the series are submitted for consideration in Web of Science.

More information about this series at <https://link.springer.com/bookseries/11236>

Manvandra Kumar Singh · Rakesh Kumar Gautam
Editors

Recent Trends in Design, Materials and Manufacturing

Selected Proceedings of ICRADMM 2020

 Springer

Editors

Manvandra Kumar Singh
Department of Mechanical Engineering,
Amity School of Engineering
and Technology
Amity University
Madhya Pradesh, India

Rakesh Kumar Gautam
Department of Mechanical Engineering
IIT(BHU) Varanasi
Uttar Pradesh, India

ISSN 2195-4356

ISSN 2195-4364 (electronic)

Lecture Notes in Mechanical Engineering

ISBN 978-981-16-4082-7

ISBN 978-981-16-4083-4 (eBook)

<https://doi.org/10.1007/978-981-16-4083-4>

© The Editor(s) (if applicable) and The Author(s), under exclusive license to Springer Nature Singapore Pte Ltd. 2022

This work is subject to copyright. All rights are solely and exclusively licensed by the Publisher, whether the whole or part of the material is concerned, specifically the rights of translation, reprinting, reuse of illustrations, recitation, broadcasting, reproduction on microfilms or in any other physical way, and transmission or information storage and retrieval, electronic adaptation, computer software, or by similar or dissimilar methodology now known or hereafter developed.

The use of general descriptive names, registered names, trademarks, service marks, etc. in this publication does not imply, even in the absence of a specific statement, that such names are exempt from the relevant protective laws and regulations and therefore free for general use.

The publisher, the authors and the editors are safe to assume that the advice and information in this book are believed to be true and accurate at the date of publication. Neither the publisher nor the authors or the editors give a warranty, expressed or implied, with respect to the material contained herein or for any errors or omissions that may have been made. The publisher remains neutral with regard to jurisdictional claims in published maps and institutional affiliations.

This Springer imprint is published by the registered company Springer Nature Singapore Pte Ltd.

The registered company address is: 152 Beach Road, #21-01/04 Gateway East, Singapore 189721, Singapore

Conference Organizing Committee

Chief Patron

Dr. Aseem Chauhan
Chancellor and Chairman, Amity University Madhya Pradesh, Gwalior
Additional President, RBEF (An Umbrella Foundation of Amity Institutions)

Chairman

Lt. Gen. V. K. Sharma, AVSM (Retd)
Vice-Chancellor, Amity University Madhya Pradesh, Gwalior

Vice-Chairman

Prof. (Dr.) M. P. Kaushik
Pro Vice-Chancellor, Amity University Madhya Pradesh, Gwalior

Organizing Secretary

Maj. Gen. (Dr.) S. C. Jain, VSM** (Retd)
Director, Amity School of Engineering and Technology, Amity University Madhya Pradesh, Gwalior

Convenor

Dr. C. P. Jawahar
Professor & Head

Department of Mechanical Engineering, Amity School of Engineering and Technology, Amity University Madhya Pradesh, Gwalior

Co-Convenor

Dr. Sandeep Rathee

Assistant Professor, Department of Mechanical Engineering, Amity School of Engineering and Technology, Amity University Madhya Pradesh, Gwalior

Members

Mr. Nasir Khan, Assistant Professor
Mr. Nagendra Kumar Sharma, Assistant Professor
Mr. Rohit Kumar Pandey, Assistant Professor
Dr. Manvandra Kumar Singh, Assistant Professor
Mr. Anurag Mukherjee, Teaching Associate

International Advisory Committee

Dr. Amit Kumar Jain, University of Cambridge, United Kingdom
Dr. B. D. Youn, Seoul National University, South Korea
Dr. Deepak R. Selvakumar, Harbin University, China
Dr. Jegalakshimi Jewaratnam, University of Malaya, Malaysia
Dr. Manoj Gupta, National University of Singapore, Singapore
Dr. Mayank Modak, POSTECH, South Korea
Dr. Mayur S. Sawant, University of Alberta, Canada
Dr. Nikhil Gupta, New York University, United States
Dr. Sagar H. Nikam, Ulster University, Ireland
Dr. Seung-Han Yang, Kyungpook National University, South Korea
Dr. Sunil Pathak, University Malaysia Pahang, Malaysia
Dr. Tarasankar Debro, Pennsylvania State University, United States

Technical Committee

Dr. Pulak Mohan Pandey, Professor, IIT Delhi
Dr. Sachin Maheshwari, Dean, FOT, University of Delhi
Dr. Arshad Noor Siddiquee, Professor, Jamia Millia Islamia, New Delhi
Dr. Akhilesh Kumar Singh, Associate Professor, IIT (BHU) Varanasi
Dr. R. K. Gautam, Associate Professor, IIT (BHU) Varanasi
Dr. U. S. Rao, Associate Professor, IIT (BHU) Varanasi
Dr. Md. ZaheerYusufzal, Associate Professor, IIT (BHU) Varanasi
Dr. MeghanshuVashista, Associate Professor, IIT (BHU) Varanasi
Dr. M. Joseph Davidson, Associate Professor, NIT Warangal
Dr. Ravindra Rana, Associate Professor, MANIT Bhopal
Dr. S. J. Vijay, Associate Professor, KITS, Coimbatore
Dr. Arun Tom, Associate Professor, VIT, Vellore
Dr. M. S. Alphin, Associate Professor, SSN College of Engineering, Chennai
Dr. Chaitanya Sharma, Associate Professor, RJIT, Gwalior
Dr. Shiva Sekar, Assistant Professor, IIT Jammu
Dr. Nishant Kumar Singh, Assistant Professor, NIT Raipur
Dr. Yogesh Singh, Assistant Professor, NIT Silchar
Dr. Rajeev Nayan Gupta, Assistant Professor, NIT Silchar
Dr. Gaurav Tiwari, Assistant Professor, VNIT Nagpur
Dr. Yogesh Kumar, Assistant Professor, NIT Patna
Dr. Rajbahadur Singh, Assistant Professor, NIT Hamirpur
Dr. N. Yuvaraj, Assistant Professor, DTU, New Delhi
Dr. Naresh K. Raghuvanshi, Assistant Professor, MITS, Gwalior
Dr. Rajkumar S. Rai, Assistant Professor, KITS, Coimbatore
Dr. Sandesh Chougule, Assistant Professor, LNMIIT, Jaipur
Dr. Anil Kumar, Assistant Professor, KNIT, Sultanpur

Preface

The book “Recent Trends in Design, Materials and Manufacturing” has covered a detailed discussion about the problems related to structural mechanics, kinematics and dynamics of machines, mechanical structures and stress analysis, noise and vibration analysis, fault detection and condition monitoring, optimization techniques, mechatronics and robotics, product design and development, and tribology. The book also discusses various properties and performance attributes of modern-age design in mechanical engineering, including their durability, workability, and carbon footprint. The book can be a valuable reference for industries, beginners, researchers, and professionals interested in sustainable development in mechanical engineering design and allied fields.

Recent trends in design, materials, and manufacturing offer versatility, in terms of utilization over other conventional technologies in the Indian scenario and worldwide. To explore and report the recent developments in the fields of design, materials, and manufacturing, the International Conference on Recent Advances in Design, Materials and Manufacturing 2020 (ICRADMM 2020) is organized during October 15–16, 2020 at Amity University Madhya Pradesh, India. More than 200 delegates from India and outside India have actively participated in this event and shared their findings. Also, some renowned speakers from premier institutes were invited to the event to share their experiences on the new design and development in technology with the audience.

Gwalior, Madhya Pradesh, India
October 2021

Manvandra Kumar Singh
Rakesh Kumar Gautam

Reviewers

Dr. Nishant K Singh

Department of Biomedical Engineering, National Institute of Technology, Raipur, Chhattisgarh, India

Dr. Khemraj

Department of Mechanical Engineering, Government College of Engineering, Bandopala Post-Risigaon, Bhawanipatna, Odisha, India

Dr. Rajeev Nayan Gupta

Department of Mechanical Engineering, National Institute of Technology Silchar, Cachar, Assam, India

Dr. Gaurav Tiwari

Department of Mechanical Engineering, Visvesvaraya National Institute of Technology Nagpur, India

Dr. Pushkar Jha

School of Mechanical Engineering, Kalinga Institute of Industrial Technology Deemed to be University, Bhubaneswar, India

Dr. Shushant Singh

Department of Mechanical Engineering, Uttarakhand University, Dehradun, India

Dr. A. Vasanthanathan

Department of Mechanical Engineering, Mepco Schlenk Engineering College, Sivakasi, India

Mr. Ashish Singh Pareta

Department of Mechanical Engineering, Indian Institute of Technology (BHU), Varanasi, India

Mr. Aamod

Department of Mechanical Engineering, Indian Institute of Technology (BHU), Varanasi, India

Dr. Yogesh Kumar

Department of Mechanical Engineering, National Institute of Technology, Patna, Bihar, India

Dr. Sudesh Kumar Singh

Department of Mechanical Engineering, Sharda University, Greater Noida, Uttar Pradesh, India

Dr. Pallav Gupta

Department of Mechanical Engineering, Amity University Noida, Amity Rd, Sector 125, Noida, Uttar Pradesh, India

Dr. M. K. Singh

Department of Mechanical Engineering, Amity School of Engineering & Technology, Amity University Madhya Pradesh, Gwalior, India

Dr. Manisha Singh

Department of Physics, Amity School of Engineering & Technology, Amity University Madhya Pradesh, Gwalior, India

Dr. Ashish Srivastava

Department of Mechanical Engineering, Presidency University, Bangalore, India

Contents

Structural Mechanics

F-Contractive-Type Mappings in Soft Metric Space	3
Ramakant Bhardwaj, Sarla Chouhan, H. G. Sanath Kumar, and Sudeep Kumar Pandey	

Fixed Point Results in b-Metric Spaces Over Banach Algebra and Contraction Principle	15
Abid Khan, Santosh Kumar Sharma, Girraj Kumar Verma, Ramakant Bhardwaj, and Qazi Aftab Kabir	

Common Invariant Point Theorem for Multi-valued Generalized Fuzzy Mapping in b-Metric Space	23
Umashankar Singh, Naval Singh, Ruchi Singh, and Ramakant Bhardwaj	

Mechanical Materials Design and Analysis

An Experimental Analysis for Temperature Dependency of Photovoltaic Cell Parameters Under Artificial Illumination	39
Abhishek Bhushan and Rakesh Kumar	

Performance Analysis of Combined Cycle with Supplementary Heating	47
Nagendra Kumar Sharma and Rohit Pandey	

Effect of Laser Spot Diameter on Melt Pool Thermal History During Laser Cladding on Inconel 718 Coatings	65
Nikhil Thawari, Chaitanya Gullipalli, and T. V. K. Gupta	

Impact of Forthcoming Price Increase for Maximum Fixed Lifetime Product with Preservation Technology Investment and Price-Sensitive Demand	75
Mrudul Y. Jani, Manish R. Betheja, and Urmila Chaudhari	

Industry 4.0 Research: Information and Communication	
Technology Capability Index for Supply Chain Management	97
Prashant R. Nair, S. P. Anbudayasankar, R. Kishore, and R. Pradeep	
Productivity Improvement in Foundry Using IoT	119
Yash Patel, Bhavesh Mewada, Bharat Tank, and Prashant Singh Tomar	
Mechanical Structures and Stress Analysis	
Strain Measurement of Aluminium in Tensometer Using Digital Image Correlation (DIC)	135
A. Vijaya, N. Kannan, M. Palaniappan, and G. S. Lohith Kumar	
Structural and Thermal Analyses of Gas Turbine Blades with Internal Cooling System Under Steady-State Conditions	149
K. Balaji, G. Jims John Wessley, and S. V. Khandal	
Response of Modified 9Cr-1Mo Steel Under Asymmetrical Stress Loading at 600 °C	163
Prerna Mishra, N. C. Santhi Srinivas, and Vakil Singh	
Finite Element Analysis of Bending Response of Aluminum 1100-H12 and Mild Steel Hat Shape Beam	173
Amita Shinde and Gaurav Tiwari	
Ballistic Response of CFRP Armor Helmet Against Ogive Nosed Projectile	181
S. L. S. Hamsi, N. Gharde, N. Khaire, and Gaurav Tiwari	
Tensile-Microstructure Evaluation for LM6 Alloys Synthesized by Solid–Liquid Mixed Casting	191
Mayank Agarwal, Devendra Pratap Singh, Manvandra Kumar Singh, and Rajeev Srivastava	
FEM-Based Impact Analysis of Roll Cage of an All-Terrain Vehicle	199
Jitendra Yadav, Santosh Kumar Kurre, and Shubham Thakur	
Noise and Vibration Analysis	
Fault Investigation of Rolling Element Bearing Using Vibration Signature Analysis and Artificial Neural Network	213
Pavan Agrawal, Arvind Singh Tomar, and Pratesh Jayaswal	
Enhancement of Aerodynamic Efficiency of a Formula Car by Incorporating a Passive Device in the Front Wing	225
K. Balaji, G. Jims John Wessley, S. V. Khandal, and Mayuri Gore	

Design and Analysis of Exoskeleton with a Torque Prediction Algorithm 239
 R. Venkatesh, B. Satish Kumar, K. Umamaheswara Rao, S. S. Mantha, and K. Dileep

Characterization of Noise Sources, Built Material and Acoustic Parameters of a Newly Renovated Special Purpose Space 261
 Mohd Zaid, Yasser Rafat, Sameen Mustafa, Rashid Ali, and Bashmal Salem

Fault Detection and Condition Monitoring

A Comparative Study on Mathematical Approaches to Determine the Time Lag and Synchrony Between Two Time-Series Data in Different Engineering Applications 281
 N. Abinson Paul, Rajakumar S. Rai, and S. J. Vijay

Envelope Spectrum Analysis of Noisy Signal with Spectral Kurtosis to Diagnose Bearing Defect 291
 Arvind Singh Tomar and Pratesh Jayaswal

Semi-Automatic Boundary Detection of Weak Edges for Medical Image Analysis 305
 Neha Bhadrawale, Rajeev Kumar Gupta, and Arti Jain

An Efficient and Lightweight Intrusion Detection System for Mobile Ad Hoc Networks 317
 Y. Sharmasth Vali, N. Prakash, and L. Shakkeera

Synchronization of Uncertain and External Disturbance Time Delay Chaotic Systems 331
 Ajit K. Singh

Optimization Techniques

Optimization of Machining Parameters on Vertical Milling Machine for Al-CNT Composites Using Taguchi Design of Experiments 345
 Sachchida Nand, Manvandra Kumar Singh, and C. M. Krishna

Numerical Study on Domain Independency for Prediction of Vortex Shedding Parameters of a Circular Cylinder 353
 Vidya Chandran, Sheeja Janardhanan, and M. Sekar

Design and Performance—Analysis of Hybrid Drive Optimized for Torque–Speed Characteristic Requirements of Heavy Vehicles 365
 Kumaran Duraikannu, Yuddhveer Singh Kachhawa, Abhishek Vats, and Sahil Purushotham Kanchan

Handling and Scheduling of Inner-City Lagoon Water Through Numerical Index and Multivariate Statistics	383
Yogesh Shukla, Nasir Khan, and Sonia Shivhare	
Multi-objective Optimization and Numerical Analysis of Coil Spring Used in Automobile Suspensions	389
Anurag Tripathi, K. Rameshkumar, and S. Saravanamurugan	
Mechatronics and Robotics	
Replicating the Natural Limb Structure of a Mammal-Type Quadruped on a Highly Compact 12-DoF Robot to Deduce a Relation Between Limb Structure and Canine Gait Efficiency	409
Divyaansh Singh and Apurv Verma	
Automation in Robotics with Artificial Intelligence	423
Yogini Borole and C. G. Dethe	
Modeling and Path Planning of a Grocery Robot	435
R. Venkatesh, B. Satish Kumar, K. Umamaheswara Rao, and K. Dileep	
Mechatronic System for an Automated Dynamics Staircase for Walking Difficulty People to Travel in Public Road Transportation Vehicles	449
Mrunal Swaroop Peravali, Gadudasu Babu Rao, Praveen Kumar Bannaravuri, Mona Sahu, Dasariraju Lakshmi Deepak, Sumanth Ratna Kandavalli, Kumara swamy Pulisheru, and Srinivasa Rao Gorrepati	
Design and Development of Mechatronic System for an Automated Ergonomic Keyboard Tray	461
Mona Sahu, Gadudasu Babu Rao, Wilson M. Kumar, S. J. Vijay, Achsah Phebe Chrysolin, Ajith Purushothaman Madan, Samuel Jebish, and Joseph J. John	
Product Design and Development	
Comparative Study of the Rear and Rear Side Impact on a Roll Cage Using FEM	475
Santosh Kumar Kurre, Jitendra Yadav, and Shubham Thakur	
Design and Analysis of a Structure to Support Two Star Sensors	485
S. Rai Rajakumar, X. Ajay Vasanth, I. Kantharaj, and R. Srinivasan	
Designing and Fabrication of a Device for Automation of the Film Transfer Process in Floating Film Transfer Method	493
Nitesh Kumar, Gopal Ji, and Manvandra Kumar Singh	

Filter Design for Radar Signal Analysis Using Field Programmable Gate Array 501
Anil Kumar Sahu, Abhishek Singh, and Harish Kumar Shakya

A Greener Framework for Start-Up Involving Order Management 511
R. Akaash, S. Aswin, M. Jayashuriya, Enoch Somana, and S. P. Anbuudayasankar

Tribology

Prediction of Brake Pad Wear Using Various Machine Learning Algorithms 529
John Jeyaraj Steffan, Immanuel Johnraja Jebadurai, Lazarus Godson Asirvatham, Stephen Manova, and Jeffry Pon Larkins

Abrasive Wear Behavior of Bio-Fiber-Reinforced Epoxy Composites with Taguchi Approach 545
Tanusree Bera, Lopamundra Mohapatra, Ved Prakash, and S. K. Acharya

Effect of Surface-Treated Calcium-Copper-Titanate as a Lubricant Additive in Cottonseed Oil on Tribo Performance in Sliding Contacts 555
Rajeev Nayan Gupta, A. P. Harsha, and Tej Pratap

About the Editors

Dr. Manvandra Kumar Singh is currently an Assistant Professor at the Department of Mechanical Engineering, Amity School of Engineering and Technology, Amity University Madhya Pradesh, India. He obtained his B.Tech. in Mechanical Engineering from Uttar Pradesh Technical University (U.P.T.U.) Lucknow, India, in 2009. He completed his M.Tech. in Materials Science & Technology from Indian Institute of Technology (Banaras Hindu University) Varanasi, India, in 2011. He received his Ph.D. in Mechanical Engineering (Design) from Indian Institute of Technology (Banaras Hindu University) Varanasi, India, in 2018. Major areas of his research-interest include study of development and design of metal matrix composite and hybrid composite materials and its microstructural, physical, mechanical and tribological behaviors including its applications. He has published more than 25 papers in reputed journals, book chapter and conference proceedings. Dr. Singh is life member of “Tribology Society of India (TSI)” affiliated to International Tribology Council, U.K. Senior member of Indian Society of Mechanical Engineers (ISME) and Associate member of “The Indian Institute of Metals (IIM)”. Currently, he is an editorial board member of the International Journal of Teknika: Jurnal Sains dan Teknologi”, “Composite Materials Research” and “Metallic Material Research”.

Dr. Rakesh Kumar Gautam is currently an Professor at the Department of Mechanical Engineering, Indian Institute of Technology (Banaras Hindu University) Varanasi, India. He received his B.E. from Madan Mohan Malviya Engineering College, Gorakhpur (1999), M.Tech. from Institute of Technology (2001) presently Indian Institute of Technology (BHU) Varanasi and Ph.D. degree from Indian Institute of Technology, Roorkee (2009). His major areas of research interest includes copper-based in-situ and hybrid composite, processing of light alloy base composites and nano- composite, microwave sintered composite, tribological, mechanical and physical properties of cast in-situ composites, self-healing materials, bio-tribology, air jet erosion. Dr. Rakesh Kumar Gautam has published more than 50 articles in international journals, conference proceedings and a book chapter. He has guided more than 20 M.Tech and 05 Ph.D students. Currently, he is a reviewer/editorial board member of the International Journal of Tribology-Transaction, ASME, Journal of Materials

Science, Springer, Journal of Tribology Transactions, STLE, Taylor and Francis, Journal of Engineering Tribology Proceedings of the Institution of Mechanical Engineers (IMEchE), Part J: Journal of Engineering Tribology, Tribology - Materials, Surfaces & Interfaces.

Structural Mechanics

F-Contractive-Type Mappings in Soft Metric Space



Ramakant Bhardwaj , Sarla Chouhan, H. G. Sanath Kumar,
and Sudeep Kumar Pandey

Abstract In the present paper, some fixed point results are established in soft metric spaces for F-contractive-type mappings for random operator. The obtained results generalized the basic results in fixed point theory. The obtained results are useful to solve the uncertainty as well as decision-making problems. To find the required results, the basic concepts of Banach contraction principle are used for complete soft metric spaces.

Keywords Fixed point · Soft sets · F-contraction · Random operator

1 Introduction and Preliminaries

In the year 1999, Molodtsov [1] initiated a novel concept of soft sets theory as a new mathematical tool for dealing with uncertainties. A soft set is a collection of approximate descriptions of an object. Soft systems provide a very general framework with the involvement of parameters. The detail about soft set theory can be studied in [1–3] and brief for soft metric space, in [4–9]. The detail about fixed point theorem for random operator and convergence of an iteration leading to a solution of a random operator equation can be viewed in [10–13]. The definition can be modified for random operator easily. Throughout this paper (Ω, Σ) denotes a measurable space consisting of a set Ω and sigma algebra Σ of subset of Ω . X stands for a metric space and C is non-empty subset of X . In 2012, Wardowski [14] introduces a new type of

R. Bhardwaj (✉)

Department of Mathematics, Amity University, Kolkata 700157, India

Department of Mathematics, APS University, Rewa, MP, India

S. Chouhan

Department of Mathematics and Computational Science, SGSITS, Indore 453441, India

H. G. Sanath Kumar

Department of Science, Shanghai United International School Minhang, Shanghai, China

S. K. Pandey

Department of Mathematics, Government Degree College Amarapur, Dindori 481880, India

© The Author(s), under exclusive license to Springer Nature Singapore Pte Ltd. 2022

M. K. Singh and R. K. Gautam (eds.), *Recent Trends in Design, Materials*

and Manufacturing, Lecture Notes in Mechanical Engineering,

https://doi.org/10.1007/978-981-16-4083-4_1

contractions called F-contraction and proves a new fixed point theorem concerning F-contraction. More about F-contraction can be seen in [15–17]. All are modification of Banach's contraction principle [18] in different form. The detail about Suzuki-type mapping can be seen in [19, 20]. The modification form of F-contraction can be written as follows.

Definition 1.1 Let (X, d) be a metric space. A function $T : X \rightarrow X$ is said to be an F-contraction for random operator if there exists $\tau > 0$ such that for all $\xi x, \xi y \in X$

$$d(T\xi x, T\xi y) > 0 \Rightarrow \tau + F(d(T\xi x, T\xi y)) \leq F(d(\xi x, \xi y)),$$

where $F : \mathbb{R}_+ \rightarrow \mathbb{R}$ is a mapping satisfying the following conditions:

(F1) F is strictly increasing, i.e., for all $\xi x, \xi y \in \mathbb{R}_+$ such that $\xi x < \xi y$, $F(\xi x) < F(\xi y)$;

(F2) For each sequence $\{\xi\alpha_n\}_{n=1}^\infty$ of positive numbers, $\lim_{n \rightarrow \infty} \xi\alpha_n = 0$ if and only if $\lim_{n \rightarrow \infty} F(\xi\alpha_n) = -\infty$;

(F3) There exists $k \in (0, 1)$ such that $\lim_{n \rightarrow 0^+} \xi\alpha^k F(\xi\alpha) = 0$.

Lemma 1.2 Let $F : \mathbb{R}_+ \rightarrow \mathbb{R}$ be an increasing mapping and $\{\xi\alpha_n\}_{n=1}^\infty$ be a sequence of positive real numbers. Then the following assertions hold:

(F1') (a) if $\lim_{n \rightarrow \infty} F(\xi\alpha_n) = -\infty$ then $\lim_{n \rightarrow \infty} \xi\alpha_n = 0$;

(b) if $\inf F = -\infty$ and $\lim_{n \rightarrow \infty} \xi\alpha_n = 0$ then $\lim_{n \rightarrow \infty} F(\xi\alpha_n) = -\infty$.

(F2') $\inf F = -\infty$ or also by

(F2'') there exists a sequence $\{\alpha\xi_n\}_{n=1}^\infty$ of positive real numbers such that $\lim_{n \rightarrow \infty} F(\xi\alpha_n) = -\infty$.

(F3') F is continuous on $(0, \infty)$.

We denote by \mathcal{F} the set of all functions satisfying the conditions (F1), (F2'), and (F3').

2 Main Results

Theorem 2.1 Let $(\tilde{X}, \tilde{d}, E)$ be a complete soft metric space and let (f, φ) be a self-mapping of a \tilde{X} into itself. ξ is a measurable selector and (Ω, Σ) denotes a measurable space consisting of a set Ω and sigma algebra Σ of subset of Ω . Suppose $F \in \mathcal{F}$ and there exists $\tau > 0$ such that for all $\tilde{\xi}x_\lambda, \tilde{\xi}y_\mu \in SP(X)$

$$\tilde{d}\left((f, \varphi)\left(\tilde{\xi}x_\lambda\right), (f, \varphi)\left(\tilde{\xi}y_\mu\right)\right) > 0$$

$$\Rightarrow \tau + F\left(\tilde{d}\left((f, \varphi)\left(\tilde{\xi}x_{\lambda}\right), (f, \varphi)\left(\tilde{y}\tilde{\xi}_{\mu}\right)\right)\right) \leq F\left(\tilde{d}\left(x\tilde{\xi}_{\lambda}, \tilde{\xi}y_{\mu}\right)\right). \quad (1)$$

Then (f, φ) has a unique random soft fixed point in \tilde{X} and for every $\tilde{\xi} \tilde{x}_{\lambda}^* \in \tilde{X}$ the sequence $(f, \varphi)^n\left(\tilde{\xi} \tilde{x}_{\lambda_0}^0\right)$ converges to $\tilde{\xi} \tilde{x}_{\lambda}^*$.

Proof Let $\tilde{\xi} \tilde{x}_{\lambda}^0$ be any soft point in $SP(X)$.

$$\begin{aligned} \text{Set} \quad \tilde{\xi}x_{\lambda_1}^1 &= (f, \varphi)\left(\tilde{\xi}x_{\lambda}^0\right) = \left(f\left(\tilde{\xi}x_{\lambda}^0\right)\right)_{\varphi(\lambda)} \\ \tilde{\xi}x_{\lambda_2}^2 &= (f, \varphi)\left(\tilde{\xi}x_{\lambda_1}^1\right) = \left(f^2\left(\tilde{\xi}x_{\lambda}^0\right)\right)_{\varphi^2(\lambda)} \\ &\text{-----} \\ \tilde{\xi}x_{\lambda_{n+1}}^{n+1} &= (f, \varphi)\left(\tilde{\xi}x_{\lambda_n}^n\right) = \left(f^{n+1}\left(\tilde{\xi}x_{\lambda}^0\right)\right)_{\varphi^{n+1}(\lambda)}. \text{---} \end{aligned}$$

If there exists $n \in \mathbb{N}$ such that $\tilde{d}\left(\tilde{\xi}x_{\lambda_n}^n, (f, \varphi)\left(\tilde{\xi}x_{\lambda_n}^n\right)\right) = 0$, the proof is complete.

So we assume that $0 < \tilde{d}\left(\tilde{\xi}x_{\lambda_n}^n, (f, \varphi)\left(\tilde{\xi}x_{\lambda_n}^n\right)\right) = \tilde{d}\left((f, \varphi)\left(\tilde{\xi}x_{\lambda_{n-1}}^{n-1}\right), (f, \varphi)\left(\tilde{\xi}x_{\lambda_n}^n\right)\right)$.

For any $n \in \mathbb{N}$, we have

$$\begin{aligned} \tau + F\left(\tilde{d}\left((f, \varphi)\left(\tilde{\xi}x_{\lambda_{n-1}}^{n-1}\right), (f, \varphi)\left(\tilde{\xi}x_{\lambda_n}^n\right)\right)\right) &\leq F\left(\tilde{d}\left(\tilde{\xi}x_{\lambda_{n-1}}^{n-1}, \tilde{\xi}x_{\lambda_n}^n\right)\right), \\ F\left(\tilde{d}\left((f, \varphi)\left(\tilde{\xi}x_{\lambda_{n-1}}^{n-1}\right), (f, \varphi)\left(\tilde{\xi}x_{\lambda_n}^n\right)\right)\right) &\leq F\left(\tilde{d}\left(\tilde{\xi}x_{\lambda_{n-1}}^{n-1}, \tilde{\xi}x_{\lambda_n}^n\right)\right) - \tau. \end{aligned}$$

Continuing this process n - times, we get

$$\begin{aligned} F\left(\tilde{d}\left((f, \varphi)\left(\tilde{\xi}x_{\lambda_{n-1}}^{n-1}\right), (f, \varphi)\left(\tilde{\xi}x_{\lambda_n}^n\right)\right)\right) &\leq F\left(\tilde{d}\left(\tilde{\xi}x_{\lambda_{n-1}}^{n-1}, \tilde{\xi}x_{\lambda_n}^n\right)\right) - \tau \\ &= F\left(\tilde{d}\left((f, \varphi)\left(\tilde{\xi}x_{\lambda_{n-2}}^{n-2}\right), (f, \varphi)\left(\tilde{\xi}x_{\lambda_{n-1}}^{n-1}\right)\right)\right) - \tau \\ &\leq F\left(\tilde{d}\left(\tilde{\xi}x_{\lambda_{n-2}}^{n-2}, \tilde{\xi}x_{\lambda_{n-1}}^{n-1}\right)\right) - 2\tau \\ &= F\left(\tilde{d}\left((f, \varphi)\left(\tilde{\xi}x_{\lambda_{n-3}}^{n-3}\right), (f, \varphi)\left(\tilde{\xi}x_{\lambda_{n-2}}^{n-2}\right)\right)\right) - 2\tau \\ &\leq F\left(\tilde{d}\left(\tilde{\xi}x_{\lambda_{n-3}}^{n-3}, \tilde{\xi}x_{\lambda_{n-2}}^{n-2}\right)\right) - 3\tau \\ &\text{-----} \\ &\leq F\left(\tilde{d}\left(\tilde{\xi}x_{\lambda_0}^0, \tilde{\xi}x_{\lambda_1}^1\right)\right) - n\tau. \end{aligned} \quad (2)$$

From (2), we obtain $\lim_{n \rightarrow \infty} F\left(\tilde{d}\left((f, \varphi)\left(\tilde{\xi} \tilde{x}_{\lambda_{n-1}}^{n-1}\right), (f, \varphi)\left(\tilde{\xi} \tilde{x}_{\lambda_n}^n\right)\right)\right) = -\infty$, which together with (F2') and Lemma 1.2 gives $\lim_{n \rightarrow \infty} \tilde{d}\left((f, \varphi)\left(\tilde{\xi} \tilde{x}_{\lambda_{n-1}}^{n-1}\right), (f, \varphi)\left(\tilde{\xi} \tilde{x}_{\lambda_n}^n\right)\right) = 0$,

i.e.,

$$\lim_{n \rightarrow \infty} \tilde{d}\left(\tilde{\xi} \tilde{x}_{\lambda_n}^n, (f, \varphi)\left(\tilde{\xi} \tilde{x}_{\lambda_n}^n\right)\right) = 0. \quad (3)$$

Now, we claim that $\left\{\tilde{\xi} \tilde{x}_{\lambda_n}^n\right\}$ is a Cauchy sequence. Suppose, on the contrary, that there exists $\epsilon_0 > 0$ and sequence $\{\lambda_{m(k)}\}$ and $\{\lambda_{n(k)}\}$ of natural numbers such that

$$\lambda_{m(k)} > \lambda_{n(k)} > k, \tilde{d}\left(\tilde{\xi} \tilde{x}_{\lambda_{m(k)}}^{m(k)}, \tilde{\xi} \tilde{x}_{\lambda_{n(k)}}^{n(k)}\right) \geq \epsilon_0, \tilde{d}\left(\tilde{x} \tilde{\xi}_{\lambda_{m(k)-1}}^{m(k)-1}, \tilde{\xi} \tilde{x}_{\lambda_{n(k)}}^{n(k)}\right) < \epsilon_0 \forall k \in \mathbb{N}. \quad (4)$$

Applying the triangle inequality, we have

$$\begin{aligned} \epsilon_0 &\leq \tilde{d}\left(\tilde{\xi} \tilde{x}_{\lambda_{m(k)}}^{m(k)}, \tilde{\xi} \tilde{x}_{\lambda_{n(k)}}^{n(k)}\right) \leq \tilde{d}\left(\tilde{\xi} \tilde{x}_{\lambda_{m(k)}}^{m(k)}, \tilde{\xi} \tilde{x}_{\lambda_{m(k)-1}}^{m(k)-1}\right) + \tilde{d}\left(\tilde{\xi} \tilde{x}_{\lambda_{m(k)-1}}^{m(k)-1}, \tilde{\xi} \tilde{x}_{\lambda_{n(k)}}^{n(k)}\right) \\ &\leq \tilde{d}\left(\tilde{\xi} \tilde{x}_{\lambda_{m(k)}}^{m(k)}, \tilde{\xi} \tilde{x}_{\lambda_{m(k)-1}}^{m(k)-1}\right) + \epsilon_0 \\ &\leq \tilde{d}\left(\tilde{\xi} \tilde{x}_{\lambda_{m(k)-1}}^{m(k)-1}, (f, \varphi)\left(\tilde{\xi} \tilde{x}_{\lambda_{m(k)-1}}^{m(k)-1}\right)\right) + \epsilon_0. \end{aligned}$$

From (3) and the above inequality that

$$\epsilon_0 \leq \lim_{n \rightarrow \infty} \tilde{d}\left(\tilde{\xi} \tilde{x}_{\lambda_{m(k)}}^{m(k)}, \tilde{\xi} \tilde{x}_{\lambda_{n(k)}}^{n(k)}\right) \leq 0 + \epsilon_0,$$

i.e.,

$$\lim_{n \rightarrow \infty} \tilde{d}\left(\tilde{\xi} \tilde{x}_{\lambda_{m(k)}}^{m(k)}, \tilde{\xi} \tilde{x}_{\lambda_{n(k)}}^{n(k)}\right) = \epsilon_0. \quad (5)$$

On the other hand, from (3) there exists $k \in \mathbb{N}$, such that

$$\begin{aligned} \tilde{d}\left(\tilde{\xi} \tilde{x}_{\lambda_{m(k)}}^{m(k)}, (f, \varphi)\left(\tilde{\xi} \tilde{x}_{\lambda_{m(k)}}^{m(k)}\right)\right) &= \frac{\epsilon_0}{4} \\ \text{and } \tilde{d}\left(\tilde{\xi} \tilde{x}_{\lambda_{n(k)}}^{n(k)}, (f, \varphi)\left(\tilde{\xi} \tilde{x}_{\lambda_{n(k)}}^{n(k)}\right)\right) &= \frac{\epsilon_0}{4}. \end{aligned} \quad (6)$$

Next, we claim that

$$\tilde{d}\left((f, \varphi)\left(\tilde{\xi} \tilde{x}_{\lambda_m(k)}^{m(k)}\right), (f, \varphi)\left(\tilde{\xi} \tilde{x}_{\lambda_n(k)}^{n(k)}\right)\right) = \tilde{d}\left(\tilde{\xi} \tilde{x}_{\lambda_m(k)+1}^{m(k)+1}, \tilde{\xi} \tilde{x}_{\lambda_n(k)+1}^{n(k)+1}\right) > 0. \quad (7)$$

Suppose, on the contrary, there exists $l \geq \mathbb{N}$ such that

$$\tilde{d}\left(\tilde{\xi} \tilde{x}_{\lambda_m(l)+1}^{m(l)+1}, \tilde{\xi} \tilde{x}_{\lambda_n(l)+1}^{n(l)+1}\right) = 0. \quad (8)$$

It follows from (4), (6), and (8), we get

$$\begin{aligned} \epsilon_0 &\leq \tilde{d}\left(\tilde{\xi} \tilde{x}_{\lambda_m(k)}^{m(k)}, \tilde{\xi} \tilde{x}_{\lambda_n(k)}^{n(k)}\right) \leq \tilde{d}\left(\tilde{\xi} \tilde{x}_{\lambda_m(k)}^{m(k)}, \tilde{\xi} \tilde{x}_{\lambda_m(k)+1}^{m(k)+1}\right) + \tilde{d}\left(\tilde{\xi} \tilde{x}_{\lambda_m(k)+1}^{m(k)+1}, \tilde{\xi} \tilde{x}_{\lambda_n(k)}^{n(k)}\right) \\ &\leq \tilde{d}\left(\tilde{\xi} \tilde{x}_{\lambda_m(k)}^{m(k)}, \tilde{\xi} \tilde{x}_{\lambda_m(k)+1}^{m(k)+1}\right) + \tilde{d}\left(\tilde{\xi} \tilde{x}_{\lambda_m(k)+1}^{m(k)+1}, \tilde{\xi} \tilde{x}_{\lambda_n(k)+1}^{n(k)+1}\right) + \tilde{d}\left(\tilde{\xi} \tilde{x}_{\lambda_n(k)+1}^{n(k)+1}, \tilde{\xi} \tilde{x}_{\lambda_n(k)}^{n(k)}\right) \\ &\leq \tilde{d}\left(\tilde{\xi} \tilde{x}_{\lambda_m(k)}^{m(k)}, (f, \varphi)\left(\tilde{\xi} \tilde{x}_{\lambda_m(k)}^{m(k)}\right)\right) \\ &\quad + \tilde{d}\left(\tilde{\xi} \tilde{x}_{\lambda_m(k)+1}^{m(k)+1}, \tilde{\xi} \tilde{x}_{\lambda_n(k)+1}^{n(k)+1}\right) + \tilde{d}\left(\tilde{\xi} \tilde{x}_{\lambda_n(k)}^{n(k)}, (f, \varphi)\left(\tilde{\xi} \tilde{x}_{\lambda_n(k)}^{n(k)}\right)\right) \\ &< \frac{\epsilon_0}{4} + 0 + \frac{\epsilon_0}{4} = \frac{\epsilon_0}{2}. \end{aligned}$$

This contradiction establishes relation (7). Therefore, it follows from (7) and the assumption of the theorem that $\forall k \in \mathbb{N}$,

$$\tau + F\left(\tilde{d}\left((f, \varphi)\left(\tilde{\xi} \tilde{\lambda}_{m(k)}\right), (f, \varphi)\left(\tilde{\xi} \tilde{\lambda}_{n(k)}\right)\right)\right) \leq F\left(\tilde{d}\left(\tilde{\lambda} \tilde{\xi}_{m(k)}, \tilde{\xi} \tilde{\lambda}_{n(k)}\right)\right). \quad (9)$$

From (F3'), (5), and (9), we get $\tau + F(\epsilon_0) \leq F(\epsilon_0)$. This contradiction shows that $\left\{\tilde{\xi} \tilde{x}_{\lambda_n}^n\right\}$ is a Cauchy sequence. By completeness of $(\tilde{X}, \tilde{d}, E)$, $\left\{\tilde{\xi} \tilde{x}_{\lambda_n}^n\right\}$ converges to some point $\tilde{\xi} \tilde{x}_\lambda^* \in \tilde{X}$.

Finally, the continuity of (f, φ) yields

$$\tilde{d}\left((f, \varphi)\tilde{\xi} \tilde{x}_{\lambda_n}^n, \tilde{\xi} \tilde{x}_\lambda^*\right) = \lim_{n \rightarrow \infty} \tilde{d}\left(\tilde{\xi} \tilde{x}_{\lambda_{n+1}}^{n+1}, \tilde{\xi} \tilde{x}_\lambda^*\right) = \tilde{d}\left(\tilde{\xi} \tilde{x}_\lambda^*, \tilde{\xi} \tilde{x}_\lambda^*\right) = 0.$$

Uniqueness: Let \tilde{y}_μ^* is another fixed point of (f, φ) in \tilde{X} such that

$$(f, \varphi)\left(\tilde{\xi} \tilde{x}_\lambda^*\right) = \tilde{x}_\lambda^* \neq \tilde{\xi} \tilde{y}_\mu^* = (f, \varphi)\left(\tilde{\xi} \tilde{y}_\mu^*\right).$$

Therefore, $\tilde{d}\left((f, \varphi)\tilde{\xi}x_\lambda^*, (f, \varphi)\tilde{\xi}y_\mu^*\right) = \tilde{d}\left(\tilde{\xi} \tilde{x}_\lambda^*, \tilde{\xi} \tilde{y}_\mu^*\right) > 0$.

Then we get

$$F\left(\tilde{d}\left(\tilde{\xi}x_\lambda^*, \tilde{\xi}y_\mu^*\right)\right) = F\left(\tilde{d}\left((f, \varphi)\tilde{\xi}x_\lambda^*, (f, \varphi)\tilde{\xi}y_\mu^*\right)\right) < \tau$$

$$+ F\left(\tilde{d}\left((f, \varphi)\tilde{\xi} \tilde{x}_\lambda^*, (f, \varphi)\tilde{\xi} \tilde{y}_\mu^*\right)\right) \leq F\left(\tilde{d}\left(\tilde{\xi}x_\lambda, \tilde{\xi}y_\mu\right)\right),$$

which is a contraction. Therefore, the fixed point is unique.

Definition 2.2 Let $(\tilde{X}, \tilde{d}, E)$ be a soft metric space. A mapping $(f, \varphi) : \tilde{X} \rightarrow \tilde{X}$ is said to be generalized F-Suzuki contraction for random operator if there exists $\tau > 0$ and $F \in \mathcal{F}$ such that for all $\tilde{\xi} \tilde{x}_\lambda, y \tilde{\xi}_\mu \in SP(X)$ with $(f, \varphi)(\tilde{\xi}x_\lambda) \neq (f, \varphi)(\tilde{\xi}y_\mu)$

$$\frac{1}{2}\left[\tilde{d}\left((f, \varphi)(\tilde{\xi}x_\lambda), (f, \varphi)(\tilde{\xi}y_\mu)\right)\right] < \tilde{d}\left(\tilde{\xi}x_\lambda, \tilde{\xi}y_\mu\right)$$

$$\Rightarrow \tau + F\left(\tilde{d}\left((f, \varphi)(\tilde{\xi}x_\lambda), (f, \varphi)(\tilde{\xi}y_\mu)\right)\right) \leq F\left(\tilde{d}\left(\tilde{\xi}x_\lambda, \tilde{\xi}y_\mu\right)\right).$$

Theorem 2.3 Let $(\tilde{X}, \tilde{d}, E)$ be a complete soft metric space and let (f, φ) be generalized F-Suzuki contraction of a \tilde{X} into itself. ξ is a measurable selector and (Ω, Σ) denotes a measurable space consisting of a set Ω and sigma algebra Σ of subset of Ω . Then (f, φ) has a unique random soft fixed point in \tilde{X} .

Proof Let $\tilde{\xi}x_\lambda^0$ be any soft point in $SP(X)$

$$\text{Set } \tilde{\xi} \tilde{x}_{\lambda_1}^1 = (f, \varphi)\left(\tilde{\xi} \tilde{x}_\lambda^0\right) = \left(f\left(\tilde{\xi}x_\lambda^0\right)\right)_{\varphi(\lambda)}$$

$$\tilde{\xi} \tilde{x}_{\lambda_2}^2 = (f, \varphi)\left(\tilde{\xi} \tilde{x}_{\lambda_1}^1\right) = \left(f^2\left(\tilde{\xi} \tilde{x}_\lambda^0\right)\right)_{\varphi^2(\lambda)}$$

$$\tilde{\xi} \tilde{x}_{\lambda_{n+1}}^{n+1} = (f, \varphi)\left(\tilde{\xi} \tilde{x}_{\lambda_n}^n\right) = \left(f^{n+1}\left(x \tilde{\xi}_\lambda^0\right)\right)_{\varphi^{n+1}(\lambda)} \dots$$

If there exists $n \in \mathbb{N}$ such that $\tilde{d}\left(\tilde{\xi}x_{\lambda_n}^n, (f, \varphi)\left(\tilde{\xi} \tilde{x}_{\lambda_n}^n\right)\right) = 0$, the proof is complete.

So we assume that $0 < \tilde{d}\left(\tilde{\xi} \tilde{x}_{\lambda_n}^n, (f, \varphi)\left(\tilde{\xi}x_{\lambda_n}^n\right)\right), \forall n \in \mathbb{N}$.

Therefore

$$\begin{aligned}
 & \frac{1}{2} \left[\tilde{d} \left(\tilde{\xi} \tilde{x}_{\lambda_n}^n, (f, \varphi) \left(\tilde{\xi} \tilde{x}_{\lambda_n}^n \right) \right) \right] < \tilde{d} \left(\tilde{\xi} \tilde{x}_{\lambda_n}^n, (f, \varphi) \left(\tilde{\xi} \tilde{x}_{\lambda_n}^n \right) \right) \\
 \Rightarrow & \tau + F \left(\tilde{d} \left((f, \varphi) \left(\tilde{\xi} \tilde{x}_{\lambda_n}^n \right), (f, \varphi)^2 \left(\tilde{\xi} \tilde{x}_{\lambda_n}^n \right) \right) \right) \leq F \left(\tilde{d} \left(\tilde{\xi} \tilde{x}_{\lambda_n}^n, (f, \varphi) \left(\tilde{\xi} \tilde{x}_{\lambda_n}^n \right) \right) \right) \\
 \Rightarrow & F \left(\tilde{d} \left(\tilde{\xi} \tilde{x}_{\lambda_{n+1}}^{n+1}, (f, \varphi) \left(\tilde{\xi} \tilde{x}_{\lambda_{n+1}}^{n+1} \right) \right) \right) \leq F \left(\tilde{d} \left(\tilde{\xi} \tilde{x}_{\lambda_n}^n, (f, \varphi) \left(\tilde{\xi} \tilde{x}_{\lambda_n}^n \right) \right) \right) - \tau.
 \end{aligned}$$

Repeating this process, we get

$$\begin{aligned}
 F \left(\tilde{d} \left(\tilde{\xi} \tilde{x}_{\lambda_n}^n, (f, \varphi) \left(\tilde{\xi} \tilde{x}_{\lambda_n}^n \right) \right) \right) & \leq F \left(\tilde{d} \left(\tilde{\xi} \tilde{x}_{\lambda_{n-1}}^{n-1}, (f, \varphi) \left(\tilde{\xi} \tilde{x}_{\lambda_{n-1}}^{n-1} \right) \right) \right) - \tau \\
 & \leq F \left(\tilde{d} \left(\tilde{\xi} \tilde{x}_{\lambda_{n-1}}^{n-1}, (f, \varphi) \left(\tilde{\xi} \tilde{x}_{\lambda_{n-1}}^{n-1} \right) \right) \right) - 2\tau \\
 & \leq F \left(\tilde{d} \left(\tilde{\xi} \tilde{x}_{\lambda_{n-1}}^{n-1}, (f, \varphi) \left(\tilde{\xi} \tilde{x}_{\lambda_{n-1}}^{n-1} \right) \right) \right) - 3\tau \\
 & \quad \text{-----} \\
 & \quad \text{-----} \\
 & \leq F \left(\tilde{d} \left(\tilde{\xi} \tilde{x}_{\lambda_0}^0, (f, \varphi) \left(\tilde{\xi} \tilde{x}_{\lambda_0}^0 \right) \right) \right) - n\tau.
 \end{aligned} \tag{10}$$

From (10), we obtain $\lim_{n \rightarrow \infty} F \left(\tilde{d} \left(\tilde{\xi} \tilde{x}_{\lambda_n}^n, (f, \varphi) \left(\tilde{\xi} \tilde{x}_{\lambda_n}^n \right) \right) \right) = -\infty$, which together with (F2') and Lemma 1.2 gives

$$\lim_{n \rightarrow \infty} \tilde{d} \left(\tilde{\xi} \tilde{x}_{\lambda_n}^n, (f, \varphi) \left(\tilde{\xi} \tilde{x}_{\lambda_n}^n \right) \right) = 0. \tag{11}$$

Now, we claim that $\left\{ \tilde{\xi} \tilde{x}_{\lambda_n}^n \right\}$ is a Cauchy sequence. Suppose, on the contrary, that there exists $\epsilon_0 > 0$ and sequence $\{\lambda_m(k)\}$ and $\{\lambda_n(k)\}$ of natural numbers such that

$$\begin{aligned}
 \lambda_{m(k)} > \lambda_{n(k)} > k, \tilde{d} \left(\tilde{\xi} \tilde{x}_{\lambda_{m(k)}}^{m(k)}, \tilde{\xi} \tilde{x}_{\lambda_{n(k)}}^{n(k)} \right) & \geq \epsilon_0, \\
 \tilde{d} \left(\tilde{\xi} \tilde{x}_{\lambda_{m(k)-1}}^{m(k)-1}, \tilde{\xi} \tilde{x}_{\lambda_{n(k)}}^{n(k)} \right) & < \epsilon_0 \forall k \in \mathbb{N}.
 \end{aligned} \tag{12}$$

Applying the triangle inequality, we have

$$\begin{aligned}
 \epsilon_0 & \leq \tilde{d} \left(\tilde{\xi} \tilde{x}_{\lambda_{m(k)}}^{m(k)}, \tilde{\xi} \tilde{x}_{\lambda_{n(k)}}^{n(k)} \right) \leq \tilde{d} \left(\tilde{\xi} \tilde{x}_{\lambda_{m(k)}}^{m(k)}, \tilde{\xi} \tilde{x}_{\lambda_{m(k)-1}}^{m(k)-1} \right) + \tilde{d} \left(\tilde{\xi} \tilde{x}_{\lambda_{m(k)-1}}^{m(k)-1}, \tilde{\xi} \tilde{x}_{\lambda_{n(k)}}^{n(k)} \right) \\
 & \leq \tilde{d} \left(\tilde{\xi} \tilde{x}_{\lambda_{m(k)}}^{m(k)}, \tilde{\xi} \tilde{x}_{\lambda_{m(k)-1}}^{m(k)-1} \right) + \epsilon_0
 \end{aligned}$$

$$\leq \tilde{d}\left(\tilde{\xi} \tilde{x}_{\lambda_m(k)-1}^{m(k)-1}, (f, \varphi)\left(\tilde{\xi} \tilde{x}_{\lambda_m(k)-1}^{m(k)-1}\right)\right) + \epsilon_0.$$

From (11) and the above inequality that

$$\lim_{n \rightarrow \infty} \tilde{d}\left(\tilde{\xi} \tilde{x}_{\lambda_m(k)}^{m(k)}, \tilde{\xi} \tilde{x}_{\lambda_n(k)}^{n(k)}\right) = \epsilon_0. \quad (13)$$

From (11) and (12), we can choose a positive integer such that

$$\frac{1}{2} \left[\tilde{d}\left(\tilde{\xi} \tilde{x}_{\lambda_m(k)}^{m(k)}, (f, \varphi)\left(\tilde{\xi} \tilde{x}_{\lambda_m(k)}^{m(k)}\right)\right) \right] < \frac{\epsilon_0}{2} < \tilde{d}\left(\tilde{\xi} \tilde{x}_{\lambda_m(k)}^{m(k)}, \tilde{\xi} \tilde{x}_{\lambda_n(k)}^{n(k)}\right).$$

So, from the assumption of the theorem, we get

$$\begin{aligned} \tau + F\left(\tilde{d}\left((f, \varphi)\left(\tilde{\xi} \tilde{x}_{\lambda_m(k)}^{m(k)}\right), (f, \varphi)\left(\tilde{\xi} \tilde{x}_{\lambda_n(k)}^{n(k)}\right)\right)\right) &\leq F\left(\tilde{d}\left(\tilde{\xi} \tilde{x}_{\lambda_m(k)}^{m(k)}, \tilde{\xi} \tilde{x}_{\lambda_n(k)}^{n(k)}\right)\right) \\ \tau + F\left(\tilde{d}\left(\tilde{\xi} \tilde{x}_{\lambda_m(k)+1}^{m(k)+1}, (f, \varphi)\left(\tilde{\xi} \tilde{x}_{\lambda_n(k)+1}^{n(k)+1}\right)\right)\right) &\leq F\left(\tilde{d}\left(\tilde{\xi} \tilde{x}_{\lambda_m(k)}^{m(k)}, \tilde{\xi} \tilde{x}_{\lambda_n(k)}^{n(k)}\right)\right). \end{aligned} \quad (14)$$

From (F3'), (11), and (13), we get $\tau + F(\epsilon_0) \leq F(\epsilon_0)$. This contradiction shows that $\left\{\tilde{\xi} \tilde{x}_{\lambda_n}^n\right\}$ is a Cauchy sequence. By completeness of $(\tilde{X}, \tilde{d}, E)$, $\left\{\tilde{\xi} \tilde{x}_{\lambda_n}^n\right\}$ converges to some point $\tilde{\xi} \tilde{x}_\lambda^* \in \tilde{X}$.

Therefore,

$$\lim_{n \rightarrow \infty} \tilde{d}\left(\tilde{\xi} \tilde{x}_{\lambda_n}^n, \tilde{\xi} \tilde{x}_\lambda^*\right) = 0. \quad (15)$$

Now, we claim that

$$\begin{aligned} \frac{1}{2} \left[\tilde{d}\left(\tilde{\xi} \tilde{x}_{\lambda_n}^n, (f, \varphi)\left(\tilde{\xi} \tilde{x}_{\lambda_n}^n\right)\right) \right] &< \tilde{d}\left(\tilde{\xi} \tilde{x}_{\lambda_n}^n, \tilde{\xi} \tilde{x}_\lambda^*\right) \\ \frac{1}{2} \left[\tilde{d}\left((f, \varphi)\left(\tilde{\xi} \tilde{x}_{\lambda_n}^n\right), (f, \varphi)^2\left(\tilde{\xi} \tilde{x}_{\lambda_n}^n\right)\right) \right] &< \tilde{d}\left((f, \varphi)\left(\tilde{\xi} \tilde{x}_{\lambda_n}^n\right), \tilde{\xi} \tilde{x}_\lambda^*\right) \forall n \in \mathbb{N}. \end{aligned} \quad (16)$$

Again, assume that there exists $m \in \mathbb{N}$ such that

$$\begin{aligned} \frac{1}{2} \left[\tilde{d}\left(\tilde{\xi} \tilde{x}_{\lambda_m}^m, (f, \varphi)\left(\tilde{\xi} \tilde{x}_{\lambda_m}^m\right)\right) \right] &\geq \tilde{d}\left(\tilde{\xi} \tilde{x}_{\lambda_m}^m, \tilde{\xi} \tilde{x}_\lambda^*\right) \\ \text{or } \frac{1}{2} \left[\tilde{d}\left((f, \varphi)\left(\tilde{\xi} \tilde{x}_{\lambda_m}^m\right), (f, \varphi)^2\left(\tilde{\xi} \tilde{x}_{\lambda_m}^m\right)\right) \right] &\geq \tilde{d}\left((f, \varphi)\left(\tilde{\xi} \tilde{x}_{\lambda_m}^m\right), \tilde{\xi} \tilde{x}_\lambda^*\right). \end{aligned} \quad (17)$$

Therefore,

$$\begin{aligned}
2\tilde{d}\left(\tilde{\xi}x_{\lambda_m}^m, \tilde{\xi}x_{\lambda}^*\right) &\leq \tilde{d}\left(\tilde{\xi}x_{\lambda_m}^m, (f, \varphi)\left(\tilde{\xi}x_{\lambda_m}^m\right)\right) \leq \tilde{d}\left(\tilde{\xi}x_{\lambda_m}^m, \tilde{\xi}x_{\lambda}^*\right) + \tilde{d}\left(\tilde{\xi}x_{\lambda}^*, (f, \varphi)\left(\tilde{\xi}x_{\lambda_m}^m\right)\right) \\
&\tilde{d}\left(\tilde{\xi}x_{\lambda_m}^m, \tilde{\xi}x_{\lambda}^*\right) \leq \tilde{d}\left(\tilde{\xi}x_{\lambda}^*, (f, \varphi)\left(\tilde{\xi}x_{\lambda_m}^m\right)\right).
\end{aligned} \tag{18}$$

It follow from (15) and (16) that

$$\begin{aligned}
\tilde{d}\left(\tilde{\xi}x_{\lambda_m}^m, \tilde{\xi}x_{\lambda}^*\right) &\leq \tilde{d}\left(\tilde{\xi}x_{\lambda}^*, (f, \varphi)\left(\tilde{\xi}x_{\lambda_m}^m\right)\right) \leq \\
&\frac{1}{2}\left[\tilde{d}\left((f, \varphi)\left(\tilde{\xi}x_{\lambda_m}^m\right), (f, \varphi)^2\left(\tilde{\xi}x_{\lambda_m}^m\right)\right)\right].
\end{aligned} \tag{19}$$

Since $\frac{1}{2}\left[\tilde{d}\left(\tilde{\xi}x_{\lambda_m}^m, (f, \varphi)\left(\tilde{\xi}x_{\lambda_m}^m\right)\right)\right] < \tilde{d}\left(\tilde{\xi}x_{\lambda_m}^m, (f, \varphi)\left(\tilde{\xi}x_{\lambda_m}^m\right)\right)$ by the assumption of the theorem, we get

$$\tau + F\left(\tilde{d}\left((f, \varphi)\left(\tilde{\xi}x_{\lambda_m}^m\right), (f, \varphi)^2\left(x\tilde{\xi}_{\lambda_m}^m\right)\right)\right) \leq F\left(\tilde{d}\left(\tilde{\xi}x_{\lambda_m}^m, (f, \varphi)\left(\tilde{\xi}x_{\lambda_m}^m\right)\right)\right)$$

Since $\tau > 0$, this implies that

$$F\left(\tilde{d}\left((f, \varphi)\left(\tilde{\xi}x_{\lambda_m}^m\right), (f, \varphi)^2\left(\tilde{\xi}x_{\lambda_m}^m\right)\right)\right) < F\left(\tilde{d}\left(\tilde{\xi}x_{\lambda_m}^m, (f, \varphi)\left(\tilde{\xi}x_{\lambda_m}^m\right)\right)\right).$$

So, from (F1), we get

$$\tilde{d}\left((f, \varphi)\left(\tilde{\xi}x_{\lambda_m}^m\right), (f, \varphi)^2\left(\tilde{\xi}x_{\lambda_m}^m\right)\right) < \tilde{d}\left(\tilde{\xi}x_{\lambda_m}^m, (f, \varphi)\left(\tilde{\xi}x_{\lambda_m}^m\right)\right). \tag{20}$$

It follows from (17), (18), and (20) that

$$\begin{aligned}
&\tilde{d}\left((f, \varphi)\left(\tilde{\xi}x_{\lambda_m}^m\right), (f, \varphi)^2\left(\tilde{\xi}x_{\lambda_m}^m\right)\right) < \tilde{d}\left(\tilde{\xi}x_{\lambda_m}^m, (f, \varphi)\left(\tilde{\xi}x_{\lambda_m}^m\right)\right) \\
&< \tilde{d}\left(\tilde{\xi}x_{\lambda_m}^m, \tilde{\xi}x_{\lambda}^*\right) + \tilde{d}\left(\tilde{\xi}x_{\lambda}^*, (f, \varphi)\left(\tilde{\xi}x_{\lambda_m}^m\right)\right) \\
&\leq \frac{1}{2}\left[\tilde{d}\left((f, \varphi)\left(\tilde{\xi}x_{\lambda_m}^m\right), (f, \varphi)^2\left(\tilde{\xi}x_{\lambda_m}^m\right)\right)\right] + \frac{1}{2}\left[\tilde{d}\left((f, \varphi)\left(\tilde{\xi}x_{\lambda_m}^m\right), (f, \varphi)^2\left(\tilde{\xi}x_{\lambda_m}^m\right)\right)\right] \\
&\leq \tilde{d}\left((f, \varphi)\left(\tilde{\xi}x_{\lambda_m}^m\right), (f, \varphi)^2\left(\tilde{\xi}x_{\lambda_m}^m\right)\right).
\end{aligned}$$

This is a contraction. Hence, (16) holds. So, from (16), for every $n \in \mathbb{N}$,

$$\begin{aligned} & \tau + F\left(\tilde{d}\left((f, \varphi)\left(\tilde{\xi}x_{\lambda_n}^n\right), (f, \varphi)\left(x \begin{smallmatrix} \tilde{\xi} \\ \tilde{\xi}^* \end{smallmatrix} \right)\right)\right) \leq F\left(\tilde{d}\left(\tilde{\xi}x_{\lambda_n}^n, \tilde{\xi}x_{\lambda}^*\right)\right) \\ \text{or } & \tau + F\left(\tilde{d}\left((f, \varphi)^2\left(\tilde{\xi} \tilde{x}_{\lambda_n}^n\right), (f, \varphi)\left(\tilde{\xi}x_{\lambda}^*\right)\right)\right) \\ & \leq F\left(\tilde{d}\left((f, \varphi)\left(\tilde{\xi}x_{\lambda_n}^n\right), \tilde{\xi} \tilde{x}_{\lambda}^*\right)\right) = F\left(\tilde{d}\left(\tilde{\xi}x_{\lambda_{n+1}}^{n+1}, \tilde{\xi}x_{\lambda}^*\right)\right) \end{aligned}$$

holds. In the first case, from (15), (F2'), and Lemma 1.2, we obtain

$$\lim_{n \rightarrow \infty} F\left(\tilde{d}\left((f, \varphi)\left(\tilde{\xi} \tilde{x}_{\lambda_n}^n\right), (f, \varphi)\left(\tilde{\xi} \tilde{x}_{\lambda}^*\right)\right)\right) = -\infty.$$

It follows from (F2') and Lemma 1.2 that $\lim_{n \rightarrow \infty} \tilde{d}\left((f, \varphi)\left(\tilde{\xi} \tilde{x}_{\lambda_n}^n\right), (f, \varphi)\left(\tilde{\xi} \tilde{x}_{\lambda}^*\right)\right) = 0$. Therefore,

$$\begin{aligned} \tilde{d}\left(\tilde{x}_{\lambda}^*, (f, \varphi)\left(\tilde{\xi}x_{\lambda}^*\right)\right) &= \lim_{n \rightarrow \infty} \tilde{d}\left(\tilde{\xi} \tilde{x}_{\lambda_{n+2}}^{n+2}, (f, \varphi)\left(\tilde{\xi}x_{\lambda}^*\right)\right) \\ &= \lim_{n \rightarrow \infty} \tilde{d}\left((f, \varphi)^2\left(\tilde{\xi}x_{\lambda_n}^n\right), (f, \varphi)\left(\tilde{\xi} \tilde{x}_{\lambda}^*\right)\right) = 0. \end{aligned}$$

In the second case, from (F2'), and Lemma 1.2, we obtain

$$\lim_{n \rightarrow \infty} F\left(\tilde{d}\left((f, \varphi)^2\left(\tilde{\xi}x_{\lambda_n}^n\right), (f, \varphi)\left(\tilde{\xi} \tilde{x}_{\lambda}^*\right)\right)\right) = -\infty.$$

It follows from (F2') and Lemma 1.2 that $\lim_{n \rightarrow \infty} \tilde{d}\left((f, \varphi)\left(\tilde{\xi}x_{\lambda_n}^n\right), (f, \varphi)\left(\tilde{\xi} \tilde{x}_{\lambda}^*\right)\right) = 0$. Therefore,

$$\begin{aligned} \tilde{d}\left(\tilde{\xi}x_{\lambda}^*, (f, \varphi)\left(\tilde{\xi} \tilde{x}_{\lambda}^*\right)\right) &= \lim_{n \rightarrow \infty} \tilde{d}\left(\tilde{\xi} \tilde{x}_{\lambda_{n+2}}^{n+2}, (f, \varphi)\left(\tilde{\xi} \tilde{x}_{\lambda}^*\right)\right) \\ &= \lim_{n \rightarrow \infty} \tilde{d}\left((f, \varphi)^2\left(\tilde{\xi}x_{\lambda_n}^n\right), (f, \varphi)\left(\tilde{\xi} \tilde{x}_{\lambda}^*\right)\right) = 0. \end{aligned}$$

Hence, $\tilde{\xi} \tilde{x}_{\lambda}^*$ is a random soft fixed point of (f, φ) .

Uniqueness: Let $\tilde{\xi} \tilde{y}_{\mu}^*$ is another fixed point of (f, φ) in \tilde{X} such that

$$(f, \varphi)\left(\widetilde{\xi}x_{\lambda}^*\right) = \widetilde{x}_{\lambda}^* \neq \widetilde{\xi}y_{\mu} = (f, \varphi)\left(\widetilde{\xi}y_{\mu}\right), \text{ then } \widetilde{d}\left(\widetilde{\xi}x_{\lambda}^*, \widetilde{\xi}y_{\mu}\right) > 0.$$

So, we have $0 = \frac{1}{2}\widetilde{d}\left(\widetilde{\xi}x_{\lambda}^*, (f, \varphi)\widetilde{\xi}x_{\lambda}^*\right) < \widetilde{d}\left(\widetilde{\xi}x_{\lambda}^*, \widetilde{\xi}y_{\mu}\right)$ and from the assumption of the theorem, we obtain

$$\begin{aligned} F\left(\widetilde{d}\left(\widetilde{\xi}x_{\lambda}^*, \widetilde{\xi}y_{\mu}\right)\right) &= F\left(\widetilde{d}\left((f, \varphi)\widetilde{\xi}x_{\lambda}^*, (f, \varphi)\widetilde{\xi}y_{\mu}\right)\right) < \tau + F\left(\widetilde{d}\left((f, \varphi)\widetilde{\xi}x_{\lambda}^*, (f, \varphi)\widetilde{\xi}y_{\mu}\right)\right) \\ &\leq F\left(\widetilde{d}\left(\widetilde{\xi}x_{\lambda}, \widetilde{\xi}y_{\mu}\right)\right), \end{aligned}$$

which is a contraction. Therefore, the random soft fixed point is unique.

References

1. Molodtsov D (1999) Soft set-theory-first results. *Comput Math Appl* 37:19–31
2. Maji PK, Roy AR, Biswas R (2002) An application of soft sets in a decision-making problem. *Comput Math Appl* 44:1077–1083
3. Maji PK, Biswas R, Roy AR (2003) Soft set theory. *Comput Math Appl* 45:555–562
4. Das S, Samanta SK (2013) On soft metric spaces. *J Fuzzy Math* 21(3):707–734
5. Das S, Samanta SK (2013) Soft metric. *Ann Fuzzy Math Inform* 6(1):77–94
6. Das S, Samanta SK (2013) Soft linear operators in soft normed linear spaces. *Ann Fuzzy Math Inform* 6(2):295–314
7. Wadkar BR, Bhardwaj R, Mishra VN, Singh BK (2017) Coupled Soft Fixed Point Theorems in Soft Metric and Soft b- Metric Space. *Sci Publ State Univ Novi Pazar Ser Appl Math Inform Mech* 9(1):59–73
8. Gupta S, Bhardwaj R, Rao WBR, Sharraf RM (2020) Fixed point theorems in fuzzy metric spaces. *Mater Today Proc* 29(P2):611–616
9. Rao WB, Bhardwaj R, Sharraf RM (2020) Couple fixed point theorems in soft metric spaces. *Mater Today Proc* 29(P2):617–624
10. Choudhary BS, Ray M (1999) Convergence of an iteration leading to a solution of a random operator equation. *J Appl Math Stochastic Anal* 12:161–168
11. Choudhary BS, Upadhyay A (1999) An iteration leading to random solutions and fixed points of operators. *Soochow J Math* 25:395–400
12. Choudhary BS (2002) A common unique fixed point theorem for two random operators in Hilbert spaces. *IJMMS* 32:177–182
13. Dhagat VB, Sharma A, Bhardwaj RK (2008) Fixed point theorem for random operators in Hilbert spaces. *Int J Math Anal* 2:557–561
14. Wardowski D (2012) Fixed point theory of a new type of contraction mapping in complete metric spaces. *Fixed Point Theory Appl* 94
15. Chen C, Wen L, Dong J, Gu Y (2016) Fixed point theorems for generalized F-contractions in b-metric-like spaces. *J Nonlinear Sci Appl* 9:2161–2174
16. Chen D (2005) The parameterization reduction of soft sets and its applications. *Comput Math Appl* 49:757–763
17. Piri H, Kumam P (2014) Some fixed point theorems concerning F-contraction in complete metric spaces. *Fixed Point Theory Appl* 1–11
18. Banach S (1922) Surlesoperation dans les ensembles abstraits et leur application aux equationsintegrals. *Fund Math* 3:133–181

19. Suzuki T (2009) A new type of fixed point theorem in metric spaces. *Nonlinear Anal* 71:5313–5317
20. Suzuki T (2001) Generalized distance and existence theorems in complete metric spaces. *J Math Anal* 253:440–458

Fixed Point Results in b-Metric Spaces Over Banach Algebra and Contraction Principle



Abid Khan, Santosh Kumar Sharma, Girraj Kumar Verma, Ramakant Bhardwaj, and Qazi Aftab Kabir

Abstract The main purpose of this paper is to present some fixed point results concerning the generalized contraction principle mappings in b-metric spaces over Banach algebras. We also give an example to support our main theorem. To obtain the results, basic concept of fixed point, that is, Banach's contraction principle is mainly used and extension is obtained for various types of expressions. Obtained results are useful in image processing as well as in materials research for phase transition study and initial value and boundary value problems.

Keywords Fixed point (FP) · Contraction mapping · B-metric space (BMS) · Banach algebra

1 Introduction

Bakhtin [1] introduced BMS in 1989. This is based on Banach's contraction principle. Many authors extended the concept detail can be seen in [2–5, 6–21]. The concept of BMS coincides with the concept of metric space. In the present paper, the generalization of contraction principle mappings is done in BMS over Banach algebras.

A. Khan · S. K. Sharma · G. K. Verma
Department of Mathematics, Amity University, Gwalior, Madhya Pradesh, India
e-mail: sksharma1@gwa.amity.edu

G. K. Verma
e-mail: gkverma@gwa.amity.edu

R. Bhardwaj (✉)
Department of Mathematics, Amity University Kolkata (W.B.), Kolkata, India

Q. A. Kabir (✉)
Department of Mathematics, Govt. Gandhi Memorial Science College, Jammu, India

© The Author(s), under exclusive license to Springer Nature Singapore Pte Ltd. 2022
M. K. Singh and R. K. Gautam (eds.), *Recent Trends in Design, Materials and Manufacturing*, Lecture Notes in Mechanical Engineering,
https://doi.org/10.1007/978-981-16-4083-4_2

2 Definitions Preliminaries

Definition 2.1 ([12]) $X \neq \emptyset$ with metric d and $s \geq 1 \in \mathbb{R}$.

A function $d : X \times X \rightarrow [0, \infty)$ is a b-metric if, for all $x, y, z \in X$, the following conditions are satisfied:

- (b1) $d(x, y) = 0$ if and only if $x = y$,
- (b2) $d(x, y) = d(y, x)$,
- (b3) $d(x, z) \leq s[d(x, y) + d(y, z)]$

(X, d) is called a BMS.

Note Every metric is a BMS with $s = 1$.

Definition 2.2 ([11]) If $\langle x_n \rangle$ is a seq in a BMS X

- a. $\langle x_n \rangle$ is known as b-conv iff $\exists x \in X: d(x_n, x) \rightarrow 0$ as $n \rightarrow \infty$.
- b. $\langle x_n \rangle$ is a b-Cauchy seq iff $d(x_n, x_m) \rightarrow 0$ as $n, m \rightarrow \infty$.
- c. A BMS X is called complete iff \forall b-Cauchy seq in this space is b-conv.

Lemma 2.3 ([12]) Let (X, d) be a b-metric space with $s \geq 1$.

- i. If a sequence $\{x_n\} \subset X$ is a b-convergent sequence, then it admits a unique limit.
- ii. Every b-convergent sequence in X is b-Cauchy.

Definition 2.4 ([11]) Suppose X is a b-metric space with d , $Y \subset X$ is known as closed if f iff $\forall \langle x_n \rangle \in Y$ in which b-converges to an element x .

$$x \in Y$$

3 Main Results

Definition 3.1 ([14]) If $X \neq \emptyset$ and $\theta : X \times X \rightarrow [1, \infty)$. A function $d_\theta : X \times X \rightarrow [0, \infty)$ is called an extended b-metric if for all $x, y, z \in X$ it satisfies the following:

- $d_\theta 1$ $d_\theta(x, y) = 0$ iff $x = y$;
- $d_\theta 2$ $d_\theta(x, y) = d_\theta(y, x)$;
- $d_\theta 3$ $d_\theta(x, z) \leq \theta(x, z)[d_\theta(x, y) + d_\theta(y, z)]$.

The pair (X, d_θ) is called an extended b-metric.

Remark 3.2 If $\theta(x, y) = s$ for $s \geq 1$ then we obtain the definition of a b-metric space.

Definition 3.3 ([14]) Let (X, d_θ) be an extended b-metric space.

- i. A sequence $\{x_n\}$ in X is called to converge $x \in X$, if for every $\epsilon > 0, \exists N = N(\epsilon) \in \mathbb{N}$ such that $d_\theta(x_n, x) < \epsilon, \forall n \geq N$. In this case, we write $\lim_{n \rightarrow \infty} x_n = x$.
- ii. A sequence $\{x_n\}$ in X is said to be Cauchy, if for every $\epsilon > 0$ there exists $N = N(\epsilon) \in \mathbb{N}$ such that $d_\theta(x_m, x_n) < \epsilon, \forall m, n \geq N$.

Definition 3.4 ([14]) An extended BMS (X, d_θ) is complete if every Cauchy sequence in X is convergent.

Theorem 3.5 Let (X, d_θ) be a complete extended *bms – ba* such that d_θ is a continuous functional with parameter $s \geq 1$ and let the mappings $T : X^2 \rightarrow X$ satisfying the contractive condition:

$$d_\theta(Tx, Ty) \leq k[d_\theta(x, Tx) + d_\theta(y, Ty) + d_\theta(x, y)] \forall x, y \in X, \tag{1}$$

where $k \in [0, 1)$ such that for each $x \in X$. T will contain unique FP X :

$$d_\theta(x, x) = 0.$$

Proof Let $x \in X$ From (1) we have

$$d_\theta(T^n x, T^{n+1} x) \leq k d_\theta(T^{n-1} x, T^n x) \leq \dots \leq k^n d_\theta(x, Tx). \tag{2}$$

Repeating this process, we obtain

$$d_\theta(T^n x, T^{n+1} x) \leq k^n d_\theta(x, Tx). \tag{3}$$

Here the proof is divided into two cases.

Case 1

Let $T^n x = T^m x$ for some $m, n \in \mathbb{N}, n \neq m$. if $m > n$ then $T^{m-n}(T^n x) = T^n x$, that is, $T^n x = y$, where $p = m - n$, then

$$T^p y = y. \tag{4}$$

By (1) and (2), we have

$$d_\theta(y, Ty) = d_\theta(T^p y, T^{p+1} y) \leq k^p d_\theta(y, Ty) \tag{5}$$

$k \in (0, 1) \Rightarrow d_\theta(y, Ty) = 0$, so $y = Ty$, that is, y is a FP of T .

Case 2

Suppose $T^n x \neq T^m x, \forall m, n \in \mathbb{N}, n \neq m$. We rewrite (2) as

$$\begin{aligned}
 d_\theta(T^n x, T^{n+1} x) &\leq s[k^n d_\theta(x, Tx)] \\
 &\leq s[k^n d_\theta(x, Tx) + k^{n+1} d_\theta(x, Tx) + k^{n+2} d_\theta(x, Tx)] \\
 &\leq s \sum_m^{\infty} s^m k^{n+m} (d_\theta(x, Tx)) \\
 &\leq s \sum_m^{\infty} s^m k^m (d_\theta(x, Tx))
 \end{aligned}$$

Since

$$d_\theta(T^n x, T^{n+m} x) \leq s \sum_m^{\infty} s^m k^m (d_\theta(x, Tx)). \quad (6)$$

Similarly, by (1), we have

$$d_\theta(T^n x, T^{n+2} x) \leq k d_\theta(T^{n-1} x, T^{n+1} x) \leq k^n d_\theta(x, T^2 x) \leq s \sum_m^{\infty} s^m k^{n+m} (d_\theta(x, Tx)). \quad (7)$$

For $m > 3$ and $m = 3p + 1, p \geq 1$ and using the fact that $g^q x \neq g^r x, \forall q, r \in \mathbb{N}, q \neq r$, we have

$$\begin{aligned}
 d_\theta(T^n x, T^{n+m} x) &\leq d_\theta(T^n x, T^{n+1} x) \\
 &\quad + s[d_\theta(T^{n+1} x, T^{n+2} x) + \dots + d_\theta(T^{n+2p} x, T^{n+2p+1} x)] \\
 &\leq s[k^n d_\theta(x, Tx) + k^{n+1} d_\theta(x, Tx) + \dots + k^{n+2p} d_\theta(x, Tx)] \\
 &\leq s \sum_m^{\infty} s^m k^{n+m} (d_\theta(x, Tx)) \\
 &\leq s \sum_m^{\infty} s^m k^m (d_\theta(x, Tx)).
 \end{aligned}$$

Thus, for $m > n$ above inequality implies

$$d_\theta(T^n x, T^{n+m} x) \leq s \sum_m^{\infty} s^m k^m (d_\theta(x, Tx)).$$

Similarly, for $m > 4$ and $m = 3b + 2, b \geq 1, g^q x \neq g^r x, \forall q, r \in \mathbb{N}, q \neq r$, By triangular property, we have

$$\begin{aligned}
& d_\theta(T^n x, T^{n+3b+2} x) \\
& \leq s \left[d_\theta(T^{n+3b+2} x, T^{n+3b+1} x) + d_\theta(T^{n+3b+1} x, T^{n+3b} x) + d_\theta(T^{n+3b} x, T^{n+3b-1} x) + d_\theta(T^{n+3b-1} x, T^n x) \right] \\
& \leq s \left[d_\theta(T^n x, T^{n+1} x) + d_\theta(T^{n+1} x, T^{n+2} x) + \dots + d_\theta(T^{n+3b-1} x, T^{n+3b} x) + d_\theta(T^{n+3b} x, T^{n+3b-1} x) \right] \\
& \leq s \left[k^n d_\theta(x, Tx) + k^{n+1} d_\theta(x, Tx) + \dots + k^{n+3b-1} d_\theta(x, Tx) + k^{n+3b} d_\theta(x, Tx) \right] \\
& \leq s \sum_m^{\infty} s^m k^{n+m} (d_\theta(x, Tx)) \\
& \leq s \sum_m^{\infty} s^m k^m (d_\theta(x, Tx)).
\end{aligned}$$

Finally

$$d_\theta(T^n x, T^{n+m} x) \leq s \sum_m^{\infty} s^m k^m (d_\theta(x, Tx)). \quad (8)$$

We deduce from all cases that

$$d_\theta(T^n x, T^{n+m} x) \leq s[k^n d_\theta(x, T^2 x) + \frac{k^n}{1-k} d_\theta(x, Tx)] \forall n, m \geq 0. \quad (9)$$

Therefore, we have

$$\lim_{n \rightarrow \infty} s d_\theta(T^n x, x) = \lim_{n \rightarrow \infty} s d_\theta(T^n x, T^m x) = d_\theta(x, x).$$

Since, $\lim_{n \rightarrow \infty} \frac{k^n}{1-k} s \|d_\theta(x, Tx)\| = 0$.

We have $\lim_{n \rightarrow \infty} \|d_\theta(T^n x, T^{n+m} x)\| = 0, \forall n, m \in \mathbb{N}$,

which implies $\{T^n x\}$ is a CS in X .

By completeness of X , there exists $u \in X$ such that

$$\lim_{n \rightarrow \infty} T^n x = u.$$

Now we will show that u is a FP of T , i.e., $Tu = u$. without loss of generality, assume that $T^k \neq u$ for any $k \in \mathbb{N}$. Therefore, the triangular inequality implies that

$$\begin{aligned}
d_\theta(u, Tu) & \leq s \left[d_\theta(u, T^n x) + d_\theta(T^n x, T^{n+1} x) + d_\theta(T^{n+1} x, Tu) \right] \\
& \leq d_\theta(u, T^n x) + s \left[d_\theta(T^n x, T^{n+1} x) + k \left[d_\theta(Tu, u) + d_\theta(T^n x, u) \right] \right] \\
& \Rightarrow d_\theta(u, Tu) \\
& \leq \frac{1}{1-k} s \left[d_\theta(u, T^n x) + d_\theta(T^n x, T^{n+1} x) + k d_\theta(T^n x, u) \right]. \quad (10)
\end{aligned}$$

Taking limit as $n \rightarrow \infty$, and using (4) and (10), we have $\|d_\theta(u, Tu)\| = 0$.

Hence, $Tu = u$, i.e., u is a FP of T .

To show the individuality of u . If u^* is alternative FP of T , that is, $Tu^* = u^*$. Therefore,

$$\begin{aligned} d_\theta(u, u^*) &= d_\theta(Tu, Tu^*) \leq k[d_\theta(u, Tu^*) + d_\theta(Tu, u^*) + d_\theta(u, u^*)] \\ &= 0, \end{aligned}$$

which implies that

$$\|d_\theta(u, Tu)\| = 0,$$

that is, $u = u^*$.

Example 3.2 Let $\mathcal{A} = \{a = (a_{ij})_{4 \times 4} : a_{ij} \in \mathbb{R}, 1 \leq i, j \leq 4\}$ and $\|a\| = \frac{1}{4} \sum_{1 \leq i, j \leq 4} |a_{ij}|$. Take $P = \{a \in \mathcal{A} : a_{ij} \geq 0, 1 \leq i, j \leq 4\}$ in \mathcal{A} . Let $X = \{1, 2, 3, 4\}$.

Define a mapping $d_{bms} : X^2 \times X \rightarrow \mathcal{A}$ by $d(1, 1) = d(2, 2) = d(3, 3) = d(4, 4) = \theta$

$$d_{bms}(x, y) = \begin{cases} (2, 1) \begin{pmatrix} 1, 1, 4, 1 \\ 4, 2, 3, 1 \\ 1, 4, 3, 1 \\ 1, 2, 3, 4 \end{pmatrix} & \text{if } x, y \in X; \\ (3, 1) \begin{pmatrix} 4, 1, 4, 1 \\ 4, 3, 5, 2 \\ 2, 3, 1, 4 \\ 3, 4, 2, 1 \end{pmatrix} & \text{if } x, y \in X; \\ (4, 1) \begin{pmatrix} 4, 1, 1, 1 \\ 2, 3, 4, 2 \\ 3, 2, 1, 1 \\ 4, 3, 2, 1 \end{pmatrix} & \text{if } x, y \in X; \\ (4, 3) \begin{pmatrix} 16, 9, 12, 7 \\ 20, 8, 6, 2 \\ 9, 8, 4, 4 \\ 16, 12, 9, 4 \end{pmatrix} & \text{if } x, y \in X; \end{cases}$$

then (X, d_{bms}) is a $bMS - BA$ over \mathcal{A} with coefficient $p = \begin{pmatrix} 4, 0, 0, 0 \\ 0, 4, 0, 0 \\ 0, 0, 4, 0 \\ 0, 0, 0, 4 \end{pmatrix}$.

References

1. Bakhtin IA (1989) The contraction mapping principle in almost metric spaces. *Func Anal* 30:26–37
2. Aamri M, Moutawakil El (2002) Some new common fixed point theorems under strict contractive conditions. *J Math Anal Appl* 270:181–188
3. Akkouchi M (2011) Common fixed point theorems for two self-mappings of a b-metric space under an implicit relation. *Hacet J Math Stat* 40:805–810
4. Aydi H, Bota MF, Karapinar E, Moradi S (2012) A common fixed point for weak θ -contractions on b-metric spaces. *Fixed Point Theory* 13:337–346
5. Aydi H, Felhi A, Sahmim S (2017) Common fixed points via implicit contractions on b-metric like spaces. *J. Nonlinear Sci Appl* 10:1524–1537
6. Beg I, Abbas M (2011) Coincidence and common fixed points of non-compatible maps. *J. Appl. Math. Inform.* 29:743–752
7. Bhardwaj R, SanathKumar HG (2020) B-metric space: an application of fixed point. *Mater Today Proc* 29(2):659–663
8. Boriceanu M (2009) Strict fixed point theorems for multi-valued operators in b-metric spaces. *Int J Mod Math* 4:285–301
9. Czerwik S (1993) Contraction mappings in b-metric spaces. *Acta Math Inform Univ Ostraviensis* 1:5–11
10. Demma M, Vetro P (2015) Picard sequence and fixed point results on b-metric spaces. *J Funct Spaces* 6–12
11. Faraji H, Savić D, Radenović S (2019) Fixed point theorems for Geraghty contraction type mappings in b-metric spaces and applications. *Axioms* 8:34–40
12. Huang S, Xu (2013) Fixed point theorems of contractive mappings in cone b-metric spaces and applications. *Fixed Point Theory Appl* 10–20
13. Jungck G (1986) Compatible mappings and common fixed points. *Int J Math Math Sci* 9:771–779
14. Kamran T, Samreen M, UL Ain Q (2017) A generalization of b-metric space and some fixed point theorems. *Math MDPI* 5(19)
15. Karapinar E, Czerwik S, Aydi H (2018) Meir-Keeler contraction mappings in generalized b-metric spaces. *J Funct Spaces* 3
16. Mudgal S (2014) Fixed points theorems for weakly compatible maps along with property (E.A.). *Int J Comput Appl* 96(24):241–247
17. Nazir T, Abbas M (2014) Common fixed points of two pairs of mappings satisfying (E.A)-property in partial metric spaces. *J Inequal Appl* 12–24
18. Ozturk V, Radenovi S (2016) Some remarks on b-(E.A)-property in b-metric spaces. *Springer Plus* 5:544
19. Ozturk V, Turkoglu D (2015) Common fixed point theorems for mappings satisfying (E.A)-property in b-metric spaces. *J Nonlinear Sci Appl* 8:1127–1133
20. Raghunath WB, Bhardwaj R, Mishra VN, Singh BK (2017) Coupled soft fixed-point theorems in soft metric and soft b-metric space. *Scientific Publ State Univ Novi Pozar Ser A: Appl Math Inform Mech* 9(1):59–73
21. Mlaiki N, Kucik K, Filipovic M, Aydi H (2019) On almost b-metric spaces and related fixed point results. *Axioms* 8(70):1–12
22. Roshan JR, Parvaneh V, Altun I (2014) Some coincidence point results in ordered b-metric spaces and applications in a system of integral equations. *Appl Math Comput* 226:725–737

Common Invariant Point Theorem for Multi-valued Generalized Fuzzy Mapping in b-Metric Space



Umashankar Singh, Naval Singh, Ruchi Singh, and Ramakant Bhardwaj 

Abstract An effort is being made in this research paper to establish α -fuzzy invariant point and common α -fuzzy invariant point for multi-valued fuzzy mapping in complete b-metric space. Some results have been drawn to attain α -fuzzy invariant point and common α -fuzzy invariant point with new coherent contractive conditions. In this paper, we have extended and generalized the results of Shahzad et al. (Math 38:419–427, [12]) and proved the existence and uniqueness of invariant point results for multi-valued fuzzy mapping in b-metric space. The contractive conditions used in this article can be extended to derive other contractive conditions such as Hardy–Roger contraction or some new extended rational contractive conditions. The conclusion so drawn can be implemented in various fields of engineering especially mechanical engineering, electronics, and computer engineering. The result of this research paper satisfies all the well-known contractive conditions and spaces so defined. Further some examples were also been quoted in support of the theorems of this research paper.

Keywords Multi-valued mapping · b-Metric space · Invariant point · Common invariant point

U. Singh

Sagar Institute of Research and Technology Excellence, Bhopal, Madhya Pradesh, India

N. Singh

Govt. Dr. Shyama Prasad Mukherjee Science and Commerce College, Bhopal, Madhya Pradesh, India

R. Singh

Institute for Excellence in Higher Education, Bhopal, Madhya Pradesh, India

R. Bhardwaj (✉)

Department of Mathematics, Amity University, Kolkata, West Bengal, India

© The Author(s), under exclusive license to Springer Nature Singapore Pte Ltd. 2022

23

M. K. Singh and R. K. Gautam (eds.), *Recent Trends in Design, Materials and Manufacturing*, Lecture Notes in Mechanical Engineering,

https://doi.org/10.1007/978-981-16-4083-4_3

1 Introduction

Invariant point theory has a pivotal role in development of various fields with its applications on computer science, physical science, medical science, applied science, and different areas. In the present scenario with the concept of invariant theory are fuzzy locking system, fuzzy machine has been develop. In 1922, Banach gave invariant point theorem for contractive mapping in complete metric space. In 1969, Zadeh evidenced the concept of fuzzy set and then many authors obtain invariant point results for fuzzy mapping. In 1981, Heilpern contributes some invariant point results for contraction mapping. After that, the idea of b-metric space was [5, 6] defined and proved invariant point theorem with b-metric space and generalized usual metric space. After his contribution, many researchers proved many invariant point theorems for fuzzy contraction mapping using b-metric space. In 2009, Boriceanu; in 2016, Joseph; and in 2017, Jinakul and Shahzad proved invariant point and common invariant point results for multi-valued mapping in b-metric space. In this paper, we are establishing α -fuzzy invariant point and common α -fuzzy invariant point theorems for multi-valued fuzzy mapping in complete b-metric space and extending and generalizing the result of Shahzad et al. [12] with new rational inequality and we are given for support of them some examples which were quoted. For detail one can read references [2–4, 9, 10, 13].

2 Preliminaries

Definition 2.1 (Nadler [11]) Let X and Y be nonempty sets. T is said to be multi-valued mapping from X to Y if T is a function for X to the power set Y . We denote a multi-valued map by $T: X \rightarrow 2^Y$.

Definition 2.2 (Nadler [11]) A fixed point $x_0 \in X$ is said to be invariant point of the multi-valued mapping T if $x_0 \in Tx_0$.

Example (Heilpern [7]) Every single-valued mapping can be multi-valued mapping. Let $f: X \rightarrow Y$ be single-valued mapping define $T: X \rightarrow 2^Y$ by $Tx = \{f(x)\}$. Note that T is a multi-valued mapping iff for each $x \in X, Tx \subseteq Y$. Unless otherwise stated we always assume Tx is nonempty for each $x, y \in X$.

Definition 2.3 (Jinakul et al. [8]) Let (X, d) be a metric space. A map $T: X \rightarrow Y$ is called contraction if there exist $0 \leq \rho < 1$ such that

$$d(Tx, Ty) \leq \rho d(x, y) \text{ for } x, y \in X.$$

Definition 2.4 (Nadler [11]) Let (X, d) be a metric space. A map $T: X \rightarrow CB(X)$ is called multi-valued contraction if there exist $0 \leq \rho < 1$ such that

$$H(Tx, Ty) \leq \rho d(x, y) \text{ for } x, y \in X.$$

Definition 2.5 (Czerwik [5]) Let X be any nonempty set and $b \geq 1$ be any real number. A function $d: X \times X \rightarrow R^+$ is called b -metric if it satisfies the following conditions for all $x, y \in X$:

1. $d(x, y) = 0$ if and only if $x = y$.
2. $d(x, y) = d(y, x)$.
3. $d(x, z) \leq b[d(x, y) + d(y, z)]$.

Then the pair (X, d) is called b -metric space.

Definition 2.6 (Ayadi et al. [12]) Let (X, d) be a b -metric space. Then the sequence $\{x_n\}$ in X is called Cauchy sequence if and only if for all $\epsilon > 0$ there exists $n(\epsilon) \in N$ such that for each $m, n \geq n(\epsilon)$ we have $d(x_n, x_m) < \epsilon$.

Definition 2.7 (Czerwik [5]) Let (X, d) be a metric space. We define the Hausdorff metric space $CB(X)$ induced by d .

Then

$$H(A, B) = \max\{\sup_{x \in A} d(x, B), \sup_{y \in B} d(A, y)\}.$$

For all $A, B \in CB(X)$, where $CB(X)$ denotes the family of closed and bounded subset of X and

$$d(x, B) = \inf\{d(x, a) : a \in B\}, \text{ for all } x \in X.$$

A fuzzy set X is a function with domain X and values in $[0, 1]$, $F(X)$ is the collection of all fuzzy sets in X . If A is a fuzzy set and $x \in X$, then the function value $A(x)$ is called grade of membership of x in X . The α —level set of a fuzzy set A is denoted by $[A]_\alpha$ and defined as

$$[A]_\alpha = \{x: A(x) \geq \alpha\}, \text{ where } \alpha \in (0, 1]$$

$$[A]_0 = \{x: A(x) > 0\},$$

Let X be any nonempty set and Y be a metric space. A mapping T is called a fuzzy mapping, if T is a mapping from X into $F(X)$. A fuzzy mapping T is a fuzzy subset on $X \times Y$ with membership function $T(x)(y)$. The function $T(x)(y)$ is the grade of membership of y in $T(x)$. For convenience, we denote the α —level set of $T(x)$ by $[Tx]_\alpha$ instead of $[T(x)]_\alpha$ [1].

Definition 2.8 (Nadler [11]) A point $x \in X$ is called α -fuzzy fixed point of a fuzzy mapping $T: X \rightarrow F(X)$ if there exist $\alpha \in (0, 1]$ such that $x \in [Tx]_\alpha$.

Lemma 2.9 (Nadler [11]) Let A and B be a nonempty closed and bounded subsets of a metric space (X, d) , if $\alpha \in A$ then

$$d(a, B) \leq H(A, B).$$

Lemma 2.10 (Nadler [11]) Let A and B be a nonempty closed and bounded subsets of a metric space (X, d) , and $0 < \alpha \in R$ then

for $a \in A$, there exist $b \in B$ such that $d(a, b) \leq H(A, B) + \epsilon$.

Theorem 2.11 (Shahzad et al. [12]) Let (X, d) be a complete b-metric with constant $b \geq 1$ and $T: X \rightarrow F(X)$ be a fuzzy mapping and for $x \in X, \alpha(x) \in (0, 1]$ if satisfying the following conditions:

$$\begin{aligned} H([Tx]_{\alpha(x)}, [Ty]_{\alpha(y)}) &\leq a_1 d(x, [Tx]_{\alpha(x)}) + a_2 d(y, [Ty]_{\alpha(y)}) \\ &+ a_3 d(x, [Ty]_{\alpha(y)}) + a_4 d(y, [Tx]_{\alpha(x)}) + a_5 d(x, y) \\ &+ a_6 \left[\frac{d(x, [Tx]_{\alpha(x)}) + (1 + d(x, [Tx]_{\alpha(x)}))}{1 + d(x, y)} \right]. \end{aligned}$$

For all $x, y \in X$ and $a_i \geq 0, i = 1, 2, 3$. with $(ba_1 + a_2 + b(b+1)a_3 + b(a_5 + a_6)) < 1$

and

$$\sum_{i=1}^6 a_i < 1 \quad (1)$$

then T has a fixed point.

Now we present our main theorems with new coherent contractive conditions.

3 Main Theorem

Theorem 3.1 Let (X, d) be a complete b-metric with constant $s \geq 1$ and $U: X \rightarrow CB(X)$ be a multi-valued generalized fuzzy mapping and $x \in X, \alpha(x) \in (0, 1]$ if satisfying the following conditions:

$$\begin{aligned} H([Ux]_{\alpha(x)}, [Uy]_{\alpha(y)}) &\leq \alpha_1 d(x, y) + \alpha_2 d(x, [Uy]_{\alpha(y)}) + \alpha_3 d(y, [Ux]_{\alpha(x)}) \\ &+ \alpha_4 \min\{d(x, [Ux]_{\alpha(x)}), d(y, [Uy]_{\alpha(y)})\} \\ &+ \alpha_5 \left[\frac{d(y, [Ux]_{\alpha(x)}) + d(y, [Uy]_{\alpha(y)})}{1 + d(y, [Ux]_{\alpha(x)}) \cdot d(y, [Uy]_{\alpha(y)})} \right] \\ &+ \alpha_6 d(x, [Ux]_{\alpha(x)}) \left[\frac{1 + d(x, [Ux]_{\alpha(x)}) + d(y, [Ux]_{\alpha(x)})}{1 + d(x, y)} \right]. \end{aligned}$$

For all

$$x, y \in X \text{ and } \alpha_i \geq 0, i = 1, 2, 3. \text{ with } (\alpha_1 + 2s\alpha_2 + \alpha_3 + \alpha_5 + \alpha_6) < 1 \quad (2)$$

and $\sum_{i=1}^6 \alpha_i < 1$,

then U have a α -fuzzy invariant point.

Proof Let x_0 be a random point of X and let $x_1 \in [Ux_0]_{\alpha(x_0)}$ then by Lemma 2.10, we may choose $x_2 \in [Ux_1]_{\alpha(x_1)}$

$$\text{such that } d(x_1, x_2) \leq H([Ux_0]_{\alpha(x_0)}, [Ux_1]_{\alpha(x_1)}) + (\alpha_1 + s\alpha_2 + \alpha_6).$$

Now,

$$\begin{aligned} d(x_1, x_2) &\leq H([Ux_0]_{\alpha(x_0)}, [Ux_1]_{\alpha(x_1)}) + (\alpha_1 + s\alpha_2 + \alpha_6) \\ &\leq \alpha_1 d(x_0, x_1) + \alpha_2 d(x_0, [Ux_1]_{\alpha(x_1)}) + \alpha_3 d(x_1, [Ux_1]_{\alpha(x_1)}) \\ &\quad + \alpha_4 \min\{d(x_0, [Ux_0]_{\alpha(x_0)}), d(x_1, [Ux_0]_{\alpha(x_0)})\} \\ &\quad + \alpha_5 \left[\frac{d(x_1, [Ux_0]_{\alpha(x_0)}) + d(x_1, [Ux_1]_{\alpha(x_1)})}{1 + d(x_1, [Ux_0]_{\alpha(x_0)}) \cdot d(x_1, [Ux_1]_{\alpha(x_1)})} \right] \\ &\quad + \alpha_6 d(x_0, [Ux]_{\alpha(x_0)}) \left[\frac{1 + d(x_0, [Ux_0]_{\alpha(x_0)}) + d(x_1, [Ux_0]_{\alpha(x_0)})}{1 + d(x_0, x_1)} \right] \\ &\leq (\alpha_1 + s\alpha_2 + \alpha_6) \cdot \leq \alpha_1 d(x_0, x_1) + \alpha_2 d(x_0, x_2) + \alpha_3 d(x_1, x_2) \\ &\quad + \alpha_4 \min\{d(x_0, x_1), d(x_1, x_1)\} + \alpha_5 \left[\frac{d(x_1, x_1) + d(x_1, x_2)}{1 + d(x_1, x_1) \cdot d(x_1, x_2)} \right] \\ &\quad + \alpha_6 d(x_0, x_1) \left[\frac{1 + d(x_0, x_1) + d(x_1, x_1)}{1 + d(x_0, x_1)} \right] + (\alpha_1 + s\alpha_2 + \alpha_6) \\ &\leq \alpha_1 d(x_0, x_1) + \alpha_2 d(x_0, x_2) + \alpha_3 d(x_1, x_2) \\ &\quad + \alpha_5 d(x_1, x_2) + \alpha_6 d(x_0, x_1) + (\alpha_1 + s\alpha_2 + \alpha_6) \\ &\leq \alpha_1 d(x_0, x_1) + \alpha_2 s[d(x_0, x_1) + d(x_1, x_2)] \\ &\quad + \alpha_3 d(x_1, x_2) + \alpha_5 d(x_1, x_2) + \alpha_6 d(x_0, x_1) + (\alpha_1 + s\alpha_2 + \alpha_6) \\ &\quad [1 - s\alpha_2 + \alpha_3 + \alpha_5] d(x_1, x_2) \leq (\alpha_1 + s\alpha_2 + \alpha_6) d(x_0, x_1) \\ &\quad + (\alpha_1 + s\alpha_2 + \alpha_6) \\ d(x_1, x_2) &\leq \frac{(\alpha_1 + s\alpha_2 + \alpha_6)}{[1 - (s\alpha_2 + \alpha_3 + \alpha_5)]} d(x_0, x_1) + \frac{(\alpha_1 + s\alpha_2 + \alpha_6)}{[1 - (s\alpha_2 + \alpha_3 + \alpha_5)]}. \end{aligned}$$

Similarly there exist

$$\begin{aligned} x_3 \in [Px_2]_{\alpha(x_2)} \text{ such that } d(x_2, x_3) &\leq H([Ux_1]_{\alpha(x_1)}, [Ux_2]_{\alpha(x_2)}) \\ &\quad + \frac{(\alpha_1 + s\alpha_2 + \alpha_6)^2}{[1 - (s\alpha_2 + \alpha_3 + \alpha_5)]}. \end{aligned}$$

Now,

$$\begin{aligned}
 d(x_2, x_3) &\leq H([Ux_1]_{\alpha(x_1)}, [Ux_2]_{\alpha(x_2)}) + \frac{(\alpha_1 + s\alpha_2 + \alpha_6)^2}{[(1 - (s\alpha_2 + \alpha_3 + \alpha_5))]} \\
 &\leq \alpha_1 d(x_1, x_2) + \alpha_2 d(x_1, [Ux_2]_{\alpha(x_2)}) + \alpha_3 d(x_2, [Ux_2]_{\alpha(x_2)}) \\
 &\quad + \alpha_4 \min\{d(x_1, [Ux_1]_{\alpha(x_1)}), d(x_2, [Ux_1]_{\alpha(x_1)})\} \\
 &\quad + \alpha_5 \left[\frac{d(x_2, [Ux_1]_{\alpha(x_1)}) + d(x_2, [Ux_2]_{\alpha(x_2)})}{1 + d(x_2, [Ux_1]_{\alpha(x_1)}) \cdot d(x_2, [Ux_2]_{\alpha(x_2)})} \right] \\
 &\quad + \alpha_6 d(x_1, [Ux_1]_{\alpha(x_1)}) \left[\frac{1 + d(x_1, [Ux_1]_{\alpha(x_1)}) + d(x_2, [Ux_1]_{\alpha(x_1)})}{1 + d(x_1, x_2)} \right] \\
 &\quad + \frac{(\alpha_1 + s\alpha_2 + \alpha_6)^2}{[(1 - (s\alpha_2 + \alpha_3 + \alpha_5))]} \\
 &\leq \alpha_1 d(x_1, x_2) + \alpha_2 d(x_1, x_3) + \alpha_3 d(x_2, x_3) \\
 &\quad + \alpha_4 \min\{d(x_1, x_2), d(x_2, x_2)\} + \alpha_5 \left[\frac{d(x_2, x_2) + d(x_2, x_3)}{1 + d(x_2, x_2) \cdot d(x_2, x_3)} \right] \\
 &\quad + \alpha_6 d(x_1, x_2) \left[\frac{1 + d(x_1, x_2) + d(x_2, x_2)}{1 + d(x_1, x_2)} \right] + \frac{(\alpha_1 + s\alpha_2 + \alpha_6)^2}{[(1 - (s\alpha_2 + \alpha_3 + \alpha_5))]} \\
 &\leq \alpha_1 d(x_1, x_2) + \alpha_2 s[d(x_1, x_2) + d(x_2, x_3)] + \alpha_3 d(x_2, x_3) + \alpha_5 d(x_2, x_3) \\
 &\quad + \alpha_6 d(x_1, x_2) + \frac{(\alpha_1 + s\alpha_2 + \alpha_6)^2}{[(1 - (s\alpha_2 + \alpha_3 + \alpha_5))]} \\
 &\quad [1 - s\alpha_2 + \alpha_3 + \alpha_5] d(x_2, x_3) \leq (\alpha_1 + s\alpha_2 + \alpha_6) d(x_1, x_2) \\
 &\quad + \frac{(\alpha_1 + s\alpha_2 + \alpha_6)^2}{[(1 - (s\alpha_2 + \alpha_3 + \alpha_5))]} d(x_2, x_3) \leq \frac{(\alpha_1 + s\alpha_2 + \alpha_6)}{[(1 - (s\alpha_2 + \alpha_3 + \alpha_5))]} d(x_1, x_2) \\
 &\quad + \frac{(\alpha_1 + s\alpha_2 + \alpha_6)^2}{[(1 - (s\alpha_2 + \alpha_3 + \alpha_5))^2]} d(x_2, x_3) \\
 &\leq \left\{ \frac{(\alpha_1 + s\alpha_2 + \alpha_6)}{[(1 - (s\alpha_2 + \alpha_3 + \alpha_5))]} \right\}^2 d(x_0, x_1) \\
 &\quad + 2 \left\{ \frac{(\alpha_1 + s\alpha_2 + \alpha_6)}{[(1 - (s\alpha_2 + \alpha_3 + \alpha_5))]} \right\}^2
 \end{aligned}$$

$d(x_2, x_3) \leq k^2 d(x_0, x_1) + 2k^2$, where $k = \frac{(\alpha_1 + s\alpha_2 + \alpha_6)}{[(1 - (s\alpha_2 + \alpha_3 + \alpha_5))]}$.
Continuing this process, we inherit a sequence $\{x_n\}$ such that

$$d(x_2, x_3) \leq k^2 d(x_0, x_1) + 2k^2,$$

then

$$d(x_n, x_{n+1}) \leq k^n d(x_0, x_1) + nk^n.$$

Let $u, v > 0$ with $v > u$

$$\begin{aligned}
 d(x_u, x_v) &\leq s[d(x_u, x_{u+1}) + d(x_{u+1}, x_v)] \\
 d(x_u, x_v) &\leq sd(x_u, x_{u+1}) + s^2[d(x_{u+1}, x_{u+2}) + d(x_{u+2}, x_v)] \\
 d(x_u, x_v) &\leq s[k^u d(x_0, x_1) + uk^u] + s^2[k^{u+1}d(x_0, x_1) + (u + 1)k^{u+1}] \\
 &\quad + \dots + s^{v-u}[k^{v-1}d(x_0, x_1) + (v - 1)k^{v-1}] \\
 d(x_u, x_v) &\leq sk^u(1 + sk + \dots + s^{v-u}k^{v-u})d(x_0, x_1) + \sum_{i=u}^{v-1} s^{i-u}ik^i \\
 d(x_u, x_v) &\leq \frac{sk^u}{1 - sk}d(x_0, x_1) + \sum_{i=u}^{v-1} s^{i-u}ik^i.
 \end{aligned}$$

Since $sk < 1$ by Cauchy root test. $\sum_{i=u}^{v-1} s^{i-u}ik^i$ is convergent. Hence $\{x_n\}$ is Cauchy sequence in X . Since (X, d) is a complete b-metric space then their exist $z \in X$ such that $\lim_{n \rightarrow \infty} d(x_n, z) = 0$.

Now we prove z is a common α -fuzzy invariant point of U . We have

$$\begin{aligned}
 d(z, [Uz]_{\alpha(z)}) &\leq s[d(z, x_{n+1}) + d(x_{n+1}, [Uz]_{\alpha(z)})] \\
 d(z, [Uz]_{\alpha(z)}) &\leq sd((z, x_{n+1}) + sH([Ux_n]_{\alpha(x_n)}, [Uz]_{\alpha(z)})) \\
 d(z, [Uz]_{\alpha(z)}) &\leq sd(z, x_{n+1}) + s\{\alpha_1 d(x_n, z) + \alpha_2 d(x_n, [Uz]_{\alpha(z)}) + \alpha_3 d(z, [Uz]_{\alpha(z)}) \\
 &\quad + \alpha_4 \min\{d(x_n, [Ux_n]_{\alpha(x_n)}), d(z, [Ux_n]_{\alpha(x_n)})\} \\
 &\quad + \alpha_5 \left[\frac{d(z, [Ux_n]_{\alpha(x_n)}) + d(z, [Uz]_{\alpha(z)})}{1 + d(z, [Uz]_{\alpha(z)}) \cdot d(z, [Ux_n]_{\alpha(x_n)})} \right] \\
 &\quad + \alpha_6 d(x_n, [Ux_n]_{\alpha(x_n)}) \left[\frac{1 + d(x_n, [Ux_n]_{\alpha(x_n)}) + d(z, [Ux_n]_{\alpha(x_n)})}{(1 + d(x_n, z))} \right] \}.
 \end{aligned}$$

Taking $n \rightarrow \infty$ then we get

$$\begin{aligned}
 d(z, [Uz]_{\alpha(z)}) &\leq sd(z, z) \\
 &\quad + s\{\alpha_1 d(z, z) + \alpha_2 d(z, [Uz]_{\alpha(z)}) + \alpha_3 d(z, [Uz]_{\alpha(z)}) + \alpha_4 \min\{d(z, z), d(z, z)\} \\
 &\quad + \alpha_5 \left[\frac{d(z, z) + d(z, [Uz]_{\alpha(z)})}{1 + d(z, [Uz]_{\alpha(z)}) \cdot d(z, z)} \right] + \alpha_6 d(z, z) \left[\frac{1 + d(z, z) + d(z, z)}{1 + d(z, z)} \right] \} \\
 d(z, [Uz]_{\alpha(z)}) &\leq s[\alpha_2 d(z, [Uz]_{\alpha(z)}) + \alpha_3 d(z, [Uz]_{\alpha(z)}) + \alpha_5 d(z, [Uz]_{\alpha(z)})] \\
 d(z, [Uz]_{\alpha(z)}) &\leq s(\alpha_2 + \alpha_3 + \alpha_5)d(z, [Uz]_{\alpha(z)}) \\
 [1 - s(\alpha_2 + \alpha_3 + \alpha_5)]d(z, [Uz]_{\alpha(z)}) &\leq 0,
 \end{aligned}$$

which is incongruity then we have $d(z, [Uz]_{\alpha(z)}) = 0$, thus $z = [Uz]_{\alpha(z)}$.

Hence z is an α -fuzzy invariant point of U .

Theorem 3.2 Let (X, d) be a complete b-metric with constant $s \geq 1$ and $U, P: X \rightarrow CB(X)$ be a two multi-valued generalized fuzzy mapping and $x \in X, \alpha_U(x), \alpha_P(y) \in (0, 1]$ if satisfying the following conditions:

$$\begin{aligned} \mathbf{H}([Ux]_{\alpha_U(x)}, [Py]_{\alpha_P(y)}) &\leq \alpha_1 d(x, y) + \alpha_2 d(x, [Py]_{\alpha_P(y)}) + \alpha_3 d(y, [Py]_{\alpha_P(y)}) \\ &\quad + \alpha_4 \min\{d(x, [Ux]_{\alpha_U(x)}), d(y, [Ux]_{\alpha_U(x)})\} \\ &\quad + \alpha_5 \left[\frac{d(y, [Ux]_{\alpha_U(x)}) + d(y, [Py]_{\alpha_P(y)})}{1 + d(y, [Ux]_{\alpha_U(x)}) \cdot d(y, [Py]_{\alpha_P(y)})} \right] \\ &\quad + \alpha_6 d(x, [Ux]_{\alpha_U(x)}) \left[\frac{1 + d(x, [Ux]_{\alpha_U(x)}) + d(y, [Ux]_{\alpha_U(x)})}{1 + d(x, y)} \right]. \end{aligned}$$

For all $x, y \in X$ and $\alpha_i \geq 0, i = 1, 2, 3$. with $(\alpha_1 + 2s\alpha_2 + \alpha_3 + \alpha_5 + \alpha_6) < 1$ and

$$\sum_{i=1}^6 \alpha_i < 1, \quad (3)$$

Then U and P have common α -fuzzy invariant point.

Proof Let x_0 be a random point of X and let $x_1 \in [Ux_0]_{\alpha(x_0)}$ then by Lemma 2.10, we may choose $x_2 \in [Px_1]_{\alpha(x_1)}$, such that $d(x_1, x_2) \leq \mathbf{H}([Ux_0]_{\alpha(x_0)}, [Px_1]_{\alpha(x_1)}) + (\alpha_1 + s\alpha_2 + \alpha_6)$.

Now,

$$\begin{aligned} d(x_1, x_2) &\leq \mathbf{H}([Ux_0]_{\alpha(x_0)}, [Px_1]_{\alpha(x_1)}) + (\alpha_1 + s\alpha_2 + \alpha_6) \\ &\leq \alpha_1 d(x_0, x_1) + \alpha_2 d(x_0, [Px_1]_{\alpha(x_1)}) + \alpha_3 d(x_1, [Px_1]_{\alpha(x_1)}) \\ &\quad + \alpha_4 \min\{d(x_0, [Ux_0]_{\alpha(x_0)}), d(x_1, [Ux_0]_{\alpha(x_0)})\} \\ &\quad + \alpha_5 \left[\frac{d(x_1, [Ux_0]_{\alpha(x_0)}) + d(x_1, [Px_1]_{\alpha(x_1)})}{1 + d(x_1, [Ux_0]_{\alpha(x_0)}) \cdot d(x_1, [Px_1]_{\alpha(x_1)})} \right] \\ &\quad + \alpha_6 d(x_0, [Ux_0]_{\alpha(x_0)}) \left[\frac{1 + d(x_0, [Ux_0]_{\alpha(x_0)}) + d(x_1, [Ux_0]_{\alpha(x_0)})}{1 + d(x_0, x_1)} \right] \\ &\quad + (\alpha_1 + s\alpha_2 + \alpha_6). \\ &\leq \alpha_1 d(x_0, x_1) + \alpha_2 d(x_0, x_2) + \alpha_3 d(x_1, x_2) + \alpha_4 \min\{d(x_0, x_1), d(x_1, x_1)\} \\ &\quad + \alpha_5 \left[\frac{d(x_1, x_1) + d(x_1, x_2)}{1 + d(x_1, x_1) \cdot d(x_1, x_2)} \right] \\ &\quad + \alpha_6 d(x_0, x_1) \left[\frac{1 + d(x_0, x_1) + d(x_1, x_1)}{1 + d(x_0, x_1)} \right] \end{aligned}$$

$$\begin{aligned}
& + (\alpha_1 + s\alpha_2 + \alpha_6). \\
& \leq \alpha_1 d(x_0, x_1) + \alpha_2 d(x_0, x_2) + \alpha_3 d(x_1, x_2) + \alpha_5 d(x_1, x_2) + \alpha_6 d(x_0, x_1) \\
& \quad + (\alpha_1 + s\alpha_2 + \alpha_6). \\
& \leq \alpha_1 d(x_0, x_1) + \alpha_2 s[d(x_0, x_1) + d(x_1, x_2)] + \alpha_3 d(x_1, x_2) \\
& \quad + \alpha_5 d(x_1, x_2) + \alpha_6 d(x_0, x_1) + (\alpha_1 + s\alpha_2 + \alpha_6). \\
& [1 - s\alpha_2 + \alpha_3 + \alpha_5]d(x_1, x_2) \leq (\alpha_1 + s\alpha_2 + \alpha_6)d(x_0, x_1) \\
& \quad + (\alpha_1 + s\alpha_2 + \alpha_6) \\
d(x_1, x_2) & \leq \frac{(\alpha_1 + s\alpha_2 + \alpha_6)}{[(1 - (s\alpha_2 + \alpha_3 + \alpha_5))]}d(x_0, x_1) + \frac{(\alpha_1 + s\alpha_2 + \alpha_6)}{[(1 - (s\alpha_2 + \alpha_3 + \alpha_5))]} .
\end{aligned}$$

Similarly there exist

$$\begin{aligned}
x_3 \in [Px_2]_{\alpha(x_2)} \text{ such that } d(x_2, x_3) & \leq H([Ux_1]_{\alpha(x_1)}, [Px_2]_{\alpha(x_2)}) \\
& \quad + \frac{(\alpha_1 + s\alpha_2 + \alpha_6)^2}{[(1 - (s\alpha_2 + \alpha_3 + \alpha_5))]} .
\end{aligned}$$

Now,

$$\begin{aligned}
d(x_2, x_3) & \leq H([Ux_1]_{\alpha(x_1)}, [Px_2]_{\alpha(x_2)}) + \frac{(\alpha_1 + s\alpha_2 + \alpha_6)^2}{[(1 - (s\alpha_2 + \alpha_3 + \alpha_5))]} \\
& \leq \alpha_1 d(x_1, x_2) + \alpha_2 d(x_1, [Px_2]_{\alpha(x_2)}) + \alpha_3 d(x_2, [Px_2]_{\alpha(x_2)}) \\
& \quad + \alpha_4 \min \left\{ d(x_1, [Ux_1]_{\alpha(x_1)}), d(x_2, [Ux_1]_{\alpha(x_1)}) \right\} \\
& \quad + \alpha_5 \left[\frac{d(x_2, [Ux_1]_{\alpha(x_1)}) + d(x_2, [Px_2]_{\alpha(x_2)})}{1 + d(x_2, [Ux_1]_{\alpha(x_1)}) \cdot d(x_2, [Px_2]_{\alpha(x_2)})} \right] \\
& \quad + \alpha_6 d(x_1, [Ux_1]_{\alpha(x_1)}) \left[\frac{1 + d(x_1, [Ux_1]_{\alpha(x_1)}) + d(x_2, [Ux_1]_{\alpha(x_1)})}{1 + d(x_1, x_2)} \right] \\
& \quad + \frac{(\alpha_1 + s\alpha_2 + \alpha_6)^2}{[(1 - (s\alpha_2 + \alpha_3 + \alpha_5))]} \\
& \leq \alpha_1 d(x_1, x_2) + \alpha_2 d(x_1, x_3) + \alpha_3 d(x_2, x_3) \\
& \quad + \alpha_4 \min \{d(x_1, x_2), d(x_2, x_2)\} + \alpha_5 \left[\frac{d(x_2, x_2) + d(x_2, x_3)}{1 + d(x_2, x_2) \cdot d(x_2, x_3)} \right] \\
& \quad + \alpha_6 d(x_1, x_2) \left[\frac{1 + d(x_1, x_2) + d(x_2, x_2)}{1 + d(x_1, x_2)} \right] + \frac{(\alpha_1 + s\alpha_2 + \alpha_6)^2}{[(1 - (s\alpha_2 + \alpha_3 + \alpha_5))]} \\
& \leq \alpha_1 d(x_1, x_2) + \alpha_2 s[d(x_1, x_2) + d(x_2, x_3)] + \alpha_3 d(x_2, x_3) + \alpha_5 d(x_2, x_3) \\
& \quad + \alpha_6 d(x_1, x_2) \\
& \quad + \frac{(\alpha_1 + s\alpha_2 + \alpha_6)^2}{[(1 - (s\alpha_2 + \alpha_3 + \alpha_5))]}
\end{aligned}$$

$$\begin{aligned}
 & [1 - (s\alpha_2 + \alpha_3 + \alpha_5)]d(x_2, x_3) \leq (\alpha_1 + s\alpha_2 + \alpha_6)d(x_1, x_2) \\
 & \quad + \frac{(\alpha_1 + s\alpha_2 + \alpha_6)^2}{[(1 - (s\alpha_2 + \alpha_3 + \alpha_5))]} \\
 d(x_2, x_3) & \leq \frac{(\alpha_1 + s\alpha_2 + \alpha_6)}{[1 - (s\alpha_2 + \alpha_3 + \alpha_5)]}d(x_1, x_2) + \frac{(\alpha_1 + s\alpha_2 + \alpha_6)^2}{[1 - (s\alpha_2 + \alpha_3 + \alpha_5)]^2} \\
 d(x_2, x_3) & \leq \left\{ \frac{(\alpha_1 + s\alpha_2 + \alpha_6)}{[1 - (s\alpha_2 + \alpha_3 + \alpha_5)]} \right\}^2 d(x_0, x_1) + 2 \left\{ \frac{(\alpha_1 + s\alpha_2 + \alpha_6)}{[1 - (s\alpha_2 + \alpha_3 + \alpha_5)]} \right\}^2
 \end{aligned}$$

$d(x_2, x_3) \leq k^2 d(x_0, x_1) + 2k^2$, where $k = \frac{(\alpha_1 + s\alpha_2 + \alpha_6)}{[1 - (s\alpha_2 + \alpha_3 + \alpha_5)]}$.

Continuing this process, we obtain a sequence $\{x_n\}$ such that

$$d(x_2, x_3) \leq k^2 d(x_0, x_1) + 2k^2$$

then

$$d(x_n, x_{n+1}) \leq k^n d(x_0, x_1) + nk^n.$$

Let $u, v > 0$ with $v > u$

$$\begin{aligned}
 d(x_u, x_v) & \leq s[d(x_u, x_{u+1}) + d(x_{u+1}, x_v)] \\
 d(x_u, x_v) & \leq sd(x_u, x_{u+1}) + s^2[d(x_{u+1}, x_{u+2}) + d(x_{u+2}, x_v)] \\
 d(x_u, x_v) & \leq s[k^u d(x_0, x_1) + uk^u] + s^2[k^{u+1} d(x_0, x_1) + (u + 1)k^{u+1}] \\
 & \quad + \dots + s^{v-u}[k^{v-1} d(x_0, x_1) + (v - 1)k^{v-1}] \\
 d(x_u, x_v) & \leq sk^u(1 + sk + \dots + s^{v-u}k^{v-u})d(x_0, x_1) + \sum_{i=u}^{v-1} s^{i-u}ik^i \\
 d(x_u, x_v) & \leq \frac{sk^u}{1 - sk}d(x_0, x_1) + \sum_{i=u}^{v-1} s^{i-u}ik^i.
 \end{aligned}$$

Since $sk < 1$ by Cauchy root test. $\sum_{i=u}^{v-1} s^{i-u}ik^i$ is convergent. Hence $\{x_n\}$ is Cauchy sequence in X . Since (X, d) is a complete b-metric space then their exist $z \in X$ such that $\lim_{n \rightarrow \infty} d(x_n, z) = 0$.

Now we prove z is a Common α -fuzzy invariant point of U . We have

$$\begin{aligned}
 d(z, [Uz]_{\alpha(z)}) & \leq s[d(z, x_{2n+1}) + d(x_{2n+1}, [Uz]_{\alpha(z)})] \\
 d(z, [Uz]_{\alpha(z)}) & \leq sd(z, x_{2n+1}) + sH([Ux_{2n}]_{\alpha(x_{2n})}, [Uz]_{\alpha(z)}) \\
 d(z, [Uz]_{\alpha(z)}) & \leq sd(z, x_{2n+1}) + s\{\alpha_1 d(x_{2n}, z) + \alpha_2 d(x_{2n}, [Uz]_{\alpha(z)}) \\
 & \quad + \alpha_3 d(z, [Uz]_{\alpha(z)}) + \alpha_4 \min\{d(x_{2n}, [Ux_{2n}]_{\alpha(x_{2n})}), d(z, [Ux_{2n}]_{\alpha(x_{2n})})\}\}
 \end{aligned}$$

$$\begin{aligned}
 & + \alpha_5 \left[\frac{d(z, [Ux_{2n}]_{\alpha(x_{2n})}) + d(z, [Uz]_{\alpha(z)})}{1 + d(z, [Ux_{2n}]_{\alpha(x_{2n})}) \cdot d(z, [Uz]_{\alpha(z)})} \right] \\
 & + \alpha_6 d(x_{2n}, [Ux_{2n}]_{\alpha(x_{2n})}) \left[\frac{1 + d(x_{2n}, [Ux_{2n}]_{\alpha(x)}) + d(z, [Ux_{2n}]_{\alpha(x_{2n})})}{1 + d(x_{2n}, z)} \right] \Big\}.
 \end{aligned}$$

Taking $n \rightarrow \infty$, then we get

$$\begin{aligned}
 d(z, [Uz]_{\alpha(z)}) & \leq sd(z, z) \\
 & + s \{ \alpha_1 d(z, z) + \alpha_2 d(z, [Uz]_{\alpha(z)}) + \alpha_3 d(z, [Uz]_{\alpha(z)}) + \alpha_4 \min\{d(z, z), d(z, z)\} \\
 & + \alpha_5 \left[\frac{d(z, z) + d(z, [Uz]_{\alpha(z)})}{1 + d(z, z) \cdot d(z, [Uz]_{\alpha(z)})} \right] + \alpha_6 d(z, z) \left[\frac{1 + d(z, z) + d(z, z)}{1 + d(z, z)} \right] \Big\} \\
 d(z, [Uz]_{\alpha(z)}) & \leq s [\alpha_2 d(z, [Uz]_{\alpha(z)}) + \alpha_3 d(z, [Uz]_{\alpha(z)}) + \alpha_5 d(z, [Uz]_{\alpha(z)})] \\
 d(z, [Uz]_{\alpha(z)}) & \leq s (\alpha_2 + \alpha_3 + \alpha_5) d(z, [Uz]_{\alpha(z)}) \\
 [1 - s(\alpha_2 + \alpha_3 + \alpha_5)] d(z, [Uz]_{\alpha(z)}) & \leq 0,
 \end{aligned}$$

which is an opposition then we have $d(z, [Uz]_{\alpha(z)}) = 0$, thus $z = [Uz]_{\alpha(z)}$

$$\begin{aligned}
 d(z, [Pz]_{\alpha(z)}) & \leq s [d(z, x_{2n+1}) + d(x_{2n+1}, [Pz]_{\alpha(z)})] \\
 d(z, [Pz]_{\alpha(z)}) & \leq sd(z, x_{2n+1}) + sH([Px_{2n}]_{\alpha(x_{2n})}, [Pz]_{\alpha(z)}) \\
 d(z, [Pz]_{\alpha(z)}) & \leq sd(z, x_{2n+1}) + s \{ \alpha_1 d(x_{2n}, z) + \alpha_2 d(x_{2n}, [Pz]_{\alpha(z)}) + \alpha_3 d(z, [Pz]_{\alpha(z)}) \\
 & + \alpha_4 \min[d(x_{2n}, [Px_{2n}]_{\alpha(x_{2n})}), d(z, [Px_{2n}]_{\alpha(x_{2n})})] \\
 & + \alpha_5 \left[\frac{d(z, [Px_{2n}]_{\alpha(x_{2n})}) + d(z, [Pz]_{\alpha(z)})}{1 + d(z, [Px_{2n}]_{\alpha(x_{2n})}) \cdot d(z, [Pz]_{\alpha(z)})} \right] \\
 & + \alpha_6 d(x_{2n}, [Px_{2n}]_{\alpha(x_{2n})}) \left[\frac{1 + d(x_{2n}, [Px_{2n}]_{\alpha(x)}) + d(z, [Px_{2n}]_{\alpha(x_{2n})})}{1 + d(x_{2n}, z)} \right] \Big\}.
 \end{aligned}$$

Taking $n \rightarrow \infty$, then we get

$$\begin{aligned}
 d(z, [Pz]_{\alpha(z)}) & \leq sd(z, z) + s \left\{ \begin{aligned} & \alpha_1 d(z, z) + \alpha_2 d(z, [Pz]_{\alpha(z)}) + \alpha_3 d(z, [Pz]_{\alpha(z)}) \\ & + \alpha_4 \min\{d(z, z), d(z, z)\} + \alpha_5 \left\{ \frac{d(z, z) + d(z, [Pz]_{\alpha(z)})}{1 + d(z, z) \cdot d(z, z)} \right\} \\ & + \alpha_6 d(z, z) \left[\frac{1 + d(z, z) + d(z, z)}{1 + d(z, z)} \right] \end{aligned} \right\} \\
 d(z, [Pz]_{\alpha(z)}) & \leq s \{ \alpha_2 d(z, [Pz]_{\alpha(z)}) + \alpha_3 d(z, [Pz]_{\alpha(z)}) + \alpha_5 d(z, [Pz]_{\alpha(z)}) \} \\
 d(z, [Pz]_{\alpha(z)}) & \leq s (\alpha_2 + \alpha_3 + \alpha_5) d(z, [Pz]_{\alpha(z)}) \\
 [1 - s(\alpha_2 + \alpha_3 + \alpha_5)] d(z, [Pz]_{\alpha(z)}) & \leq 0,
 \end{aligned}$$

which is an inconsistency then we have $d(z, [Pz]_{\alpha(z)}) = 0$, thus $z = [Pz]_{\alpha(z)}$.

Hence z is a common α -fuzzy invariant point of U and P .

Example 3.3 Let $X = [0, 1]$ and $U(x, y) = |x - y| \forall x, y \in X$, and then (X, d) be a complete b -metric space.

Define a fuzzy mapping $U: X \rightarrow F(X)$ by $U(x)(t) = \begin{cases} 1, & 0 \leq t \leq \frac{x}{8} \\ \frac{1}{2}, & \frac{x}{8} < t \leq \frac{x}{4} \\ \frac{1}{4}, & \frac{x}{4} < t \leq \frac{x}{2} \\ 0, & \frac{x}{2} < t \leq 1 \end{cases}$.

For all $x \in X$, there exists $\alpha(x) = 1$, such that $[Ux]_{\alpha(x)} = [0, \frac{x}{8}]$, then

$$\begin{aligned} H\left(\frac{x}{8}, \frac{y}{8}\right) &\leq \frac{1}{2}|x - y| + \frac{1}{4}\left|x - \frac{y}{8}\right| + \frac{1}{8}\left|y - \frac{y}{8}\right| \\ &+ \frac{1}{16}\min\left\{\left|x - \frac{x}{8}\right|, \left|y - \frac{x}{8}\right|\right\} \\ &+ \frac{1}{32}\left[\frac{|x - \frac{x}{8}| + (1 + |x - \frac{x}{8}|)}{1 + \left|y - \frac{x}{8}\right|}\right] + \frac{1}{64}\left[\frac{|x - \frac{x}{8}| + (1 + |x - \frac{x}{8}|)}{1 + |x - y|}\right]. \end{aligned}$$

Therefore, $0 \in X$ is the invariant point of U .

4 Conclusion

By using b -metric space, many authors have invariant point results for self-mapping. In this paper by using b -metric space, we prove the existence and uniqueness of invariant point results for multi-valued fuzzy mapping. Our result extent and generalized the result of Shahzad et al. [12] with new coherent expression.

References

1. Aydi H et al (2012) A Fixed point theorem for set valued quasi-contractions in b -metric spaces. *Fixed Point Theory Appl* 88
2. Azam A (2011) Fuzzy fixed points of fuzzy mapping via a rational inequality. *Hacettepe J Math Stat* 40(3):421–431
3. Banach S (1922) Sur les operations dans les ensembles abstraits et leur application aux equations integrals. *Fundam Math* 3:133–181
4. Boriceanu M (2009) Fixed Point Theory for Multi-valued generalized contraction on a set with two b -metric space. *Stud Univ Babes-Bolyai Math*
5. Czerwik S (1998) Nonlinear set-valued contraction mappings in b -metric spaces. *Atti Semin Math Fis Univ Modena* 46(2):263–276
6. Czerwik S (1993) Contraction mapping in b -metric spaces. *Acta Math Inform Univ Ostraviensis* 1:5–11
7. Heilpern S (1981) Fuzzy Mapping and fixed point theorems. *J Math Anal Appl* 83(2):566–569
8. Jinakul C et al (2017) Common fixed point theorems for multi-valued mapping on b -metric spaces. *Int J Pure Appl Math* (3):1–14

9. Maria Joseph J, Ramaganesh E () Fixed point theorem on multi-valued mapping. *Int J Anal Appl* 1:123–127
10. Maria Joseph J, Roselin D, Marudai M (2016) Fixed point theorem on multi-valued mappings in b-metric spaces. *Springer Plus*, 5:217 *Math*, 113(1):167–179
11. Nadler S.B (1969) Multi-valued contraction mapping. *Pac J Math* 30: 475–488, no 2:123–127
12. Shahzad A et al (2017) Common fixed point theorems for fuzzy mapping in b-metric space. *Italian J Pure App Math* 38:419–427
13. Zadeh LA (1965) Fuzzy sets. *Inf Control* 8:338–353

Mechanical Materials Design and Analysis

An Experimental Analysis for Temperature Dependency of Photovoltaic Cell Parameters Under Artificial Illumination



Abhishek Bhushan and Rakesh Kumar

Abstract Solar energy is gaining tremendous importance to solve the electricity problem of remote areas by converting available solar energy into electrical power using a photovoltaic module (PVM). The present work focused on the effect of PVM temperature on the electrical efficiency (η_{ele}) of the PVM by performing an indoor test. The performance of the PVM depends on many factors such as solar radiation, module temperature, PVM condition, wind velocity, dust, etc. The solar radiation and other factors help in increasing the PVM temperature, and this rise in temperature adversely affects the η_{ele} of the PVM. In this paper, a relation between intensity, temperature, and η_{ele} of the PVM is established. Halogen lamps are installed above PVM and, by adjusting the distance between the PVM and lamp, we control the radiation level for the PVM. The average radiation at the PVM top surface is observed to be 912 W/m^2 . At these radiation values, the experiment is performed for natural cooling and forced cooling in indoor condition. The experimental result shows that with forced air cooling the PVM temperature decreases which result in an increase in η_{ele} by 3.6%.

Keywords Photovoltaic module · Electrical efficiency · Module temperature · Artificial illumination · Halogen lamp

1 Introduction

Energy plays a crucial role in the socio-economic progress of mankind. Presently, mankind is in search of more and more application of renewable energy sources so as the dependency on non-renewable energy can be reduced. The renewable energy sources such as wind energy, solar energy, biomass, geothermal energy, and ocean energy are environmental friendly, economical, and almost unlimited. For the year 2018, the growth rate for solar energy is 28.9%, wind is 12.6%, and other renewable

A. Bhushan · R. Kumar (✉)
Department of Mechanical Engineering, Indian Institute of Technology (ISM),
Dhanbad 826004, India
e-mail: rakesh@iitism.ac.in

© The Author(s), under exclusive license to Springer Nature Singapore Pte Ltd. 2022
M. K. Singh and R. K. Gautam (eds.), *Recent Trends in Design, Materials and Manufacturing*, Lecture Notes in Mechanical Engineering,
https://doi.org/10.1007/978-981-16-4083-4_4

energy sources 7.0% [1]. Thus, we can say that solar energy is the most popular one among all the renewable energy sources because it is available in abundance, free of cost, and environment-friendly. Solar energy is used in two ways: as thermal source and as electricity generation.

For the conversion of solar energy into useful electrical energy, PVM is used. The PVM is an array of photovoltaic cell arranged in an array to generate electricity. The photovoltaic cell is made of semiconductors (Si, GaAs, CdTe, etc.), semiconductors are capable of generating DC electricity when exposed to light source [2]. The low conversion rate from available solar energy to electricity is the main concern for the researchers. Only a maximum of 15–25% total incident energy can be converted to electrical energy [7, 11]. The performance of PVM largely depends on factors such as intensity of solar energy or artificial light, condition of a module, environmental condition (dust, wind, temperature, etc.) and temperature of module [6]. The effect of module temperature on the η_{ele} the PVM is discussed by [3] and it is found that as with rise in temperature the η_{ele} decreases. The maximum output of any PVM is calculated at 25 °C and 1000 W/m² intensity in a controlled environment [4]. In Indian climate for any sunny day, the module temperature easily exceeds the 25 °C mark [16] and thus it affects the output. Many works are done in regards to improve the η_{ele} of the PVM by regulating the PVM temperature [10]. In order to regulate the PVM temperature, scientist designs different methods to extract the heat from the module [5]. This heat extraction is done either by air cooling or by water cooling of the PVM [8]. With the application of different types of fins at the bottom of the module, we can also reduce the module temperature [14]. Halogen lights are installed in order to have a sufficient light source for the performance analysis of PVM [9, 13].

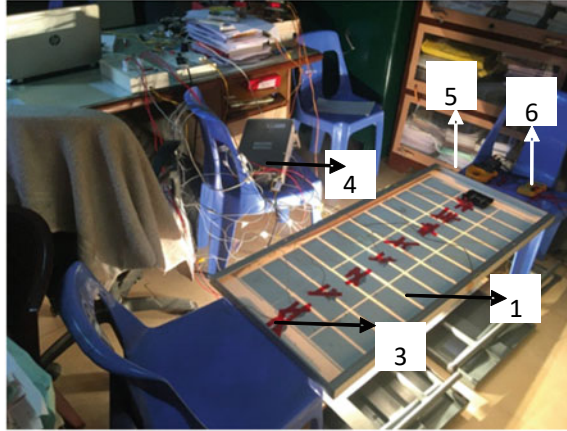
From the literature review, it has been observed that not much work has been done to experimentally study the effect of PVM temperature on performance output under controlled environmental conditions. It has been also seen that work related to the comparative study of the performance of the PVM for forced and natural cooling condition is also very less.

Based on the research gap, the objective of the present study is to experimentally study the effect of air cooling on the η_{ele} of a PVM is performed. And a comparative study of the PVM output for forced and natural cooling has been done and a relation between the module temperature, light intensity, voltage, η_{ele} , and current at equal interval of time has been discussed.

2 Experimental Setup

A very simple experimental setup has been designed with the available resources in the mechanical engineering workshop of IIT (ISM) Dhanbad to conduct indoor test. For the setup design, the instruments and parts needed are as follows:

Fig. 1 Experimental set up for natural cooling



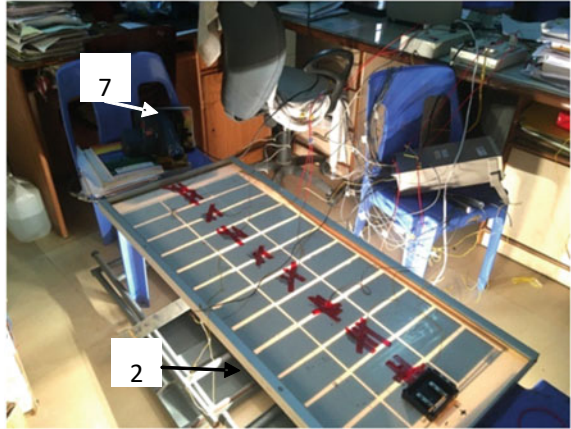
1. 100 W PV module,
2. Four halogen lamp of 500 W each,
3. K-type thermocouple,
4. Data acquisition system (DAS),
5. Multimeter,
6. Solar meter, and
7. Blower.

As shown in the Fig. 1, four halogen lamps were placed below the 100 W polycrystalline silicon PVM. The distance between the lamp and module are adjusted to control the average intensity. K—type thermocouples have been used for temperature measurement because it is accurate and fast [12]. Eight K-type thermocouples are fixed on the back side of PVM and four on the front side of the module. These thermocouples are attached to DAS to record the temperature, an average of the recorded temperature is found and this average value is taken as the back side and front side temperatures. The light intensity at four different places of the PVM is measured and recorded with the help of a solar meter and the average value is taken for the analysis. A multimeter is used to carry out the measurement of the open circuit voltage (V_{oc}) and short circuit current (I_{sc}). The temperature, voltage, and current are measured for intensity value 912 W/m^2 at an equal time interval. The experiment is conducted for both naturally cooling and forced cooling process, 620 W Bosch blowers is used to provide forced cooling.

3 Results and Discussion

The present experiment is conducted for both natural cooling and forced cooling conditions, Fig. 1 shows the actual figure for natural cooling and similarly, Fig. 2 is for forced convection. The PVM is exposed to a constant light source and all the

Fig. 2 Experimental set up for forced cooling



readings are recorded at an equal time interval. After a certain time, the change in PVM temperature is almost constant and we consider that system attains a steady-state condition. The experiments have been repeated for five times for both the conditions and the averaged value for all the parameters are taken. Based on the collected data, following outcome have been observed.

3.1 Front Temperature and Back Temperature

Figure 3 shows the change in front and back sides PVM temperature at an equal time interval. From the figure, it is clear that the front side temperature rises from 23 °C to a maximum of 65 °C for natural cooling. Once the temperature reaches its

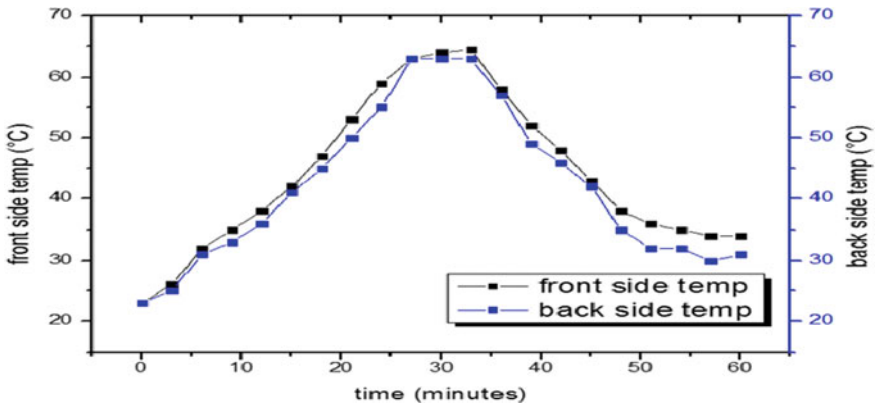
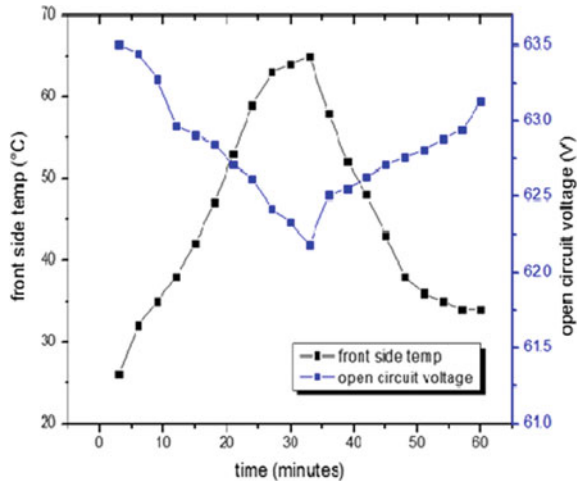


Fig. 3 Front and back side module temperature with time

Fig. 4 Variation of open circuit voltage and front side temperature with time



steady state, the blower has been switched ON and as a result, the temperature starts decreasing and reaches a constant value of 34 °C. Similarly, it has been observed that the initial reading for the back side is 23 °C and it reaches to a maximum of 63 °C, and again decreases to 31 °C when Blower was switched ON.

3.2 Effect on Voc and Isc

Figure 4 shows the change in voltage and temperature with respect to time, from the figure, it is very much clear that as the temperature increases voltage decreases and, once we start forced cooling of the module, then again voltage increases. Similarly, Fig. 5 shows the graph between temperature and current for equal time interval, and from the figure, it is clear that the current doesn't change much with change in temperature the maximum change in the current is of 0.07 A.

3.3 Power and Electrical Efficiency Results

Power output (Pout) of a PVM, having Isc, Voc, and fill factor (FF) is given by Eq. (1) and ηele of the PVM having area (A) and irradiation (I) is given by Eq. (2) [15]:

$$P_{out} = (V_{oc} * I_{sc} * FF) \tag{1}$$

$$\eta_{ele} = (P_{out}) / (I * A) \tag{2}$$

Fig. 5 Variation of closed circuit current and front side temperature with time

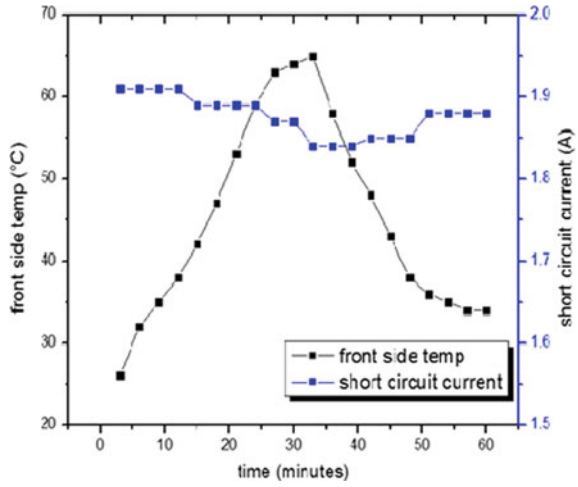


Fig. 6 Variation of power output and front side temperature with time

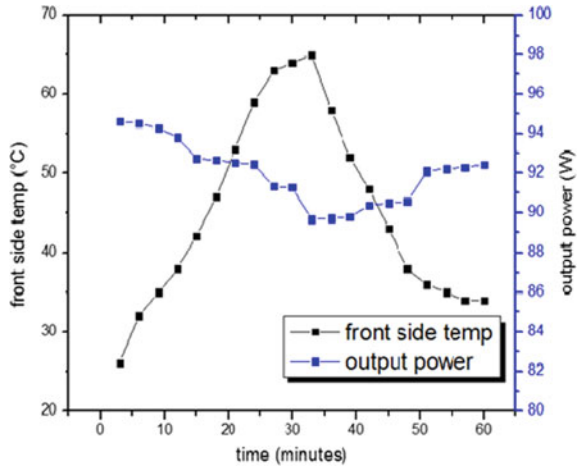
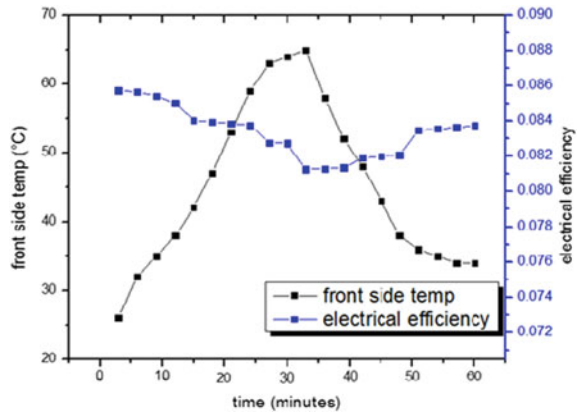


Fig. 6 shows the graph between P_{out} and temperature for equal time interval and it has been reported that, as the temperature increases, the power output decreases and same is the trend for electrical efficiency as shown in Fig. 7.

Fig. 7 Variation of electrical efficiency and front side temperature with time



4 Conclusion

From the experimental result, it is clear that the rise in temperature of the PVM have a negative impact on the electrical efficiency for a constant light intensity. As the temperature increases, the voltage decreases and, as a result, the net power output also decreases. And it is also concluded that, by cooling the PVM, the electrical efficiency again starts increasing. The percentage increase in the electrical efficiency is 3.6%. Thus, it is better to use PVM along with solar heater so that the latter will extract heat from PVM and results in increased electrical efficiency and thermal energy extracted can be used for other purposes.

References

1. Dudley B (2018) BP statistical review of world energy. BP Statistical Review, London, UK. Accessed 6 Aug 2018
2. Dubey S, Sarvaiya JN, Seshadri B (2013) Temperature dependent photovoltaic (PV) efficiency and its effect on PV production in the world—a review. *Energy Procedia* 33:311–321
3. El Mays A, Ammar R, Hawa M, Akroush MA, Hachem F, Khaled M, Ramadan M (2017) Improving photovoltaic panel using finned plate of aluminum. *Energy Procedia* 119:812–817
4. Fesharaki VJ, Dehghani M, Fesharaki JJ, Tavasoli H (2011) The effect of temperature on photovoltaic cell efficiency. In: *Proceedings of the 1st international conference on emerging trends in energy conservation—ETEC*, Tehran, Iran, pp 20–21
5. Gaur A, Tiwari GN (2014) Performance of a-Si thin film PV modules with and without water flow: an experimental validation. *Appl Energy* 128:184–191
6. Gupta A, Chauhan YK (2016) Detailed performance analysis of realistic solar photovoltaic systems at extensive climatic conditions. *Energy* 116:716–734
7. Hasan MA, Sumathy K (2010) Photovoltaic thermal module concepts and their performance analysis: a review. *Renew Sustain Energy Rev* 14(7):1845–1859
8. Idoko L, Anaya-Lara O, McDonald A (2018) Enhancing PV modules efficiency and power output using multi-concept cooling technique. *Energy Rep* 4:357–369

9. Irwan YM, Leow WZ, Irwanto M, Fareq M, Amelia AR, Gomesh N (2015) Indoor test performance of PV panel through water cooling method, vol 79. Elsevier, Hoboken
10. Kim JH, Park SH, Kim JT (2014) Experimental performance of a photovoltaic-thermal air collector. *Energy Procedia* 48:888–894
11. Messenger RA, Abtahi A (2010) *Photovoltaic systems engineering*. CRC Press
12. Manjhi SK, Kumar R (2019) Performance assessment of K-type, E-type and J-type coaxial thermocouples on the solar light beam for short duration transient measurements. *Measurement*, 146:343–355
13. Sarwar J, Georgakis G, LaChance R, Ozalp N (2014) Description and characterization of an adjustable flux solar simulator for solar thermal, thermochemical and photovoltaic applications. *Sol Energy* 100:179–194
14. Saxena A, Deshmukh S, Nirali S, Wani S (2018) Laboratory based experimental investigation of photovoltaic (PV) thermo-control with water and its proposed real-time implementation. *Renewable Energy* 115:128–138
15. Skoko SM, Ciric RM (2017) Laboratory exercises of photovoltaic systems—Review of the equipment, methodology, trials and results. *Renew Sustain Energy Rev* 79:293–303
16. Tiwari A, Sodha MS, Chandra A, Joshi JC (2006) Performance evaluation of photovoltaic thermal solar air collector for composite climate of India. *Sol Energy Mater Sol Cells* 90(2):175–189

Performance Analysis of Combined Cycle with Supplementary Heating



Nagendra Kumar Sharma and Rohit Pandey

Abstract Hydraulic power turbine uses water as working fluid were the only means of energy generation in the beginning of technological development; later steam and gas turbine came into existence. Water turbine plants do not develop the power throughout the year. Thermal efficiency gas turbine is very poor approximate sixty percent of total heat generated in combustion chamber goes waste in the form of exhausted flue gases. To utilize the thermal energy of these exhausted gases of gas turbine idea of combined cycle has been introduced. The gas turbine exhaust gas energy is used to generate the steam used for running steam turbines. It arrangement results in increased efficiency and increased power and increased efficiency. In the present work, mathematical modeling for the specific work output of combined cycle with variable supplementary heating has been done. Steam is generated in two stages, for high pressure turbine steam it is at 20 bar and 813 K and for low pressure turbine steam at 10 bar and 623 K. The turbine inlet temperature is variable. Specific work output combined cycle with variable supplementary heating has been calculated with different pressure ratios. The pressure has been varied in the range of 4–10. A/F ratio has been kept constant. Supplementary heating range is taken from 0.0 to 0.5. The optimum point has been searched and its analysis has been done.

Keywords Combined cycle · Supplementary heating · Air–fuel ratio · Pressure ratio

Nomenclature

C_{pa}	Specific heat of air
C_{pg}	Specific heat of flue gases
h_1	Enthalpy of High Pressure Turbine inlet
h_2	Enthalpy of High Pressure Turbine exit

N. K. Sharma (✉) · R. Pandey

Department of Mechanical Engineering, Amity University Madhya Pradesh, Maharajpura Dang, Gwalior 474005, Madhya Pradesh, India

h_3	Enthalpy of low Pressure Turbine inlet
h_4	Enthalpy of low Pressure Turbine exit
h_{f3}	Enthalpy of water at condenser pressure
H.R.S.G.	Heat Recovery Steam Generator
L.C.V.	Lower calorific value
T_1	Ambient Temperature
T_2	Compressor Exit Temperature
T_{2a}	Actual Compressor Temperature
T_3	Exit Temperature of flue gases
T_4	Exit Temperature of Gas Turbine
T_{4a}	Actual Temperature of Gas Turbine
T_9	Stack Temperature
W_T	Work output of Gas Turbine
W_C	Work input to Compressor
Z	Part of flue gas passed through Gas Turbine
Z_a	Part of flue gas bypassed through HRSG

1 Introduction

On account of ever increasing demand of electric power several new technologies have been developed during last few decades and turbines are one of the extensively used prime movers. In any type of turbine, either thermal, hydel or gas turbine, there are no reciprocating parts as in case of steam, diesel or petrol engines hence turbines offers best means to produce mechanical power. For the operation of steam turbines high pressure and temperature steam are required which need heavy and costly equipment for the generation of steam. Heating equipment, conventional boiler, and nuclear reactors employ inefficient indirect heating.

Gas turbine is the later development which derives its power from the high pressure and temperature combustion products air and fuel. Flue gases are allowed to expand through turbine blades. Gas turbine power cycle is of open type and close type.

In an open cycle gas turbine air enters from atmosphere and combustion products are discharged to atmosphere. Main components are compressor, combustion chamber, and turbine. A major part of power developed is consumed in running the compressor. If efficiency of turbine and compressor is 50%, the net out is zero.

In closed cycle gas turbine working fluid is confined within the plant and is not exhausted into atmosphere and is re-circulated. Significant feature of closed cycle gas turbine is that pressure is very high throughout the cycle which results in reduced size of plant. Power output can be altered by changing the pressure level in the circuit. This type of control can accommodate wide range of load conditions without change in maximum cycle temperature and thus there is not much variation in overall efficiency.

Efficiency of gas turbine is low and a big fraction of energy is wasted as exhausted high temperature flue gases, means have been developed to use energy of these flue gases to raise steam for steam turbine such an arrangement is called combined cycle power plant. This combined cycle power plant gaining more attention due to their increased output and enhanced overall efficiency in comparison to individual steam power plants and gas turbine power plants.

In a combined cycle exhaust heat loss from gas turbine is significantly reduced by utilizing this heat in a ‘Bottoming Cycle’, here the high temperature exhaust gas transfer a large portion of its heat to raise the temperature of steam for steam turbine. Thus the power output and the thermal efficiency of the plant are increased. On the basis of exhaust heat utilization method combined cycle can of two types, namely,

- a. Basic combined cycle power plant.
- b. Supplementary heating combined cycle.

The capacity of unfired HRSG depends on the temperature and mass flow rates of the gas turbine exhaust. Supplementary heating is often employed to increase output of steam turbine power plant. More air is required for burning additional quantity of fuel during supplementary heating. This is obtained by employing higher A/F ratio in the combustion chamber of the gas turbine power plant. Thus the exhaust gases have ample air to support combustion of additional quantity of fuel in the HRSG. Combustion of additional fuel takes place in the gas turbine exhaust gases before they enter unfired section of HRSG. Supplementary heating is also advantageous if the gas turbine plant has to operate at the reduced load. Supplementary heating of required quantity of fuel can compensate for the reduced heat input to HRSG and thus maintained its full load operation without any disturbance.

Literature shows that gas turbines cogeneration system is nowadays a prominent area for research and development. Various thesis work has been done and running simultaneously too. Main focus of this project is the papers of ASME which deals with the Power Boosting of Gas turbines cogeneration system by using various modifications.

The power enhancement of gas turbines sytem with the help of regeneration. It consists of considering the real situation with all the efficiencies not equal to 100%. The regeneration improves the efficiency of the system, further modification is done by adding an inlet air cooling system to it. Gas turbines cogeneration system analysis with alternative regeneration is another paper which deals with improvement in performance [1]. The critical analysis of reheat cycle performance of the gas turbines cogeneration system. This paper deals with the modification of gas turbines cogeneration system with Reheat [2]. The thermal modeling of the combined power cycle develops a logical tool to know the power developing capacity in advance. The level of uncertainty was kept <2% [3]. A critical review of advanced gas turbine cycles for power generation and compared the various power generation cycle. Power generation and thermal efficiency can be increased by enhancing the exhaust heat recovery [4]. A vast study of gas turbine cycles which are characterized by low thermal efficiency and short commissioning duration. Combined power cycle is a way of improving the thermal efficiency of the power generation system [5]. The

heat recovery from the steam generator and the energy losses were minimized. Gas turbine efficiency can be enhanced by raising the gas turbine inlet temperature. Authors explored the possibilities of increasing the combined cycle efficiency up to 60% by limiting the maximum pressure up to 220 bar. With the help of reheating combined cycle efficiency can be enhanced up to 65% [7]. Experimental work with novel method was used to increase the efficiency of combined gas turbine cycle by connecting two supercritical (s-CO₂) power cycles in series, run by waste heat of gas turbine cycle and solar energy and compared this system with the conventional combined cycles [8]. A combined model was developed for heat utilization and economic dispatch for natural gas combined power plant and the effect of heat load on combined heat and power economic dispatch (CHPED) was analyzed [9]. An innovative system was applied to 200 MW power plant to achieve latent heat recovery by applying dehumidification of the exhaust gas. This method was applied to 200 MW power plant, the results showed an improvement of thermal efficiency of the system by 7.4% [10]. It was found that the quality of steam at the exit of low pressure steam turbine has a significant impact on the output and efficiencies of turbine [11]. The effect of the quality of exhaust steam on the output of combined power plant was studied, obtained results showed that steam quality should be constant at 88% for technical feasibility. It was found that an increase in HRSG high pressure reduces the total cost of the system and increases the efficiency of the system [12]. Author used the experience graph to determine the economic feasibility of natural gas-based combined cycle gas turbine cycle (CCGT). It was found that in last decade the price of specific investment for larger CCGTs has reduced up to 35% in practical terms. This trend of fall in price can be expected to continue in the future. It will affect the future price of CCGT plants and electricity generation in a positive way [13]. Theoretical study of combined steam and gas cycle processes was carried and determined the overall efficiency of the cycle. In this work supplementary firing of the gas turbine exhaust, efficiency of recovery boiler, and efficiency of heat exchanger efficiency in steam and gas turbine were considered. It was found that heat production has more effect on overall efficiency of the combined plant than overall exergy efficiency. Supplementary firing of gas turbine exhaust affects the energy efficiency and exergy efficiency in the same manner [14].

From the above-discussed literature review combined cycle performance can be altered by using the concept of supplementary heating. In this analysis of effect of supplementary heating on the performance of individual turbines output, the combined cycle has been discussed.

2 Mathematical Formulation

Specific work output and thermal efficiency depend on several parameters, all parameters cannot be taken into analysis as it would be a tedious task. So for the analysis of combined cycle, some important assumptions have been considered.

- The ambient pressure and temperature are 1 bar and 288 K.
- Highest permissible temperature of gas turbine is 1400 K.
- The isentropic efficiency for compressor and turbine is 85%.
- Calorific value of naphthalene fuel used is 44963.5 kJ/kg.
- The specific heat of flue gases is taken as 1.148 kJ/kg-K.
- Temperature of stack is 413 K.
- Steam used in high pressure turbine at 20 bar & 813 K and low pressure turbine at 10 bar & 623 K.
- Condenser pressure is 0.07 bar.

(a) **Without reheat and without supplementary heating**

$$W_T = (m_a + m_f) \times c_{pg} \times (T_3 - T_{4a}) \quad (1)$$

$$W_C = m_a \times c_{pa} \times (T_{2a} - T_1) \quad (2)$$

$$Work_1 = W_T - W_C \quad (3)$$

$$Worknet_1 = Work_1 / (m_a + m_f) \quad (4)$$

For high pressure turbine working at 20 bar 813 K

$$M_w = (m_a + m_f) \times c_{pg} \times (T_{4a} - T_9) / (h_1 - h_{f3}) \quad (5)$$

If ($T_{4a} > 813$ K & $T_3 < 1400$ K)

$$Work_2 = m_f \times (h_1 - h_2) \quad (6)$$

$$Worknet_2 = Work_2 / (m_a + m_f) \quad (7)$$

For low pressure turbine working at 10 bar, 623 K

$$M_{w1} = (m_a + m_f) \times c_{pg} \times (T_{4a} - T_9) / (h_3 - h_{f3}) \quad (8)$$

If ($623 < T_{4a} > 813$ K & $T_3 < 1400$ K)

$$Work_3 = m_{w1} \times (h_3 - h_4) \quad (9)$$

$$Worknet_3 = Work_3 / (m_a + m_f) \quad (10)$$

Total work of plant

$$Work_4 = Worknet_1 + Worknet_2 + Worknet_3 \quad (11)$$

(b) **Without reheat with supplementary heating**

Gas turbine work

$$W_T = z \times (m_a + m_f) \times c_{pg} \times (T_3 - T_{4a}) \quad (12)$$

where, $z = 1 - z_a$

$$W_C = m_a \times c_{pa} \times (T_{2a} - T_1) \quad (13)$$

$$Work_1 = W_T - W_C \quad (14)$$

$$Worknet_1 = Work_1 / (m_a + m_f) \quad (15)$$

For high pressure turbine working at 20 bar & 813 K

$$M_w = \frac{\{Z_a \times (m_a + m_f) \times c_{pg} \times T_3 + z \times (m_a + m_f) \times c_{pg} \times T_{4a} - (m_a + m_f) \times c_{pg} \times T_9\}}{(h_1 - h_{f3})} \quad (16)$$

If ($T_{4a} > 813$ K & $T_3 < 1400$ K)

$$Work_2 = m_w \times (h_1 - h_2) \quad (17)$$

$$Worknet_2 = Work_2 / (m_a + m_f) \quad (18)$$

For low pressure turbine working at 10 bar & 623 K (Fig. 1)

$$M_{w1} = \frac{\{Z_a \times (m_a + m_f) \times c_{pg} \times T_3 + z \times (m_a + m_f) \times c_{pg} \times T_{4a} - (m_a + m_f) \times c_{pg} \times T_9\}}{(h_3 - h_{f3})} \quad (19)$$

If (623 K < $T_{4a} > 813$ K & $T_3 < 1400$ K)

$$Work_3 = m_{w1} \times (h_3 - h_4) \quad (20)$$

$$Worknet_3 = Work_3 / (m_a + m_f) \quad (21)$$

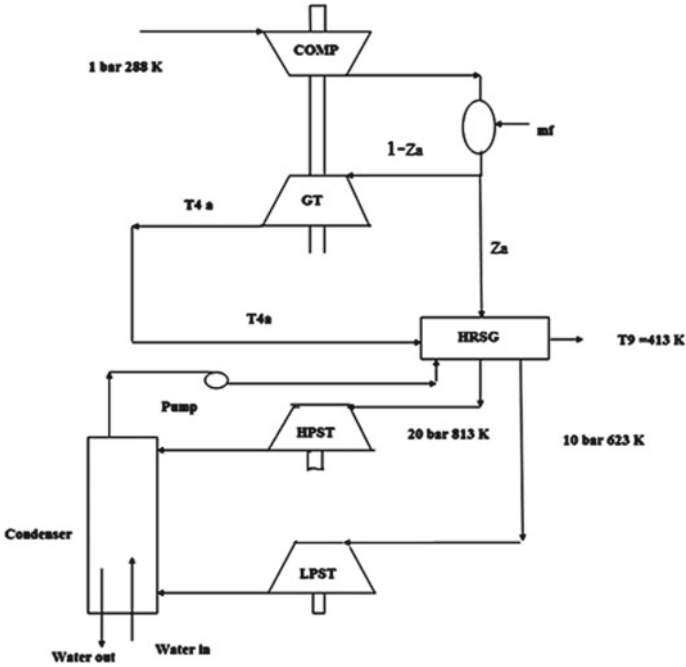


Fig. 1 Combined power cycle

3 Results and Discussion

It is clear from Figs. 2, 3, 4, 5, 6, 7, 8, 9, 10, 11, 12, 13, 14, 15, 16, 17, 18 and 19 that when a part of flue gases is fed to HRSG, the gas turbine efficiency decreases and low pressure steam turbine efficiency increases irrespective of compressor pressure ratio. Gas turbine efficiency and low pressure steam turbine become equal at particular value of z_a which depends upon the pressure ratio. Low pressure steam turbine efficiency increase as z_a increases and reaches its limit after that no improvement is observed. This limiting value of z_a varies slightly with pressure ratio. Total efficiency of the combined cycle depends upon the fraction of flue gases supplied to HRSG, and it decreases up to $z_a = 0.4$ for pressure ratio of 4–8. In the high pressure ratio range (12–20) total efficiency becomes maximum at 10% of flue gases by pass to HRSG.

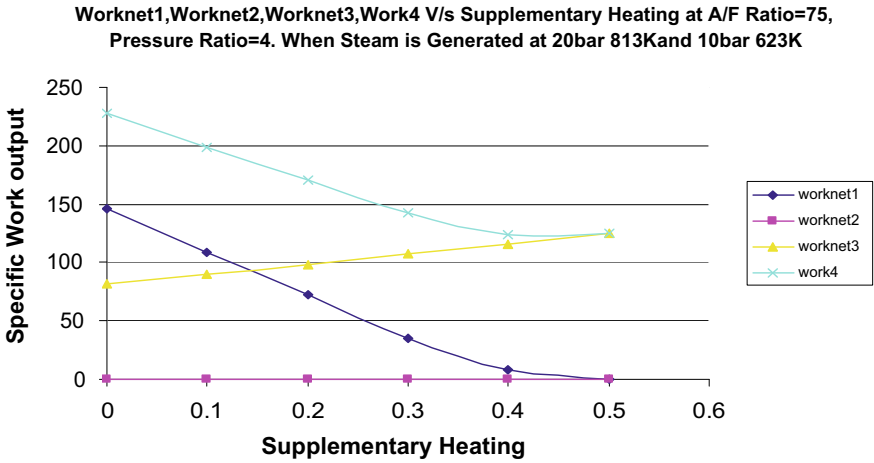


Fig. 2 Specific work output of combined cycle with supplementary heating at air fuel ratio 75 and pressure ratio 4

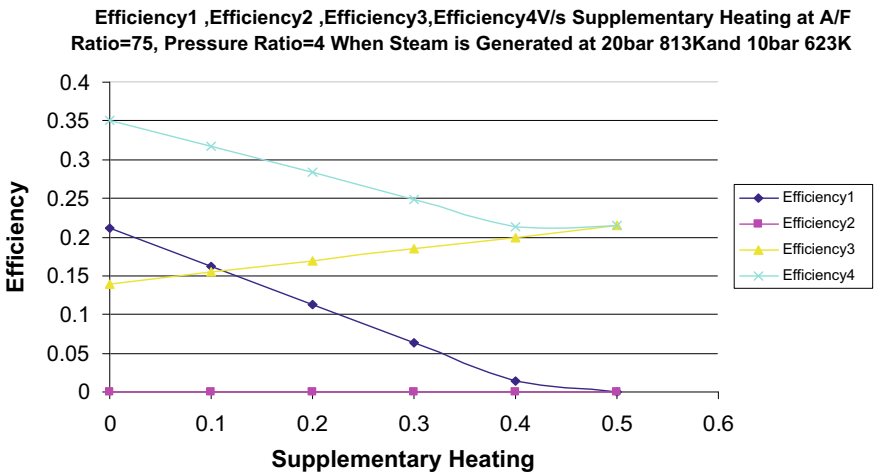


Fig. 3 Efficiency of combined cycle with supplementary heating at air fuel ratio 75 and pressure ratio 4

4 Conclusion

In this study mathematical modeling of combined power cycle is developed and computer programming is developed. It is observed from the graphs plotted for efficiency and specific work out that supplementary heating is not effective when

Worknet1,Worknet2,Worknet3,Work4 V/s Supplementary Heating at A/F Ratio=75, Pressure Ratio=6. When Steam is Generated at 20bar 813Kand 10bar 623K

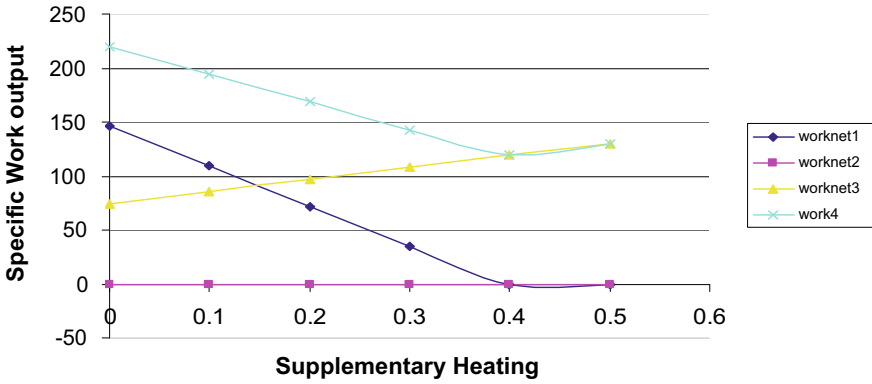


Fig. 4 Specific work output of combined cycle with supplementary heating at air fuel ratio 75 and pressure ratio 6

Efficiency1 ,Efficiency2 ,Efficiency3,Efficiency4V/s Supplementary Heating at A/F Ratio=75, Pressure Ratio=6 When Steam is Generated at 20bar 813Kand 10bar 623K

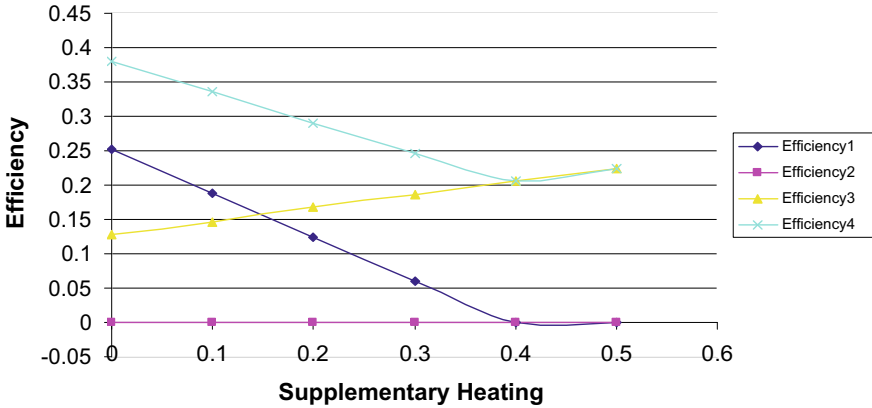


Fig. 5 Efficiency of combined cycle with supplementary heating at air fuel ratio 75 and pressure ratio 6

compression ratio is <12, for compression ratio 12–20 supplementary heating useful. Higher compression ratio range (12–20) only 10% supplementary heating is suffice to obtain maximum efficiency of combined power cycle.

Worknet1,Worknet2,Worknet3,Work4 V/s Supplementary Heating at A/F Ratio=75, Pressure Ratio=8. When Steam is Generated at 20bar 813Kand 10bar 623K

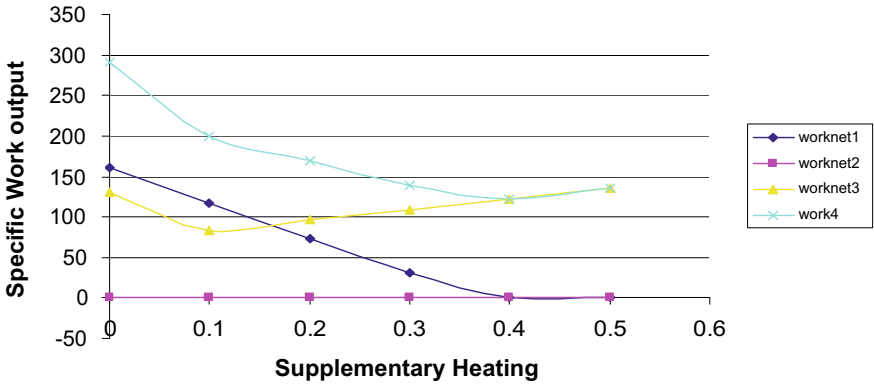


Fig. 6 Specific work output of combined cycle with supplementary heating at air fuel ratio 75 and pressure ratio 8

Efficiency1 ,Efficiency2 ,Efficiency3,Efficiency4V/s Supplementary Heating at A/F Ratio=75, Pressure Ratio=8 When Steam is Generated at 20bar 813Kand 10bar 623K

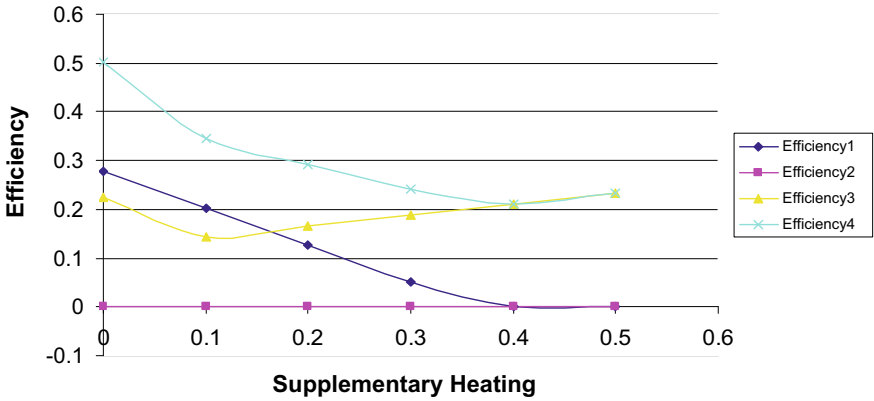


Fig. 7 Efficiency of combined cycle with supplementary heating at air fuel ratio 75 and pressure ratio 8

Worknet1,Worknet2,Worknet3,Work4 V/s Supplementary Heating at A/F Ratio=75, Pressure Ratio=10. When Steam is Generated at 20bar 813Kand 10bar 623K

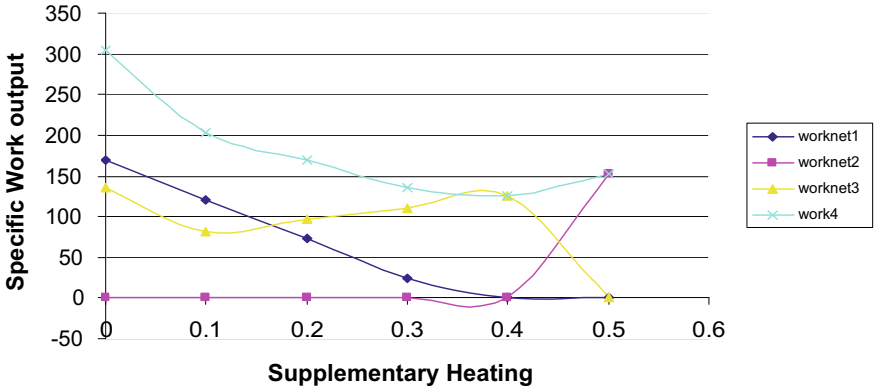


Fig. 8 Specific work output of combined cycle with supplementary heating at air fuel ratio 75 and pressure ratio 10

Efficiency1 ,Efficiency2 ,Efficiency3,Efficiency4V/s Supplementary Heating at A/F Ratio=75, Pressure Ratio=10 When Steam is Generated at 20bar 813Kand 10bar 623K

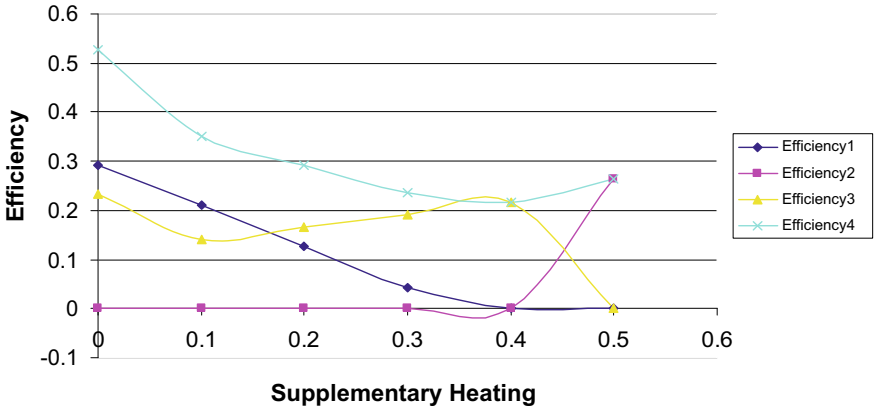


Fig. 9 Efficiency of combined cycle with supplementary heating at air fuel ratio 75 and pressure ratio 10

Worknet1,Worknet2,Worknet3,Work4 V/s Supplementary Heating at A/F Ratio=75, Pressure Ratio=12. When Steam is Generated at 20bar 813Kand 10bar 623K

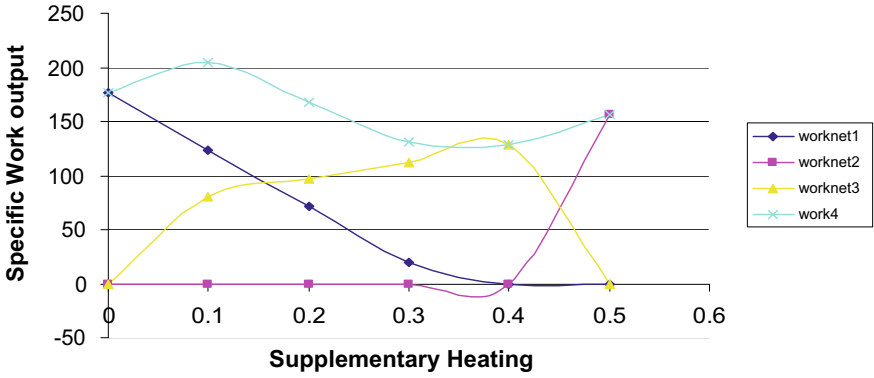


Fig. 10 Specific work output of combined cycle with supplementary heating at air fuel ratio 75 and pressure ratio 12

Efficiency1 ,Efficiency2 ,Efficiency3,Efficiency4V/s Supplementary Heating at A/F Ratio=75, Pressure Ratio=12 When Steam is Generated at 20bar 813Kand 10bar 623K

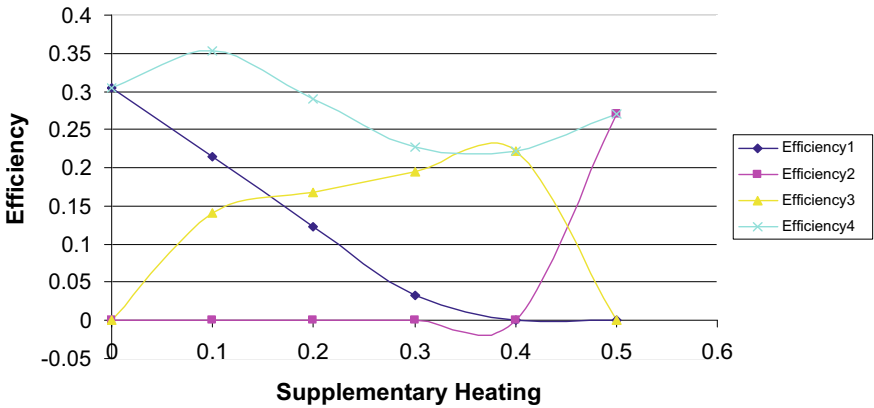


Fig. 11 Efficiency of combined cycle with supplementary heating at air fuel ratio 75 and pressure ratio 12

Worknet1,Worknet2,Worknet3,Work4 V/s Supplementary Heating at A/F Ratio=75, Pressure Ratio=14. When Steam is Generated at 20bar 813Kand 10bar 623K

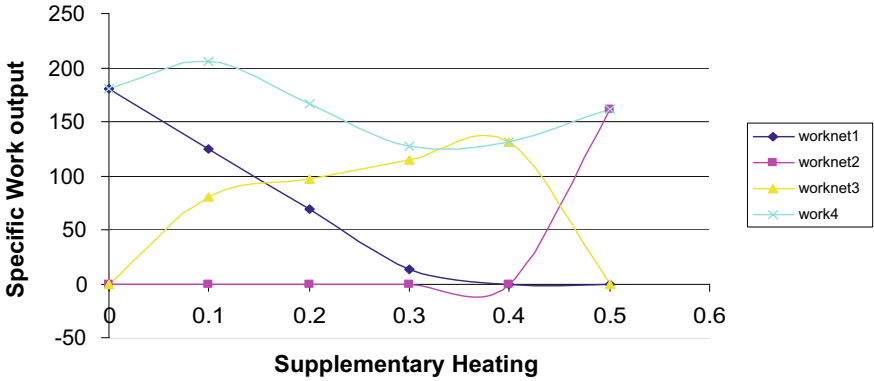


Fig. 12 Specific work output of combined cycle with supplementary heating at air fuel ratio 75 and pressure ratio 14

Efficiency1 ,Efficiency2 ,Efficiency3,Efficiency4V/s Supplementary Heating at A/F Ratio=75, Pressure Ratio=14 When Steam is Generated at 20bar 813Kand 10bar 623K

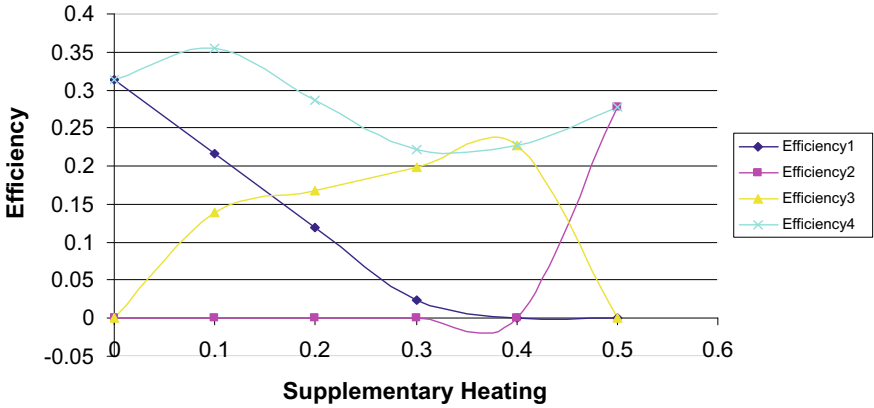


Fig. 13 Efficiency of combined cycle with supplementary heating at air fuel ratio 75 and pressure ratio 14

Worknet1,Worknet2,Worknet3,Work4 V/s Supplementary Heating at A/F Ratio=70, Pressure Ratio=16. When Steam is Generated at 20bar 813Kand 10bar 623K

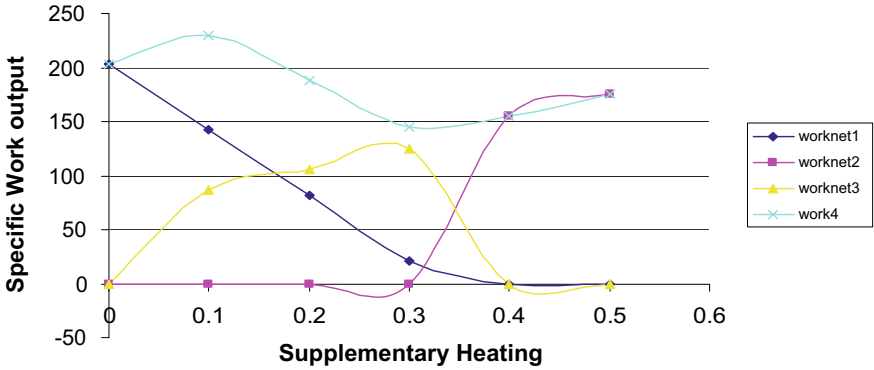


Fig. 14 Specific work output of combined cycle with supplementary heating at air fuel ratio 75 and pressure ratio 16

Efficiency1 ,Efficiency2 ,Efficiency3,Efficiency4V/s Supplementary Heating at A/F Ratio=70, Pressure Ratio=16 When Steam is Generated at 20bar 813Kand 10bar 623K

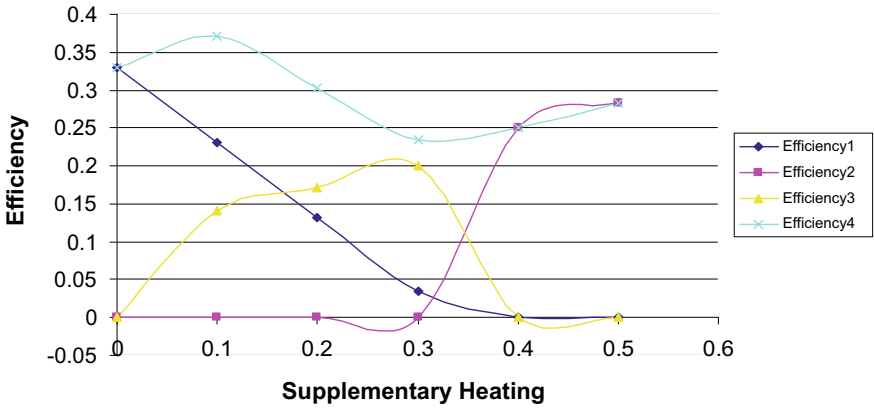


Fig. 15 Efficiency of combined cycle with supplementary heating at air fuel ratio 75 and pressure ratio 16

Worknet1,Worknet2,Worknet3,Work4 V/s Supplementary Heating at A/F Ratio=70, Pressure Ratio=18. When Steam is Generated at 20bar 813Kand 10bar 623K

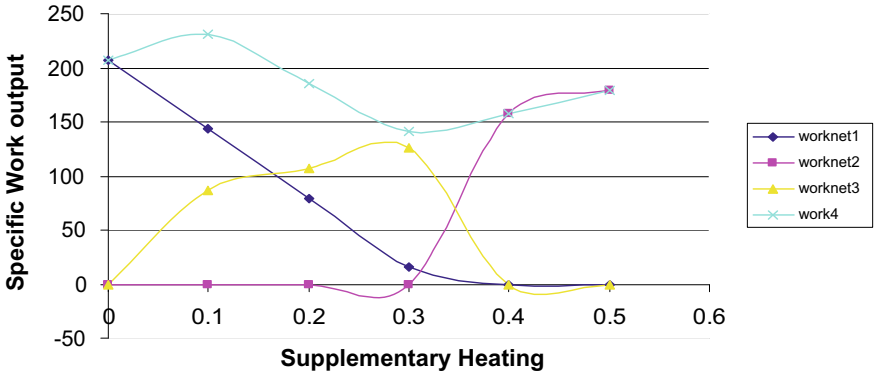


Fig. 16 Specific work output of combined cycle with supplementary heating at air fuel ratio 75 and pressure ratio 18

Efficiency1 ,Efficiency2 ,Efficiency3,Efficiency4V/s Supplementary Heating at A/F Ratio=70, Pressure Ratio=18 When Steam is Generated at 20bar 813Kand 10bar 623K

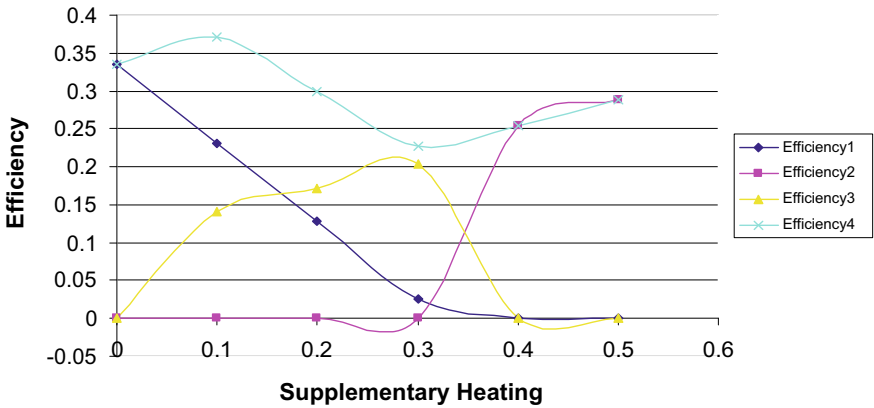


Fig. 17 Efficiency of combined cycle with supplementary heating at air fuel ratio 75 and pressure ratio 20

Worknet1,Worknet2,Worknet3,Work4 V/s Supplementary Heating at A/F Ratio=75, Pressure Ratio=20. When Steam is Generated at 20bar 813Kand 10bar 623K

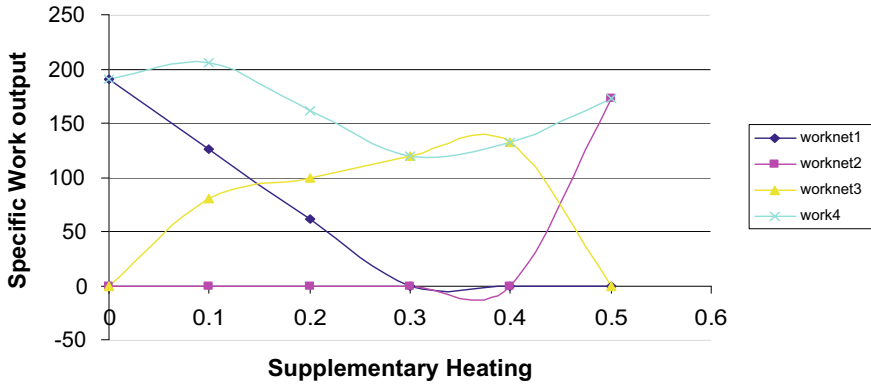


Fig. 18 Efficiency of combined cycle with supplementary heating at air fuel ratio 75 and pressure ratio 20

Efficiency1 ,Efficiency2 ,Efficiency3,Efficiency4V/s Supplementary Heating at A/F Ratio=75, Pressure Ratio=20 When Steam is Generated at 20bar 813Kand 10bar 623K

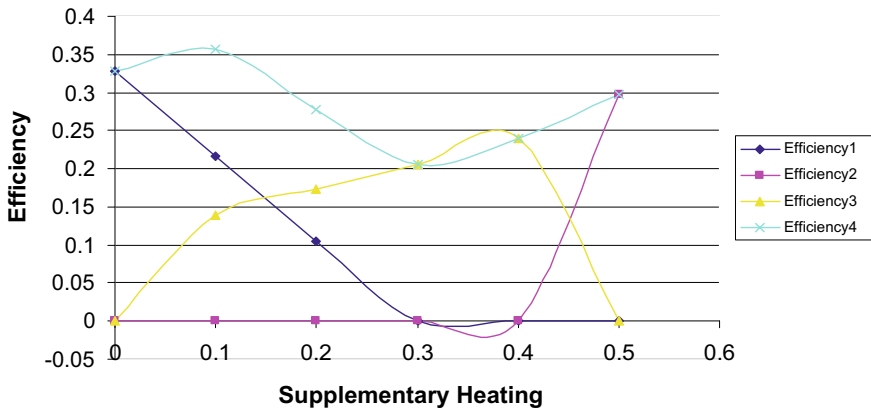


Fig. 19 Specific work output of combined cycle with supplementary heating at air fuel ratio 75 and pressure ratio 20

References

1. Oh S (1996) Exergy analysis for a gas turbines cogeneration system. ASME J Eng Gas Turb Power 118:782-791
2. Popiel CO, Wojtkowek J (1998) Heat and fluid flow research group. Environmental Engineering Institute, Pozan Univ 19(3)
3. Lee JH, Kim TS, Kim EH (2017) Prediction of power generation capacity of a gas turbine combined cycle cogeneration plant, vol 124. Elsevier B.V. (2017)

4. Heppenstall T (2003) Advanced gas turbine cycles for power generation: a critical review. *Appl Therm Eng* 18(9–10):837–846
5. Najjar YSH (2003) Efficient use of energy by utilizing gas turbine combined systems. In: *Proceedings of IASTED International conference Power Con 2002-Spec. Theme Blackout*, vol 21, pp 262–267
6. Franco FA, Russo A (2002) Combined cycle plant efficiency increase based on the optimization of the heat recovery steam generator operating parameters. *Int J Thermal Sci* 41:843–859
7. Franco A, Casarosa C (2002) On some perspectives for increasing the efficiency of combined cycle power plants. *Appl Therm Eng* 22:1501–1518
8. Mohammadi K, Ellingwood K, Powell K (2020) Novel hybrid solar tower-gas turbine combined power cycles using supercritical carbon dioxide bottoming cycles. *Appl Thermal Eng* 178:115588
9. Yu H, Nord LO, Yu C, Zhou J, Si F (2020) An improved combined heat and power economic dispatch model for natural gas combined cycle power plants. *Appl Thermal Eng* 181(2):115939
10. Yuan–Hu L, Kim J, Kim S, Han H (2019) Use of latent heat recovery from liquified natural gas combustion for increasing the efficiency combined-cycle gas turbine plant. *Appl Thermal Eng* 161:114177
11. Aliyu M, Al Qudaihi AB, Said SAM, Habib MA (2019) Energy, exergy and parametric analysis of a combined cycle power plant. *Thermal Sci Eng Progr* 15:114177
12. Ganjehkaviri A, MohdJaafar MN, Hosseini SE (2015) Optimization and the effect of steam turbine outlet quality on the output power of a combined cycle power plant. *Energy Convers Manage* 89:231–243
13. Copley UC, Cornland D (2002) The economics of the combined cycle gas turbine-an experience curve analysis. *Energy Policy* 30(4):309–316
14. Tuma M, Oman J, Sekavcnik M (1999) Efficiency of a combined gas-steam process. *Energy Conv Manag* 40(11):1163–1175

Effect of Laser Spot Diameter on Melt Pool Thermal History During Laser Cladding on Inconel 718 Coatings



Nikhil Thawari , Chaitanya Gullipalli, and T. V. K. Gupta

Abstract Laser cladding is a surface coating technique used to repair the worn-out components. In this work, effect of laser spot diameter on the melt pool thermal history during laser cladding on Inconel 718 substrate is studied using finite element-based numerical modeling. COMSOL Multi-physics heat transfer module is used for analysis. Six different laser spot diameters of varying size from 1 to 6 mm are considered in the study and the results are compared. The results show that, increase in spot diameter reduces the melt pool temperature, as about 45% reduction in temperature is observed as the spot diameter increases from 1 to 2 mm and further the temperature difference reduces with increase in diameter. The substrate melting was not observed for larger diameters which indicate the absence of metallurgical bond (no cladding) formation with the substrate, whereas the rapid heating observed in all the samples, and a decrease in rapid cooling of the melt pool is noticed with increase in laser spot size; this could be due to decrease in the energy density. Also, the melt pool size is smaller for low spot diameters, due to the dominant radiation over conduction which results of high surface temperatures. The overall analysis suggests that high powers must be incorporated for laser cladding with larger spot diameters and vice versa.

Keywords Laser cladding · Numerical analysis · Thermal history · Laser spot diameter · COMSOL+

1 Introduction

Laser cladding (LC) is a surface enhancement technique used to repair or rebuild the worn-out components damaged due to harsh working environment [1]. In LC, laser is used for melting the coating material, fed coaxially into the clad region depositing a layer of the coating [2] as shown in Fig. 1. The clad materials used in the process are of either in powder or wire form, which produces a strong metallurgical bond between the clad and the substrate material [3]. The low heat input, minimum distortion, lower

N. Thawari (✉) · C. Gullipalli · T. V. K. Gupta
Department of Mechanical Engineering, Visvesvaraya National Institute of Technology, Nagpur
440010, India

© The Author(s), under exclusive license to Springer Nature Singapore Pte Ltd. 2022
M. K. Singh and R. K. Gautam (eds.), *Recent Trends in Design, Materials
and Manufacturing*, Lecture Notes in Mechanical Engineering,
https://doi.org/10.1007/978-981-16-4083-4_6

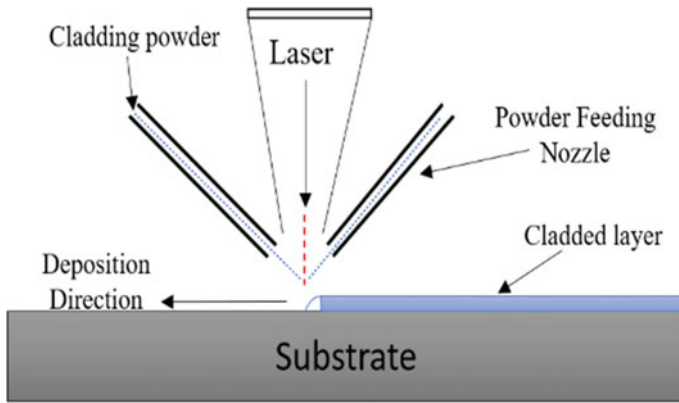


Fig. 1 Laser cladding process

HAZ, near neat shape cladding, higher process flexibility, etc., are some of the major advantages of this process [4]. A variety of cladding materials can be used in this process to produce functionally graded coatings with thickness varying from 0.1 to 2 mm [5].

The quality of laser cladding process depends on various process parameters like laser power, scanning speed, powder feed rate, overlapping %, spot diameter, stand of distance (SOD), etc. Most of the studies reported are based on laser power, speed, powder feed rate due to the system constraints. Also, laser cladding process involves complex physical phenomena like heat transfer, rapid solidification, phase transformation, and melting. As a result, it is not preferred all the times to perform experiments to optimize the parameters to study their effect on the clad quality which involves huge amount of cost. These problems can be eliminated using Finite Element (FE)-based numerical modelling to access and predict the process.

Several attempts were made on laser cladding process using FE-based modeling. Like, Wirth et al. used FE methodology to validate the effect of process parameters on thermal history, clad geometry, and absorptivity [6]. Benoit et al. performed numerical analysis to evaluate the role of process parameters on stresses and temperature in the coating and substrate materials [7]. Farahmand et al. used numerical modeling to investigate the heat distribution and the stresses with scanning speed [8]. Peyre et al. studied the temperature distribution considering Arbitrary Lagrangian–Eulerian (ALE) procedure in multi-layer cladding [9]. Jendrzejewski et al. developed a model to evaluate the temperature and stresses in LC process [10]. Though several researchers attempted to study the process performance with FE-based modeling, there has been no reports on the role of laser spot diameters on melt pool temperature history. Hence, in the present study, an FE model is developed to investigate the effect of different laser spot diameters on melt pool temperatures using COMSOL Multi-physics 5.4 software; and compared, evaluated the influence of spot diameters on temperature history in laser cladding.

2 Simulation Work

The present study is on the use of COMSOL Multiphysics software (version 5.4) for developing an FE-based numerical model, which is capable of analyzing the thermal history and to monitor melt pool dynamics during laser cladding. As mentioned above, LC process involves complex heat transfer phenomena; and hence, to simplify the analysis assumptions were taken like (i) validation of simple theory of heat conduction, (ii) both substrate and clad materials are isotropic, and (iii) ignoring chemical reaction in the clad region. A model geometry, size: 120 mm × 30 mm × 10 mm is developed as the substrate in COMSOL, shown in Fig. 2a. The governing equations of heat transfer are defined and the necessary boundary conditions are applied to the substrate with Eq. (1) is the heat conduction in model considered

$$\rho C_p \frac{\partial T}{\partial t} + \rho C_p u \nabla T + \nabla q = Q \quad (1)$$

where ρ = density of material, C_p = heat capacity, T = temperature, and t = time in sec.

The boundary conditions for the substrate are (i) top surface is exposed to moving heat source and (ii) remaining all surfaces are subjected to heat losses (due to convection and radiation). Equation (2) gives the Gaussian shape distribution of the moving heat source, shown in Fig. 3:

$$Q = \frac{2 P}{\pi R_b^2} \exp \left(-\frac{2R}{R_b} \right) \quad (2)$$

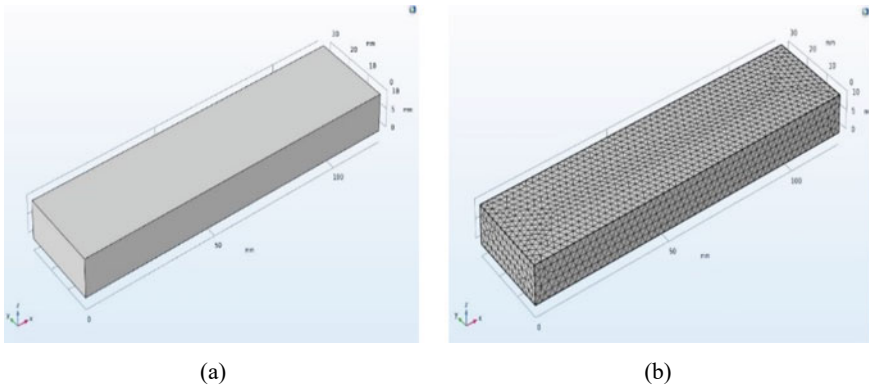


Fig. 2 a 3D block created in COMSOL as substrate. b Meshed model of geometry with quadrilateral elements

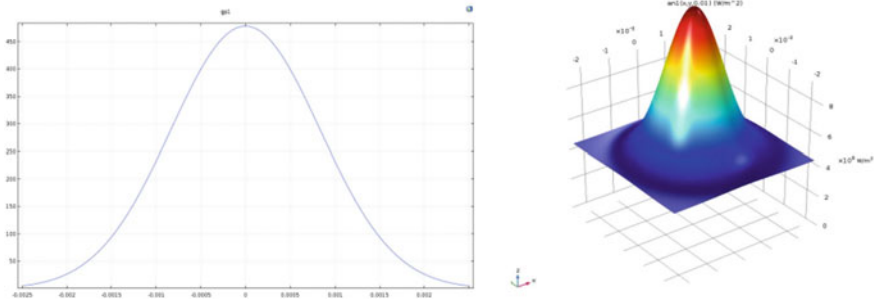


Fig. 3 Gaussian distribution of the laser power source

where P is laser power, R_b spot diameter, and R is the position of spot, which changes with time. The heat loss from surface, due to convection and radiation, are given in Eqs. (3) and (4). Here, h is convective heat transfer coefficient, σ is Stefan Boltzmann constant, and ε is surface emissivity.

$$q_{conv} = h(T_s - T_{amb}) \tag{3}$$

$$-n \cdot q = \varepsilon\sigma(T_{amb}^4 - T_s^4) \tag{4}$$

The model is specified with Inconel 718 properties for the geometry, available in the software material library. The Physics controlled mesh (Extremely fine) with tetrahedral element is adopted in the present study to discretize the block into number of finite elements. The geometry block and meshed model are shown in Fig. 2b. Time dependent study is incorporated to simulate the laser cladding process. In the analysis, laser is moved over the substrate material with a laser power of 1000 W, scanning speed 20 mm/s with traveling length of 100 mm, respectively. During numerical modeling, the laser spot diameter is varied with a constant interval of 1 mm as specified in Table 1. In each case, the thermal history is recorded at the midpoint of the substrate for a time period of 2.5 s.

Table 1 Process parameters used for analysis with obtained temperature results

Sr. no	Laser power (W)	Scanning speed (mm/s)	Spot diameter (mm)	Max. melt pool temperature (K)
1	1500	20	1	4500
2			2	2820
3			3	1780
4			4	1410
5			5	1180
6			6	1050

3 Results and Discussion

The melt pool thermal history observed for different laser spot diameters have been evaluated and the maximum melt pool temperatures recorded for each spot diameter is listed in Table 1. From the results, it is observed that as the spot diameter increases from 1 to 6 mm, the melt pool temperature decreases drastically from 4500 to 1050 K for the same laser power. Almost 45% temperature reduction is seen when the spot diameter is increased from 1 to 2 mm, respectively. Further reduction in the temperatures were observed as the diameter increases. It is predicted that, with increase in spot size, the energy density at the point of contact during deposition is reduced resulting in lower temperatures.

It can be seen that substrate melting hasn't occurred for 4–6 mm spot diameters, as shown in Fig. 4. This indicates the absence of metallurgical bond (no cladding) formation between the clad and substrate materials. For 1–2 mm spot dia., the melt pool temperatures were observed to be too high, i.e., 2–3 times the melting point of Inconel 718 (1670 K). As a result, larger substrate melting occurred along the depth which may result in increased dilution in the coating. It indicates that cladding with large spot diameters requires high laser powers and vice versa.

The temperature history measured for different laser spot diameters are shown in Fig. 5, gives that in cladding, rapid heating is observed for all the samples, whereas, with increase in spot size, rapid cooling of the substrate material decreases, which is due to decrease in the heat concentration at the contact point for larger diameters.

The surface temperature contours developed in laser heating is shown in Fig. 6. It is observed that, for lower spot diameters, melt pool size is small; this phenomenon is due to the domination of radiation effect over conduction. It is noticed from the results that at smaller diameters the temperatures obtained are very high which shows that radiation has a dominating role in heat transfer over conduction. On the other hand, high spot diameters generate lower temperatures, allowing conduction to be primary mode of heat transfer; thus the melt pool size expands resulting larger area.

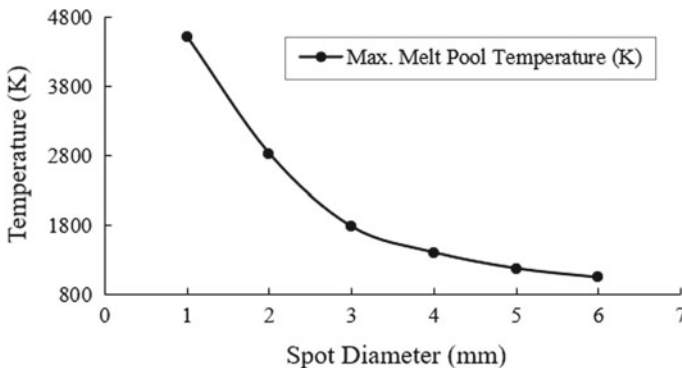


Fig. 4 Melt pool temperature variation for different spot diameters

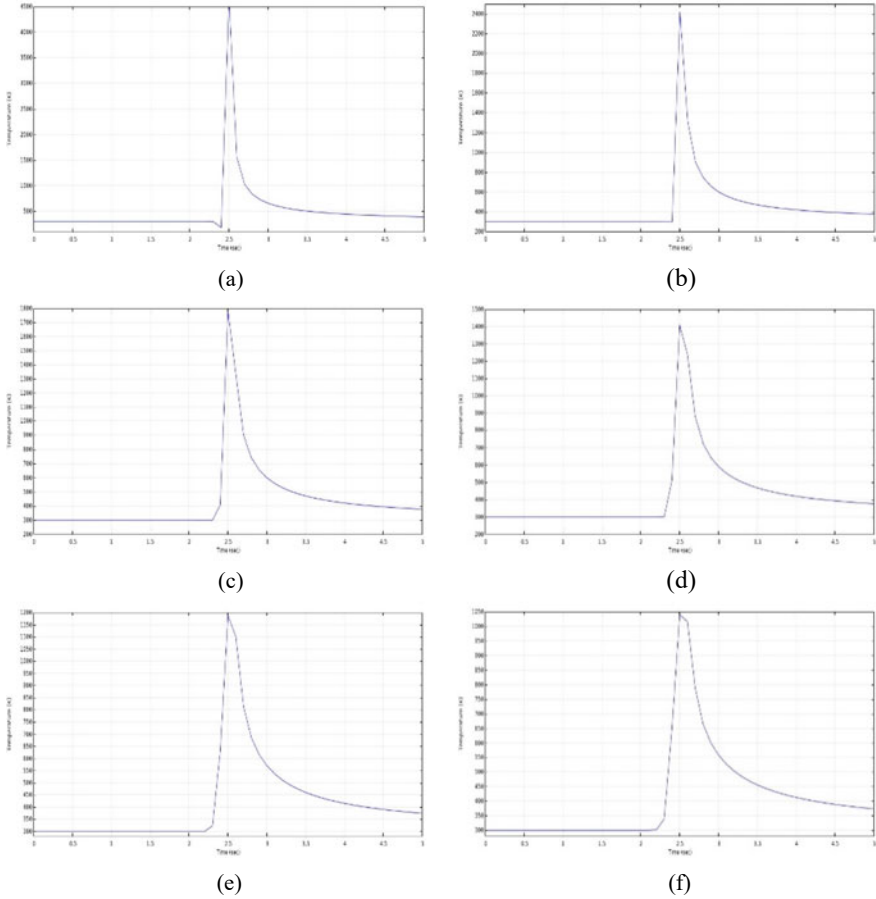


Fig. 5 Melt pool thermal history obtained for different spot diameters. **a–f** indicates spot diameter from 1 to 6 mm, respectively

From the overall analysis, it is concluded that laser spot diameter plays an important role in laser cladding process. It is also a deciding factor for laser power which generates the melt pool history during deposition. Also, to investigate the effect of spot diameter on clad geometry and powder catchment efficiency, an exhaustive analysis is required with coating layer addition and also to need to be validated with experiments, which are planned for future work.

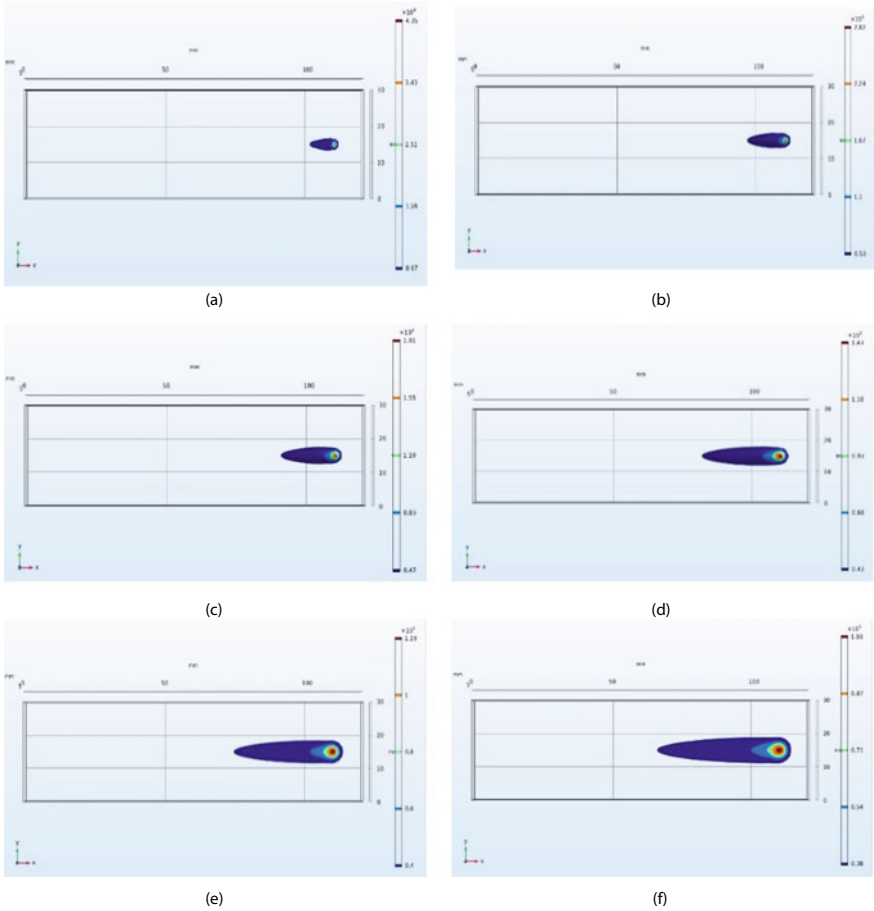


Fig. 6 Temperature contours for varying spot diameters. **a–f** indicates spot diameter from 1 to 6 mm, respectively

4 Conclusions

The FE-based numerical model developed in COMSOL Multiphysics software predicts the effect of laser spot diameter on melt pool thermal history in laser cladding. The following conclusions can be made based on the analysis:

- The increase in laser spot diameter, maximum temperature generated in melts pool region decreases drastically, due to lower energy density concentration.
- Increase in spot size decreases the rapid cooling of substrate material.
- For small spot diameters, area generated for the melt pool is small and it increases with spot diameters.

- High laser powers with large spot diameters are to be used to developed a metallurgical bond between the clad and substrate materials, and vice versa.

Acknowledgements The authors acknowledge DST, Govt. of India, for the financial support and testing equipment under the Project No. DST/ECR/2016/001403.

References

1. Toyserkani E, Khajepour A, Corbin SF (2004) Laser cladding. CRC Press
2. Kumar V, Rakshit R, Das AK (2020) Mechanical and tribological performance of fiber laser clad h-BN+ SS316 composite on SS316 surface. *J Mater Process Technol* 278:116509
3. Jendrzewski R, Navas C, Conde A, de Damborenea JJ, Sliwinski G (2008) Properties of laser-clad stellite coatings prepared on preheated chromium steel. *Mater Des* 29(1):187–192
4. Thawari N, Gullipalli C, Chandak A, Gupta TVK (2021) Influence of laser cladding parameters on distortion, thermal history and melt pool behaviour in multi-layer deposition of stellite 6: in-situ measurement. *J Alloys Compd* 860:157894
5. Song L, Zeng G, Xiao H, Xiao X, Li S (2016) Repair of 304 stainless steel by laser cladding with 316L stainless steel powders followed by laser surface alloying with WC powders. *J Manuf Process* 24:116–124
6. Liu H, Hu Z, Qin X, Wang Y, Zhang J, Huang S (2017) Repair of 304 stainless steel by laser cladding with 316L stainless steel powders followed by laser surface alloying with WC powders. *Int J Adv Manuf Tech* 91(9–12):3967–3975
7. So H, Chen CT, Chen YA (1996) Wear behaviours of laser-clad stellite alloy 6. *Wear* 192(1–2):78–84
8. Aubry P, Blanc C, Demirci I, Dal M, Malot T, Maskrot H (2017) Laser cladding and wear testing of nickel base hardfacing materials: Influence of process parameters. *J Laser Appl* 29(2):022504
9. Näkki J, Tuominen J, Vuoristo P (2017) Effect of minor elements on solidification cracking and dilution of alloy 625 powders in laser cladding. *J Laser Appl* 29(1):012014
10. Vostrak M, Houdkova S, Hruska M (2019) Comparison of WC and (TiW) C in nickel-based alloy coatings prepared by laser cladding. *Int IOP Conf Ser Mater Sci Eng* 461:012092
11. Korsmik RS, Turichin GA, Klimova-Korsmik OG, Alekseeva EV, Novikov RS (2018) Development of laser powder cladding technology for restoration of heat-resistant nickel alloys turbine blades. *J Phys Conf Ser* 1109:12–23
12. Stanciu EM, Pascu A, Tierean MH, Voiculescu I, Roata IC, Croitoru C, Hulka I (2016) Dual coating laser cladding of NiCrBSi and Inconel 718. *Mater Manuf Process* 31(12):1556–1564
13. Zhou S, Zeng X, Hu Q, Huang Y (2008) Analysis of crack behavior for Ni-based WC composite coatings by laser cladding and crack-free realization. *Appl Surf Sci* 255(5):1646–1653
14. Wang DS, Liang EJ, Chao MJ, Yuan B (2008) Investigation on the microstructure and cracking susceptibility of laser-clad V₂O₅/NiCrBSiC alloy coatings. *Surf Coat Technol* 202(8):1371–1378
15. Huang Y, Zeng X (2010) Investigation on cracking behavior of Ni-based coating by laser-induction hybrid cladding. *Appl Surf Sci* 256(20):5985–5992
16. Thawari N, Gullipalli C, Katiyar JK, Gupta TVK (2021) Influence of buffer layer on surface and tribomechanical properties of laser clad Stellite 6. *Mat Sci Eng B* 263:114799
17. Sun S, Durand Y, Brandt M (2005) Parametric investigation of pulsed Nd: YAG laser cladding of stellite 6 on stainless steel. *Surf Coat Technol* 194(2–3):225–231
18. Lin WC, Chen C (2006) Characteristics of thin surface layers of cobalt-based alloys deposited by laser cladding. *Surf Coat Technol* 200(14–15):4557–4563

19. Luo X, Li J, Li GJ (2015) Effect of NiCrBSi content on microstructural evolution, cracking susceptibility and wear behaviors of laser cladding WC/Ni–NiCrBSi composite coatings. *J Alloys Compd* 626:102–111
20. D'Oliveira ASC, da Silva PSC, Vilar RM (2002) Microstructural features of consecutive layers of Stellite 6 deposited by laser cladding. *Surf Coat Technol* 153(2–3):203–209
21. Fallah V, Alimardani M, Corbin SF, Khajepour A (2010) Impact of localized surface preheating on the microstructure and crack formation in laser direct deposition of Stellite 1 on AISI 4340 steel. *Appl Surf Sci* 257(5):1716–1723

Impact of Forthcoming Price Increase for Maximum Fixed Lifetime Product with Preservation Technology Investment and Price-Sensitive Demand



Mrudul Y. Jani , Manish R. Betheja , and Urmila Chaudhari 

Abstract Whenever a supplier proclaims a price rise, the effect is amplified at a predetermined point in the future. At that point, each retailer should decide whether to buy more stock or to purchase at a higher price to take benefit of the present lower price. The result of price changes on the retailer's daily replenishment strategy for deteriorating items with expiry dates is discussed in this model. Price-sensitive demand is addressed in this research and is appropriate for products whose demand falls rapidly as the price of the product rises. This article advocates two scenarios: (I) when the special-order time coincides with the retailer's replenishment time; and (II) when the special-order time occurs during the retailer's sales period. The crucial objective of this article is to determine the best ordering policies for the retailer in all cases that reduce the profit difference function between the regular order and the special order during the reduction time of the special-order quantity concerning cycle time, selling price, and investment for preservation technology. The scenarios are set up and demonstrated with numerical illustrations. Additionally, to investigate the impacts of key parameters on an optimum solution, a sensitivity analysis is carried out.

Keywords Inventory · Price increase · Price-sensitive demand · Maximum fixed lifetime · Preservation technology investment

1 Introduction

Merchandise prices have risen globally as a result of the worldwide rise in oil prices. It has become a severe issue for originalities. Especially once administrators make decisions about their inventory strategy, they wish to consider increments in trade

M. Y. Jani (✉) · M. R. Betheja
Department of Applied Sciences, Faculty of Engineering and Technology, Parul University,
Vadodara, Gujarat 391760, India

U. Chaudhari
Government Polytechnic Dahod, Dahod, Gujarat 389151, India

good prices. When a supplier proposes a potential price increase on a commodity over a fixed period, each manufacturer must determine whether to buy enough supply to meet the current low-cost contract margin before the price increase. In many industries, demand is also a big factor and it directly proportional to profit. Thus, the vendor will purchase products as per the demand and make a higher profit. Nowadays, because of the influence of COVID, customers are demanding more products like masks, sanitizers, gloves, and handwash, which are all time-dependent. Furthermore, the price has a huge effect on demand, as consumers are more interested in consuming lower priced goods. When dealing with objects that appear at the time of deterioration, the study of inventory management is critical. (For example, perishable goods and inventory that is about to expire). Products like chemicals, blood banks, pharmaceuticals, food packets, vegetables, juices, and even electronic gadgets have an expiration date. They all begin to deteriorate over time and lose their original value. Customers' main concern when ordering goods is that they want to buy products with an expiration date so that they can be stored for an extended period. As a result, scholars consider the significances of deteriorating objects over time and consider them. To diminish the decay of goods, sellers are investing some amount to conserve the item. Several methods are used to maintain the quality of deteriorating products and for sellers such as freeze-drying, radiation, electromagnetic radiation, chemical sterilization, etc.

The rise in product prices is a big source of anxiety for consumers these days. Fuel, gasoline, diesel, and raw materials costs are increasingly rising in everyday life. As a result, analysts have considered the idea of price growth. Naddor [1] was the first researcher who designed "an infinite horizon economic order quantity (EOQ) model". Then after the expectation of future price fluctuations, Lev and Soyster [2] identified "a finite horizon inventory model" and established an optimal ordering strategy. Goyal [3] strained the [2] EOQ model and offered alternative techniques to specify the optimal strategy. Lev and Weiss [4] established the formation of optimal strategies and behaviors for calculating the best strategy. Goyal et al. [5] analyzed and given a written report of inventory strategies, under one-time incentives. Khouja and Park [6] proposed a new EOQ model that incorporated the constant dynamics of price peaks and troughs into account. With small special-order quantities, Ouyang et al. [7] discovered optimum order policy under-declared price rises.

Demand is vital to the growth of every company. Benefit in every industry is determined by the goods that consumers want. Harris [8] was the initial to create a simple EOQ model that assumed constant demand. Seasonal products, electronics, cosmetics, etc., all are examples of time-dependent ingredients. As a result, the researchers considered this, and Hariga [9] developed an EOQ model under time-dependent demand. Panda et al. [10] addressed an optimal replenishment strategy for seasonal goods with time-dependent demand in a ramp-type pattern. Since demand are influenced by price. Customers' appetite for goods declines as the price of the products grows and they are mainly obsessed with and dependent on the price. As a consequence, price-dependent demands are taken into account. Hossen et al. [11] created a price and time-dependent fuzzy inventory model. Shah et al. [12] used a price credit-dependent trapezoidal demand to construct an EOQ model on

optimal strategies. Under partly backlogged shortages, Mashud et al. [13] established a mathematical model of stock and price-dependent demand. Agi and Soni [14] recently proposed a deterministic model of price-dependent demand that combined pricing and inventory management policies.

Keeping deteriorating items like vegetables, juices, drugs, and fruits in storage for an extended period would ruin them. As a consequence, when decide the optimum order technique, goods of this form that are decaying due to deterioration must be considered. As a result, researchers consider perishable goods, and Ghare and Schrader [15] remained the initial to consider a time-dependent inventory model with a steady rate of demand decrease. After that, Philip [16] cultivated a mathematical model and used three-parameters to consider the Weibull perishable rate. Yang [17] addressed a two-warehouse dilemma for decaying goods under constant demand rate. Skouri et al. [18] created an inventory model that took into account a Weibull deterioration rate, ramp style demand rate, and partial backlog. Tripathi and Tomar [19] looked at the appropriate way to set a constant rate of deterioration for time-varying demand in response to an indirect market discount. With the supposition of quadratic demand with a constant rate of deteriorating goods by following the stimulus of probable price increases, Shah et al. [20] expanded the [19] model and obtained an optimum ordering strategy. Jani et al. [21] recently addressed a mathematical model for the goods' maximum lifespan and variable demand.

As a result of diminishing products, the consistency of the goods deteriorates over time. As an effect, consumers are hesitant to purchase the product. The preservation technology can now be applied to the researcher's account to preserve consistency and reduce deterioration. Hwang et al. [22] proposed a multiproduct capacitated economic production quantity model with a one-time initial investment that reduced startup time and improved efficiency. Hsu et al. [23] identified an inventory model in which preservation technology investment was considered in the context of constant demand. With preservation technology investment, Dye and Hsieh [24] created an inventory model for deterioration rate with expiry dates. Under the sale price–trade credit quadratic in nature, Shah et al. [25] established an optimum ordering strategy and considered the maximum lifespan of deteriorated goods with preservation technology investment. Chaudhari et al. [26] recently discussed the mathematical model for the early payment scheme and spent money on perishable material preservation technology (Table 1).

Rendering to the report, before the cost increase, the vendor is more likely to take on special order to make a better profit, and the supplier is still ready to supply the unit to the manufacturer as quickly as possible. As a consequence, to understand the above business topics, this survey considers the impact of a price rise on a retailer's replacement approaches. The purpose of this report is to determine the economic order quantity model for each of the four cases. The resultings are among them: (1) The retailer deliberates the supplier's forthcoming price rise and decides whether to choose a special-order time; (2) The goods are deteriorating and have a fixed lifespan; (3) The demand for a product is proportional to its price, which falls exponentially as the price of the product grows; (4) To save the deteriorating piece, the retailer spends money on preservation technology. Additionally, two provisions refer to the retailer's

Table 1 Summary of works related to a price increase, demand, deterioration, and preservation technology investment

Source	Price increase	Demand	Deterioration	Preservation technology investment
Ouyang et al. [7]	Yes	Constant	Constant	No
Shah et al. [8]	Yes	Quadratic	Constant	No
Mashud et al. [13]	No	Stock-price dependent	Non-instantaneous	No
Hsu et al. [23]	No	Constant	Constant	Yes
Dye and Hsieh [24]	No	Constant	Constant	Yes
Shah et al. [25]	No	Price-trade credit-dependent quadratic	Maximum fixed life-time	Yes
Chaudhari et al. [26]	No	Quadratic	Maximum fixed life-time	Yes
In this paper	Yes	Price-sensitive demand	Maximum fixed life-time	Yes

replenishment policies during the special-order period. (I) when the special-order period coincides with the retailer's replenishment period; (II) when the special-order period coincides with the retailer's sales period. The special-order quantity is always higher than the standard EOQ in both cases. By minimizing the total profit difference between the regular order and the special order, this analysis defines the retailer's optimum order strategy under the expectation of future price increases. The algorithm is also designed to estimate the optimum value for a total profit difference function. Finally, numerical examples are given to test the theoretical results and sensitivity analysis is done for the best optimal solution under the main parameters.

The resulting flow of the article is controlled as follows. Section 2 demonstrates the notation and assumptions that are used to model a problem. Section 3 is about the derivation of mathematical models of the inventory problem. Section 4 provides an algorithm for determining the total profit difference function's optimality. Section 5 authorizes the resultant inventory model with numerical illustration and sensitivity analysis of the key parameters is too accomplished. Finally, Sect. 6 contains the conclusion of this article and its future possibilities.

2 Notation and Assumptions

For deriving a mathematical model of the problem, this article contains subsequent notations and assumptions.

2.1 Notations

C	Purchasing cost per unit (\$/unit)
A	Ordering cost per order (\$/order)
h	Inventory holding cost (\$/unit/unit time)
a	Scale demand, $a > 0$ (units)
b	Price elasticity constant, $0 < b < 1$ (units)
p	Selling price before the price rise(\$/unit)
$R(p)$	$= a \exp(-bp)$; demand rate (units)
m	The maximum fixed lifetime (in years)
$\theta(t)$	$= \frac{1}{1+m-t}$ deterioration rate; $0 \leq \theta(t) \leq 1$
u	Preservation technology investment before the price rise (\$/unit)
μ	Rate of preservation; $\mu > 0$
$f(u)$	$= 1 - \frac{1}{1+\mu u}$; the amount of condensed deterioration item (in years)
T	The cycle time before the price rise (in years)
$I(t)$	The level of inventory before the price rise, $0 \leq t \leq T$ (units)
Q	The order quantity; before the price rise (units)
$\pi(T, p, u)$	Overall profit throughout the cycle time T (\$/unit time)
k	Price increase of the product (\$/unit)
p_1	Selling price after the price rise (\$/unit)
u_1	Preservation technology investment after the price rise (\$/unit)
T_1	The cycle time after the price rise (in years)
$I_1(t)$	The level of inventory after the price rise, $0 \leq t \leq T_1$ (units)
Q_1	The order quantity; after the price rise (units)
$\pi_1(T_1, p_1, u_1)$	Overall profit throughout the cycle time T_1 (\$/unit time)
p_s	The selling price of the special-order quantity Q_s (\$/unit) (decision variable)
u_s	Preservation technology investment of the special-order quantity Q_s (\$/unit) (decision variable)
T_s	Depletion time for the special-order quantity Q_s (in years) (decision variable)
$I_s(t)$	The level of inventory when the special-order is adopted, $0 \leq t \leq T_s$ (units)
Q_s	Order Quantity of the special-order (units) (decision variable)
q	Remaininglevel of inventory when the special order is placed (units)
t_q	The cycle time for remaining stock q (in years)
T_q	Reduction time for quantity $Q_s + q$ (in years)
$I_q(t)$	Inventory level at the time t during the time interval $[0, T_q]$ (units)
$\pi_{S_i}(T_s, p_s, u_s)$	The overall profit of a special order during the time interval $[0, T_s]$ for the case $i, i = 1, 2$ (\$/unit time)
$\pi_{r_i}(T_s, p_s, u_s)$	The overall profit of a regular order during the time interval $[0, T_s]$ for case $i, i = 1, 2$ (\$/unit time)

(continued)

(continued)

$g_i(T_s, p_s, u_s)$	Total profit difference between the special-order and regular order during the special cycle time for case $i, i = 1, 2$ (\$/unit time)
*	The superscript denotes the optimal value

2.2 Assumptions

1. The scheme under review contracts with a single item.
2. The demand rate is $R(p) = a \exp(-bp)$, where $a > 0$ denotes the scaling demand, b denotes the constant of price elasticity. The functional form of demand rate suggests that when the selling price of the product increases then demand will decrease exponentially.
3. The instantaneous rate of deterioration is $\theta(t) = \frac{1}{1+m-t}, 0 \leq t \leq T \leq m$. For any finite value, m , the range is $0 \leq \theta(t) \leq 1$. If $m \rightarrow \infty$, then $\theta(t) \rightarrow 0$, i.e., the item is non-deteriorating.
4. The amount of reduced deterioration rate, $f(u)$, is a concave function of investment “ u ” on preservation technology, i.e., $f'(u) > 0$, and $f''(u) < 0$. WLOG, assume $f(0) = 0$.
5. To imitate the extra cost of raw textiles, the dealer announces that the unit price of a commodity will be increased by a certain amount k in the future.
6. The retailer has only one chance to refill its inventory at the current amount earlier to the price increase.
7. The refilling amount is unlimited with no lead time.
8. Shortages are not allowed.
9. During cycle time, there is not an alternative or restoration for the deteriorating item.

3 Mathematical Model

The combined impact of price-sensitive demand and maximum lifetime deteriorating goods with preservation technology investment leads to diminishing inventory levels in this report, which reflects largely on the possible effects of price rises on a retailer’s replenishment strategy. Hence, the rate of change in the level of inventory can be described by the following equation:

$$\frac{dI}{dt} = -R(p) - \theta(t)(1 - f(u))I(t) \text{ with boundary condition } I(T) = 0 \quad (1)$$

and the solution is given by

$$I(t) = \frac{-a(\mu u + 1) \left[(1 + m - T)^{\frac{\mu u}{\mu u + 1}} (1 + m - t)^{\frac{1}{\mu u + 1}} - m + t - 1 \right] \exp(-bp)}{\mu u} \tag{2}$$

Also, by using $I(0) = Q$, gives

$$Q = I(0) = \frac{-a(\mu u + 1) \left[(1 + m - T)^{\frac{\mu u}{\mu u + 1}} (1 + m)^{\frac{1}{\mu u + 1}} - m - 1 \right] \exp(-bp)}{\mu u} \tag{3}$$

Now, before the price increase, the generated sales revenue of retailer, per cycle time T can be evaluated as

$$SR = p \int_0^T R(p) dt.$$

Next, before the price increase, the retailer’s total cost components, per cycle time T is comprised by.

• Ordering cost per unit;	$OC = A$
• Purchasing cost;	$PC = CQ$
• Average holding cost per unit;	$HC = hC \int_0^T I(t) dt$
• Preservation technology investment;	$PTI = uT$

Before the price increase and on the original purchase rate C , the retailer implements a standard economic order strategy. Therefore, the retailer’s total profit before the price increase can be evaluated as

$$\begin{aligned} \pi(T, p, u) &= \frac{1}{T} (SR - OC - PC - HC - PTI) \\ &= \frac{1}{T} \left(p \int_0^T R(p) dt - A - CQ - hC \int_0^T I(t) dt - uT \right). \end{aligned} \tag{4}$$

By applying the necessary conditions $\frac{\partial \pi(T, p, u)}{\partial T} = 0$, $\frac{\partial \pi(T, p, u)}{\partial p} = 0$, and $\frac{\partial \pi(T, p, u)}{\partial u} = 0$ in (4), it is easily checked that $\pi(T, p, u)$ is a concave function T , p and u .

Hence, there exists a unique value for T (say T^*), p (say p^*), u (say u^*) which maximizes $\pi(T, p, u)$.

Now, the upcoming price increase is announced by the supplier, k , per unit, so the unit price changes $C + k$ from the original purchasing cost C . Thus, the inventory level at the time t and order quantity Q_1 becomes

$$I_1(t) = \frac{-a(\mu u_1 + 1) \left[(1 + m - T_1)^{\frac{\mu u_1}{\mu u_1 + 1}} (1 + m - t)^{\frac{1}{\mu u_1 + 1}} - m + t - 1 \right] \exp(-bp_1)}{\mu u_1} \tag{5}$$

and $Q_1 = I_1(0) = \frac{-a(\mu u_1 + 1) \left[(1 + m - T_1)^{\frac{\mu u_1}{\mu u_1 + 1}} (1 + m)^{\frac{1}{\mu u_1 + 1}} - m - 1 \right] \exp(-bp_1)}{\mu u_1}$. (6)

Now, the retailer’s sales revenue, per cycle time T_1 can be evaluated as

$$SR_1 = p_1 \int_0^{T_1} R(p_1) dt.$$

Next, after the price increase, the retailer’s total cost components, per cycle time T_1 is comprised by

• Purchasing cost;	$PC_1 = (C + k)Q_1$
• Average holding cost per unit	$HC_1 = h(C + k) \int_0^{T_1} I_1(t) dt$
• Preservation technology investment;	$PTI_1 = u_1 T_1$

Therefore, the total profit of the retailer (i.e., $\pi_1(T_1, p_1, u_1)$) during the replenishment period T_1 is given by

$$\begin{aligned} \pi_1(T_1, p_1, u_1) &= \frac{1}{T_1} (SR_1 - OC - PC_1 - HC_1 - PTI_1) \\ &= \frac{1}{T_1} \left(p_1 \int_0^{T_1} R(p_1) dt - A - (C + k)Q_1 - h(C + k) \int_0^{T_1} I_1(t) dt - u_1 T_1 \right). \end{aligned} \tag{7}$$

Similarly, there are unique values T_1 (say T_1^*), p_1 (say p_1^*), u_1 (say u_1^*) that maximize $\pi_1(T_1, p_1, u_1)$. The values T_1^* , p_1^* and u_1^* are obtained by solving the equations

$$\frac{d\pi_1(T_1, p_1, u_1)}{dT_1} = 0, \quad \frac{d\pi_1(T_1, p_1, u_1)}{dp_1} = 0, \quad \text{and} \quad \frac{d\pi_1(T_1, p_1, u_1)}{du_1} = 0$$

Because the supplier may supply the retailer with an increasing number of products, the retailer may consider placing a special order before the price increase. As stated above, two conditions may arise for special-order times: (1) the special-order time coincides with the retailer’s replenishment time; and (2) the special-order time occurs during the retailer’s sales period. The primary goal of this model is to find the

best special-order quantity that minimizes the profit difference between regular and special orders. For the above-mentioned two factors, this analysis now formulates the profit difference function.

3.1 Case 1: The Special-Order Time Coincides with the Retailer’s Replenishment Time

Here, the retailer adopts the special-order with its regular replenishment order and if the retailer orders Q_s units then the level of inventory at a time t can be given by

$$I_s(t) = \frac{-a(\mu u_s + 1) \left[(1 + m - T_s)^{\frac{\mu u_s}{\mu u_s + 1}} (1 + m - t)^{\frac{1}{\mu u_s + 1}} - m + t - 1 \right] \exp(-bp_s)}{\mu u_s} \tag{8}$$

and the special-order quantity Q_s is given by

$$Q_s = I_s(0) = \frac{-a(\mu u_s + 1) \left[(1 + m - T_s)^{\frac{\mu u_s}{\mu u_s + 1}} (1 + m)^{\frac{1}{\mu u_s + 1}} - m - 1 \right] \exp(-bp_s)}{\mu u_s}. \tag{9}$$

Now, for this case, the generated sales revenue for the retailer, per cycle time T_s can be evaluated as

$$SR_s = p_s \int_0^{T_s} R(p_s) dt.$$

Next, the total cost components per unit time for cycle time T_s is comprised of

• Purchasing cost;	$PC_s = C Q_s$
• Average holding cost per unit	$HC_s = hC \int_0^{T_s} I_s(t) dt$
• Preservation technology investment;	$PTI_s = u_s T_s$

Therefore, for the coinciding special order, the net profit during the cycle time T_s can be evaluated as

$$\begin{aligned} \pi_{S_1}(T_s, p_s, u_s) &= (SR_s - OC - PC_s - HC_s - PTI_s) \\ &= p_s \int_0^{T_s} R(p_s) dt - A - C Q_s - hC \int_0^{T_s} I_s(t) dt - u_s T_s. \end{aligned} \tag{10}$$

If the retailer does not wish to place a special order, as seen in Fig. 1, the retailer orders Q^* units at the initial cost price before the price rise, C . As a consequence, before a price rise, the profit of a regular order is given by

$$\frac{1}{T^*} \left(p^* \int_0^{T^*} R(p^*) dt - A - CQ^* - hC \int_0^{T^*} I(t) dt - u^* T^* \right) \tag{11}$$

which is close to Eq. (4)

Now, after the price increase, the retailer again orders Q_1^* units at the purchasing cost, $C + k$. Thus, the profit of regular orders after the price increase is comparable to Eq. (7) and is given by

$$\frac{T_s - T^*}{T_1^*} \left(p_1^* \int_0^{T_1^*} R(p_1^*) dt - A - (C + k)Q_1^* - h(C + k) \int_0^{T_1^*} I_1(t) dt - u_1^* T_1^* \right). \tag{12}$$

Therefore, for a regular order, the total profit, by using Eqs. (11) and (12) is given by

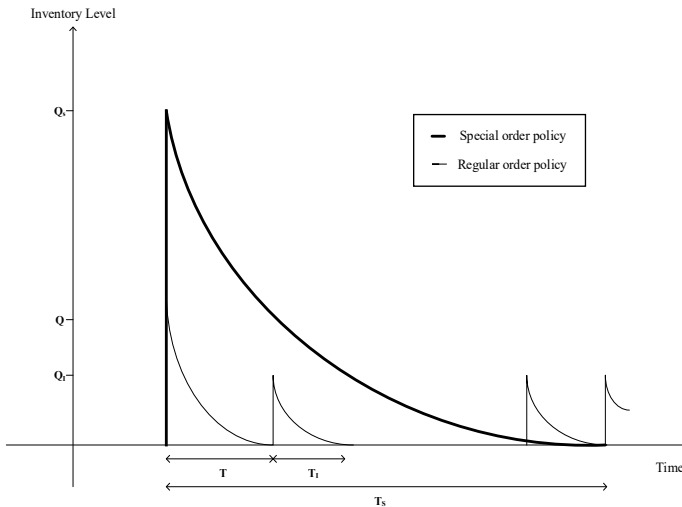


Fig. 1 Special versus regular order policies when the special-order time coincides with the retailer’s replenishment

$$\pi_{r_1}(T_s, p_s, u_s) = \frac{1}{T^*} \left(p^* \int_0^{T^*} R(p^*) dt - A - CQ^* - hC \int_0^{T^*} I(t) dt - u^* T^* \right) + \frac{T_s - T^*}{T_1^*} \left(p_1^* \int_0^{T_1^*} R(p_1^*) dt - A - (C+k)Q_1^* - h(C+k) \int_0^{T_1^*} I_1(t) dt - u_1^* T_1^* \right). \tag{13}$$

Hence, by using (10) and (13), the profit difference function for the coincide special-order is given by

$$g_1(T_s, p_s, u_s) = \pi_{r_1}(T_s, p_s, u_s) - \pi_{s_1}(T_s, p_s, u_s) = \frac{1}{T^*} \left(p^* \int_0^{T^*} R(p^*) dt - A - CQ^* - hC \int_0^{T^*} I(t) dt - u^* T^* \right) + \frac{T_s - T^*}{T_1^*} \left(p_1^* \int_0^{T_1^*} R(p_1^*) dt - A - (C+k)Q_1^* - h(C+k) \int_0^{T_1^*} I_1(t) dt - u_1^* T_1^* \right) - p_s \int_0^{T_s} R(p_s) dt - A - CQ_s - hC \int_0^{T_s} I_s(t) dt - u_s T_s. \tag{14}$$

3.2 Case 2: The Special-Order Time Occurs During the Retailer’s Sales Period

Here, the retailer places the special order during its selling time. From Fig. 2, when only q units are left in the retailer’s inventory, at that time, the retailer places its special order and orders Q_s units. Thus, the inventory level immediately reaches $Q_s + q$ when the retailer received the special order and that level can be evaluated as

$$Q_s + q = \frac{-a(\mu u_s + 1) \left[(1 + m - T_s)^{\frac{\mu u_s}{\mu u_s + 1}} (1 + m)^{\frac{1}{\mu u_s + 1}} - m - 1 \right] \exp(-bp_s)}{\mu u_s} + \frac{-a(\mu u^* + 1) \left[(1 + m - (T^* - t_q))^{\frac{\mu u^*}{\mu u^* + 1}} (1 + m)^{\frac{1}{\mu u^* + 1}} - m - 1 \right] \exp(-bp^*)}{\mu u^*}. \tag{15}$$

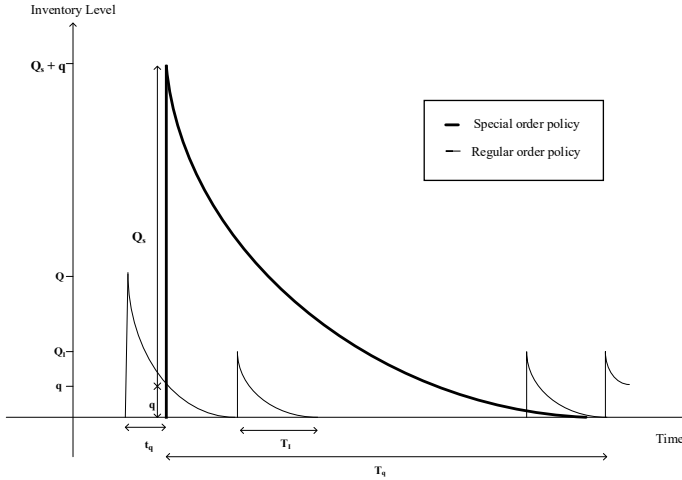


Fig. 2 Special versus regular order policies when the special-order time occurs during the retailer’s sales period (Shah et al. [20])

Moreover, during the time interval $[0, T_q]$, the level of inventory at any time t can be given by

$$I_q(t) = \frac{-a(\mu u_s + 1) \left[(1 + m - T_q)^{\frac{\mu u_s}{\mu u_s + 1}} (1 + m - t)^{\frac{1}{\mu u_s + 1}} - m + t - 1 \right] \exp(-bp_s)}{\mu u_s} \tag{16}$$

Since, $I_q(0) = Q_s + q$, By equating Eqs. (15) and (16), gives

$$\begin{aligned} & \frac{-a(\mu u_s + 1) \left[(1 + m - T_q)^{\frac{\mu u_s}{\mu u_s + 1}} (1 + m)^{\frac{1}{\mu u_s + 1}} - m - 1 \right] \exp(-bp_s)}{\mu u_s} \\ &= \frac{-a(\mu u_s + 1) \left[(1 + m - T_s)^{\frac{\mu u_s}{\mu u_s + 1}} (1 + m)^{\frac{1}{\mu u_s + 1}} - m - 1 \right] \exp(-bp_s)}{\mu u_s} \\ &+ \frac{-a(\mu u_s + 1) \left[(1 + m - (T^* - t_q))^{\frac{\mu u_s}{\mu u_s + 1}} (1 + m)^{\frac{1}{\mu u_s + 1}} - m - 1 \right] \exp(-bp_s)}{\mu u_s} \end{aligned} \tag{17}$$

Thus, T_q can be expressed in terms of T_s as

$$T_q = -\exp\left(\frac{1}{\mu u}\right) \left(\ln \left(\frac{1}{u_s(\mu u + 1)} \left(\begin{aligned} &2F \exp(-bp_s)m\mu u u_s - F \exp(-bp)m\mu u u_s - \\ &G(1+m-T+tq) \frac{\mu u_s}{\mu u_s+1} \exp(-bp_s)\mu u u_s - \\ &G(1+m-T)_s \frac{\mu u_s}{\mu u_s+1} \exp(-bp_s)\mu u u_s + \\ &2F \exp(-bp_s)\mu u u_s - F \exp(-bp)\mu u u_s + \\ &2F \exp(-bp_s)mu - F \exp(-bp)mu_s - \\ &G(1+m-T+tq) \frac{\mu u_s}{\mu u_s+1} \exp(-bp_s)u - \\ &G(1+m-T_s) \frac{\mu u_s}{\mu u_s+1} \exp(-bp_s)u + \\ &2F \exp(-bp_s)u - F \exp(-bp)u_s \end{aligned} \right) + bp(\mu u + 1) + 1 + m \right) \quad (18)$$

where $(1+m)^{\frac{-1}{\mu u+1}} = F$, $(1+m)^{\frac{\mu(u-u_s)}{(\mu u+1)(\mu u_s+1)}} = G$.

Here, in this case, the average holding cost, per unit time T_q , for the retailer’s is comprised of

$$HC_q = hC \int_0^{T_q} I_q(t) dt.$$

Therefore, for the sales period special order, the overall profit during the cycle time T_s can be evaluated as

$$\begin{aligned} \pi_{S_2}(T_s, p_s, u_s) &= (SR_s - OC - PC_s - HC_q - PTI_s) \\ &= p_s \int_0^{T_s} R(p_s)dt - A - CQ_s - hC \int_0^{T_q} I_q(t)dt - u_s T_s. \end{aligned} \quad (19)$$

Conversely, if the retailer doesn’t want to place any special order, then the retailer chooses its regular order and it will consist of two stages: (1) the retailer orders Q^* units before the price increase and (2) orders Q_1^* units after the price increase.

In phase 1, the retailer only earns the profit through the depletion time of remaining q . Thus, the profit before the price increase is given by

$$\frac{T^* - t_q}{T^*} \left(p^* \int_0^{T^*} R(p^*)dt - A - CQ^* - hC \int_0^{T^*} I(t)dt - u^* T^* \right) \quad (20)$$

and, in phase 2, the price is increased k per unit, so the purchasing cost becomes $C + k$. Thus, the profit after the price increase is given by

$$\frac{T_q - (T^* - t_q)}{T_1^*} \left(p_1^* \int_0^{T_1^*} R(p_1^*) dt - A - (C + k)Q_1^* - h(C + k) \int_0^{T_1^*} I_1(t) dt - u_1^* T_1^* \right). \quad (21)$$

Therefore, for a regular order, the total profit by using Eqs. (20) and (21) is given by

$$\begin{aligned} \pi_{r_2}(T_s, p_s, u_s) &= \frac{T^* - t_q}{T^*} \left(p^* \int_0^{T^*} R(p^*) dt - A - CQ^* - hC \int_0^{T^*} I(t) dt - u^* T^* \right) \\ &\quad + \frac{T_q - (T^* - t_q)}{T_1^*} \\ &\quad \left(p_1^* \int_0^{T_1^*} R(p_1^*) dt - A - (C + k)Q_1^* - h(C + k) \int_0^{T_1^*} I_1(t) dt - u_1^* T_1^* \right). \end{aligned} \quad (22)$$

Hence, by using (21) and (22), the profit difference function during the sales period special order is given by

$$\begin{aligned} g_2(T_s, p_s, u_s) &= \pi_{r_2}(T_s, p_s, u_s) - \pi_{S_2}(T_s, p_s, u_s) \\ &= \frac{T^* - t_q}{T^*} \left(p^* \int_0^{T^*} R(p^*) dt - A - CQ^* - hC \int_0^{T^*} I(t) dt - u^* T^* \right) \\ &\quad + \frac{T_q - (T^* - t_q)}{T_1^*} \\ &\quad \left(p_1^* \int_0^{T_1^*} R(p_1^*) dt - A - (C + k)Q_1^* - h(C + k) \int_0^{T_1^*} I_1(t) dt - u_1^* T_1^* \right) \\ &\quad - p_s \int_0^{T_s} R(p_s) dt - A - CQ_s - hC \int_0^{T_q} I_q(t) dt - u_s T_s. \end{aligned} \quad (23)$$

Remark It's worth reminding that the retailer could place the special order only if the total profit is positive; otherwise, the retailer will disregard the chance of using a special order.

4 Algorithm

For both cases, the total profit difference function is given by

$$g_i(T_s, p_s, u_s) = \pi_{r_i}(T_s, p_s, u_s) - \pi_{s_i}(T_s, p_s, u_s); \quad i = 1, 2.$$

Here, this study implements the following algorithm to check the optimality of decision parameters in mathematical software Maple *XVIII*.

Step 1: Apply the necessary conditions

$$\frac{\partial g_i(T_s, p_s, u_s)}{\partial T_s} = 0, \quad \frac{\partial g_i(T_s, p_s, u_s)}{\partial p_s} = 0, \quad \frac{\partial g_i(T_s, p_s, u_s)}{\partial u_s} = 0; \quad i = 1, 2.$$

for the optimal values T_s^* , p_s^* and u_s^* to making the total profit difference function minimum or maximum.

Step 2: Find all the possible second-order partial derivatives

$$\begin{aligned} & \frac{\partial^2 g_i(T_s^*, p_s^*, u_s^*)}{\partial T_s^2}, \quad \frac{\partial^2 g_i(T_s^*, p_s^*, u_s^*)}{\partial T_s \partial p_s}, \quad \frac{\partial^2 g_i(T_s^*, p_s^*, u_s^*)}{\partial T_s \partial u_s}, \quad \frac{\partial^2 g_i(T_s^*, p_s^*, u_s^*)}{\partial p_s \partial T_s}, \\ & \frac{\partial^2 g_i(T_s^*, p_s^*, u_s^*)}{\partial p_s^2}, \quad \frac{\partial^2 g_i(T_s^*, p_s^*, u_s^*)}{\partial p_s \partial u_s}, \quad \frac{\partial^2 g_i(T_s^*, p_s^*, u_s^*)}{\partial u_s \partial T_s}, \quad \frac{\partial^2 g_i(T_s^*, p_s^*, u_s^*)}{\partial u_s \partial p_s}, \\ & \frac{\partial^2 g_i(T_s^*, p_s^*, u_s^*)}{\partial u_s^2} \end{aligned}$$

Step 3: Generate the Hessian Matrix

$$H_i(T_s^*, p_s^*, u_s^*) = \begin{bmatrix} \frac{\partial^2 g_i(T_s^*, p_s^*, u_s^*)}{\partial T_s^2} & \frac{\partial^2 g_i(T_s^*, p_s^*, u_s^*)}{\partial T_s \partial p_s} & \frac{\partial^2 g_i(T_s^*, p_s^*, u_s^*)}{\partial T_s \partial u_s} \\ \frac{\partial^2 g_i(T_s^*, p_s^*, u_s^*)}{\partial p_s \partial T_s} & \frac{\partial^2 g_i(T_s^*, p_s^*, u_s^*)}{\partial p_s^2} & \frac{\partial^2 g_i(T_s^*, p_s^*, u_s^*)}{\partial p_s \partial u_s} \\ \frac{\partial^2 g_i(T_s^*, p_s^*, u_s^*)}{\partial u_s \partial T_s} & \frac{\partial^2 g_i(T_s^*, p_s^*, u_s^*)}{\partial u_s \partial p_s} & \frac{\partial^2 g_i(T_s^*, p_s^*, u_s^*)}{\partial u_s^2} \end{bmatrix}; \quad i = 1, 2.$$

to obtain the concavity of the total profit difference.

Step 4: In Hessian Matrix, assign theoretical values to inventory parameters.

Step 5: Find eigenvalues of Hessian Matrix $H_i(T_s^*, p_s^*, u_s^*)$; $i = 1, 2$.

Step 6: According to Cardenas-Barron et al. [27], if all the eigenvalues of the Hessian matrix at the solution (T_s^*, p_s^*, u_s^*) are positive, then the total profit difference function $g_i(T_s^*, p_s^*, u_s^*)$ has a minimum value at the solution and if all are negative, then the total profit difference $g_i(T_s^*, p_s^*, u_s^*)$ has a maximum value at the solution.

5 Numerical Illustrations and Sensitivity Analysis

5.1 Numerical Illustrations

For the numerical illustrations, the theoretical data are given in Table 2 and the optimum solution is shown in Table 3.

Case 1 has the best optimal solution in the above two scenarios since the total profit difference is minimal and positive. This consequence validates that if the retailer follows the case 1 approach, the profits of the regular and special orders are virtually equivalent. This means that if the retailer uses a special order that coincides with its regular order, the retailer would probably double its profit.

Now, by applying the above algorithm, this paper next shows the total profit difference function $g_1(T_s^*, p_s^*, u_s^*)$ has a minimum value at the solution.

Table 2 Parameter measures for the numerical illustrations

Inventory parameters	Examples	
	Case 1	Case 2
a (units)	4000	4000
b	0.04	0.04
h (\$/unit/unit time)	0.1	0.1
C (\$/unit)	100	100
A (\$/order)	100	100
m (in years)	2	2
k (\$/unit)	6	6
$\mu > 0$	8.8	8.8
q (units)	–	20

Table 3 Optimum solution

	Case 1	Case 2
T_s (in years)	1.542	3.000
p_s (in \$)	133.15	154.52
u_s (in \$)	8.52	10.79
Q_s (units)	30.12	25.09
$\pi_{S_i}(T_s, p_s, u_s)$ (in \$)	636.78	1025.93
$\pi_{r_i}(T_s, p_s, u_s)$ (in \$)	636.80	748.01
$g_i(T_s, p_s, u_s) = \pi_{r_i}(T_s, p_s, u_s) - \pi_{S_i}(T_s, p_s, u_s)$ (in \$)	0.02	-277.93

Step 1: By applying the necessary conditions

$$\frac{\partial g_1(T_s, p_s, u_s)}{\partial T_s} = 0, \quad \frac{\partial g_1(T_s, p_s, u_s)}{\partial p_s} = 0, \quad \frac{\partial g_1(T_s, p_s, u_s)}{\partial u_s} = 0$$

in mathematical software Maple *XVIII*, the optimal values are

$$T_s^* = 1.542 \text{ years}, \quad p_s^* = \$ 133.15 \text{ and } u_s^* = \$8.52$$

Step 2: The values of all possible second-order partial derivatives are

$$\begin{aligned} \frac{\partial^2 g_1(T_s^*, p_s^*, u_s^*)}{\partial T_s^2} &= 214.93, & \frac{\partial^2 g_1(T_s^*, p_s^*, u_s^*)}{\partial T_s \partial p_s} &= -6.46, & \frac{\partial^2 g_1(T_s^*, p_s^*, u_s^*)}{\partial T_s \partial u_s} &= -1.34, \\ \frac{\partial^2 g_1(T_s^*, p_s^*, u_s^*)}{\partial p_s \partial T_s} &= -6.46, & \frac{\partial^2 g_1(T_s^*, p_s^*, u_s^*)}{\partial p_s^2} &= 1.99, & \frac{\partial^2 g_1(T_s^*, p_s^*, u_s^*)}{\partial p_s \partial u_s} &= 0.06, \\ \frac{\partial^2 g_1(T_s^*, p_s^*, u_s^*)}{\partial u_s \partial T_s} &= -1.34, & \frac{\partial^2 g_1(T_s^*, p_s^*, u_s^*)}{\partial u_s \partial p_s} &= 0.06, & \frac{\partial^2 g_1(T_s^*, p_s^*, u_s^*)}{\partial u_s^2} &= 0.36 \end{aligned}$$

Step 3: The Hessian Matrix is given by

$$H_1(T_s^*, p_s^*, u_s^*) = \begin{bmatrix} \frac{\partial^2 g_1(T_s^*, p_s^*, u_s^*)}{\partial T_s^2} & \frac{\partial^2 g_1(T_s^*, p_s^*, u_s^*)}{\partial T_s \partial p_s} & \frac{\partial^2 g_1(T_s^*, p_s^*, u_s^*)}{\partial T_s \partial u_s} \\ \frac{\partial^2 g_1(T_s^*, p_s^*, u_s^*)}{\partial p_s \partial T_s} & \frac{\partial^2 g_1(T_s^*, p_s^*, u_s^*)}{\partial p_s^2} & \frac{\partial^2 g_1(T_s^*, p_s^*, u_s^*)}{\partial p_s \partial u_s} \\ \frac{\partial^2 g_1(T_s^*, p_s^*, u_s^*)}{\partial u_s \partial T_s} & \frac{\partial^2 g_1(T_s^*, p_s^*, u_s^*)}{\partial u_s \partial p_s} & \frac{\partial^2 g_1(T_s^*, p_s^*, u_s^*)}{\partial u_s^2} \end{bmatrix}$$

Step 4: The theoretical values to the inventory parameters in Hessian Matrix are

$$H_1(T_s^*, p_s^*, u_s^*) = \begin{bmatrix} 214.93 & -6.46 & -1.34 \\ -6.46 & 1.19 & 0.06 \\ -1.34 & 0.06 & 0.36 \end{bmatrix}$$

Step 5: The eigenvalues of the Hessian Matrix $H_1(T_s^*, p_s^*, u_s^*)$ are 0.35, 1.01, and 215.14.

Step 6: One can observe in step 5, all the eigenvalues are positive, hence it suggests that the profit difference function $g_1(T_s^*, p_s^*, u_s^*)$ has a minimum value at the solution (T_s^*, p_s^*, u_s^*) .

$$\text{(i.e., } g_1(T_s^*, p_s^*, u_s^*) = 0.02 \text{ is minimum at } (T_s^*, p_s^*, u_s^*) = (1.542, 133.15, 8.52) \text{)}$$

5.2 Sensitivity Analysis for the Inventory Parameters

In this portion, sensitivity analysis is implemented on ex. (1) and reflects a shift in decision variables by adjusting inventory parameters up to -20% , -10% , 10% , and 20% along with the overall profit difference function.

The following insights are obtained from Table 4:

1. Once the purchasing cost C increase, both the profit difference function $g_i(T_s, p_s, u_s)$ and the special-order quantity Q_s decrease. The simple commercial clarification for this is that if the purchasing cost is higher, the retailer will place a special order for a lower quantity, ensuing in a minimum profit difference. Moreover, the optimal special-order quantity and the profit difference function both are sensitive to the purchasing cost.
2. The price elasticity constant and purchase cost increases cycle time speedily although scale demand, ordering cost, and holding cost of the product decreases cycle time slowly. Often, the maximum fixed lifetime of the product and rate of preservation increases cycle time slowly.
3. The parameter (h), a maximum fixed lifetime of the product, and purchase cost increase the price of selling the product slowly. However, scale demand, price elasticity constant, ordering cost, and the parameter (μ) decreases the price of selling the product slowly.
4. The price elasticity constant, holding cost of the product, purchase cost, a maximum fixed lifetime, and rate of preservation decrease investment slowly. However, scale demand and ordering cost increase preservation technology investment slowly.
5. The parameter (a), (A), a maximum fixed lifetime of the product, and (μ) increases the special-order quantity slowly although the holding cost of the product decreases the special-order quantity slowly. However, price elasticity constant and purchase cost decrease the special-order quantity rapidly.
6. The parameter (a) increases the profit difference function rapidly although the parameter (b) and purchase cost decreases the profit difference function rapidly. However, the holding cost of the product rises the profit difference function slowly wherever a maximum fixed lifetime, ordering cost, and the rate of preservation decreases the profit difference function slowly.

From the result shown in Table 5, one can see that as the unit price of the product increases the cycle time increases speedily through the selling price of the product, preservation technology investment, and the special-order quantity increase slowly. However, the profit difference function decreases slowly. The graph of parameter k and profit difference function $g_1(T_s, p_s, u_s)$ is shown in Fig. 3, which suggests that the price increase has a positive effect on the total profit difference function as the price of the products increases the difference will decrease and tends to the minimum.

Table 4 Sensitivity analysis

Parameters	Change %	Values	T_s (in years)	p_s (in \$)	u_s (in\$)	Q_s (units)	π_{S_1} (in \$)	π_{r_1} (in \$)	g_1 (in \$)
<i>a</i>	-20	3600	1.665	133.86	7.92	25.32	516.68	476.50	-40.18
	-10	3800	1.598	133.47	8.23	27.75	577.48	556.16	-21.32
	0	4000	1.542	133.15	8.53	30.12	636.78	636.80	0.02
	10	4200	1.494	132.88	8.81	32.45	694.83	718.29	23.46
	20	4400	1.453	132.65	9.08	34.73	751.80	800.51	48.71
<i>b</i>	-20	0.032	1.197	137.47	11.56	58.98	1724.96	2257.39	532.43
	-10	0.036	1.348	134.84	9.91	42.16	1054.18	1217.25	163.07
	0	0.04	1.542	133.15	8.53	30.12	636.78	636.80	0.02
	10	0.044	1.796	132.34	7.39	21.39	369.92	312.77	-57.15
	20	0.048	2.131	132.43	6.44	14.92	194.52	133.71	-60.81
<i>h</i>	-20	0.08	1.761	132.52	9.42	35.29	761.66	713.56	-48.10
	-10	0.09	1.642	132.85	8.93	32.47	693.55	672.01	-21.54
	0	0.1	1.542	133.15	8.53	30.12	636.78	636.80	0.02
	10	0.11	1.458	133.45	8.19	28.14	588.69	606.42	17.73
	20	0.12	1.385	133.73	7.89	26.44	547.36	579.81	32.45
<i>C</i>	-20	80	1.419	110.92	11.30	67.38	1563.72	1854.56	290.84
	-10	90	1.458	121.88	9.78	44.65	998.26	1099.90	101.64
	0	100	1.542	133.15	8.53	30.12	636.78	636.80	0.02
	10	110	1.679	144.86	7.49	20.56	398.63	353.11	-45.52
	20	120	1.878	157.17	6.62	14.08	237.05	180.84	-56.21
<i>A</i>	-20	80	1.426	132.55	8.20	28.54	618.93	669.87	50.94
	-10	90	1.486	132.86	8.37	29.36	628.59	652.87	24.28
	0	100	1.542	133.15	8.53	30.12	636.78	636.80	0.02
	10	110	1.597	133.44	8.68	30.84	643.72	621.53	-22.19
	20	120	1.649	133.71	8.83	31.50	649.56	606.95	-42.61
<i>m</i>	-20	1.6	1.530	133.13	9.34	29.92	630.29	632.19	1.90
	-10	1.8	1.537	133.15	8.91	30.03	633.82	634.70	0.88
	0	2	1.542	133.15	8.53	30.12	636.78	636.80	0.02
	10	2.2	1.547	133.16	8.20	30.20	639.31	638.58	-0.73
	20	2.4	1.551	133.17	7.903	30.27	641.50	640.12	-1.38
μ	-20	7.04	1.533	133.16	9.49	29.96	630.92	632.68	1.76
	-10	7.92	1.538	133.16	8.97	30.04	634.09	634.90	0.81
	0	8.8	1.542	133.15	8.53	30.12	636.78	636.80	0.02
	10	9.68	1.546	133.15	8.15	30.19	639.12	638.43	-0.69
	20	10.56	1.549	133.15	7.82	30.25	641.17	639.88	-1.29

Table 5 Effect of the parameter k (Unit price increase) on $T_s, p_s, u_s, Q_s, \pi_{S_1}(T_s, p_s, u_s), \pi_{r_1}(T_s, p_s, u_s)$, and $g_1(T_s, p_s, u_s)$

Parameters	Values	T_s (in years)	p_s (in \$)	u_s (in\$)	Q_s (units)	π_{S_1} (in \$)	π_{r_1} (in \$)	g_1 (in \$)
k	2	1.130	130.99	7.29	24.03	490.59	523.02	32.43
	3	1.235	131.55	7.62	25.71	530.98	557.86	26.88
	4	1.339	132.09	7.94	27.28	568.73	588.23	19.49
	5	1.441	132.63	8.24	28.75	603.96	614.44	10.48
	6	1.542	133.15	8.53	30.12	636.78	636.80	0.02
	7	1.642	133.68	8.81	31.41	667.31	655.60	-11.71
	8	1.739	134.19	9.08	32.60	695.65	671.09	-24.56

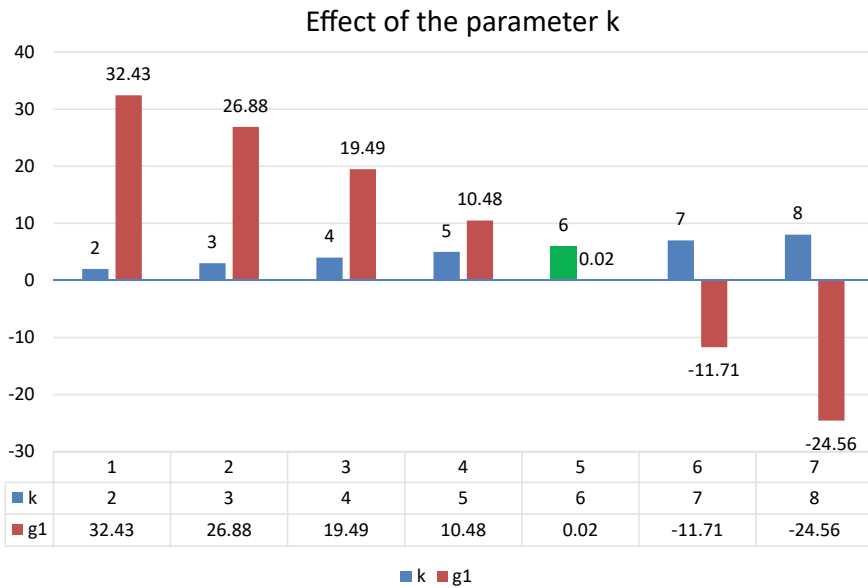


Fig. 3 Graph of profit difference function w.r.t inventory parameter k

6 Conclusions

This study investigates the influence of a supplier’s announcement of future price increases on a retailer’s replenishment strategy. Price-dependent demand is discussed in this study; which suggests that demand declines speedily as the price of the products rises. Besides, products are deteriorating over time and also have a maximum fixed lifetime. In addition, to preserve the deteriorating inventories, buyers invest some amount on preservation technology investment. Moreover, this work deliberates the two possible scenarios for the special-order time: (I) when the special-order time

coincides with the retailer's replenishment time (II) when the special-order time occurs during the retailer's sales period. The consequences and observations of this paper are (1) to reach a minimum profit difference, the retailer should order a special order that coincides with the replenishment time; (2) The higher the unit price, the more likely it is that the retailer would need to place a special order to take advantage of the current low price; (3) increasing a product's maximum lifetime and preservation rate decreases the total profit difference; (4) increasing holding costs raises the total profit difference; (5) when the manufacturer has a special-order period during the sales period, the profit differential function will be minimized by providing a higher residual inventory. The main aim of this article is to minimize the total profit difference between the regular order and the special order. The results are verified using numerical results, and an algorithm for optimizing the total profit difference function is constructed. Lastly, the sensitivity analysis is performed on the optimal solution concerning the key parameters. Current research has several possible extensions like the model can be further comprehensive by allowing shortages, trade credit, quantity discounts, and take more items at a time. Also, it can be additional deliberate for probabilistic demand, fuzzy stochastic demand, stock time-dependent demand, etc.

References

1. Naddor E (1966) Inventory systems. Wiley, New York, NY
2. Lev B, Soyster AL (1979) An inventory model with finite horizon and price changes. *J Oper Res Soc* 30(1):43–53
3. Goyal SK (1979) A note on the paper: an inventory model with the finite horizon and price changes. *J Oper Res Soc* 30(9):839–842
4. Lev B, Weiss HJ (1990) Inventory models with cost changes. *Oper Res* 38(1):53–63
5. Goyal SK, Srinivasan GF, Arcelus F (1991) One-time only incentives and inventory policies. *Eur J Oper Res* 54(1):1–6
6. Khouja M, Park S (2003) Optimal lot sizing under continuous price decrease. *Omega* 31(6):539–545
7. Ouyang LY, Wu KS, Yang CT, Yen HF (2014) Optimal order policy in response to the announced price increase for deteriorating items with limited special-order quantity. *Int J Syst Sci* 47(3):718–729
8. Harris FW (1913) How many parts to make at once. *Fact Mag Manag* 10(2):135–136, 152
9. Hariga M (1996) Optimal EOQ models for deteriorating items with time-varying demand. *J Oper Res Soc* 47(10):1228–1246
10. Panda S, Senapati S, Basu M (2008) Optimal replenishment policy for perishable seasonal products in a season with ramp-type time-dependent demand. *Comput Ind Eng* 54(2):301–314
11. Hossen MA, Hakim MdA, Ahmed SS, Uddin MS (2016) An inventory model with price and time-dependent demand with fuzzy valued inventory costs under inflation. *Ann Pure Appl Math* 11(2):21–32
12. Shah NH, Jani MY, Chaudhari B (2017) Retailer's optimal policies for price-credit dependent trapezoidal demand under two-level trade credit. *Int J Oper Quant Manag* 23(02):115–130
13. Mashud A, Khan M, Uddin M, Islam M (2018) A non-instantaneous inventory model having different deterioration rates with stock and price dependent demand under partially backlogged shortages. *Uncertain Supply Chain Manag* 6(1):49–64

14. Agi MAN, Soni HN (2020) Joint pricing and inventory decisions for perishable products with age-, stock-, and price-dependent demand rate. *J Oper Res Soc* 71(1):85–99
15. Ghare PM, Schrader GH (1963) A model for the exponentially decaying inventory system. *J Ind Eng* 14(5):238–243
16. Philip GC (1974) A generalized EOQ model for items with weibull distribution deterioration. *AIIE Trans* 6(2):159–162
17. Yang HL (2004) Two-warehouse inventory models for deteriorating items with shortages under inflation. *Eur J Oper Res* 157(2):344–356
18. Skouri K, Konstantaras I, Papachristos S, Ganas I (2009) Inventory models with ramp type demand rate, partial backlogging, and Weibull deterioration rate. *Eur J Oper Res* 192(1):79–92
19. Tripathi RP, Tomar SS (2015) Optimal order policy for deteriorating items with time-dependent demand in response to temporary price discounts linked to order quantity. *Int J Math Anal* 23(9):1095–1109
20. Shah NH, Jani MY, Chaudhari UB (2016) Impact of future price increase on ordering policies for deteriorating items under quadratic demand. *Int J Ind Eng Comput* 7(3):423–436
21. Jani MY, Shah NH, Chaudhari UB (2020) Inventory control policies for time-dependent deteriorating item with variable demand and two-level order linked trade credit. *Optim Inven Manag* 55–67
22. Hwang H, Kim D, Kim Y (1993) Multiproduct economic lot size models with investment costs for setup reduction and quality improvement. *Int J Prod Res* 31(3):691–703
23. Hsu PH, Wee HM, Teng HM (2010) Preservation technology investment for deteriorating inventory'. *Int J Prod Econ* 124(1):388–394
24. Dye CY, Hsieh TP (2012) An optimal replenishment policy for deteriorating items with effective investment in preservation technology. *Eur J Oper Res* 218(1):106–112
25. Shah NH, Chaudhari UB, Jani MY (2017) Optimal policies for a time-varying deteriorating item with preservation technology under selling price and trade credit-dependent quadratic demand in a supply chain. *Int J Appl Comput Math* 3(2):363–379
26. Chaudhari UB, Shah NH, Jani MY (2020) Inventory modelling of deteriorating item and preservation technology with advance payment scheme under quadratic demand. *Optim Inven Manag* 69–79
27. Cárdenas-Barrón LE, Sana SS (2015) Multi-item EOQ inventory model in a two-layer supply chain while demand varies with a promotional effort. *Appl Math Model* 39(21):6725–6737

Industry 4.0 Research: Information and Communication Technology Capability Index for Supply Chain Management



Prashant R. Nair, S. P. Anbuudayasankar, R. Kishore, and R. Pradeep

Abstract Purpose—The objective of this paper is to suggest methods to compute an effective Information and Communication Technology (ICT), Capability Index for Supply Chain Management (SCM) as part of assessment framework on ICT impact on SCM. The other part of this assessment framework is an empirical model based on SCOR level I performance indicators. This framework can be seamlessly dovetailed into the universally accepted and popular APICS Supply Chain Operations Reference (SCOR) model as its constructs are based on SCOR. The assessment framework will be a welcome addition to the Industry 4.0 research underway. **Design/methodology/approach**—Survey questionnaire was administered and collected from 200 + SCM professionals in sectors such as manufacturing, services, MSMEs, international companies as well as SCM/ERP professionals working as domain experts in IT and service companies. Snowball sampling was primarily used with the support of various industrial associations and professional body chapters. This questionnaire combines quantitative and qualitative inputs with adequate provision for open-ended questions with user input as a means of eliciting case interviews. After Confirmatory Factor Analysis (CFA) using SEM was employed to validate the empirical model, its performance indicators are ranked using AHP and the weights are ascertained. Computing the ICT Capability Index for SCM from the metrics of the assessment model is done using tools such as Balanced Scorecard (BSC) and Snorm De Boer standardized normalization (SNORM) method. **Findings**—An ICT capability index for SCM is computed based on user input with respect to the impact of ICT on the supply chain performance indicator as part of this framework using the methods of BSC & SNORM. 2 industry case studies are used

P. R. Nair (✉)

Department of Computer Science and Engineering, Amrita School of Engineering Coimbatore, Amrita Vishwa Vidyapeetham, Coimbatore, India

e-mail: prashant@amrita.edu

S. P. Anbuudayasankar · R. Kishore · R. Pradeep

Department of Mechanical Engineering Amrita School of Engineering Coimbatore, Amrita Vishwa Vidyapeetham, Coimbatore, India

e-mail: sp_anbu@cb.amrita.edu

© The Author(s), under exclusive license to Springer Nature Singapore Pte Ltd. 2022

M. K. Singh and R. K. Gautam (eds.), *Recent Trends in Design, Materials*

and Manufacturing, Lecture Notes in Mechanical Engineering,

https://doi.org/10.1007/978-981-16-4083-4_9

for the computation and analysis of this index. **Research limitations/implications**—Discussion with an enterprise is needed to take input on the impact of ICT on each supply chain performance indicator in our calculation for the index. This investigation considers ICT deployment as the variable which encompasses the entire gamut of ICT tools and technologies. There could be different granular approaches to ICT as a variable. A scoring system, scale, and rubric are proposed to be evolved based on multiple case studies of various enterprises as an extension to this research work. There is tremendous scope to extend the investigation into SCOR level II metrics which are diagnostics of strategic metrics and level III metrics which are context or sector-specific and also considering various geographies. **Originality/value**—The managerial implications of this ICT Capability Index for SCM assumes greater significance as a result of the present situation due to Covid-19 pandemic, which has accelerated the need for Industry 4.0, digitalization and embracing of ICT not only for supply chain but also all aspects of the enterprise. There is also an identified lacuna in terms of performance scoring and assessment framework with respect to impact of ICT in SCM. The advantages of this index are that it is universal and can be used by any enterprise irrespective of the geography or country, vertical or domain, manufacturing or services. This index will provide insights to enterprises on their ICT capabilities and help them to further leverage ICT so as to adapt their organizations, digitize their operations and also benchmark with their peers and competitors. A scoring system and rubric is proposed to be evolved based on multiple case studies of various enterprises as an extension to this research work.

Keywords Supply Chain Management (SCM) · Information and Communication Technology (ICT) · Industry 4.0 · Capability Index · Balanced Scorecard (BSC) · Snorm De Boer standardized normalization (SNORM)

1 Introduction

Speedy technology advancements and ever-changing market dynamics have altered the enterprise landscape as fundamentally translated current business models. Information and Communication Technology (ICT) applications and deployment have unlocked the flood gates for all enterprises to compete in any marketplace. Enterprises from all geographies and verticals, manufacturing and services, profit and non-profit are exposed to the current-day challenges of larger competition, pricing pressures and global marketplace. These challenging settings are popularly referred to as VUCA short for *Volatility, Uncertainty, Complexity and Ambiguity* [1] and have been further complicated by the worldwide web and Information Superhighway. The following examples illustrate the power of innovation enabled through ICT:

- The largest car company globally is Uber, but fascinatingly Uber does not own any cars.
- The largest media company globally is Facebook, but interestingly Facebook does not create any content.

- The largest retailer globally is Alibaba, but amusingly, Alibaba does not own any malls or superstore

The deployment of cutting-edge ICT tools such as big data analytics, Internet of things (IoT), Cyber-Physical Systems (CPS), mobile apps, and the like are revolutionizing automation in enterprises. This wave dubbed Industry 4.0 is fast emerging as an inflection point in manufacturing and is being touted as the fourth industrial revolution. Interestingly, in today’s interconnected world, it is not the companies that are competing, but their supply chains and stakeholder networks.

2 Industry 4.0

Industry 4.0 is the latest wave of computerization in manufacturing. This comprises cutting-edge ICT tools and technologies such as robotics, IoT, CPS, Artificial Intelligence (AI), machine learning, mobile apps, and cloud computing. This fosters what has been popularly referred to as a smart factory, fourth industrial revolution, and Industrial IoT (IIoT). Within modular smart factories, CPS monitor physical processes in all aspects such as manufacturing, supply chain, and logistics, creating a digital twin of the physical world and making distributed decisions. Over the IoT connectivity of physical assets, CPS collaborate and engage in dialogue with one other and with humans in real time. Both internal and cross-organizational services are provided and employed by various stakeholders [2]. Industry 4.0 seamlessly transforms the supply chain into a value chain (Fig. 1).

CPS consists of collaborating computational elements controlling physical objects, whose processes are seamlessly monitored, coordinated, controlled, and integrated. The resultant value chain thereby becomes more agile, collaborative, visible,

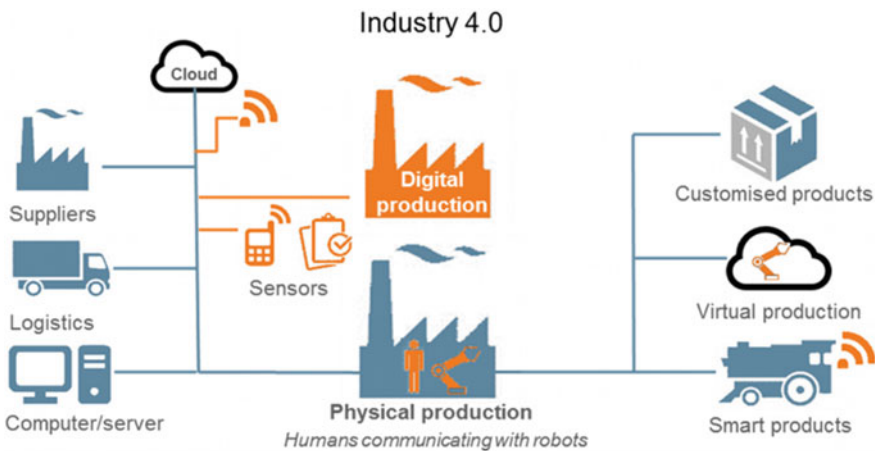


Fig. 1 Industry 4.0 constituents

and responsive. An example would be a totally connected and retooled supply chain, which can reconfigure itself on receipt of any new data point. If a weather delay ties up a shipment, a connected system can proactively adjust itself and modify manufacturing priorities bringing about perfect alignment between supply chain planning and execution. Digital technologies are transforming supply chain management from linear to circular models. This trend of transformation and reorganization of SCM due to the digital technologies of Industry 4.0 is also cited as Supply Chain 4.0 [3]. Industry 4.0 has rendered supply chains to be more transparent, visible, resilient, adaptable, and pro-active in decision-making. This is in terms of effective access to timely and actionable information as also communication, collaboration, and dialogue with various stakeholders. And this benefit has percolated to their partners and suppliers, who are connected to the enterprise through an extranet.

Adoption of Industry 4.0 technologies has become all the more relevant considering the fact that annual global supply chain losses run into billions of dollars. Cargo theft has resulted in loss of \$ 23 billion dollars as per BSI in 2015. Three out of 4 companies have seen disruptions in their supply chains in 2015. A couple of years ago supply chain disruptions resulted in closure of almost 65% of 900 Kentucky Fried Chicken restaurants in England [3].

Industry 4.0 adoption and deployment are gathering steam. German manufacturing powerhouse, Siemens is executing an Industry 4.0 application in biomedical engineering for artificial knee and hip joints, which are standardized products needing high level of customization for patients. With industry 4.0 software tools, Siemens can produce an implant within 3–4 h. Predix, the Operating System for the Industrial IoT is the engine for enterprises in the new knowledge economy. Predix-based apps are unleashing new levels of performance for General Electric (GE) [3].

3 Motivation, Background and Relevance of the Research

This effectual investigation assumes greater significance as a result of the present situation due to Covid-19 pandemic, which has accelerated the need for Industry 4.0, digitalization and embracing of ICT not only for supply chain but also all aspects of the enterprise. Indices and metrics for measurement of ICT at an enterprise level or even at a national level are dime a dozen. The International Telecommunications Union (ITU), which is part of the United Nations has taken leadership and emerged as the primary source of global ICT and telecom statistics. One of the major metrics developed by ITU is ICT Development Index (IDI) used for ranking nations based on ICT readiness and digital divide with knowledge, social, or economic dimensions. Consequent to this, there are now 20 similar indices like ICT Diffusion Index by UNCTAD, Global Innovation Index by WIPO, and Networked Readiness Index by INSEAD-World Economic Forum (WEF) [4, 5]. On similar lines, there are metrics developed for industry. McKinsey Global Institute (MGI) has developed MGI India Firm Digitization Index, which shows how digitally advanced firms are pulling ahead of their peers and Country Digital Adoption Index [6]. The firm digitization index

for India is built on digital strategies, organization, and capabilities and is a variant of the indices developed by MGI for US and European companies. Interesting insights from these indices and studies are that digital adoption by India's businesses has so far been uneven. Rather, ICT adoption is uneven not only across firms, but sectors and countries.

While most supply chain professionals from both academia and industry are in complete agreement of the reality that ICT conclusively impacts performance and fulfillment of the supply chain with many frameworks having been suggested, there is an identified lacuna in terms of performance scoring and assessment framework with respect to the impact of ICT in SCM [7]. Various factors that contribute to this gap in measurement include intangibility of measures in the knowledge economy [8, 9]; the dynamic nature of supply chains [10] and multiplicity of performance metrics [11]. In the latest release of SCOR Process Reference model version 11 by APICS [12], a new process addition is 'enable' processes largely concerned with collaboration and dialogue amongst various stakeholders like suppliers and partners in the enterprise, which are now primarily through ICT. But APICS does not have list any ICT metric. Nor does other SCM models like GSCF, balanced scorecard and benchmarking [7]. There is only a casual mention of ICT as a KPA in OPQR framework [13]. A recent study reinforces this position that a coherent picture or metric of ICT impact on SCM performance is not available [14, 15]. It is also observed that there is asymmetry and variability in ICT adoption for SCM across various sectors and companies [7].

The motivation of this investigation is to append an original addition to the existing knowledge archive in providing enterprises with a universal benchmark in form of an assessment framework on their ICT deployment in SCM and its dovetailing into Supply Chain Operations Reference (SCOR) model of the APICS professional body, which has 45,000 members. SCOR model is very popular and the de facto benchmark for process enhancement for SCM [3] with over 200 process elements, 550 measures, and 500 good practices [16, 17]. This assessment framework includes an empirical model and ICT capability index for SCM derived from performance constructs of the empirical model, which is built on SCOR Level I metrics. The managerial implications and benefits of the assessment framework will be discussed in later sections.

4 Research Methodology

To address this research problem, which is exploratory in nature, an assorted research method consisting of both descriptive and numerical means seemed appropriate considering the scope and nature of the research problem. A detailed survey questionnaire combines quantitative and qualitative inputs with adequate provision for open-ended questions with user input as a means of eliciting case interviews of ICT deployment for SCM in the enterprises as well as the quantitative inputs.

In a pilot phase, the survey questionnaire was administered to a cross section of supply chain professionals from industry and experts from academia. This includes

both supply chain managers in manufacturing and services directly dealing in supply chain planning and execution as also professionals working on the automation side in ERP and software solutions for SCM. Initial feedback and respondents' point of view included insights such as respondent needs to be very well-versed in supply chain concepts and that almost 20 min are needed to fill the questionnaire. These inputs were factored in with the pilot phase contributing to face validity for the research instrument. Snowball sampling was employed and support for the survey was enlisted from industry associations and professional body chapters such as Indian Institute of Materials Management, MSME Development Institute (DI), CIO Forum of Computer Society of India (CSI), Institute for Supply Chain Management (ISM), Coimbatore District Small and Medium Scale industries association (CODISSIA) and Coimbatore Management Association (CMA), all of whom, have a large member and subscriber base. More than a thousand e-mails were sent using these good offices and networks.

An empirical model which is the first part of the assessment framework on impact of ICT in SCM is propounded based on the SCOR performance indicators details of which are provided in the next section. After getting a turnaround of 200 respondents, analysis using Structural Equation Modeling (SEM) method was used. These respondents were SCM professionals in sectors such as manufacturing, services, MSMEs, international companies as well as SCM/ERP professionals working as domain experts in IT and service companies. Confirmatory Factor Analysis (CFA) was used to validate this empirical model and the proposed supply chain performance constructs. After validation, using these supply chain performance indicators, the second part of the assessment framework, i.e., the ICT capability index for SCM is computed using 2 methods, namely, Snorm De Boer standardized normalization (SNORM), Balanced Scorecard (BSC), and ranking of these constructs done using Analytic Hierarchy Process (AHP).

5 Empirical Model on ICT for SCM

The first part of the assessment framework is an empirical model for measurement of ICT impact in SCM based on SCOR model, which has been proposed and validated using Structural Equation Modeling (SEM). This model is based on exogenous latent variable & endogenous and latent & measured variables. Exogenous variables are independent and this investigation uses ICT Deployment, which refers to the entire gamut of ICT tools and technologies as the exogenous variable. In the next stage of research, different granular approaches to ICT deployment variable are proposed. Endogenous variables are dependent variables and are adopted from SCOR Level I metrics. As given below in Tables 1 and 5 latent endogenous factors and its 13 measurable endogenous factors are taken from SCOR to develop the empirical model of supply chain. These factors or variables are based on theoretical foundation [12]

Table 1 Endogenous latent and measured variables [12]

Endogenous latent variable	Endogenous measured variables
Reliability	Complete Delivery (CD) On-time Delivery (OD) Accurate Documentation (AD) No Damage (ND)
Responsiveness	Order Fulfillment Cycle Time (OCT)
Agility	Upside Supply Chain Flexibility (UPCA) Upside Supply Chain Adaptability (UPSA) Downside Supply Chain Adaptability (DSCA) Overall Value at Risk (Risk)
Costs	Total Cost to Serve (Cost)
Asset management efficiency	Cash to Cash Cycle Time (CCR) Return on Supply Chain Assets (RFA) Return on Working Capital (ROW)

and validated through expert opinion [7]. Variables list are given above in Table 1 and the validated empirical models are shown in Fig. 2. Here all λ are factor loadings, ϵ & δ are measurement errors and γ are regression weights.

6 Computation of ICT Capability Index for SCM

The second part of the assessment framework, i.e., the ICT capability index for SCM is computed using the supply chain performance indicators from the validated empirical model and questionnaire responses. ICT Capability Index for SCM has the potential to serve as a universal benchmark for measuring of the impact, effectiveness, and benefits of ICT enablement in SCM. Based on the multiple indicators of ICT impact on SCM, this ICT Capability Index is one that requires Multi-Criteria Decision-Making (MCDM).

MCDM is used in addressing the real-world decision problems by using both qualitative and quantitative information. This is peeled down into a ranking of alternatives. Building on this, a tool that will help us rank the attributes would be helpful [18]. MCDM can also be used as an approach to pick the best alternative from the list of available alternatives [19]. Techniques to address MCDM include PCA, Data Envelopment Analysis (DEA), fuzzy methods, non-linear programming, ISM, TOPSIS, and Analytic Hierarchy Process (AHP) [20]. This research investigation has used two methods to compute the ICT Capability Index for SCM, namely, Snorm De Boer standardized normalization (SNORM), Balanced Scorecard (BSC), and ranking of these indicators is done using AHP.

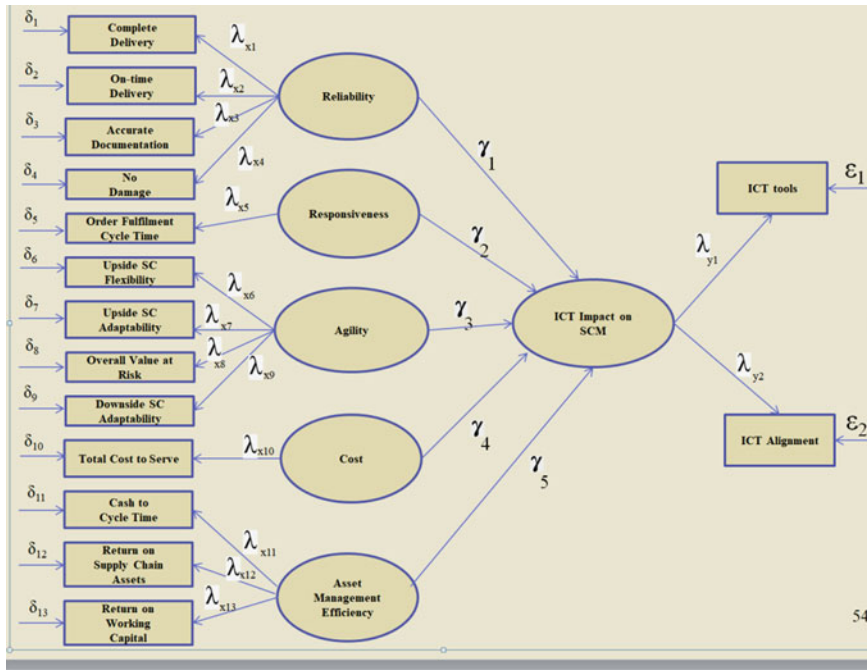


Fig. 2 Empirical model on benefits of ICT for SCM

6.1 AHP Method for Ranking Indicators to Compute ICT Capability Index for SCM

AHP is a structured tool for analyzing complicated and multifarious courses of action. AHP helps managers ascertain the alternative that is best suited to fulfill their aims. It provides a logical and coherent framework for providing a hierarchy to a decision problem, for constituting its elements, linking them to overall goals, and for assess alternative courses of action. The problem is broken down to elements, which are easy to understand and a hierarchy is built as also independent analysis of each element and the inter-relationships between these elements [21]. AHP is well-suited for MCDM as it is possible to determine the relative ranking of alternatives or attributes [22], which in this case is supply chain performance indicators impacted by ICT. This led to the selection of AHP and its extensions as the tool that ranks and quantifies the attributes in the order of importance and preference.

170 valid responses from the 200 respondents of the survey questionnaire are converted from Likert scale translated to Saaty Scale and the following methodology is used as shown in Fig. 3 and supported by Table 2 which is the AHP importance scale and Table 3 which is the pair-wise comparison matrix so as to get the AHP ranks and weights of the supply chain performance indicators reproduced in Table 4. These weights in Table 4 are utilized in the computation of the ICT Capability Index.

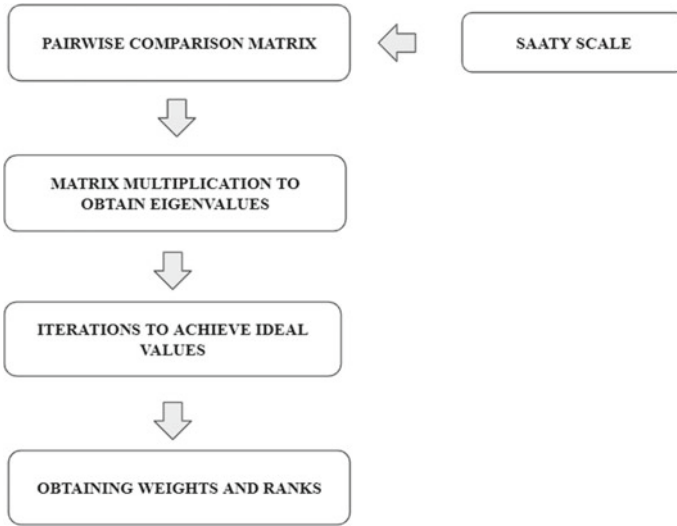


Fig. 3 AHP ranking methodology

Table 2 AHP importance scale

Importance scale	Definition of importance scale
1	Equally important
2	Equally to moderately important
3	Moderately important
4	Moderately to strongly important
5	Strongly important
6	Strongly to very strongly important
7	Very strongly important
8	Very strongly to extremely important
9	Extremely important

6.2 SNORM Method for Computing ICT Capability Index for SCM

Snorm De Boer standardized normalization (SNORM) method is used to normalize supply chain performance constructs and used in conjunction with SCOR as a method for measuring business performance. Companies can use this tool to assess and gauge each business practice and also find out the ones that need improvements to be made [23]. This method is used to calculate the ICT Capability Index for SCM.

Weight of each construct is obtained by AHP from the values in Table 4. SNORM method is defined as follows [24]:

If large value of a performance indicator or construct is better:

Table 3 AHP pair-wise comparison matrix from questionnaire responses in likert scale translated to saaty scale

ICT impact on	Accurate Documentation	Complete Delivery	Cost	No Damage	On-time Delivery	Order Fulfillment Cycle Time	Upside Supply Chain Adaptability	Downside Supply Chain Adaptability	Cash to Cash cycle time	Risk	Return on Supply Chain Fixed Assets	Upside Supply Chain Flexibility	Return on Working Capital
Accurate Documentation	1/1	2/1	3/1	4/1	5/1	6/1	7/1	7/1	8/1	8/1	8/1	9/1	9/1
Complete Delivery	1/2	1/1	3/1	3/1	3/1	3/1	3/1	4/1	5/1	6/1	6/1	7/1	8/1
Cost	1/3	1/3	1/1	3/1	3/1	4/1	5/1	6/1	7/1	8/1	9/1	9/1	9/1
No Damage	1/4	1/3	1/3	1/1	4/1	4/1	5/1	6/1	7/1	8/1	8/1	9/1	9/1
On-time Delivery	1/5	1/3	1/3	1/4	1/1	5/1	5/1	6/1	6/1	7/1	8/1	9/1	9/1
Order Fulfillment Cycle Time	1/6	1/3	1/4	1/4	1/5	1/1	6/1	6/1	7/1	8/1	9/1	9/1	9/1
Upside Supply Chain Adaptability	1/7	1/3	1/5	1/5	1/5	1/6	1/1	7/1	7/1	8/1	8/1	9/1	9/1
Downside Supply Chain Adaptability	1/7	1/4	1/6	1/6	1/6	1/6	1/7	1/1	8/1	8/1	9/1	9/1	9/1
Cash to Cash cycle time	1/8	1/5	1/7	1/7	1/6	1/7	1/7	1/8	1/1	7/1	8/1	9/1	9/1
Risk	1/8	1/6	1/8	1/8	1/7	1/8	1/8		1/7	1/1	9/1	9/1	9/1
Return on Supply Chain Fixed Assets	1/8	1/6	1/9	1/8	1/8	1/9	1/8	1/9	1/8	1/9	1/1	8/1	9/1
Upside Supply Chain Flexibility	1/9	1/7	1/9	1/9	1/9	1/9	1/9	1/9	1/9	1/9	1/8	1/1	9/1
Return on Working Capital	1/9	1/8	1/9	1/9	1/9	1/9	1/9	1/9	1/9	1/9	1/9	1/9	1/1

Table 4 AHP ranks and weights

ICT impact on	Weights	Ranks
Accurate documentation	0.217861815	1
Complete delivery	0.137556089	3
Cost	0.141317992	2
No damage	0.126162194	4
On-time delivery	0.104515685	5
Order fulfillment cycle time	0.085308167	6
Upside supply chain adaptability	0.062960113	7
Downside supply chain adaptability	0.044615283	8
Cash to cash cycle time	0.02854347	9
Risk	0.020812043	10
Return on supply chain fixed assets	0.014019403	11
Upside supply chain flexibility	0.009737723	12
Return on working capital	0.006590024	13

$$\text{SNORM is } ((S_i - S_{\min}) / (S_{\max} - S_{\min})) * 100$$

If smaller value of a performance indicator or construct is better:

$$\text{SNORM is } ((S_{\max} - S_i) / (S_{\max} - S_{\min})) * 100$$

where

- S_i is Actual performance value of the indicator/construct.
- S_{\max} is Maximum value of the indicator/construct.
- S_{\min} is Minimum value of the indicator/construct.

Actual performance value of the indicator/construct is given by a company based on the maximum and minimum value of the construct. Actual value of a particular indicator is given by the enterprise as company value. Finally by multiplying the weights of the factors and the SNORM value, the performance score for the five performance attribute is obtained and adding these gives the overall performance score which is converted to an ICT Capability index for SCM.

6.3 *Balanced Scorecard (BSC) Method for Computing ICT Capability Index for SCM*

Balanced Scorecard (BSC) is a comprehensive business performance measure to measure overall performance in diverse aspects of an enterprise. Using this tool, an organization is viewed from the following four important perspectives which cover both operational and financial aspects.

- Customer.
- Internal business.
- Innovation and learning.
- Financial.

Each perspective is constituted of objectives and metrics [25]. This is again an application of MCDM. BSC impacts decision-makers with insights on whether enhancements in one perspective are attained at the cost of the other. In our investigation, BSC is applied in conjunction with matrix goals and interpolation formula method. Weights are taken from AHP for each indicator in the same method employed in SNORM method from Table 4. Target and stretch are defined as lower and upper threshold values for each indicator in the attainment of performance. The actual company value of a particular indicator is obtained for the enterprise. The attainment value for each indicator is calculated using the following interpolation formula [26]:

$$y_2 = \frac{(x_2 - x_1)(y_3 - y_1)}{(x_3 - x_1)} + y_1$$

x_1, x_2 and x_3 are target, actual, and stretch values of the indicator.

y_1 and y_3 are lower and upper threshold values of the indicator.

From the attainment value, the score is computed by multiplying weight of indicator with the attainment value of indicator. And total score is the sum of all performance scores, which is our index [26]. Enterprise case studies are hereby explored based on selected respondents which contained both quantitative data points and qualitative data points with provision for some open-ended responses as well.

6.3.1 Industry Case Study # 1: Manufacturing Company # 1

The first case study is of a manufacturing company headquartered at Coimbatore with the following details:

- Respondent: Senior Vice-President.
- Total Number of Employees: 3000.
- Name of Business Vertical/SBU/Description: Horn/Industrial Cleaning Equipment's/Die Casting/Plastic components/Medical Equipment, etc.
- Total Turnover (In Indian Rupees): Rs. 700 crores.
- Years of Operating experience of enterprise: 40 Years.
- ICT Deployment.
 - ERP Package.
 - Bar Code.
 - DSS.
 - Software Agents.
 - Cloud Computing.
 - Business Analytics.
 - High Performance Computing.
 - Mobile Apps.
 - Social Media.
 - CRM package.
 - E-business software suite.
 - IoT.
- ICT Deployment benefits described by respondent
 - Visibility of order status.
 - Visibility of shipping and transportation details.
 - Accuracy of demand forecasts.
 - Decrease of manual work.
- ICT Capability Index computed and shown in Tables 5 and 6 using:
 - SNORM: 0.9172.
 - BSC: 0.947.

- Recommendations & Inference from the ICT Capability Index for SCM
 - SNORM & BSC are different methods for computing the index and as such as the range of values and scale will show some variation between the two methods.
 - This is an enterprise which has not only adopted high-end ERP software package but also cutting-edge ICT tools like analytics, mobile apps, etc. for their supply chain processes. More or less the enterprise has leveraged the power of ICT for all aspects of the SCM.
 - As such the values of the index are high and this can be compared with other case studies.
 - There is scope to maximize the ICT usage of internal process and financial measures as evidenced from scores from both methods.
 - ICT tools have already been deployed and improvement of internal process like OCT, UPCA, UPSA can be done by maximizing the usage of these tools as also look for operational gaps in the ICT-enabled processes like poor communication between stakeholders, technology incompatibility, etc.
 - There is scope for maximization of financial measures, but this requires management actions and audits.
 - As and when required, the enterprise can upgrade their ICT tools.

6.3.2 Industry Case Study # 2: MSME # 1

The second case study is of a MSME headquartered at Coimbatore with the following details:

- Respondent: Senior General Manager.
- Total Number of Employees: 400.
- Name of Business Vertical/SBU/Description: Food processing.
- Total Turnover (In Indian Rupees): Rs. 15 crores.
- Years of Operating experience of enterprise: 15 Years.
- ICT Deployment
 - Bar Code.
 - Inventory management software package.
 - Fleet.
 - Management software package.
 - Cloud Computing—ESDS.
 - Mobile Apps—Local startup.
 - Social Media.
 - CRM software package—Salesforce.com.
 - Management Information System (MIS) package—Tally for finance, Benny Impex.

Table 5 Index computation using SNORM method of industry case study # 1

ICT	Impact on construct	Abbreviation	Minimum (in %)	Maximum (in %)	Company value (in %)	AHP weights	SNORM	Score
ICT+	Complete delivery	CD	0	100	100	0.137556089	100	13.7556089
ICT+	On-time delivery	OD	0	100	100	0.104515685	100	10.4515685
ICT+	Accurate documentation	AD	0	100	100	0.217861815	100	21.7861815
ICT +	No damage	ND	0	100	100	0.126162194	100	12.6162194
ICT –	Order fulfillment cycle time	OCT	100	0	80	0.085308167	80	6.82465336
ICT+	Upside supply chain flexibility	UPCA	100	0	80	0.009737723	80	0.77901781
ICT+	Upside supply chain adaptability	UPSA	0	100	80	0.062960113	80	5.03680904
ICT+	Downside supply chain adaptability	DSCA	100	0	80	0.044615283	80	3.56922265
ICT–	Cash to cash cycle time	CCR	100	0	80	0.02854347	80	2.28347761
ICT+	Return on supply chain fixed assets	RFA	0	100	80	0.014019403	80	1.12155222
ICT+	Return on working capital	ROWC	0	100	80	0.006590024	80	0.52720189
ICT–	Cost	Cost	100	0	80	0.141317992	80	11.3054393
ICT–	Risk	Risk	100	0	80	0.020812043	80	1.66496347
							Score	91.7219156
							Index	0.9172

Table 6 Index computation using BSC method of industry case study # 1

Balanced score card	ICT impact on construct	Abbreviation	Target	Stretch	Actual	Weights	Score	Weight * score
Customer	ICT+	Complete delivery	80	100	100	0.137556	100	13.75560885
	ICT+	On-time delivery	80	100	100	0.104516	100	10.45156851
	ICT+	Accurate documentation	90	100	100	0.217862	100	21.78618148
	ICT+	No damage	90	100	100	0.126162	100	12.61621941
	ICT-	Order fulfillment cycle time	100	80	95	0.085308	85	7.251194195
Internal process	ICT+	Upside supply chain flexibility	100	80	95	0.009738	85	0.827706428
	ICT+	Upside supply chain adaptability	0	100	85	0.06296	97	6.107130958
	ICT+	Downside supply chain adaptability	100	80	95	0.044615	85	3.792299066
	ICT-	Cash to cash cycle time	100	80	95	0.028543	85	2.426194963
Financial	ICT+	Return on supply chain fixed assets	0	100	85	0.014019	97	1.359882064
	ICT+	Return on working capital	0	100	80	0.00659	96	0.632642266
	ICT-	Cost	100	80	95	0.141318	85	12.01202931
Learning and growth	ICT-	Risk	100	0	85	0.020812	83	1.727399601
							Score	94.7460571
							Index	0.947

- ICT Deployment benefits described by the respondent
 - Better visibility of milk movements [both at procurement and distribution stages].
 - Better Planning for milk and milk products sales and stocking.
 - Better utilization of the production facilities.
 - Effective manpower deployment.
 - Reduction in the milk transaction and storage timings.
 - Increase in the shelf life of milk and milk products.
- ICT Capability Index computed and shown in Tables 7 and 8 using:
 - SNORM: 0.65
 - BSC: 0.8571
- Recommendations and Inference from the ICT Capability Index for SCM
 - SNORM and BSC are different methods for computing the index and as such as the range of values and scale will show some variation between the 2 methods.
 - This enterprise is a progressive MSME in dairy and food processing with ICT deployed for various activities of the enterprise. Even though ERP has not been procured, MIS packages for operations, finance, etc. are available as also cutting-edge tools like mobile apps, cloud, etc.
 - When this is compared with other case studies, it is clear that there is a tremendous room for improvement in ICT deployment. From stand-alone MIS, the MSME can explore a capital investment in procuring an ERP to integrate the enterprise operations.
 - As evidenced from the scores, internal processes to a large extent have been improved by the stand-alone MIS packages and few cutting-edge tools.
 - There is tremendous scope to improve customer, financial, and risk measures.
 - If procuring an ERP is not possible, customer measures can be improved using web services for better dialogue and communication.
 - Reducing risk will require more integration and this is best served by integrating all the MIS packages for various functional areas of the enterprise.

7 Managerial Implications and Future Research Directions

The managerial implications of this ICT Capability Index for SCM assume greater significance as a result of the present situation due to Covid-19 pandemic, which has accelerated the need for Industry 4.0, digitalization, and embracing of ICT not only for the supply chain but also all aspects of the enterprise. The index is derived from the empirical model which together constitutes assessment framework on impact of ICT for SCM. The advantages of this index are that it can be used by any enterprise irrespective of the geography or country, vertical or domain, manufacturing,

Table 7 Index computation using SNORM method of industry case study # 2

ICT	Impact on construct	Abbreviation	Minimum (in %)	Maximum (in %)	Company value (in %)	AHP weights	SNORM	Score
ICT+	Complete delivery	CD	0	100	60	0.137556089	60	8.25336531
ICT+	On-time delivery	OD	0	100	60	0.104515685	60	6.2709411
ICT +	Accurate documentation	AD	0	100	60	0.217861815	60	13.0717089
ICT+	No damage	ND	0	100	60	0.126162194	60	7.56973165
ICT –	Order fulfillment cycle time	OCT	100	0	60	0.085308167	60	5.11849002
ICT+	Upside supply chain flexibility	UPCA	100	0	80	0.009737723	80	0.77901781
ICT+	Upside supply chain adaptability	UPSA	0	100	80	0.062960113	80	5.03680904
ICT+	Downside supply chain adaptability	DSCA	100	0	80	0.044615283	80	3.56922265
ICT–	Cash to cash cycle time	CCR	100	0	80	0.02854347	80	2.28347761
ICT+	Return on supply chain fixed assets	RFA	0	100	60	0.014019403	60	0.84116416
ICT+	Return on working capital	ROWC	0	100	20	0.006590024	20	0.13180047
ICT–	Cost	Cost	100	0	80	0.141317992	80	11.3054393
ICT–	Risk	Risk	100	0	40	0.020812043	40	0.83248174
							Score	65.0636498
							Index	0.65

Table 8 Index computation using BSC method of industry case study # 2

Balanced score card	ICT impact on construct	Abbreviation	Target	Stretch	Actual	Weights	Score	Weight * score
Customer	ICT+	Complete delivery	80	100	90	0.137556	90	12.38004797
	ICT+	On-time delivery	80	100	85	0.104516	85	8.88383323
	ICT+	Accurate documentation	90	100	90	0.217862	80	17.42894518
	ICT+	No damage	90	100	90	0.126162	80	10.09297553
	ICT-	Order fulfillment cycle time	100	80	95	0.085308	85	7.251194195
Internal process	ICT+	Upside supply chain flexibility	100	80	85	0.009738	95	0.925083655
	ICT+	Upside supply chain adaptability	0	100	95	0.06296	99	6.233051184
	ICT+	Downside supply chain adaptability	100	80	85	0.044615	95	4.238451897
	ICT-	Cash to cash cycle time	100	80	90	0.028543	90	2.568912314
	ICT+	Return on supply chain fixed assets	0	100	55	0.014019	91	1.275765648
Financial	ICT+	Return on working capital	0	100	25	0.00659	85	0.560152006
	ICT-	Cost	100	80	95	0.141318	85	12.01202931
	ICT-	Risk	100	0	50	0.020812	90	1.873083905
							Score	85.72352602
							Index	0.857

or services. This index not only provides insights to enterprises on their ICT capabilities for SCM but also assesses to what extent digital matters to them and how it might transform their business models and supply chains and affect financial performance and diagnostics. This will help them to adapt their organizations, leverage ICT, digitize their operations, and also benchmark with their peers and competitors. The index can also provide insights on selection of appropriate ICT tool after measurement of its impact on the supply chain paradigm and understanding success factors and operational challenges for adoption of various ICT tools [27].

This index calculation has been done using 2 methods, namely, SNORM and BSC. Discussion with an enterprise is needed to take input on the company value on the effect of ICT on each supply chain performance indicator in our calculation for the index. Two case studies are showcased with calculation of the index using the 2 methods. Inferences and recommendations are also provided to these respective companies.

A scoring system and rubric are proposed to be evolved based on multiple case studies of various enterprises as an extension to this research work. This will essentially involve not only providing the enterprise with an index but also a gradation model with specific recommendations on moving up the ladder in terms of ICT adoption. The investigation has focused primarily on strategic supply chain metrics or level I metrics as per the SCOR model. There is ample scope to extend the investigation into SCOR level II metrics which are diagnostics of strategic metrics and level III metrics which are context or sector-specific. A cluster-based or sector-based analysis approach with or without geographical limitations can also be considered as an extension to the research.

8 Conclusion

Industry 4.0 is the latest cutting-edge wave of ICT deployment in enterprises. The present situation due to Covid-19 pandemic has only accelerated the need for Industry 4.0, digitalization, and embracing of ICT not only for supply chain but also all aspects of the enterprise. While most supply chain professionals are in complete agreement of the fact that ICT conclusively impacts performance and fulfillment of the supply chain with many frameworks having been suggested, there is an identified lacunae in terms of performance scoring and assessment framework with respect to impact of ICT in SCM. This investigation proposes an ICT Capability Index for SCM as one part of an assessment framework on ICT impact on SCM. The other part is an empirical model based on SCOR level 1 performance constructs, which is validated using SEM from the survey questionnaire responses. These constructs are ranked using AHP and the weights are ascertained. Computing the ICT Capability Index for SCM from the metrics of the assessment model is done using tools such as Balanced Scorecard (BSC) and Snorm De Boer standardized normalization (SNORM) method. Enterprises irrespective of sector or vertical can use this index as a universal benchmark to assess to what extent digital technologies and ICT matters to them and how

it might transform their supply chains and business models as also affect financial performance and diagnostics. A scoring system and rubric is proposed to be evolved based on multiple case studies of various enterprises as an extension to this research work. Enterprises may be provided with specific recommendations on moving up the ladder in terms of ICT adoption as also from a cluster or sector-based approach.

References

1. Bennett N, Lemoine J (2014) What VUCA really means for you. *Harv Bus Rev* 92(1/2)
2. Mueller E, Chen XL, Riedel R (2017) Challenges and requirements for the application of industry 4.0: a special insight with the usage of cyber-physical system. *Chin J Mech Eng* 30(5):1050–1057
3. Ferrantino MJ, Koten EE (2019) Understanding supply chain 4.0 and its potential impact on global value chains. In: *Global value chain development report 2019*, p 103. https://www.wto.org/english/res_e/booksp_e/gvc_dev_report_2019_e_ch5.pdf
4. Kauffman RJ, Kumar A (2005) A critical assessment of the capabilities of five measures for ICT development. misrc.umn.edu/workingpapers/fullpapers/2005/0506_031805.pdf
5. Kononova K (2015) Some aspects of ICT measurement: comparative analysis of E-indexes. In: *HAICTA*, pp 938–945
6. McKinsey Global Institute (2019) Digital India: technology to transform a connected nation. <https://www.mckinsey.com/~media/McKinsey/Business%20Functions/McKinsey%20Digital/Our%20Insights/Digital%20India%20Technology%20to%20transform%20a%20connected%20nation/Digital-India-technology-to-transform-a-connected-nation-Full-report.ashx>
7. Nair PR, Anbuudayasankar SP (2016) An investigation on the benefits of ICT deployment in supply chain management (SCM). *Indian J Sci Technol* 9(30):1–7
8. Fahimnia B, Tang CS, Davarzani H, Sarkis J (2015) Quantitative models for managing supply chain risks: a review. *Eur J Oper Res* 247(1):1–15
9. Gunasekaran A, Kobu B (2007) Performance measures and metrics in logistics and supply chain management: a review of recent literature (1995–2004) for research and applications. *Int J Prod Res* 45(12):2819–2840
10. Hassini E, Surti C, Searcy C (2012) A literature review and a case study of sustainable supply chains with a focus on metrics. *Int J Prod Econ* 140(1):69–82
11. Bhagwat R, Sharma MK (2007) Performance measurement of supply chain management: a balanced scorecard approach. *Comput Ind Eng* 53(1):43–62
12. APICS (2015) Supply chain operations reference model, revision 11.0. <https://docs.huihoo.com/scm/supply-chain-operations-reference-model-r11.0.pdf>
13. Sardana GD (2009) Exploring the performance of a responsive supply chain. In: *Supply chain forum: an international journal*, vol 10, no 2, pp 38–39. Taylor & Francis
14. Birkel HS, Hartmann E (2019) Impact of IoT challenges and risks for SCM. *Supply Chain Manag Int J* 24(1):39–61
15. Gunasekaran A, Subramanian N, Papadopoulos T (2017) Information technology for competitive advantage within logistics and supply chains: a review. *Transp Res Part E Logist Transp Rev* 99:14–33
16. de Barros AP, Ishikiriya CS, Peres RC, Gomes CFS (2015) Processes and benefits of the application of information technology in supply chain management: an analysis of the literature. *Procedia Comput Sci* 55:698–705
17. Simchi-Levi D, Kaminsky P, Simchi-Levi E (2004) *Managing the supply chain: definitive guide*. Tata McGraw-Hill Education
18. Zhou T, Maumbe K, Deng J, Selin SW (2015) Resource-based destination competitiveness evaluation using a hybrid analytic hierarchy process (AHP): the case study of West Virginia. *Tour Manag Perspect* 15:72–80

19. Lavasani SMM, Wang J, Yang Z, Finlay J (2012) Application of MADM in a fuzzy environment for selecting the best barrier for offshore wells. *Expert Syst Appl* 39(3):2466–2478
20. Sudarshan SV, Priyadarshuan A, Anbuudayasankar SP (2019) Analysis of the barriers in implementing green supply chain management (GSCM) practices: a hybrid approach. In: IOP conference series: materials science and engineering, vol 577, no 1, p 012005. IOP Publishing
21. Saaty TL (2008) Relative measurement and its generalization in decision making why pairwise comparisons are central in mathematics for the measurement of intangible factors the analytic hierarchy/network process. *RACSAM-Revista de la Real Academia de Ciencias Exactas Fisicas y Naturales. Serie A Matematicas* 102(2):251–318
22. Mani V, Agrawal R, Sharma V (2014) Supplier selection using social sustainability: AHP based approach in India. *Int Strat Manag Rev* 2(2):98–112
23. Hasibuan A, Arfah M, Parinduri L, Hernawati T, Harahap B, Sibuea SR, Sulaiman OK (2018) Performance analysis of supply chain management with supply chain operation reference model. *J Phys Conf Ser* 1007(1):012029
24. Trienekens JH, Hvolby HH (2000) Performance measurement and improvement in supply chains. In: Proceedings of the third CINET conference; CI 2000 from improvement to innovation, Aalborg, September 18–19, pp 399–409
25. Kaplan RS, Norton DP (1998) Putting the balanced scorecard to work. *Econ Impact Knowl* 27(4):315–324
26. PeopleSoft (2006) PeopleSoft enterprise human resources 9.0 PeopleBook: manage variable compensation. https://docs.oracle.com/cd/E13053_01/hr9pbr1_website_master/eng/psbooks/hhvc/chapter.htm?File=hhvc/htm/hhvc09.htm
27. Nair PR, Sahay M, Anbuudayasankar SP (2017) Investigation through system dynamics for the benefits of ICT intervention in distribution. *Prabandhan Indian J Manag* 10(8):42–51

Productivity Improvement in Foundry Using IoT



Yash Patel, Bhavesh Mewada, Bharat Tank, and Prashant Singh Tomar

Abstract In today’s rapid changing scenario in manufacturing industries, implementation of Internet of Things is essential for a manufacturing unit in order to respond effectively and work efficiently. Internet of Things is a system of sensing, processing, and interacting among devices to transfer data over the network from anywhere and at any time. Internet of Things is capable of collecting data in real time, resulting in enhancing the productivity of the manufacturing industries. Nowadays, many industries, organizations, and enterprises are urging to equip the fourth industrial revolution, i.e., Industry 4.0 as it is based on automation which include Internet of Things, Cyber Physical System, and Industrial Internet of Things, helping in easy data exchange in manufacturing technologies and processes. Nonetheless there are still some challenges that need to be investigated in order to implement IoT in industries and enterprises. This paper addresses the design and implementation of a real-time temperature monitoring and controlling system with the help of DS18B20 temperature sensor interfaced with Node MCU and 4-channel relay module that can access data from anywhere and anytime over the internet. The system will continuously monitor the temperature through mobile app Blynk and if the temperature exceeds the predefined limit set by the user, a notification will be sent to the registered Email ID that “the temperature is above predefined limit”.

Keywords Node MCU microcontroller · DS18B20 temperature sensor · Temperature monitoring · Wireless communication · Internet of Things

1 Introduction

Internet of Things comprises different types of sensors and actuators, which has the capability of communicating, interconnecting, and interacting with one other over the network from anywhere, anytime, with anything, and with anyone. Nowadays, IoT is gaining more attention from scientists and researchers as it has the ability

Y. Patel (✉) · B. Mewada · B. Tank · P. S. Tomar
Parul Institute of Technology, Vadodara, Gujarat, India

© The Author(s), under exclusive license to Springer Nature Singapore Pte Ltd. 2022
M. K. Singh and R. K. Gautam (eds.), *Recent Trends in Design, Materials and Manufacturing*, Lecture Notes in Mechanical Engineering,
https://doi.org/10.1007/978-981-16-4083-4_10

to transform the current systems into smart ones. IoT is an emerging technology, offering users to continuously monitor the system and in acquiring real-time data of the system. The foundry industries are facing challenges due to lack of proper temperature monitoring system. Especially in the foundry industries, in order to melt the molten metal the temperature of the furnace reaches nearly 1500 °C or even high, which is a security risk for the workers. In order to ensure the safety of the workers, the paper focuses on implementing IoT in foundry industries in order to increase their productivity by monitoring and controlling the temperature using DS18B20 temperature sensor. It aims at controlling the temperature via mobile app Blynk using WiFi as communication protocol and Node MCU as microcontroller. The microcontroller is interfaced with the DS18B20 and the 4-channel relay module that controls the device for controlling the temperature. The temperature monitoring system can be used in manufacturing industries, power plants, and other industries that need the data to be saved and analyzed.

2 Literature Study

In [1], the author had made an attempt to develop a low cost IoT solution for smart manufacturing in foundry. Simulation was done using Autocast_XI software for detecting defects during solidification. Simulation software helped in early checking of effective gating system and defect prediction, saving reasonable productivity and quality. Thermocouple was placed in the mold cavity to monitor temperature, which helped in studying cooling curves and quality check of solidification defects. Data obtained using controller and amplifier were stored in mobile for live monitoring. IoT platform saved time by providing casting solidification data in real time.

In [2], the author designed, prototyped, and tested an integrated sensor platform that can record physiological changes-heart rate, oxygen saturation, physical activity levels, skin temperature, and galvanic skin response. Wearable sensor includes skin temperature sensor, pulse oximetry sensor, accelerometer sensor for assessments of activity level, and galvanic skin response sensor for measuring the skin moisture. The wearable system was compared with clinical measures such as fingertip pulse oximetry and infrared thermometry which resulted in high accuracy and correlation. MATLAB software was used for comparing, analyzing, and visualizing the data. This device offers a variety of versatile uses especially with athletes, military personnel, laborers, and elderly individuals as it helps in multi-parameter health monitoring.

In [3], the author revealed that IoT improves business effectiveness in various ways which include enhancing collaboration, improving productivity and efficiency, coordinating business operations, reducing cost and waste, tracking manufacturing processes, enhancing human resource at workplace, reducing maintenance times, improving supply chain of goods and services, connecting machinery together, improving customer experience, supporting data collection, developing new business models and remote mobile device management.

In [4], the author discussed an IoT evolution, IoT ecosystem, and IoT architecture. A well-structured IoT architecture helps enterprises and industries to create innovative and state-of-the-art services. It also ensures that a variety of enterprise applications connects with enterprise IoT devices for better access of data to users, customers, consumers, and subscribers. The author also discussed challenges faced by enterprises and industries in adopting IoT, which makes it difficult for the industries to make decision on IoT adoption.

In [5], the author designed heterogeneous wearable IoT sensor for safety and health applications, suitable for industrial workplace. Multiple wearable sensors were attached to the worker's body to monitor environmental and physiological parameters. Workers body was equipped with two nodes: Safe node for environmental condition monitoring (ambient temperature, relative humidity, ultraviolet radiation, and carbon monoxide) and Health node for physiological signal monitoring (body temperature and heart rate). The wearable sensors communicate through a gateway via LoRa network which forms heterogeneous IoT platform and provides invaluable information to the system operator and workers regarding their safety and health monitoring. Aspects such as sensor node hardware and software design, gateway, and cloud implementation were also discussed.

3 Design and Discussion

In the proposed system, DS18B20 temperature sensor and 4-channel relay module are interfaced with the Node MCU microcontroller. The sensors data is processed by the Node MCU and is updated to the Blynk app using the WiFi as a communication protocol. The whole system is designed in Embedded C language and simulation of the written code is done in Arduino IDE.

3.1 Components Used

See Table 1

3.2 Interfacing DS18B20 and 4-Channel Relay Module with Node MCU

In this project, the 1-wire temperature sensor DS18B20 is interfaced with the microcontroller Node MCU. A 4.7 k Ω pull-up resistor is used for the proper connection. The temperature sensor requires 3.3–5 V power supply, which means that it can be

Table 1 Components listing

Sr. no.	Components	Quantity
1	Node MCU	1
2	DS18B20 temperature sensor	1
3	4-channel relay circuit	1
4	USB Jack cable	1
5	4.7 kΩ resistor	1
6	Electric heater	1
7	Bulb	1

powered from one of the 3.3 V Node MCU. The sensor has three wires: black represents GRD, red represents VCC, and yellow represents 1-wire data. The advantage of using this temperature sensor is that it occupies only one digital I/O pin of the microcontroller. D1 pin of Node MCU is connected to the DS18B20 temperature sensor for acquiring the data from the temperature sensor. The circuit diagram of Node MCU interfaced with DS18B20 temperature sensor is shown in Fig. 1.

The 4-channel relay circuit is then interfaced with the microcontroller Node MCU. An electric heater and a bulb are connected to the relay circuit. The D2 pin of Node MCU is connected to the IN2 pin of the 4-channel relay circuit. As the data arriving from the DS18B20 temperature sensor reaches above the predefined limit, the relay circuit turns off the power supply to the electric heater and the bulb (Fig. 2).

In order to get the data on the mobile app Blynk, a unique ID needs to be generated. After generating the ID, the next step is to include the authentication key, SSID, and password in the coding for communication between Node MCU and Blynk server. The process is described in Figs. 3, 4 and 5).

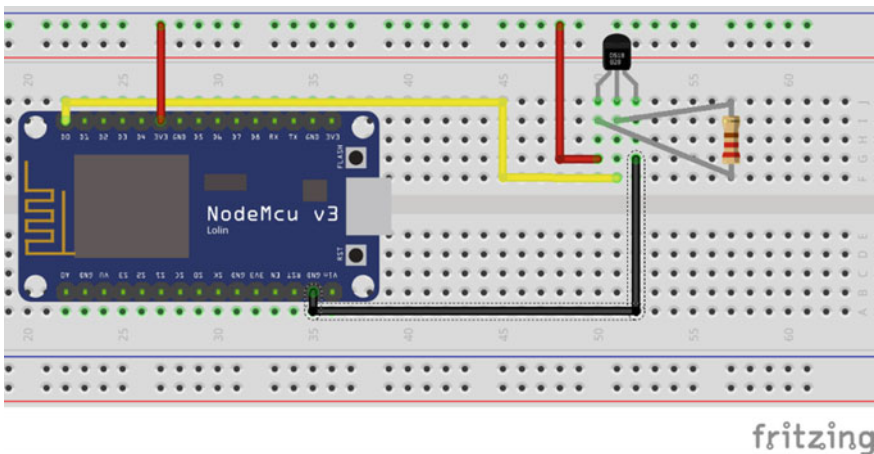


Fig. 1 Circuit diagram of DS18B20 with Node MCU

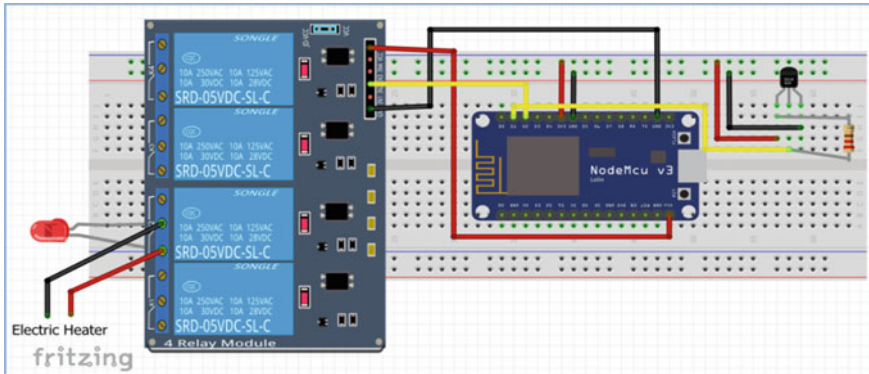


Fig. 2 Circuit diagram of DS18B20 and relay circuit with Node MCU

4 Hardware Implementation and Testing

Figure 6 shows the hardware setup of DS18B20 temperature sensor with the Node MCU. On uploading the program in Arduino IDE, the DS18B20 temperature sensor shows a result of 33 °C when it is set free in the room which is the room temperature (Figs. 7 and 8).

The hardware connection of electric heater and the bulb with the Node MCU and DS18B20 temperature sensor through 4-channel relay module is shown in Fig. 9.

If the temperature is below 35 °C, then the bulb will glow and the electric heater will heat the water (Fig. 10).

As the temperature reaches above 35 °C (predefined limit), then the relay module will turn off the electric heater and the bulb (Figs. 11, 12 and 13).

5 Conclusion

- In this project, a circuit is developed which regulate and monitor the temperature using IoT.
- It helps in overcoming the challenge of lack of proper monitoring system in industries and homes.
- The microcontroller Node MCU needs to be connected to WiFi in order to show the temperature on mobile app Blynk. It continuously monitors the temperature and if the temperature exceeds the predefined limits, a notification will be sent to the registered email id that “the temperature is above predefined limit”.

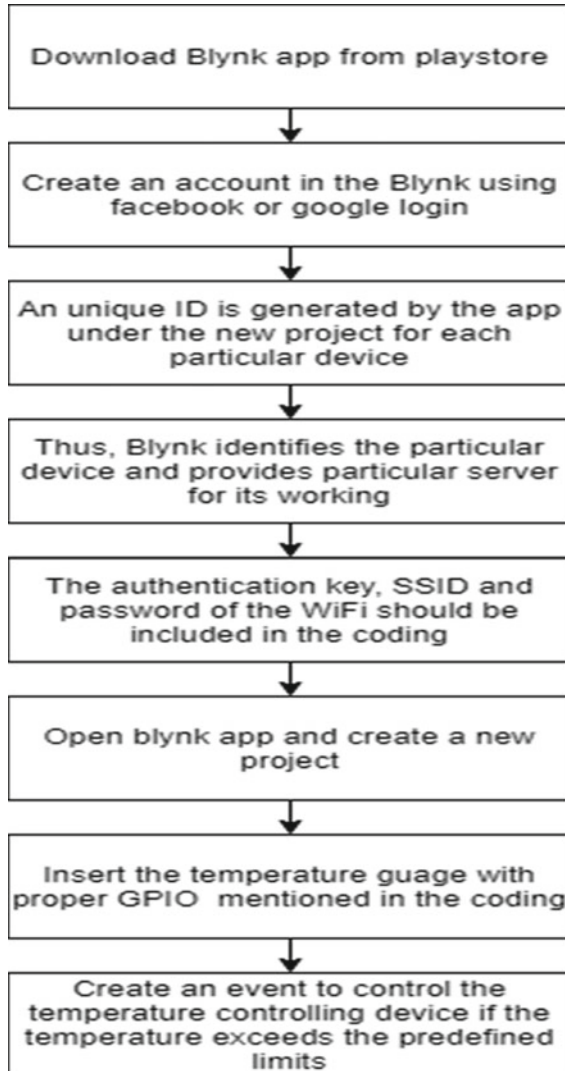


Fig. 3 Account creation and working process in Blynk app

- The proposed project was done on pilot level. After this project, the aim is to implement IoT in foundry. Firstly, in furnace in order to monitor the temperature inside the furnace through mobile app Blynk over WiFi. And secondly, implementing it in casting in order to reduce the defects which occur during solidification, as it causes a large amount of loss to the industries.

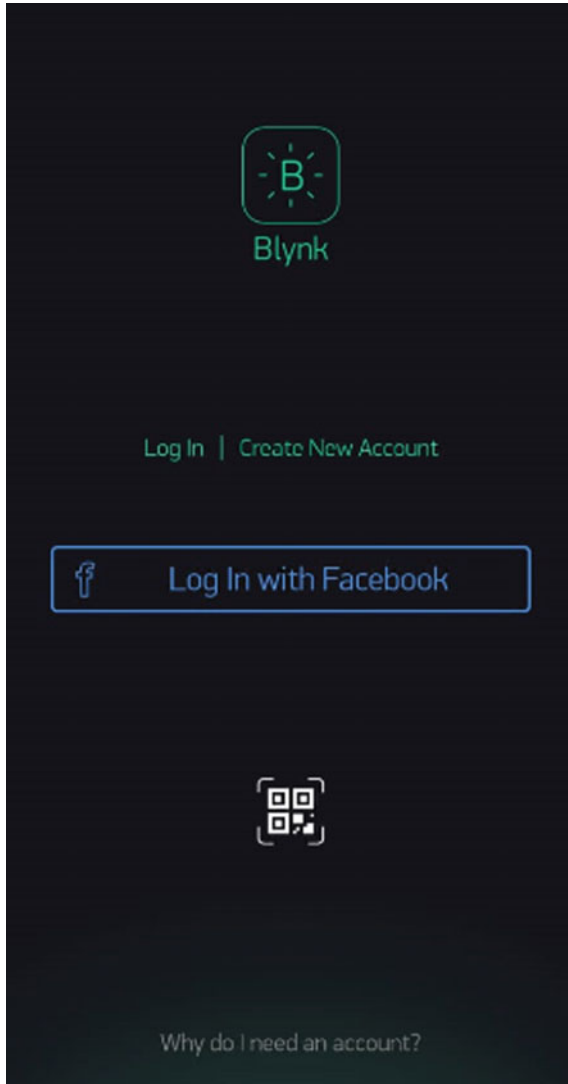


Fig. 4 Blynk App User Interface

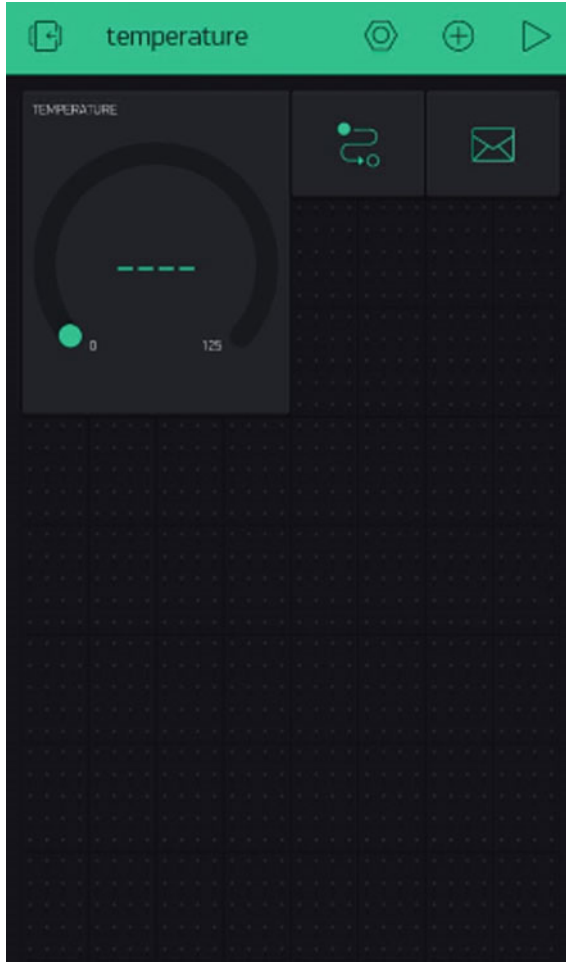


Fig. 5 Created a new project named temperature

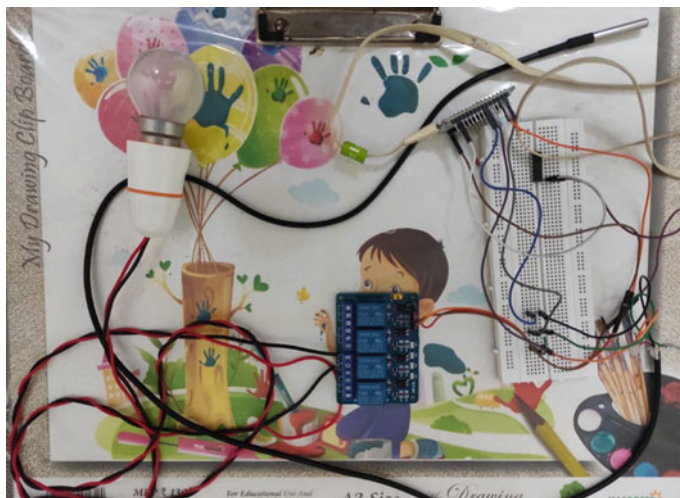


Fig. 6 Hardware implementation of DS18B20 with Node MCU

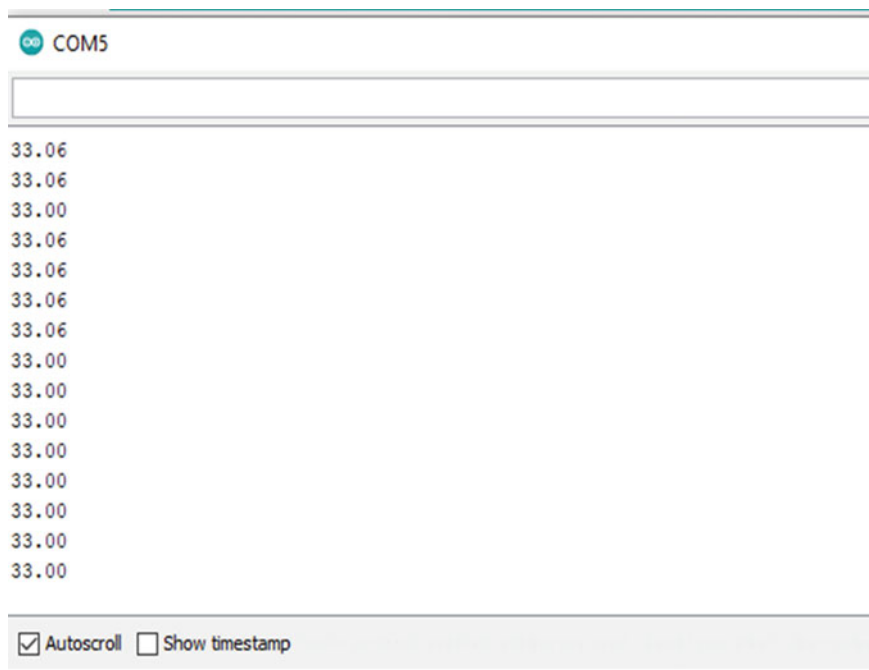


Fig. 7 Temperature sensor shows 33 °C (room temperature) in Arduino IDE serial monitor

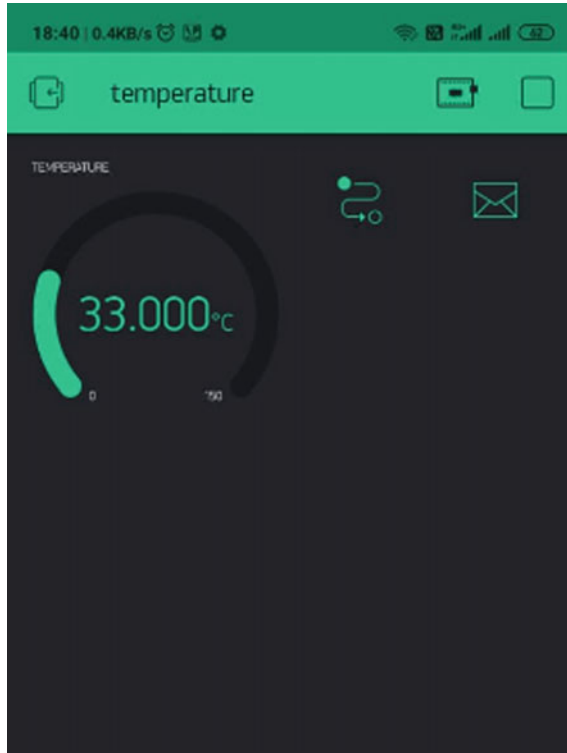


Fig. 8 Temperature (33 °C) shown in Blynk app

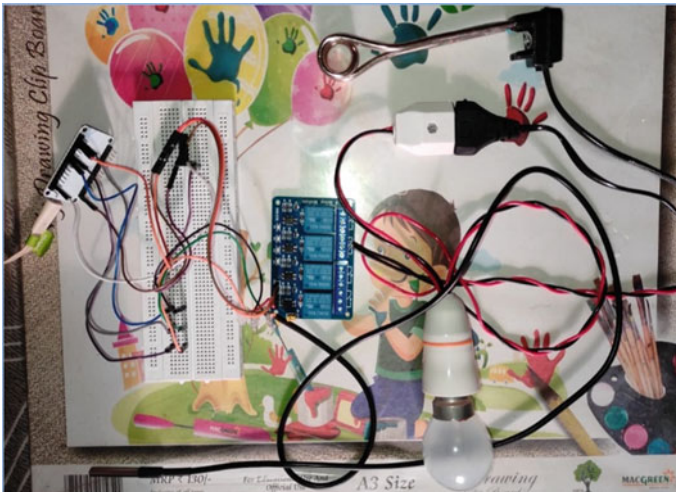


Fig. 9 Hardware implementation of the proposed system

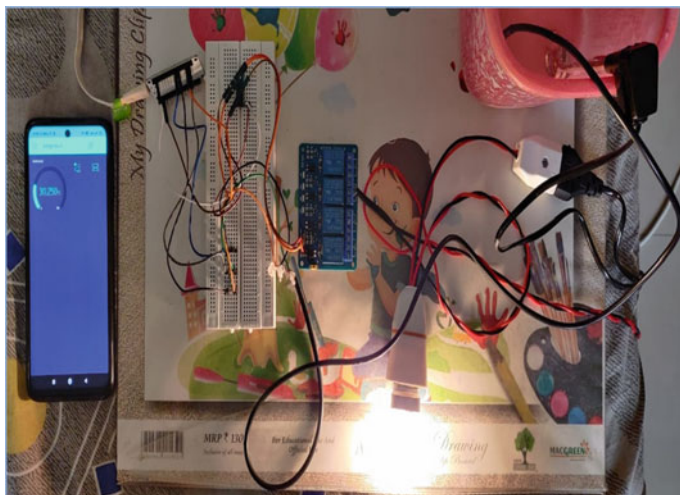


Fig. 10 Connection at 30 °C (below 35 °C)

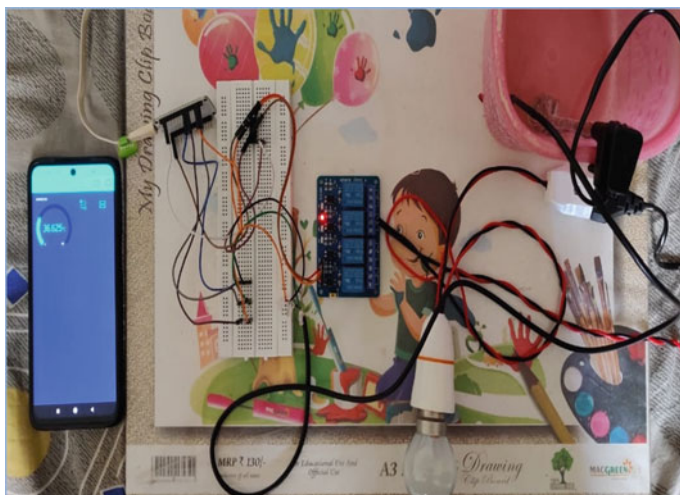


Fig. 11 Connection at 36 °C (above 35 °C)

Fig. 12 Temperature (36.5 °C) shown in Blynk app

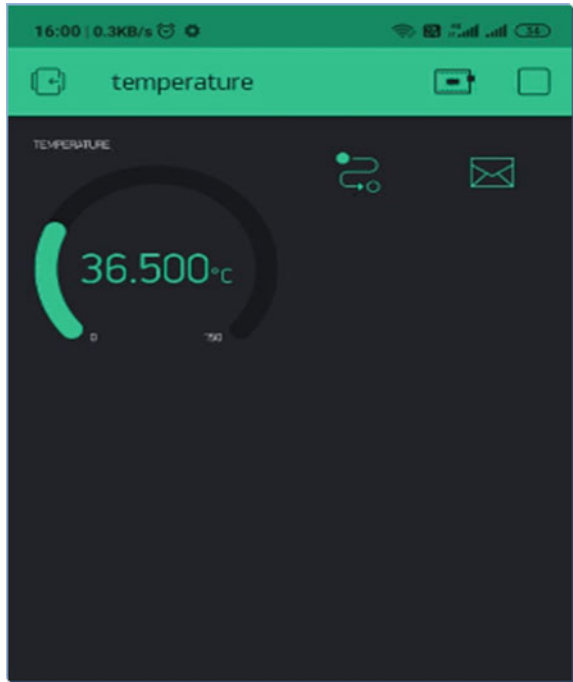
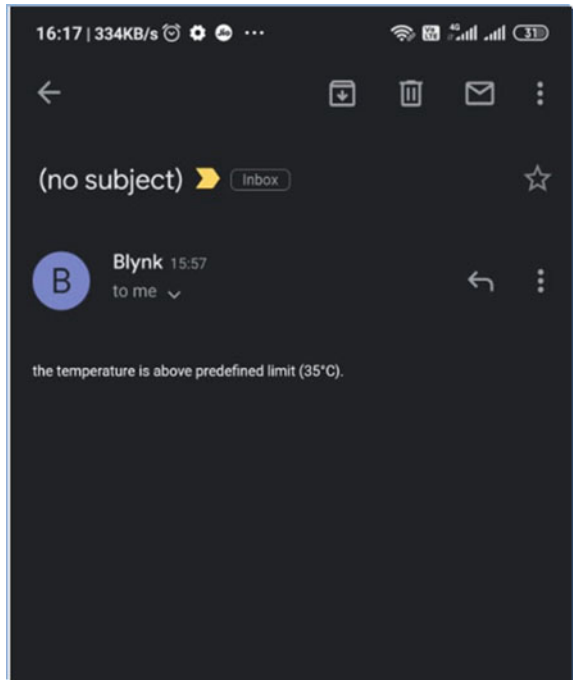


Fig. 13 Notification sent by Blynk on registered Email ID



References

1. Barot RS, Patel H, Devmurari R, Shah K, Sharma B, Jay Shah (2020) IoT feasibility aspects of mould temperature monitoring and casting simulation for smart foundry. *Mater Today Proc* 28(3):1732–1738
2. Pham S, Yeap D, Escalera G, Basu R, Wu X, Kenyon NJ, Hertz-Picciotto I, Ko MJ, Davis CE (2020) Wearable sensor system to monitor physical activity and the physiological effects of heat exposure. *MDPI Sensors* 20(3):855
3. Abubakari S (2019) Improving business effectiveness using internet of things. *Diverse Gen Comp Inform Sci (DJCIS)* 1(2):1–5
4. Padhen M (2019) Internet of things for industries and enterprises. *Int Res J Eng Technol (IRJET)* 06(09):1010–1014
5. Wu F, Wu T, Yuce MR (2019) Design and implementation of a wearable sensor network system for IoT-connected safety and health applications. In: 2019 IEEE 5th World Forum on Internet of Things (WF-IoT), pp 87–90

Mechanical Structures and Stress Analysis

Strain Measurement of Aluminium in Tensometer Using Digital Image Correlation (DIC)



A. Vijaya , N. Kannan, M. Palaniappan, and G. S. Lohith Kumar

Abstract Digital Image Correlation (DIC) is an evolving optical image technique to measure deformation. DIC technique correlates a series of images captured during deformation. Based on the position of speckle pattern on the image, the displacement and strain field are estimated. The aluminium sample is prepared as per ASTM standard added with speckle pattern spray-painted on its surface. A simple stand-alone CCD camera—lighting system is used to record the deformation along uniaxial tensile testing carried out in Tensometer. A series of captured images during deformation are tracked using open-source DIC program in MATLAB software. The static and dynamic analysis of specimen is also carried out in ANSYS workbench. The stress and strain values obtained from the experimental readings (Tensometer) and the image correlations (DIC) closely match each other whereas simulation results obtained in ANSYS have 16% error compared with experimental. This error may be reduced by decreasing the element size and reducing errors in meshing and loading.

Keywords Mechanical testing · Tensometer · Aluminium · DIC · Dynamic analysis

1 Introduction

The knowledge of stress and strain of a material is essential for structural design and other purposes. Thus, its determination is very significant for all engineering applications. A strain in any material can be defined as the ratio of change in length to the original length. It is essential in critical investigation parameters to study the property of material behaviour. The traditional measuring instruments are not capable of creating strain plots, mostly due to high costs and not practical, and the conventional optical measurement methods require tedious experimental setup [1–3]] compared to digital image correlation (DIC) methods [4]. Digital Image Correlation

A. Vijaya (✉) · N. Kannan · M. Palaniappan · G. S. L. Kumar
Department of Mechanical Engineering, SRM Institute of Science and Technology,
Kattankulathur, Chennai, India
e-mail: vijayaa@srmist.edu.in

technique can be tested from small to large test specimen without any restriction for its size or shape. It uses image correlation principle to measure the strain field by analyzing the movement of the points marked on the test specimen. The recent development of inexpensive CCD cameras and rapid growth in image processing with powerful and affordable laptops makes this non-contact measurement technique more attractive [5–7]. These computer-based optical techniques have the advantage of direct sensing and non-complex systems, which avoids the tedious process. The data acquisition by DIC is faster compared to other traditional methods. This technique comprises of creating speckle pattern comprising with finer block dots preferably on a white background on the specimen and subjecting it to deformation while capturing the deformation continuously, either with high-speed camera [8, 9] or with slower frame rate.

A series of acquired images correlate with each other depending on the subtle movement of speckle pattern based on the strain it subjected to. Digital image correlation algorithm is an iterative algorithm, which searches for the intensity of speckle patterns as a subset, inconsequent images from its reference image. The difference between initial and final positions of speckle pattern gives us full-field displacement and strain of the test specimen.

Peter and Ranson [4] introduced the concept of DIC digital image correlations and now many researchers adopted DIC methods for various applications starting from strain measurement in structural applications [5, 10] to biomechanics [11]. Out of plane measurement and large deformation are achieved through stereo DIC [12], and in some cases, DIC is combined with interferometry in a hybrid manner to find the deformation [13]. Few researchers used DIC to measure the strain of crystal grains by capturing images in optical microscope and SEM [14]. The literature presented here is representative and not exhaustive.

There are various contact and non-contact techniques for measurement of strain. Some software can be used for measurement of strain using 2D DIC. Companies like correlated solution; Dantec Dynamic produces 2D DIC software. There are also several other open-source software such as NCORR [15] and MATLAB.

Two-dimensional digital image correlation (2D DIC) is now widely accepted and commonly used in the field of experimental mechanics. 2D DIC directly provides full-field displacements to sub-pixel accuracy and full-field strains by comparing the digital images of a test object surface acquired before and after deformation. Ma Quanjin et al. [16] investigated the mechanical properties of materials like aluminium, GFRP and plastics using DIC by carrying out tensile test in the universal testing machine.

In this present study, methodologies of the 2D DIC technique for displacement and strain field estimation are determined for aluminium rod while extension is carried out in extensometer. In this experiment, Tensometer is used for the application of load for obtaining the experimental strain values as well as deformations are captured continuously using a stand-alone CCD camera. These images are then correlated using MATLAB software. The following study compares the results obtained from DIC using experimental input speckle images collected from the experiment as well

as dynamic analysis carried in ANSYS along with experimental strain values from Tensometer.

2 Methodology

The methodology describes the techniques that are to be followed for the image acquisition to perform the DIC process in MATLAB. The specimen is subjected to tensile loading and images are captured at certain desired intervals until the failure of the specimen. These images are obtained by using a CCD Camera. The images are then correlated and measured for required parameters using DIC process in MATLAB. The following Fig. 1 shows a schematic diagram of the experimental setup. Tensometer, a testing machine, is used to analyze the tensile behaviour of the material, such as the tensile strength and Young's modulus. In this present work, Electronic Tensometer, which is fitted with load cells of capacity 0.2KN, 2KN and 20KN, is used for conducting experiments.

2.1 Specimen

The material for the specimen is selected Aluminium 6061 as per dimensions (ASTM A370-8). Figure 2a, b shows 3D model of the specimen. Speckle patterns are sprayed on the specimen, and continuous periodic images are acquired through WATEC 902B Camera during the entire loading process.

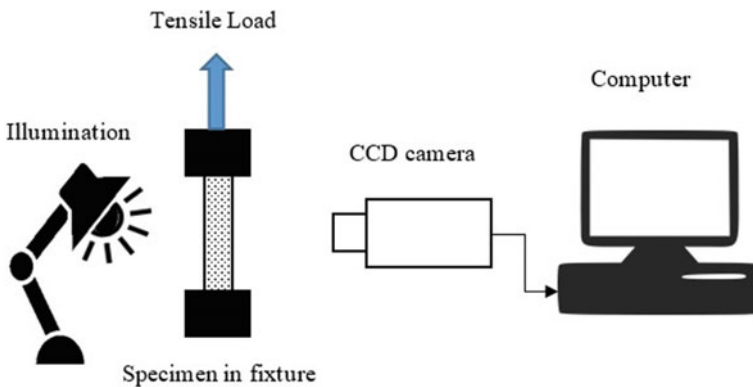


Fig. 1 Schematic setup diagram for strain measurement in tensometer using DIC

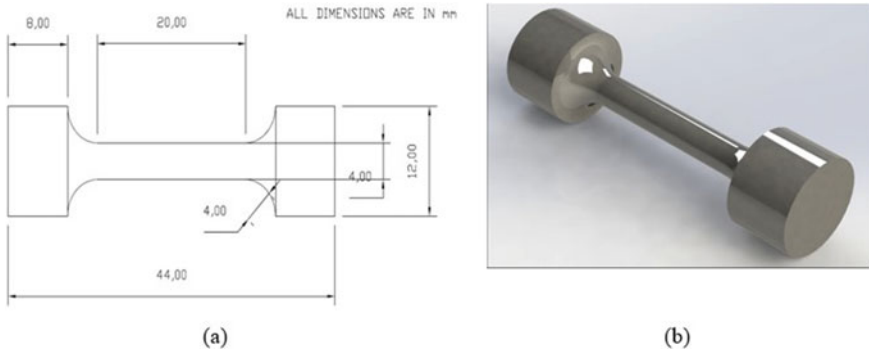


Fig. 2 a 2D Drawing of Specimen as per ASTM b Specimen designed in Solid Works

2.2 Spray Painting Technique

The commonly used speckle preparation technique is the spray paint technique. The background surface of the specimen should always be painted in white. The specimen is coated with white aerosol paint, throughout its surfaces. The specimen is allowed to dry for a minimum of 4–5 h. A temporary disposable toothbrush is painted with the black aerosol paint on the bristles of the toothbrush and is kept at 45 degrees towards the specimen and flicked gently to paint speckle pattern on it. The specimen is allowed to dry again before using it for testing.

3 Experimental Procedure

The specimen painted with speckle pattern is fixed on two ends of fixture, which in turn fitted on electronic Tensometer as shown in Fig. 3. This machine has a data transfer unit along with the provision of display unit. The data entry for specimen code, batch code, specimen grade, area of applied load, maximum load (20 kN), and minimum load (10 N) is fed through the display unit. The camera is fixed in a proper position to focus it on detection of the speckle pattern and connected to laptop through interfacing software. The lights are fixed in such a way that the specimen is adequately illuminated. Once the experiment starts, the experimental data for strain measurement from electronic Tensometer are transferred through DTU to PC, and simultaneously specimen images are acquired continuously for analyzing the same via DIC using CCD camera. The graphs are generated for Stress versus Strain for the process conducted. The images taken from the camera are being carried out for the correlation process as in Fig. 4.

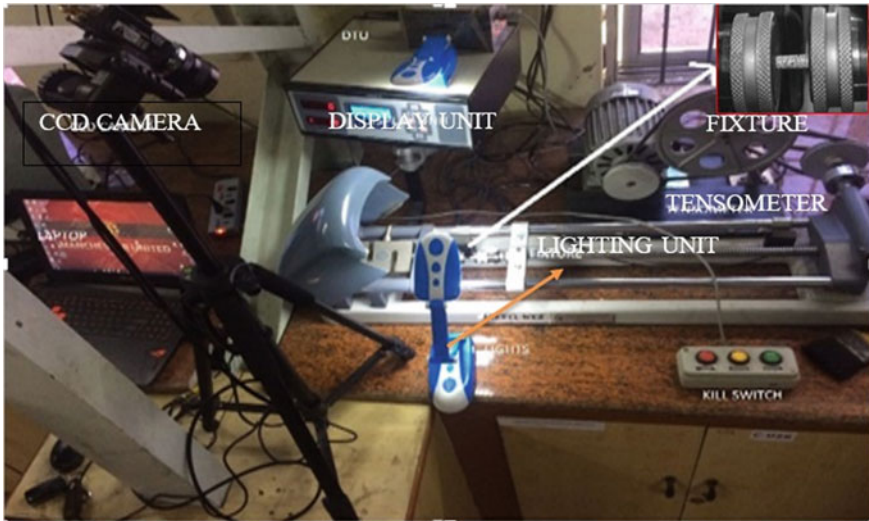
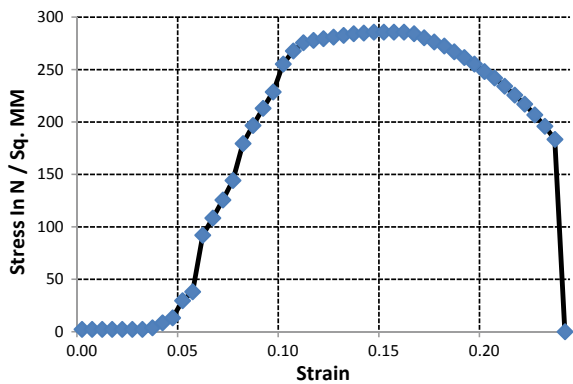


Fig. 3 Experimental setup: image acquisition for DIC in tensometer: fixture and specimen (subset)

Fig. 4 Stress versus strain graph obtained for aluminium specimen from electronic tensometer



3.1 Experimental Verification

The specimen is clamped and attached with the tensometer, the focus lights are used to illuminate the specimen and the cameras are placed near normal to specimen surface and focus towards the specimen as shown in Fig. 5a. Once the tensile loading on the specimen starts to increase, the specimen elongates. At a load of around 2 KN, this part of the specimen is observed as shown in Fig. 5b. The necking starts after a load of around 4.8 KN in the specimen. The necking process involves elongation of around 3.8 mm of total length of the specimen as shown in Fig. 5c. The specimen breaks into two due to ultimate tensile loading. At a load of around 9KN, this part of the specimen is observed as shown in Fig. 5d.

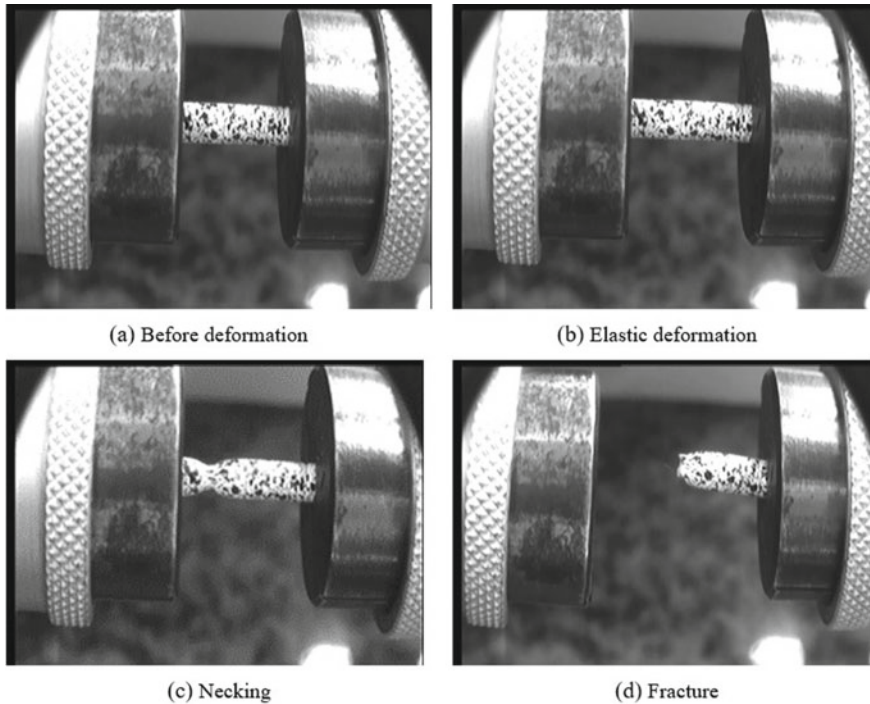


Fig. 5 Experimental Images of specimen acquired through CCD

3.2 Digital Image Correlation Using MATLAB [17]

In 2D-DIC method, the region of interest in the reference image is defined first, which is again divided into evenly spaced grid, the displacements are calculated at each point of the grid and deformation is calculated. The basic principle of 2D DIC is that matching of same points or pixels of series of images recorded before and after deformation.

Digital image correlation is an image processing technique used to measure displacement field and strain by the movement of points marked on the specimen. DIC falls into three main stages like pre-processing, processing and post-processing.

The gradual application of tensile load, the behaviour of the specimen is recorded as a video by use of the HONESTECH software. This video, saved in the system, is acquired into snapshots at periodic intervals. Any desirable number of images can be obtained. For image acquisition from the video, VLC Media Player Software can be used.

For the image to be processed in MATLAB, the size of the image must not be greater than 1024 kb. The images are supposed to be in greyscale only. The images are to be named as in order sequentially without any spaces in between. The image *.tif format is preferred.

In the processing stage, a series of text files that contain the MATLAB code with an extension of ‘*.m’ called m-files need to be executed. The m-files used for this experiment are as follows. The commands of these m files can be downloaded from [17]

- `filelist_generator.m`
- `grid_generator.m`
- `automate_image.m`
- `displacement.m`

The ‘`filelist_generator`’ generates the list of series images assigned with preferred filename given by the user. It can be done manually as well as automatically. The series of images as in Fig. 6a are stored for processing in a particular folder. The ‘`grid_generator.m`’ is a command that is used to define the region of interest in the captured images. The speckle pattern in the tensile specimen lies in 2D plane as a rectangle, and rectangular ROI is chosen. After marking the lower left part of the specimen and upper right part of the specimen using the markers, the grid is generated on the specimen within the ROI with the desired pixel resolution as shown in Fig. 6b. The correlation between the images is carried out using ‘`automate_image.m`’ file. It can be noticed that the markers placed on the specimen surface gradually move, thus measuring the total deformation that has occurred during the application of tensile load. The red dots indicate the markers of the deformed specimen, whereas the green dots are the initial markers, as shown in Fig. 6c. The computed displacement is plotted and viewed in the post-processing stage using ‘`displacement.m`’. This is a collection of function, which helps us to review the displacement field, calculate the strain and even delete the unwanted trackers.

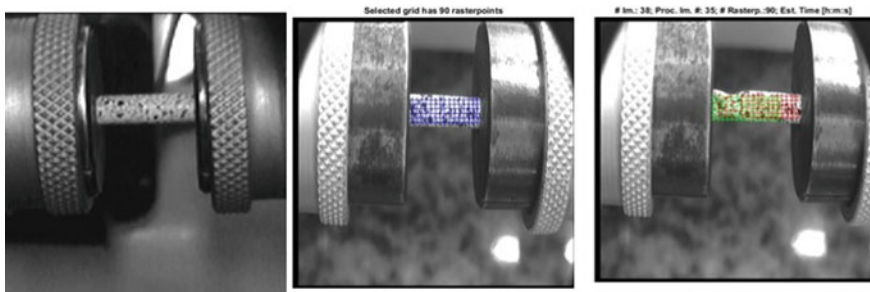


Fig. 6 a Sample Image b Grid Generator c Movement of grid points during deformation

3.3 Digital Image Correlation and Tracking with MATLAB [17]

The displacement of initial markers (Green) in the ROI is plotted as 3D mesh plot as in Fig. 7. The blue markers show the displacement along x-axis. After filtering the poorly correlated tracker, 1D Average Strain measurement is plotted for aluminium in Fig. 8. The stress that has been calculated using the load–displacement graph

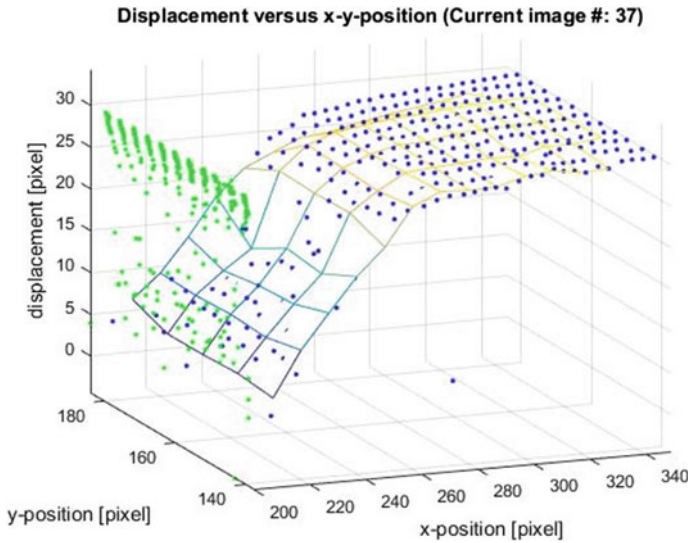
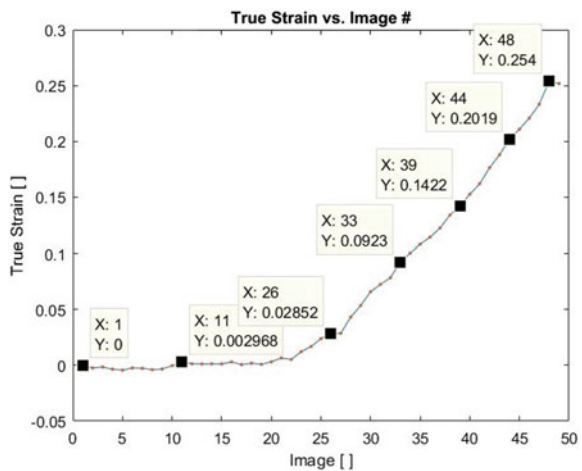


Fig. 7 Three-dimensional displacement obtained for aluminium specimen

Fig. 8 1D Average strain measurement (aluminium)



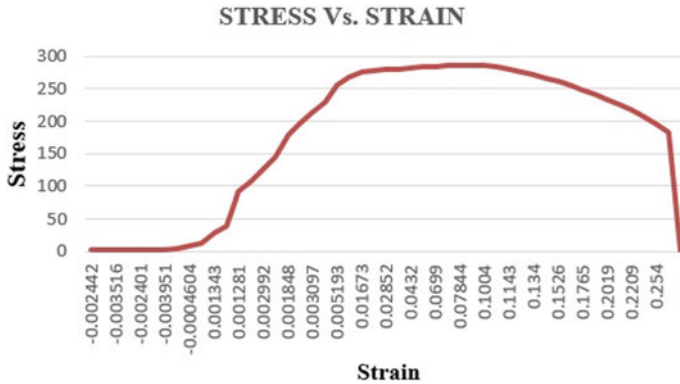


Fig. 9 Stress versus strain (aluminium)

obtained from the experimental result is plotted against the strain from DIC and shown in Fig. 9.

4 Static and Dynamic Analysis of Aluminium in ANSYS

Static analysis is performed to determine the stress, strains, displacements and forces in structures or components due to applied loads, which do not include significant inertia and damping effects. The tensile specimen was designed according to the ASTM standards of Tensometer using SOLIDWORKS, 3D modelling CAD software. The file is then converted into Initial Graphics Exchange Specification (IGES), a neutral file format that facilitates to exchange information to other software. The static analysis was performed using ANSYS V16.0 workbench software. The static analysis consists of selecting engineering material, mesh generation, giving constraint and solving the problem.

The material selected is aluminium. The properties of the chosen grade material such as yield strength, ultimate tensile strength, Poisson ratio, Young’s modulus are provided. Meshing is vital for rendering solutions. Mesh generation is a process of generating a polygonal or polyhedral mesh that approximates the geometry as shown in Fig. 10a. The type of mesh used was tetrahedrons, and the element size is given as 1 mm. The quality of the mesh is checked once meshing is complete. To perform static analysis, constraints are to be provided, since it’s a tensile testing specimen one end of the dog bone structure is fixed, and another end is subjected to tensile loading as shown in Fig. 10b. The load was provided in transient condition with time interval of 1 s load was gradually increased from 220 N to 10 KN. In Fig. 10b, the blue region or A is the fixed portion, and the red region or B is the force applied. The force applied was in positive x-direction.

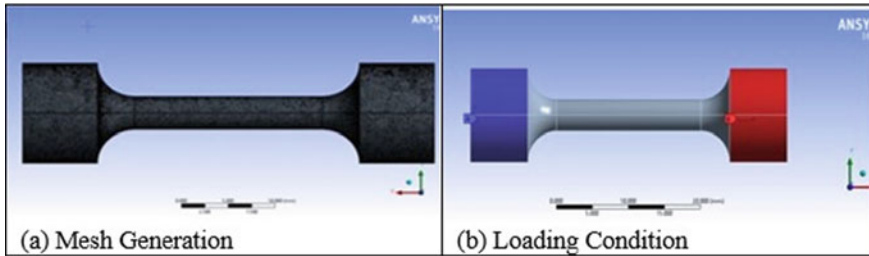


Fig. 10 a Meshing of tensile specimen and b constraints for tensile specimen

ANSYS software provides us with various options. Solution such as stress, strain, total deformation of the specimen can be evaluated. The stress and strain values obtained under the applied loading conditions are shown in Fig. 11a–c are taken for comparison. Explicit dynamic analysis was also carried out to determine the response of the specimen to the real-time data, especially when it is impossible to perform physical testing. Here also, material is defined first, and then meshing is done. Once meshing is complete, the constraints are provided. Making one end fixed and another end is applied with the load of 10 KN. The real-time animation is generated. The elastic deformation that occurs during dynamic analysis is shown in Fig. 12a. The neck formation that occurs during dynamic analysis has been shown in Fig. 12b. The failure of the specimen that occurs during dynamic analysis has been shown in Fig. 12c.

5 Results and Discussions

The results are obtained in the form of the graph from the entire three-tensile test, done by Tensometer, ANSYS and DIC. The comparison for all three tests is carried and plotted in Figs. 13 and 14. The experimental results obtained from tensometer closely match with DIC results. As the tensile strain increases, the tensile stress also increases, reaches the UTS 285pa and breaks into two pieces when the tensile strain reaches to a maximum of 0.24.

The error percentage between the experimental values, DIC and ANSYS is shown in Table 1. From the above results, one can find that the test result of DIC technique is closely matched with experimental values. The strain measurement using DIC provides accurate strain measurement at less cost and fast data acquisition.

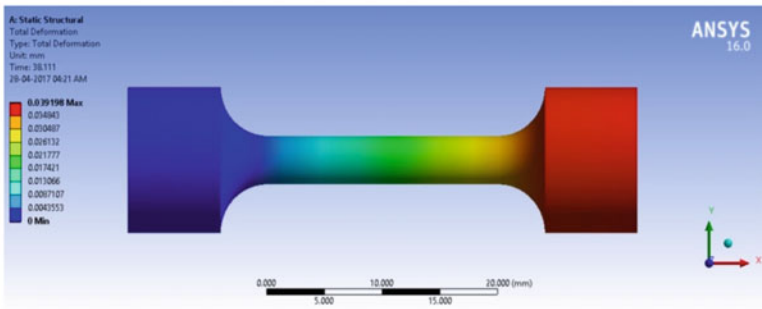
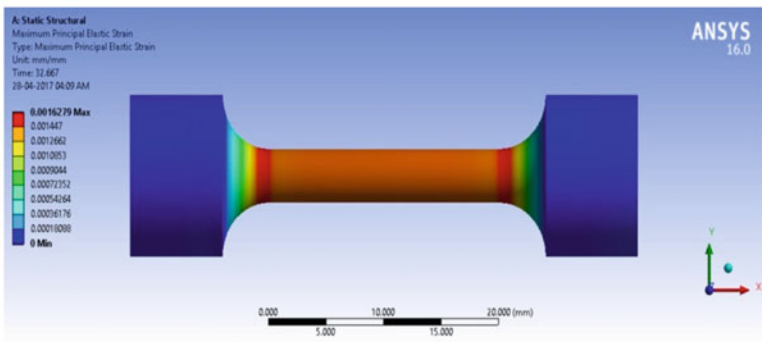
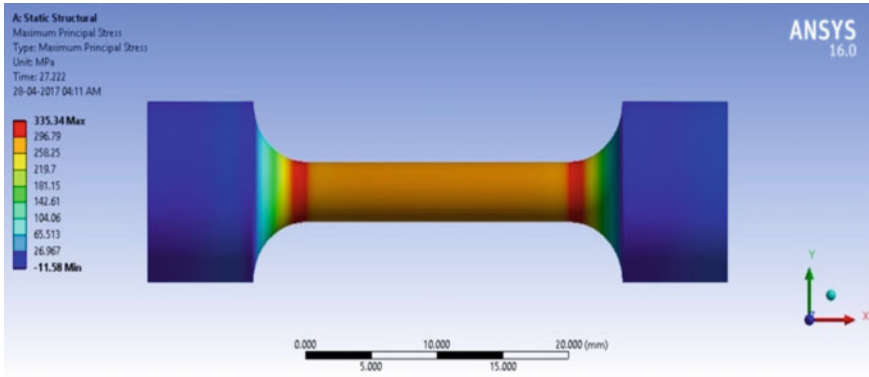
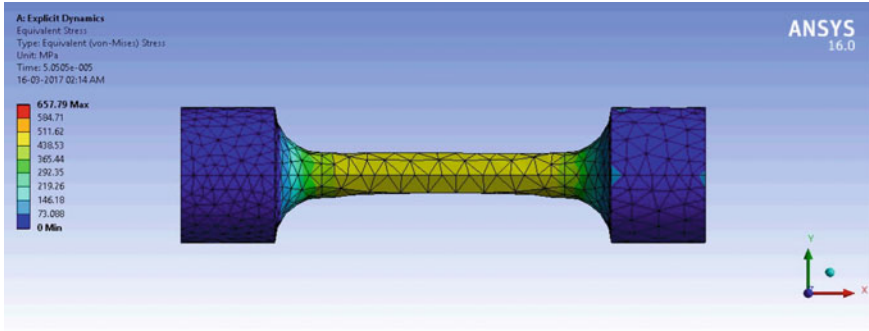
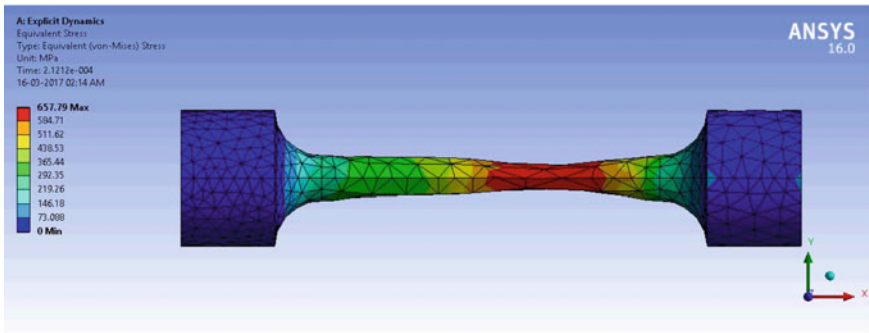


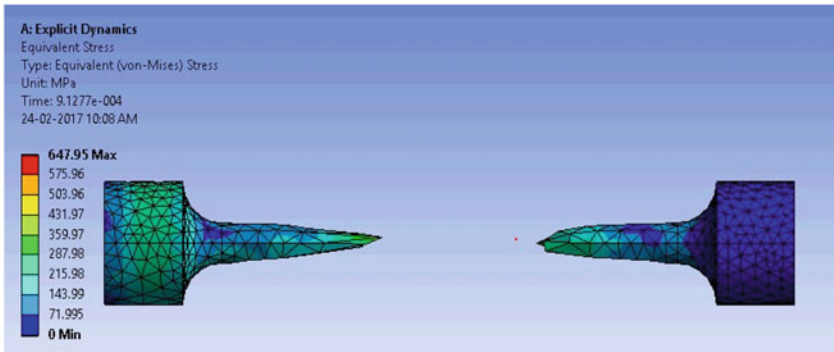
Fig. 11 Stress, strain and deformation (aluminium)



(a) Deformation



(b) Necking



(c) Fracture

Fig. 12 Dynamic analysis of aluminium under tensile loading **a** deformation **b** necking **c** fracture

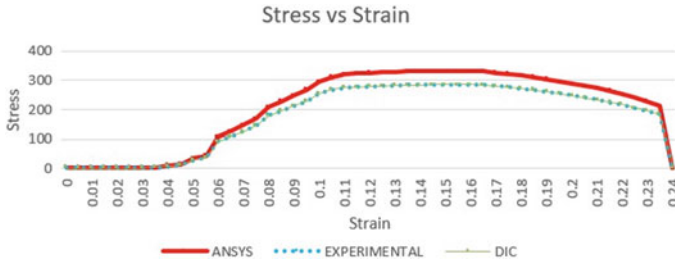


Fig. 13 2D Stress versus strain plot (aluminium)

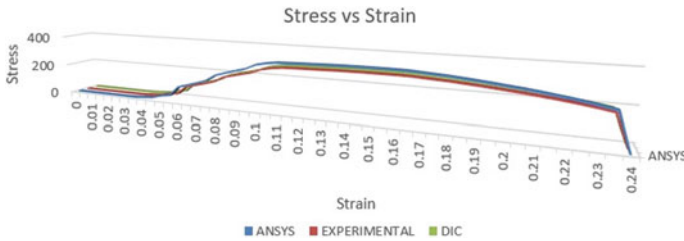


Fig. 14 3D Plot for Stress versus strain plot (aluminium)

Table 1 Error analysis (aluminium)

S.no	Content	Theoretical	Experimental	ANSYS	DIC
1	Maximum stress	285 Pa	285.7 Pa	333.08 Pa	285.668 Pa
2	Maximum Strain	0.24	0.24	0.06	0.254
3	Error% (Stress)	–	0.25%	16.87%	0.23%
4	Error% (Strain)	–	0%	75%	5.83%

6 Conclusion

This present study discusses the application of digital image correlation (DIC) technique for strain measurement of aluminium specimen under uni-axial tensile testing in Tensometer. A stand-alone camera and the lighting setup are set to capture the series of images during deformation. The captured images are digitally tracked and correlated using MATLAB. The results obtained through DIC closely match with the strain values obtained from the load cell in Tensometer. Static and dynamic analysis for the tensile specimen is carried out in ANSYS, and the results obtained through ANSYS have an error percentage around 16%. This may be due to error in the selection of mesh size as well as loading conditions in ANSYS. Hence, it can be concluded that DIC is best suited for mechanical testing, and one can apply the same for unknown material for research purposes. This experiment can be used as

a student's experiment in the material testing lab if one has a good resolution CCD camera and proper lighting system.

References

1. Patorski K, Kujawinska M (1993) Handbook of the Moire Fringe Technique. Elsevier Science
2. Reid GT (1984) Moiré fringes in metrology. *Opt Lasers Eng* 5:63–93. [https://doi.org/10.1016/0143-8166\(84\)90012-5](https://doi.org/10.1016/0143-8166(84)90012-5)
3. Subramanian G, Nair SM (1985) Direct determination of curvatures of bent plates using a double-glass-plate shearing interferometer. *Exp Mech* 25:376–380. <https://doi.org/10.1007/BF02321336>
4. Sutton M, Wolters W, Peters W, Ranson W, McNeill S (1983) Determination of displacements using an improved digital correlation method. *Image Vis Comput* 1:133–139. [https://doi.org/10.1016/0262-8856\(83\)90064-1](https://doi.org/10.1016/0262-8856(83)90064-1)
5. He T, Liu L, Makeev A, Shonkwiler B (2016) Characterization of stress-strain behavior of composites using digital image correlation and finite element analysis. *Compos Struct* 140. <https://doi.org/10.1016/j.compstruct.2015.12.018>
6. Hassan GM (2019) Digital Image Correlation for discontinuous displacement measurement using subset segmentation. *Opt Lasers Eng* 115:208–216. [https://doi.org/10.1016/J.OPTLAS.ENG.\(2018\).12.003](https://doi.org/10.1016/J.OPTLAS.ENG.(2018).12.003)
7. Pan B, Yu LP, Zhang QB (2018) Review of single-camera stereo-digital image correlation techniques for full-field 3D shape and deformation measurement. *Sci China Technol Sci* 61. <https://doi.org/10.1007/s11431-017-9090-x>
8. Krishnan SA, Baranwal A, Moitra A, Sasikala G, Albert SK (2014) Assessment of deformation field during high strain rate tensile tests of RAFM steel using DIC technique. *Procedia Eng* 86:131–138. <https://doi.org/10.1016/j.proeng.2014.11.021>
9. Leclerc H, Périé J-N, Roux S, Hild F (2009) Integrated digital image correlation for the identification of mechanical properties. *Comput Vision/Computer Graph Collab Tech* 161–71. https://doi.org/10.1007/978-3-642-01811-4_15
10. Zappa E, Hasheminejad N (2017) Digital image correlation technique in dynamic applications on deformable targets. *Exp Tech* 41. <https://doi.org/10.1007/s40799-017-0184-3>
11. Genovese K (2019) An omnidirectional DIC system for dynamic strain measurement on soft biological tissues and organs. *Opt Lasers Eng* 116:6–18. [https://doi.org/10.1016/j.optlaseng.\(2018\).12.006](https://doi.org/10.1016/j.optlaseng.(2018).12.006)
12. Genovese K, Sorgente D (2018) A morphing-based scheme for large deformation analysis with stereo-DIC. *Opt Lasers Eng* 104:159–172. <https://doi.org/10.1016/j.optlaseng.2017.06.020>
13. Malesa M, Kowalczyk P, Dymny G, Skrzypczak P, Salbut L, Pakula A (2019) Hybrid GI-DIC measurement procedure for hierarchical assessment of strain fields. *Meas J Int Meas Confed* 134:83–88. [https://doi.org/10.1016/j.measurement.\(2018\).10.078](https://doi.org/10.1016/j.measurement.(2018).10.078)
14. Guery A, Hild F, Latourte F, Roux S (2016) Identification of crystal plasticity parameters using DIC measurements and weighted FEMU. *Mech Mater* 100:55–71. <https://doi.org/10.1016/j.mechmat.2016.06.007>
15. Ncorr - Open source 2D digital image correlation MATLAB software n.d. <http://www.ncorr.com/> (accessed June 15, 2017)
16. Quanjin M, Rejab MRM, Halim Q, Merzuki MNM, Darus MAH (2020) Experimental investigation of the tensile test using digital image correlation (DIC) method. *Mater Today Proc* 27:757–763. <https://doi.org/10.1016/j.matpr.2019.12.072>
17. Eberl C Digital Image Correlation and Tracking 2017

Structural and Thermal Analyses of Gas Turbine Blades with Internal Cooling System Under Steady-State Conditions



K. Balaji, G. Jims John Wessley , and S. V. Khandal

Abstract Turbine is a rotating mechanical device that is used to convert the kinetic energy available in a fluid into useful work. The high-velocity fluid creates an impact on the blades as it flows over the turbine blades and causes the rotor to rotate, thus producing useful work that can be coupled to any application. In this present work, gas turbine blade made of Inconel 718 is modelled using CATIA, and the structural and thermal analyses are carried out using ANSYS. Four different configurations were developed for the study, with different number of holes and hole sizes. Also, the distance between these holes and surfaces were also varied in the analysis. This analysis revealed that a blade configuration with 12 holes each with a diameter of 1.5 mm shows better cooling effectiveness and more advantageous in terms of stress and deformation when compared to other three configurations analyzed in this study. The temperature of the blade and the deformation and stress obtained for this configuration were found to be 1090 K, 2.7 mm and 1481 MPa, respectively.

Keywords Cooling system · Gas turbine blade · Steady state · Structural and thermal analyses · ANSYS software

1 Introduction

Turbines produce power by allowing fast-moving flow of water, gas, steam, air, or any fluid to impinge on a wheel or rotor fitted with vanes. The working fluid may be compressible or incompressible but contains a huge amount of potential energy and kinetic energy. The performance of the turbine blade depends on the temperature of the blades during energy conversion and hence cooling of turbine

K. Balaji · G. J. J. Wessley (✉)
Department of Aerospace Engineering, Karunya Institute of Technology and Sciences,
Coimbatore, Tamil Nadu, India
e-mail: jims_john@karunya.edu

K. Balaji · S. V. Khandal
Department of Aeronautical Engineering, Sanjay Ghodawat University, Kolhapur, Maharashtra,
India

blade material is very critical. In general, to improve the performance of the blades by maintaining them at minimum possible temperatures during operation, data on internal heat transfer and flow are vital in understanding the functionalities behind the flow and heat generation so as to design effective cooling mechanisms. Few designs and techniques have been widely used in the turbine blades to increase the cooling of the blades. The most widely used is the implementation of cold passages in the middle of the aerofoil lined with rib turbulators and jet impingement along the stator vanes and also by using pin-fin or dimples along the trailing edge of the vanes. In order to increase the heat transfer, all the above methods can be combined appropriately.

The related literature on the cooling of turbine blades reported in the literature is summarized in this section. In the reviews conducted by Muniyandi [1] and Ugade and Bhambere [2] on the structural and thermal analyses of turbine blades, it is found that the number of holes in the turbine blade and the material used in the construction play major roles in the efficient functioning of the same. The numerical study performed by Prasad et al. [3], it was concluded that Inconel 717 is the suitable material for gas turbine blades, and the optimum number of holes for efficient operation is found to be 13. However, in the simulation work carried out by Begum et al. [4] by finite element analysis (FEA) using two different materials, N155 and Chromium, it is seen that N155 gives better results compared to Chromium, and it is also concluded that the cooling increases with an increase in the number of holes. Mahesh et al. [5] used solid works to analyze four different turbine models with 7, 8, 9, and 10 holes, respectively, and it was reported that the model with 9 holes yielded better results, and the model with 10 holes yielded very poor results. Krishnam Raju et al. [6] conducted similar studies with CAE software to analyze a gas turbine blade profile with different models using 7, 8, and 9 holes. It is found that the structural and thermal analyses were better when the number of holes used was maximum. The study conducted by Kini et al. [7] on a high-pressure stage gas turbine blade with different helicoidal duct configurations for cooling shows that a parameter defined by the ratio of diameter to length of the cooling duct plays a major role in the performance. The work of Theju et al. [8] compared the structural and thermal performance of two different materials, namely, Inconel 716 and Titanium in turbine blades using CAE tools and found that Inconel 718 showed better performance parameters. A similar study conducted by Hari and Kumar [9] showed that the performances were getting better with the increase in the number of holes across the turbine blades structure. Few other researches like Saif et al. [10] reported the use of advanced materials as coating on the blades, and Balaji et al. [11] reported on the effect of hole orientation angle on the cooling effectiveness of the turbine blades. The work of Veerarahavan [12] reported that molybdenum alloys have good temperature resistance capabilities when compared with Titanium, Zirconium and super alloys. Sagar [13] analyzed the deformation due to stress induced in the blade geometry and reported that the maximum temperature and elongations were found in the blade tip while the temperature remained almost uniform over the maximum curvature of the profile with the distribution linearly decreasing from the tip to the root of the blade.

Ganta [14] and Xie [15] suggested various failure mechanisms and suggestions for a good blade profile configuration and also the use of dimples in optimal design of blades.

However, the literatures reveal that the availability of work on the mechanical and thermal analyses of internal cooling of gas turbine blade system with different configurations made of Inconel 718 material is not reported. Hence, this research attempts to perform structural and thermal analyses of gas turbine blade with internal cooling system under different conjunctions using Inconel 718 material applying ANSYS software.

2 Modelling and Analysis of Gas Turbine Blade

The modelling of turbine blade is done in CATIA software as per the dimensions of the configuration shown in Fig. 1. A high pressure turbine blade from a military aircraft engine is selected for this analysis. It is assumed that hot air from combustion chamber directly hits the high-pressure turbine. CATIA V5 design software is used to create in-part design aerofoil shape according to the coordinates. The Sketcher work is completed by using Sketch-based features, dress-up features and transformation features.

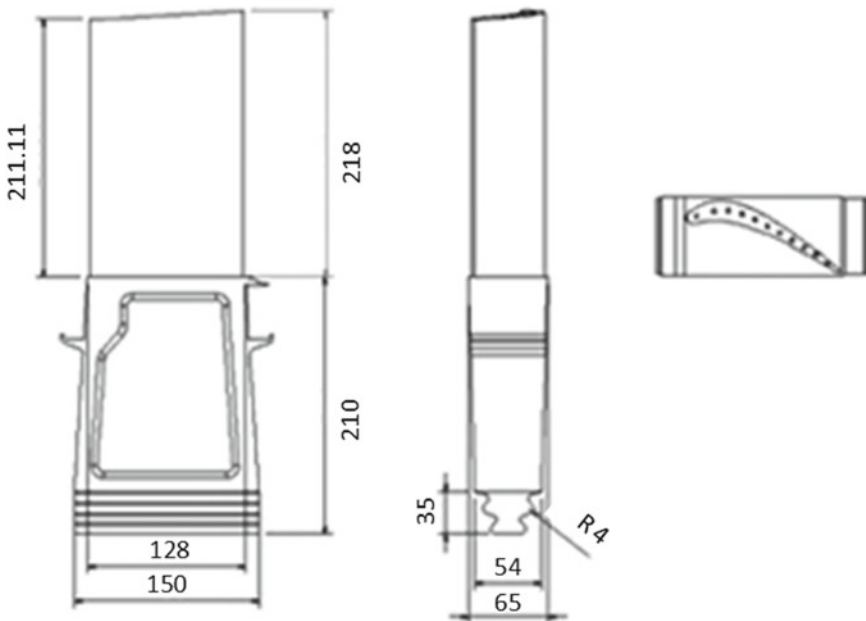


Fig. 1 Dimensions of the turbine blade used in the study

Four different configurations are created with different size of holes, and the part design is loaded into the workbench to convert the design into a 3D model. Analysis of the turbine blade model assembly by creating different views of blade assembly is also completed. The turbine blade model developed in CATIA is depicted in Fig. 2.

Various configurations of the turbine blade used in the current study are provided in Figs. 3, 4, 5 6. The number of holes, hole size and the distance between the holes and surface in each configuration can be seen in the figures as well as in Table 1. ANSYS software was used to perform structural and thermal analyses in these models. The material for the blade chosen in the study is Inconel 718.

The summary of the different configurations and its specifications used in the study are given in Table 1.

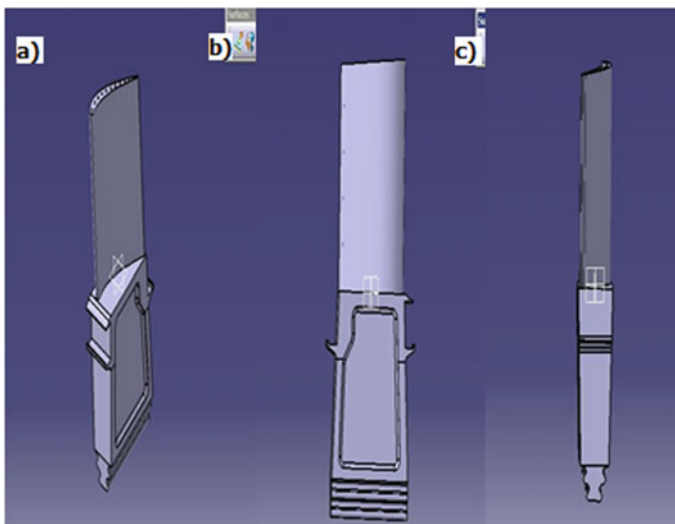


Fig. 2 Various views of turbine blade model. **a** Holes are shown over turbine blade tip for cooling. **b** Side view of the turbine blade with the cross-section in the form of an aerofoil. **c** Model of turbine blade with turbine disk attachment

Fig. 3 Various configurations of blades used in the study

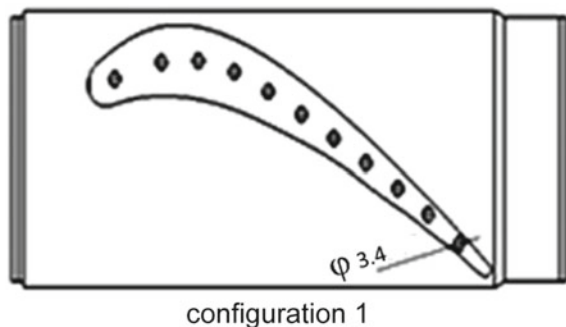


Fig. 4 Various configurations of blades used in the study

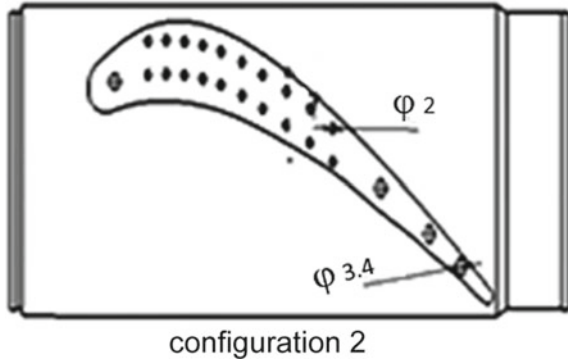


Fig. 5 Various configurations of blades used in the study

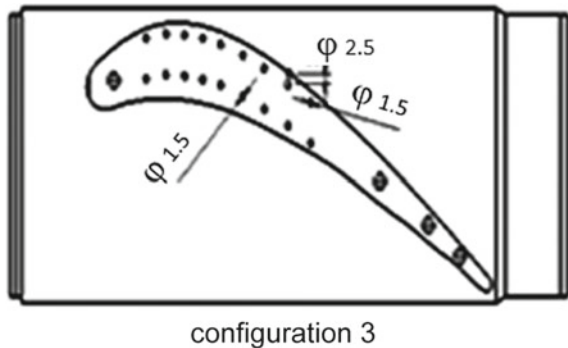
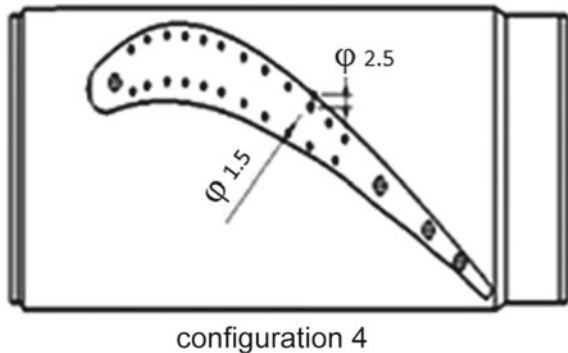


Fig. 6 Various configurations of blades used in the study



The blade configurations are analyzed using displacement and stiffness method under steady-state structural analysis system. The engineering data like stiffness and inertial loads of the component are added. Tetrahedral and hexahedral type of meshing is used, and the material properties of Inconel 718 are chosen. The boundary conditions are set, and the rotation speed of the blade is fixed as 1000 rpm. The pressure, temperature and deformations over the turbine blade are analyzed.

Table 1 Summary of parameters used in the various blade configurations

Configuration	Number of holes	X (Dia) (first row)	Y (Dia) (second row)	Z (Distance between wall and topside hole)	Number of rows
1	10	3.4	-	-	1
2	10	2	2	4	2
3	10	1.5	1.5	2.5	2
4	12	1.5	1.5	2.5	2

3 Results and Discussion

The temperature and stress distribution across the blade and the deformation are analyzed.

3.1 Configuration 1

Configuration 1 has 10 holes created in the mid of the blade with a diameter of 3.4 mm. These holes are used to reduce the temperature over the body.

In Figs. 7, 8, 9, and 10, the pressure, temperature and deformation results are shown. The temperature is observed to be 1143 K, and deformation is recorded as 1.94 mm with a maximum stress carrying capacity of 1462 MPa. From the result, it is seen that the hot air from combustion chamber directly striking the turbine blade is cooled by the air flowing through the holes created on the blade. Hence, this configuration is found to improve the performance of engine and in turn the lifetime of the component.

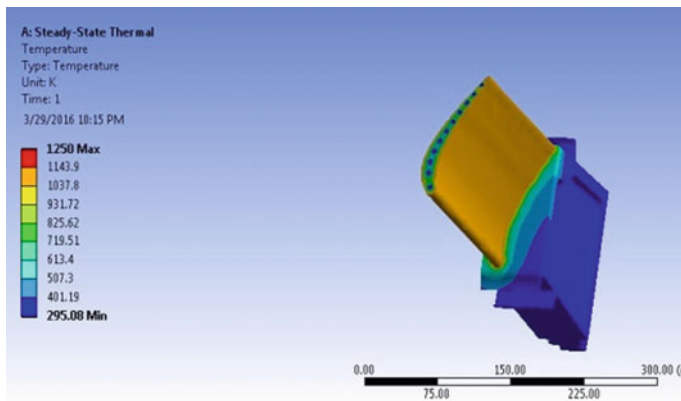


Fig. 7 Temperature distribution (Configuration 1)

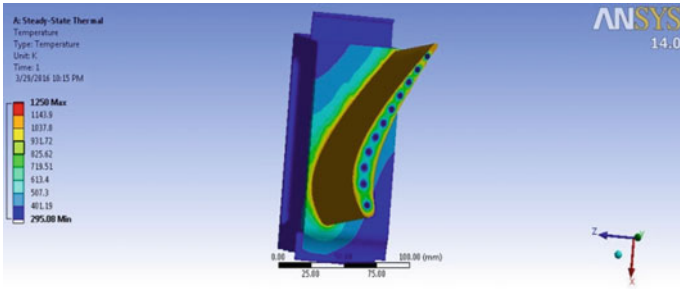


Fig. 8 Temperature across cross-section (Configuration 1)

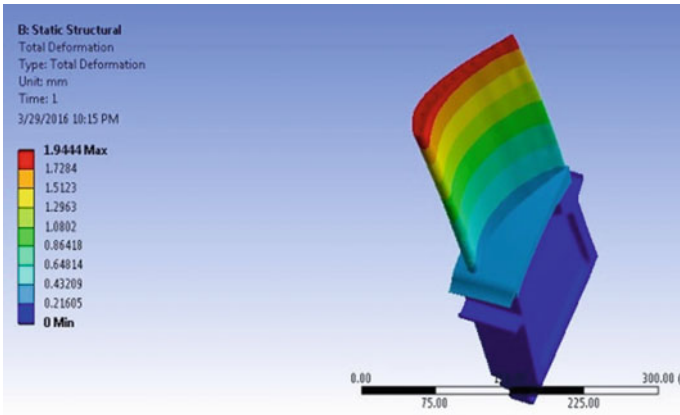


Fig. 9 Deformation (Configuration 1)

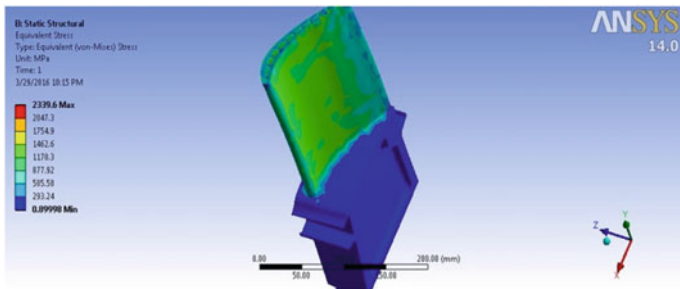


Fig. 10 Equivalent Stress (Configuration 1)

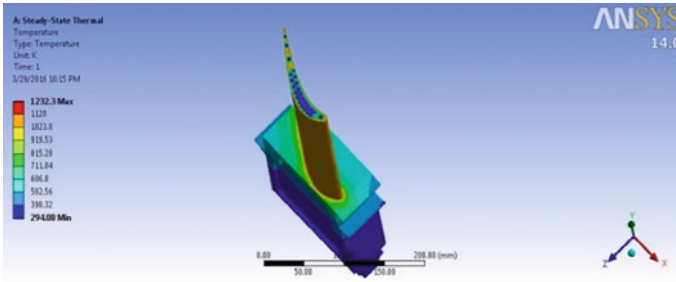


Fig. 11 Temperature distribution(Configuration 2)

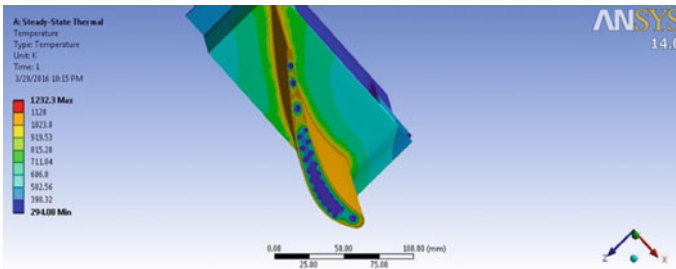


Fig. 12 Temperature across cross-section(Configuration2)

3.2 Configuration 2

In this configuration, the number of holes is maintained as 10, as in the previous configuration, while the diameter of the hole is reduced to 2 mm. Also, the holes are introduced in two rows in an attempt to increase the heat transfer rate. This configuration is seen to reduce the temperature by 2% but, however, the deformation is significantly more with the stress distribution also increased by 27%. This configuration may lead to damage of the blade material and failure compared to the previous configuration. The results of the analysis for configuration 2 are shown in Figs. 11, 12, 13, and 14.

3.3 Configuration 3

In configuration 3, the hole size is further reduced to 1.5 mm while the other boundary conditions remain the same as in configuration 2. The results show that the deformation, stress increased significantly though the cooling provided by the holes is better for this configuration. Though the thermal performance of this configuration looks

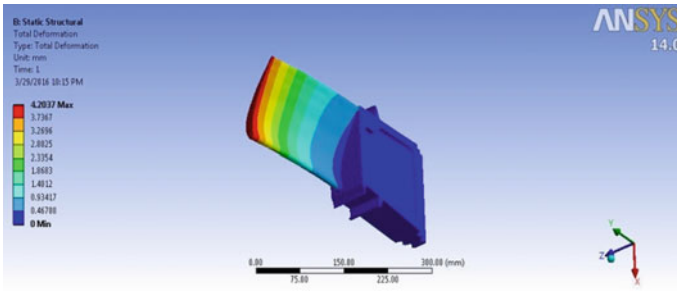


Fig. 13 Deformation (Configuration 2)

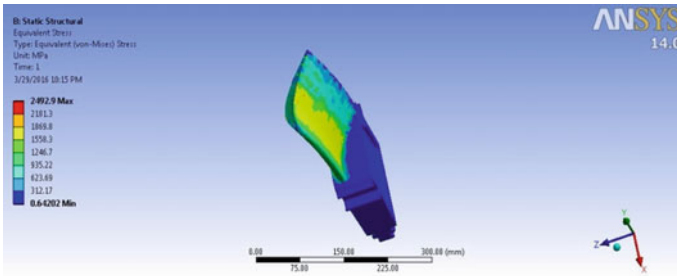


Fig. 14 Equivalent stress (Configuration 2)

good, the configuration may not be advisable from the structural point of view as the lifetime will be reduced. Figures 15, 16, 17 and 18 show the results of the analysis using configuration 3.

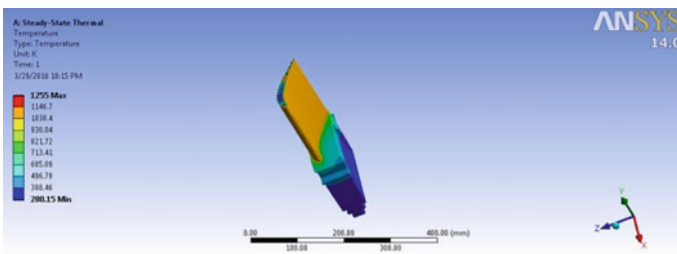


Fig. 15 Temperature distribution (Configuration 3)

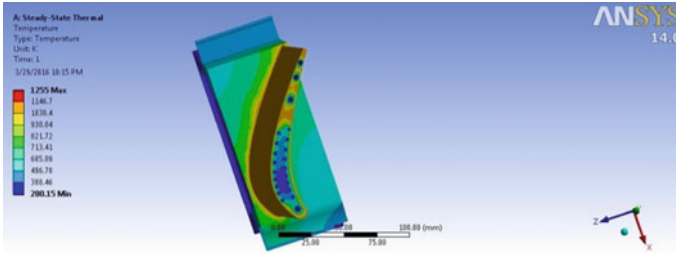


Fig. 16 Temperature across cross section (Configuration 3)

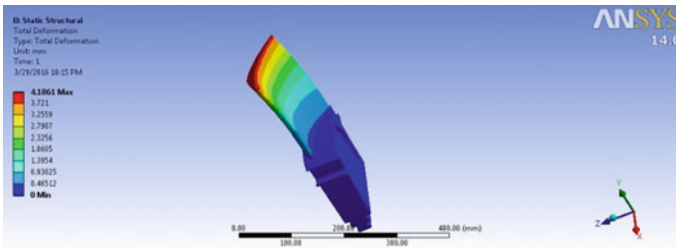


Fig. 17 Deformation (Configuration 3)

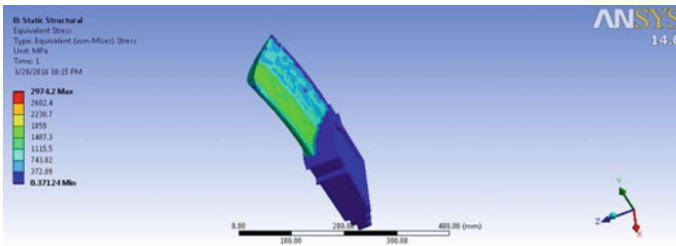


Fig. 18 Equivalent stress (Configuration 3)

3.4 Configuration 4

In configuration 4, the hole dimensions are maintained as in the previous configuration while the diameter of the holes is increased to 12 mm. Results show that the temperature is reduced more than the baseline configuration, while the stress level increases by 1.3%, and the deformation also increases to 39%. The analysis results are shown in Figs. 19, 20, 21, and 22 as shown below.

Table 2 provides the summary of results obtained from the analysis on the four different blade configurations.

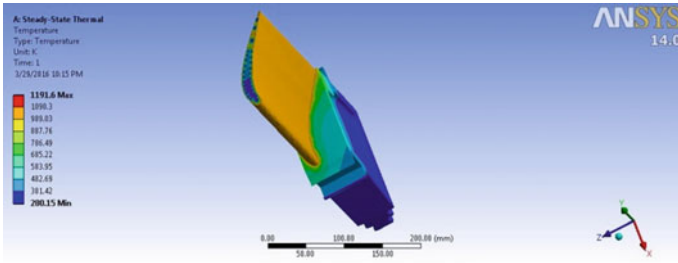


Fig. 19 Temperature distribution (Configuration 4)

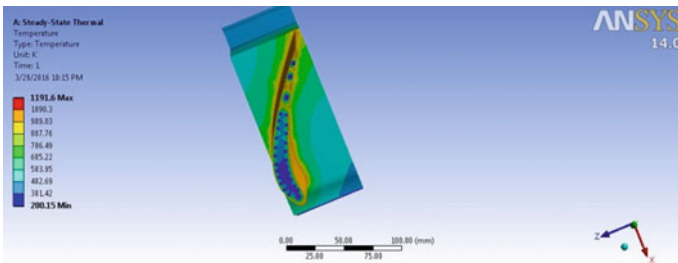


Fig. 20 Temperature across cross section (Configuration 4)

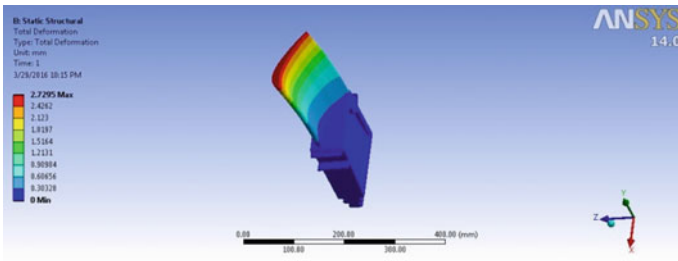


Fig. 21 Deformation (Configuration 4)

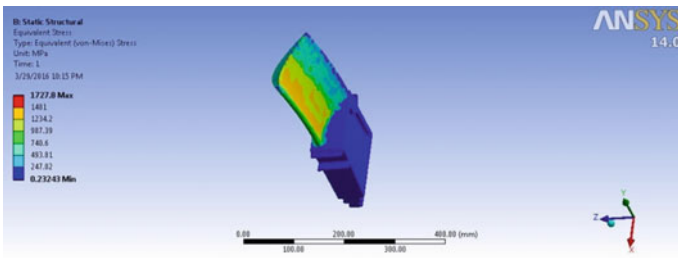


Fig. 22 Equivalent stress (Configuration 4)

Table 2 Comparison of the analysis of various configurations

S.no	Configuration	Temperature (K)	Deformation (mm)	Stress (Mpa)
1	Configuration 1	1143	1.94	1462
2	Configuration 2	1128	4.2	1869
3	Configuration 3	1116	4.18	1859
4	Configuration 4	1090	2.7	1481

While configurations 3 and 4 showed better results in terms of cooling effectiveness, the deformation and stress are found to be more when compared to configurations 1 and 2. This could be due to less distance between the holes and the surface in configurations 3 and 4. Configuration 4 showed better results when compared to configuration 3. The minimum temperature, deformation and stress obtained in this configuration are 1090 K, 2.7 mm, and 1481 MPa, respectively.

4 Conclusions

In the present work, the gas turbine blade model with four different configurations is developed using CATIA and analyzed using ANSYS software for structural and thermal analyses assuming Inconel 718 as the material. From the analysis results, the following conclusions are drawn:

1. The cooling of turbine blade is better with an increase in the number of holes and with a decrease in the hole diameter.
2. The structural deformation is better with single row of holes while the thermal cooling is poor. The increase in row numbers increases the strength of the blade showing less deformation when the number of holes increases and decrease in hole diameter.
3. A trade-off must be performed to choose the best configuration with better cooling characteristics and also good structural capabilities. Out of the four configurations analyzed, configuration 4 gives better heat transfer characteristics with reasonably less deformation and stress levels.

The life of the blades will be increased by using proper configuration for cooling, and also the need for maintenance is reduced thereby increasing the efficiency of the engine.

References

1. Muniyandi G (2017) Review on steady state thermal & structural analysis of gas turbine blade with cooling system using FEA. *Int Res J Eng Sci* 3(2)
2. Ujade GD, Bhambere MB (2014) Review of structural and thermal analysis of gas turbine blade. *Int J Mech Eng Robot Res* 3(2) ISSN: 2278-0149

3. Prasad RDV, Narasa Raju G, Srinivasa Rao MS, Vasudeva Rao N (2013) Steady state thermal & structural analysis of gas turbine blade cooling system. *Int J Eng Res Technol (IJERT)* 2(1) ISSN: 2278-0181
4. Begum F, Reddy VR, Ramanjaneyulu S (2017) Design and thermal analysis of cooling of gas turbine blade through radial holes. *Mater Today Proc* 4, 7714-7722
5. Mahesh R, Sreekar Reddy A, Lokesh K, Baba Fakruddin D, Videetha D (2016) Structural and thermal analysis on gas turbine blade using solid works. *Int J Adv Sci Technol Eng Manag Sci* 2(4) IJASTEMS-ISSN: 2454-356X
6. Venkata Krishnam Raju NN, Vinoth Kumar AM, ChandrashekarGoud V (2017) Design and structural, thermal analysis of gas turbine rotor blade. *Int J Prof Eng Stud* 8(2)
7. Kini CR, Shenoy SB, Sharma NY (2014) Thermo-structural analysis of HP stage gas turbine blades having helicoidal cooling ducts. *Int J Adv Mech Aeronaut Eng-IJAMAE* 1(2) ISSN: 2372-4153
8. Theju V, Uday PS, Gopinath Reddy PLV, Manjunath CJ (2014) Design and analysis of gas turbine blade. *Int J Innov Res Sci Eng Technol* 3(6)
9. Hari Brahmaiah K, Lava Kumar M (2014) Heat transfer analysis of gas turbine blade through cooling holes. *Int J Comput Eng Res (IJCER)* 4(7) ISSN (e): 2250-3005
10. Saif M, Mullick P, Imam A (2019) Analysis and structural design of various turbine blades under variable conditions: a review. *Adv Mater Res* 8(1), 11-24. <https://doi.org/10.12989/amr.2019.8.1.011>
11. Balaji K, Azhagesan C, Vinoth Pandian R, MuthuMurugan N, Aravinth N (2016) Review of cooling effect on gas turbine blade. *Int Conf Syst Sci Control Commun Eng Technol* 2 ISBN: 978-81-929866-6-1
12. Veeraragavan V (2012) Effect of temperature distribution in gas turbine blade model using finite element analysis. *Int J Eng Res Technol (IJERT)* 1(10) ISSN: 2278-0181
13. Kauthalkar SP (2008) Analysis of thermal stresses distribution pattern on gas turbine. *Int J Eng Educ Technol (ARDIJEET)* ISSN: 2320-8
14. Nagaraju G (2008) Study on design of turbine blade and its failures. *Int J Innov Res Eng Sci Technol*
15. Xie G, Sundén B (2010) Numerical predictions of augmented heat transfer of an internal blade tip-wall by hemispherical dimples. *Int J Heat Mass Transf* 53(25-26):5639-5650

Response of Modified 9Cr-1Mo Steel Under Asymmetrical Stress Loading at 600 °C



Prerna Mishra , N. C. Santhi Srinivas, and Vakil Singh

Abstract Response of materials under cyclic loading depends on loading type (symmetrical and asymmetrical). Modified 9 Cr-1 Mo steel is an important material used as tube or pipe in steam generator, superheater and reheater components in thermal/nuclear power plants. This investigation deals with cyclic stress–strain behaviour of this steel in asymmetric loading under different combinations of the mean stress (σ_m), stress amplitude (σ_a), stress rate ($\dot{\sigma}$) at 600 °C. Fatigue tests under asymmetrical loading were performed with various combinations of σ_m (80–100 MPa), σ_a (215–255 MPa) and $\dot{\sigma}$ (50–450 MPa/s) at 600 °C. Cyclic hardening and softening behaviour were studied from hysteresis loops in forms of loop width, area and plastic strain energy. There was cyclic softening with rise in σ_m and σ_a , whereas with rise in $\dot{\sigma}$ there was cyclic hardening. The fractographs revealed striation like marks on the cylindrical surface and dimples on the fracture surface.

Keywords Ratcheting · Hardening · Softening · Plastic strain energy · Hysteresis loop width

1 Introduction

Modified 9Cr-1Mo steel among various ferritic-martensitic steels is preferred as tubing/piping material in advanced thermal/nuclear power generating industries. This steel possesses combination of mechanical properties at elevated temperature and resistance to stress corrosion cracking beside higher thermal conductivity and lower coefficient of thermal expansion. Its other attractive features are weldability and stable microstructure on long exposure at high temperature. The high temperature strength resulted due to the formation of Nb and V carbides [1–3].

P. Mishra (✉) · N. C. Santhi Srinivas · V. Singh
Department of Metallurgical Engineering, Indian Institute of Technology (Banaras Hindu University), Varanasi 221005, India
e-mail: prernam.rs.met16@iitbhu.ac.in

N. C. Santhi Srinivas
e-mail: ncssrinivas.met@iitbhu.ac.in

© The Author(s), under exclusive license to Springer Nature Singapore Pte Ltd. 2022
M. K. Singh and R. K. Gautam (eds.), *Recent Trends in Design, Materials and Manufacturing*, Lecture Notes in Mechanical Engineering,
https://doi.org/10.1007/978-981-16-4083-4_13

The design of piping network in power plants involves the factor like operational pressure, cyclic loading during start-up and shut down and seismic effect. Cyclic loads are induced in the system from thermal stresses resulting from variation in temperature as well cyclic bending due to seismic or other events of repeated loading. During service, due to these conditions, the phenomenon of ratcheting occurs. Ratcheting is progressive development of plastic strain resulting from asymmetric stressing. Ratcheting strain degrades the fatigue life causing premature failure. Thus, the study of ratcheting is primarily important for the reliability and integrity of the piping components [4, 5].

Several investigators have studied the ratcheting behaviour of different structural materials both experimentally [6–12] as well as through simulation modelling [13–17]. Materials usually exhibit hardening/softening, depending on the material and operating parameters such as the amplitude of stress and the history of loading. Metallic materials in hardened state due to cold working or phase transformation exhibit cyclic softening whereas in the soft condition following annealing treatment displays cyclic hardening.

The present investigation examines cyclic stress response of the normalized modified 9Cr-1Mo steel under different combinations of the controlling parameters σ_m , σ_a and $\dot{\sigma}$ at 600 °C.

2 Experimental Procedure

The modified 9Cr-1Mo steel was obtained from IGCAR, Kalpakkam, India in normalized and tempered condition as plate of 25 mm thickness. Normalizing had been done at 1060 °C for 1 h, and tempering was carried out at 780 °C for 1 h, and the material was air-cooled to room temperature (Table 1).

Table 1 Chemical composition of the material (mass %)

S	0.002
Al	0.013
P	0.018
C	0.1
V	0.21
Si	0.26
Ni	0.33
N	0.044
Mn	0.41
Nb	0.074
Mo	0.95
Cr	9.27
Fe	Balance

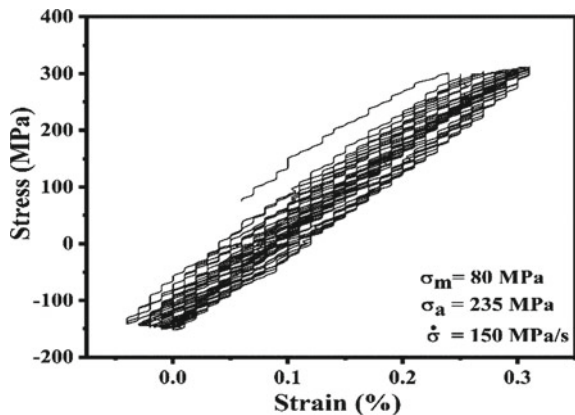
The geometry and sketch of the cylindrical specimens used during testing have been described in our previous investigation [18]. Ratcheting fatigue experiments were conducted at 600 °C with the help of three zone resistance heating furnace for heating the specimens. Uniaxial asymmetrical stress-controlled ratcheting tests were performed using servo-hydraulic testing system (MTS model 810). MTS extensometer (Model 632.53E) was used to measure strain. Three operating variables (σ_m , σ_a and $\dot{\sigma}$) were used while one variable was varied, the other two were kept constant. The tests were carried out till failure. Length of approximately 4 mm from the fracture ends was transversely sectioned and examined under field emission scanning electron microscope (FEI Quanta 200 F).

3 Results

Hardening and softening of structural materials under repeated strain loading are displayed, respectively, by increase and decrease in stress level. Contrarily hardening/softening under stress-controlled cycling is reflected by decrease/increase in plastic strain, respectively.

Response of the modified 9 Cr-1 Mo steel under asymmetric cyclic stressing at 600 °C was assessed by change in the width and area of hysteresis loops with the number of cycles by conducting fatigue tests with different sets of σ_m , σ_a and $\dot{\sigma}$. Cyclic loading with tensile mean stress leads to a progressive increase in the plastic strain. The hysteresis loop translation with number of cycles (N) for $\sigma_m = 80$ MPa, $\sigma_a = 235$ MPa and $\dot{\sigma} = 150$ MPa/s is shown in Fig. 1. It is noticed that the hysteresis loop for the first cycle exhibits the largest plastic strain accumulation.

Fig. 1 Hysteresis loop with number of cycles at $\sigma_m = 80$ MPa, $\sigma_a = 235$ MPa and $\dot{\sigma} = 150$ MPa/s



3.1 Effect of Tensile Mean Stress on Cyclic Strain Response

The impact of σ_m from 60 to 100 MPa at $\sigma_a = 235$ MPa and $\dot{\sigma} = 150$ MPa/s on the hysteresis loops at 5, 50 and 500 cycles is shown in Fig. 2. In general, an increase in the area of hysteresis loop demonstrates an increase in plastic strain energy and consequent fall in fatigue life [18, 20].

Figure 2a–c shows that as σ_m increases from 60 to 100 MPa, the width as well as hysteresis loop area increases, and the plastic strain accumulates in positive direction because of the tensile σ_m . It may be seen that at $\sigma_m = 100$ MPa, area as well as

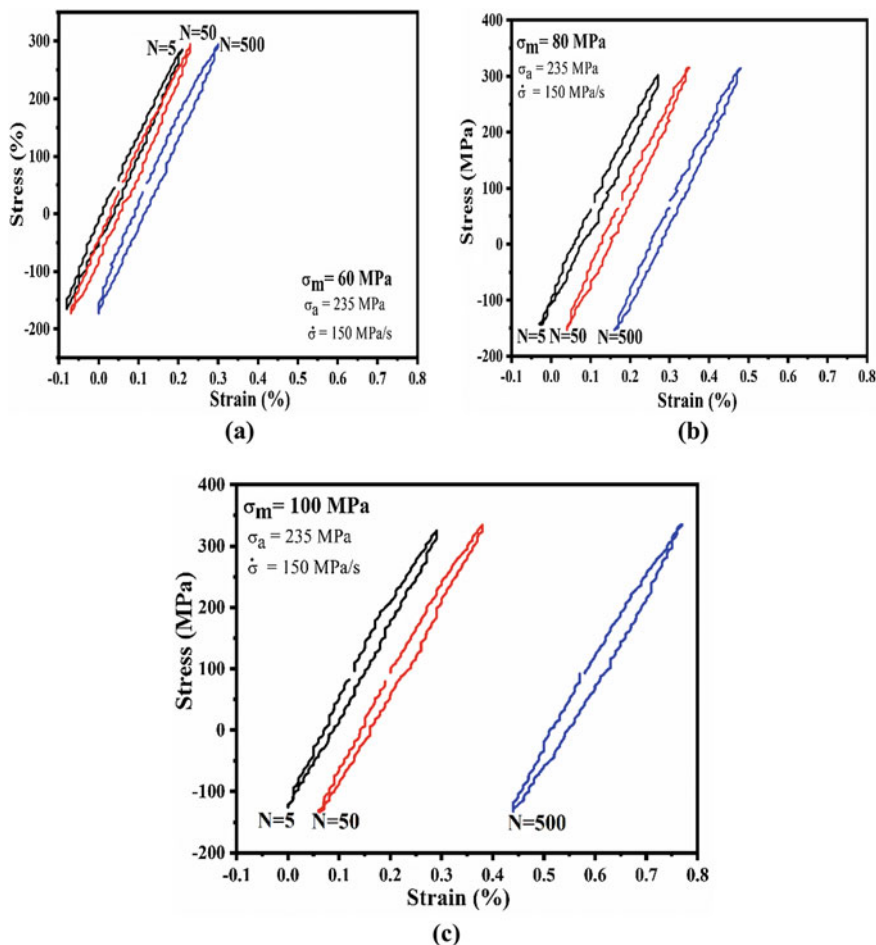
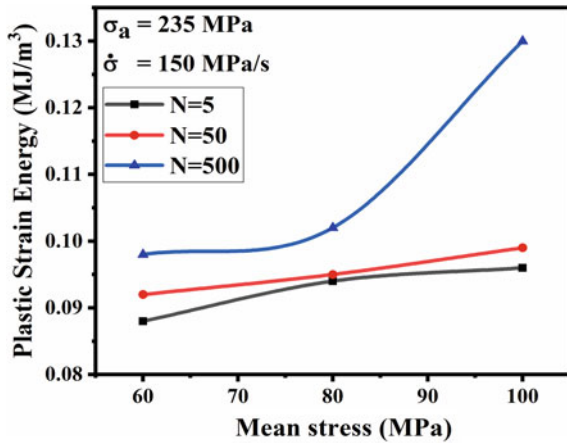


Fig. 2 Effect of tensile mean stress on the hysteresis loops corresponding to 5, 50 and 500 cycles: **a** 60 MPa, **b** 80 MPa, **c** 100 MPa at constant $\sigma_a = 235$ MPa and $\dot{\sigma} = 150$ MPa/s

Fig. 3 Plastic strain energy variation with tensile mean stress corresponding to different number of cycles 5, 50 and 500 cycles



hysteresis loop width increases more than at lower σ_m with number of cycles (N) due to an increase in softening.

It may be understood from Fig. 3 that plastic strain energy corresponding to $\sigma_m = 100$ MPa is highest and is lowest at $\sigma_m = 60$ MPa. Further, the plastic strain energy increases with an increase in number of cycles. Thus, the plastic strain energy is dependent on both the tensile mean stress and the number of cycles [18, 20].

3.2 Effect of Stress Amplitude on Cyclic Strain Response

The effect of σ_a is similar to that of σ_m effect on the hysteresis loops. It is evident that the width of hysteresis loops increases with an increase in σ_a from 215 to 255 MPa for the respective cycles 5, 50 and 500 as observed in Fig. 4a–c.

Figure 5 displays the variation in plastic strain energy on the σ_a for 5, 50 and 500 cycles. It shows that there is a linear increase in the plastic strain energy with an increase in σ_a from 215 to 255 MPa. Further, the level of the plots increases with an increase in the number of cycles. Thus, there is cyclic softening with an increase in σ_a and the number of cycles (N) [18, 20].

3.3 Effect of Stress Rate on Cyclic Strain Response

It may be seen from Fig. 6 in contrast to the increase in size of hysteresis loops with an increase in σ_m and σ_a , there is the opposite effect of increase from 50 to 450 MPa/s. The size of hysteresis loops decreases with an increase in the respective number of cycles. Both the width as well as area of the loops decreases with increase in σ .

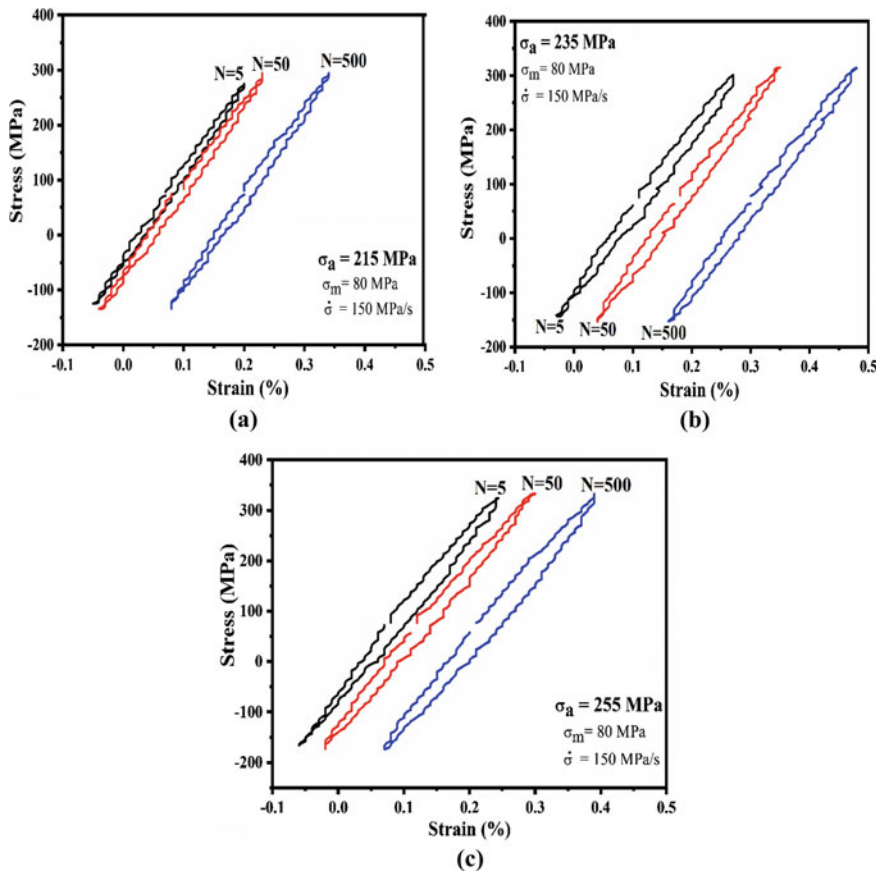


Fig. 4 Effect of stress amplitude on the hysteresis loops corresponding to 5, 50 and 500 cycles: **a** 215 MPa, **b** 235 MPa, **c** 255 MPa at constant $\sigma_m = 80$ MPa and $\dot{\sigma} = 150$ MPa/s

Further, the accumulation of plastic strain decreases and moves towards negative strain (Fig. 7).

The variation of plastic strain energy shows negative slope. This may be attributed to cyclic hardening effect with an increase in [18, 20].

3.4 Fracture Behaviour Under Asymmetric Stressing

It may be seen that in contrast to symmetrical cyclic stress/strain loading exhibiting fracture surface with features of striations resulting from crack propagation, and the region of dimples forming due to overload the fracture behaviour under asymmetric stressing is quite different. The necking area does not occur under symmetric loading,

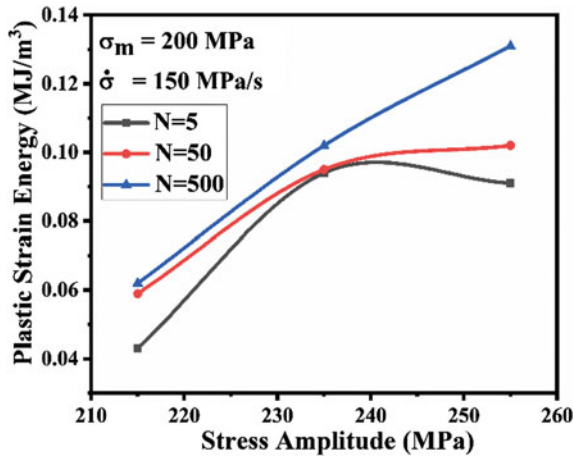


Fig. 5 Plastic strain energy variation for 5, 50 and 500 cycles at different σ_a : **a** 215 MPa, **b** 255 MPa at constant $\sigma_m = 80$ MPa and $\dot{\sigma} = 150$ MPa/s

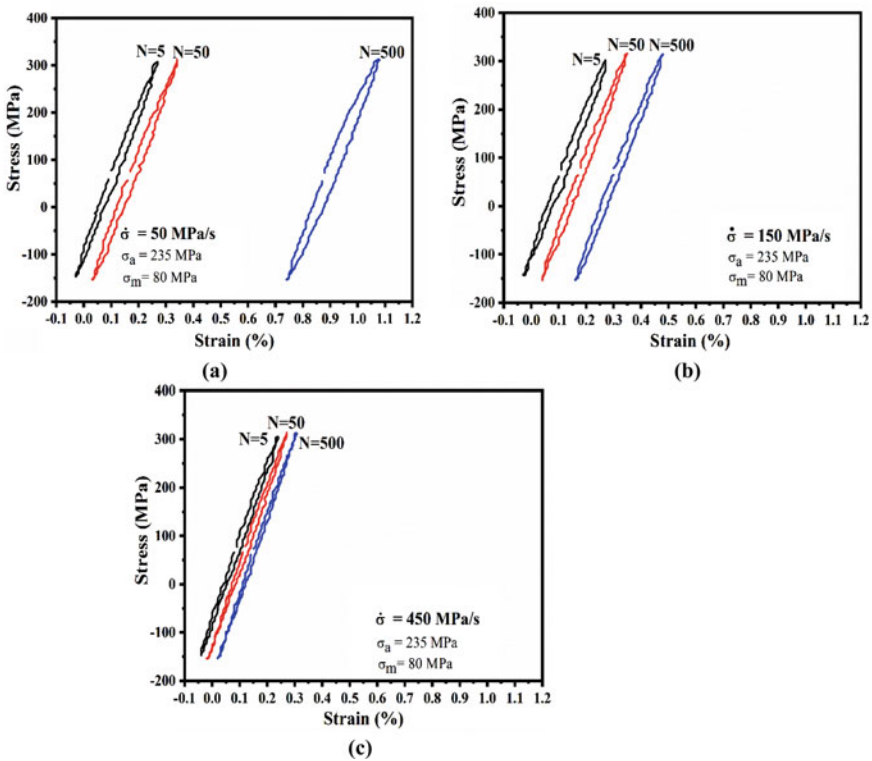


Fig. 6 Effect of stress rate on the hysteresis loops corresponding to 5, 50 and 500 cycles: **a** 50 MPa/s, **b** 150 MPa/s, **c** 450 MPa/s at constant $\sigma_m = 80$ MPa and $\sigma_a = 235$ MPa

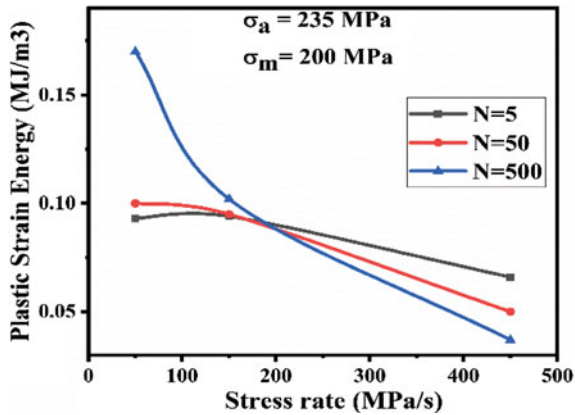


Fig. 7 Variation of plastic strain energy for 5, 50 and 500 cycles at different: **a** 50 MPa/s, **b** 150 MPa/s, **c** 450 MPa/s at constant $\sigma_m = 80$ MPa and $\sigma_a = 235$ MPa

there is necking under asymmetric stressing (Fig. 8a). Further, there are features like striations on the periphery in the necked region close to fracture end (Fig. 8c). There are no striations on the fracture surface, and there are well-defined dimples, characteristic of tensile fracture (Fig. 8b) [3, 19].

4 Conclusions

The outcome of asymmetrical loading on variation in width, area and plastic strain energy of the modified 9 Cr-1Mo steel was studied at 600 °C. The role of variables such as σ_m , σ_a , $\dot{\sigma}$ was examined for 5, 50 and 500 cycles. The following conclusions are drawn:

- Cyclic softening was exhibited due to tensile mean stress from 60 to 100 MPa. The softening effect was found to increase with an increase in the number of cycles.
- Cyclic softening effect under asymmetric stressing increased with an increase in stress amplitude from 215 to 255 MPa and also with an increase in the number of cycles.
- The impact of increase in the stress rate under asymmetrical stressing was found to cause hardening and consequent decrease in the width and plastic strain energy with an increase in the stress rate.
- Unlike symmetrical loading, the fracture behaviour under asymmetric stressing was quite different. There was striation like marks on the peripheral surface and dimples on the fracture surface.

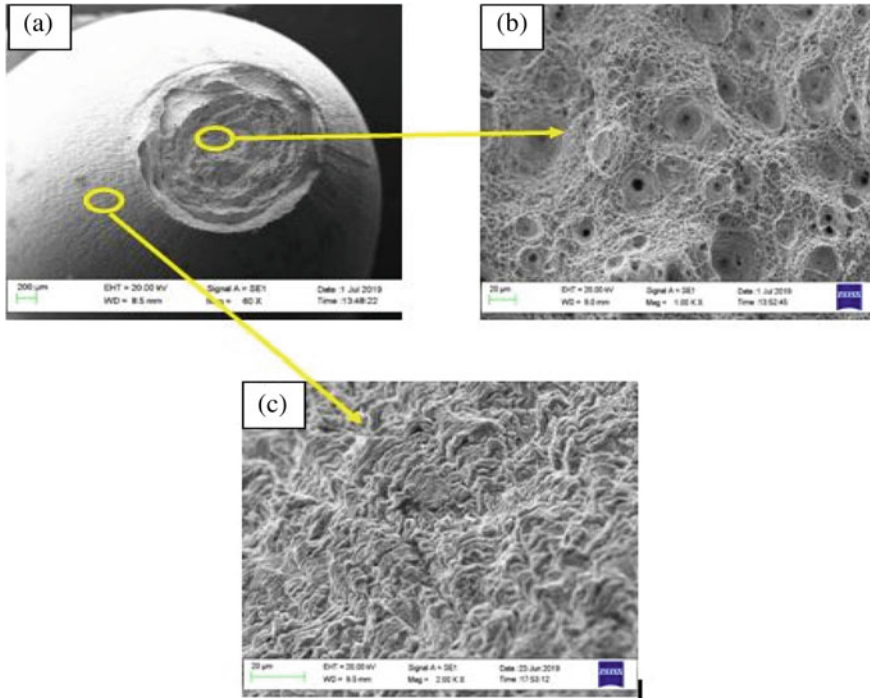


Fig. 8 Fractographs of the failed specimen (at $\sigma_m = 80$ MPa; $\sigma_a = 235$ MPa; $\dot{\sigma} = 150$ MPa/s and $T = 600$ °C): **a** full view, **b** enlarged view of central region showing dimples (tensile feature), **c** enlarged view of peripheral region showing striations like features (fatigue feature)

References

1. Das B, Singh A (2019) Understanding strain controlled low cycle fatigue response of P91 steel through experiment and cyclic plasticity modelling. *Fusion Eng Des* 138:125–137
2. Verma P, Rao GS, Chellapandi P, Mahobia GS, Chattopadhyay K, Srinivas NS, Singh V (2015) Dynamic strain ageing, deformation, and fracture behavior of modified 9Cr-1Mo steel. *Mater Sci and Eng A* 621:39–51
3. Verma P, Srinivas NS, Singh V (2016) Low cycle fatigue behaviour of modified 9Cr-1Mo steel at 600 °C. *Trans Indian Inst Metals* 69(2):331–335
4. De PS, Kundu A, Chakraborti PC (2014) Effect of prestrain on tensile properties and ratcheting behaviour of Ti-stabilised interstitial free steel. *Mater Des* 57:87–97
5. Mukhopadhyay CK, Jayakumar T, Haneef TK, Kumar SS, Rao BPC, Goyal S, Gandhi P (2014) Use of acoustic emission and ultrasonic techniques for monitoring crack initiation/growth during ratcheting studies on 304LN stainless steel straight pipe. *Int J Press Vessels Piping* 116:27–36
6. Paul SK, Sivaprasad S, Dhar S, Tarafder S (2010) Cyclic plastic deformation and cyclic hardening/softening behavior in 304LN stainless steel. *Theor Appl Fract Mech* 54(1):63–70
7. Shi H, Chen G, Wang Y, Chen X (2013) Ratcheting behavior of pressurized elbow pipe with local wall thinning. *Int J Press Vessels Piping* 102:14–23

8. Wang Y, Yu D, Chen G, Chen X (2013) Effects of pre-strain on uniaxial ratcheting and fatigue failure of Z2CN18. 10 austenitic stainless steel. *Int J Fat* 52:106–113
9. Lin YC, Chen XM, Chen G (2011) Uniaxial ratcheting and low-cycle fatigue failure behaviors of AZ91D magnesium alloy under cyclic tension deformation. *J Alloys Comp* 509(24):6838–6843
10. Paul SK, Sivaprasad S, Dhar S, Tarafder S (2010) Ratcheting and low cycle fatigue behavior of SA333 steel and their life prediction. *J Nucl Mater* 401:1–3, 17–24 (2010)
11. Lim CB, Kim KS, Seong JB (2009) Ratcheting and fatigue behavior of a copper alloy under uniaxial cyclic loading with mean stress. *Int J Fat* 31(3):501–507
12. Tao G, Xia Z (2007) Ratcheting behavior of an epoxy polymer and its effect on fatigue life. *Polym Test* 2(4):451–460
13. Kang G, Gao Q, Yang X (2004) Uniaxial and non-proportionally multiaxial ratcheting of SS304 stainless steel at room temperature: experiments and simulations. *Int J Nonlinear Mech* 39(5):843–857
14. Chaboche JL (1991) On some modifications of kinematic hardening to improve the description of ratcheting effects. *Int J Plast* 7(7):661–678
15. Jiang Y, Kurath P (1996) Characteristics of the Armstrong-Frederick type plasticity models. *Int J Plasticity* 12(3):387–415
16. Kang G, Li Y, Gao Q (2005) Non-proportionally multiaxial ratcheting of cyclic hardening materials at elevated temperatures: experiments and simulations. *Mech Mater* 37(11):1101–1118
17. Kang G, Gao Q, Yang X (2002) Uniaxial cyclic ratcheting and plastic flow properties of SS304 stainless steel at room and elevated temperatures. *Mech Mater* 34(3):145–159
18. Mishra P, Rajpurohit RS, Srinivas NS, Singh V (2020) Stress–strain behaviour of modified 9Cr-1Mo steel in asymmetric cyclic stressing at room temperature. *Structural integrity assessment* Springer Singapore, pp 713–724
19. Mishra P, Rajpurohit RS, Srinivas NS, Sastry GVS, Singh V (2020) Ratcheting fatigue behavior of modified 9Cr-1Mo steel at room temperature. *Metals Mater Inter* 1–15
20. Rajpurohit RS, Santhi Srinivas NC, Singh V (2016) Ratcheting strain accumulation due to asymmetric cyclic loading of Zircaloy-2 at room temperature. *Procedia Struct Integr* 2:2757–2763

Finite Element Analysis of Bending Response of Aluminum 1100-H12 and Mild Steel Hat Shape Beam



Amita Shinde and Gaurav Tiwari

Abstract In this paper, the study was performed out to explore the bending response of hat-shaped beams subjected to quasi-static bending for application in vehicle bumper systems to reduce injury of vehicle as well as passenger. Two distinct materials, aluminum 1100-H12 and mild steel, were taken for hat shape beam to know the influence of material strength and ductility on the specific energy absorption (SEA). The length and thickness of the hat shape beam (both aluminum and steel) were considered as 500 mm and 2 mm, respectively, whereas height and width of flange were taken as 80 and 20 mm. The bending response was explored by a three-point bending test. Three-dimensional finite element analysis was done by using commercial code ANSYS. From the study it is clear that the ductility and weight is one of the critical parameter which is affecting the energy absorption capability which tends to increase in specific energy absorption during the tests.

Keywords Single hat shape beam · Aluminum and mild steel material · Specific energy absorption · Plastic strain · Deformation

1 Introduction

Whenever front or rear collision happens on the vehicles, the bumper is the first part that comes in contact. At the time of collision, energy gets transmitted to the bumper, then it goes to the crash box and finally to the safety cage, which leads to happen damage in the passenger safety cage. If the energy generated at the time of collision is large in amount and it reaches the safety cage, it may harm the passenger or may lead to death. There are some different number of ways to keep passengers safe, such as maintaining speed, using a seatbelt, avoiding distractions, etc. Nowadays, in cars, the number of safety features are available like airbags, antilock braking system (ABS), traction control, electron stability control, seatbelts, tire pressure monitors, and many more. All these safety features are added to keep passengers safe. In this context,

A. Shinde (✉) · G. Tiwari

Department of Mechanical Engineering, Visvesvaraya National Institute of Technology, Nagpur, Maharashtra 440010, India

a plenty of studies are available wherein the characteristics of energy absorption of different structures have been studied either through crushing test in axial and lateral directions or through bending test.

Bumper beam is a key structure for which manufacturing and careful design should be performed to get good impact behaviors. In this paper, we are focusing on the bumper beam. Most of the bumpers are made out of plastic and feature an aluminum or steel bar hidden in the middle. In addition to crushable brackets and bar, bumpers are sometimes made up of polypropylene foam or thermoplastic. There are different shapes of the bumper beam like T shape, C, or hat shape. In hat shape also, there is a single hat or double hat. In accidents, mainly, transverse loading comes in picture.

Zarei and Kroger [1] performed a dynamic bending test on an empty as well as foam-filled aluminum square beam using LS-DYNA and reported that bending collapse of a thin-walled beam was localized in the plastic hinge, and other some parts of beam undergo rigid body rotation. Huang [2] studied the load and boundary condition effect for bending of thin-walled tubes in transverse direction using finite element code LS-DYNA and declared that the deformation force responses of thin-walled tubes were greatly affected by their load position, angle, and span. Chen et al. [3] studied the design of crashworthiness for hat-shaped composite structures subject to the three-point bending and transverse compression loading and found that increasing thickness of wall gives best way to increase the crashworthiness performance. Belingardi [4] investigated experimentally on a bending behavior of steel and hybrid thin-walled boxes and explained the importance of joints, which are adhesive. Reyes et al. [5] studied the capability of energy-absorbing and behavior of obliquely loaded thin-walled square aluminum columns through quasi-static experiments and realizes that the energy absorption drops drastically when a global bending mode is initiated instead of progressive buckling. Díaz-Álvarez et al. [7] studied the energy absorption and bending of biocomposite bumper and studied the post-impact behavior of beam, which shows that failure is caused because of matrix cracking. Pyrzowski and Sobczyk [8] studied global and local responses of beams (sandwich) made of PET foam cores and GFRP face sheets in three-point bending tests and found accurate estimation of failure, elastic response and damage of beam. Nassir Husain et al. [9] studied energy absorption characteristics for GFRP (glass fiber reinforced plastics) crash boxes made of different types of geometries and concluded that square geometry gives high energy absorption. Magnucki et al. [10] studied sandwich beams that are expanded-tapered in three-point bending and determined the maximum deformation of the beam with shear effect consideration.

The available studies mainly reported the bending analysis of steel structures having conventional cross-section. Therefore, in-depth studies are required to explain how the response of the structures having non-conventional cross-section. In given study, the bending analysis of hat shape beam was done through three-dimensional finite element analyses, which are made of two distinct materials, mild steel and aluminum alloy. Three-point bending tests were performed for both the beam for analyzing energy absorption capability, total deformation, plastic strain effects. The quasi-static loading condition was applied. With a bending deflection of 100 mm, all the parameters were analyzed.

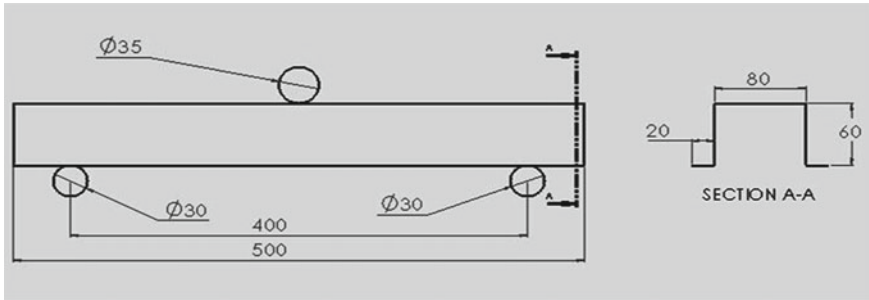


Fig. 1 Quasi-static loading three-point bending test setup for a beam

Table 1 Mechanical property of hat materials

Material	Density (gm/cm ³)	Elastic modulus (GPa)	Poisson's ratio
Mild steel	7.85	210	0.29
Aluminum 1100-H12	2.71	70	0.3

2 Quasi-Static Loading Condition for Single Hat Shape Thin-Walled Beam

The geometric configuration for a single hat shape thin-walled beam is shown in Fig. 1. The specimen has a length $L = 500$ mm and a thickness of 2 mm. The flange width and side length were kept as 20 mm and 80 mm, respectively. The height of this beam is 60 mm. The single hat profiles were placed on two cylindrical supports with a 30 mm diameter and 400 mm span. The middle cylinder has a diameter 35 mm, which is a pusher. Pusher and supports were made from structural steel with a elasticity modulus higher than mild steel and aluminum 1100-H12. Table 1 shows the mechanical properties of mild steel and aluminum 1100-H12. Figure 2 shows the true stress–strain curve for mild steel and aluminum 1100-H12.

3 Finite Element Modeling

The model for this finite element structure of a single hat shape thin-walled beam made in finite element analysis software ANSYS has been shown in Fig. 3, which shows the part model and mesh assembly model. For model boundary condition is given in such manure that the pusher will show displacement up to 100 mm.

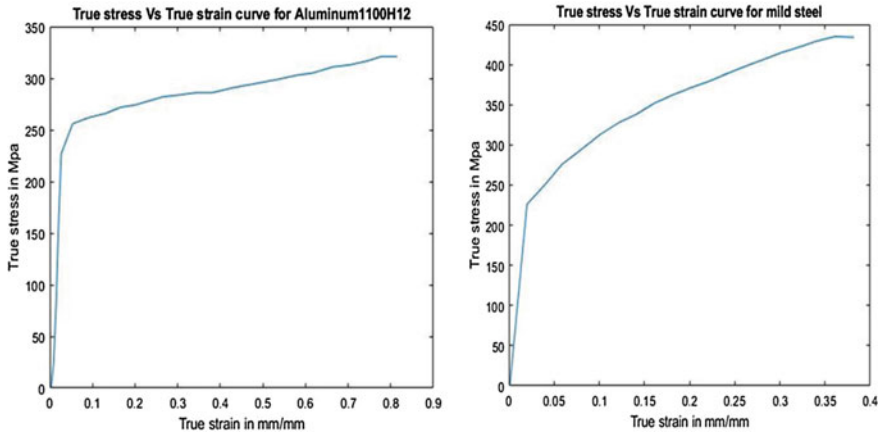


Fig. 2 True stress–strain curve for **a** aluminum 1100-H12 **b** mild steel [6]

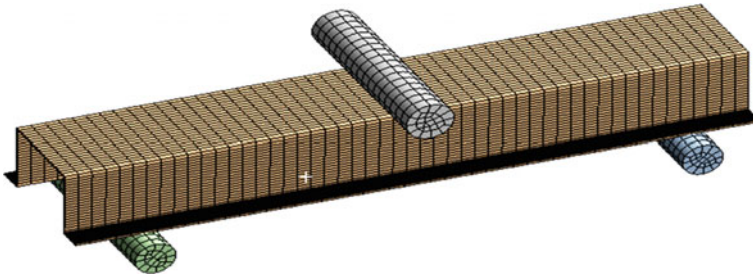


Fig. 3 Mesh model of single thin-walled hat beam

The single hat thin-walled beam part was modeled using Creo software whereas analysis was done through finite element code ANSYS, which is commercially available. In geometry, we have assigned the thickness of the material as 2 mm. Meshing done with the number of the division made for the length section is 50 for the beam. The number of divisions for height and flange portion is kept as 20. The total number of nodes and elements were 11,784 and 6343, respectively. Surface to surface contacts was defined between punch and beam, as well as between beam and support. Then boundary conditions were defined as making the bottom two supports as fixed and pusher to displace up to 100 mm. For the lower part of the beam, displacement is kept free in the bottom direction.

4 Simulation Result

A quasi-static three-point bending test was implemented for aluminum 1100-H12 and mild steel. The specimen was placed on two rigid cylindrical support with a span of 400 mm with diameter 30 mm. Pusher has diameter 35 mm was displaced up to 100 mm. Figure 4a and b shows the force–displacement curve and final deformation obtained from simulation for a hat made up of aluminum 1100-H12 as well as Fig. 5a and b shows force–displacement curve and final deformation obtained from simulation for a hat made up of mild steel.

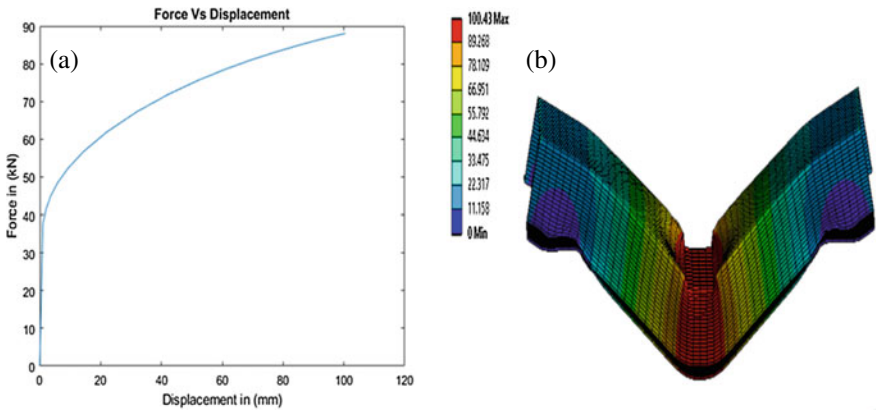


Fig. 4 Quasi-static three-point bending test for aluminum 1100-H12. **a** Force–displacement curve. **b** Final deformation (mm)

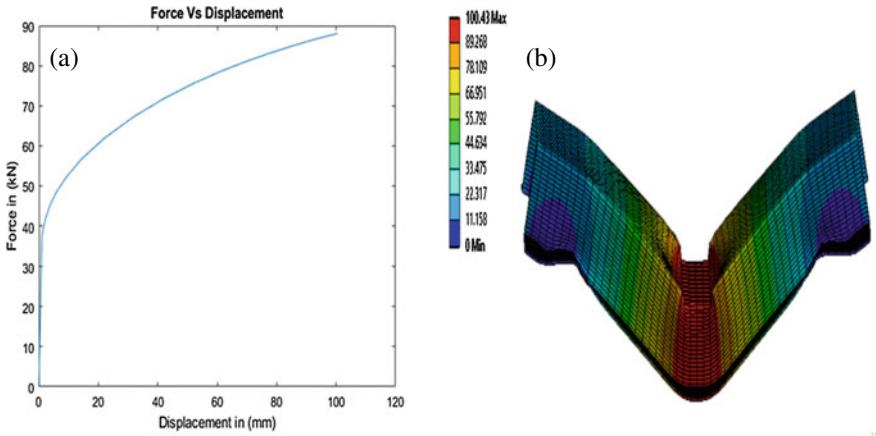


Fig. 5 Quasi-static three-point bending test for mild steel. **a** Force–displacement curve. **b** Final deformation

The fold of an inward cylindrical is similar to a punch profile, which was formed in middle part of geometry. To compare the crashworthiness and systematically evaluate and deformation of a single hat thin-walled beam, it is important to define crashworthiness indices, which are appropriate. Among the various indices, SEA (specific energy absorption) is used generally to indicate the capability of energy absorption of structures with weights and different materials. SEA is the energy absorbed per unit mass of the structure. This is expressed as:

$$SEA = \frac{EA}{M} \tag{1}$$

where, EA is the total energy absorbed during the deformation of the structure and M is the whole mass for the given structure. After simulation, specific energy absorption, the plastic strain was discovered. Table 2 shows the result of materials, aluminum 1100-H12 and mild steel.

From the result shown in Table 2, it was clear that aluminum 1100-H12 offered more amount of specific energy absorption compared to mild steel. The error shows that energy absorption capability in aluminum 1100-H12 is 30.36% higher than that of mild steel. Also, the weight of aluminum 1100-H12 was less compared to mild steel. Figure 6a and b shows the graph for strain energy versus time for aluminum 1100-H12 and mild steel, respectively.

Table 2 FE model results based on quasi-static loading for aluminum 1100-H12 and mild steel single hat beam

Material	Strain energy (J)	SEA (J/kg)	Mass (kg)	%
Aluminum 1100-H12	26.327	41.168	0.6395	30.3
Mild steel	23.142	12.491	1.8526	

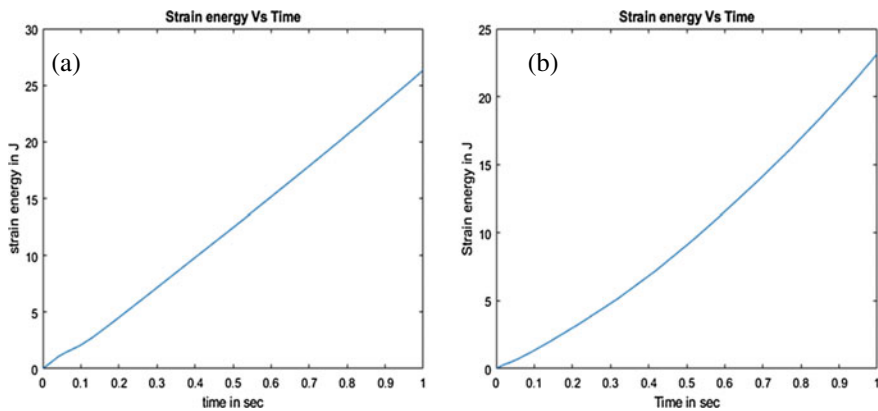


Fig. 6 Graph for strain energy versus time for **a** aluminum 1100-H12 **b** mild steel

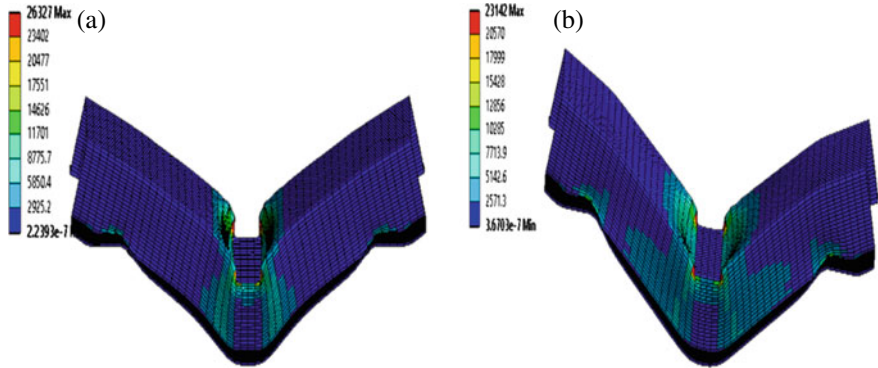


Fig. 7 Strain energy in mJ for a aluminum 1100-H12 b mild steel

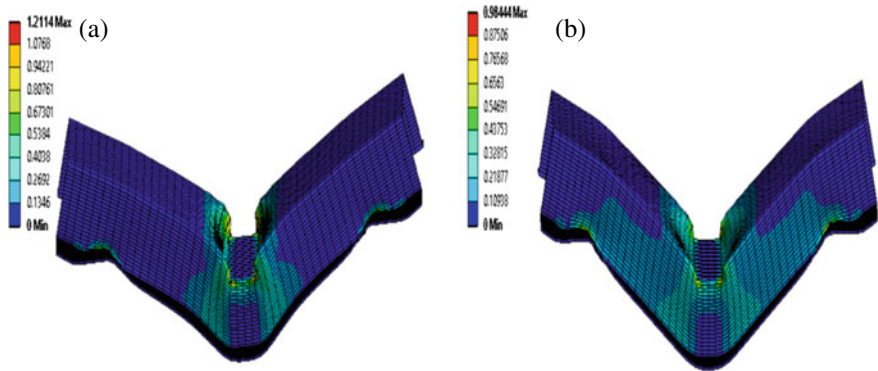


Fig. 8 Equivalent plastic strain for a aluminum 1100-H12 b mild steel

Figure 7 shows that strain energy in aluminum 1100-H12 and mild steel is 26327 mJ and 23142 mJ, respectively.

From Fig. 8, it is clear that plastic strain in aluminum 1100-H12 and mild steel is 1.2114 mm/mm and 0.9844 mm/mm, respectively. It shows that when load is removed, deformation observed in aluminum 1100-H12 will be higher than mild steel.

5 Conclusion

In this work, the bending response of single hat thin-walled beam made up of aluminum 1100-H12 and mild steel was analyzed through finite element analysis. The beams were made of two distinct materials, aluminum and mild steel, and the quasi-statically load was applied. Specific energy absorption found for given the material.

It is concluded that aluminum 1100-H12 gives higher specific energy compared to mild steel. The weight is also an important parameter that affects specific energy absorption.

References

1. Zarei HR, Kroger M (2008) Bending behavior of empty and foam-filled beams: structural optimization. *Int J Impact Eng* 35:521–529
2. Huang Z, Zhang X, Fu X. On the bending force response of thin-walled beams under transverse loading. *J Thin Walled Struct*
3. Chena D, Sun G, Jinc X, Lib Q. Quasi-static bending and transverse crushing behaviors for hat-shaped composite tubes made of CFRP, GFRP and their hybrid structures. *J Compos Struct*
4. Belingardin G, Scattina A. Experimental investigation on the bending behaviour of hybrid and steel thin walled box beams—the role of adhesive joints. *Int J Adhesion Adhesives*
5. Reyes A, Langseth M, Hopperstad OS (2003) Square aluminum tubes subjected to oblique loading. *Int J Impact Eng* 28:1077–1106
6. Gupta NK, Iqbal MA, Sekhon GS. Experimental and numerical studies on the behavior of thin aluminum plates subjected to impact by blunt- and hemispherical-nosed projectiles. *Int J Impact Eng*
7. Díaz-Álvarez A, Jiao-Wang L, Feng C, Santiuste C. Energy absorption and residual bending behavior of biocomposites bumper beams. *J Compos Struct*
8. Pyrzowski Ł, Sobczyk B. Local and global response of sandwich beams made of GFRP facings and PET foam core in three point bending test. *J Compos Struct*
9. Nassir Husain N, Regalla SP, Daseswara Rao YV. Low velocity impact characterization of glass fiber reinforced plastics for application of crash box.
10. Magnucki K, Lewinski J, Far M, Michalak P. Three-point bending of an expanded-tapered sandwich beam—analytical and numerical FEM study. *Mech Res Commun*

Ballistic Response of CFRP Armor Helmet Against Ogive Nosed Projectile



S. L. S. Hamsi, N. Gharde, N. Khaire, and Gaurav Tiwari

Abstract The present study was performed to explore the ballistic response of unidirectional CFRP composite laminates helmet subjected to impact by ogive nosed projectile within subordnance velocity regime with aim of development of lightweight body armors. The ply stacking sequence in the helmet was kept as (0/90/0/90/0/90). Three-dimensional FE analysis was carried out through an explicit module of the commercial FEA software “Abaqus”. Hashin’s damage criteria were employed to record the impact behavior of CFRP helmet. The ballistic limit was obtained by varying the incidence velocity of the projectile. Further, ballistic performance was evaluated.

Keywords CFRP · Ballistic limit · Energy absorption · Damage pattern · Ogive projectile

1 Introduction

Ballistic helmets are important and basic personal protective equipment (PPE) used by the front head soldiers. Potential threats in the form of advanced jacketed bullets and fragmenting munitions from missiles, etc., became a concern in recent years. With the rapid advancement in explosive devices, a major factor considered in modern helmet design is the enhanced strength along with the comfortability with reference to reduction in weight of the helmet. So, in this context, it is very crucial to study and predict the ballistic response of helmet using non-conventional materials. On the other hand, composite materials have been grabbing the attention of researchers because of their high strength to weight characteristics. The usage of composite materials has been rapidly increasing in many military applications due to their excellent mechanical properties like high specific stiffness, specific strength, resistance to corrosion, increased fatigue life, etc. Experimental and numerical studies have been carried out on composite materials to find the ballistic performance.

S. L. S. Hamsi (✉) · N. Gharde · N. Khaire · G. Tiwari
Department of Mechanical Engineering, Visvesvaraya National Institute of Technology, Nagpur,
Maharashtra 440010, India

© The Author(s), under exclusive license to Springer Nature Singapore Pte Ltd. 2022
M. K. Singh and R. K. Gautam (eds.), *Recent Trends in Design, Materials
and Manufacturing*, Lecture Notes in Mechanical Engineering,
https://doi.org/10.1007/978-981-16-4083-4_15

181

Tham et al. [1] conducted numerical analysis and experiments on PASGT helmets when impacted by different projectiles. The outcome showed that helmet was able to stop the projectile, a 9 mm FMJ bullet. Van Hoof et al. [2] evaluated back-face deformation of the helmet. In the later studies, Van Hoof et al. [3] compared the helmet and flat laminate deformations having the same impact conditions and found that the BFD of the flat laminate was smaller than that of the helmet made of Kevlar 29. Sharma et al. [4] and Zhang et al. [5, 6] performed numerical simulations to study the capability of Advanced Combat Helmet and found that wearing ACH 10 would mitigate the intracranial pressure. Aare and Kleiven [7] studied the effect of impact angle and helmet shell thickness on the load levels in human head and concluded that helmet shell should not deflect more than the gap between head and helmet. Cantwell and Morton [8] performed impact tests at low and high velocity on a number of CFRP laminates to study the commencement and development of damage under different loading conditions and found that impact under high velocities generates local deformation near contact point, whereas low-velocity impacts indicate the global deformation. The thickness of laminate, type of fiber, and matrix are some factors that affect the response of composites to different impact loads. Gold Smith [9] carried out an analytical investigation regarding the static and ballistic resistance of carbon fiber laminate plates with thickness up to 6.35 mm which were penetrated and perforated by a cylindroid-conical projectile. The results showed that the ballistic limit and energy absorption increased with an increase in thickness and the mechanisms through which the damage occurred are crack propagation, delamination, fiber failure and hole enlargement. Similarly, many experiments were conducted on stitched and non-stitched fibers [10, 11]. Hosur et al. [10] performed experiments and simulations on woven carbon composites at higher velocities. They found that the damage size and ballistic limit was lower for stitched plates than the unstitched plates. It was also been reported that due to high thickness and fabric architecture, the satin weave laminates have higher ballistic limits than plain wave laminates. This was agreed by Larsson [11], who also performed ballistic tests on stitched and unstitched carbon fiber laminates. Hazell and Appleby-Thomas [12] compared the ballistic response of a woven laminate to a non-woven laminate and found that the ballistic performance of both the laminates was similar at high impact energies. In few papers, the result of oblique impact was studied [13, 14]. Hazell and Kister [13] studied CFRP laminate when it was impacted by a steel sphere and concluded that the degree of delamination in the thicker targets appeared to approach an asymptotic level. Puente [14] evaluated the CFRP laminates under higher velocity oblique impacts. The results showed that, after a number of impact tests at velocities between 70 and 540 m/s, the ballistic limit was around 100 m/s for normal impact and around 150 m/s for impacts at 45°. It was revealed that the damage is less for oblique impact when compared to the normal impact and for higher velocities the damage would be more for oblique impacts. Chocron [15] performed Ballistic tests on 2D composite as well as a 3D composite to determine the ballistic limit and he found that 3D composite had a lower ballistic limit when compared to 2D. Although having a low ballistic limit, the 3D composite has a damaged area 70% smaller than the 2D composite. The ballistic limit of the 2D and 3D composites which are having the same densities is

similar, whereas Smith's theory [16] also predicted the same. Tanabe et al. [17, 18] examined the behavior of CFRP damaged when steel sphere impacts on it and showed that stress and strain–time plots were strongly affected by the fiber/matrix interface strength and the carbon fiber type used. Similar observations were made by Fujii et al. [19] and stated that the failure modes varied with the mechanical properties of the fiber. Karthikeyan et al. [20] compared the ballistic performance of UHMWPE, CFRP with stainless-steel plates. The results concluded that the highest ballistic limit was present for UHMWPE and the least was present for steel plate. Mines and Li [21] performed experiments on 32-layers unidirectional CFRP laminates to determine the energy absorbed and structure behavior. The results indicated that there was only little effect on energy absorption due to in-plane loading. Jenq et al. [22] conducted an experiment on glass/epoxy composite laminates subjected to higher velocities using hemispherical shaped nose projectiles. They found that the damage was mostly due to delamination and fiber breakage. The ballistic limit was compared experimentally and numerically. Sevkat et al. [23] studied the damage behavior of FRP plates subjected to impacts at higher velocities and compared both the simulation and the experimental data, and showed that the main reason for the failure is delamination of the FRP. Furthermore, some researchers reported the effect of thickness of CFRP on ballistic [24–27]. Ramachandran et al. [24] studied the ballistic performance of woven carbon CFRP composites made of two different thicknesses were experimentally and theoretically. The results obtained showed that the residual velocity decreases, whereas the ballistic limit and energy absorption capacity of the plates increases with an increase in thickness. Caprino et al. [25] performed ballistic tests on CFRP panels and compared with the results obtained from previously proposed papers by Reid and Wen [26] and by Cantwell and Morton [8]. Both proved that energy is a function of thickness. Bland and Dear [27] performed experiments when different projectiles impacted on CFRP, and analysis of different failures resulting from these regimes and both models provided that the perforation energy depends on target thickness. Hazell [12] said that improvements in the ballistic performance of CFRP-based structures can be done by increasing c.a. 25% in areal density.

Tse [28] proved that the highest skull stress was present when the projectile impacted on top. He also concluded that both lateral, rear impacts have the highest principal shear strains and highest principle strains. Figure 1 shows the von Mises stresses of the skull obtained when it was impacted at various impact directions. It indicated that the top impact was the most severe reaching the peak skull stress up to 15 MPa which is followed by frontal and lateral impacts. Thus, the central impact on the helmets is of prime concern.

In the available literature, there were only few numerical studies because of the complex response of composite material with orthotropic behavior. However, FEA can be used to obtain information on parameters affecting impact phenomena in the most economical and effective way. CFRP composites have been given promising responses against ballistic impacts. Most of the studies were performed on woven (2D) architecture of CFRP composite material with laminated structures. Further, studies reporting the ballistic performance evaluation of a unidirectional CFRP composite helmet under the parameters of ballistic limit, energy absorption, and

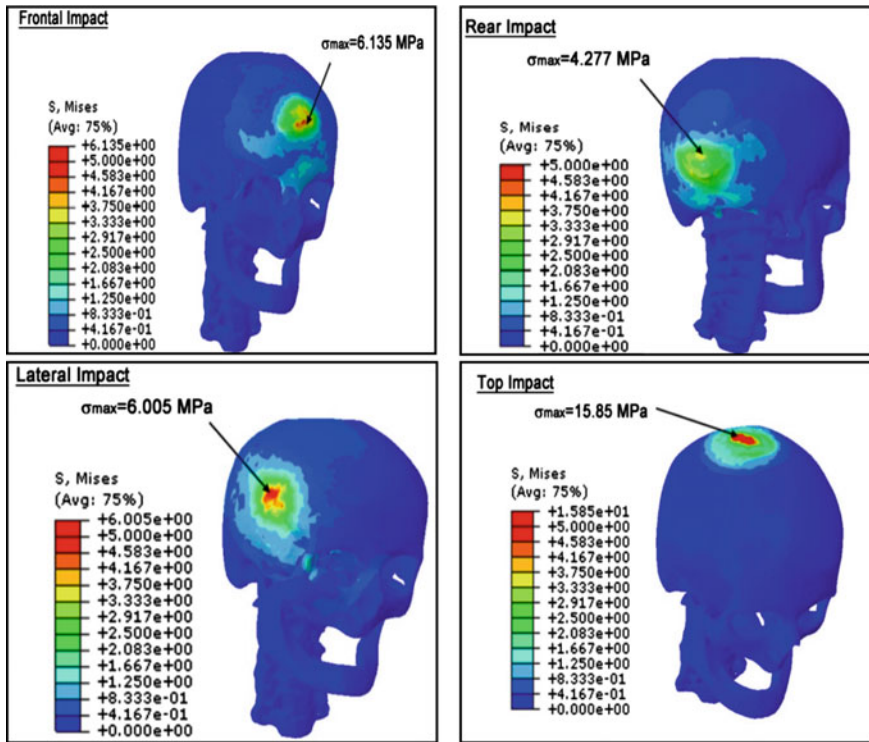


Fig. 1 Von Mises stresses under different impact directions [28]

damage pattern are rare in findings. Therefore, it was decided to perform numerical simulations to investigate the ballistic response of unidirectional CFRP helmet against sharp nosed ogival projectile. The ballistic limit, energy absorption and damage pattern within the CFRP helmet was studied within a sub ordnance regime.

2 Numerical Modeling

2.1 Helmet

In the present study, numerical analysis was performed to find the ballistic limit of CFRP helmet, when the ogive nosed projectile strikes the helmet at the top with different impact velocities. The simulations were performed using Abaqus software. The 3D cad model of the helmet was developed in Solid works and was imported to Abaqus to create the FE mesh. Hashin's damage criteria of Abaqus/Explicit was included. A laminated approach for composite modeling was used with the assignment of material, orientation, and thickness through composite layup module. The

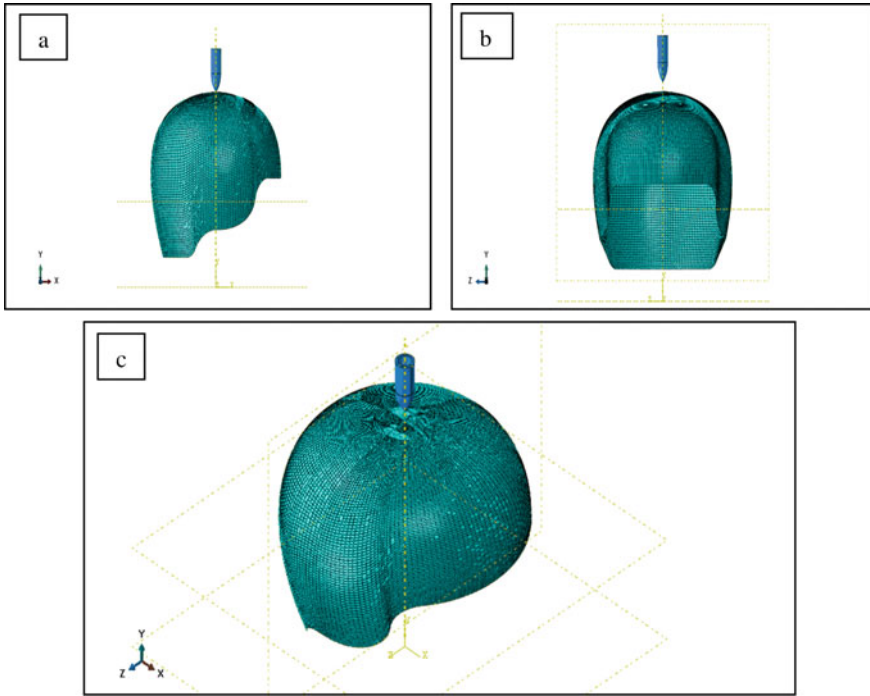


Fig. 2 Finite element model for unidirectional CFRP helmet–bullet assembly. **a** Side View, **b** Front view, and **c** Isometric view

FE model for helmet bullet assembly is shown in Fig. 2. The constants for the considered material model for the unidirectional CFRP helmet are provided in Table 1. Fine meshing was done on the area under impact as shown in Fig. 3. This was achieved by partitioning the topmost surface of the helmet. The conventional shell element of size $1\text{ mm} \times 1\text{ mm}$ is considered at the impact region.

2.2 Ogive Projectile

The Ogive nosed projectile is shown in Fig. 4. The ogive projectile was modeled as an analytical rigid (non-deformable) body where the reference point was given inside the body. Therefore, meshing was not required for the projectile. The projectile was assigned with a mass of 52.5 g and having an overall length of 50.8 mm. Only translational degree of freedom in the impact direction was provided to the projectile.

Table 1 Material properties of unidirectional CFRP [29]

Material property	Symbol	Value
Modulus of elasticity in fiber direction (a), (GPa)	E_a	132
Modulus of elasticity in transverse direction (b), (GPa)	E_b	7.8
Modulus of elasticity in transverse direction (c), (GPa)	E_c	7.8
Poisson's ratio, ab plane	ν_{ab}	0.33
Poisson's ratio, ac plane	ν_{ac}	0.33
Poisson's ratio, bc plane	ν_{bc}	0.35
Shear modulus, ab plane, (GPa)	G_{ab}	4.81
Shear modulus, ac plane, (GPa)	G_{ac}	4.81
Shear modulus, bc plane, (GPa)	G_{bc}	3.76
Tensile strength in fiber direction (a), (MPa)	Xa^T	2070
Compressive strength in fiber direction (a), (MPa)	Xa^C	1300
Tensile strength in transverse direction (b), (MPa)	Ya^T	61
Compressive strength in transverse direction (b), (MPa)	Ya^C	150
Shear strength, ab plane, (MPa)	Sa^L	110
Shear strength, ac plane, (MPa)	Sb^T	110
Shear strength, bc plane, (MPa)	Sc^T	110
Density (Kg/m^3)	ρ	1600

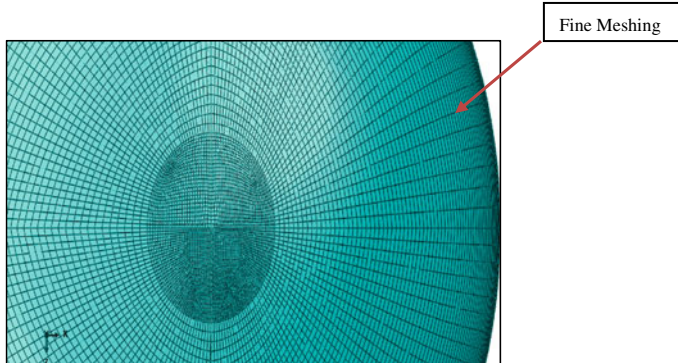
**Fig. 3** Fine meshing

Fig. 4 Ogive projectile

3 Results and Discussion

3.1 Ballistic Resistance

In the present study, simulations were performed on the unidirectional CFRP composite helmet subjected to ogive nosed projectile impact within the subordnance velocity regime in order to obtain the ballistic limit of the helmet. Analysis was carried on a 2 mm thick CFRP helmet with a layup sequence of (0/90/0/90/0/90). The values of impact velocities and the values of respective residual velocities were shown in Table 2. The velocity at which there is a 50% chance of penetration of the projectile is known as the V50 ballistic limit. In this analysis, V50 ballistic limit was determined by averaging the minimum velocity at which the projectile completely perforates the target and the maximum velocity at which the projectile would not be able to perforate the target. Based on the numerical simulations, the ballistic limit for the helmet was found to be 45 m/s. From Table 2, it was found that with a decrease in the impact velocity of the projectile, there was an increase in the drop of velocity (the difference between projectile incidence velocity and residual velocity).

3.2 Energy Absorption

The amount of kinetic energy lost by the ogive projectile is absorbed by the helmet. Therefore, energy absorption is an important phenomenon for the change in ballistic

Table 2 2 mm thick (90/0/90/0/90/0) unidirectional CFRP helmet against central impact by ogive nosed projectile

Impact velocity (m/)	Residual velocity (m/s)	Ballistic limit (m/s)	Energy absorption (J)
250	247.85	45	28.09740938
200	195.12		50.614872
150	142.63		56.61293138
80	69.11		42.62495738
60	46.79		37.03076738
50	25.44		48.636168
47	18.98		48.5299395
43	0		48.53625
40	0		42

limit. From Table 2, we can infer that the energy absorption by the CFRP helmet was increased for the velocities nearer to the ballistic limit as compared to the higher velocities. Thus, we can conclude that the CFRP laminates can be effectively used as the backing plate as the effective energy absorber.

3.3 Damage Pattern

The images of simulation results are shown in Fig. 5. It was observed that rupture of fibers is the major phenomenon due to which the helmet was failed. As the projectile penetrates into the helmet the elements failed progressively due to the sharp nose shape of the ogive projectile. A cross failure pattern was seen due to the directional straining from the fiber rupture. Thus, tensile failure of CFRP against sharp nosed ogival projectile was observed with minimum fiber stretching.

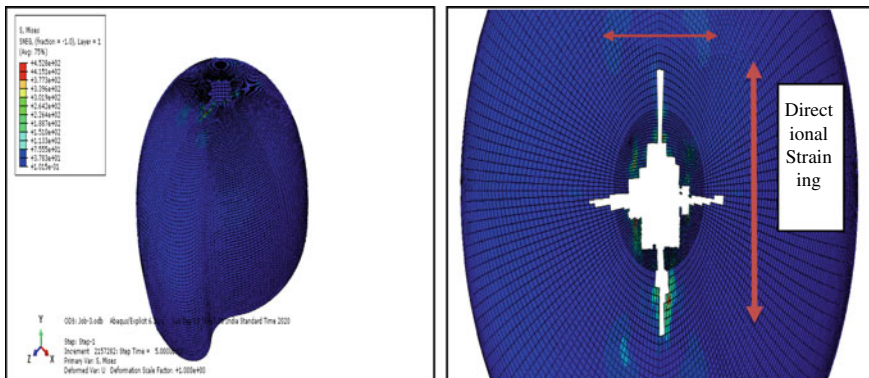


Fig. 5 Damage assessment in CFRP helmet

4 Conclusion

In this paper, the ballistic performance of unidirectional CFRP helmet was evaluated against the ogive nosed projectile impact within subordnance velocity regime. The CFRP helmet has a ply stacking of (0/90/0/90/0/90). The ballistic limit was achieved by varying the incidence velocity of the projectile. Ballistic performance was evaluated under the ballistic limit, energy absorption, and damage pattern. From the results, it was concluded that the ballistic limit of a unidirectional CFRP helmet is 45 m/s. Localized damage zone and tensile failure due to fiber rupture of CFRP helmet against ogival nosed projectile were observed.

References

1. Tham CY, Tan VBC, Lee HP (2008) Ballistic impact of a KEVLAR(R) helmet: experiment and simulations. *Int J Impact Eng* 35:304–318. <https://doi.org/10.1016/j.ijimpeng.2007.03.008>
2. Van Hoof J, Deutekom MJ, Worswick MJ, Bolduc M (1999) Experimental and numerical analysis of the ballistic impact response of composite helmet materials. In: 18th international symposium on ballistics, San Antonio, TX
3. Van Hoof, J & Cronin, D & Worswick, M & Williams, K & Nandlall, Dennis. (2001). Numerical head and composite helmet models to predict blunt trauma
4. Sharma S, Makwana R, Zhang L (2020) Evaluation of blast mitigation capability of advanced combat helmet by finite element modeling
5. Zhang L, Makwana R, Sharma S (2011) Comparison of the head response in blast insult with and without combat helmet. *J HFM-207: Survey of Blast Injury Across the Full Landscape of Military 3 Science* 4:33–31
6. Zhang L, Rahul M, Sumit S (2013) Brain response to primary blast wave using validated finite 5 element models of human head and advanced combat helmet. *Front Neurol* 4:88
7. Aare M, Kleiven S (2007) Evaluation of head response to ballistic helmet impacts using the finite element method. *Int J Impact Eng* 34:596–608. <https://doi.org/10.1016/j.ijimpeng.2005.08.001>
8. Cantwell WJ, Morton J (1989) Comparison of low and high velocity impact response of CFRP. *Composites* 20(6):545–551
9. Goldsmith W, Dharan H, Chang H (1995) Quasi-static and ballistic perforation of carbon fiber laminates. *Int J Solids Struct* 32:89–103. [https://doi.org/10.1016/0020-7683\(94\)00109-A](https://doi.org/10.1016/0020-7683(94)00109-A)
10. Hosur M, Vaidya U, Ulven C, Jeelani S (2004) Performance of stitched/unstitched woven carbon/epoxy composites under high velocity impact loading. *Compos Struct* 64:455–466. <https://doi.org/10.1016/j.compstruct.2003.09.046>
11. Larsson F (1997) Damage tolerance of a stitched carbon/epoxy laminate. *Compos A Appl Sci Manuf* 28:923–934. [https://doi.org/10.1016/S1359-835X\(97\)00063-8](https://doi.org/10.1016/S1359-835X(97)00063-8)
12. Hazell P, Appleby-Thomas G (2009) A study on the energy dissipation of several different CFRP-based targets completely penetrated by a high velocity projectile. *Compos Struct* 91:103–109. <https://doi.org/10.1016/j.compstruct.2009.04.036>
13. Hazell P, Kister G, Stennett C, Bourque P, Cooper G (2008) Normal and oblique penetration of woven CFRP laminates by a high velocity steel sphere. *Compos Part A—Appl Sci Manuf* 39:866–874. <https://doi.org/10.1016/j.compositesa.2008.01.007>
14. Puente J, Zaera R, Navarro C (2008) Experimental and numerical analysis of normal and oblique ballistic impacts on thin carbon/epoxy woven laminates. *Compos A Appl Sci Manuf* 39:374–387. <https://doi.org/10.1016/j.compositesa.2007.10.004>

15. Chocron S, Carpenter A, Scott N, Bigger R, Warren K (2019) Impact on Carbon fiber composite: ballistic tests, material tests, and computer simulations. *Int J Impact Engi* 131. <https://doi.org/10.1016/j.ijimpeng.2019.05.002>
16. Smith J, Blandford J, Schiefer H (1960) Stress–strain relationships. in yarns subjected to rapid impact loading: Part VI: velocities of strain waves resulting from impact. *Text Res J* 30:752–760. <https://doi.org/10.1177/004051756003001002>
17. Tanabe Y, Aoki M, Fujii K, Kasano H, Yasuda E (2003) Fracture behavior of CFRPs impacted by relatively high-velocity steel sphere. *Int J Impact Eng* 28:627–642. [https://doi.org/10.1016/S0734-743X\(02\)00126-4](https://doi.org/10.1016/S0734-743X(02)00126-4)
18. Tanabe Y, Aoki M (2003) Stress and strain measurements in carbon-related materials impacted by a high-velocity steel sphere. *Int J Impact Eng* 28:1045–1059. [https://doi.org/10.1016/S0734-743X\(03\)00035-6](https://doi.org/10.1016/S0734-743X(03)00035-6)
19. Fujii K, Aoki M, Kiuchi N, Yasuda E, Tanabe Y (2002) Impact perforation behavior of CFRPs using high-velocity steel sphere. *Int J Impact Eng* 27:497–508. [https://doi.org/10.1016/S0734-743X\(01\)00152-X](https://doi.org/10.1016/S0734-743X(01)00152-X)
20. Karthikeyan K, Russell B, Fleck N, Wadley HNG, Deshpande VS (2013) The effect of shear strength on the ballistic response of laminated composite plates. *Eur J Mech A Solids* 42:35–53. <https://doi.org/10.1016/j.euromechsol.2013.04.002>
21. Mines RAW, Li QM (2008) Static behaviour of transversely loaded CFRP laminate panels subject to in-plane tension. *Strain* 36:71–80. <https://doi.org/10.1111/j.1475-1305.2000.tb01176.x>
22. Jenq S-T, Jing H-S, Chung C (1994) Predicting the ballistic limit for plain woven glass/epoxy composite laminate. *Int J Impact Eng* 15:451–464. [https://doi.org/10.1016/0734-743X\(94\)80028-8](https://doi.org/10.1016/0734-743X(94)80028-8)
23. Sevkat E, Liaw B, Delale F, Raju B (2009) A combined experimental and numerical approach to study ballistic impact response of S2-glass fiber/toughened epoxy composite beams. *Compos Sci Technol* 69:965–982. <https://doi.org/10.1016/j.compscitech.2009.01.001>. Accessed 1 Jan 2009
24. Ramachandran V, Kakur N, Shankar K (2017) Influence of fibre orientation and thickness on the response of CFRP composites subjected to high velocity impact loading, 4:1–12. <https://doi.org/10.1080/2374068X.2017.1410688>
25. Caprino G, Lopresto V, Santoro D (2007) Ballistic impact behaviour of stitched graphite/epoxy laminates. *Compos Sci Technol* 67:325–335. <https://doi.org/10.1016/j.compscitech.2006.04.015>
26. Reid S, Wen H (2000) Perforation of FRP laminates and sandwich panels subjected to missile impact. <https://doi.org/10.1533/9781855738904.239>
27. Bland PW, Dear J (2001) Observations on the impact behaviour of carbon-fibre reinforced polymers for the qualitative validation of models. *Compos A Appl Sci Manuf* 32(9):1217–1227. [https://doi.org/10.1016/S1359-835X\(01\)00076-8](https://doi.org/10.1016/S1359-835X(01)00076-8)
28. Tse KM, Long Bin T, Yang B, Tan VBC, Lee HP (2016) Effect of helmet liner systems and impact directions on severity of head injuries sustained in ballistic impacts: a finite element (FE) study. *Med Biol Eng Comput* 55. <https://doi.org/10.1007/s11517-016-1536-3>
29. Gharde N (2020) Impact behavior of unidirectional CFRP composite laminates, MTech Thesis

Tensile-Microstructure Evaluation for LM6 Alloys Synthesized by Solid–Liquid Mixed Casting



Mayank Agarwal, Devendra Pratap Singh, Manvandra Kumar Singh, and Rajeev Srivastava

Abstract This experimental work represents a new process for the sand casting of LM6 Al–Si alloy based on the different amounts of powder-chip reinforcement of LM6 alloy. In the process, semi-solid slurry was prepared by mechanical stirring during the solid–liquid mixed processing. In the processing, initially, reinforcement has been synthesized by the impact of ball milling for a combination of microchips and nano-size powder particles. Finally, fabricated reinforcement particulates were well stirred inside the melt of the same alloy for a temperature between 580 and 640 °C. The addition amount of LM6 Al–Si inside the melt ranges from 10 to 25% with an incremental rate of 5%. The experimental results indicate that the tensile properties of LM6 are improved due to the addition of powdery-chip particulates. Simultaneously, experimental data confirms the effect of temperature on the mechanical properties in which mechanical strength directly increases with the drop of pouring temperature, whereas it has been found a combined effect generated by reinforced particulates and pouring temperature of slurry confirms an optimal effect for the tensile strength. The effect of these parameters has been analyzed by the microstructure evaluation at different levels.

Keywords LM6 · Pouring temperature · Tensile strength · Elongation rate · Microstructure

M. Agarwal (✉) · D. P. Singh
Pranveer Singh Institute of Technology, Kanpur, India

M. K. Singh
Department of Mechanical Engineering, Amity School of Engineering and Technology, Amity University Madhya Pradesh, Gwalior, India
e-mail: mksingh@gwa.amity.edu

R. Srivastava
Motilal Nehru National Institute of Technology, Allahabad, India
e-mail: rajmnnit@mnnit.ac.in

1 Introduction

In aluminum industries, Al-MMC based on ceramic particulates are highly attracted toward the designers and engineers due to their excellent metallurgical properties with respect to weight. These alloys have excellent casting characteristics and forming ability [1–8]. The trend towards the composite with using semi-solid processing is considerable of Al–Si alloys which used more in past several years [3]. The processing parameters in silicon-rich aluminum casting due to the effect of semi-solid temperature offers a lot of advantages such as improved mechanical and metallurgical properties, low segregation, excellent wear strength, and so on [4, 5]. During the processing of semi-solid casting, slurries are obtained by several methods, mostly by use of the stirring process, in which melts are cooled down below the liquid temperature and solid particles are used to fabricate a thick slurry [5–7]. This research work was conducted for powder-chip reinforcement of the same alloy matrix instead of pure molten metal and a combined effect of powder-chip reinforcement and temperature has been investigated for the improved tensile strength of LM6 Al–Si alloy due to the effect of processing.

2 Experimental

2.1 Material and Slurry Preparation

LM6 alloy is shown in Table 1, which was used in the process for melting, and slurry preparation was done with help of an open heat furnace. In the processing, an initial temperature of about $840\text{ }^{\circ}\text{C} \pm 20\text{ }^{\circ}\text{C}$ was maintained for all the replicates. This temperature of the melt is controlled with help of displacement for the crucible made by china clay for a very short duration. According to weight percentage, powder-chip reinforcement was mixed at the temperature range between 740 and $760\text{ }^{\circ}\text{C}$. A mechanically stirring process has been used until the temperature of the mixed melt reaches $680\text{ }^{\circ}\text{C} \pm 10\text{ }^{\circ}\text{C}$. The pouring temperature of the melt was about $640\text{ }^{\circ}\text{C}$ for higher pouring temperature casting replicates, whereas $580\text{ }^{\circ}\text{C}$ for lower pouring temperature castings. Detailed procedure of the cast part and processing has been discussed in [9–11].

Table 1 Composition of LM6 aluminum alloy according to wt.%

Cu	Fe	Mg	Mn	Ni	Pb	Si	Sn	Ti	Zn	Al
0.097	0.57	0.11	0.521	0.12	0.09	11.88	0.05	0.22	0.12	86.22

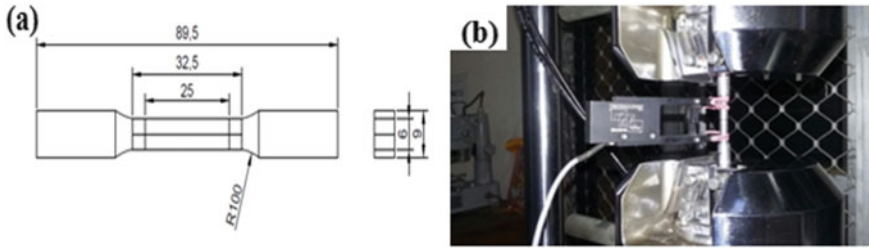


Fig. 1 **a** Schematic diagram for tensile test sample. **b** Sample test of the mini UTM

2.2 Tensile Testing

To evaluate the tensile properties, test specimens were synthesized by the machining of cast composite. A tensile test was conducted and the analysis has been reported according to the tensile specimen of 6 mm diameter and 25 mm gauge length, with all dimensions conforming to the ASTM E8-00 standards shown in Fig. 1a. These tests have been performed on the mini Universal Testing Machine BISS model 25 KN capacity shown in Fig. 1b.

2.3 Microstructure Sample Preparation

Microstructural analysis was conducted by the polished cast samples. After polished to 2000 mesh emery papers, samples were swabbed with 2% picral solution in order to perform scanning electron microscopy. This was conducted to evaluate the effect of powdery-chip particulates and other processing parameters on the cast morphology of the fabricated composite, by the help of Scanning Electron Microscope A-ZEISS EVO MA 15.

3 Results and Discussion

3.1 Tensile Properties

The tensile tests were performed for all 4 series with 5 replicates of each and the results are shown in Table 2. It is noticed that the solidification rate increases directly with the multiple additions of solid fractions. As per the results tabulated in the table, elongation of the series 'C' is higher in comparison to other all series. In this casting, the actual solid fraction was about 20% by weight providing better results with an increase in ductility due to sudden incomplete recrystallization under low pouring temperature. The ultimate tensile strength is much higher for low solid fraction and

Table 2 Typical tensile properties of all series of LM 6 solid fraction cast sample

Series	Fs (%)	Tp (°C)	E (in GPa)	YS (in MPa)	UTS (in MPa)	Elongation (in %)	Pm (in KN)
A	10	580	73.173	94.25	175.75	0.4475	6.781
B	10	680	64.8	105	157.8	0.271	6.294
C	25	580	74.75	79.4	171.5	0.6225	6.243
D	25	680	66.46	132.5	189	0.348	6.087

high temperature cast for the series ‘D’ and ductility of the cast becomes greater due to a higher rate of solid fraction increase. It is observed from the obtained results that the peak load (Pm) for all the series is the same with sufficient change in the yield strength.

Figure 2a shows the variation in the stress value with the corresponding strain rate for 580 and 680 °C temperature casting. It is observed that marginal difference in the deformation appears for the 580 °C temperature casting in the curve ‘A’ and ‘D’ as shown in Fig. 2a. Further, low deformation for the cast composite fabricated under 680 °C temperature and 10% reinforcement addition has been observed, which is shown by the curve ‘B’ in Fig. 2a. As the wt% of reinforcement increases with 680 °C, strength increase with low deformation is shown in the curve ‘C’. This change has been observed due to the faster internal cooling effect generated during the process of stirring [12]. Finally, it has been observed that 580 °C with a higher amount of reinforcement samples gives the moderate change in ductility with a reasonable increase in the strength of the LM6 alloy.

Furthermore, percentage elongations with the corresponding amount of reinforcement can be identified from Fig. 2b. Lower rate for the mixing of reinforced particles and 580 °C shows minimum elongation and confirms the lower ductility of the casting whereas this observed maximum for 580 °C with 25% wt. of reinforcement particulates. The average young’s modulus values of the 580 °C and high added amount

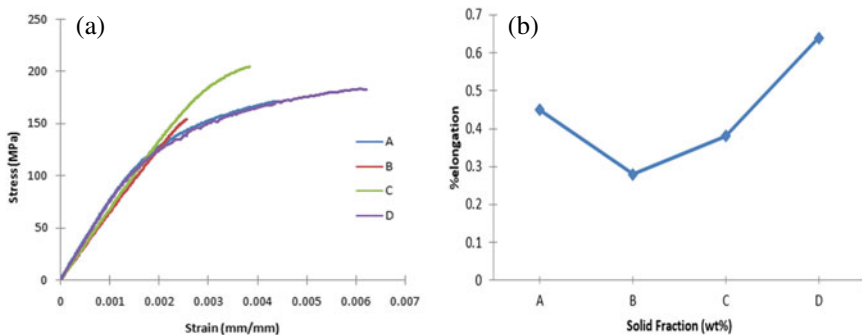


Fig. 2 a Stress–strain diagram for all series of tensile tests of LM 6 powder-chip reinforcement cast samples. **b** Variation in % elongations for corresponding solid fraction

of reinforcement during the investigation were 75.67 GPa and 181.67 MPa UTS for the 8 samples. The decrease in the tensile strength value of the fabricated composite samples, containing low addition of the reinforced particulates can also be justified by dislocation density and by relative density. A drop in the temperature during the slurry formation results in elevation of dislocation density during solidification of the cast metal leads to a reduction in resistance to plastic deformation and a decrease in strength [5, 11–14].

3.2 Microstructure Analysis

Figure 3 shows the scanning electron micrographs for the cast of various temperature and reinforcement combinations. It is evident that the grains appear finer after the addition of chip particulates in higher density at low pouring temperature shown in Fig. 3a.

The microstructure of the cast of series ‘C’ (25% reinforcement with 580 °C) shown in Fig. 3b is fully equiaxed and the inside porosity of the cast specimen is very less compared to the cast of the series ‘A’ (10%–680 °C), as shown in Fig. 3a. Diffusion (partial) of the solid chip particles in the microstructure is observed inside the bigger cavity as shown in Fig. 3a, d (in white phase), which provides sufficient

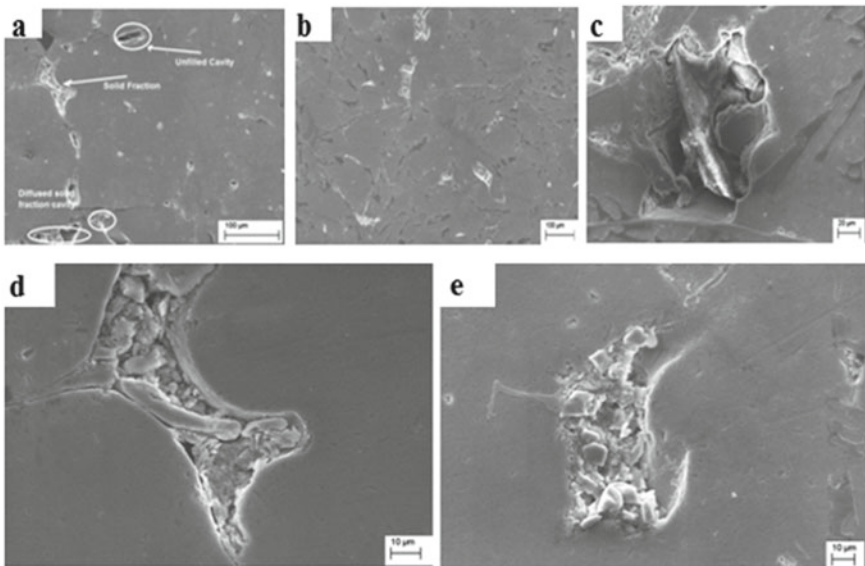


Fig. 3 Microstructure of **a** 10% reinforcement and 680 °C **b** 25% reinforcement and 580 °C **c** Diffused chips for 20% reinforcement and 680 °C, casting, closer Microstructure of **d** 10% reinforcement and 680 °C **e** 25% reinforcement and 580 °C casting

increase in the ductility of the materials. For 25% reinforcement addition in Series 'D', solid particles diffuse more along the sidewall of the cavity shown in Fig. 3c, this is accepted due to inoculation of the master solid particle as secondary shrinkage of the chips and powder particles inside the cavity [9, 10]. The combined conjugation bunch of small chips and powder particles with a mean radius of more than 81 microns diffuses inside the melt construct due to primary shrinkage at the time of pouring clearly appears on the images [9]. The happening shows in two forms first the diffusion rate is more for the pouring temperature about 680 °C about the walls of the cavities when solid fraction was about 25%, but this type of diffusion has not taken place for 10 and 15% reinforcement addition [8, 9]. Further from Fig. 3e, it is clear that a consolidated effect of the solid fraction and pouring temperature for the 20% reinforcement under a pouring temperature range below 600 °C. This depicted incomplete recrystallization for the semi-solid slurry which affects the shrinkage behavior of the melt. The basic mechanism of secondary shrinkage of the melt and solid fraction takes place in this series [11, 14].

4 Conclusions

- The inoculation of powdery-chip particulates of LM6 with the same parent matrix melt improves the tensile properties of the cast with an influence of semi-solid liquid slurry. Experimental results for percentage elongation during the test showed the significant improvement in the ultimate tensile strength of the modified cast composite with respect to parent material.
- With the addition of LM6 powder-chip ball-milled particulates, the solidification rate of the cast increases due to faster heterogeneous nucleation which provides finer and equiaxed grain distribution for the low pouring temperature along the cavities generated during the solidification.
- Multiple shrinkages during the process between the melt and solid chips reduce the inside porosity, as well as increase the relative density of the cast.
- The microstructural analysis concludes that the combined effect of pouring temperature and powder-chip reinforcement is the primary factor according to the diffusion of solid particles and internal reduction of the defects against the short cavities.
- The thermomechanical process for the semi-solid casting owing to the extensive plastic flow of the reinforcement particulates and inside annexing of the fibrous α -Al grains provides the distinct microstructural and tensile behavior.

References

1. Nampoothiri J, Muthuraja C, Balasundar I et al (2018) Microstructure evolution during semi-solid isothermal holding of liquidus cast strontium-modified A356 alloy. *Trans Indian Inst Met* 71:2707–2712
2. Liu Z, Mao W, Wan T et al (2021) Study on semi-solid A380 aluminum alloy slurry prepared by water-cooling serpentine channel and its rheo-diecasting. *Met Mater Int* 27: 2067–2077
3. Huang X, Ma Y, Zhang Q et al (2019) Effects of trace Cr on as-cast microstructure and microstructural evolution of semi-solid isothermal heat treatment ZC61 magnesium alloy. *China Foundry* 16:53–62
4. Liu Z, Mao W, Wang W et al (2017) Investigation of rheo-diecasting mold filling of semi-solid A380 aluminum alloy slurry. *Int J Miner Metall Mater* 24:691–700
5. Acharya M, Mandal A (2021) Effect of semi-solid heat treatment on the microstructure and dry sliding wear behavior of Al–20Si alloy at optimized parametric conditions. *Met Mater Int* 27:1578–1586.
6. Sheykh-jaberi F, Cockcroft SL, Maijer DM, Phillion AB (2019) Comparison of the semi-solid constitutive behaviour of A356 and B206 aluminum foundry alloys. *J Mater Process Technol* 266:37–45
7. Zhang J, Guan R-G, Tie D, Wang X, Guan X-H, Chen B-C, Chen Y (2015) Effects of technical parameters of semi-solid stirring and rheo-rolling on microstructure of A356–5wt.% B4C composite strip. *Mater Manuf Process* 30(3):340–345
8. Sheikh-Ansari MH, Aghaie-Khafri M (2019) An extension of Rice localization criterion to predict the onset of shear localization in semi-solid materials. *Int J Mater Form* 12:703–716
9. Agarwal M, Srivastava R (2016) influence of solid fraction casting on microstructure of aluminum alloy 6061. *Mater Manuf Process* 31(15):1958–1967
10. Agarwal M, Singh A, Srivastava R (2018) Influence of powder-chip based reinforcement on tensile properties and fracture behaviors of LM6 aluminum alloy. *Trans Indian Inst Met* 71:1091–1098
11. Agarwal M, Srivastava R (2019) Friction, Wear and Mechanical Properties of Al–Si LM6 Cast Alloy Processed in Semi-solid Stage. *SILICON* 11:355–366
12. Agarwal M, Srivastava R (2019) Influence of fine Al₂O₃ and aluminium nano-particles on the 6061 aluminium alloy near the grain boundary of the semi-solid cast microstructure. *Trans Indian Ceram Soc* 78(2):94–100
13. Arun Prakash J, Shanmugasundaram P, Sreelakshmy PS (2020) Optimization of mechanical, tribological and machining parameters of aluminium MMC's LM6 and ADC 12. In: *Materials today: proceedings* (In press)
14. Jerold S, Chelladurai S, Arthanari R (2019) Investigation on mechanical and wear properties of zinc-coated steel wires reinforced LM6 aluminium alloy composites by squeeze casting. *Surf Rev Lett* 26(1):1850125

FEM-Based Impact Analysis of Roll Cage of an All-Terrain Vehicle



Jitendra Yadav, Santosh Kumar Kurre, and Shubham Thakur

Abstract The paper explains the crashworthiness of the car in order to ensure the safety of the occupants. The anticipated work is projected to study the effect of impact loads on the chassis frame/roll cage of an off-road vehicle. The dynamics are captured through transient for impact testing. The results highlight the dynamics of roll cage under the front impact. The response of the system for the cases without and with bumper are compared. The impact severity has been determined by pinpointing the nodes at which maximum and minimum deflection, velocity, and stresses occur. The simulating is done with the transient dynamic analysis of the roll cage on ANSYS. Results of the work with transient dynamic analysis ensure the sufficiency of the design. The FOS is found to be higher in case of bumper.

Keywords Roll cage · All terrain · FEM · ANSYS · Crashworthiness · Chassis

1 Introduction

The drastic crash conditions of vehicle structures are analyzed to check the capabilities of sustaining impact loads. The common example of various loading is frontal impact, pole impacts offset, angular impact, and side collisions. On the other hand, non-crash functional requirements such as vibration, durability, and fatigue life cycle are also important in the vehicle design. The high impact bearing ability for improved safety of the vehicle is one of the important criteria like others such as fuel economy, cost, performance, etc. Researchers are using various software tools to capture the impact dynamics of automobiles. These software tools ensure quick results in identifying feasible solutions before building a prototype. So far from the guideline, one should expose the drastic complex crash situations toward the computer simulation to

J. Yadav (✉) · S. K. Kurre · S. Thakur
Department of Mechanical Engineering, University of Petroleum and Energy Studies,
Dehradun 248007, India
e-mail: [jyadav@ddn.upes.ac.in](mailto: jyadav@ddn.upes.ac.in)

S. K. Kurre
e-mail: [skurre@ddn.upes.ac.in](mailto: skurre@ddn.upes.ac.in)

© The Author(s), under exclusive license to Springer Nature Singapore Pte Ltd. 2022
M. K. Singh and R. K. Gautam (eds.), *Recent Trends in Design, Materials and Manufacturing*, Lecture Notes in Mechanical Engineering,
https://doi.org/10.1007/978-981-16-4083-4_17

save labor, time, and money. However, a lot of work on the vehicle dynamics has been described but the changing demands of comfortable drive conditions encourage the automobile engineers to have more study. Vehicle dynamics include model design, chassis design, chassis analysis, rapid prototyping of model, and transient dynamic analysis. Thompson et al. [1] determined the effects on stiffness and camber response with overall chassis flexibility by using a FEM model. In this analysis, they have taken care that the roll stiffness the suspensions the values by model of rigid body kinematics. Lonny et al. [2] found that baseline chassis torsional stiffness is directly proportional to the sensitivity of individual component. Thus, knowledge of individual structure members' sensitivity is helpful in modifying baseline chassis. In this manner, the targeted torsional stiffness of baseline chassis is achievable with minimum weight and the lowest possible placement of Szcotka et al. [3] proposed multibody dynamics modeling with open and closed kinematic chains, thus ensuring the analysis of different applications with these approaches. Leiva et al. [4] used the GENESIS program effectively to get the optimized solution in automobile designing. Kuti [5] modeled vehicle dynamics for 3D motion by FEM. They suggested that proper placement of elasticity and mass may be decisive in getting the ensured dynamics. Fischer et al. [6] worked on the comfort of passengers by dealing with the vibration control and interior soundproofing by FEM in contrary to the high vibration with light structures. They suggested that by combining the theoretical study and measurement, a better noise level for a 3-cylinder engine could be achieved in comparison with a 4-cylinder engine. Hadri et al. [7] analyzed vehicle for independent suspension at both the axle by a step-by-step algorithm which is based on tire force calculation based on sliding mode observation. Yaw motion results in the acceleration of the vehicle in the longitudinal and lateral directions. They concluded that vehicle transient response is influenced by load transfer effect. According to Johansson et al. [8], there is a need for efficient tools to cope with the requirement of extra features in trucks to focus on optimization and modularization. According to Sun [9], crashworthiness is the technology applied to protect occupants, in case of an impact to the vehicle's structural integrity, by absorbing the kinetic energy, and at the same time, by lowering the crashing force, thus ensuring safety to the occupants. Joao et al. [10] emphasized the requirement of an accurate model that is capable of dealing with the composite behavior of systems that are subjected to large motion with small elastic deformation. The rollover propensity of an ATV is determined mainly by its stability [11].

So far from the above discussion, it becomes clear that a lot of work has been done in the field of modeling the structures/vehicles. However, the work in analyzing the structures/vehicles is comparatively less but it keeps on increasing with the availability of new software tools for the designers for analyzing their models and prototypes. In literature, very less work is reported for off-road vehicles. An intensive study of the effect of impact loads on the whole chassis frame of an off-road vehicle is still an untouched work of research, which is the main motive of the present paper. The present work is intended to have an impact analysis on off-road vehicles to know the weak areas to cater the scope of improving the design. The simulation is done with the transient dynamic analysis of the roll cage on ANSYS.

2 Modeling of the System

The roll cage is modeled kinematic, dynamic and FEM. The attributes, which are provided to elements, are the element type, real constraints, material properties, and cross section of elements. Firstly, the significant points are set using a Cartesian coordinate system and then lines are created by joining the key points, to mesh the model with particular attributes. At last, the FEA model is created (see Fig. 1). There are 103 elements and 80 nodes have been created. The boundary conditions at different nodes varies according to situations. Depending on the points of application of force, the dynamic response of the model changes. The boundary conditions change with time, therefore, the final conditions differ from the initial ones. When the vehicle strikes with the roll cage with some velocity, then due to the impact forces, load is applied on some definite points/nodes of the roll cage due to which deformation takes place. The results are in the form of graphs, e.g., deflection versus time plot, velocity versus time plot, acceleration versus time plot, etc., for different nodes and in form of animations of deformed shape. The stresses can also be obtained for different boundary conditions. The output of the program can be stored in the form of a figure, which is easy to handle and store.

2.1 Kinematic Modeling

The kinematic modeling for the analysis on model, which is made up of steel hollow pipes, is done by considering the case of front impact in which a vehicle coming with a speed of 40 km/h strikes at the front portion. The damping controls the vibration of

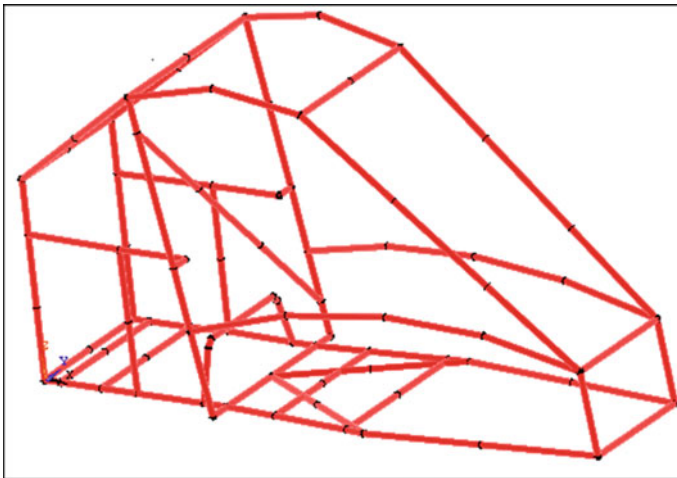


Fig. 1 Roll cage FE-Model

Table 1 Data for front impact. Velocity of striking vehicle = 40 km/h

Time (sec)	Force on each node (N)	Node of application (without bumper)	Node of application (with bumper)	Total impact load (IN)
1.1	175	12,14,50,51	81,82,83,84	700
1.2	350	12,14,50,51	81,82,83,84	1400
1.3	525	12,14,50,51	81,82,83,84	2100
1.4	700	12,14,50,51	81,82,83,84	2800
1.5	875	12,14,50,51	81,82,83,84	3500
1.6	1050	12,14,50,51	81,82,83,84	4200
1.7	1225	12,14,50,51	81,82,83,84	4900
1.8	1400	12,14,50,51	81,82,83,84	5600
1.9	1575	12,14,50,51	81,82,83,84	6300
2	1750	12,14,50,51	81,82,83,84	7000

a body or system by dissipation of energy internally or by radiation [12]. The amount of dissipated power from the vehicle suspension depends on the vehicle bounce and pitch modes [13]. The analysis is done considering two cases, viz., with and without damper. In the present case, the maximum amplitude of impact force acting is of the order 7000 N. This impact force is assumed to be gradually increasing from 700 to 7000 N in 10 steps, i.e., the application of force starts from 700 N and after 10 steps; it reaches to the highest value that is 7000 N within one second. For the case the time, force applied, and node number of force application are tabulated and represented (see Table 1).

2.2 Dynamic Modeling

Chassis supports upper lumped masses and distributes these loads to the axle through the suspension system to the wheels. The roll cage is engineered and constructed frame is designed for occupants' safety at the time of misshapes especially rollover [14]. The chassis for the off-road vehicle has an unconventional shape, above which supporting beams are mounted to provide extra support to the lumped masses such as engine, etc. The FEM model of the roll cage is formulated (see Fig. 1).

The Roll cage is made up of steel having material property tabulated below (see Table 2).

Table 2 Material properties of steel

Modulus of elasticity	Ultimate tensile stress	Yield stress	Poisson’s ratio	Density
$E \text{ (N/m}^2\text{)}$	$\sigma_{ut} \text{ (N/m}^2\text{)}$	$\sigma_{yt} \text{ (N/m}^2\text{)}$	μ	$P \text{ (kg/m}^3\text{)}$
205×10^9	4.83×10^8	2.18×10^8	0.30	7850

3 Finite Element Modeling

3.1 General Procedure

Several tools are applied for the optimization of the design [15]. The flow block diagram (see Fig. 2) is the procedure for FEA of the Roll cage model by ANSYS (Reference ANSYS Tutorial).

3.2 Element Type

For the analysis, it is essential to select appropriate elements from a library of element types for finite element modeling. In case of modeling of the Roll cage, the required element is Pipe16.

Pipe16. PIPE16 is considered a uniaxial element capable of modeling all loading conditions, i.e., tension, compression, torsion, bending, etc. With six degrees of freedom and two nodes (see Fig. 3).

3.3 Real Constraints

Properties of the element types are represented by the real constraints. The FEA model behaves like the original element after giving these values as an input. The property of the FEA model is the same as that of the original elements. The following are the real constraints for Pipe 16 element type (see Table 3).

4 Results of Simulation

The results in form of dynamic responses, i.e., deflection-time and velocity-time plot are obtained by the simulation performed on the roll cage model for different prevailing boundary conditions for all five cases. The roll cage is considered to be applied with a gradually increasing load from 700 to 7000 N in ten steps commencing in 1 s at a speed of 40 kmph. The results are also compared for different nodes.

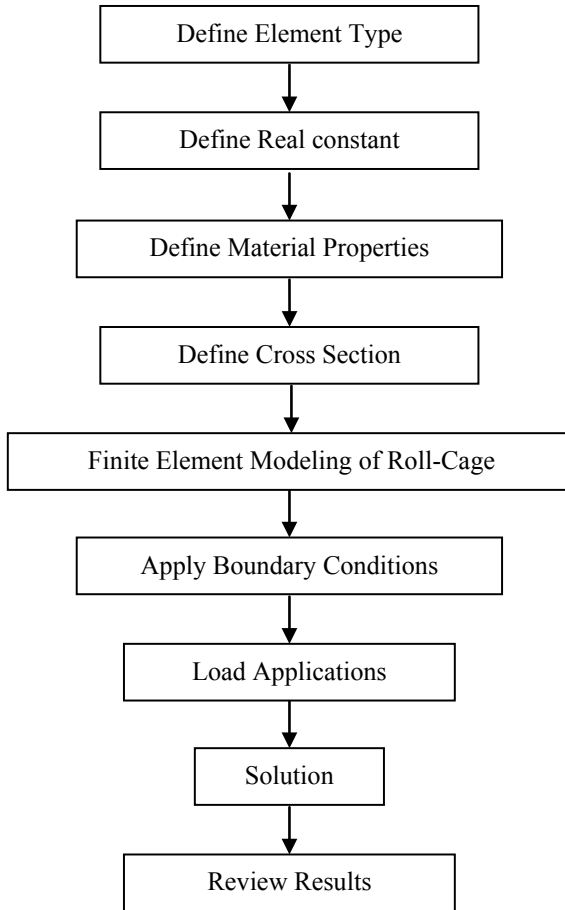


Fig. 2 Finite element analysis procedure in ANSYS

In this case, a vehicle coming at a speed of 40 kmph, strikes the roll cage at its front portion. The purpose of this analysis is to check the strength and stability of the roll cage in case where a vehicle strikes it from the front. ANSYS gives the results after applying the boundary conditions to the FE-model of the roll cage.

Relative deflection is the deflection in UZ direction (means deflection in vertical upward or downward direction) at each node of the roll cage with respect to time in a global coordinate system. The relative deflections of all nodes on the roll cage and the relative velocities of all nodes on the roll cage are obtained in for of Relative deflection verses time plot. The sample results are shown below (see Figs. 4 and 5).

From the nodal solution (see Figs. 6 and 7), it is shown by the study that without bumper the maximum deflection occurs at node 79 of the magnitude 2.1 mm and maximum velocity occurs at the same node, i.e., 2.6 mm/s. For the case with bumper, maximum deflection occurs at node 52 of the magnitude 1.55 mm.

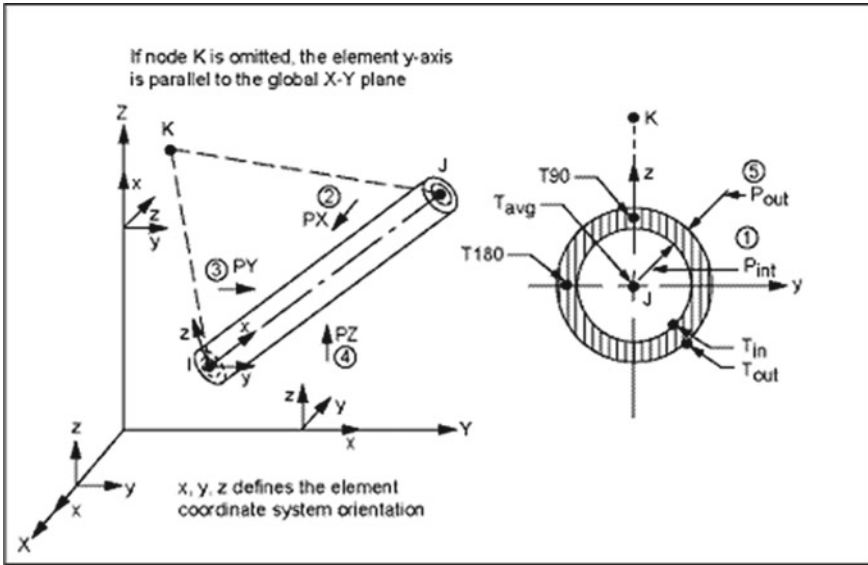


Fig. 3 Pipe16 geometry

Table 3 Set of real constants for the Pipe16 Element

S. no	Name	Description
1	OD	Outer diameter of pipe
2	TKWALL	Thickness of the pipe

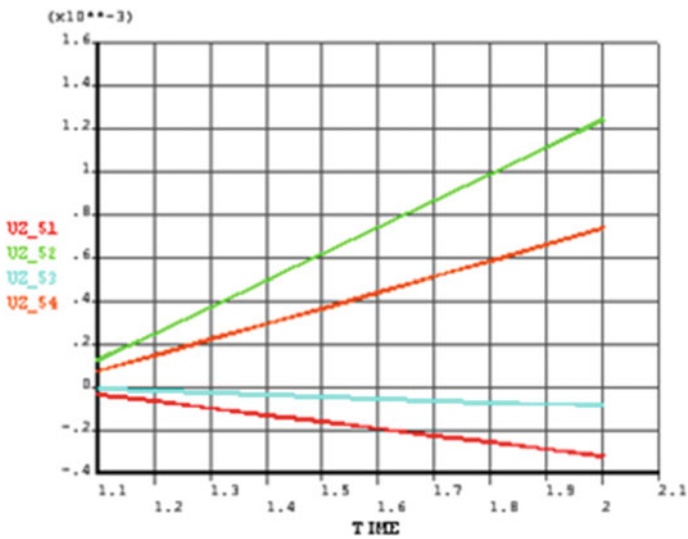


Fig. 4 Relative deflections versus time Plot for nodes 51, 52, 53, 54. (Without bumper)

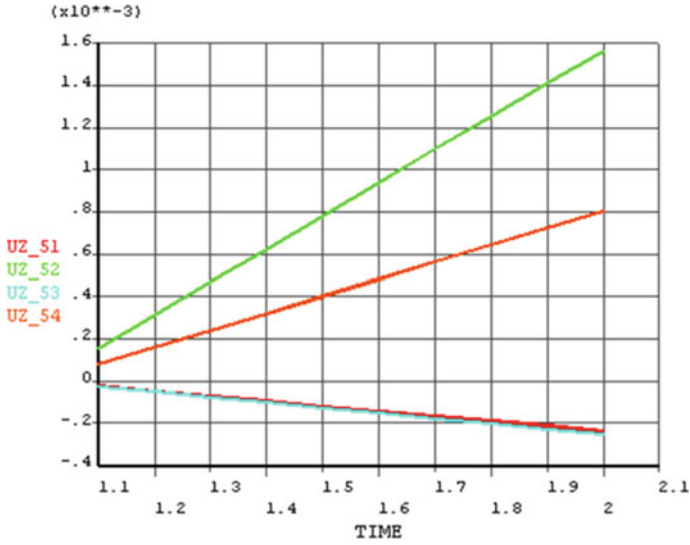


Fig. 5 Relative deflection versus Time for nodes 51, 52, 53, 54 (with bumper)

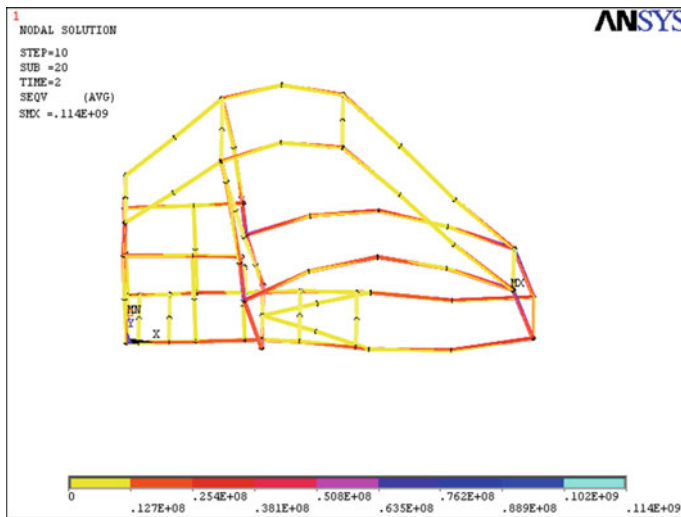


Fig. 6 Nodal solution (without bumper)

The deflection at each critical node is calculated and tabulated. The deflection of the critical nodes for the cases without damper and with damper is shown below (see Fig. 8).

The FOS for both cases are shown below (see Table 4).



Fig. 7 Nodal solution (with bumper)

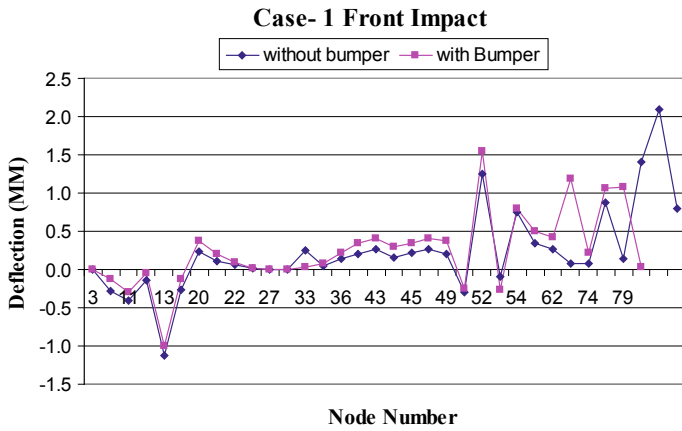


Fig. 8 Node number versus Deflection (without bumper and with bumper)

Table 4 Stress analysis

Case –1	Yield stress (N/mm ²)	Induced stress (N/mm ²)	Factor of safety
Without bumper	218	114	1.9
With bumper	218	106	2.05

5 Conclusion

It is palpable from the study that the induced stress is less in the case with bumper. The percentage reduction in induced stress is of the magnitude 7%. Thus, more safety can be provided to the vehicle by employing a bumper. The proposed analysis for a car model for different impact forces and speeds to estimate the critical speed and force amplitude for a car model at the time of crashing at the design stage. Such type of analysis prior to manufacturing can save time, labor, and money as well as provide the safest modes of performance. The present work also can be extended to have the results of all possible kinds of impact like rear impact, left side impact, right side impact, and bottom impact. Thus, one can compare the results and identify the most severe impact. Such analysis will be useful for car manufacturers to take care of the safety of vehicle and passenger effectively.

References

1. Thompson LL, Thompson LY, Soni PH, Raju S, Law EH (1998) The effects of chassis flexibility on roll stiffness of a winston cup race car. *SAE Trans* 2558–2570
2. Thompson LL, Raju S, Law EH (1998) Design of a winston cup chassis for torsional stiffness. *SAE Trans* 2571–2584
3. Szczotka M, Wojciech S (2008) Application of joint coordinates and homogeneous transformations to modeling of vehicle dynamics. *Nonlinear Dyn* 52:377–393
4. Leiva JP, Wang L, Recek S, Watson BC (2001) Automobile design using the GENESIS structural optimization program. In: *Nafems seminar: advances in optimization technologies for product design*, Chicago, Illinois, USA
5. Kuti I (2001) Dynamic analysis of vehicle manoeuvres on the basis of the finite element method. *Period Polytech Transp Eng* 29:47–58
6. Fischer MP, Kamla T, Wieser A, Waras H, Premstaller R (2001) Coupled multi-body and FE analysis to simulate engine induced chassis vibrations
7. Hadri AE, Cadiou J-C, Chikhi F (2003) Four-wheeled vehicle modelling toward on board dynamics observer. In: *Proceedings 2003 IEEE/RSJ international conference on intelligent robots and systems (IROS 2003)*(Cat. No. 03CH37453). pp 3534–3539
8. Johansson I, Gustavsson M (2000) FE-based Vehicle Analysis of Heavy Trucks Part I. In: *Proceedings of 2nd MSC worldwide automotive conference*, MSC
9. Sun J (2005) Optimization using sequential approach for triangular tube structure in crashworthiness
10. Goncalves JPC, Ambrosio JAC (2005) Road vehicle modeling requirements for optimization of ride and handling. *Multibody Syst Dyn* 13:3–23
11. Khorsandi F, Ayers PD, Fong EJ (2019) Evaluation of crush protection devices for agricultural all-terrain vehicles. *Biosyst Eng* 185:161–173
12. He R, Sandu C, Mousavi H, Shenvi MN, Braun K, Kruger R, Els PS (2020) Updated standards of the international society for terrain-vehicle systems. *J. Terramechanics* 91:185–231
13. Taghavifar H (2021) A novel energy harvesting approach for hybrid electromagnetic-based suspension system of off-road vehicles considering terrain deformability. *Mech Syst Signal Process* 146:106988

14. Safiuddeen T, Balaji P, Dinesh S, ShabeerHussain BM, Giridharan MR (2021) Comparative design and analysis of roll cage for automobiles. *Mater Today Proc* 39:183–200
15. Gautam GD, Singh KP, Prajapati A, Norkey G (2020) Design optimization of roll cage for formula one vehicle by using finite element analysis. *Mater Today Proc* 28:2068–2076

Noise and Vibration Analysis

Fault Investigation of Rolling Element Bearing Using Vibration Signature Analysis and Artificial Neural Network



Pavan Agrawal, Arvind Singh Tomar, and Pratesh Jayaswal

Abstract The bearing is the heart component of any revolving machine and is utilized in enormous applications like surgical machines to ship engines, etc. In the present research, an experimental exploration has done using vibration signature, continuous wavelet transform (CWT), and machine learning techniques, i.e., decision tree (DT) and artificial neural network (ANN) for defect investigation of bearing. Vibration signatures in the time domain have been captured from the healthy and defective bearings. Two real-valued wavelets were examined in this experimental investigation. The mother wavelet is chosen from two real-valued wavelets using the energy entropy ratio (EER) criterion, which selects the analytical uniqueness from the raw vibration signal's wavelet coefficient. These analytical characteristics are adopted as an input of decision tree and artificial neural networks for the categorization of faults. Eventually, the Morlet wavelet is decided and communicates more reliable outcomes with an artificial neural network algorithm.

Keywords Bearing defects · Energy entropy ratio · Wavelets · ANN · DT

1 Introduction

The vibration analysis is the non-destructive health monitoring technique used to detect the location and severity of the faults. To be precise, researchers such as Lu et al. [1] and Cui et al. [2] have employed time-domain signal processing for bearing health monitoring. Agrawal et al. [3] have reviewed the vibration signature analysis to find out the faults in rolling element bearings using the time and frequency domains. Hassan et al. [4] monitored the structural health of welded steel pipes using frequency response function and vibration-based fault detection techniques. Kankar et al. [5]

P. Agrawal (✉) · A. S. Tomar · P. Jayaswal
Department of Mechanical Engineering, Madhav Institute of Technology and Science,
Gwalior, India

A. S. Tomar
e-mail: arvind_tomar25@rediffmail.com

have detected the severity of defects in ball bearings utilizing time-domain statistical features such as log energy entropy, kurtosis, skewness, etc. Vibration analysis-based monitoring provides early information regarding the critical faults when compared with the healthy vibration signals [6–8]. The effectiveness of damping and stiffness of the bearing is investigated based on the natural frequency of the rotor-bearing system [9]. Naeini et al. [10] have utilized the ANN techniques for pattern recognition of the control chart via statistical process control technology. There are a variety of complex and real base wavelets like Morlet wavelet, Meyer wavelet, Daubechies wavelet, complex Morlet wavelet, etc. [11–13].

In the present manuscript, a methodology for early defect investigation and categorization of faults of REB has been suggested. The assortment of mother wavelets has been manifested by implementing the wavelet selection criterion. Initially, two real-valued mother wavelets were used. It has been identified from the consequences that the Morlet wavelet fitted with the selection criteria. Additionally, with the ANN classifier, the statistical parameters selected based on the Morlet wavelet furnish defects classification with augmented performance. The proposed methodology is shown in Fig. 1.

2 Experimental Setup (Vibration Data Collection)

An SKF experimental simulator is employed to extract vibration signatures for healthy and faulty bearings like outer race defect, inner race defect, defects on ball, and outer race surface roughness. The simulator consists of an induction motor (1 HP) that allows for variable speed up to 2000 rpm. An accelerometer has been mounted on the bearing housing. The self-aligned ball bearing model SKF 2207 EKTN9 has been used in the present experimental work. Vibration signals from healthy and faulty bearings have been taken using a handheld FFT analyzer. The fault is inserted on various elements of bearing using the electro-discharge machine (EDM). All tests have been conducted in SKF Reliability and Maintenance Center, MITS, Gwalior. The proposed methodology's soft computing and code generation have been done on MATLAB.

2.1 Feature Extraction

The vibration signatures in terms of acceleration are acquired from bearing housing using an accelerometer. The accelerometer converts the mechanical movements into analog signals and transferred them to the FFT analyzer. The captured signal is sampled and converted into a discrete signal in the FFT analyzer. The signals from healthy and defective bearings are acquired at a shaft speed of 820 rpm in the time domain. The sample signal of inner race fault bearing in the time domain is shown in Fig. 2.

Fig. 1 Proposed methodology flowchart using for bearing fault investigations

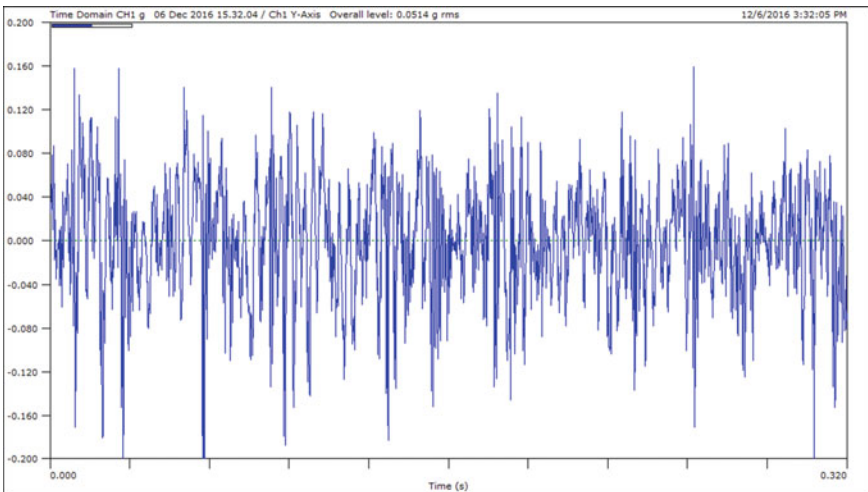
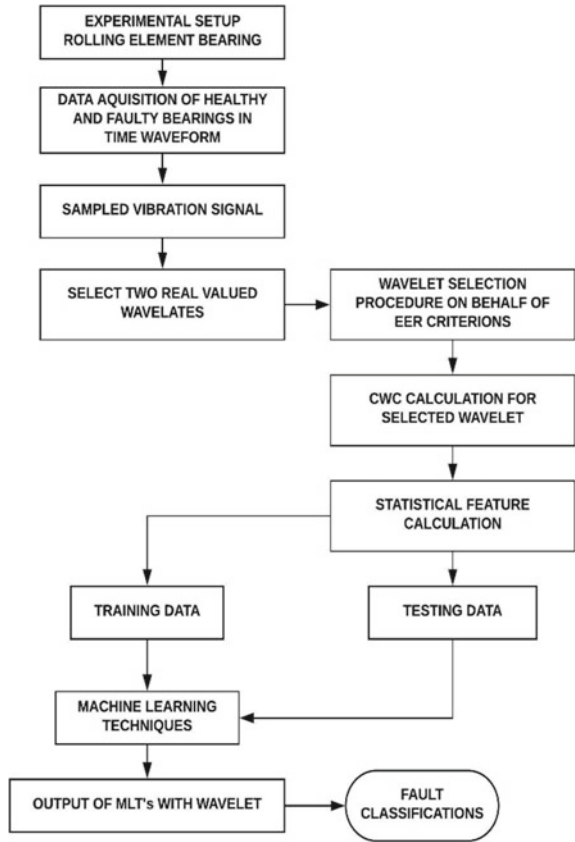


Fig. 2 The signature of inner race fault in the time domain

A total of 275 signals (55 of each bearing) of five bearings (one healthy and four faulty) are acquired from the experimental test rig.

3 Wavelet Transform

Wavelet investigation is the current method applied to examine the health condition of the bearing and determine the critical problems of industrial machines. The wavelet transform's principal roles are small waves placed at different times, enhancing the resolution of complex signals. To obtain preferred relevant data from raw vibration signatures, each of them is then converted into their generalized form of 2^7 sub-signals. Using two real wavelets such as Meyer and Morlet, the CWCs (continuous wavelet coefficients) are calculated for every signal for each bearing class. For a selection of appropriate mother wavelets, the maximum energy entropy ratio criterion has been selected.

3.1 Maximum Energy-to-Entropy Ratio Criterion (MEER)

The best-suited selection criteria of wavelets are to maximize the energy to the wavelet coefficients and minimize its Shannon entropy. Consequently, the combined tasks required to form a ratio of those measures called as energy to entropy ratio [14] are given by

$$\zeta(n) = \frac{E(n)}{S_{entropy}(n)} \quad (1)$$

where entropy of wavelet coefficient is given by

$$S_{entropy} = - \sum_{i=1}^m p_i \cdot \log_z p_i \quad (2)$$

where p_i is the energy probability distribution of wavelet coefficient and is given by

$$p_i = \frac{|C_{n,i}|^2}{E(n)} \quad (3)$$

where $C_{n,i}$ is the i th wavelet coefficient of the n th scale (Table 1).

The value of EER was observed as maximum for the Morlet wavelet. Hence, the Morlet wavelet is selected as a base wavelet for feature extraction for defect diagnosis of SABB. At 820 rpm, the high value of EER is seen for inner race fault at the 25th

Table 1 MEER criterion for real wavelets at 820 RPM

Wavelet type	Bearing condition	MEER	Signal no	Scale no
Meyer	Ball fault	0.2058	16	22
	Healthy bearing	0.0546	48	17
	Inner race fault	0.2675	25	25
	Outer race fault	0.2457	52	29
	Surface roughness	0.0250	37	17
Morlet	Ball fault	0.2506	16	23
	Healthy bearing	0.0641	48	17
	Inner race fault	0.2974	25	25
	Outer race fault	0.2759	17	25
	Surface roughness	0.0291	37	17

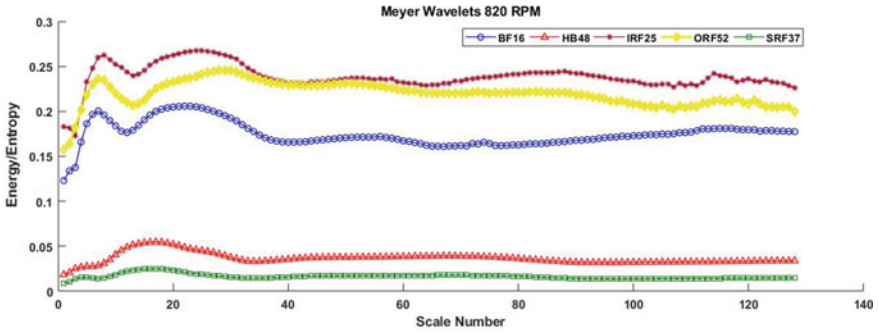
scale of the 25th signal using Meyer wavelet as shown in Fig. 3a. A high value of EER is seen for inner race fault at the 25th scale of the 25th signal using Morlet wavelet as shown in Fig. 3b. On behalf of the maximum energy entropy ratio criterion, the Morlet wavelet is selected as a mother wavelet. Estimated the statistical features like peak value, RMS, mean value, skewness, crest factor, standard deviation, variance, and kurtosis [8, 15–17] for Morlet wavelet at speed 820 rpm and then fed to machine learning techniques.

4 Machine Learning Techniques

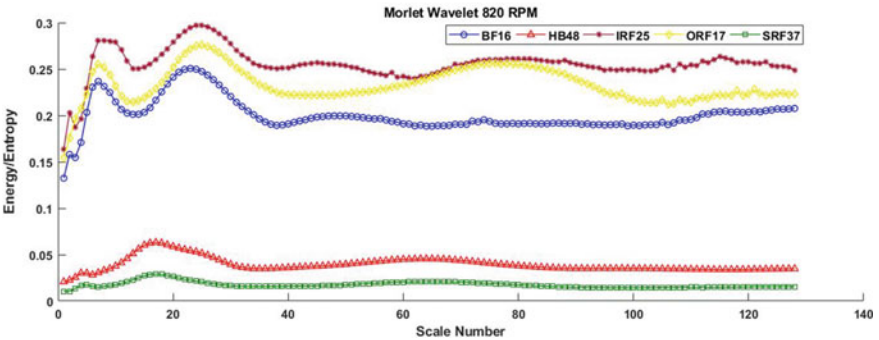
The machine learning is a method for generating an artificial model from vibration data and predicting bearing vibrations. Machine learning is divided into two types: supervised learning and unsupervised learning.

4.1 Artificial Neural Network (ANN)

The human brain has an exceptional capability to think, remember, and consistent excellence, which becomes prompted various researchers to improve artificial models whose necessary learning process is comparable to such natural neurons. Rao et al. [13] have reviewed the ANN’s structure and its history. It has further applied concerning defects and the life prediction of bearing. Samanta et al. [18] have studied the defect identification of bearings experimentally utilizing the ANN classification algorithm. The statistical features of time-domain vibration data have been applied directly as input data to the ANN. The construction of ANN is as shown in Fig. 4.



(a) A plot between MEER and scale No. for Meyer wavelet at 820 rpm



(b) A plot between MEER and scale No. for Morlet wavelet at 820 rpm

Fig. 3 The plot between MEER and scale number at 820 rpm for **a** Meyer **b** Morlet wavelet

Fig. 4 Structure of ANN [19]

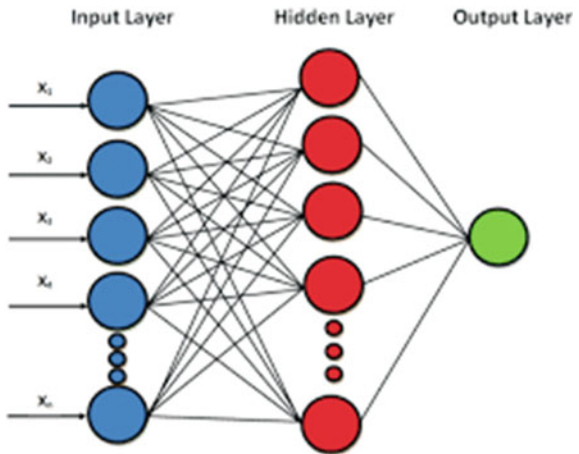
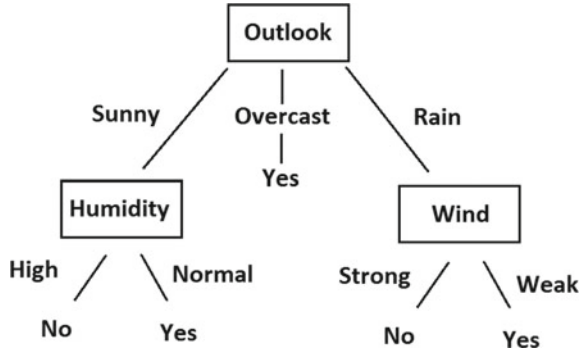


Fig. 5 Example of a decision tree [20]



4.2 Decision Tree (DT)

The decision tree (DT) is a supervised machine learning method which is based on regression theory. The decision tree is also known as a regression tree or classification tree. The classification tree is a binary tree and accompanies the tree’s decisions from the root (beginning) node down to a leaf node (contains the response) to predict these responses. Classification tree gives a True and False response given in Fig. 5 [20, 21].

In Fig. 5, the sample used pair predictors, sunny, and rain, and start at the top node (outlook). The decision tree shows the decision about playing tennis or not according to weather conditions. The tree’s leftmost branch has represented the negative instances (humidity-high and wind-robust), while the right side branches show the positive instances (humidity-normal and wind-weak). On behalf of the above positive instances, the decision tree predicts that tennis may have been played.

5 Results and Discussion

Totally 50 instances for an individual bearing (healthy and defective bearings), Morlet wavelet, and 9 features including speed are used for testing and training objectives. The testing and training purposes, two classifiers ANN and DT have been carried out in the existing examination. These classifiers are shown in Tables 2 and 3 for Morlet wavelet in the sort of confusion matrices. The confusion matrices are formed with the number of experiment samples precisely classified and wrongly classified. The actual class made the rows, and prognosticated class made the columns of confusion matrices (Fig. 6).

In machine learning techniques, the confusion matrix is used to represent the classifier of statistical features. The confusion matrix is a precise table arrangement that authorizes a visualization of a classification algorithm’s performance. Each column of the confusion matrix shows the predicted class instances, and each row of the

Table 2 Result of ANN for Morlet wavelet utilizing EER criterion (confusion matrix)

Using test set						Using tenfold cross validation					
BF	IRF	ORF	SRF	HB	Classified as	BF	IRF	ORF	SRF	HB	Classified as
9	0	1	0	0	BF	10	0	0	0	0	BF
0	9	1	0	0	IRF	0	8	2	0	0	IRF
0	0	10	0	0	ORF	2	0	8	0	0	ORF
0	0	0	10	0	SRF	0	0	0	10	0	SRF
0	0	0	0	10	HB	0	0	0	4	6	HB

Table 3 The result of DT for Morlet wavelet utilizing EER criterion (confusion matrix)

Using test set						Using 10-fold cross validation					
BF	IRF	ORF	SRF	HB	Classified as	BF	IRF	ORF	SRF	HB	Classified as
10	0	0	0	0	BF	3	1	5	0	1	BF
0	9	0	1	0	IRF	0	7	1	2	0	IRF
0	0	10	0	0	ORF	5	0	5	0	0	ORF
0	0	0	9	1	SRF	0	2	0	7	1	SRF
0	0	0	0	10	HB	1	2	1	0	6	HB

matrix represents the real class. It is also known as the error matrix. In the present research, the work above matrix is used to classify healthy and different faulty bearings. Figure 7 shows the confusion matrix diagram of a decision tree for the Morlet wavelet without and with 10-fold cross validation. The layout is a plot between actual and predicted classes. In Fig. 7a for ball fault, outer race fault, and health bearings, instances are classified in 100% corrected while inner race fault and surface roughness faults are classified in 90% corrected. In a total of 50 cases, 48 cases are found correct and 2 incorrect. It shows the accuracy of the classifier i.e., 96%.

Figure 7b, confusion matrix with 10-fold cross validation, represents that ball fault, inner race fault, and outer race fault bearings are classified as 30, 70, and 50% corrected. In comparison, surface roughness fault and healthy bearing have been organized in 70 and 60% correct. In a total of 50 instances, 28 instances are found right and 22 incorrect. It shows the accuracy of the classifier, i.e., 56%.

A scatter plot diagram is the representation of correct and incorrect instances on screen for classification purposes. Figure 8 has been drawn on MATLAB using machine learning statics. In the present work, statistical features like kurtosis and standard deviation of 50 instances for five different bearings (each 10) are entered in the decision tree. After processing software, results are shown in terms of correct (dot) and incorrect (cross) instances. Similarly, Figure 9 displays the scatter plot for 10-fold cross validation.

Table 4 shows the classification accuracies of the same classifiers for the EER criterion. Using the test set correctly classified instances for ANN and DT, are 96% and 96%, respectively. Using a 10-fold cross-validation set correctly classified instances

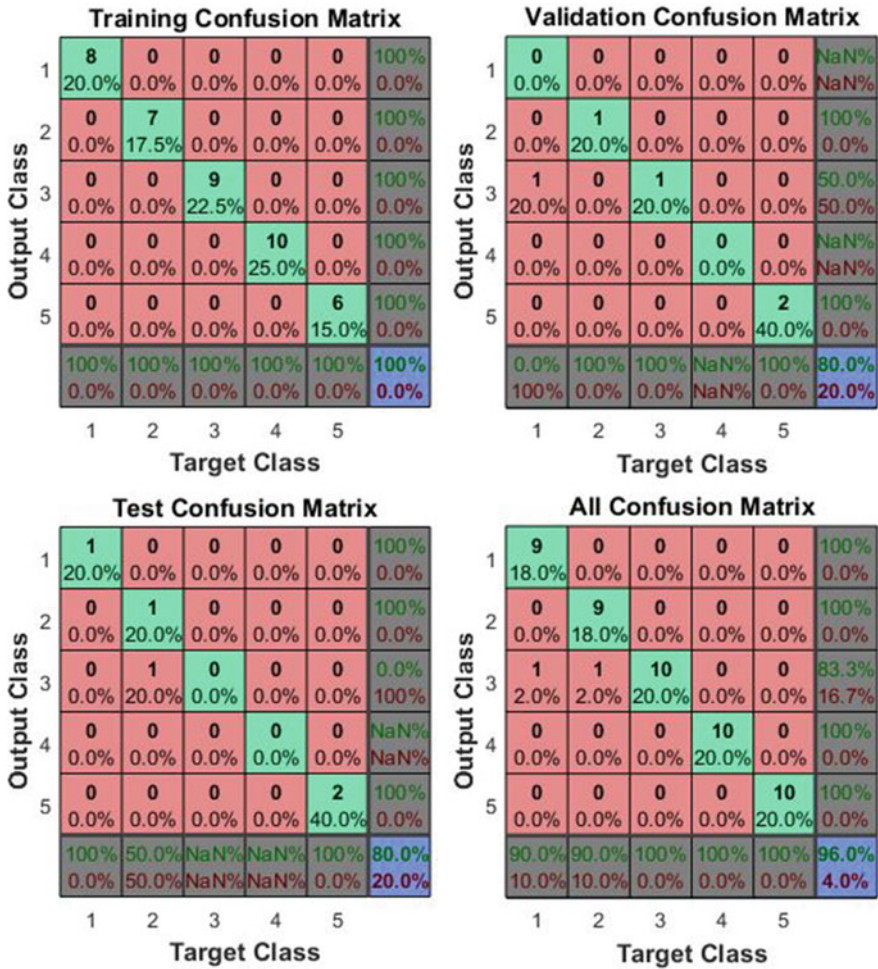


Fig. 6 All confusion matrix diagram of ANN without and with validation (for EER)

for ANN and DT, are 80% and 28%, respectively. The classification performance of the ANN classifier has come out best than DT classifiers with the use of Morlet wavelet.

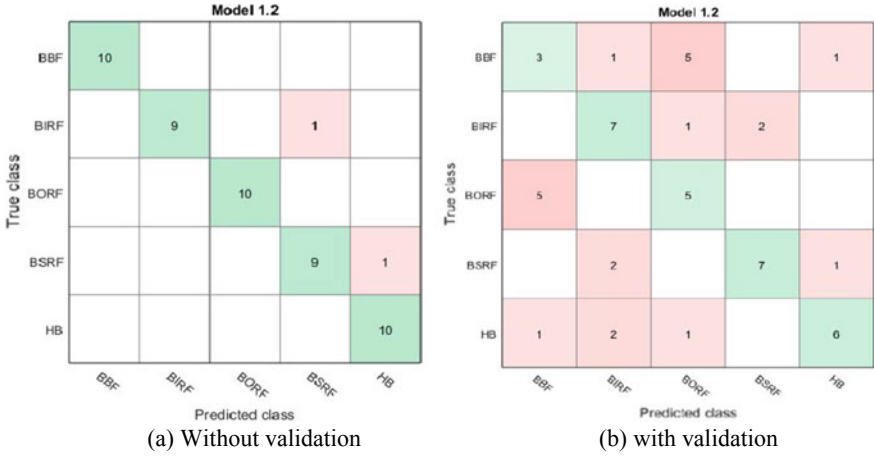


Fig. 7 Confusion matrix diagram of DT without and with validation (for EER)

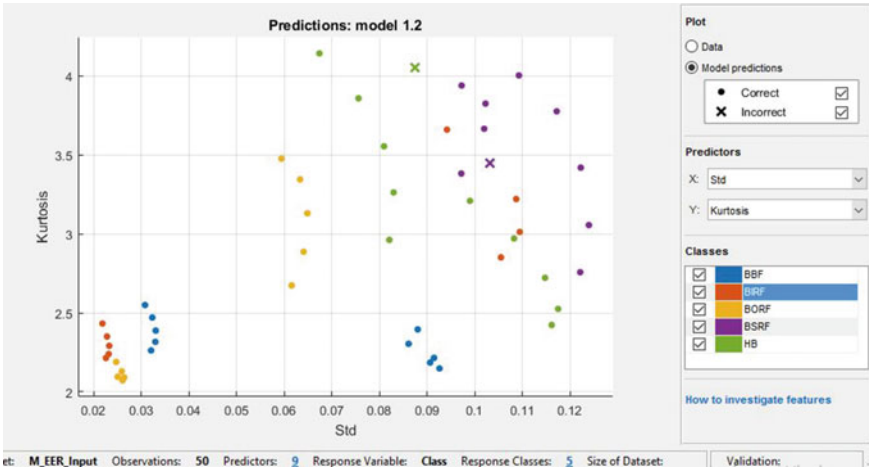


Fig. 8 Scatter plot diagram of DT for all bearings without validation

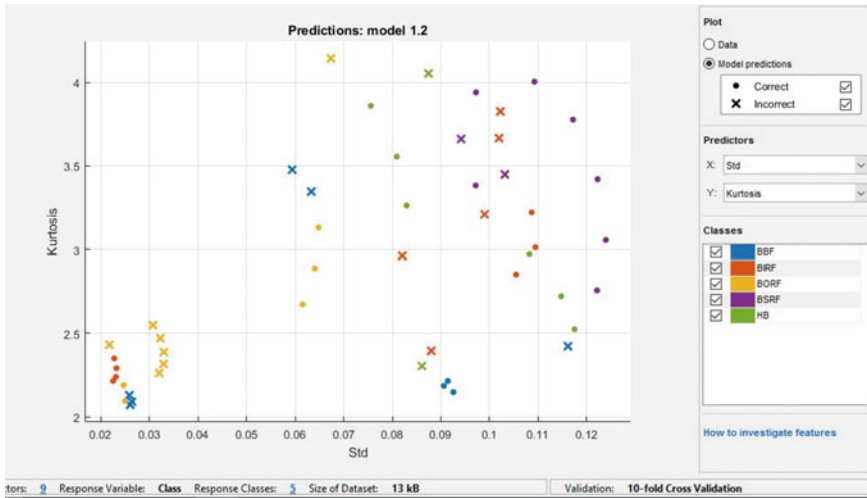


Fig. 9 Scatter plot diagram of DT for all bearings with 10-fold cross validation

Table 4 Assessment of the success of prediction using Morlet wavelet (EER criterion)

Parameters	ANN		Decision tree (DT)	
	Test set	10-fold cross validations	Test set	10-fold cross validations
Instances classified correctly	48 (96%)	40 (80%)	48 (96%)	28 (56%)
Instances classified incorrectly	02 (4%)	10 (20%)	02 (4%)	22 (44%)
Total number of instances	50 (100%)	50 (100%)	50 (100%)	50 (100%)

6 Conclusion

The methodology of bearing defect investigation concerns the energy entropy ratio criterion for the selection of the mother wavelet. Bearing defects based on defect location and generalized roughness has been considered for research. Wavelet-based eight statistical characteristics are estimated from vibration data utilizing the Morlet wavelet as an optimally chosen base wavelet between two wavelets. Two Machine Learning Techniques (MLTs), viz., ANN and DT have been used for bearing faults analysis. The defect classification efficiency of these MLTs for the energy entropy ratio criterion is represented in Table 4. Comparable research exhibited that ANN offers a more reliable classification execution than DT. The classification efficiency of ANN has been evaluated by 80%, which is higher than DT (56%) due to its extra unique generalization inclinations.

References

1. Lu S, Guo J, He Q, Liu F, Liu Y, Zhao J (2016) A novel contactless angular resampling method for motor bearing fault diagnosis under variable speed. *IEEE Trans Instrum Meas* 65(11):2538–2550
2. Cui L, Zhang Y, Zhang F, Zhang J, Lee S (2016) Vibration response mechanism of faulty outer race rolling element bearings for quantitative analysis. *J Sound Vib* 364:67–76
3. Agrawal P, Jayaswal P (2020) A review of fault detection, diagnosis, and prognosis of rolling element bearing using advanced approaches and vibration signature analysis
4. Hassan AA, El-Wazery MS, Zoalfakar SH (2015) Health monitoring of welded steel pipes by vibration analysis. *Int J Eng Trans A Basics* 28(10):1782–1789
5. Kankar PK, Sharma SC, Harsha SP (2011) Fault diagnosis of ball bearings using continuous wavelet transform. *Appl Soft Comput J* 11(2):2300–2312
6. Lee J, Wu F, Zhao W, Ghaffari M, Liao L, Siegel D (2014) Prognostics and health management design for rotary machinery systems—reviews, methodology, and applications. *Mech Syst Signal Process* 42(1–2):314–334
7. Sharma V, Parey A (2017) Case study on the effectiveness of gear fault diagnosis technique for gear tooth defects under fluctuating speed. *IET Renew Power Gener* 11(14):1841–1849
8. Jayaswal P, Wadhvani AK (2015) Application of artificial neural networks, fuzzy logic, and wavelet transform in fault diagnosis via vibration signal analysis: a review. *Aust J Mech Eng ISSN* 7(2):157–171
9. Eftekhari M (2017) The effect of damping and stiffness of bearing on the natural frequencies of rotorbearing system. *Int J Eng* 30(3):448–455
10. Naeini MK, Bayati N (2017) Pattern recognition in control chart using neural network based on a new statistical feature. *Int J Eng* 30(9):1372–1380
11. Agrawal P, Jayaswal P (2019) Diagnosis and classifications of bearing faults using artificial neural network and support vector machine. *J Inst Eng Ser C*
12. Yan R (2007) Base wavelet selection criteria for non-stationary vibration analysis in bearing health diagnosis
13. Rao BKN, Pai SP, Nagabhushana TN (2012) Failure diagnosis and prognosis of rolling – element bearings using artificial neural networks: a critical overview. In: 25th International congress on condition monitoring and diagnostic engineering, vol 364, pp 1–29
14. Rodrigues AP, Mello GD, SPP (2016) Selection of mother wavelet for wavelet analysis of vibration signals in machining. *J Mech Eng Autom* 6(5A):81–85
15. Pratyusha LP, Priya SV, Naidu VPS (2014) Bearing health condition monitoring, time domain analysis. *Int J Adv Res Electr Electron Instrum Eng* 3:75–82
16. Bafroui HH, Ohadi A (2014) Application of wavelet energy and Shannon entropy for feature extraction in gearbox fault detection under varying speed conditions. *Neurocomput Elsevier* 133:437–445
17. Bhavaraju KM, Kankar PK, Sharma SC, Harsha SP (2010) A Comparative study on bearings faults classification by artificial neural networks and self-organizing maps using wavelets. *Int J Eng Sci Technol* 2(5):1001–1008
18. Samanta B, Al-Balushi KR (2003) Artificial neural network-based fault diagnostics of rolling element bearings using time-domain features. *Mech Syst Signal Process* 17(2):317–328
19. Khademi F, Jamal SM (2016) Predicting the 28 days compressive strength of concrete using artificial neural network, *i-manager's*. *J Civ Eng* 6(2):1–6
20. Mitchell TM (1997) Machine learning. McGraw-Hill Science/Engineering/Math
21. Agrawal P, Jayaswal P (2019) Selection of best classification algorithm for fault diagnosis of bearing using vibration signature analysis. *Int J Innov Technol Explor Eng* 8(5):538–546

Enhancement of Aerodynamic Efficiency of a Formula Car by Incorporating a Passive Device in the Front Wing



K. Balaji, G. Jims John Wessley, S. V. Khandal, and Mayuri Gore

Abstract The formula cars are designed and developed based on aerodynamic shapes to meet out the high speed demand and efficiency. In connection to this, the current work introduces the concept of using a passive flap over a high lift passive device in front of the wing of a car aiming at improving the down force and stability. Models were designed using ANSYS software with different angle conditions of detached passive flap and without the passive flap and analysis carried out with ANSYS CFX at different velocities. This work also compares the results of down force generated in a typical formula one car without high lift device and with high lift device in the front wing. The down force generated was found to be about 8.67, 8.70, 8.73, and 8.76% in formula car with high lift passive device attached to the front wing at 250 kmph, 275 kmph, 300 kmph, and 350 kmph, respectively, when angle of attack (AOA) was varied from 16 to 20° for the same L/D ratio. It is observed that the flap system is used to increase the down force and increase the drag which leads to improved stability of the vehicle at high speeds and turning the car is made without reducing the speed.

Keywords Down force · Stability enhancement · Formula car · Front wing · Passive device

K. Balaji · G. J. J. Wessley (✉)
Department of Aerospace Engineering, Karunya Institute of Technology and Sciences,
Coimbatore, Tamil Nadu, India
e-mail: jims_john@karunya.edu

K. Balaji · S. V. Khandal · M. Gore
Department of Aeronautical Engineering, Sanjay Ghodawat University, Kolhapur, Maharashtra,
India
e-mail: khandal.sv@sanjayghodawatuniversity.ac.in

1 Introduction

Modern formula one (F1) cars have a single seat, open wheel, and open cockpit with substantial front and rear wings with the engine placed behind the driver. These cars have to be developed by the manufacturers considering aerodynamics according to the rules and regulations specified for the race and are unique to the championship. A lot of time as well as money are invested in designing the shape of these cars aerodynamically which plays a vital role in the success of the design. The principal forces acting on a F1 car are lift, drag, down force, and thrust. The prime objective of the designer is to create a down force and to minimize the drag. While the down force helps to stabilize the car tires onto the track and improve cornering forces the drag force slows down the speed of the car. F1 cars have aerodynamic features in-built in the rear spoiler, front wing, and bottom plate. Any defect in these components will disturb the balance of the car on the track. Also, positioning the engine, gearbox, and driver plays an equally important role in the successful design of these cars. Bernoulli's principle that is used widely to determine the lift force on an aerofoil in aircraft is applied in these cases as the cars use an inverted aerofoil. Applying Bernoulli's principle to the cars, the pressure is maintained greater on the upper side of the aerofoil than the lower side which results in a net down force. Thus, the down force which is a force opposite to the lift force is always more than lift. Primarily, the design community works on perfecting the down force properties of a car rather than addressing its drag.

Attempts have been made by various researchers to improve the aerodynamic performance of F1 car using different add-on devices and alternate configurations through steady-state CFD simulations. These studies show that there is a considerable reduction in both drag and lift forces due to streamlining the airflow across the car. The most appropriate configuration for improved aerodynamic performance in F1 car is suggested by Devaiah and Umesh [1]. Another study [2] showed that the aerofoils showed stall between 10° and 30° angle of attack (AOA) and as the AOA increased, the lift increased initially and the wing-tip (free) vortex strength increases proportionally. At some point of the flow across the suction side of the wing, the flow separated and the wing will stall. In a study by Jeffrey and Zhang [3], the aerodynamics of a single element wing fitted with Gurney flaps at trailing-edge region shows that a twin vortex structure developed downstream of the Gurney flap. The spectral analysis of the Laser Doppler Anemometry (LDA) data shows that the wake consists of a von Karman vortex street of alternately shed vortices and the same was confirmed by smoke visualization. The vortex shedding enhanced the trailing-edge suction while upstream face of the device showed reverse trend. Circulation is the result of pressure difference acting across the trailing edge because of these two changes. In a similar study, it is seen that the front and rear wings have more effect on aerodynamic performance of a racing car. The computational study on front wing of a FSAE race car was used to determine the ratio of lift to drag coefficients. NACA 23,012 aerofoil profiles were analyzed using ANSYS 14.0 by which ground clearance and effect of AOA on wing performance were studied. The results revealed

that 50 mm above the ground with an AOA of 4 degrees the drag coefficient was 0.008 and lift coefficient was 0.130 which provides best operational settings [4]. A study by Mortel [5] aimed to use a front wing to generate a load of around 600 kg at 330 kmph and simultaneously deflect the air from the wing tip to the inside of the front wheels so as to reduce the flow interaction between wheels and front wing. The study also discusses the importance of vertical endplates near to the front wing which is responsible for the flow deflection from wheels. A study by Seljak [6] is done to research the reason of using inverted aerofoil for front wing in the F1 cars and it is seen that generation of a down force by incorporating front wing provides greater control and stability to the cars by making use of the negative lift the wing experiences due to the minimal effect of ground proximity. At a given AOA, this led to higher drag with reduced lift. Near-ground fly-trailing vortices are partially blocked by ground due to which the downwash generated by the wing reduces. Downwash decrease led to increase in AOA of wing thereby resulting in more lift and less drag.

Analysis of low Reynolds number flow past single element in a wing fitted with Gurney flap at trailing-edge region was carried out by Horia and Ion [7]. The complex flow separation phenomena on aerofoils were observed with unstalled incidences and it is seen that Gurney flaps increased the overall loading enabling maximum suction. The Gurney flap with attached flow increases the circulation around aerofoil by which lift increases as compared to the normal aerofoil. Generally pressure is more at windward side of the flap as compared to leeward side and this lower pressure tendency on upper surface of trailing edge makes the flow to follow the flap and turn downward and the entire circulation over the aerofoil was enhanced. With a given AOA, the bubble stretch at leading edge showed maximum lift and further increase in AOA initiated flow separation leading to stall. Also, as the size of flap increased, the forward moving bubble led to the reduced occurrence of stall. Joseph [8] performed study on the aerodynamics of race cars observing the air motion on moving vehicle and its components. The vehicle stability control depends on down force distribution between front and rear wheels. The aerodynamic down force generated with higher drag enabled the ability to corner faster in a controlled manner with increase in speed. The paper also explains that the inverse aerofoil in the front wing adds a greater downward force about 30%. Another study by Brown and Filippone [9] on the aerodynamic shape of a formula car with Gurney flap focuses on the optimization of the height of Gurney at very low-speed region to find an analytical expression among optimal height, aerofoil's chord, and free stream velocity. The experimental results showed that a height less than the thickness of the boundary layer at the trailing edge have negligible drag. Therefore, flaps can be attached to low Reynolds number systems like gliders, micro-air vehicles, wind turbines, etc.

Design and testing of a model formula car has been carried out experimentally and using CFD by Desai and Channiwala [10]. The model is made up of thermocol with multi-holes for connecting it to the manifolds. The model is kept stationary within the test section of the subsonic wind tunnel and is tested at various subsonic speeds. The drag coefficient (CD) found for exterior profile was 0.4, which is acceptable for fuel savings. Suresh and Sitaram [11] studied the energy efficiency of a centrifugal fan and found that the efficiency was low at low Reynolds number as compared to

high Reynolds number with Gurney flap. This affects the operating range due to higher static pressure on shroud and diffuser hub of centrifugal fan and is observed to be good in elimination of laminar separation bubble at low Reynolds numbers of LP turbine blade besides reduction in loss coefficients. Syazrul [12] observed that in the front wing of a formula one car, the generation of down force is to be maximized to keep the car on the track without tire slip. This also improves the cornering force of the formula one car.

In the work of Stephen [13], six turbulence models were developed to quantify surface pressure, sectional forces, and wake flow field that showed better results compared to the earlier results. This work highlighted that flaps are the main element contributing to down force while also contributing to drag. The works of William and Michael [14] show that the front portion of a car plays a vital role in downstream flow field behavior, while the Reynolds number is insignificant causing only 3–4% variation in lift and drag. It is seen that a change in flap deflection by 10° increased CL by 0.5 with no effect on drag coefficient at a constant lift coefficient. Also, the endplate design plays a vital role on the performance of a race-car front wing. An increase in endplate area led to increase in lift coefficient without much reduction in drag coefficient. Zhang and Zerihan [15] showed that a maximum down force was achieved by increase in the lower surface suction and loss in down force was caused by upper surface pressure and lower surface suction losses, with a reduction in height. For a high flap angle, it is observed that there is a sharp reduction in boundary layer separation and circulation loss in the main element.

The formula car generates lift instead of generating down force when it is designed with poor aerodynamics and makes the formula car unstable besides losing its control. Also it has a negative effect on its speed at the corners of the track. The front wing of formula car is a highly critical component that plays a vital role in controlling the airflow around the rest of the formula car. The front wing alone accounts to about 30% of the total down force. The balance of the formula car is based on the load acting on the front wing and the airflow around it. Scarce literature is available on the design of passive device for front wing that generates more down force. Therefore, an attempt is made to increase the down force by choosing effective aerofoils in the elements of front wing and for high lift passive devices. The models were designed using ANSYS software with different angle conditions of detached passive flap and without the passive flap and the analyses were carried out with ANSYS CFX at different velocities.

2 Modeling and Analysis of Formula Car

The methodology followed in this work is as follows:

- Identification of aerofoil (NACA 632–215, NACA 9414) and passive device for front wing.

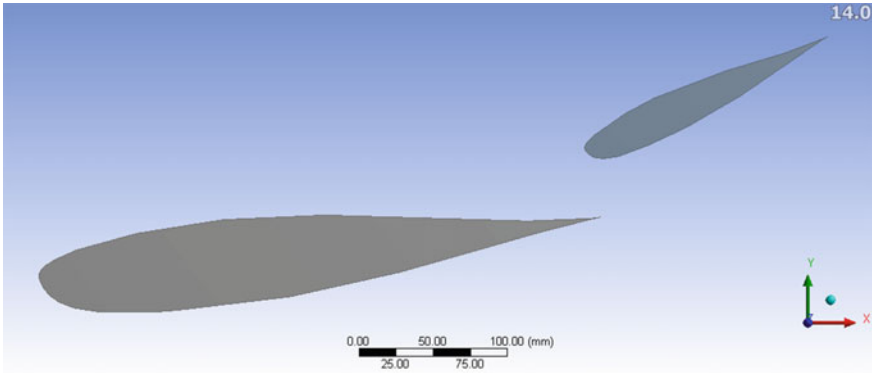


Fig. 1 Model without flap

- Modeling of main and secondary elements of front wing with detached passive flap at different AOA (Angle = 16° , 18° , 20°) using ANSYS software.
- Analysis of the modeled components using ANSYS CFX over a moving ground surface.
- Result comparison of the models at various subsonic velocities for better down force at same L/D ratio.

A schematic representation of the aerofoil used in the study is shown in Fig. 1.

Figure 1 represents the model without detached passive flap, with main element wing fixed at 6° and secondary element wing fixed at 25° . Figure 2 shows the model with detached passive flap, with main element wing fixed at 6° , secondary element wing fixed at 25° , and Gurney flap fixed at 16° . Figure 3 shows the model with detached passive flap, with main element wing fixed at 6° secondary element wing fixed at 25° and Gurney flap fixed at 18° . Figure 4 shows model with detached passive

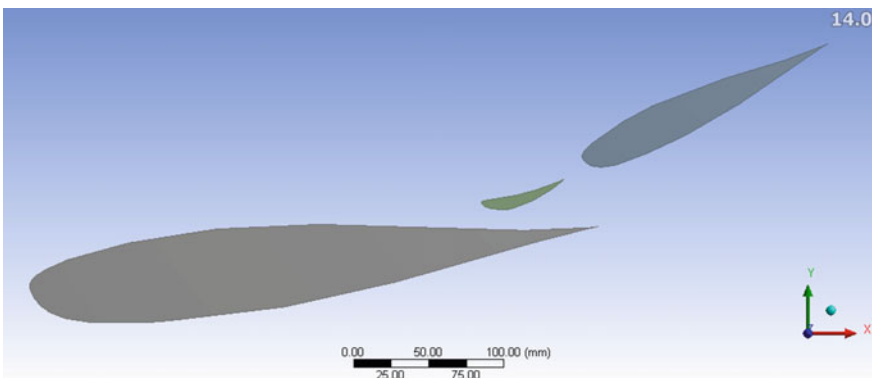


Fig. 2 Model with flap at 16°

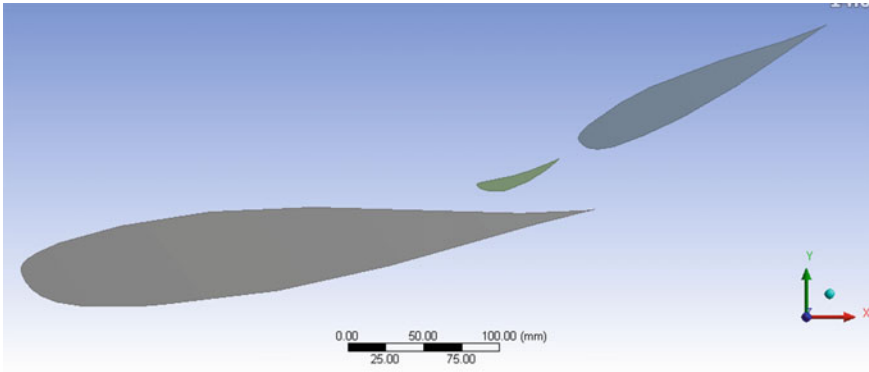


Fig. 3 Model with flap at 18°

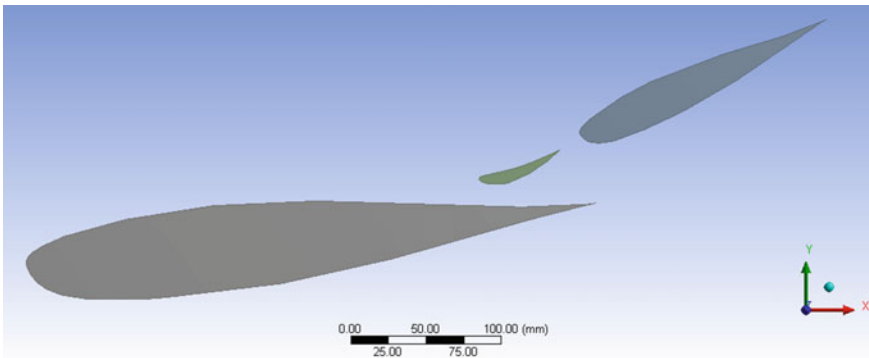


Fig. 4 Model with flap at 20°

flap, with main element wing fixed at 6°, secondary element wing fixed at 25°, and Gurney flap fixed at 20° (Table 1).

3 Results and Discussion

From the analysis, it is seen that the down force increases with the detached passive flap compared to the front wing without the Gurney flap. The converged result of the analysis is shown in Fig. 5.

Table 1 Specifications of passive device

Sr. no	Details	Dimensions	Units
1	Aerofoil	NACA 632–215	–
2	Detached passive flap	NACA 9414	–
3	First element angle	6	Degree
4	Second element angle	25	Degree
5	First element length	380	mm
6	Second element length	180	mm
7	Detached passive flap chord	57	mm
8	Horizontal distance between the two elements	367	mm
9	Vertical distance between the two elements	85	mm

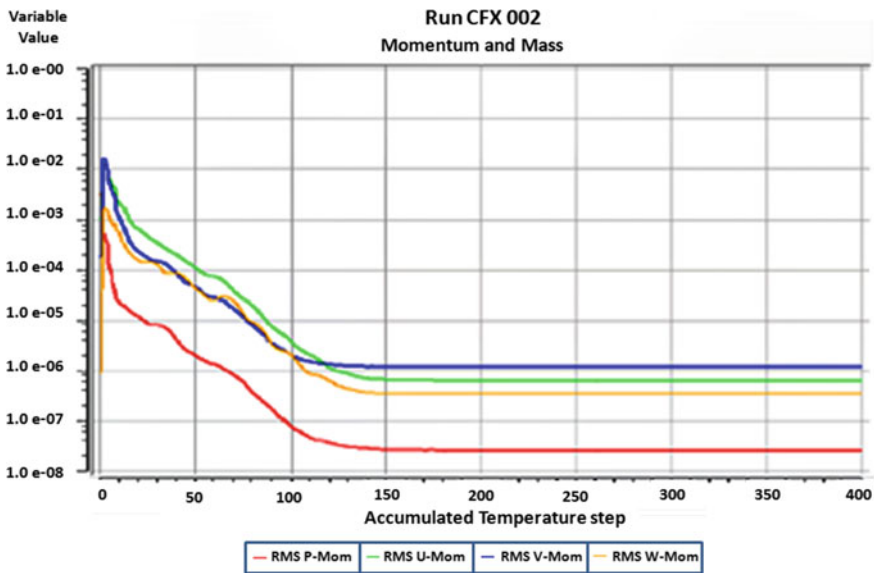


Fig. 5 Converged result of the analysis

3.1 Case 1: Analysis at 250 Km/h

Four different models with varying detached flap conditions (1, 2, 3, and 4) are analyzed at a velocity of 250 km/h. The results of the four models are compared for the down force generated and it is depicted in Fig. 6.

There is a gradual increase in the down force at different AOA with the flap system. A maximum of about 12.67% increase is seen using the detached passive flap as compared to the existing model. On the contrary, the drag force is found to increase. The increase in down force and drag is provided in Table 2.

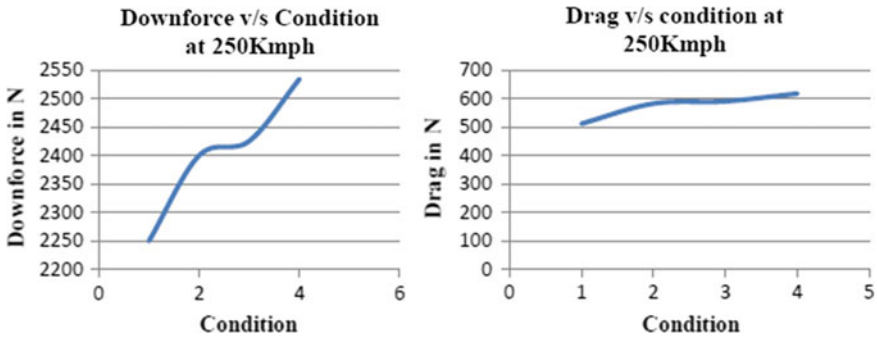


Fig. 6 Down force and drag comparisons at 250 kmph

Table 2 Results for speed 250 kmph

Condition	Position of flap	Downward force (N)	Drag (N)
1	No flap	-2249.16	511.816
2	Flap at 16°	-2399.73	582.594
3	Flap at 18°	-2425.52	590.64
4	Flap at 20°	-2534.53	617.67

3.2 Case 2: Analysis at 275 Kmph

The models with varying detached flap conditions are analyzed at a velocity of 275 kmph and the down force and drag generated are provided in Fig. 7.

It is seen that the down force gradually increased with increasing angle of attack. Improvement of about 12.70% was observed with detached passive flap as compared to existing model at 20°. The drag force is also found to increase. The increase in down force and drag is provided which is shown in Table 3.

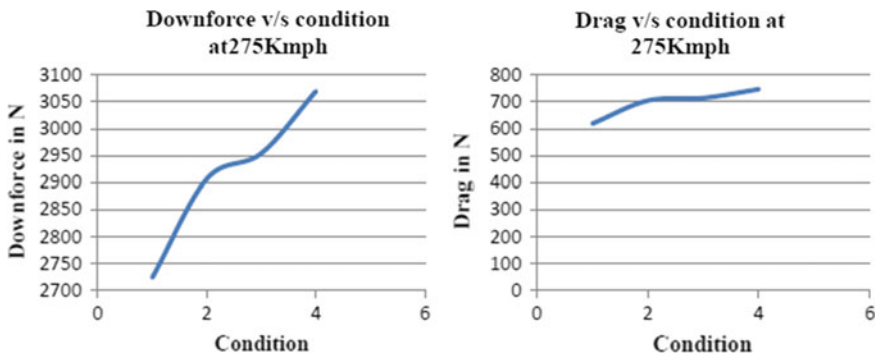


Fig. 7 Down force and drag comparisons at 275 kmph

Table 3 Results for speed 275 kmph

Condition	Position of flap	Downward force (N)	Drag (N)
1	No flap	-2723.7	619.057
2	Flap at 16°	-2906.85	704.781
3	Flap at 18°	-2954.26	714.334
4	Flap at 20°	-3069.73	747.132

3.3 Case 3: Analysis at 300 kmph

Figure 8 shows the four different models with varying detached flap conditions analyzed at a velocity of 300 kmph.

The analysis shows that a down force increases gradually with increasing angle of attack. A maximum of about 12.73% improvement is obtained with detached passive flap as compared to the existing model at 20°. The increase in down force and drag is shown in Table 4.

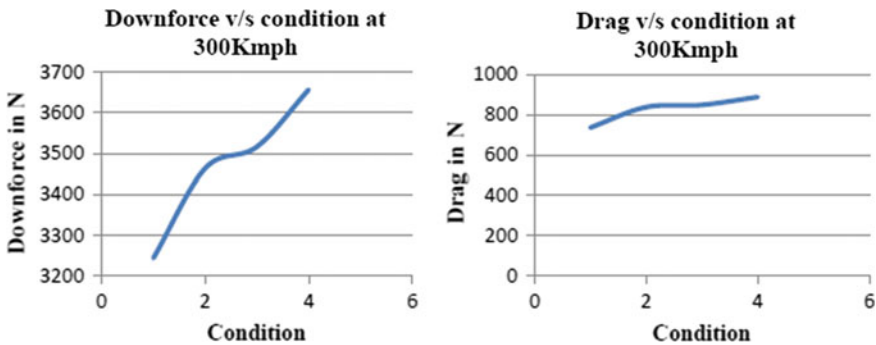


Fig. 8 Down force and drag comparisons at 300 kmph

Table 4 Results for speed 300 kmph

Condition	Position of flap	Downward force (N)	Drag (N)
1	No flap	-3243.32	736.48
2	Flap at 16°	-3462.79	838.582
3	Flap at 18°	-3516.03	849.763
4	Flap at 20°	-3656.47	888.941

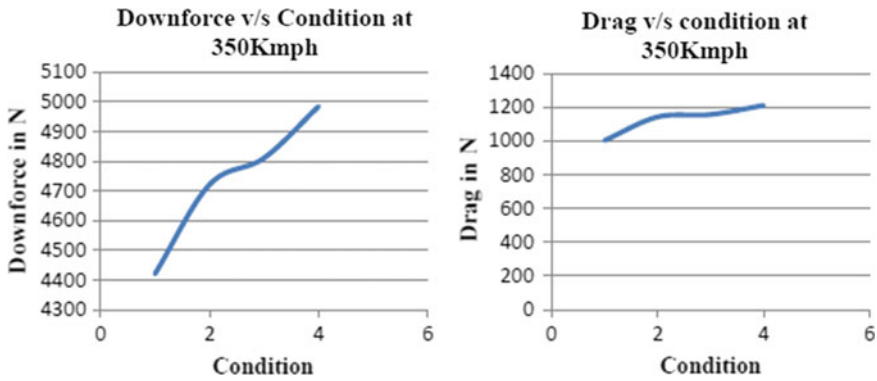


Fig. 9 Down force and drag comparisons at 350 kmph

Table 5 Results for speed 350 kmph

Condition	Position of flap	Downward force (N)	Drag (N)
1	No flap	-4420.94	1001.87
2	Flap at 16°	-4721.28	1141
3	Flap at 18°	-4811.15	1155.82
4	Flap at 20°	-4984.7	1209.42

3.4 Case 4: Analysis at 350 kmph

The four different models with varying detached flap conditions are analyzed at a velocity of 350 kmph. The down force and drag results are shown in Fig. 9.

Down force gradually increases with increasing angle of attack. Maximum increase of downward force of 12.76% was observed with detached passive flap compared to existing model at 20°. The increase in down force and drag is provided in Table 5.

3.5 Down Force Generated at Various Velocities

Down force variation at various velocities and at different AOA is illustrated in Fig. 10. Nearly about 12% down force increase is observed at same L/D ratio.

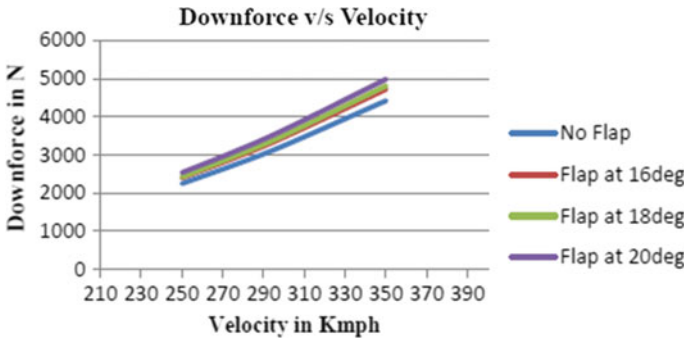


Fig. 10 Down force with different conditions

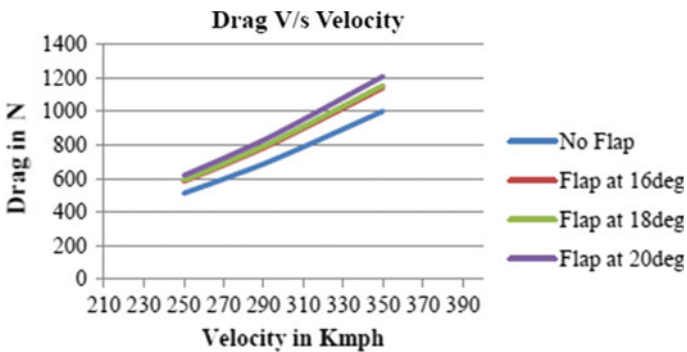


Fig. 11 Drag force with different conditions

3.6 Drag Force at Various Velocities

Figure 11 shows the drag variation with different velocities and various AOA for a fixed L/D ratio. This increase is due to increase in down force.

4 Conclusions

In the present work, four different models of flap in a formula car have been designed and analyzed at varying conditions of the detached passive flap using ANSYS and CFX for different velocity conditions. Based on the analysis, the following results are concluded:

- The down force generated was about 8.67, 8.70, 8.73, and 8.76% with detached passive flap at 250 kmph, 275 kmph, 300 kmph, and 350 kmph, respectively, and when AOA was varied from 16 to 20° at constant L/D ratio.

- The down force is increased by 21% at 16° compared to the existing model for all velocity conditions.
- The down force is increased by 19% at 18° compared to 16° for all velocity conditions.
- The down force is increased by 36% at 20° compared to 18° model for all velocity conditions.
- The drag value also increases constantly at all speeds and maximum drag of 20% at an angle of 20° compared to existing model. Further, the drag increases with increase in velocity.

It is concluded that high down force can be generated by flaps and enables the formula car to have a stable turn at the corners of the track at high speeds with high stability.

References

1. Devaiah BN, Umes S Enhancement of aerodynamic performance of a formula-1 race car using add-on devices, automotive and aeronautical engineering department. Bangalore–58
2. Walter DJ (2007) Study of aerofoils at high angle of attack in ground effect, school of aerospace, mechanical & manufacturing engineering. Portfolio of science, engineering & technology, Rmit University
3. Jeffrey D, Zhang X (2000) Aerodynamics of gurney flaps on a single-element high-lift wing, vol 37, 2nd edn. University of Southampton, Southampton, England S0171BJ, United Kingdom
4. Walker P Efficiency of a front wing on a FSAE car. School Of Mechanical Engineering
5. Mortel F (2003) Cranfield team F1: the front wing. Cranfield University, School Of Engineering Cranfield College Of Aeronautics
6. Seljak G (2008) Race Car Aerodynamics
7. Dumitrescu H, Malael I Analysis of low reynolds number flow past gurney flap. POLITEHNICA, University Bucharest, Faculty of Aerospace Engineering Str, Gheorghe Polizu, sector 1, 011061, Bucharest, Romania
8. Katz J (2008) Aerodynamics of race cars. Department of Aerospace Engineering, San Diego State University, San Diego, California, Annu. Fluid Mech, 2006.38:27–63, University Of South Australia
9. Brown L, Filippone A Aerofoil at low speeds with gurney flaps. Department of Mechanical Aerospace, Manufacturing Engineering, UMIST Manchester, UK, page no 539–546
10. Desai M, Channiwala SA (2008) Experimental and computational aerodynamic investigations of a car. Mechanical Engineering Department, Sardar Vallabhbhai National Institute of Technology (SVNIT), Surat, Gujarat, India, vol 3
11. Suresh M, Sitaram N (2011) Gurney flap applications for aerodynamic flow control, International Conference on Mechanical Engineering 2011. Department of Mechanical Engineering IIT Madras, India
12. Saad MSSB (2010) Study of F1 car aerodynamics front wing using computational fluid dynamics (CFD). Faculty of Mechanical Engineering University Malaysia Pahang
13. Mahon S, Zhang X (2006) Computational analysis of an inverted double- element airfoil in ground effect, Aerospace Engineering. School of Engineering Sciences, University of Southampton, Southampton SO17 1BJ, UK, vol-128

14. Jasinski WJ, Selig MS (1998) Experimental study of open-wheel race-car front wings. University of Illinois at Urbana-Champaign
15. Zhang X, Zerihan J (2003) Aerodynamics of a double-element wing in ground effect. University of Southampton, Southampton, England SO17 1BJ, United Kingdom, vol 41(6)

Design and Analysis of Exoskeleton with a Torque Prediction Algorithm



R. Venkatesh , B. Satish Kumar , K. Umamaheswara Rao ,
S. S. Mantha, and K. Dileep 

Abstract This paper gives accurate prediction values for selection of actuator for exoskeleton robot. After carefully analysing various research works conducted by researchers, modelling of exoskeleton is done using SolidWorks software. The main aim of this paper is to suggest the suitable motor at knee joint in exoskeletons. So, to find the torque, Python software is used by considering the three independent parameters, namely, speed, height and angle of the human leg. These three parameters can be calculated by using a motion analysis software—Kinovea. Later analysis software ANSYS is used to complete the stress analysis of each component of exoskeleton. Exoskeletons are suits or wearable devices that are placed round the human body. Lower extremity exoskeletons are used for various functions—performance amplification, locomotion (ambulatory) and rehabilitation. This kind of skeleton is incredibly helpful for the military applications particularly in carrying weapons and providing ease to the soldiers. Within the alternative hand, exoskeletons for ambulant and rehabilitation assist patients to steer by providing joint trajectories of the gait cycle.

Keywords Exoskeleton · Solidworks · Ansys · Kinovea · Python · Deep learning

1 Introduction

Every year nearly 1.25 million people lose their lives in accidents and almost 3 million people suffer from serious injurious across the world [5]. Many of these injured people might be paraplegic. So, they need exoskeletons to enhance their strength. This paper provides a way to select the type of actuator for the exoskeleton based on the experimental results. This paper also gives complete information about the current technologies regarding construction and controlling of exoskeletons and predicts the torque at different joints with the help of machine learning algorithm,

R. Venkatesh (✉) · B. S. Kumar · K. Umamaheswara Rao · S. S. Mantha · K. Dileep
KLEF, Guntur, AP, India

i.e. multivariate algorithm and the accuracy of prediction have been carried out with deep learning technology.

2 Literature Survey

Singla et al. [1] gave an alternative power sources for the exoskeletons, with the rapid growth in usage of exoskeletons. Most of the exoskeletons commercially available use lithium-ion battery. The charging of the battery becomes a large bottleneck when the individual who wears the exoskeleton must go on trekking or mountaineering for a week journey. An alternative power source can be a useful choice to make batteries more efficient and rugged. These appliances were also regarded as cost-effective and environmentally friendly.

Spanda et al. [2] define the testing exercise performed on an exoskeleton of a commercial passive lower limb: The Chair less Chair, wearable sitting support that enables employees to switch between a standing position and a seated position. Tests were conducted on FCA employees who volunteered for the research. In the second step, anthropometry and postural angles of the worker are reproduced by considering some static postures. The greater the proportion reduced the strain on the limbs of the subject.

Srinath et al. [3] proposed an exoskeleton for lower limb amputees and dynamic analysis was performed using ADAMS software that gave better results for time versus force and time versus torque. Modelling of exoskeletons is done using SolidWorks software.

Kumar and Chakravarthy [4] designed a model for torque prediction of selecting appropriate motor in exoskeletons. Machine learning algorithms were used to validate the prediction of torque values generated by the model. Data from knee and hip joints is obtained from motion analysis software, i.e. Kinovea.

3 Theoretical Analysis

3.1 Torque Calculation Methods

The first step within the exoskeletons or active orthoses style is mechanism sort choice. There are some essential problems that ought to be thought of within the style method, viz., steady-state potency, power/mass magnitude relation, strain, power/volume magnitude relation, power consumption, stress, bandwidth, auxiliary gear mechanism, auxiliary power offer instrumentation and ease management procedures. Additionally, the actuators ought to be chosen considering the aim of the body coverage. The primary step within the mechanism choice is, deciding the amount of torsion and power needed for driving the exoskeleton. The specified torsion

and power are often calculated in three totally different ways: full build modelling, estimation mistreatment CGA1 knowledge, and experimental procedure [6].

The torsion on every joint has three parts in 3D area. Throughout level walking, within the articulation, the part that is within the direction of region flexion is the biggest one. Sometimes within the alternative two directions, passive actuators area unit used equally in knee and hip the direction of extension needs a lot of power and torsion whether you wear a backpack or not. It ought to be thought of that if the mission of the body covering changes appreciate occupancy a circular path, the opposite parts become necessary. Since the complete body modelling methodology is simply too sophisticated thanks to high DOF of build, the tactic can cause awfully troublesome procedure. If no simplification is used, it might be therefore troublesome to unravel the equations and calculate the torques and powers required.

3.2 Estimating Torques Using CGA Data

Lots of experiments are done on traditional human gait. They accordingly normalized that knowledge, relative to human weight throughout level walking; however, none of them investigated the impact of carrying backpack on torques and walking patterns. During this technique of torsion estimation, it is assumed that of having linear scaling if traditional CGA knowledge can cause a decent estimation of joint torques and joint powers [7]. This suggests that backpack mass has constant impact and because of this the body mass increases and therefore the frame would not greatly influence the gait patterns of the user. Therefore, addition of the backpack mass to the body mass is considered while calculating the torques [8]. Examining the CGA results shows that not solely there's heaps of variance within the most torsion and power, however additionally there are some variations between the patterns. On the opposite hand, there is no complete experimental knowledge to verify the results of this estimation.

3.3 Determining Torques Based on Experiment

Earlier the strategies of dynamic modelling and CGA based mostly would not essentially give reliable knowledge to style the system. In this methodology, the mean square measure tested below the condition of carrying a 35 kgs backpack [9]. The walking gait cycle is recorded employing a motion capture system and two force plates. Then the information would be analysed and therefore the joint torques are calculated. Earlier it is assumed that the human will bear his/her weight, and therefore the exploit system should tolerate the burden of automation and backpack and conjointly overcome the automation inertia. By subtracting the traditional level walking torsion and power knowledge from the experiment results, the specified motor torques and power are calculated. The advantage of this methodology is its reliability (Fig. 1).

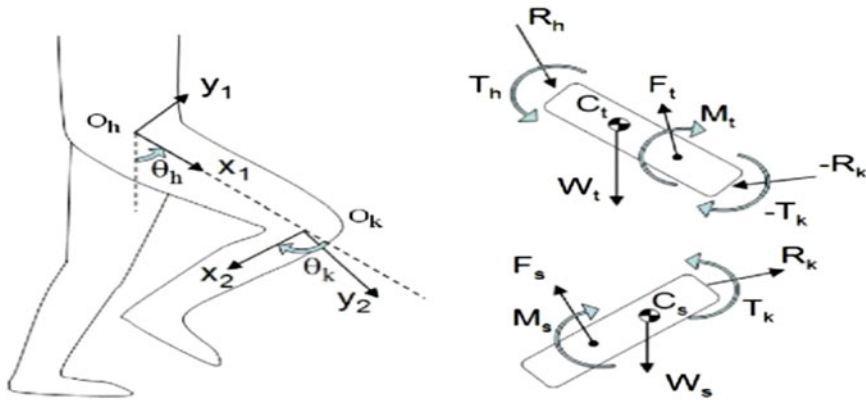


Fig. 1 Force acting at hip, knee, ankle

4 Video Motion Analysis

Video movement analysis is used to get data about moving subjects from video. Instances of this incorporate step examination, sports replays, speed and increasing speed computations and, on account of group or individual games, task execution investigation. The movement's examination method for the most part includes a fast camera and a PC that has programming permitting outline-by-outline playback of the video [10].

A computerized camcorder is fixed on a tripod. Utilizing video movement investigation programming, the picture on screen can be adjusted to the size of the scale empowering estimation of true qualities [11]. The product likewise observes the time between edges to give a development versus time informational index. This is helpful in ascertaining gravity, for example, from dropping a ball. Complex game examination frameworks, for example, those by Verusco technology advancements in New Zealand utilize different strategies, direct feeds from satellite TV to give ongoing investigation to mentors over the Internet and progressively point-by-point post-game investigation after the game has finished.

Customarily, video movement examination has been utilized in logical circles for computation of velocities of shots, or in sport for improving play of competitors. As of late, PC innovation has permitted different utilizations of video movement investigation to surface including things like showing principal laws of material science to class understudies, or general instructive undertakings in game and science.

In sport, frameworks have been created to give an elevated level of assignment, execution and physiological information to mentors, groups and players [12]. The goal is to improve individual and group execution or potentially examine restriction examples of play to give strategic bit of leeway. Police and measurable researchers dissect CCTV video when exploring crime. Police use programming, for example,

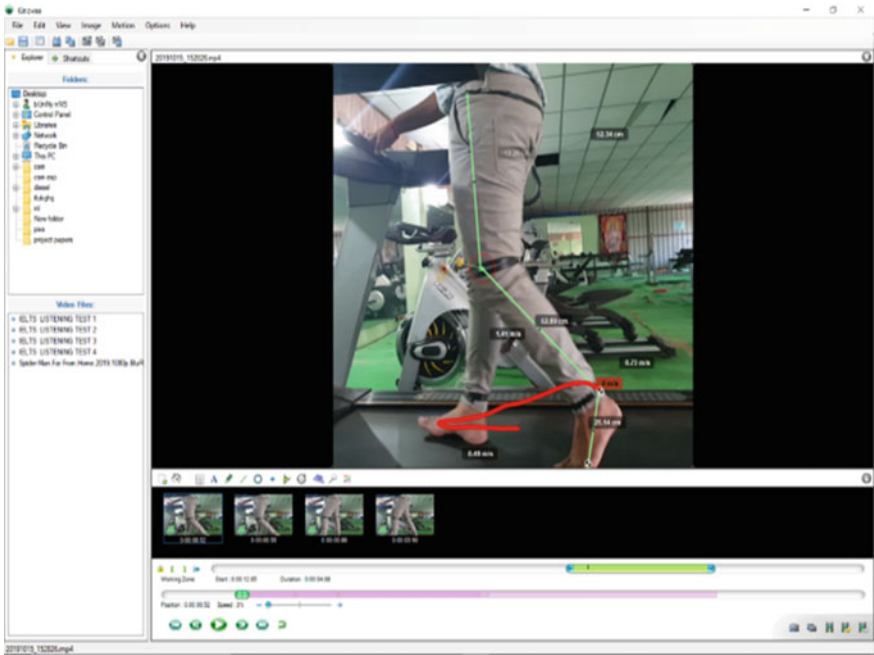


Fig. 2 Video motion analysis

Kinesense, which performs video movement examination to look for key occasions in video and discover suspects (Fig. 2).

5 Drive System and Controllers

Harmonic drive system may be a power gear mechanism that is an awfully fashionable alternative in electrical motivated systems. Drive system and controller section will reduce the output speed additionally and improves the output force for entire system. Besides no backlash, high-accuracy and high-torque quantitative relation we employed drive system unit. Besides, it is compact in size; this is often because of the special style that produces its input homocentric with its output [13]. The harmonic drive system is opted for construction of exoskeleton by considering its merits [14].

Raspberry Pi is now widely used even in analysis, like for weather observation thanks to its low value and movability [15]. Exoskeletons are empowered with the Raspberry Pi controllers for controlling signals from the actuators, as Raspberry controllers are very fast and rugged in nature, and complete controlling of the system is efficiently carried out with this controller.

Table 1 Materials

	Aluminium 7075	Duralumin (Aluminium 2024)	Prosthetic aluminium (Aluminium 7068)
Yield strength	503 (Mpa)	503	683
Density	2.80 (g/cc)	2.77	2.85
Availability	High	High	Low
Machinability	Medium	High	Medium

6 Material

In planning associate degree skeletal system, a fabric that is lightweight and robust is needed to make the frame of the exoskeleton. This is often because of low-weight frame that needs low power to actuate the piece. Skeletal system ought to be onerous enough to resist the force generated by the mechanism and additionally the weight of the user. Studies are done by metallic element alloys area unit chosen as their main material for the frame of the skeletal system. Though different types of metallic element alloys are employed in completely different studies, the most reason metallic element alloys are one in each of the foremost fashionable material because of its lightness and strength. In combination of metal or metallic element 2024 and chrome steel is employed to construct the structure of the skeletal system. The metal is employed to form the frame and therefore the chrome steel is employed to make the joints. On the opposite hand, combination of metallic element alloy 7075 and polymer six area was used to form the structure of the skeletal system [16]. The metallic element alloy 7075 area unit is employed in high load structure whereas the polymer six area unit is applied in low load structure to create the skeletal system as lightweight as potential. In combination of carbon fibre and prosthetic metallic element tube that uses metallic element 7068 is employed to construct the skeletal system. The prosthetic metallic element tube is chosen because it is designed for human use and lightweight. Carbon fibre area unit is solely employed in a little portion as it's lighter than metallic element alloys (Table 1).

7 Modelling

Modelling of the exoskeletons has been done with the help of SolidWorks software. Following figures depict how the modelling work is carried out for construction of exoskeletons. All the modelled parts have been assembled at the final stage which is shown in Fig. 11 (Figs. 3, 4, 5, 6, 7, 8, 9, 10 and 12).

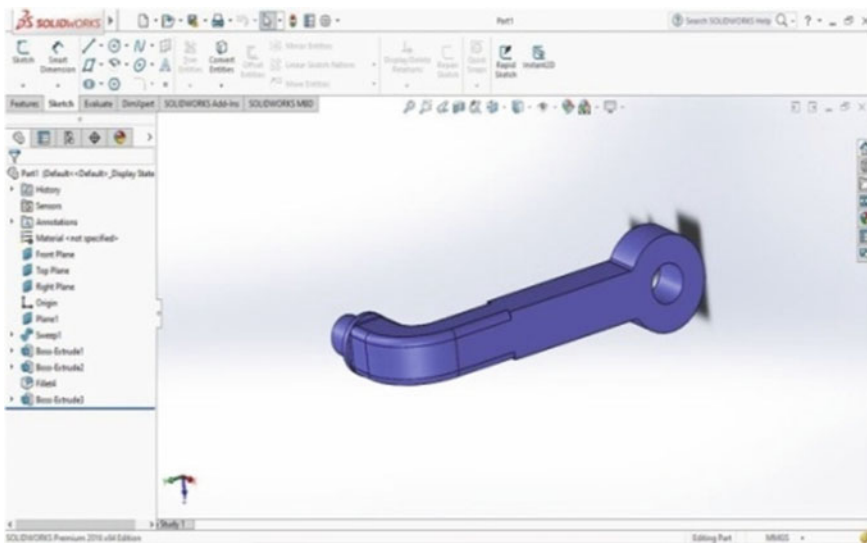


Fig. 3 Support link 1

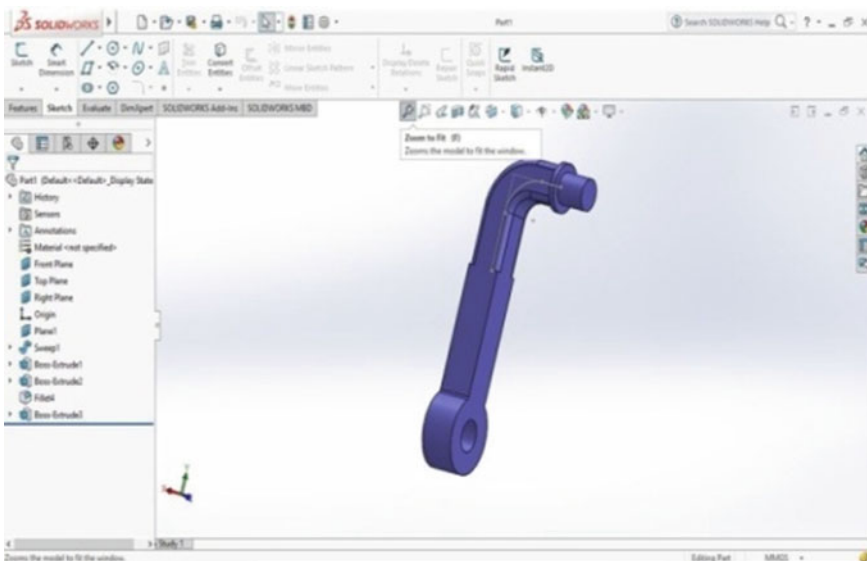


Fig. 4 Support link 2

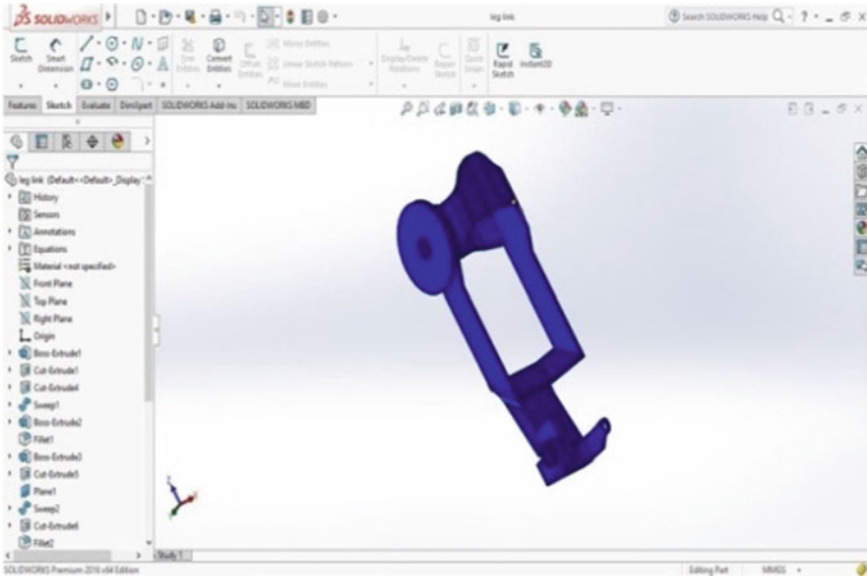


Fig. 5 Leg link

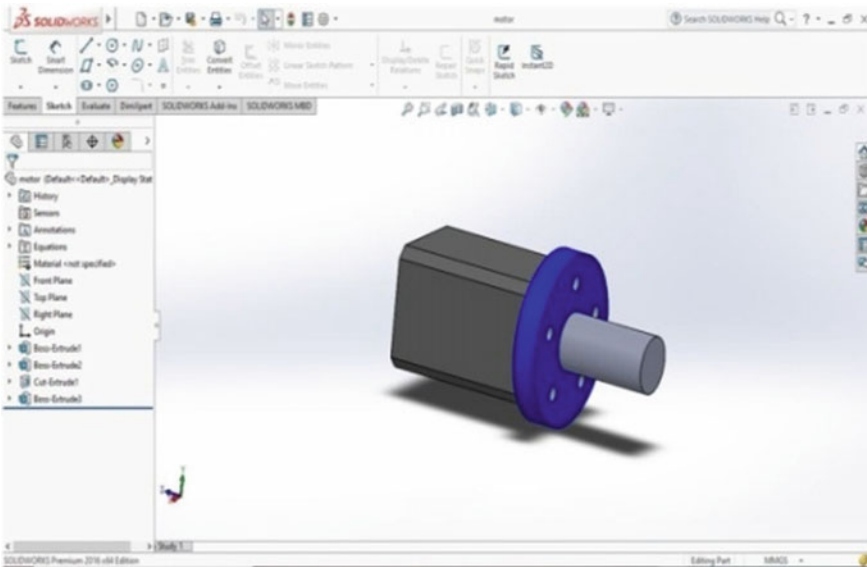


Fig. 6 Motor

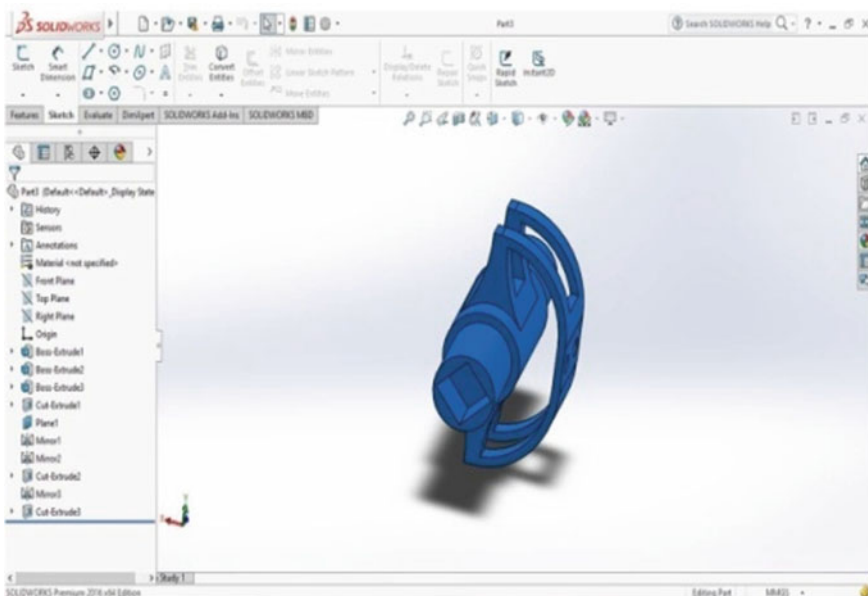


Fig. 7 Waist support

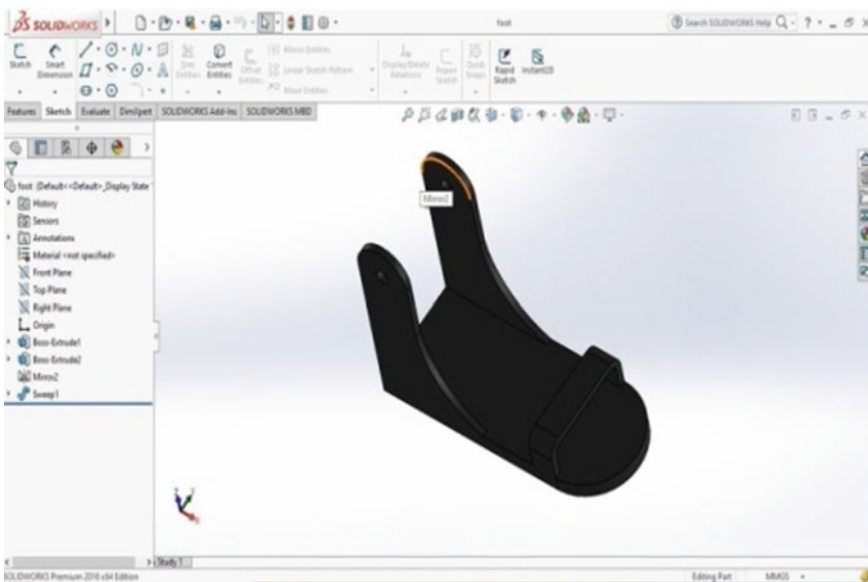


Fig. 8 Foot

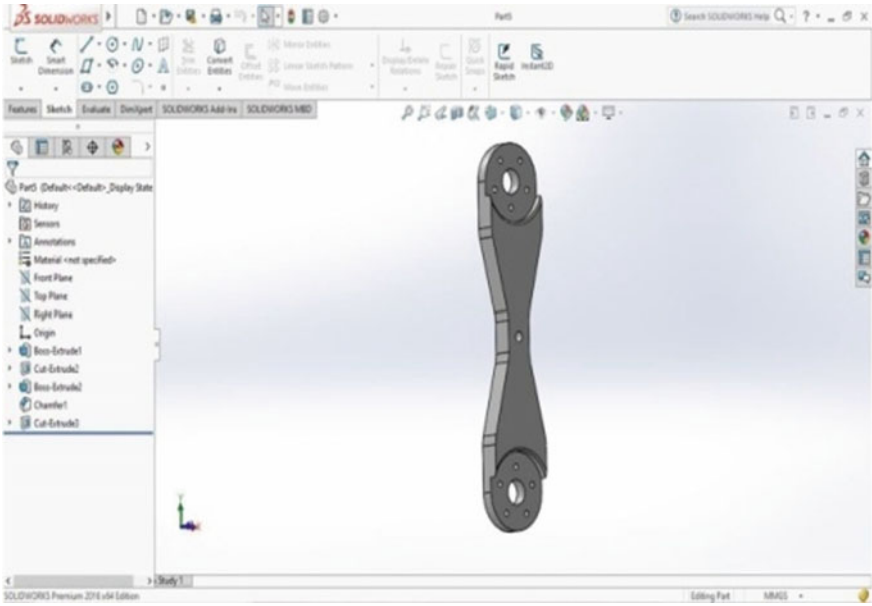


Fig. 9 Upper leg link

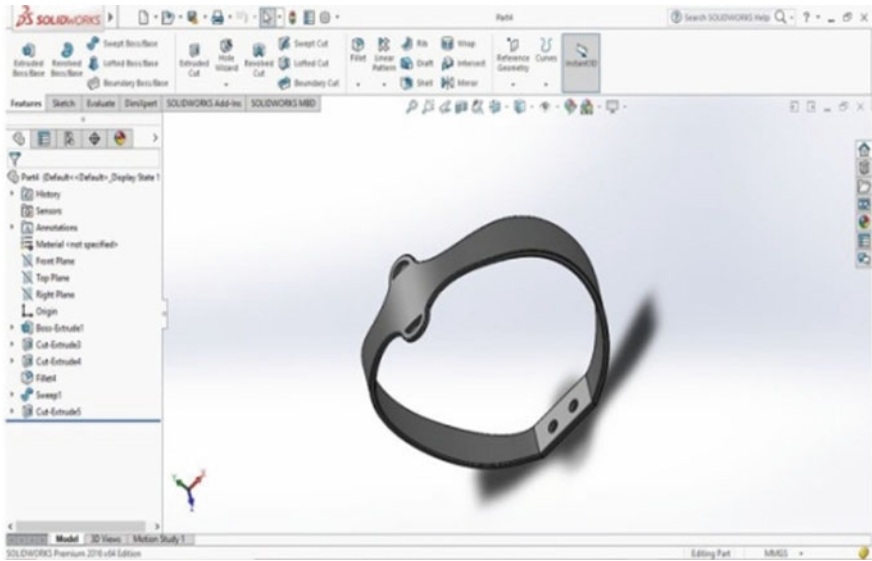


Fig. 10 Support belt

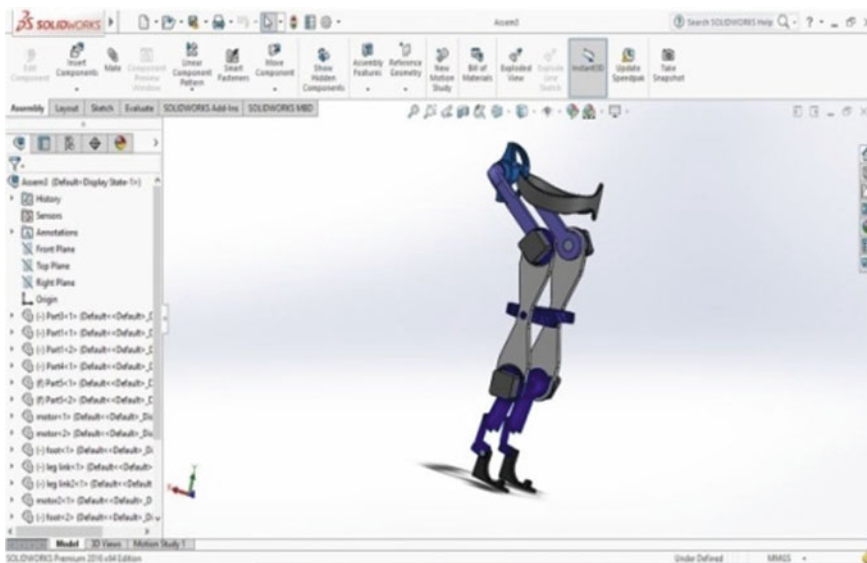


Fig. 11 Final assembly

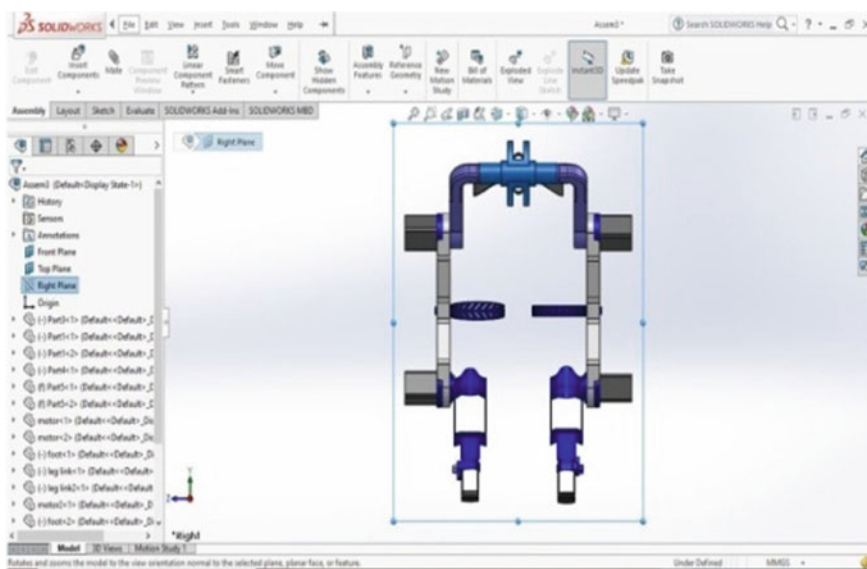


Fig. 12 Front view

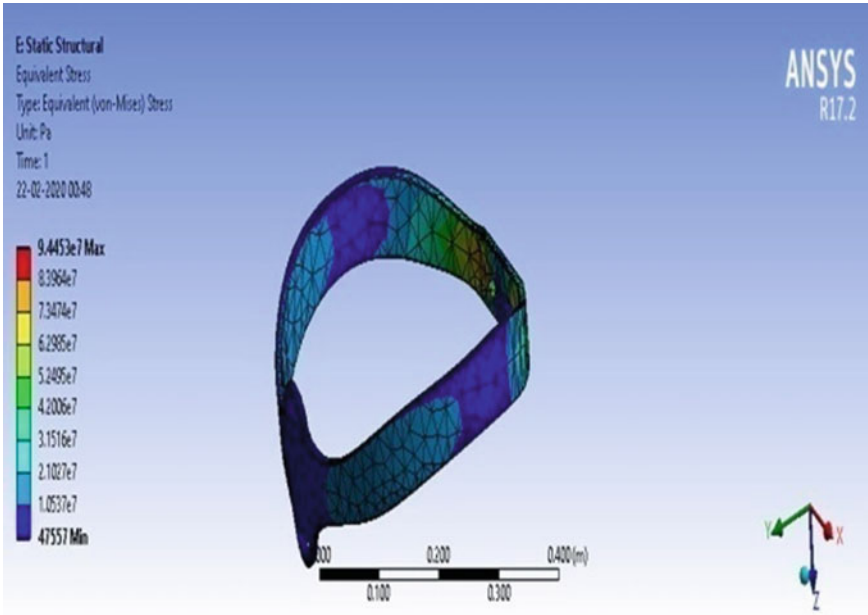


Fig. 13 Equivalent von Mises stress

8 Analysis

Analysis of the modelled exoskeleton parts has been done under extreme load conditions and the analysis work has been carried out by Ansys software (Figs. 13, 14, 15, 16, 17 and 18).

9 Experimental Results

See Table 2.

10 Video Motion Analysis

Video motion analysis has been done with the help of Kinovea software, where a person is made to walk on the treadmill and video has been recorded [17]. That video has been analysed by Kinovea software through which ankle, knee and hip angles data has been recorded [18]. Based on this data, using torque calculation methods, required torque has been calculated by substituting these values, respectively. It is

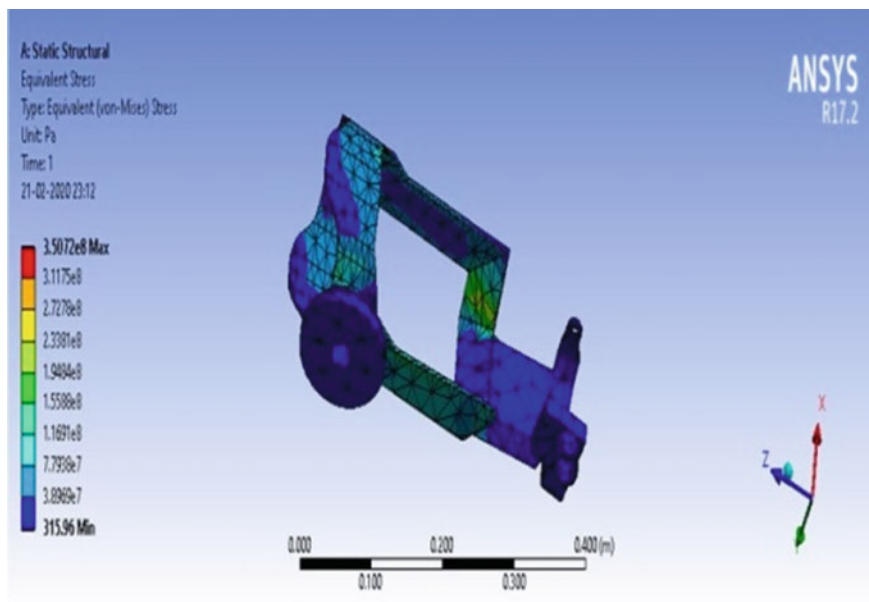


Fig. 14 Equivalent von Mises stress

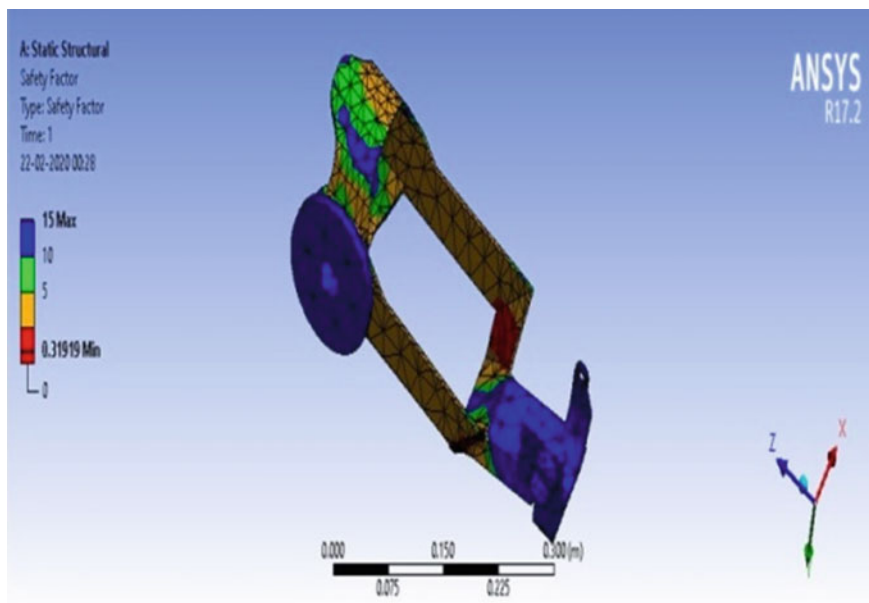


Fig. 15 Safety factor

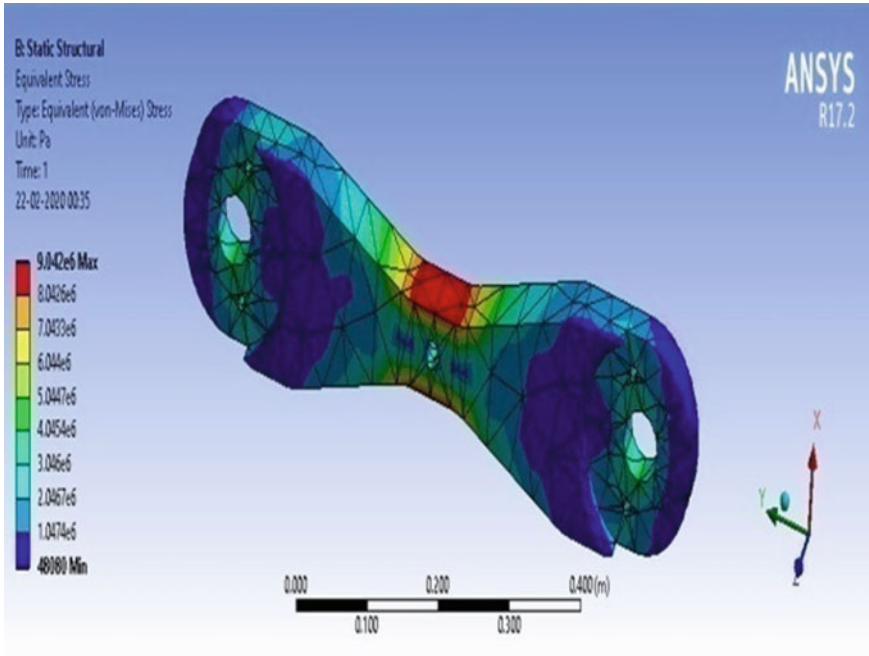


Fig. 16 Equivalent von Mises stress

very hectic and complex task to calculate the torque values repeatedly, and hence this process has been automated with the help of Python software (Fig. 19).

10.1 Torque Calculations

Torque calculation requires the estimated values of mass of the actuators and the mass of the links the user is assumed of weighing 85 kg.

Formulas for torque at different joints (Table 3).

$$\begin{aligned}
 \tau_1 = \sin\theta & \left[(m_1 + m_{L1})g\left(\frac{l_1}{2}\right) + m_3g(l_1) \right] \\
 & + \sin\theta \left[(m_4 + m_{L2})g\left(l_1 + \frac{l_1}{2}\right) \right] \\
 & + \sin\theta[m_4g(l_1 + l_2)] \\
 & + \sin\theta[(m_6 + m_{L3})g(l_1 + l_2)] \\
 & + \cos\theta \left[(m_6 + m_{L3})g\left(\frac{l_3}{2}\right) \right]
 \end{aligned}$$

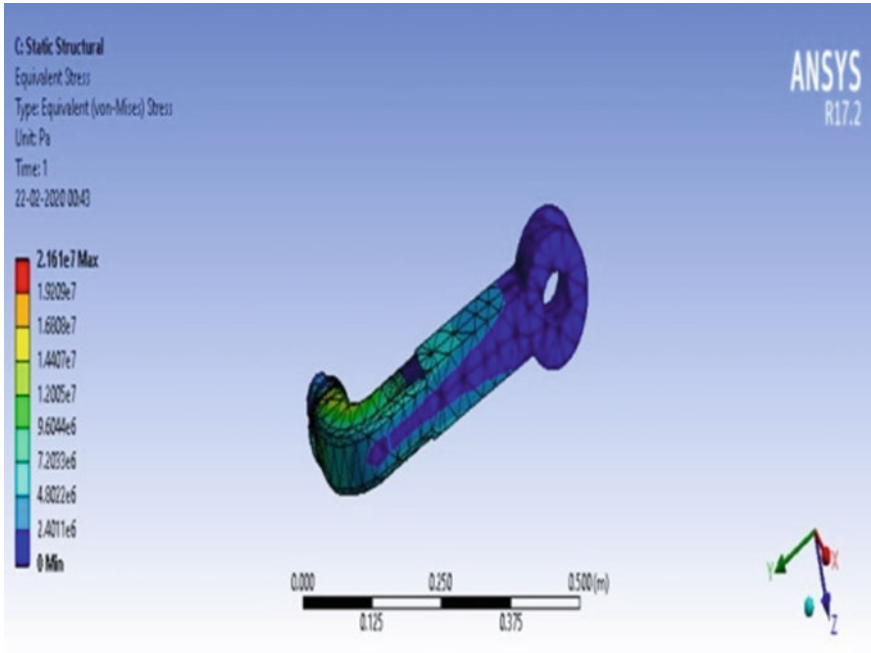


Fig. 17 Equivalent von Mises stress

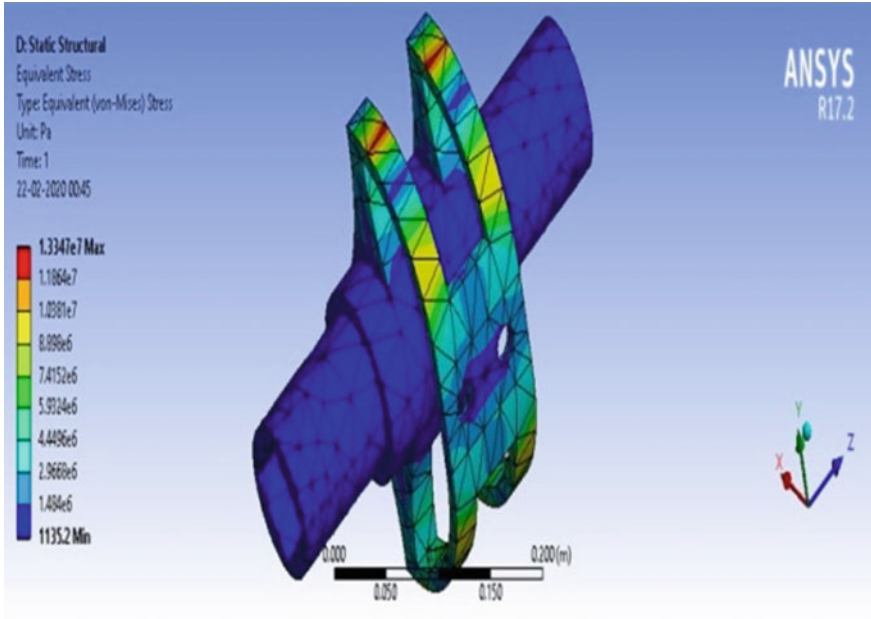


Fig. 18 Equivalent von Mises stress

Table 2 Speed obtained from KINOVEA software

Motion	Speed of foot (m/s)	Speed of knee (m/s)	Speed of hip (m/s)
At rest	0	0	0
Walking forward	0.32	0.17	0.13
Walking backward	0.73	0.89	0.13

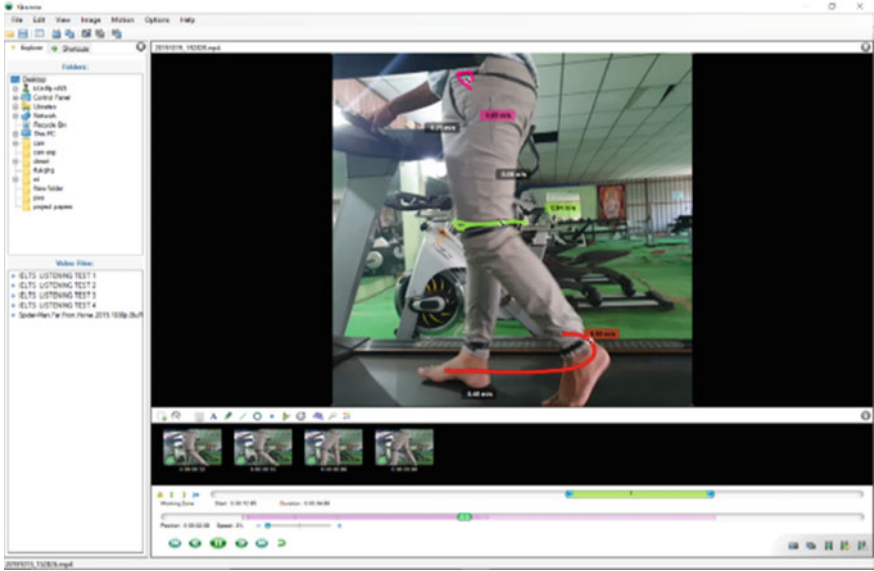


Fig. 19 Walking on treadmill

$$\tau_2 = \sin\theta \left[(m_4 + m_{L2})g \left(\frac{l_2}{2} \right) \right] + \sin\theta [m_5g(l_2)]$$

$$+ \cos\theta \left[(m_6 + m_{L3})g \left(\frac{l_3}{2} \right) \right] + \sin\theta [m_6g(l_2)]$$

$$\tau_3 = \cos\theta \left[(m_6 + m_{L3})g \left(\frac{l_3}{2} \right) \right]$$

From the above calculations, the

- Torque required at hip joint = 560 Nm.
- Torque required at knee joint = 289 Nm.
- Torque required at ankle joint = 129 Nm.

Prediction of torques has been done using machine learning techniques. Multi-variate algorithm is employed to predict the output torque. To validate the results,

Table 3 Body segment weights/lengths

Parameters	Notation	Values/ units
Mass of actuator at hip joint	m_1	0.920 kg
Mass of thigh	m_2	18.275 kg
Mass of actuator at knee joint	m_3	0.513 kg
Mass of shank	m_4	8.16 kg
Mass of actuator at ankle joint	m_5	0.196 kg
Mass of foot	m_6	2.89 kg
Mass of thigh link	m_{L1}	3.5 kg
Mass of shank link	m_{L2}	4.75
Mass of ankle link	m_{L3}	1.85
Length of thigh	l_1	50×10^{-2} m
Length of shank	l_2	48.5×10^{-2} m
Length of foot	l_3	23.55×10^{-2} m
Angle of thigh joint	θ_1	23^0
Angle of knee joint	θ_2	57^0
Angle of ankle joint	θ_3	45^0

whether the predicted value is correct or not, deep learning concept has been employed in this research.

11 Deep Learning

The predicted output data has been compared with the output processed in neural networks. The best possible means of validation of the predicted outputs is done through deep learning technique. The deep learning technique involves numerous numbers of neurons connecting each other with specified weights on them. The input data is processed through the hidden layers, cost function and accuracy has been calculated precisely using deep learning technique [19].

TensorFlow methodology is imbibed in the deep learning algorithm and the input data has been tested and trained for a specific number of cycles [20]. The output obtained after processing of TensorFlow technique has been recorded and the average loss for testing and training of data set has been recorded. The data has been processed in the deep learning module using TensorFlow and employing mean optimizer, obtained average loss value for the trained data set is 21.69% and average loss value for testing data set is 34.10% for hip torque and 1.50%, 3.19% for knee torques, respectively (Figs. 20, 21 and 22).

The data obtained from Kinovea is compared with the previous methods of data retrieving processes. The data when compared is more or less similar to the previous methods and hence the processing of that data by machine learning algorithm and

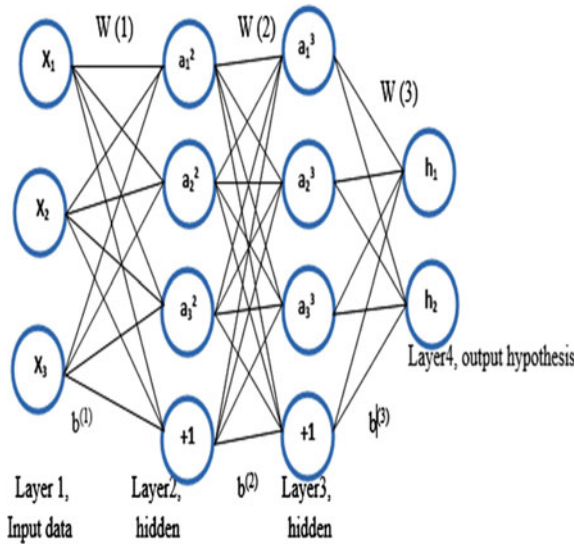
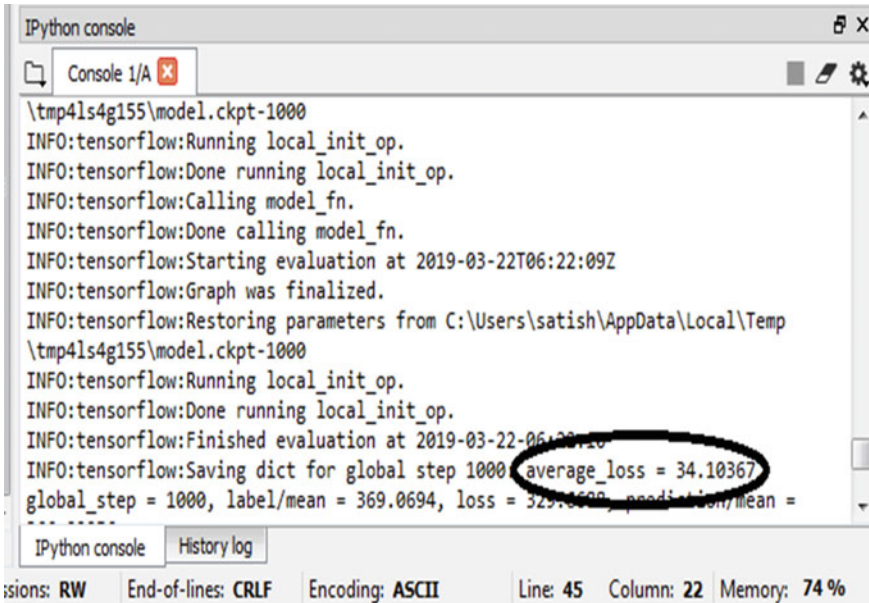


Fig. 20 Deep learning block diagram (with three input variables and two outputs variables)

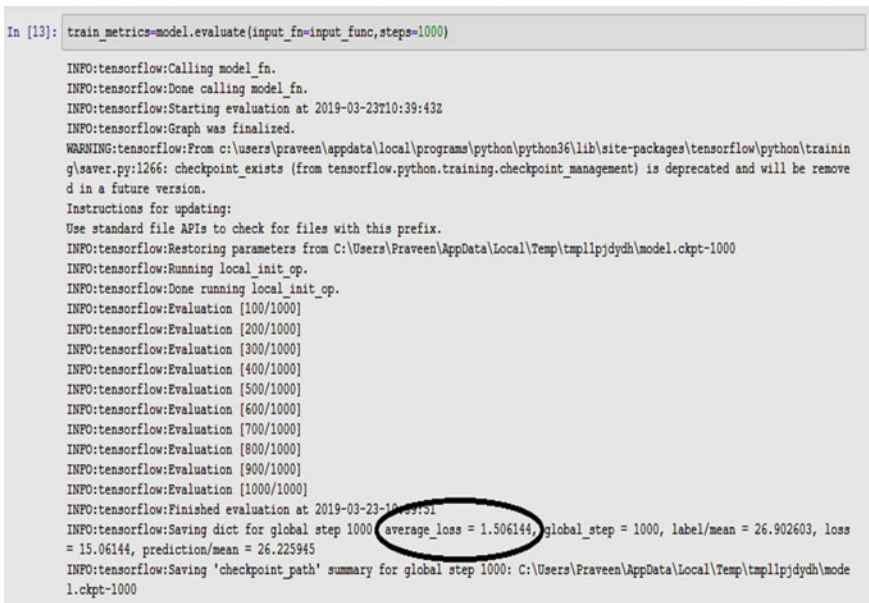
```
IPython console
Console 1/A
INFO:tensorflow:Done running local_init_op.
INFO:tensorflow:Evaluation [100/1000]
INFO:tensorflow:Evaluation [200/1000]
INFO:tensorflow:Evaluation [300/1000]
INFO:tensorflow:Evaluation [400/1000]
INFO:tensorflow:Evaluation [500/1000]
INFO:tensorflow:Evaluation [600/1000]
INFO:tensorflow:Evaluation [700/1000]
INFO:tensorflow:Evaluation [800/1000]
INFO:tensorflow:Evaluation [900/1000]
INFO:tensorflow:Evaluation [1000/1000]
INFO:tensorflow:Finished evaluation at 2019-03-22-06:33:06
INFO:tensorflow:Saving dict for global step 1000: average_loss = 21.694235
global_step = 1000, label/mean = 367.74323, loss = 21.694235, prediction/mean =
IPython console History log
ions: RW End-of-lines: CRLF Encoding: ASCII Line: 45 Column: 22 Memory: 74 %
```

Fig. 21 Average loss value of hip-torque (trained sets)



```
IPython console
Console 1/A
\tmp41s4g155\model.ckpt-1000
INFO:tensorflow:Running local_init_op.
INFO:tensorflow:Done running local_init_op.
INFO:tensorflow:Calling model_fn.
INFO:tensorflow:Done calling model_fn.
INFO:tensorflow:Starting evaluation at 2019-03-22T06:22:09Z
INFO:tensorflow:Graph was finalized.
INFO:tensorflow:Restoring parameters from C:\Users\satish\AppData\Local\Temp\tmp41s4g155\model.ckpt-1000
INFO:tensorflow:Running local_init_op.
INFO:tensorflow:Done running local_init_op.
INFO:tensorflow:Finished evaluation at 2019-03-22-06-22-10
INFO:tensorflow:Saving dict for global step 1000: average_loss = 34.10367
global_step = 1000, label/mean = 369.0694, loss = 329.8600, prediction/mean =
IPython console History log
Sessions: RW End-of-lines: CRLF Encoding: ASCII Line: 45 Column: 22 Memory: 74 %
```

Fig. 22 Average loss value of hip-torque (test sets)



```
In [13]: train_metrics=model.evaluate(input_fn=input_func,steps=1000)
INFO:tensorflow:Calling model_fn.
INFO:tensorflow:Done calling model_fn.
INFO:tensorflow:Starting evaluation at 2019-03-23T10:39:43Z
INFO:tensorflow:Graph was finalized.
WARNING:tensorflow:From c:\users\praveen\appdata\local\programs\python\python36\lib\site-packages\tensorflow\python\trainin
g\saver.py:1266: checkpoint_exists (from tensorflow.python.training.checkpoint_management) is deprecated and will be remove
d in a future version.
Instructions for updating:
Use standard file APIs to check for files with this prefix.
INFO:tensorflow:Restoring parameters from C:\Users\Praveen\AppData\Local\Temp\tmpl1pjdydh\model.ckpt-1000
INFO:tensorflow:Running local_init_op.
INFO:tensorflow:Done running local_init_op.
INFO:tensorflow:Evaluation [100/1000]
INFO:tensorflow:Evaluation [200/1000]
INFO:tensorflow:Evaluation [300/1000]
INFO:tensorflow:Evaluation [400/1000]
INFO:tensorflow:Evaluation [500/1000]
INFO:tensorflow:Evaluation [600/1000]
INFO:tensorflow:Evaluation [700/1000]
INFO:tensorflow:Evaluation [800/1000]
INFO:tensorflow:Evaluation [900/1000]
INFO:tensorflow:Evaluation [1000/1000]
INFO:tensorflow:Finished evaluation at 2019-03-23-10-39-51
INFO:tensorflow:Saving dict for global step 1000: average_loss = 1.506144, global_step = 1000, label/mean = 26.902603, loss
= 15.06144, prediction/mean = 26.225945
INFO:tensorflow:Saving 'checkpoint_path' summary for global step 1000: C:\Users\Praveen\AppData\Local\Temp\tmpl1pjdydh\mode
l.ckpt-1000
```

Fig. 23 Average loss value of knee-torque (trained sets)

```

In [15]: predictions=list(preds)
         final_pred=[]
         for pred in predictions:
             final_pred.append(pred*"predictions")

         test_metric=model.evaluate(input_fn=pred_input_func,steps=1000)

INFO:tensorflow:Calling model_fn.
INFO:tensorflow:Done calling model_fn.
INFO:tensorflow:Graph was finalized.
INFO:tensorflow:Restoring parameters from C:\Users\Praveen\AppData\Local\Temp\tmp1ljdydh\model.ckpt-1000
INFO:tensorflow:Running local_init_op.
INFO:tensorflow:Done running local_init_op.
INFO:tensorflow:Calling model_fn.
INFO:tensorflow:Done calling model_fn.
INFO:tensorflow:Starting evaluation at 2019-03-23T10:40:13Z
INFO:tensorflow:Graph was finalized.
INFO:tensorflow:Restoring parameters from C:\Users\Praveen\AppData\Local\Temp\tmp1ljdydh\model.ckpt-1000
INFO:tensorflow:Running local_init_op.
INFO:tensorflow:Done running local_init_op.
INFO:tensorflow:Finished evaluation at 2019-03-23-10:40:14
INFO:tensorflow:Saving dict for global step 1000: average_loss = 3.1938508, global_step = 1000, label/mean = 27.32363, loss
= 30.873892, prediction/mean = 26.95568
INFO:tensorflow:Saving 'checkpoint_path' summary for global step 1000: C:\Users\Praveen\AppData\Local\Temp\tmp1ljdydh\mode
l.ckpt-1000

```

Fig. 24 Average loss value of knee-torque (tested sets)

the prediction of the torques were said to be accurate and hence this method is recommended for prediction and calculation of torque values through gait analysis (Figs. 23 and 24).

12 Conclusion

In this paper, modelling of exoskeleton has been done with SolidWorks software and the modelled exoskeleton is validated with Ansys software which analysed the working of the model at extreme conditions. The torque required for this exoskeleton has been calculated from the hip, knee and ankle data captured from the video motion analysis software, i.e. Kinovea software and the process is automated with Python programming software. Then prediction of the torques for selecting the actuator, i.e. motor has been done with the machine learning algorithms and is validated with the accuracy rate using deep learning technology. By this, doctors can easily evaluate the type of exoskeleton actuators for the amputees/old-age people that ease the effected ones to carry out their works more efficiently and accurately. Ergonomics and safety parameters have been improved in exoskeletons from this research work.

References

1. Singla A, Dhand S, Dhawad A, Virk GS (2019) Toward human-powered lower limb exoskeletons: a review. In *Harmony search and nature inspired optimization algorithms*, pp 783–795. Springer, Singapore
2. Spada S, Ghibaudo L, Carnazzo C, Pardo MD, Chander DS, Gastaldi L, Cavatorta MP (2018) Physical and virtual assessment of a passive exoskeleton. In *Congress of the International Ergonomics Association*, pp 247–257. Springer, Cham
3. Srinath A, Rao KU, Paladugu RP, Chakravarthy YK (2019) Design & optimization of rehabilitation exoskeleton device for Indian amputees. *Int J Innov Technol Explor Eng (IJITEE)* 8(7). ISSN: 2278–3075
4. Kumar BS, Chakravarthy YK, Prediction of optimal torques from gait analysis applying the machine learning concepts
5. Ruikar M (2013) National statistics of road traffic accidents in India. *J Orthop Trauma Rehabil* 6(1):1
6. Arnold BL, Perrin DH (1993) The reliability of four different methods of calculating quadriceps peak torque and angle-specific torques at 30, 60, and 75. *J Sport Rehabil* 2(4):243–250
7. Toudeshki AG, Yousefi-Koma A, Jokar M, Taherifar A (2014) Torque and power estimation for a power-assisted lower extremity exoskeleton during level walking. *Dynamic Walking*
8. Chu A, Kazerooni H, Zoss A (2005) On the biomimetic design of the berkeley lower extremity exoskeleton (BLEEX). In *Proceedings of the 2005 IEEE international conference on robotics and automation* (pp 4345–4352). IEEE
9. Zhang J, Cheah CC, Collins SH (2015) Experimental comparison of torque control methods on an ankle exoskeleton during human walking. In: *2015 IEEE international conference on robotics and automation (ICRA)* (pp 5584–5589). IEEE
10. Borel S, Schneider P, Newman CJ (2011) Video analysis software increases the interrater reliability of video gait assessments in children with cerebral palsy. *Gait Posture* 33(4):727–729
11. Guzmán C, Valdivia A, Blanco O, Oliver-Salazar MA, Carrera-Escobedo JL (2013) Therapeutic motion analysis of lower limbs using Kinovea. *Int J Soft Comput Eng (IJSCE)* 3
12. Adnan NMN, Ab Patar MNA, Lee H, Yamamoto SI, Jong-Young L, Mahmud J (2018) Biomechanical analysis using Kinovea for sports application. In *IOP conference series: materials science and engineering* 342(1), p 012097. IOP Publishing Ltd
13. Gandhi* PS, Ghorbel F (2005) High-speed precision tracking with harmonic drive systems using integral manifold control design. *Int J Control* 78(2):112–121
14. Schäfer I, Slatter R (2013) Precision pointing and actuation systems for UAVS USING HARMONIC DRIVE GEARS. In *2nd AIAA” Unmanned Unlimited” Conf. and Workshop & Exhibit* (p 6636)
15. Sandeep V, Gopal KL, Naveen S, Amudhan A, Kumar LS (2015) Globally accessible machine automation using Raspberry pi based on Internet of Things. In: *2015 International conference on advances in computing, communications and informatics (ICACCI)* (pp 1144–1147). IEEE
16. Beving DE, McDonnell AM, Yang W, Yan Y (2006) Corrosion resistant high-silica-zeolite MFI coating: one general solution formulation for aluminum alloy AA-2024-T3, AA-5052-H32, AA-6061-T4, and AA-7075-T6. *J Electrochem Soc* 153(8):B325
17. Puig-Diví A, Padullés-Riu JM, Busquets-Faciabén A, Padullés-Chando X, Escalona-Marfil C, Marcos-Ruiz D (2017) Validity and Reliability of the Kinovea Program in 2 Obtaining Angular and Distance Dimensions 3. Preprints 2017100042
18. El-Raheem, Abd RM, Kamel RM, Ali MF (2015) Reliability of using Kinovea program in measuring dominant wrist joint range of motion. *Trends Appl Sci Res* 10(4):224
19. Deng L, Yu D (2014) Deep learning: methods and applications. *Found Trends Signal Process* 7(3–4):197–387
20. Ertam F, Aydın G (2017) Data classification with deep learning using Tensorflow. In: *2017 International conference on computer science and engineering (UBMK)*, pp 755–758. IEEE

Characterization of Noise Sources, Built Material and Acoustic Parameters of a Newly Renovated Special Purpose Space



Mohd Zaid, Yasser Rafat , Sameen Mustafa, Rashid Ali, and Bashmal Salem

Abstract The study of acoustical characteristics is important to understand sound propagation, absorption, build up and aural comfort in closed and open spaces. This article presents experimental investigation and analyses of the acoustical characteristics of a renovated room in the Mechanical Engineering Department of the Aligarh Muslim University (AMU). To design a space (room, hall, lab, etc.), the acoustic parameters such as Early Decay Time (EDT), Reverberation time (RT), Noise criterion and other parameters need to be determined. Absorption is also an important parameter to determine the acoustics of a space. The absorption coefficient of built material and objects in the room was measured using a new in situ method (sec 0). The presence of occupants and various objects inside a space can change the overall absorption performance of that space. These parameters help acousticians to correctly design and maintain the venues according to the need. The results of experimental data collected using microphones were found to be in accordance with values set by various standards. The room was found to be suitable to be used as a lecture room and laboratory, while it was unsuitable for musical purposes. These aspects should be considered before designing the space, and knowledge of the absorption coefficient of any object should be utilized for enhancing the acoustics of a space in the early designing and interior designing phases.

Keywords Noise characterization · Built material characterization · Acoustical parameters · Absorption · Background noise · Reverberation time

M. Zaid · Y. Rafat (✉) · R. Ali
Department of Mechanical Engineering, Aligarh Muslim University, Aligarh, India
e-mail: yasser.rafat@zhcet.ac.in

R. Ali
e-mail: rashidali1@zhcet.ac.in

S. Mustafa
Department of Mechanical and Aerospace Engineering, Politecnico di Torino, Turin, Italy

B. Salem
Mechanical Engineering Department, King Fahd University of Petroleum and Minerals, Dhahran, Saudi Arabia
e-mail: bashmal@kfupm.edu.sa

1 Introduction

Acoustical evaluation is an integral part of room design as the acoustical characteristics specify the purpose for which a designed closed space (room, hall and auditorium) is to be used. It is essential to know the room acoustics properly to know whether it is suitable to be used as a classroom/lab, etc. To know the acoustical features correctly, we need to go step-wise from noise characterization to acoustical parameter evaluation. In this case, we are concerned about knowing the complete acoustical features of a research lab that is newly renovated; a description of the lab is given in coming sections. First of all, noise characterization will be conducted for the room and the background noise level was measured for different operating conditions at different locations. Ambiance of the room was also assessed and an average and maximum sound levels of noisiest proximity were recorded.

After noise characterization, absorption tendencies of different objects present in the room were assessed. Absorption was measured using PU-based in situ absorption probe which gives absorption of any object in situ (refer to sec 0). The effect of the absorption by these objects on the overall acoustics of the room was discussed.

Then acoustical parameters were measured. The most commonly used method for determining the acoustic parameters and evaluating sound quality is the impulse response method in which a random noise (pink noise, white noise, balloon pop sound, etc.) is played for a short while and is received by an omnidirectional microphone. Plotting the sound pressure levels as a function of elapsed time gives the various acoustical characteristics of the space under study. In the present study, white Gaussian noise has been used to generate impulse response, and various software have been used for its analyses. Many studies have been carried out using the impulse response method to classify spaces, some of which will be discussed in coming sections.

Acoustical evaluation is an integral part of room design as the acoustical characteristics specify the purpose for which a designed closed space (room, hall and auditorium) is to be used. The most commonly used method for determining the acoustic parameters and evaluating sound quality is the impulse response method in which a random noise (pink noise, white noise, balloon pop sound, etc.) is played for a short while and is received by an omnidirectional microphone. Plotting the sound pressure levels as a function of elapsed time gives the various acoustical characteristics of the space under study. In the present study, white Gaussian noise has been used to generate impulse response, and various software have been used for its analyses. Many studies have been carried out using the impulse response method to classify spaces, some of which are discussed below.

Milner et al. studied the modal characteristics of a series of reverberation rooms with parallel ceilings and floor using the finite element method (FEM). He concluded that similar performance can be shown by the rooms having dissimilar shapes. Performance of the rooms was also found to be very responsive to the small changes in the configuration of rooms [1].

Soulodre et al. performed a series of subjective and experimental evaluations of various acoustical features in North American concert halls. Acoustical parameters such as reverberation time (RT), Clarity (C_{50}), Strength (G) and Lateral energy fraction (LEF) were measured. Relation of loudness, clarity and echo with the parameters G, C_{50} , RT, etc. were established. They concluded from the results that long RT at lower frequencies is generally recommended but at the same time low-frequency energy of sound should also be maximized [2].

Hodgson assessed acoustical performance experimentally in some randomly chosen classrooms at the University of British Columbia (UBC). Acoustical quality of the classrooms was found better when occupied than the unoccupied situation. So student occupancy in the classrooms creates a noticeable effect in the classroom acoustics, and it should be kept in mind while designing such spaces [3].

Cirillo and Martellotta performed an acoustical study on nine Romanesque churches in Apulia (Southern Italy). Monaural and Binaural parameters were calculated according to ISO 3382. The average value of whole space and also the individual value related to different positions were measured. First, it was investigated how reverberation time got affected by the architecture of a space, then average values of the other parameters that are important in acoustical calculations were assessed. It was concluded that the monaural parameters could be expressed as functions of the source-receiver distance and one or two of the following parameters: average absorption coefficient, room volume, reverberation time and absorbing surface area [4].

Knüttel et al. used an analytical method to describe the influence of the directivity of the loudspeaker on Room Impulse Response (RIR). He concluded that the influence of directivity exists in very reverberant rooms also [5].

Scannell et al. performed a subjective and objective evaluation of acoustical and architectural features of 23 Informal Learning Spaces (ILSs). 850 students participated in the survey. He pointed out that the level of generated sound by various sources including student's voices exceeded the various set standards. It was concluded that acoustical properties of such learning spaces should be sought with occupants' perception, and corrective measures should be taken to meet the required expectations [6].

Alam et al. performed an acoustical study on Kennedy Auditorium in Aligarh Muslim University with the use of active sound systems. Absorption tendencies of built material and their effect on auditorium acoustics were also assessed. Reverberation time (RT) of the auditorium was found greater than the acceptable limits especially when the frequency is low. It was concluded that the reason for high RT is the very reflecting nature of sidewalls. Some acoustic treatment on the walls was recommended for absorbing the low-frequency sound. It was also recommended that the existing sound system should be modified with some line arrays [7].

Pelegrín-García et al. presented the effect of four rooms with different acoustical features on the speech generated by some talkers when addressing the same listener from four different locations. It was realized that when talkers prolong their speech, then it is the case of difficult understanding. It was concluded that talker-listener relative distance is a key point in speech comprehension [8].

Pelegrín-García and Brunskog presented a study by conducting experiments in a laboratory to find the favourable acoustical conditions of a room for speech-related activities. An objective study was coupled with a subjective survey to find out the effect of bad acoustics on human comfort. Teachers with some voice problems were also included in this study. It was concluded that teachers having some problem with their voice perceived their surrounding very differently than the other teachers, and they prefer more decay times when they speak [9].

Zannin and Marcon performed objective and subjective evaluations of acoustical comfort in the classrooms. Around 60 teachers and 500 students were surveyed. Major sources of annoyance were found in the speaking sound from the occupants and neighbouring classrooms. Acoustical parameters such as reverberation time background noise and also the sound insulation were measured. The acoustical quality of the classroom was found to be not good according to the Brazilian Standard NBR 12,179. Simulations were also performed to suggest better acoustics with some acoustical treatment using sound absorbers [10].

Lyberg-Åhlander et al. presented a subjective survey on some teachers related to the acoustic perception of classrooms and environment. They created two groups, the first one having teachers with some voice-related problems and the other one of healthy teachers. They concluded that teachers having some voice-related problems are more concerned about the room acoustics and reacted heavily to the load-related issues than the healthy teachers [11].

It can be concluded from the above studies that from the acoustical perspective of a space, some factors such as background noise, reverberation time and absorption tendencies of built material play a very important role. Subjective surveys were also performed to point out the annoyance sources. Notice sources should be identified and characterized and also the built material should be characterized and natural absorption of the materials should be in mind at the designing phase of a building or space. An in situ method for measuring absorption was discussed in this article which can give absorption of any object in minutes. It will be discussed in coming sections.

2 Methodology

In lecture rooms and labs, a major acoustic concern is verbal communication as most of the activities in the lab are dependent on speech intelligibility (SI). The speech intelligibility in rooms and enclosures is related to signal-to-noise ratio (SNR) as well as the acoustical characteristics of the enclosures. Thus, it can be influenced by background noise (BN) and reverberation time (RT). Both BN and RT are influenced by the absorption coefficient. BN can be calculated using Sound Level Meter (SLM), and Absorption can be calculated using PU-based in situ absorption probe (refer to sec 0) which can easily give results in a few minutes. From a directional perspective, a room acoustic indicator is of three types, i.e. monophonic indicators, directionally influenced indicators and directional indicators. Pressure impulse response is a very

common and effective method to determine monophonic indicators (EDT, RT60, C50, STI and SNR). The response is taken from a single microphone [12].

3 Case study

3.1 Description of Room

The room under study was renovated under the DST project and is in the main building of Zakir Hussain College of Engineering and Technology, Aligarh Muslim University, Aligarh, Uttar Pradesh, India. The room measures $26 \times 21 \times 16$ ft and has two windows (3.75×2.6 ft) and one door (7×4 ft). Two window ACs and three fans are installed in the room. The maximum capacity of the room is x pupils. It can be used both as a lecture room as well as an acoustics measurement laboratory. The floor is covered with ceramic tiles and there is no false ceiling installed in the room. The walls of the room are made of brick, plastered with cement mortar having a thickness of about 1 ft and painted with white distemper. Two big tables are there at the centre of the room (approx. area is 24 ft^2). Five big tables are put adjacent to a wall. Tabletop surface area of each table is around 15 ft^2 . There is a metallic almirah of surface area around 12 ft^2 attached with each table. Besides a wall, five wooden board computer tables (approx. area 6 ft^2) are there. Thickness of the tabletop of each table is 2 cm. Two steel almirahs of total surface are around 30 ft^2 are there adjacent to a wall. Ten chairs with foam and Rexene covers are there each chair having a surface area of around 6 ft^2 (sitting and back). The absorption coefficient of all these objects was calculated and its effect is discussed in the coming sections.

3.2 Measurements

See Fig. 1.

4 Experimental Setup

See Figs. 2, 3, and 4.

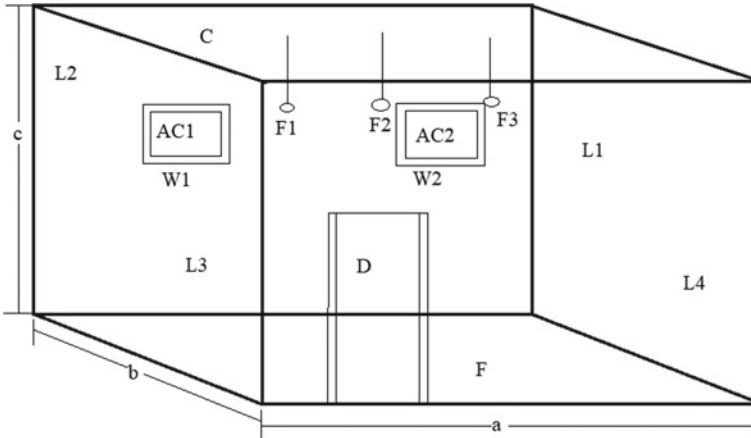


Fig. 1 Layout of the room; $a = 7.92$ m; $b = 6.4$ m; $c = 4.88$ m; F1, F2, F3 = Fans; C = Ceiling; F = Floor; W1, W2 = Windows; AC1, AC2 = Air conditioners; D = Door; L1, L2, L3, L4 = Walls



Fig. 2 Picture of the room under study

5 Background Noise and Noise Criterion

Measurements were taken at six different points under four different conditions: ACs and fans ON (S1), ACs ON and fans OFF (S2), ACs OFF and fans ON (S3) and ACs and fans OFF (S4).

One of the basic parameters that affects the acoustical comfort in a place where speech-related activities are performed such as classrooms and meeting rooms is Background Noise (BN). Many countries such as the USA, the UK, France, Germany

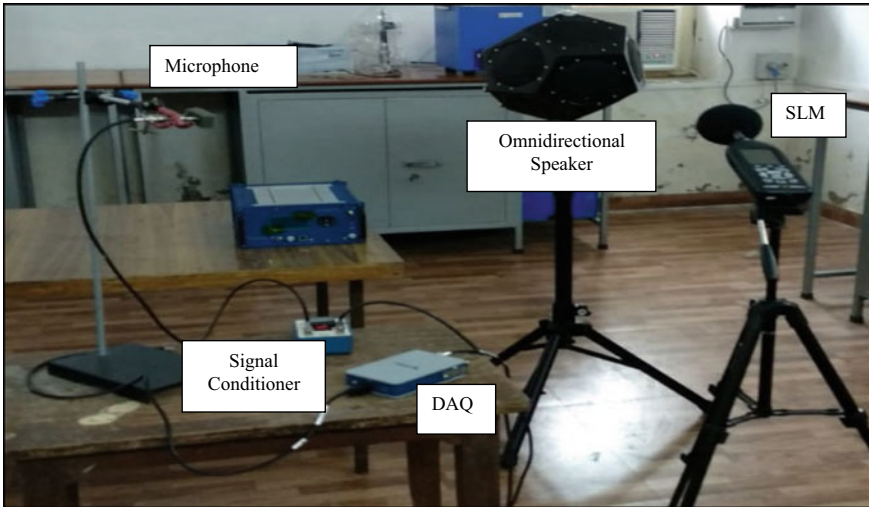


Fig. 3 Instruments used for measuring monophonic parameters from impulse response



Fig. 4 Instrument used for measuring absorption

and Brazil have set some recommendations to limit the Background. Limiting background noise level in India is 55 dB during the day and 45 dB during the night (according to the Indian standard NBC 2005). Background noise was measured using a sound level meter (Larson and Davis Soundtrack LxT1) at six different locations in the room and Noise Criterion was established using the same data.

Room under study is situated inside the premises and is not adjacent to the main road. A major source of noise is traffic noise from the road. The maximum and

Table 1 Maximum and average sound level at noisiest proximity

L _{Amax} (dBA)	L _{Aeq} (dBA)
75.2	66.4

average noise levels were measured in the noisiest proximity shown in Table 1 and background noise in different situations is shown in Table. It can be seen that the surrounding of the building is not very noisy as it is situated inside the university campus and far away from the main highway.

6 Monophonic and 1/3 Octave Band filtered Parameters

To measure the monophonic parameters (listed in Table 2), a two-channel SDG 1032X (SIGLENT) waveform generator has been used, which generates a Gaussian white noise signal to a BAS-001 (Larson and Davis) power amplifier connected to the sound source. A dodecahedral omnidirectional sound source was used. The generated sound was captured by a random incidence microphone (PCB PIEZOTRONICS) connected to the NI 9215 DAQ Assistant via a signal conditioner (refer to Figs. 2, 3 and 4), and the flow diagram for the connection is shown in Fig. 5. The impulse response was acquired using LabVIEW. MATLAB codes were then used to calculate different parameters. The measurements were taken following the specifications of the ISO 3382 standard [13].

Before the calculations of EDT and RT60, the Impulse Response was band-filtered in 1/3 Octave Bands with centre frequencies (f_c) ranging from 125 Hz to 8 kHz. Measurements were taken at six different points in each classroom under four different conditions: ACs and fans ON (S1), ACs ON and fans OFF (S2), ACs OFF and fans ON (S3) and ACs and fans OFF (S4).

Table 2 NC and BN for different situations in the room

Situation	NC	Leq (dBA)
S1	63	67.7
S2	60	63.4
S3	60.2	64.7
S4	30.6	41.5

[Signal Generator → Amplifier → Speaker]

[Microphone → Signal Conditioner → DAQ meter → Laptop]

Fig. 5 Flow diagram for connection

7 Built-Material Characterization

Our industrialized Society includes many harmful sources of noise. Noise pollution from these sources can be minimized with the help of the absorption of sound energy. It is important to characterize the built materials inside the buildings/rooms. Various materials inside a space have the tendency to absorb or attenuate the sound [14,15]. Absorption tendency affects the acoustical parameters and speech intelligibility in spaces [16,17]. These materials have to be pointed out and characterized accordingly [18,19]. Absorbers made from different materials are used to attenuate sound in many applications. If we need to attenuate noise and want to manufacture some sound absorbers or even if we need to know the absorption of the different objects in any space (which is the case now), then it is necessary to know the acoustical properties of those materials used in manufacturing the absorbers.

To calculate the absorption of built materials and other objects present in the room, a new in situ method was applied using Microflown in situ absorption probe (see Fig. 6) which can give the absorption in minutes without any destructive techniques.

7.1 Working of Absorption Probe

A spherical speaker generates the sound, and sensors are placed at a fixed distance (23 cm) from the speaker. The system is designed in such a way that it decouples the sensors from structure-borne vibrations. Pressure and velocity are measured directly

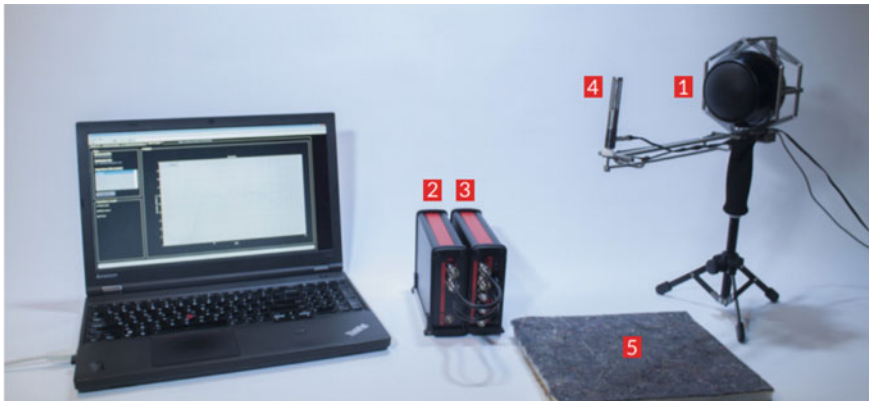


Fig. 6 (1) Impedance Gun: sound source. (2) Scout | Data Acquisition: Highly accurate 24-bit, 4-channel data acquisition. (3) MFPA-2 | Signal Conditioner. (4) PU Sensor Broadband PU probe: Having two sensors one for pressure and the other one for particle velocity. (5) Sample: minimum size of the sample should be 30×30 cm

on the surface of the sample material to be tested. Absorption and reflection coefficient can be deduced from the measured impedance which is the complex ratio of pressure and velocity [20].

7.2 Features of Microflown In Situ Absorption Probe [20]

Range of Frequency: Works for a wide range of frequencies starting from 300 Hz to 10 kHz.

- Mode of Operation: This method is truly in situ and gives results in a few minutes.
- Parameters that can be measured:
 - i Impedance
 - ii Sound reflection coefficient
 - iii Sound absorption coefficient.
- Non-destructive Method: This method is non-destructive in nature, and there is no specific requirement related to the shape and size of the sample to be tested.
- Incident Angles: This probe works on normal as well as oblique incident angles also and gives suitable results in all the situations.
- Nature of Surfaces of the Sample: It can work on plane and curved surfaces as well.
- Requirement of Material to be Tested: It works for both homogeneous and inhomogeneous materials (e.g. jetliners) as it measures the pressure and particle velocity directly on the surface of the material.

8 Results and Discussion

8.1 Background Noise and Noise Criterion

The values of A-weighted background noise levels (L_{eq}) and the corresponding noise criterion (NC) for the four situations S1, S2, S3 and S4 are listed in Table. Each value was obtained by using the SLM and recording the data for 20 s. It was observed that L_{eq} s for all cases except S4 were much higher than the recommended values. This was due to the noise coming from the fans and air conditioners. On the other hand, L_{eq} for S4 was well tolerable; hence the room seems to be well insulated from outside noise. This implies that the room is ideal for listening when there are no electronic equipment operating in it, however, this is only possible in winters when there is no need for cooling. Under the conditions of fans and ACs operating, it becomes essential to provide sound insulation inside the lab so that the noise levels could be minimized. A-weighted background noise levels (L_{eq}) were measured for different locations of the room also, as shown in Fig. 7. It can be concluded from the chart

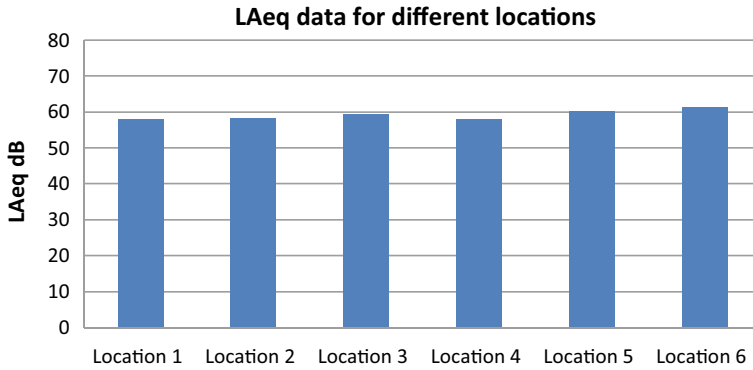


Fig. 7 Equivalent sound level at different locations

that there are no significant changes in noise with reference to the locations inside the room. The reason for this uniformity is that the room has a simple cuboid shape, and there are many similarities in the room with respect to the interiors and object placement. Major reflecting surfaces are floor tiles and walls, which has an almost similar effect at every location. The NC curve for S1 is shown in Fig. 8. Similar NC curves were used to calculate NCs for the other three situations. Noise criterion is only found suitable for S4 implying that the relative noise levels for the octave frequencies are much higher than acceptable values for S1, S2 and S3. Unacceptable NC may create fatigue and negatively affect productivity and the ability to communicate.

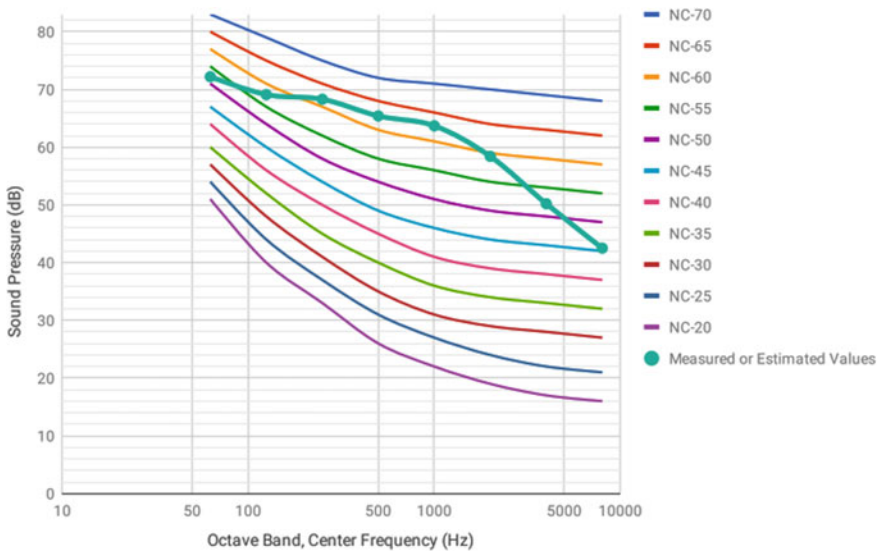


Fig. 8 NC curve for measured data in situation S1

8.2 Built-Material Characterization

Absorption tendencies of all the objects and built material present in the room were measured using in situ absorption probe, and it was established that most of the surfaces and objects in the room are reflecting in nature (see Fig. 9). The absorption coefficient of floor tiles and the wall is very low and comprises most of the surface area. It is one of the main reasons for the poor acoustics of the room and deviation from the standard reverberation time. Some objects' material have good absorption tendencies, but their surface area is very low in comparison to other reflecting surfaces so it doesn't create any noticeable effect on the overall absorption of the room (see Table 3).

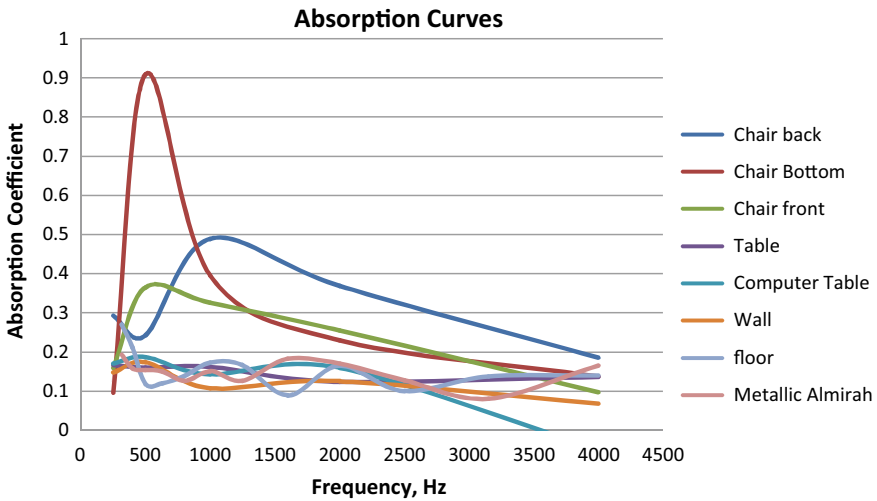


Fig. 9 Absorption coefficient versus frequency

Table 3 Absorption of different objects in the room

S. No	Description	Surface area (approx.) m ²	Fraction of total room surface area (%)	Absorption coefficient
1	Chair back	1.8	<1	0.36628
2	Chair bottom	1.8	<1	0.51103
3	Chair front	1.8	<1	0.314844
4	Table	6.5	2.7	0.148255
5	Computer table	3.2	1.3	0.162615
6	Wall	176	73.3	0.13524
7	Floor tiles	50	20.8	0.163919
8	Metallic Almirah	8.1	3.3	0.135983

The mismatch between Sabine's RT and the calculated RTs may be due to the presence of experimental equipment, apparatus, tables and other furniture in the room. These equipment and objects in the room, to some extent and for some frequencies (see Fig. 9), provide absorbing surfaces also which result in the lowering of RT. It can thus be inferred that even though there is no acoustical treatment in the room, the presence of the above-said stuff acts as a sound absorber and makes the room suitable for hearing lectures (it can be seen in Fig. 9 that in mid-frequencies, some materials acts as good absorbers).

Built material of the spaces and specific geometries has the tendencies to absorb and attenuate sound. The presence of occupants and various objects inside a space can change the overall absorption of that environment. These aspects should be considered before designing the space and information should be utilized for enhancing the acoustics of a space.

8.3 Monophonic and 1/3 Octave Band-filtered Parameters

According to the Indian standard IS: 2526–1963, the recommended reverberation time for speech category rooms of size comparable to the one under study is about 0.9 s. Sabine's relation yields RT_{60} for the room to be 2.5 s, which is due to poor or no acoustical treatment on surfaces of the room, and the absorption coefficients are lower due to the presence of mostly reflecting surfaces (as discussed in sec 0). Speech Intelligibility also got hampered by background noise which is increased by high reverberation time.

Summary of RT_{60} and EDT measured in six locations at frequencies ranging from 125 Hz to 8 kHz is shown in Table. The decibel drop (shown in Figs. 10 and 11), RT and EDT were calculated using Schroeder's model. EDT was calculated using the slope up to 10 dB drop, while RT_{60} was calculated using slope between 15 and 35 dB drop. RT was found high at lower frequencies for all the six locations (shown in Fig. 12) in the room. It indicates that the absorption of low-frequency sound is also low. Larger values of EDT than RT indicate lower clarity of sound and low speech intelligibility [21]. RT_{60} was in compliance with the Indian standard for the medium frequency range (500–2000 Hz). For other centre frequencies, the RT was much higher which indicated poor sound absorption at both low and high frequencies (as discussed in sec 0). However, human ears are more sensitive in the medium frequency range, thus the reverberation characteristics of the room are suitable for hearing (Fig. 13).

From Figs. 10 and 11, it is observed that Schroeder's model is more applicable at mid- to high frequencies as the decay curves are smoother at these frequencies and follow the characteristics of Schroeder's curve as well. This implies that the results obtained at these frequencies are more reliable. However, the values of results at other frequencies are close to these values, therefore all the measured values are accurate, and the methods used in experimentation are reliable. The fluctuation in

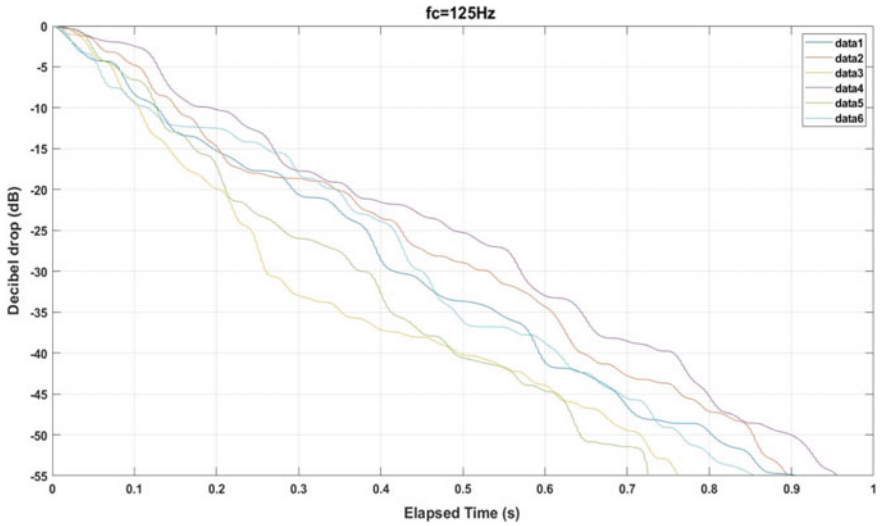


Fig. 10 Decibel drop at $f_c = 125$ Hz

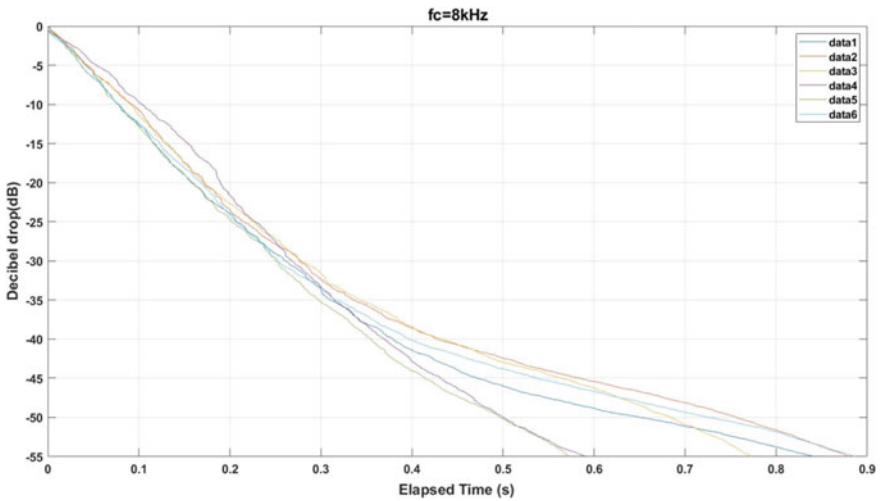


Fig. 11 Decibel drop at $f_c = 8000$ Hz

the decay curves at lower frequencies is due to poor absorption and scattering of low-frequency sound.

The average values of R , C_{50} and D_{50} (see Table 4) are much beyond the tolerance bounds [22]. Thus, the room is unsuitable for musical events as a larger value of C_{50} provides music a sensation of definition (D_{50}), while its decrement adds ‘tone-fullness’ [5]. In concert halls, a lower value of definition is preferred, but the average

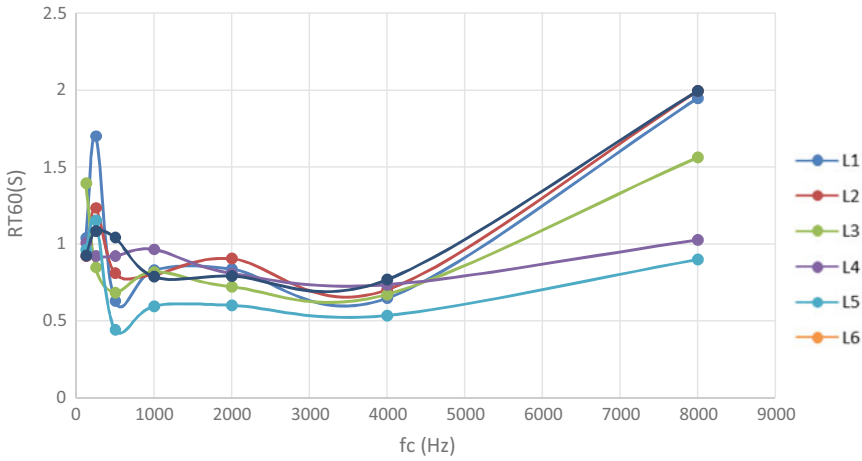


Fig. 12 Reverberation time versus centre frequency for different locations

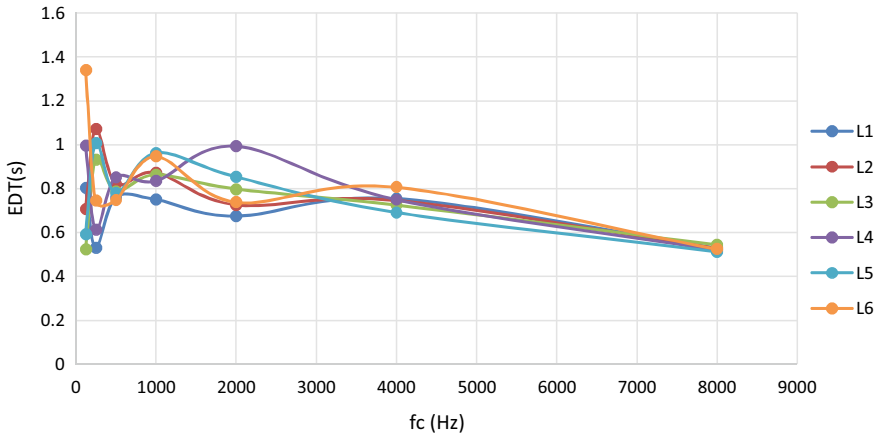


Fig. 13 Early decay time versus centre frequency for different locations

Table 4 Various parameters at different locations

Location	Unfiltered EDT60(s)	Unfiltered RT60(s)	R	C50 (dB)	D50	STI	%ALcons
L1	2.18	0.83	20.69	-21.88	0.112	0.7148	3.5465
L2	2.12	0.76	23.41	-24.33	0.087	0.7152	3.5386
L3	2.24	0.78	21.58	-22.68	0.103	0.7683	2.6535
L4	2.82	0.92	23.64	-24.54	0.086	0.7644	2.7106
L5	1.5	0.67	22.4	-23.41	0.087	0.9008	1.2947
L6	2.56	0.82	22.31	-23.33	0.097	0.7161	3.5212
Average	2.24	0.79	22.34	-23.36	0.095	0.7633	2.8772

measured D_{50} is even lower than the desired value [23]. Furthermore, high values of EDT are preferable for concert halls while the trend is reversed after 2 s, this again makes the room unsuitable for music as most of the values of EDT are greater than 2 s. The STI of the room has an average value of 0.76 which implies that the speech intelligibility of the room is quite good. Even though the D_{50} was very less, the measured STI was within a good range of intelligibility; this is due to the high value of signal-to-noise ratio ($SNR = 55$ dB) which directly influences the value of STI. It is to be noticed that SNR alone is not a measure of STI; it is also affected by band-filtered RTs and modulation frequencies. In the current study, the combination of the measured RTs and STI indicates good quality of sound and intelligibility but inappropriate clarity. It can thus be inferred that the room is suitable to be used as a classroom or a laboratory but unsuitable for musical purposes.

9 Conclusions

Background noise was found in acceptable limit only when AC and fans are OFF and windows are closed, but it is not possible in summers when opening the windows is cost-effective measure for natural ventilation. Some corrective measures should be taken to check this because depending on the level of noise, it can adversely affect the occupants of the built space. Therefore, it is necessary to first identify the various internal and external noise sources and then to characterize them. Noise or sound source characterization is the first step in the acoustical design of a built space. Corrective measures should be taken in the early designing phase.

Most of the objects and surfaces in the room were found reflective and only some small objects were found to have good absorption, but this result of obtaining absorption of various objects can be utilized in designing the interiors of the room. Built material of the spaces and specific geometries have the tendencies to absorb and attenuate sound. The presence of occupants and various objects inside a space can change the overall absorption of that environment. These aspects should be considered before designing the space and information should be utilized for enhancing the acoustics of a space.

The combination of the measured RTs and STI indicates good quality of sound and intelligibility but inappropriate clarity. It can thus be inferred that the room is suitable to be used as a classroom or a laboratory but unsuitable for musical purposes. Good room acoustics criteria include sufficient loudness, reverberance, clarity, uniformity, echo-free sound and minimal background noise. Thus, the optimum acoustic quality is a balance between clarity (requires short RT), sound strength (requires high RT) and vivacity (requires long RT).

Acknowledgements This work is a part of project (ECR/2016/002030) funded by DST-SERB. The author is thankful to the organization for funding this research work.

References

1. Milner JR, Bernhard RJ, Herrick RW (1989) An investigation of the modal characteristics of nonrectangular reverberation rooms. *J Acoust Soc Am* 85(2):772–779. <https://doi.org/10.1121/1.397549>
2. Soulodre GA, Bradley JS (1995) Subjective evaluation of new room acoustic measures. *J Acoust Soc Am* 98(1):294–301. <https://doi.org/10.1121/1.413735>
3. Hodgson M (1999) Experimental investigation of the acoustical characteristics of university classrooms. *J Acoust Soc Am* 106(4):1810–1819. <https://doi.org/10.1121/1.427931>
4. Cirillo E, Martellotta F (2003) Acoustics of Apulian-Romanesque churches: correlations between architectural and acoustic parameters. *Build Acoust* 10(1):55–76. <https://doi.org/10.1260/135101003765184816>
5. Knüttel T, Witew IB, Vorländer M (2013) Influence of ‘omnidirectional’ loudspeaker directivity on measured room impulse responses. *J Acoust Soc Am* 134(5):3654–3662. <https://doi.org/10.1121/1.4824334>
6. Scannell L, Hodgson M, García Moreno Villarreal J, Gifford R (2014) The role of acoustics in the perceived suitability of, and well-being in, informal learning spaces. *Environ Behav* 48(6):769–795. <https://doi.org/10.1177/0013916514567127>
7. Alam SF, Rafat Y, Bilgrami H (2017) Acoustical analysis of Aligarh Muslim University’s central auditorium, p 015021. <https://doi.org/10.1121/2.0000438>
8. Pelegrín-García D, Smits B, Brunskog J, Jeong C-H (2011) Vocal effort with changing talker-to-listener distance in different acoustic environments. *J Acoust Soc Am* 129(4):1981–1990. <https://doi.org/10.1121/1.3552881>
9. Pelegrín-García D, Brunskog J (2012) Speakers’ comfort and voice level variation in classrooms: laboratory research. *J Acoust Soc Am* 132(1):249–260. <https://doi.org/10.1121/1.4728212>
10. Zannin PHT, Marcon CR (2007) Objective and subjective evaluation of the acoustic comfort in classrooms. *Appl Ergon* 38(5):675–680. <https://doi.org/10.1016/j.apergo.2006.10.001>
11. Lyberg-åhlander V, Rydell R, Löfqvist A, Pelegrin-García D, Brunskog J (2015) Teachers ‘voice use in teaching environment. Aspects on speakers’ comfort. *Energy Proc* 78:3090–3095. <https://doi.org/10.1016/j.egypro.2015.11.762>
12. Abdou A, Guy RW (1996) Spatial information of sound fields for room-acoustics evaluation and diagnosis. *J Acoust Soc Am* 100(5):3215–3226. <https://doi.org/10.1121/1.417205>
13. Goydke H (1997) New international standards for building and room acoustics. *Appl Acoust* 52(3–4):185–196. [https://doi.org/10.1016/s0003-682x\(97\)00045-5](https://doi.org/10.1016/s0003-682x(97)00045-5)
14. Deželak F, Čurović L, Čudina M (2016) Determination of the sound energy level of a gunshot and its applications in room acoustics. *Appl Acoust* 105:99–109. <https://doi.org/10.1016/j.apacoust.2015.12.001>
15. Galbrun L, Scerri L (2017) Sound insulation of lightweight extensive green roofs. *Build Environ* 116:130–139. <https://doi.org/10.1016/j.buildenv.2017.02.008>
16. Scheck J, Gibbs B (2015) Impacted lightweight stairs as structure-borne sound sources. *Appl Acoust* 90:9–20. <https://doi.org/10.1016/j.apacoust.2014.09.012>
17. W. B.-S. A. VIBRATION and undefined 2015, Impact insulation data for solid-joist floor-ceiling construction
18. Del Rey R, Alba J, Ramis J, Sanchís VJ (2011) New absorbent acoustic materials from plastic bottle remnants, *materconstrucc.revistas.csic.es*
19. Bravo T, Maury C, Pinhède C (2013) Enhancing sound absorption and transmission through flexible multi-layer micro-perforated structures. *J Acoust Soc Am* 134(5):3663–3673. <https://doi.org/10.1121/1.4821215>
20. In-situ Absorption testing—Microflown. <https://www.microflown.com/products/acoustic-material-testing/in-situ-absorption>. Accessed 18-Sept 2020
21. Portuguese Theatres and Concert Halls Acoustics | Sound | Reflection (Physics). <https://www.scribd.com/document/424729722/Portugese-Opera-Houses>. Accessed 17 Sept 2020

22. Steeneken HJM, Houtgast T (1978) A physical method for measuring the quality of speech communication channels. *J Acoust Soc Am* 63(S1):S79–S80. <https://doi.org/10.1121/1.2016836>
23. Jordan VL (1981) A group of objective acoustical criteria for concert halls. *Appl Acoust* 14(4):253–266. [https://doi.org/10.1016/0003-682X\(81\)90021-9](https://doi.org/10.1016/0003-682X(81)90021-9)

Fault Detection and Condition Monitoring

A Comparative Study on Mathematical Approaches to Determine the Time Lag and Synchrony Between Two Time-Series Data in Different Engineering Applications



N. Abinson Paul, Rajakumar S. Rai, and S. J. Vijay

Abstract Time-delay estimation (TDE) and determining synchrony between two time-series signals are important aspects to analyze complex mechanical engineering systems. Time-delay estimation has been a research subject in numerous fields such as radar, sonar, seismology, geophysics, ultra-sonics, sans hands correspondences, and so on. The different mathematical approaches discussed here include finding the variance and standard deviation for distinguishing and limiting the data available at the array of sensors. This research work audits the latest mathematical approaches for time-delay estimation and defining synchrony between both periodic and non-periodic data signals. Specifically, calculations carried out incorporate the summed up cross-correlation calculation, the multichannel cross-relationship calculation, dynamic time wrapping, and proof method-based calculations. Moreover, their relations, differences in impact of various parameters considered for obtaining time delay to each other, and enhancements are also stated in an analytical approach.

Keywords Time delay · Time series · Synchrony

1 Introduction

Time-delay estimation and determining synchrony between two time-series data are challenging research fields and find applications in different domains of science and technology [1]. As far as data mining is concerned, there are several application domains with time-series data. The OECD glossary of statistical terms [2] defines a

N. A. Paul (✉) · R. S. Rai · S. J. Vijay
Department of Mechanical Engineering, Karunya Institute of Technology and Sciences,
Coimbatore, Tamilnadu 641114, India

R. S. Rai
e-mail: rajakumars@karunya.edu

S. J. Vijay
e-mail: vijayjoseph@karunya.edu

time series as “A time series is a set of regular time-ordered observations of a quantitative characteristic of an individual or collective phenomenon taken at successive, in most cases equidistant, periods/points of time.”

To analyze complex engineering systems, it is necessary to differentiate the data provided by two similar sensors. Sensors provide signals that convey data. Depending on the type of signal available, different mathematical methods are used to process the data to obtain the time delay between the signals and to establish different means of synchrony between the signals. Time-series analysis is widely used for signal processing, forecasting, econometrics, pattern recognition, statistics, earthquake prediction, mathematical finance, electroencephalography (EEG), weather forecasting, communications engineering, control engineering, astronomy, and various domains of applied science and engineering in which temporal measurements are involved [3].

2 Delay Estimation Methods

2.1 A Gradient Method

Gradient methods on TDE depend on adding the delay by a vector which depends on the cost function that is to be minimized. The cost function is defined in such a way that it defines the synchrony between two signals. The gradient algorithm normally involves expanding second-order Taylor’s series around the estimated delay. Gradient algorithms are generally defined based on Gauss–Newton and least mean squares method (LMS) [4–6].

A gradient approach called distance method finds an accuracy of less than 5% in the time-delay estimation of non-periodic data analysis of solar heating circuit. The Euclidean distance is calculated by analyzing the temperature courses on two temperature sensors placed in a solar circuit. A defined sector of the temperature curve (Ti^{S1}) from the first sensor is being cut out by selecting $\pm m$ (number of elements chosen to define the sector) measured values from a chosen point in time, about which flow rate is to be determined. The sector is shifted by time shift (t lag) positions across the second temperature curve (Ti^{S2}). For each of these offsets, mathematical distance k (t lag) is calculated using Euclidean metric represented by the equation:

$$k(t \text{ lag}) = \frac{1}{\text{sqrt}(2m + 1)} * \text{sqrt} \sum_{i=-m}^{+m} \left((Ti^{S1}(t - t \text{ lag}) - Ti^{S2}(t))^2 \right)$$

The factor $(2m + 1)^{-0.5}$ is a normalizing factor for k , which depends on the size of the number of elements chosen to define the sector ($\pm m$). The time shift (t lag) will be equivalent to the occurrence of an index position of minimum value of k

(t lag). This “k(t lag)” can be used to determine the fluid running time in the solar heating system [7–9]. The gradient method has the advantage that it can be used for determining time delay of both periodic and non-periodic data for a certain extent accurately depending on the signal available where other methods fail to give suitable inferences.

2.2 Cross Correlation

Coupled oscillator models are useful to determine the time delay of periodic signals occurring in many natural phenomena such as a laser system [10], a living system with plasmodium of *Phys arum polycephalic* [11], cardiorespiratory system [12], and neuronal populations [13–15]. Coupled oscillator models are analyzed in multivariate data [16] by instantaneous phase synchronization methods [17]. Delay estimation can be achieved to a good extent using the synchronization matrix since signals are periodic and of the same characteristics. If synchrony is far away, this method fails to determine the time shift. Finding the synchronization matrix forms the basis of the famous dynamic time wrapping methods for time-delay estimation.

The most discussed method in time-delay estimation is the cross-correlation function, which can be defined in different mathematical ways. It gives the similarity measure of the first signal with the second signal, depending on the defined cross-correlation function. Either one of the signals is fixed or the other signal is allowed to move as a sliding window to compute the summed up cross-correlation function. The delay is obtained where the similarity measure is maximum [18, 19]. Cross correlation is the most popular and widely used method in analyzing pattern recognition, probability, and statistics in various signal processing domains.

2.3 Neural Network for Time Delay Estimation

In recent years, advancement in many machine learning techniques such as artificial neural networks, supervised learning techniques, regression and classification can be implemented in the time-delay estimation problems.

Time-delay determination using neural networks is a promising approach. Artificial neural networks are trained by noisy signal, filtered signal, and delayed signal. Accurate time-delay estimates are possible through neural networks. Classical techniques of obtaining cross correlation between two signals use a method to find the correlation function by looking for the common occurrence of peaks and valleys in the signal. The positions of occurrence of peaks and valleys are used to determine the time delay between the signal. The computational effort to perform correlation is demanding when handling huge data [20, 21]. These two steps of computation of classical approaches can be replaced by a single pass of the neural network feedforward structure [22]. A direct approach and an indirect approach can be defined for

modeling of the neural network. The direct method for time-delay estimation employs a neural network-based time-delay estimator to identify the delay directly. On the other hand, the indirect approach employs a neural network model with time delay as an online nonlinear programming procedure [23]. While using neural networks, a supervised estimation time delay can be obtained as the output of a previously trained neural network which has the input of two signals as two vectors. The neural network modeled for determining a delay between two signals should be capable of system identification and interpolation of an ideal response represented by the occurrence of peaks and valleys, observed at the correct time delay with minimized errors [24].

2.4 Delay Estimation by Model Fitting

Time-delay estimation problems regarding different kinds of periodic signals can be analyzed in a way similar to analyzing sinusoidal waveforms. This method uses fast Fourier transforms (FFT) for model fitting. Reconstruction of the first time series is carried out by numerically trying to fit estimated phase derivatives of first and second series of data by a coupling function for different values of the time shift. Available data is used to create a model fitting with a probe function in the form of Fourier transforms. The method is widely used in nondestructive testing, Global Navigation Satellite Systems (GNSS), wireless communications, and instruments that use sonar methods. Algorithms using Fourier transforms search for known signal shapes. Since the sensors receiving a superimposition of an attenuated and delayed replica of a known signal with noise happens during the transformation of data, the occurrence of similar shapes can be identified and used for determining the time delay between signals.

The most common method for FFT is the matched filter approach [25]. In this algorithm, the width of the signal is matched by an autocorrelation function. If the width of the signal is good, this method is suitable. But there is a practical difficulty in increasing the width of the signal while transmitting data. As a remedy to this problem, recent developments are the estimation of high-resolution sinusoidal frequency and techniques like the Direction of Arrival (DOA) estimation [26]. Time-delay estimation can be done in both the time domain and frequency domain. The frequency domain is found to be more suitable for this approach.

For the general problem formulation, the received signal in one sensor is defined as follows:

$$y(t) = \sum_{l=1}^L (a_l s(t - d + e(t))), 0 \leq t \leq T$$

$S(t), 0 \leq t \leq T$ signifies the known transmitted signal (real valued or complex), $y(t)$ represents the received signal, having L replicas of $S(t)$, gain of (a_l) delay (d), and $e(t)$ is the noise.

2.5 *Weighted Fourier Transform and Relaxation (WRELAX) Algorithm*

Weighted Fourier transform uses the principle of minimizing nonlinear least squares (NLS) criterion and maximum likelihood approach [27]. Sometimes the defined cost function has a complicated multimodal shape in the time domain, making it very difficult to estimate the local minimum. To overcome these difficulties, a relaxation-based optimization algorithm (WRELAX) is used to obtain the NLS parameter estimates. After applying the relaxation criteria, the Euclidean norm can be computed and the location of the dominant peak can be computed using fast Fourier transform [28]. The WRELAX algorithm decouples the multidimensional matched filters with that of one-dimensional matched filter.

The EM algorithm is similar to WRELAX algorithm [29], which converts the multidimensional optimization problem into a series of a one-dimensional optimization problem. The algorithm decomposes the available data into its signal component and estimates separately the parameters of each signal component.

Time-delay estimation techniques for automatic control applications in the industry including open-loop and closed-loop systems [30, 31] can be implemented. One of the successful implementations of the TDE method is inferencing the turbulent fields (such as density, velocity, and temperature) at the locations of a last cost flux surface. Current measurements of the turbulent velocity field are limited to the outer edges of the last closed flux surface (LCFS). Measurement of the turbulent velocity inside LCFS is possible in systems such as the international thermonuclear experimental reactors [32].

3 Measurement of Synchrony Between Two Time Series

3.1 *Pearson Correlation*

Pearson correlation coefficient which is referred to as “Pearson’s r ” is the ratio of covariance of two random signals to the standard deviation of two signals. The correlation coefficient obtained after computation gives a linear relationship between two time-series data on the scale of -1 to $+1$. Correlation coefficients describe the strength and direction of the association between the variables. Correlation fails to specify nonmonotonic or nonlinear relationships. Hypothesis tests are carried out to test the null hypothesis. This helps to determine the confidence intervals, where it is feasible to find whether a correlation is possible or not for the available data. In a broader aspect, the Pearson correlation gives a simple method to compute synchrony between time-series data of different kinds. But it fails to provide insights into data signals and as which event occurs first, which is to be computed using another correlation method [33–36].

3.2 *Time Lagged Cross Correlation*

Time lagged cross correlation (TLCC) can determine the directionality between two events as a leader–follower relationship, in which the leader initiates an event that is being observed by the second signal with signal transmitting losses. There are different methods available to identify the correlation between two signals which include regression and Granger causality. One way of obtaining a correlation between two signals is by Granger causality. It uses forecasting techniques as regression methods, to find mere correlations. TLCC is measured by transferring one time-series data signal and repeatedly calculating the correlation between the first and second signal. When peak correlation is obtained, it is concluded that maximum synchrony is established between two signals. The widely used algorithms are detrended moving average cross-correlation analysis and detrended cross-correlation analysis (DCCA). A time-lagged DCCA cross-correlation coefficient quantifies the level of time-lagged cross correlation between two non-stationary time series. The detrended covariance is calculated as a lagged convolution and can be useful to obtain a delay between time-series data. This analytical approach is suitable in the fields of physiology, geology, ethnology, economics, and other related fields [37–40].

Another extension of TLCC to analyze more fine-grained dynamics in the two signals is windowed time-lagged cross correlations (WTLCC). In this method, the time-lagged cross correlations in multiple moving windows of the signal are repeated continuously. So, each window can be defined and analyzed separately comparing the difference between leader–follower interaction of the signals [41, 42].

3.3 *Dynamic Time Warping*

In the analysis of time-series data, dynamic time warping (DTW) is one of the algorithms used in measuring the similarity between two signals. DTW finds application in speech recognition and pattern matching. This method calculates an optimal match between two temporal sequences. The two sequences are warped non-linearly in the time dimension to obtain the similarity measure. The optimal warping path is computed by considering the principle of continuity and monotonicity. DTW computes the Euclidean distance at each frame across every other frame to determine the minimum path that will closely match the two signals. In classical DTW, the accumulated cost matrix is computed and from that the optimum warping path is computed by considering the condition of continuity and monotonicity. In multiscale DTW, one can make use of data-dependent constraint regions. DTW can be used to compare data with different window lengths. From one signal, we can select a greater number of points and from the other signal, we can choose a fewer number points to determine the delay [43, 44].

3.4 Peak Synchronization

Peaks are corresponding to events in a signal especially in the study of dynamic systems. Considering time-series analysis of two signals, the occurrence of peaks and valleys with mutual correspondence may lead to establishing synchrony between the two signals. By selecting a window from two signals, the most prominent feature to obtain mutual dependence is identified. To achieve peak synchronization, first detect successful peaks, which can be compared to obtain useful events in the time-series data. One common method is to obtain local maxima in the chosen window. Window threshold techniques like Hilbert transform and pattern matching can be used as the means to identify the peaks. A density function is then defined to compare the identified peaks. Suitable peak synchronization measures were found using the Gaussian function between the two signals [45–49]. Using this approach periodic wave forms such as sinusoidal wave forms can be analyzed effectively.

3.5 Synchronization Using Cumulative Signals

It is possible to estimate the time delay after finding synchronization points between the time series. This method is based on changing the input data into cumulative signals and turning points of the curves are found and the time delay is determined by the time difference of these points. In this approach, a window of data points is chosen, which contains appropriate data points that will enable time delay to be determined. The time interval of the window when the signal will permanently exceed a given threshold value can be determined. Time interval $T = N\Delta T$, where ΔT -sampling time and N is the total number of samples.

Next step is to convert the input signal $s(n)$ into the cumulative signal as follows:

$$S_c(n) = \sum_{(i=0)}^n S(i), n = 1, \dots, N$$

where N determines the time window in relation to the number of elements considered.

To determine the time of occurrence of a turning point, the following method is used (Fig. 1).

$$S_c(n) = \sum_{(i=0)}^n S(i), n = 1, \dots, N$$

Algorithm. The turning point of the cumulative signal is determined as the point of intersection of the signal S_c by a straight-line l , where l is defined based on (1) or (2).

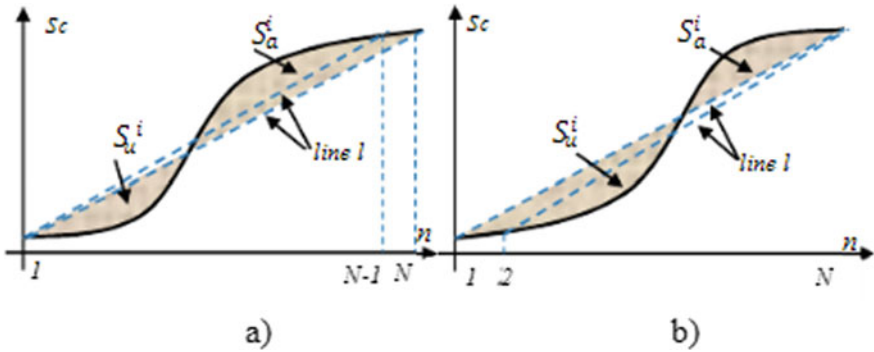


Fig. 1 Illustration of finding the infection point on comparison of the areas of S_u^i and S_a^i , determined by cumulative signal S_c and straight-line l using criteria (a) and (b)[50]

- (a) $\min(S_u^n - S_a^n), n = 1 \dots N$. When $S_u^1 \geq S_a^1$, where S_u^n, S_a^n is the area under and above the defined straight line and cumulative signal curve S_c , respectively, and the line l passes through the points $n, S_c(n)$ and $(N, S_c(N))$.
- (b) $\min(S_a^{N-n} - S_u^{N-n}), n = 1 \dots N$. When $S_u^1 < S_a^1$, where $(S_a^{N-n} - S_u^{N-n})$ is the area under and above the defined straight line and cumulative signal curve S_c , respectively. And l passes through the points $1, S_c(1)$, and $(N-n, S_c(N-n))$.

Applying the above algorithm to the two input signals separately, the delay can be obtained [50]. This new method finds applicability and gives an accuracy of less than 10% where conventional time-delay estimation method such as correlation fails due to absence of identifiable features in the window of data considered to determine time delay. Noisy signals are analyzed effectively with this approach since cumulative signals are considered for determining time delay.

4 Conclusion

A more detailed comparison of effective mathematical approaches for time-delay estimation is presented here. The selection of approach depends on the features that can be extracted from the data and compared with each other to establish a suitable synchrony which leads to time-delay estimation. The classical cross-correlation method and its modifications including weighing functions are the most popular methods for analyzing noised and periodic signals due to high accuracy and low computational complexity. Gradient approach gives better accuracy for time-delay estimation of non-periodic signals.

References

1. Azevedo JM, Almeida R, Almeida P (2012) Using data mining with time series data in short-term stocks prediction: a literature review. *Int J Intell Sci* 2:176–180
2. OECD, "Time Series," 2006. <http://stats.oecd.org/glossary/detail.asp?ID=2708>. Accessed 15 Jan 2020.
3. Kirlic A, Hasovic A (2018) A literature review on big data and time series. *Int J Sci Res Comput Sci Eng Inf Technol IJSRCSEIT* 3(1). ISSN: 2456–3307
4. Reklaitis GV, Ravindran A, Ragsdell KM (1983) *Engineering optimisation methods and applications*. Wiley
5. Smith JO, Friedlander B (1985) *IEEE Trans Aerosp Electron Syst* AES-21, 180
6. Pak HA, Li GQ (1992) *Trans ASME. J Dyn Syst Meas Control* 114, 714
7. Frank E, Krause M, Wiese F, Uecker M, Vajen K, Ackermann H (2001) Quasi-continuous flow rate determination based on analyzing temperature courses. In: *Proceedings of ISES Solar World Congress, Adelaide (AU)*, vol 26, pp 613–61
8. Kaufmann B, Boehringer V (1999) Kalibrierung des Volumensstroms bei thermischen solaranlagen durch Auswertung einer Temperaturflanke, Tagungsbericht, Symposium thermische Solarenergie, Staffelstein, pp 111–113
9. Frank E (2000) Untersuchungen zur Bestimmung von Kollektorkreis-Volumenstromen durch Auswertung von Temperaturverläufen, Examensarbeit, Philipps-Universität Marburg
10. Heil T et al (2001) *Phys Rev Lett* 86:795
11. Takamatsu TF, Endo I (2000) *Phys Rev Lett* 85, 2026
12. Keyl et al (2000) *Clin Sci* 99:113
13. Gerstner W (1996) *Phys Rev Lett* 76:1755
14. Brunel N, Hakim V (1999) *Neural Comput* 11:1621
15. Golomb D, Hansel D, Mato G (2001) In *neuro-informatics and neural modeling*. In: Moss F, Gielen S (eds) *Handbook of biological physics*, vol 4. Elsevier, Amsterdam, pp 887–968
16. Rosenblum MG et al (2001) In *neuro-informatics and neural modeling*. In: Moss F, Gielen S (eds) *Handbook of Biological Physics*, vol 4. Elsevier, Amsterdam, pp 279–321
17. Pikovsky A, Rosenblum M, Kurths J (2001) *Synchronization: a universal concept in nonlinear sciences*. Cambridge University Press, Cambridge, England
18. Billings SA (2013) *Nonlinear system identification: NARMAX methods in the time, frequency, and spatio-temporal domains*. Wiley. ISBN 978-1-118-53556-1
19. Wang C, Zhang L, Xie L, Yuan J (2018) Kernel cross-correlator. In: *The thirty-second AAAI conference on artificial intelligence*. Association for the Advancement of Artificial Intelligence, pp 4179–4186
20. Knapp CH, Carter GC (1976) The generalized correlation method for estimation of time delay. *IEEE Trans Acoust Speech Signal Process* ASSP-24(4):320–327
21. Carter GC (1987) Coherence and time-delay estimation. In: *Proceedings of the IEEE*, vol. 75, no. 2, pp. 236–255
22. Shaltaf S (2004) Neural-network-based time-delay estimation. *EURASIP J Appl Signal Process* 3:378–385c. Hindawi Publishing Corporation
23. Tan Y (2004) Time-varying time-delay estimation for nonlinear systems using neural networks. *Int J Appl Math Comput Sci* 14(1):63–68
24. Houegnigan L, Safari P, Nadeu C, Schaar M, Solé M (2017) Neural networks for high performance time-delay estimation and acoustic source localization. 137–146. <https://doi.org/10.5121/csit.2017.70114>, (2017)
25. Bell BM, Ewart TE (1986) Separating multipaths by global optimization of multidimensional matched filter. *IEEE Trans Acoust Speech Signal Process* 34(5):1029–1037
26. Karmanov VG (1977) *Programmation mathématique*. Editions Mir, Moscow
27. Wu R, Wang W, Jia Q (2012) FFT-based efficient algorithms for time delay estimation. <https://doi.org/10.5772/36242>
28. Li J, Stoica P (1996) Efficient mixed-spectrum estimation with applications to target feature extraction. *IEEE Trans Signal Process* 44(2):281–295

29. Stewart GW (1973) Introduction to matrix computations. Academic Press, Inc.
30. Feder M, Weinstein E (1988) Parameter estimation of superimposed signals using the EM algorithm. *IEEE Trans Acoust Speech Signal Process* 36(4):477–489
31. Bjorklund S, Ljung L (2003) A review of time-delay estimation techniques. In: Proceedings of the 42nd IEEE conference on decision and control Mad, Hawaii USA
32. Hollanda C, Tynan GR, McKee GR, Fonck RJ (2004) Investigation of the time-delay estimation method for turbulent velocity inference. *Rev Sci Instruments* 75:4278
33. Schober P, Boer C, Schwarte LA (2018) Correlation coefficients: appropriate use and interpretation. *Anesthesia-Analgnesia* 126:1763–1768
34. Galton F (1886) Regression towards mediocrity in hereditary stature. *J Anthropol Inst Great Britain Ireland* 15:246–263
35. Soper HE, Young AW, Cave BM, Lee A, Pearson K (1917) On the distribution of the correlation coefficient in small samples. Appendix ii to the papers of “student” and R. A. Fisher. A cooperative study. *Biometrika* 11:328–413
36. Devlin SJ, Gnanadesikan R, Kettenring JR (1975) Robust estimation and outlier detection with correlation coefficients. *Biometrika* 62:531–545
37. Wang F, Wang L, Chen Y (2017) Detecting PM2.5’s correlations between neighboring cities using a time-lagged cross-correlation coefficient. *Sci Rep* 7:10109
38. Du DK, Lee DI, Kwon BH, Kim K, Park JK (2015) Features of the detrended cross-correlation analysis in the time series between absorbable particulate matter and meteorological factors. *J Korean Phys Soc* 63:10–17
39. Singh NK, Borrok DM (2019) A Granger causality analysis of groundwater patterns over a half-century. *Sci Rep* 9:12828
40. Shen C (2014) Analysis of detrended time-lagged cross-correlation between two nonstationary time series. *Phys Lett A* 379:680–687
41. Schoenherr D, Paulick J, Strauss BM, Deisenhofer A-K, Schwartz B, Rubel JA et al (2019) Identification of movement synchrony: validation of windowed cross-lagged correlation and -regression with peak-picking algorithm. *PLoS ONE* 14(2)
42. Boker SM, Rotondo JL, Xu M, King K (2002) Windowed cross-correlation and peak picking for the analysis of variability in the association between behavioral time series. *Psychol Methods* 7:338–355
43. Chen X, Huang J, Wang Y, Tao C (2012) Incremental feedback learning methods for voice recognition based on DTW. In: Proceedings of international conference on modeling, identification and control
44. Lin YS, Ji CP (2010) Research on improved algorithm of DTW in speech recognition. In: Proceedings of the international conference on computer application and system modeling (ICCAS), Taiyuan, China
45. Müller M (2007) Dynamic time warping. Chapter 4 of *Information retrieval for music and motion*. Springer, Verlag, ISBN: 3540740473
46. Biswas R, Khamaru K, Majumdar KK (2014) A peak synchronization measure for multiple signals. *IEEE Trans Signal Process* 62:4390–4398
47. Pan J, Tompkins WJ (1985) A real-time QRS detection algorithm. *IEEE Trans Biomed Eng* BME 32(3):230–238
48. Benitez D, Gaydecki PA, Zaidi A, Fitzpatrick AP (2011) The use of the Hilbert transforms in ECG signal analysis. *Comput Biol Med* 31:399–406
49. Pieper M, Klein P (2012) Application, of simple, periodic homogenization techniques to non-linear heat conduction problems in non-periodic, porous media. *Heat Mass Transfer* 48:291–300
50. Mosorov V (2019) A cumulative-signals-based method for time delay estimation. *Measur Sci Rev* 12:61–63

Envelope Spectrum Analysis of Noisy Signal with Spectral Kurtosis to Diagnose Bearing Defect



Arvind Singh Tomar  and Pratesh Jayaswal

Abstract Rolling element bearing generates a complex vibration due to geometrical flaws, surface irregularities during production, faulty bearing used, and error in the associated component. These vibration signals are usually covered with background noise. This research paper has shown the extraction of fault feature frequency when the raw vibration signal is immersed with heavy noise and this can be achieved by applying kurtosis, spectral kurtosis, and bandpass filter before the envelope spectrum. Besides, this article has revealed several methods that can extract several frequency spectrum characteristics. In this paper, the vibration signal case study is discussed, and this vibration signal was immersed with heavy background noise. The envelope spectrum analysis fails to isolate the fault function from this signal and needs some advanced strategy to solve this kind of situation. Many researchers used the de-noising process as a pre-filter signal before enveloping. Also, de-noising has some drawbacks, like the loss of original features. The noise degrades the performance of signal-processing algorithms. Applying kurtosis, spectral kurtosis, and bandpass filter before the envelope spectrum is done to overcome these drawbacks. These frequency spectrum characteristics more efficiently serve a bearing health. For bearing diagnostics, envelope analysis is a useful vibration analysis tool. The frequency-domain characteristics allow for a quick assessment of a machine's health without the need for extensive diagnostics. The intermittent impacts of a defected bearing were collected using envelope analysis from the modulated signal. When the vibration signal is comparatively low in energy and "embedded" within additional vibration from the related part, it is still rational.

Keywords Frequency domain · Spectral kurtosis · REB · Vibration analysis

A. S. Tomar (✉) · P. Jayaswal

Department of Mechanical Engineering, Madhav Institute of Technology and Science, Gwalior, MP, India

1 Introduction

Rolling element bearing (REB) used in many applications in industry and the failure of REB may result in machinery breakdown [1, 2]. Therefore, fault investigation is necessary to avoid these types of bearing failure [2, 3]. Vibration data of bearing contains lots of information regarding fault and their location [4]. Vibration analysis is widely used in rolling part bearings to locate localized defects [5, 6]. In the presence of a defect, the periodic force impacts result from impulsivity at a fixed frequency and its frequency is calculated by the shaft speed, sampling frequency, and geometry of bearing [2–4]. Consequently, periodic impulses are critical state indicator of REBs, and the fault detection generally classifying the bearing characteristic frequencies (BCFs) by assuming the outer race is stationary in most cases [4, 5, 7].

This paper presents how to implement a rolling element bearing fault investigation. Also, this paper focuses on studying the noisy vibration signal from the associated component of the machine. The method described in this paper demonstrates how to implement envelope spectrum analysis besides with spectral kurtosis. Localized defect develops in bearing in various locations like a defect in the inner race (IR), in the outer race (OR), ball, also in cage [8]. The inner race defects systematic diagram presented in Fig. 1.

Different defect positions have different critical frequencies: The first is the ball pass frequency outer race (BPFO), which has the following formulae for the signature frequencies:

$$BPFO = \left\{ \frac{N}{2} \left[f_i \left(1 - \frac{d \cos \alpha}{PD} \right) \right] \right\} \tag{1}$$

Other critical frequencies expressing various defect positions: second is ball pass frequency inner race (BPFI), third is fundamental train frequency (FTF), and fourth is ball spin frequency (BSF). The formulae for those characteristic frequencies are as follows [9]:

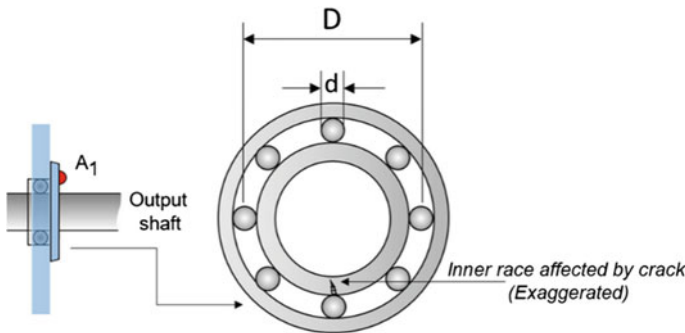


Fig. 1 Bearing with inner race affected by crack

$$BPFI = \left\{ \frac{N}{2} \left[f_i \left(1 + \frac{d \cos \alpha}{PD} \right) \right] \right\} \quad (2)$$

$$FTF = f_g = \frac{1}{2} \left[f_i \left(1 - \frac{d \cos \alpha}{PD} \right) \right] \quad (3)$$

$$BSF = f_r = \frac{D_p}{2d} (f_i) \left[1 - \left(\frac{d \cos \alpha}{PD} \right)^2 \right] \quad (4)$$

where the number of rolling element N , pitch diameter of bearing PD , diameter of ball d , angle of contact α , and the shaft speed is denoted by f_i .

2 Envelope Spectrum Analysis and Spectral Kurtosis

2.1 Envelope Spectrum Analysis

Demodulation investigation is required since signals of a defective machine are modulated by defect characteristics. Likewise, envelope analysis can obtain detailed analysis of the collected signals. High-frequency resonance analysis also called envelope analysis and it's a signal-processing method that can be viewed as a dominant and reliable classification for defecting identification in rotating machine bearings [10].

Generally, envelope spectrum analysis processed in three steps which are as follows: the first step is the original vibration data is bandpass filtered, second step is to making enveloped by wrapping the base portion of the time-domain signal across the uppermost part followed by Hilbert-Huang transform (HHT), and in the third step, it is modified by employing fast Fourier transform (FFT). Finally, the envelope spectrum derived from vibration data contains distinct details regarding peak amplitude. These peak amplitudes are not clearly seen in the FFT domain [1, 10, 11].

2.2 Spectral Kurtosis

Kurtosis is described as the fourth normalized central moment and calculates a higher peak or lower peak concerning the distribution peak [12]. Dwyer (1983) proposed a frequency-domain kurtosis (FDK) method, which is the advancement of time-domain spectral kurtosis (SK). The frequency-domain kurtosis is interpreted as the ratio of the fourth-order central moment of the short-term Fourier transforms divided by the square of the second-order central moment of the short-term Fourier transforms (STFT) (Dwyer 1984). Mathematically,

$$x_{FDK}(f) = \frac{E\{[x(q, f_p)]^4\}}{E\{[x(q, f)^2]^2\}} \tag{5}$$

where

$$x(q, f) = \sqrt{\frac{h}{m}} \sum_{i=0}^{m-1} w_i x(i, q) \exp(-j f_p i) \tag{6}$$

also

$$x(i, q,) = x[i + (q - 1)m]n \tag{7}$$

where h = the period among succeeding measurements of the method, $w_i = 1$, $f = 2\pi/m$, $q = 1, 2 \dots n$, $i = p = 0, 1, 2, \dots m$, $j = \sqrt{-1}$, and $x(i, q,)$ = signal input.

The simplest way to use the spectral kurtosis procedure is to use the kurtosis at a certain frequency to detect the appearance of non-Gaussian elements, as well as using the frequency bands where those non-Gaussian elements exist. Spectral kurtosis is a description of the kurtosis of a particular frequency element of a signal. Spectral kurtosis is calculated by signal decomposition of a time waveform in the time domain, where the value of kurtosis in the frequency group is determined locally [11, 13]. The spectral kurtosis signal $x(t)$, the fourth-order normalized cumulate is known as spectral kurtosis $x_{SK}(f)$ and is calculated by Eq. (8):

$$x_{SK}(f) = \frac{\langle |H(t, f)|^4 \rangle}{\langle |H(t, f)|^2 \rangle^2} - 2 \tag{8}$$

where $H(t, f)$ is the complex envelope function of $x(t)$ at frequency f captured utilizing the short-term Fourier transforms algorithm:

$$H(t, f) = \int_{-\infty}^{+\infty} x(\tau) w(\tau - t) e^{-j2\pi f \tau} d\tau \tag{9}$$

The Kurtogram algorithm is proposed by [14] and is obtained from the spectral kurtosis [14]. Spectral kurtosis for various window sizes is calculated by the Kurtogram algorithm and also utilizes a bandpass filter. The bandpass filtering of signal is done to optimize the Kurtogram using the central frequency (f_c) and bandwidth (bw) of the kurtogram.

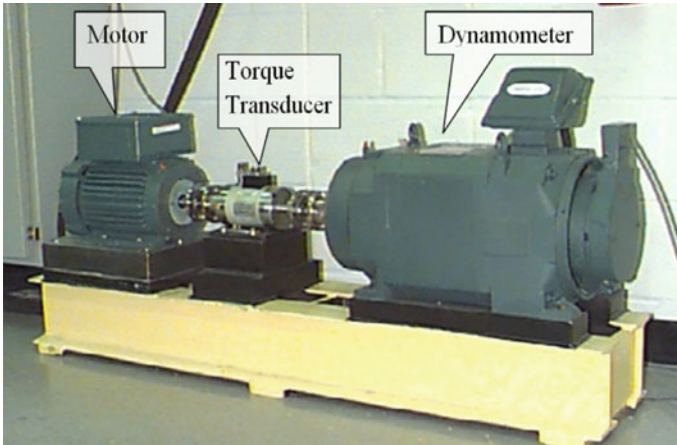


Fig. 2 Experimental setup [17]

3 Experimental Investigation

3.1 Description of Test Rigs

Bearing data of the aforementioned article is developed by Case Western Reserve University (CWRU) [17]. A SKF makes deep groove ball bearing number 6205-2RS JEM was used in this experiment. The sampling frequency is taken as 12,000 Hz for all types of faults considered. The load varies between 0 and 3 hp with shaft speed variation from 1772 to 1730 rpm, respectively. Figure 2 shows the laboratory setup used in this investigation. Electrical discharge machining is used in an experimental bearing to produce artificial defects of various diameters in various locations inside the inner and outer races [17].

3.2 Inner Race Fault Investigation (Case 1)

Case 1: The first case involves a defect on the inner race of the bearing 6205-SKF. To find the inner race defect, the envelope analysis is used. The 6205-SKF bearing's BPFI and related parameters are as follows:

$$BPFI = \left\{ \frac{N}{2} \left[f_i \left(1 + \frac{d \cos \alpha}{PD} \right) \right] \right\}$$

where the $N = 09$, $PD = 46.4$ mm, $d = 7.2$ mm, $\alpha = 0$ degree, inside diameter of bearing = 25 mm, and outside diameter of bearing = 52 mm. The sampling

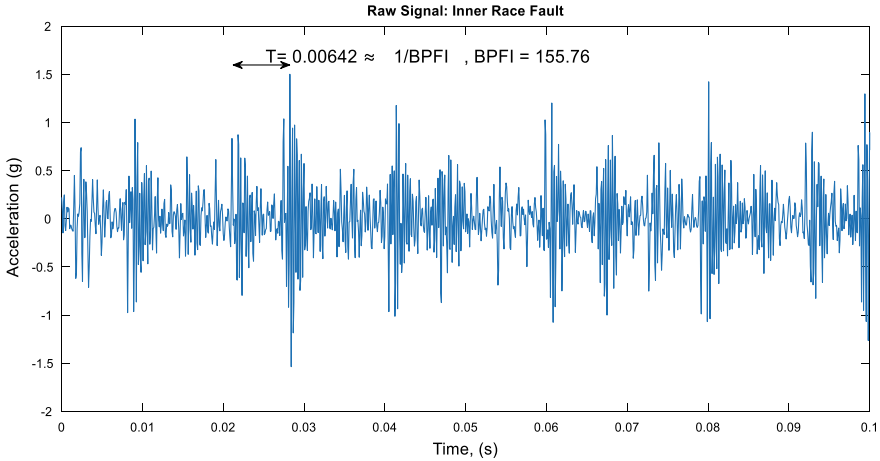


Fig. 3 Time-domain raw signal from inner race fault

frequency and total data point in the experimental investigation are 12,000 Hz and 122,917. The shaft frequency $f_i = 28.83$ Hz. Therefore, from the above equation, the corresponding BPFI is 156.1477 Hz as per the specification of the bearing.

Order monitoring is a pre-processing tool for reducing the effect of shaft speed variations. But, in this experiment, speed of the shaft is uniform, and therefore there is no requirement to complete the order tracking process. Figure 3 shows the original inner race fault signature in the time domain.

The original signal amplitude is modulated at a certain frequency, the time-domain signal, as well as the time period, and demonstrate this $T = 0.00642 \approx 1/BPFI$, $BPFI = 155.76$. It indicates that the rolling part bearing has a defect in the inner race.

In the frequency domain, visualize the raw data and Fig. 4 shows the raw signal inner race fault envelope signal and the associated envelope spectrum of inner race fault shown in Fig. 5.

Figure 5 registers the following: the different peaks are visible and provide important knowledge about the fault type. The frequency value of different peaks and their multiple of harmonics are mentioned in this diagram. The observed values of peaks at frequency 154.9 Hz with frequency harmonics are 338.5 Hz and 454.9.4 Hz. The BPFI observed with its harmonics agreeing with the calculated BPFI 156.1477 Hz is exposed. Therefore, it can be considered that the inner race defect is classified by the envelope analysis

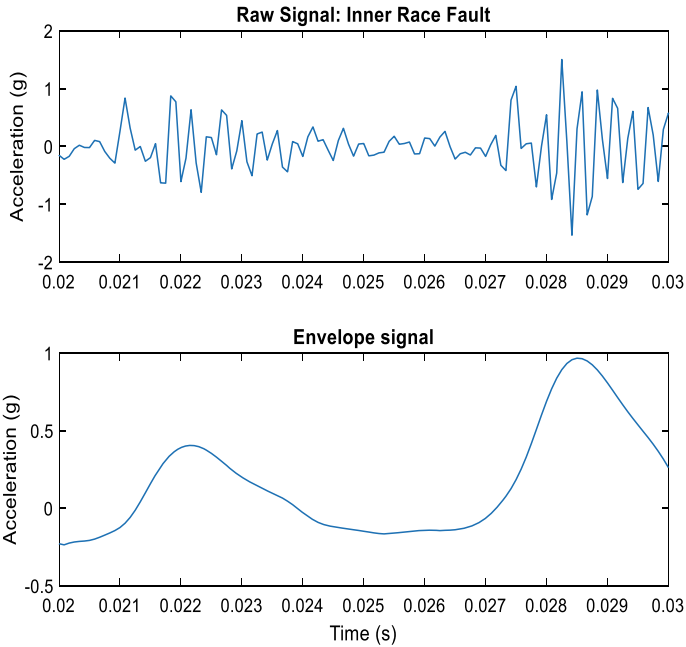


Fig. 4 Envelope signal of raw signal inner race fault

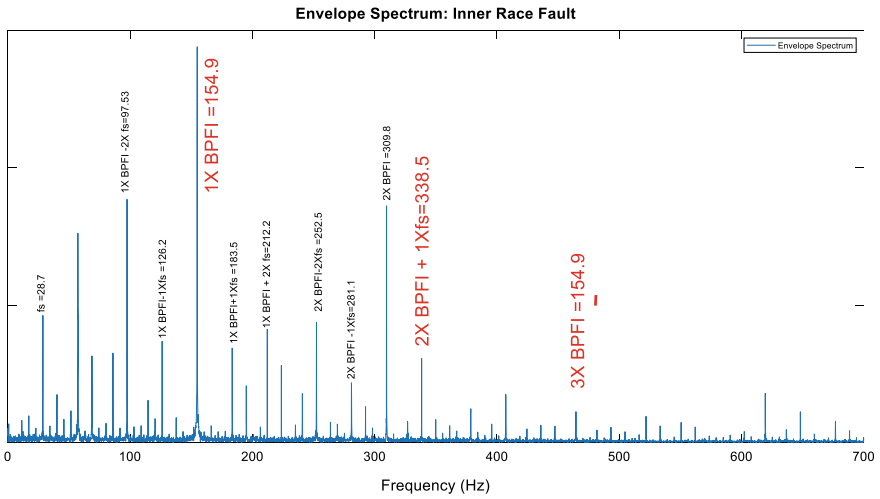


Fig. 5 IR defect observed in envelope spectrum with BPFI and its harmonics

3.3 Bearing with Outer Race Fault Investigation (Case 2)

Case 2 is the outer race fault investigation which uses bearing 6205-SKF with a defect on the outer race. The envelope analysis is applied to examine to find the outer race defect. BPFO and the relevant parameter of the 6205-SKF bearing are given as follows:

$$BPFO = \left\{ \frac{N}{2} \left[f_i \left(1 - \frac{d \cos \alpha}{PD} \right) \right] \right\}$$

where the $N = 09$, $PD = 46.4$ mm, $d = 7.2$ mm, $\alpha = 0$ degree, inside diameter of bearing = 25 mm, and outside diameter of bearing = 52 mm. The sampling frequency and total data point in the experimental investigation are 12,000 Hz and 122,136. The shaft frequency $f_i = 28.83$ Hz. Therefore, from the above equation, the corresponding BPFO is 103.3223 Hz as per the specification of the bearing.

Repeat the same procedure for finding the BPFO and its harmonic for outer race fault. Sometimes in presence of heavy background noise, normal bearing data and outer race data do not show clear peaks at BPFI, BPFO harmonics as shown in Fig. 6. When the signal is immersed with heavy noise, envelope spectrum analysis facing difficulty extracts the fault feature frequency. In this condition, kurtosis of vibration data is calculated, which indicates the signal impulsiveness. Figure 7 represents the kurtosis value for various types of bearing fault.

The IR defect signal has higher impulsiveness, as seen in Fig. 3. As a result, the envelope spectrum is effectively stored and visualizes the peaks and harmonics at (BPFI). When immersed in heavy background noise, the peaks at BPFO and its harmonics are mildly visible in the case of an OR defect. Extracting the impulsive signal or amplifying the SNR is expected prior to envelope spectrum analysis (signal-to-noise ratio). By introducing kurtogram [16] as a pre-filter process and spectrum kurtosis before envelope spectrum analysis, this heavy background noise problem is resolved.

From Fig. 6, it is easily observed that immersed noise suppressed the fault feature frequency at BPFI and BPFO means no clear pictures are visible in Fig. 6 for BPFI and BPFO. Figure 7 represents the time-domain waveform and kurtosis value of a bearing with an IR defect, an OR defect, and a normal bearing. The normal bearing's kurtosis value is 2.9572, the inner race fault's kurtosis is 5.2911, and the outer race fault's kurtosis is 8.2898. Hence, higher kurtosis value is observed when bearing faulting an inner race and outer race. Higher kurtosis represents non-stationarity of the signal, immersed with heavy background noise. The parameter shown in Fig. 8 gives the necessary information for selecting the required bandpass filtering. The bandpass filter is used as a pre-filter for the data and improves the differentiation of the non-stationary component. Following observation recorded from Fig. 8, maximum kurtosis = 7.1128 at a level of 4.6, optimum window length = 48, center frequency = 2.625 kHz, and bandwidth = 0.25 kHz. For computing kurtosis locally within the frequency band, kurtogram and spectral kurtosis are used. The bandpass filter

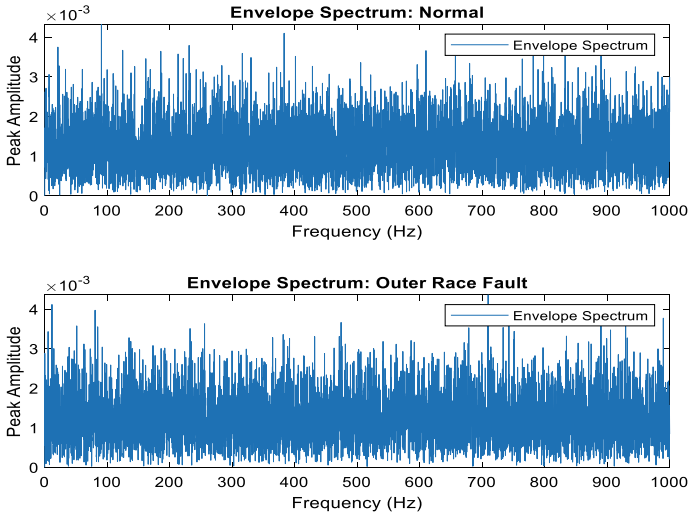


Fig. 6 Envelope spectrum normal and outer race (heavy background noise signals)

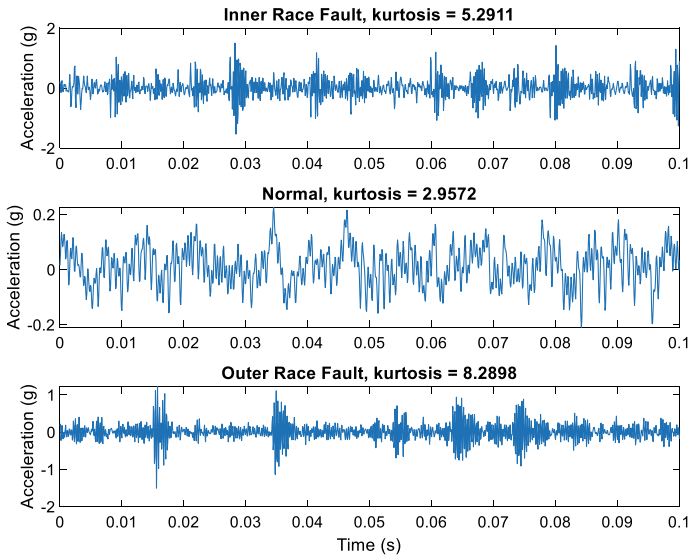


Fig. 7 Time-domain waveform and kurtosis value of bearing. a Inner race, b Normal and c Outer race

was added to the initial signal to produce a higher impulsiveness of signal for envelope spectrum analysis after deciding the maximal kurtosis value from Fig. 8 and its specific frequency band. By using the optimal window length which describes kurtogram is utilized to determine spectral kurtosis shown in Fig. 9. In addition,

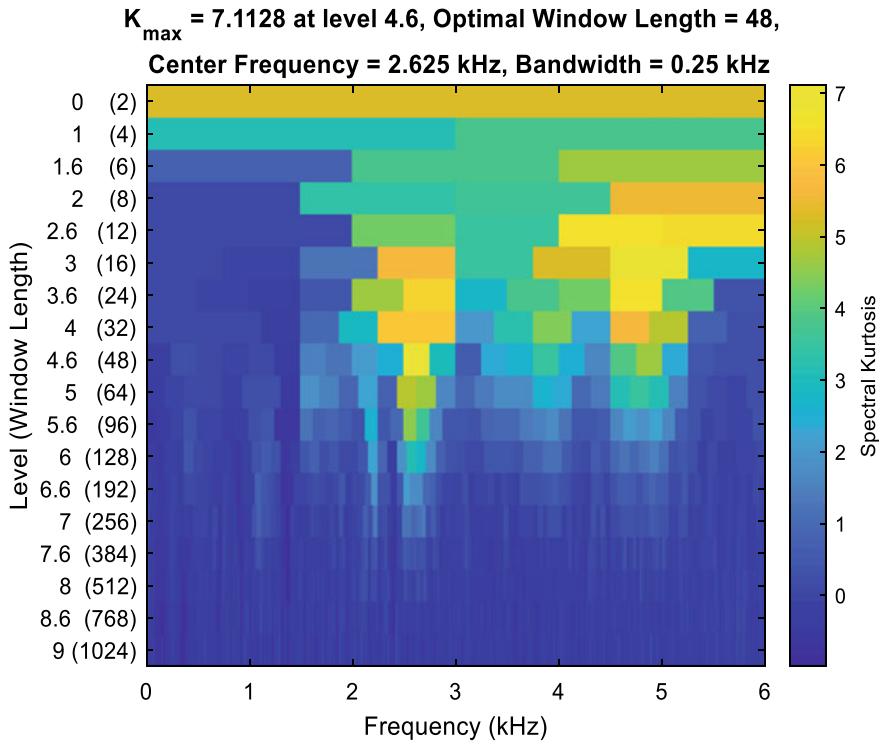


Fig. 8 Kurtogram for band selection

a strong spectral kurtosis value denotes a broad power variance (dB) at the corresponding frequency. The envelope spectrum analysis is conducted on these higher impulsive data. As a consequence, the non-stationary portion of the vibration signal is found using a spectral kurtogram.

Figure 10 represents a comparison between the kurtosis values of outer race raw signal fault with bandpass-filtered outer race raw signal fault kurtosis value. Before bandpass filtering, the kurtosis value is 8.2898 after bandpass filtering kurtosis value is 12.0876. Therefore, from Fig. 10, the higher kurtosis achieved after bandpass filtering is clearly observed.

Kurtogram diagram represented in Fig. 8 recommended the center frequency (f_c) and bandwidth (b_w) for the bandpass filtering. By applying bandpass filtering to the original signal data the value of kurtosis is increased as shown in Fig. 10. By doing this, the modulated peak amplitude of the outer race defect will regain and improve. Finally, the envelope signal is extracted as shown in Fig. 11 and represents the observed value of BPFO = 103.4 Hz and their harmonics 206.7 Hz. The observed value of BPFO and its harmonics matching with the calculated value revealed that the REB has outer race defect. After bandpass filtering with the frequency band

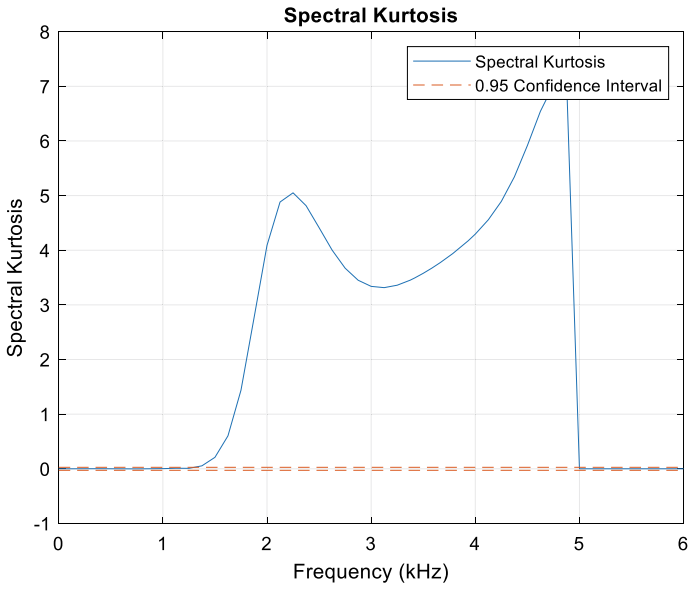


Fig. 9 Spectral kurtosis

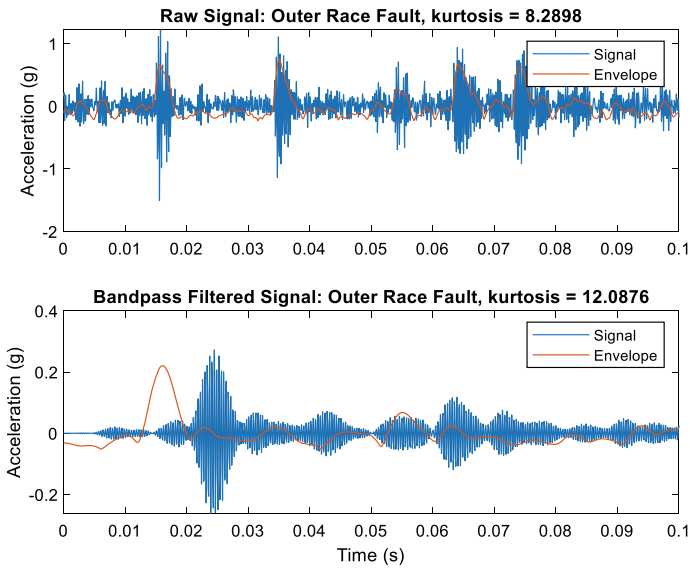


Fig. 10 Bandpass filter

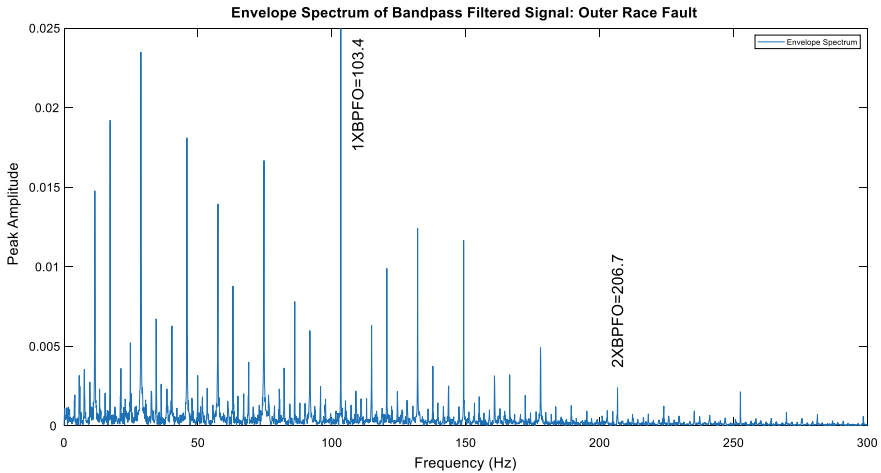


Fig. 11 Bandpass filtered signal envelope spectrum with OR defect

submitted by kurtogram and spectral kurtosis provide improved envelope spectrum. Hence, we investigate the outer race defect in the bearing envelope signal that can show the defect indication at BPFO and its harmonics.

4 Conclusion

The performance of spectral kurtosis in the diagnosis of REB defects is an interesting innovative method. This paper investigates the rolling element bearing fault at two locations, an inner and outer race. Firstly, envelope spectrum analysis is applied for determining inner race defect frequency and their harmonics. As the inner race defect frequency envelope signal shows high impulsiveness. Therefore, envelope spectrum captures the peaks and harmonics at BPFI efficiently. Secondly, the envelope spectrum is failed and did not show any peaks at BPFO and its harmonics for outer race data with heavy noise or slightly noticeable. In this situation, before the envelope spectrum investigation, it is necessary to extract the impulsive signal or amplifying the SNR (signal-to-noise ratio). By introducing kurtogram as a pre-filter process and spectrum kurtosis before envelope spectrum analysis and by applying the above steps, the problem of heavy background noisy signal is resolved. The outcome acknowledges that the suggested procedure of fault investigation is feasible and useful for the condition monitoring of the rolling element bearing. Besides, the experimental investigation here presented is distinguished by a uniform speed. Future studies directed at inquiring the robustness of the suggested approach in the presence of rotation speed fluctuations also using the empirical mode decomposition (EMD) method are adaptive and utilized for the non-stationary signal.

References

1. Zhao S, Liang L, Xu G, Wang J (2013) Quantitative diagnosis of a spall-like fault of a rolling element bearing by empirical mode decomposition and the approximate entropy method. *Mech Syst Signal Process* 1–24
2. Agrawal P (2019) Diagnosis and classifications of bearing faults using artificial neural network and support vector machine. *J Inst Eng Ser C*
3. Jayaswal P, Wadhvani AK, Mulchandani KB (2008) Machine fault signature analysis. *Int J Rotating Mach* 2008:1–10
4. El-thalji, Jantunen E (2015) A summary of fault modelling and predictive health monitoring of rolling element bearings. *Mech Syst Signal Process* 1–21
5. Yang G, Sun X, Zhang M, Li X, Liu X (2014) Study on ways to restrain end effect of Hilbert-Huang transform
6. Donoho DL (1995) De-noising by soft-thresholding. 41(3)
7. Huang NE, Wu Z, Long SR, Arnold KC, Chen X, Blank K (2009) On instantaneous frequency. 1(2), 177–229
8. Qin X, Li Q, Dong X, Lv S (2017) The fault diagnosis of rolling bearing based on ensemble empirical mode decomposition and random forest, vol 2017
9. Xiang J, Zhong Y (2017) Microelectronics reliability a fault detection strategy using the enhancement ensemble empirical mode decomposition and random decrement technique
10. Wang N, Liu X (2018) Bearing fault diagnosis method based on hilbert envelope demodulation analysis bearing fault diagnosis method based on Hilbert envelope demodulation analysis
11. Hochmann D, Bechhoefer E (2016) Envelope bearing analysis : theory and practice Ω
12. Vrabie V, Granjon P (2004) Application of spectral kurtosis to bearing fault detection in induction motors
13. Smith WA, Fan Z, Peng Z, Li H, Randall RB Optimised spectral kurtosis for bearing diagnostics under electromagnetic interference, pp 1–38
14. Sawalhi N, Randall RB (2014) The application of spectral kurtosis to bearing diagnostics. The application of spectral kurtosis to bearing diagnostics Spectral Kurtosis—background
15. Bearing Data Center, Case Western Reserve University.pdf
16. Chen X, Feng F, Zhang B (2016) Weak fault feature extraction of rolling bearings based on an improved Kurtogram
17. Bearing Data Center, Case Western Reserve University. <http://csegroups.case.edu/bearingdatacenter/pages/download-data-file>

Semi-Automatic Boundary Detection of Weak Edges for Medical Image Analysis



Neha Bhadrawale, Rajeev Kumar Gupta , and Arti Jain

Abstract The study and investigation of medical images is a crucial task for the prediction of critical diseases in our day-to-day life. The image processing gives various methods for the analysis of critical diseases using segmentation. In this paper, semi-automatic image segmentation technique for the analysis of blood vessel segmentation is proposed. The technique is quite efficient in terms of accuracy and sensitivity for the utility of the blood vessel segmentation process, demanding an improvised segmentation area and in turn enhances accuracy. From the improvement perspective, the threshold technique is used with an objective function optimization technique. This improvises the segmentation area and so increases the value of sensitivity. It is hybrid approach which uses Gabor transform, Fuzzy C Mean (FCM), and Ant Colony Optimization (ACO) for the weak edge detection. The blood vessel segmentation process uses Gabor to transform the technique with set FCM and ACO. The set level image segmentation technique improves the segmentation area as well as quality of segmentation for boundary and object detections.

Keywords Ant colony optimization · Blood vessel detection · Boundary detection · Fuzzy C means · Medical image segmentation

N. Bhadrawale
Department of Computer Science, Sagar Institute of Science and Technology, Bhopal, Madhya Pradesh, India

R. K. Gupta (✉)
Department of Computer Engineering, Pandit Deendayal Energy University, Gandhinagar, Gujarat, India

A. Jain
Department of Computer Science and Engineering, Jaypee Institute of Information Technology, Noida, Uttar Pradesh, India
e-mail: arti.jain@jiit.ac.in

1 Introduction

The process of segmentation of blood vessels is a very critical stage in detecting diabetes and heart disease. Changes in the structural composition of retinal blood vessels are signs of the initiation of essential diseases, for example, diabetes, hypertension, heart strokes, and other multiple cardiovascular diseases [1, 2]. Blood vessel morphological changes include vessel diameter changes, vessel tortuosity increases, hemorrhages, neovascularization, and arteriovenous nicking [3, 4]. The primary stage for the quantification of such changes and the identification of vessel defects in computer-aided medical diagnosis is automatic retinal blood vessel segmentation. In addition, the elimination of blood vessels in areas of the optic disk allows a clearer estimation of the extent of glaucoma in the background or in retinal images. Vessel segmentation is quite a challenging problem due to its complicated non-linear nature of blood vessels and very poor contrast between blood vessels and their context. In the related literature, several methods for detecting blood vessels have been reported. In image processing and computer vision [5, 6], image segmentation plays an important role. It is also used to divide an image into different regions that ideally correspond to various objects in the real world. One of the efficient methods for image segmentation is thresholding [7, 8]. Thresholding methods have gained a lot of attention over the last few decades due to the benefit of smaller storage space, high processing speed, and ease of manipulation. Since this is a well-researched field, several algorithms exist to determine an optimal image threshold. In the fields of remote sensing and medical sciences, an applicability of computer vision and pattern recognition is growing day by day. The need for the method of image segmentation is now growing. The segmentation method initially operates by clustering strategies such as K-means. In the latest study trend, however, the authors have suggested various techniques for image segmentation [7, 9]. The image segmentation method undermines the thesis of data and noise influence. Authors also used soft computing and the neural network approach to minimize noise and blurred areas. The segmentation techniques are distinguished as segmentation techniques based on the edge, area, and graph.

In this work, the Fuzzy C Means (FCM) and Ant Colony Optimization (ACO) techniques are used to enhance the vessel segmentation algorithm. The ACO optimizes a blood vessel's potential worth. Using the FCM algorithm, the optimized value of the vessel is segmented and the Gabor transform is quite useful to extract texture-based information from the input image.

The rest of the paper is detailed as follows. Section 2 discusses related work in the field of blood vessel segmentation. Section 3 discusses the Gabor transform and ACO. Section 4 discusses our proposed methodology. Section 5 discusses the result analysis of the proposed work. Section 6 discusses conclusion and future work.

2 Related Work

To explore the vast field of medical images, this section discusses the related work using vivid methods of image processing in different dimensions. A vessel dynamic form shows that an accelerating system is carried out by labeling the continuously advanced features and retains a strategic distance from the rehashed measurement of them on the resulting accent, provided the nearby power weighting and the vessel vector area [1]. Tests using the constructed and authentic pictures of the vessel approve the demonstration studied. Correlations with the restricted dynamic form demonstrate the nearby twofold fitting model, and vascular dynamic shape display talks about model which is more exact, productive, and appropriate for the extraction of the vessel tree from various restorative images.

In [2], a novel area-based technique is proposed for extricating valuable data from minuscule pictures under the complex conditions. It is primarily used for the division of platelets and accurate examination. The dynamic model identifies a few internal and external shapes of a protest from its experience. The model talks about moderately more alluring execution rather than the customary models, even though the outcomes are still an element over the division in the nucleolus range. From the experimental results, it looks for crossover model that catches the powerless edge limit while utilizing the nearby fitting terms. At the same time, it watches the control of territorial differences and utilizes it as a rule to shape these terms to precisely catch the limits. The analyses exhibit that it performs absolutely fine in fragmenting the cell layer as well as the nucleolus, respectively.

In [3], a new dynamic approach demonstrates variation levels which detail the picture divisions as well as confinement of the target. They join a neighborhood picture fitting term and a worldwide picture fitting term which drives toward shape advancement. Their model can portion images with power inhomogeneity, where beginning of shape occurs at anyplace within the picture. It approves its adequacy in various manmade images and genuine pictures. Here, the potential trial comes about demonstrating its preferences as far as precision, effectiveness, and vigor are concerned. This paper introduces a novel localized dynamic shape that is shown in a variable level set plan. Their representation uses both nearby and worldwide image data which controls the movement of the shape. Subsequently, it can handle force inhomogeneity with an adaptable introduction skillfully. Their model executes the GFRLS method, in order to dispose of the necessity of an initialization process. Their results exhibit that the model has preferred execution in comparison to C-V and LIF demonstrate. A versatile intertwining level set technique is displayed to join the alluring features of the two known strategies, individually. The spatial data of the picture naturally balance the weights of the ADPLS and LBF. Exploratory outcomes demonstrate that extensive execution pointers such as precision, solidness, and speed are altogether being enhanced by utilizing this enhanced technique [4]. The combined strategy examined coefficient of variable weighting to consolidate both the ADPLS technique and the LBF. Tests show that the present method is better thought about exhaustive execution than the separate calculation of ADPLS and LBF in the division accuracy, speed, and strength.

The strategy fixes various power vasculatures and the aneurysmal low-differentiation areas that are influenced by the turbulent flows. They focus on the use of philters (multi-dimensional) and neighborhood variations to strength-dependent image, highlighting on distinguishing contrast shifting vasculatures [5]. Then to a great degree, a low-force area, influenced by the turbulent flows, identifies the structural topology using filters (multi-range) and nearby differences. The technique utilizes an apparition picture volume with an aneurysm and four clinical cases. It accomplishes the dice score (0.80) in the apparition case. The strategy is assessed by using a picture volume with the vascular ghost and four clinical cases. Given a similar division system, different parts of the talked about approach: (i) round force brokenness descriptor, (ii) refined power irregularity descriptor, (iii) related DH proportions, and (iv) topology refinement are analyzed. They tentatively demonstrate that they convey promising outcomes in the distribution of aneurysms within the pictures of the PC-MRA.

The directed strategy exhibits to handle the issue of retinal vein division, which consolidates two predominant classification techniques: convolutional Neural Network (CNN) which is executed as trainable progressive element extractor and outfits another Random Forest (RF) function as a trainable approach. While coordinating the benefits of learning and customary classifiers, this technique consequently takes in components from the crude pictures and foresees the examples, and Genetic Algorithm (GA) which is used as a parametric enhancement for the CNN. Additionally, they keenly attempt the CNN max. pooling (maximum pooling) [6] as the progressive component extractor while contrasting CNN. Apart from this, they also apply the strategy over vivid biomedical pictures, e.g., layer division, etc.

The difficulty is utilizing a discriminatively prepared contingent arbitrary field which shows more expressive possibilities. Specifically, they use late outcomes, empowering amazingly quick induction in a completely associated demonstration. They observed that this rich yet experimentally effective unit is combined with principled discriminative preparation, given an ordered yield bolster vector machine. This in turn produces a fully mechanized system that is measurably indistinguishable from a human specialist annotator. Subsequently, contending techniques endure as measured by affectability [10]. Interestingly, their approach nearly coordinates the execution of a specialist (human being) both in specificity and affectability, and hence accomplishes the significantly higher affectability over rest other contending strategies. Affectability can especially be vital as it is an exact estimation for vessels pixels, an essential objective within the vessel division toward the picture investigation.

In [11], the line-formed in profiling with an application to cerebrum vein and AVM division is effective for settling the subtle elements and the calculation time. Their strategy considers both the nearby proximate and more extensive neighborhood of the handled pixel, which makes it efficient for dividing substantial vein tree structures and also fine structures of the AVMs. The outcome on apparition informational collections for different clamor and ancient rarity levels demonstrate high strength of the examined technique. The approval is performed by the examination of divided AVM locale with the portioned pictures of an onyx cast after embolization methodology which proves the effectiveness of their strategy. The acquired outcomes on genuine

CTA information pleasantly smooth tubular vessels, resultant of the outspread situating of the line-molded SEs for the solitary pixel. Their strategy precisely fragments the most astounding measure of the vein structure, contrasted with other division techniques. The first change is finished by adding a new discriminant that highlights to the components pool and is utilized as a part of the classification. The second change ends by applying the new heuristic capacity in light of the likelihood hypothesis in the insect state framework rather than the old that gives Euclidean separation and is utilized sometime recently. The after effects of the enhancements are promising while applying the enhanced approach to the STARE database for the retinal images. They have enhanced the elements while incorporating a novel discriminant highlight, which is chosen by the CFS heuristic [12] inside the best elements set, likewise enhances the execution of the ACS, utilizing new heuristic capacity in light of the likelihood hypothesis rather than the old one, which depends on the Euclidean separation. In [13], deep learning-based edge detection model is proposed which used deep neural network for semantic edge detection.

The primary issues in the medicinal picture investigation are covering tissue division. Since the veins banter into the optic plate zone and mislead the chart cut calculation through breaking the optic circle limit, to accomplish great division comes about, the MRF picture remaking calculation kills vessels in the optic circle territory with no modification of the pictures [7, 8]. In the fundus retinal images, it demonstrates a new approach to the portion veins and optic circle. In modern ophthalmology, the technique can be used to improve non-intrusive resolve. An imperative predictor for infections such as diabetic retinopathy, glaucoma, and hypertension is the morphology of an optic circle as well as of the vein. As a first step, extraction of tree of the retina vascular, the system uses the process of chart cutting [14]. In order to measure an area of the optic plate, the vein data is then used. The division of the optic plate is carried out using two techniques of choice. The Markov irregular field (MRF), remaking technique of the picture, sections the optic circle while expelling out the vessels from the optic plate district, so remuneration calculates strategy fragments that optic plate utilizes in the earlier nearby force learning of the vessels [15]. The three open datasets, namely, DiaRetDB1, DRIVE, and STARE, are attempting the technique. The findings and connation with the choice strategies reveal that their approach achieves successful execution in the vein and optic circle segmentation.

3 Feature Extraction and ACO Gabor Transform

This section discusses the Gabor transform function. The Gabor transform function is very efficient for the extraction of texture features. The extracted texture feature gives the formation of the moment and gradient. Visual content is further divided into general or domain specific. Here, we have used it for the extraction purpose. To implement the texture analyzer, use of two-dimensional Gabor functions is done to produce a strengthen correlation with the textural data in a color image [16]. The Gabor functions are Gaussian that are modulated by the complex sinusoids. In the 2-D space, it contains the form of, as is stated in Eq. (1):

$$g(x, y) = \frac{1}{2\pi\sigma_x\sigma_y} \exp\left(-\frac{1}{2}\left(\frac{x^2}{\sigma_x^2} + \frac{y^2}{\sigma_y^2}\right) + 2\pi j\mu\right) \tag{1}$$

The filters' dictionary is given by an appropriate dilatation, and $g(x, y)$ rotation of the generating function, as is stated in Eq. (2).

$$g_{mn}(x, y) = a^{-m}g(x', y') \tag{2}$$

where $m = 0, 1, \dots, S - 1$; $x' = a^{-m}(x\cos\theta + y\sin\theta)$; $y' = (-x\sin\theta + y\cos\theta)$; $\mu = n^{1/4}K$;

$$a = (U_h/U_l) - 1 / (S - 1);$$

θ : angle of rotation, K : no. of orientations, S : no. of scales in multi-resolution, U_l , U_h : lower and upper center frequencies of interest.

Then a representation in the compact form is derived from the learning and classification processes. For a given input sample image $I(x, y)$, Gabor wavelet transform is, as is stated in Eq. (3)

$$W_{mn}(x, y) = \int I(x, y)g_{mn}^*(x - x_1, y - y_1)dx_1dy_1 \tag{3}$$

where $*$ is the representation of the complex conjugate (mean: μ_{mn} , standard deviation (s.d.) as $3/4 mn$), magnitudes of transform coefficients which describe the given image, as is stated in Eq. (4).

$$\mu_{mn} = \iint |W_{mn}(x, y)|dx dy \tag{4}$$

$$\text{and, } \sigma_{mn} = \sqrt{\iint (|W_{mn}(x, y) - \mu_{mn}|)^2 dx dy}$$

To construct a feature vector, we have used mean and s.d. as μ_{mn} and σ_{mn} , i.e., the components of the feature vector, as is stated in Eq. (5):

$$f = [\mu_{00}\sigma_{00}, \mu_{01}\sigma_{01}, \dots, \mu_{mn}\sigma_{mn}] \tag{5}$$

As a consequence, for orientations and scale shifts, numerical vector of 30 dimensions is obtained. It is important to be noted that the texture function has been calculated only for the rectangular grid, since computing the texture vector for one arbitrary area is difficult. For the optimization process, the extracted texture function generates a feature matrix.

The ACO algorithm is being proposed by Dorigo and Scholar. The biological ants' action inspires the algorithm proposed. The dynamic population-dependent process [7] is supported by the algorithm. The working theory of continuity and

shortest path estimation is the working principle of ant colony optimization. Ants are creepy crawls that live or live. Since they are visually impaired animals, they use the pheromone guide to find the most restricted way from home to sustenance. The pheromone is the concoction material held by the ants, which among them serves as the primary medium of correspondence [17, 18], directing the assurance of the following progress in this way. Then again, because of the strength of pheromones that are saved in different ways [19, 20], ants find the shortest path. The strength of the pheromone and the length of the tracks are used to re-enact the insect structure, by and large. The ACO is used here, during the fusion process, to pick the local feature process.

4 Proposed Algorithm

In this research work, we have proposed an algorithm which is a combination of the algorithms ACO and FCM. For the purpose of the selection and optimization of the extracted features by the Gabor transform algorithm, former one is used. The optimized characteristics move through the later one, and the image of the blood vessel is segmented. In step-by-step mode, the process of the proposed algorithm is defined explicitly as shown in Fig. 1.

Step 1. The features that are extracted earlier are allowed to pass through the ACO and decide an initial ant’s size (say, $N = 500$).

- a. Initializes the pheromone value. All features must have different value.
- b. Uses the condition of selection for an optimal solution, as is stated in Eq. (6).

$$F_s(Mij) = \frac{[\tau(f_i, k_j)]\alpha[\rho(v_i, k_i)]\beta}{\sum_{k=0} f^{\tau(f_i,k)\alpha[\rho(v_i,k)]\beta}} \tag{6}$$

Here,

$\tau(f_i, k_i)$ is the value of mapped ants’ features.

F_s is the final solution of features.

- c. An optimal features set is estimated.

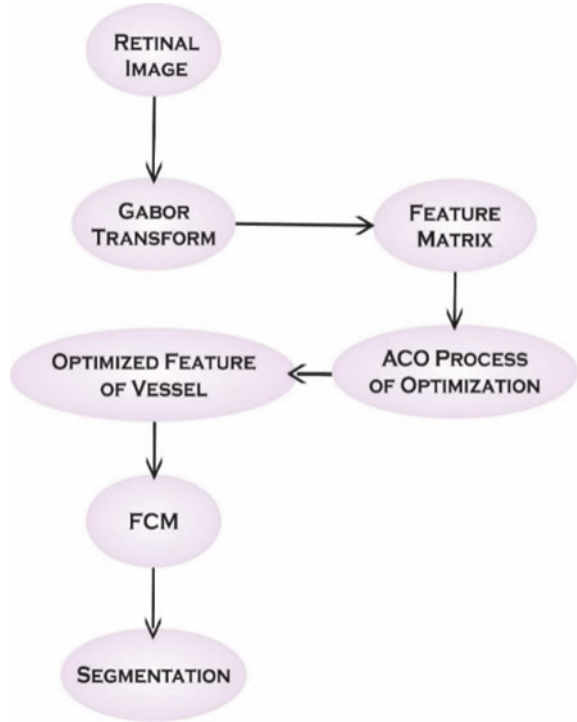
Step 2.

- a. Compute relative feature set value, as is stated in (7).

$$Rf = \frac{LSI}{Wd} \tag{7}$$

Here,

Fig. 1 Flow of proposed segmentation method



LSI is the interference value of ants.

Wd is the sum value of center FCM.

- b. The FCM processing of feature, as is stated in Eq. (8).

$$FS = \begin{cases} \frac{\max(Rf) - F_s}{\max_{h=1 : (WS)}} & \text{if } s_i \in f_j \\ 0 & \text{otherwise} \end{cases} \tag{8}$$

- c. Measure the value of center difference, as is stated in (9).

$$Rd = \sum_{fd=1}^n \sum_{pf=1}^m (x_i - FS) \tag{9}$$

- d. If the Rd value is zero, then the segmentation process is completed.

5 Result Analysis

In MATLAB 7.14.0, the suggested approach is implemented and checked with different images of blood vessels. The measurements of precision, specificity, and sensitivity are taken into consideration in this job. The two vessel segmentation datasets from the University of California, Machine Learning (ML) repository, namely, DRIVE: Digital Retinal Images for Vessel extraction and STARE: Structured Analysis of Retina are considered for evaluating the output parameters. The output comparison of metrics—specificity (SP), sensitivity (SE), and accuracy (AU) using GF, ALT, and our proposed work with respect to different input images and the threshold value (as 5) are exemplified, as shown in Table 1. The specificity is defined as True Negative Rate (TNR) and sensitivity is defined as True Positive Rate (TPR).

In Fig. 2, it is depicted that a comparative analysis among the evaluation metrics, namely, specificity, sensitivity, and accuracy rates are performed for the GF, ALT, and our proposed method that too for the threshold value set at 10. On the basis of Fig. 2, it is stated that our proposed work gives better specificity, sensitivity, and accuracy values as compared to the other comparative approaches.

Table 1 Comparative analysis of specificity (TNR), sensitivity (TPR), and accuracy (ACC) using GF, ALT, and our proposed method (here, threshold: set to 5)

Image	Method	Specificity (SP)	Sensitivity (SE)	Accuracy (AU)
1	GF	91.5151	62.5151	92.5151
	ALT	90.9676	66.3656	91.9676
	Proposed method	93.0648	67.4646	93.0648
2	GF	89.5368	60.8951	91.2551
	ALT	91.9676	62.8956	90.8476
	Proposed method	94.10648	66.4646	92.0648
3	GF	90.5251	62.5151	91.8251
	ALT	88.8576	67.8756	90.5876
	Proposed method	91.6948	65.4646	92.2448
4	GF	91.5151	64.5151	90.2451
	ALT	89.8696	66.3656	92.4876
	Proposed method	92.8748	66.8946	93.5898
5	GF	89.5151	62.5151	89.2541
	ALT	91.4676	66.5456	90.9676
	Proposed method	94.0648	68.4546	92.0648

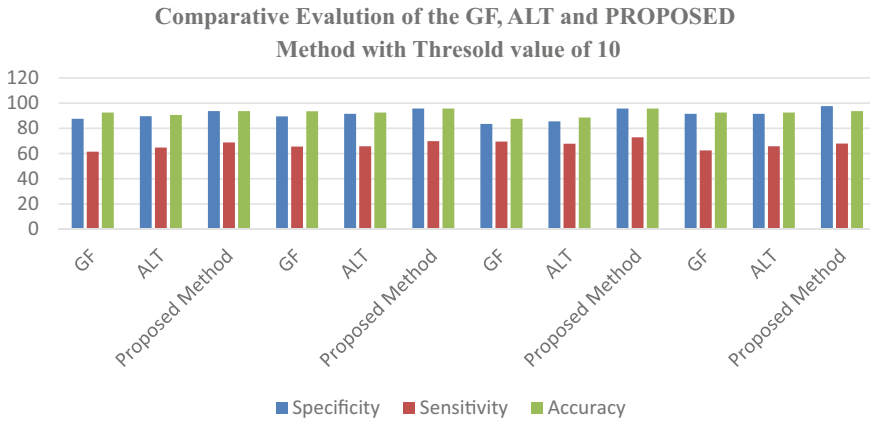


Fig. 2 Comparison of GF, ALT, and proposed method when threshold value is set to 10

6 Conclusion and Future Work

In this work, hybrid method for the blood vessel segmentation is proposed which combines the Gabor transform, ACO, and FCM algorithms. The experimentation is conducted on the MATLAB 7.14.0 platform, over different images of the blood vessels. The DRIVE and STARE vessel datasets are taken from the UCI ML repository, namely, vessel segmentation dataset. The proposed work is quite efficient in terms of evaluation metrics, namely, specificity, sensitivity, and accuracy. The method compares different set level parameters for the vessel segmentation, for which comparisons with other segmentation methods, e.g., Gabor Filter (GF) and alternate (ALT) are also done. The intensity in homogeneities can be visualized in the images that are used for the routine imaging for the boundary detections. The results depict that the proposed approach provides the better segmentation irrespective of the shape and position of an initialized contour, and resultant contours are quite thin which gives no discontinuities. The composite form of the proposed method decreases the time complexity. These region values are not recalculated for the recalculation process, they can be redefined in the future.

References

1. Tian Y, Chen Q, Wang W, Peng Y, Wang Q, Duan F, Wu Z, Zhou M (2014) A vessel active contour model for vascular segmentation. Hindawi, 1–16
2. Yao C, Zhang J, Chen M, Guan Q, Scalia M (2012) Incorporating a local binary fitting model into a maximum regional difference model for extracting microscopic information under complex conditions. Hindawi, 1–11
3. Yu X, Qi Y, Lu Z, Hu N (2013) Implicit active contours driven by local and global image fitting energy for image segmentation and target localization. Hindawi, 1–9

4. Kashyap R, Gautam P (2014) Microarray image segmentation using improved GOGAC method. *Int J Comput Sci Eng (IJCSE)* 2(4):67–74
5. Kashyap R, Gautam P (2015) Modified region-based segmentation of medical images. In: *International conference on communication networks (ICCN)*. IEEE, pp 209–216
6. Wang S, Yin Y, Cao G, Wei B, Zheng Y, Yang G (2014) Hierarchical retinal blood vessel segmentation based on feature and ensemble learning. *Neurocomputing* 1–10
7. Odstreilik J, Kolar R, Budai A, Hornegger J, Jan J, Gazarek J, Kubena T, Cernosek P, Svoboda O, Angelopoulou E (2013) Retinal vessel segmentation by improved matched filtering: evaluation on a new high-resolution fundus image database. *IET Image Process* 1–11
8. Gao X, Wang B, Tao D, Li X (2011) A relay level set method for automatic image segmentation. *IEEE Trans. Syst.* 518–525
9. Bayraktar M, Kockara S, Halic T, Mete M, Wong HK, Iqbal K (2019) Local edge-enhanced active contour for accurate skin lesion border detection. *BMC Bioinform* 20(2):87–97
10. Orlando JI, Blaschko M (2014) Learning fully-connected CRFs for blood vessel segmentation in retinal images. *MICCAI* 1–8
11. Babin D, Pižurica A, De Vylder J, Vansteenkiste E, Philips W (2016) Brain blood vessel segmentation using line-shaped profiles. *PMIB*, 1–23
12. Kashyap R, Gautam P (2016) Fast level set method for segmentation of medical images. In: *Proceedings of the international conference on informatics and analytics (ICIA-16)*, vol 20, p 7. ACM. <https://doi.org/10.1145/2980258.2980302>
13. Liu Y, Cheng MM, Fan DP, Zhang L, Bian J, Tao D (2020) Semantic edge detection with diverse deep supervision. *Int J Comput Vis* 1–17
14. Foruzan AH, Zoroofi RA, Sato Y, Hori M (2012) A Hessian-based filter for vascular segmentation of noisy hepatic CT Scans. *Int J Comput Assist Radiol Surg* 199–205
15. Farokhian F, Demirel H (2014) Fast detection and segmentation in retinal blood vessels using gabor filters. In: *22nd Signal processing and communications applications conference*. IEEE, pp 1507–1511
16. Waoon N, Kashyap R, Jaiswal A (2010) DNA nano array analysis using hierarchical quality threshold clustering. In: *2010 2nd IEEE international conference on information management and engineering*, pp 81–85. IEEE
17. Guo Y, Ashour AS (2020) Neutrosophic sets in dermoscopic medical image segmentation. In: *Neutrosophic set in medical image analysis*, pp 102–112
18. Haque RI, Neubert J (2020) Deep learning approaches to biomedical image segmentation. *Inform Med Unlocked* 18
19. Azani W, Haniza M, Kamaruddin YW (2017) Combination of grey level and moment invariant for automatic blood vessel detection on retinal image. *J Biomimetics Biomater Biomed Eng* 34:10–19
20. Guo Y, Budak Ü, Vespa LJ, Khorasani E, Şengür A (2018) A retinal vessel detection approach using convolutional neural network with reinforcement sample learning strategy. *Measurement* 125:586–591

An Efficient and Lightweight Intrusion Detection System for Mobile Ad Hoc Networks



Y. Sharmasth Vali , N. Prakash, and L. Shakkeera 

Abstract The distinctive aspects of Mobile Ad Hoc Networks (MANETs), including dynamic network topology, susceptible wireless medium, and limited battery power are highly vulnerable to various types of invasion. The traditional Intrusion Detection System (IDS) prevents the network from intruders using observation-based techniques and security algorithms. However, the limited battery power and network overhead is still a major issue to design an IDS. This paper proposes a Distributed and Cooperative Lightweight Intrusion Detection (DCLID) system to discern and eradicate the intruders from the network. The proposed system includes local detection engine, local analyzer, and trust management system. A local detection engine continuously monitors the network activity and stores the monitoring data in a table. A local analyzer examines the monitoring data periodically to evaluate a threshold based on network traffic and network connectivity. An extra field is added to a routing protocol to store the observed data for threshold measurement. The DCLID system is a lightweight system, it only turns on when the attack happens in the network and the network lifetime is high owing to lightweight designing. The threshold value measurement is used to trigger the IDS for detecting the intruders based on trust estimation. It estimates the trustworthiness of a node using Dempster–Shafer (DS) evidence theory. The DS theory provides a mathematical way to merge the observed data from different observers for deciding trustworthiness of an intruder. The simulation results demonstrate the efficacy of the DCLID system.

Y. S. Vali (✉)

Research Scholar, Department of Information Technology, B. S. Abdur Rahman Crescent Institute of Science and Technology, Chennai, Tamil Nadu, India
e-mail: sharmasth.vali@presidencyuniversity.in

Y. S. Vali · N. Prakash

Associate Professor, Department of Information Technology, B. S. Abdur Rahman Crescent Institute of Science and Technology, Chennai, Tamil Nadu, India

L. Shakkeera

Associate Professor, School of Computing Science and Engineering, Presidency University, Bengaluru, Karnataka, India
e-mail: shakkeera.l@presidencyuniversity.in

Keywords MANET · Lightweight intrusion detection system · Network layer attacks · Trust management · Dempster–Shafer theory · First keyword · Second keyword · Third keyword

1 Introduction

MANETs (mobile ad hoc networks) are comprised of mobile nodes that run in the open medium without any infrastructure [1, 2]. The topology of MANET's network changes suddenly and without notice. Person or cooperative nodes perform network tasks such as path discovery and data packet forwarding on their own. The capacity of MANET nodes to self-configure provides scalability and versatility. Because of the network operations of nodes, resources are quickly depleted. Battery capacity is one of the most important issues in an open MANET environment. Because of its distributed and transparent nature, MANET is vulnerable to a variety of attacks. Reactive and proactive routing protocols are vulnerable to routing attacks because they are based on the presumption that all nodes are cooperative. Malicious nodes use cooperative routing algorithms to conduct routing attacks. In MANET, common routing attacks include the sleep deprivation attack, the black hole attack, the link withholding attack, the replay attack, the packet dropping attack, the rushing attack, the newcomer attack, and the Sybil attack. Node mobility, battery power limits, and bandwidth must all be addressed by routing protocols. Due to these features, a conventional centralized control scheme is not feasible in MANETs. Researchers are motivated to develop an Intrusion Detection System as a result of these scenarios (IDS).

Intrusion has the potential to jeopardise a company's reputation, confidentiality, or resource availability. A device designed to detect such intrusions is known as an intrusion detection system (IDS) [3]. The most effective ways for minimizing the burden of intrusion are intrusion detection and prevention methods. Because of the constraints in achieving IDS requirements, such as the need to aggregate network audit data and detect intrusions with a low rate of false positives, developing IDS in MANET is more complex and difficult than developing IDS in fixed networks. In general, IDSs are classified as either centralized or distributed.

The centralized IDS contains a centralized monitor to observe the whole network activity. In a distributed IDS, each node contains separate IDS, and the observer nodes observe the network functions independently. The cooperative observer nodes share the independent observations between them for taking appropriate decision. A major problem in the distributed IDS is how to merge the observational information of several nodes.

This paper proposes a framework of Distributed and Cooperative Lightweight Intrusion Detection (DCLID) system to discover and mitigates the effects of intruders. It contains a local detection engine and the local analyzer. A local detection engine in the DCLID system is always on, and it frequently observes node activities. DCLID appends one field in the routing protocol for accumulating observed data. A local

analyzer, analyzes the observed data for determining intrusions. Each node keeps threshold value which depends on successful packet delivery in the network. The packet loss is measured in terms of network connectivity and traffic. With the aim of increasing the network lifetime, the DCLID system is designed as a lightweight. If the threshold is varied due to intrusion, the local analyzer provides intrusion alert to originate the IDS. The IDS uses DS theory to determine a node's trustworthiness [4]. The DS theory gathers and combines the observations of different nodes to reflect the uncertainty.

1.1 Problem Statement

The characteristics of MANETs make it susceptible to several intrusions. Intrusion detection and prevention have been used for the last decades as one of the vital security components in MANET. Intruders can compromise the nodes in the MANET and launch network layer attacks in the network. The routing protocol layer is vulnerable due to the deployment of cooperative algorithms, resource constraints of nodes, lack of clear defense mechanisms, and the transient nature of services in the network. The conventional IDS techniques do not offer complete solutions and hence, intrusion detection mechanisms are widely suggested to secure MANETs.

The detection of routing attacks is still a challenging issue due to mobile nodes and power constraints. Therefore, this work proposes a framework DCLID system to detect the attacks in MANET. The DCLID is a lightweight system, and it employs DS theory for evaluating the trustworthiness. The DS theory reflects uncertainty by collecting strong evidence from various independent observers in a secure manner.

1.2 Contribution

- The primary objective of this paper is to differentiate between the active and passive attacks in MANET. The framework DCLID comprises a local detection engine and the local analyzer. For threshold measurement, the DCLID system adds a field to the routing protocol of the MANET.
- The local detection engine observes a node behavior and the local analyzer periodically examines the observed data and independent observations are stored in the routing table. The DCLID measures the threshold using packet loss obtained in the routing table. This work differs the packet loss due to intruders by measuring the packet loss due to network traffic and connectivity.
- The local analyzer generates an intrusion alarm when the disparity occurs in threshold value. The intrusion alarm triggers the IDS to determine the intruders based on DS theory. The DCLID system mitigates the intruder using strong evidence which is collected from distinctive observers.

2 Literature Survey

It proposes the Dempster–Shafer (DS) theory [4], which is a distributed intrusion detection method that expresses uncertainty. To assess the intruders, this paper gathers and incorporates information from inaccurate observers. It calculates trustworthiness for a single node using Bayesian method. The trustworthiness is determined using a hypothesis and evidence gathered from unreliable sources. The Dempster combination rule blends the data collected by various nodes independently. It [5] proposes a collaboration system for Intrusion Detection Networks (CIDNs) that uses a Bayesian theorem for each peer’s feedback aggregation scheme. IDS is linked to the social network through this work. It models each IDS’s false positive (FP) and true positive (TP) using a beta distribution. The CIDN [6] framework offers rewards to successful nodes in order to promote them. The Bayesian approach lowers the cost of false positives. CIDN, on the other hand, has a high overhead and power consumption.

Due to their shared experience, the paper [7] proposes a robust Bayesian confidence management model to estimate the degree of trustworthiness of participating IDSs. Furthermore, the Dirichlet family of probability density purposes is applied to the self-reliance management in this analysis. For evaluating the future action of IDS built on the earlier history of IDS. This work determines the intruders effectively. The intrusion detection schemes in [8] detect packet dropping attacks and [9] detects the selfish nodes.

The work in [10] describes a sleep deprivation attack. The paper [11] presents a clustered detection technique that elects a cluster head monitoring node on a regular basis. The control node is in charge of keeping an eye on the cluster and detecting local and global intrusions. It constructs a finite state machine that abstracts the actual node’s actions in relation to the on-demand routing protocol specification (FSM). The monitor node watches each node’s activity and detects an attack if some of the node’s actions aren’t validated by the FSM. Using a hierarchical architecture, a cooperative intrusion detection system [12, 13] detects packet dropping attacks.

ARAN [14] is an authenticated hop-by-hop routing scheme that protects the network from malicious nodes. Using the certification method, ARAN detects malicious nodes that trigger denial of service, path redirection, tunneling, and routing loops. SEAD [15] is a stable routing protocol for proactive routing that uses a one-way hash function to protect against routing packet alteration, ads, false routing packets, wormhole attacks, and replay attacks. A specification and synthesis for modeling and analyzing MANET routing protocols was proposed in [16]. It extracts parameters from traffic flows and uses them to detect intrusions. The anomaly detection approach produces a behavior that nodes may use to assess the trustworthiness of other nodes [17], and it validates their process with an anomalous payload descriptor. The payload is examined in the training process, and payload is collected from various nodes to create profiles that are compared using a similarity matrix. Exchanging models between nodes, on the other hand, adds to the communication and processing overhead.

The game-theoretic paradigm is used in [18] to detect intrusion in MANETs. It simulates a two-player Bayesian game in which the attacker and the detector are

both present. It uses Bayesian hybrid detection approaches, such as lightweight and heavyweight systems, to analyze the network in two different ways. Since it uses so little resources, the lightweight networking monitoring system is still on. The heavyweight monitoring system, on the other hand, uses ABID to create profiles and compare them to tested data in order to detect intrusion. The work in [19] suggests using Markov chain classifiers to identify anomalies. There are two phases in the anomaly detection algorithm. The first step is to create a Markov chain table, and the second is to create a classifier using a Markov model.

Using a version of the chi-square goodness of fit test and control charts [20], an anomaly-based intrusion detection protocol (AIDP) detects and removes the intruder responsible for a sleep deprivation attack. An approach in [21] proposes a framework that uses three feature vectors to model the network's normal behavior and the ABID discrimination module to define the black hole attack. A neural network and watermarking techniques are used in an intrusion detection engine for mobile ad hoc networks [22]. In [23], a TWOACK scheme is proposed. The TWOACK scheme overcomes watchdog's drawbacks, such as receiver collisions and insufficient transmitting capacity. By obtaining ACK, the TWOACK scheme determines the misbehaving connection. Each data packet receives an ACK and then transmits over the next three nodes on the routing route. Each node sends an ACK to the node located two hops away. Similarly, the TWOACK scheme resolves receiver collision and minimal transmitted capacity. Receiving ACK from a node two hops away from the sender, on the other hand, greatly increases network overhead. TWOACK has a high overhead and electricity consumption.

3 Distributed and Co-operative Lightweight Intrusion Detection (DCLID) System

In DCLID, each node consists of an IDS for independent local observation. The local detection engine in the IDS monitors the actual behavior of the node and obtains the monitoring data in a table. In order to accumulate the observed data, the framework adds one extra field in the routing protocol. The threshold is calculated based on packet loss due to the normal network behavior such as traffic and connectivity. The local analyzer periodically examines the observed data for discovering intrusions. If any dissimilarity occurs in the threshold value due to intrusion, the IDS produces a local intrusion alarm. The IDS is activated to discover the intruders using trust estimation. The neighboring IDSs share their independent observations to the corresponding observer node for evaluating the trustworthiness of the suspected node.

The evidence may be uncertain due to the presence of compromised nodes. To reflect the uncertainty, the proposed DCLID system employs DS theory to estimate the trustworthiness. The DS combination rule collects and combines the evidence collects from different observer nodes. Thus, DCLID prevents the network from proactive and reactive attacks such as rushing attack, replay attack, sleep deprivation attack, black hole attack, and Link withholding attack.

3.1 System Model

The size of a network is expressed as $X*Y$. G represents the network as a communication graph (N, E) . The number of nodes in the network G is represented by N . The contact range of each node is denoted by R , and $R = 250$ is used in the simulation. The set E contains all directional links between node A and B , where $A, B \in N$. The speed of each mobile node is S . In the framework, the packet delivery threshold (P_{TH}) measurement is used to detect attacks. The probability of traffic (P_T) and connectivity (P_C) measurement is used to evaluate the packet loss (P_L). The P_{TH} measurement depends on P_L . The misbehaving probability is denoted as P_m . P_m is calculated based on DS evidence theory. The DS evidence theory estimates the belief ($Baal(H)$) and plausibility ($pl(H)$) to calculate the trustworthiness of the hypothesis. The frame of discernment (powerset) denotes as Ω , and the powerset comprises 2^Ω subsets. The basic probability assignment number considers between 0 and 1. The mass set (degree of belief) contains null set $m(\phi) = 0$ and sum of $\sum m(H_i) = 1$, and power set $m(H) = \{m(\phi), m(H_i)\}$. The $bel(H)$ and $pl(H)$ evaluates using basic mass probability.

3.2 An IDS Framework for Threshold Calculation

A local detection engine attaches to every node for detecting local intrusions. The local detection engine is always on as it consumes minimum energy. The intrusion alert is generated based on threshold measurement. The threshold is normally varied due to two conditions such as the nature of network activity and intrusions. For threshold measurement, the framework attaches one additional field with MANET routing protocols. The field counts the ACK packets to obtain the successful packet delivery rate. The network traffic and connectivity are used to measure packet loss. Routing protocols create paths for data packets to travel. The Transport Control Protocol (TCP), which is used in the transport layer, guarantees data transmission success. In the routing technique, a receiver successfully receives a packet, the receiver is required to send back an ACK to the sender along the same route. The framework counts and stores the ACK count in the routing table for measuring packet loss in the routing layer.

The threshold value estimation depends on the packet loss in the network. The packet loss is the ratio of the number of packets received to the total number of forwarded packets. The packet loss occurs due to general network functions like network traffic and connectivity. The DCLID computes the packet loss probability as follows:

$$P_L = (P_T + P_C)/2 \quad (1)$$

In Eq. (1), P_T and P_C represent the traffic probability and connectivity probability, respectively. The P_C is the ratio of node density (N_D) to the communication range of the node (N_R). It is estimated as follows:

$$P_C = N_D * N_R \quad (2)$$

The PT appraises using Round Trip Time (RTT) delay assigned on the data packet for receiving an ACK packet. RTT is the amount of time taken to forward the data packet, and receive an ACK successfully to the corresponding data packet. The traffic probability in the network is calculated using Eq. (3):

$$PT = \left(\sum_{X=1}^n RTT_{\text{delay}} / T_{RTT} \right) / n \quad (3)$$

where

$$RTT_{\text{delay}} = T_{RTT} - T_{ACK\text{receiving}} \quad (4)$$

In (4), T_{RTT} is the RTT assigned in the forwarding data packet, and $T_{ACK\text{receiving}}$ is the ACK receiving time for the corresponding data packet. The RTT_{delay} is the difference between actual RTT and ACK receiving time. A successful packet delivery probability (P_S) is the difference between the probability of the total number of generating packets (P_G) and the probability of packet loss (P_L) due to network activity. It is calculated as follows:

$$P_S = P_G - P_L \quad (5)$$

$$P_{TH} < P_S \quad (6)$$

Equation (6) depicts the relationship between the packet delivery threshold and a successful packet delivery probability. The threshold is changed dynamically owing to, network conditions. If intruders present in the network, the corresponding local analyzer generates a local intrusion alert to activate the IDS. The DCLID starts to appraise the trustworthiness using DS evidence theory.

3.3 Intrusion Detection Based on Trust Evaluation

Each node maintains a trust table in which each of its neighbors is assigned a trust value. On local independent observation, each node obtains the table. A neighbor node's trustworthiness is not spread internationally since it is held locally. Neighboring nodes receive intrusion warnings and report back to the corresponding node

on their findings of the suspicious node. Since routing attacks can compromise neighbouring nodes, the intrusion warning created node receives shaky proof. As a consequence, in order to make good choices, the corresponding node also estimates the trustworthiness of the neighboring nodes. Using DS proof theory, the node calculates neighboring node confidence and plausibility. To show that node S is an intruder, node A generates an intrusion warning. Nodes B, C, and D are nodes that are similar to nodes A and S. Nodes B, C, and D also made statements about node S. Node B could be hacked, so Node A assesses the trustworthiness of Nodes B, C, and D. A neighboring node B’s confidence is measured as follows:

$$\text{Bel}(B) = \sum_{A_n \subset B} m(A_n) \tag{7}$$

In Eq. (7), A is the collection of evidence that supports the probability of a neighboring node’s claim is true. Likewise, the observer node estimates trustworthiness of other neighboring nodes. However, the neighboring nodes provide uncertain information due to its compromised nature. It is crucial to estimate the trustworthiness of neighboring nodes for considering the claim about the suspected node. Hence, the node considers the maximum evidence that is provided with nodes intersecting with the corresponding neighbors. The plausibility is a maximum belief of neighbors and it is calculated as follows:

$$\text{Pl}(B) = \sum_{A_n \cap B \neq \phi} m(A_n) \tag{8}$$

In (8), A_n is the maximum share of the evidence from various observer nodes that intersect with the neighboring node. The pl(B) is the maximum belief for B to be true. The disbelief and dis-plausibility of B represent as $\text{bel}(\hat{B})$ and $\text{pl}(\hat{B})$. The relationship between belief and plausibility is as follows:

$$\text{pl}(B) = 1 - \text{Bel}(B) \tag{9}$$

Diversely, the Eq. (9) can be written as follows:

$$\text{Bel}(B) = 1 - \text{pl}(\hat{B}) \tag{10}$$

Likewise, node A appraises the trustworthiness of all neighboring nodes, which claims about the node S using evidence collection. It is necessary to calculate the average trust for deciding the trustworthiness of an intruder. The average trustworthiness of node S is calculated using DS combination rule.

The Dempster combination rule combines the independent observation for estimating the average trustworthiness of the suspected node. The basic mass probability of two independent observers denotes as $m_1(A)$ and $m_2(C)$ for hypothesis B.

$$m_{1,2}(B) = m_1(A) \oplus m_2(C) \quad (11)$$

$$m_{1,2}(B) = 1/(1 - k) \sum m_1(A) m_2(C) \quad (12)$$

$$A \cap B \neq \phi$$

In Eq. (12),

$$k = \sum m_1(A) m_2(C) \quad (13)$$

$$A \cap B \neq \phi \text{ efficacy}$$

In Eq. (13), the two masses $m_1(A)$ and $m_2(C)$ support to believe the node B. The three nodes B, C, and D claims trustworthiness about suspected node S. The DS theory computes the trustworthiness of each neighboring node to decide the intruder's trustworthiness. Likewise, the DCLID system effectively detects and mitigates the intruder from the network. The DCLID system determines several routing attacks as shown in the Table 1.

4 Performance Evaluation

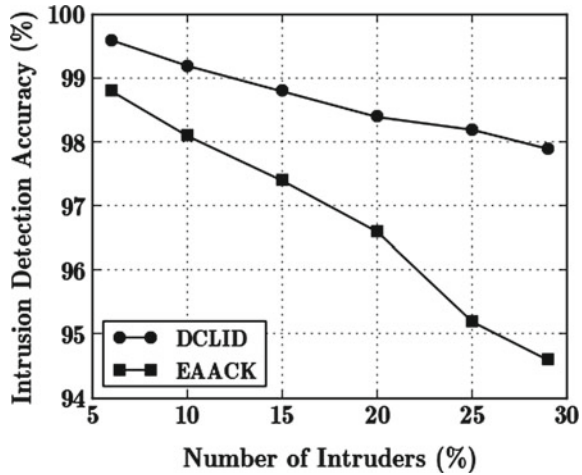
4.1 Simulation Setup

The DCLID system's efficiency is demonstrated using NS-2 simulation. The simulation was run on a random topology of 100 nodes in a 1000×1000 m network area. A mobile node has a speed of 20 m/s. A node's communication range is 250 ms. TCP traffic with File Transfer Protocol (FTP) is implemented with a packet size of 512 bytes. The initial energy of every node is fixed as 100 J. The simulation run time is 500 s. The simulation focuses on metrics such as routing overhead, energy level, Intrusion Detection Accuracy (IDA), and False Positive Error (FPE). The proposed DCLID system compares with an EAACK scheme [24] for analyzing performance.

4.2 Simulation Results

Intrusion Detection Accuracy. Intrusion detection is a term that refers to the detection of intrusion. The ratio of successfully identified intruders to the total number of intruders is called accuracy. The sensitivity of intrusion detection for different numbers of intruders is shown in Fig. 1. The DCLID system determines and substantiates the intruders based on strong evidence which is collected from distinctive independent observers. In contrast, the existing EAACK determines the intruders

Fig. 1 The number of intruders versus intrusion detection accuracy



based on ACK packets only. In DCLID, the detection accuracy is also high if a high number of intruders may present the network. Thus, the DCLID attains high detection accuracy compared to EAACK. In Fig. 1, the DCLID and EAACK accomplishes 98.2% and 95.2% detection accuracy to 25% intruders.

Routing Overhead. Routing overhead is the ratio of the number of additional packets (such as Route Request (RREQ), Route Reply (RREP), and evidence) is generated to the total number of data packets. Figure 2 illustrates the plot of misbehavior ratio and routing overhead. Fraction of misbehaving nodes denotes as pm. The nodes share their independent observations only when intruders occur in the network. DCLID did not perform computational calculations at all time due to lightweight IDS designing and thus, minimize the network overhead considerably. In Fig. 2, the DCLID and

Fig. 2 Misbehavior ratio versus routing overhead

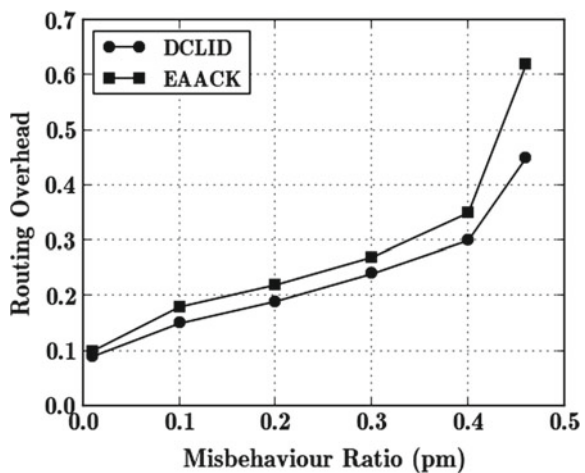
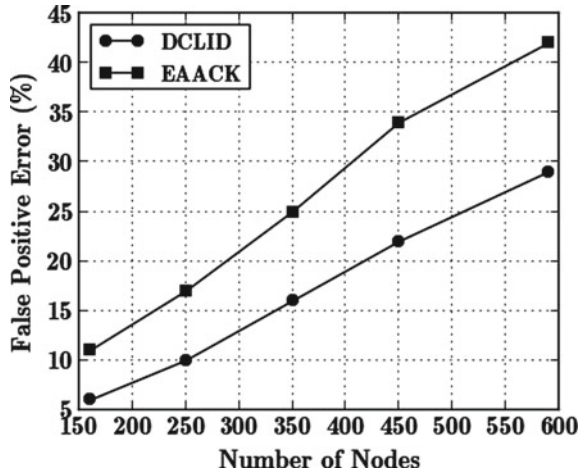


Fig. 3 The number of nodes versus false positive error

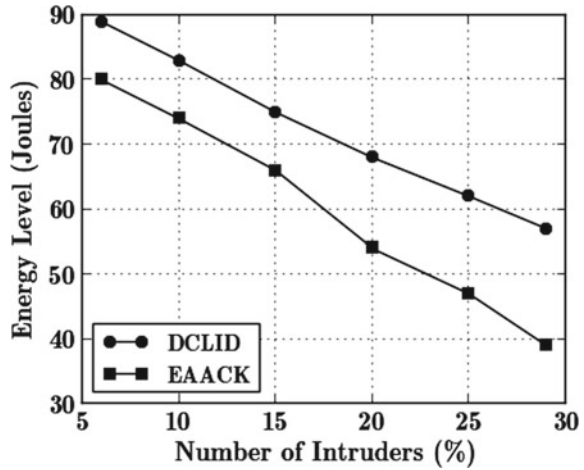


EAACK scheme attain 0.45 and 0.62, respectively, overhead for 0.46 pm. In EAACK, the misbehavior ratio exceeds the threshold value; the network overhead is increased unexpectedly. The variation depicts at 0.46 pm in Fig. 2.

False Positive Error. The percentage of all good nodes incorrectly classified as an intruder is known as the FPE. Figure 3 depicts the relationship between the number of nodes and FPE. The EAACK sends misbehavior report authentication (MRA) packets through the routing path to validate the behavior of suspected node, while it did not consider the evidence for decision-making. To minimize the FPE, the proposed DCLID method tests the trustworthiness of a suspicious node by gathering information from independent observers in two separate stages. Thus, the FPE is low in the DCLID system as strong evidence assists in decision-making. In Fig. 3, the DCLID system and EAACK attain FPE 22% and 34%, respectively, for 450 nodes.

Energy Level. Figure 4 illustrates the relationship between the number of intruders and energy level. The IDS calculates the trustworthiness value to determine and ignore the intruders from the network. If the occurrence of intruder rate is high, the IDS requires high energy to perform computational calculations by sharing evidences. In DCLID, the energy utilization level is minimum compared to a conventional EAACK scheme. In Fig. 4, the DCLID and EAACK require 43 J and 61 J of energy to detect 29% intruders, respectively.

Fig. 4 The number of intruders versus energy level



5 Conclusion

This paper focuses on the intrusion detection problem in the MANET and proposes a framework DCLID system that comprises a local detection engine and a local analyzer for discovering and mitigating intruder effects. In the MANET routing protocol, the system adds an area for obtaining independent observations. The packet loss in the network due to normal network functions determines the threshold measurement. Based on the threshold difference, the local analyzer generates an intrusion alarm. The DCLID is designed as a lightweight IDS to prolong the life of the network. It only triggers when intruders reach the network. Thus, the DCLID system diminishes energy consumption and also minimize the network overhead. The DCLID evaluates trustworthiness of a node using DS evidence theory. By gathering and integrating data from a number of objective observers, the DCLID method replicates uncertainty. The replication outcomes show that the proposed system is capable of identifying and mitigate the intruders effectively, compared to existing EAACK. The DCLID system integrates with all topologies-based MANET routing protocols, and it also extends to other wireless networks.

References

1. Chlamtac I, Conti M, Liu JJ (2003) Mobile ad hoc networking: imperatives and challenges. *Ad hoc Netw* 1(1):13–64
2. de Moraes Cordeiro C, Agrawal DP (2002) Mobile ad hoc networking. Center for Distributed and Mobile Computing, 1–63
3. Zhang Y, Lee W, Huang Y-A (2003) Intrusion detection techniques for mobile wireless networks. *Wireless Netw* 9(5):545–556

4. Chen TM, Venkataramanan V (2005) Dempster-shafer theory for intrusion detection in ad hoc networks. *Internet Comput IEEE* 9(6):35–41
5. Fung C (2011) Collaborative intrusion detection networks and insider attacks. *Ubiquitous Computing, and Dependable Applications* 2(1):63–74
6. Fung CJ et al (2011) Dirichlet-based trust management for effective collaborative intrusion detection networks. *Netw Serv Manag IEEE Trans* 8(2):79–91
7. Sen J (2010) A robust and fault-tolerant distributed intrusion detection system. *Parallel Distrib Grid Comput (PDGC)*, 123–128
8. Al-Roubaiey A, Sheltami T, Mahmoud A, Shakshuki E, Mouftah H (2010) AACK: adaptive acknowledgment intrusion detection for MANET with node detection enhancement. In: 24th IEEE international conference on advanced information networking and applications, pp 634–640
9. Mohammed N, Otrok H, Wang L, Debbabi M, Bhattacharya P. (2011) Mechanism design-based secure leader election model for intrusion detection in MANET. *IEEE Trans Dependable Secure Comput* 8(1):89–103
10. Yi P, Dai Z, Zhong Y, Zhang S (2005) Resisting flooding attack in ad hoc networks. In: *Proceedings of IEEE international conference on information technology coding & computing ITCC*
11. Ping Y, Xinghao J, Yue W, Liu N (2008) Distributed intrusion detection for mobile ad hoc networks. *Syst Eng Electron* 19(4):851–859
12. Sterne D, Balasubramanyam P, Carman D, Wilson B, Talpade R, Ko C, Balupari R, Tseng CY, Bowen T (2005) A general cooperative intrusion detection architecture for MANETs. In: *Third IEEE international workshop*, pp 57–70
13. Huang YA, Lee W (2003) A cooperative intrusion detection system for ad hoc networks. In: *Proceedings of the 1st ACM workshop on security of ad hoc and sensor networks*, pp 135–147
14. Sanzgiri K, Belding-Royer M (2002) A secure routing protocol for ad hoc networks. In: *Proceedings of IEEE international conference on network protocol (ICNP'02)*, pp 78–87
15. Hu Y, Johnson B, Perrig A (2003) SEAD: secure efficient distance vector routing for mobile wireless ad hoc networks. *Int J Adhoc Netw* 1(1):175–192
16. Stakhanova N, Basu S, Zhang W, Wang X, Wong J (2007) Specification synthesis for monitoring and analysis of MANET protocols. In: *Proceedings of international symposium on frontiers in networking with applications*
17. Cretu GF, Parekh J, Wang K, Stolfo SJ (2006) Intrusion and anomaly detection model exchange for mobile ad-hoc networks. In: *Proceedings of IEEE consumer communication and networking conference*
18. Liu Y, Comaniciu C, Man H (2006) Modeling misbehavior in ad hoc networks: a game theoretic approach for intrusion detection. *Int J Secure Netw* 1(3):243–254
19. Jiang H, Wang H (2005) Markov chain based anomaly detection for wireless ad-hoc distribution power communication networks. In: *Proceedings of IEEE power engineering conference*, pp 1–249
20. Nadeem A, Howarth M (2009) Adaptive intrusion detection & prevention of denial of service attacks in MANETs. In: *Proceedings of ACM international wireless communication and mobile computing conference (IWCMC 09)*, pp 926–930
21. Kurosawa S, Jamalipour A (2007) Detecting blackhole attack on AODV based mobile ad hoc networks by dynamic learning method. *Int J Netw Secur* 5(3), 338–345
22. Mitrokosta A, Komninos N, Douligieris C (2007) Intrusion detection with neural networks and watermarking techniques for MANETs. In: *Proceedings of IEEE international conference on pervasive services*, pp 118–127
23. Liu K et al (2007) An acknowledgment-based approach for the detection of routing misbehavior in MANETs. *IEEE Trans Mobile Comput* 6(5):536–550
24. Shakshuki EM, Kang N, Sheltami TR (2013) EAACK—a secure intrusion-detection system for MANETs. *IEEE Trans* 60(3):1089–1098

Synchronization of Uncertain and External Disturbance Time Delay Chaotic Systems



Ajit K. Singh

Abstract This article addresses the synchronization problem of a class of uncertain and external disturbance time delay chaotic systems with nonlinear inputs in a drive response structure. The high complexity of the multiple unknown parameters of system can provide a new approach for enhancing message security in chaos based encryption systems. With uncertain and external disturbance time delay, advanced Lorenz and Rössler systems have been considered to demonstrate the synchronization problem. Simulation results are presented to illustrate the effectiveness of the considered chaotic systems with and without the unknown parameters.

Keywords Active control method · Advanced Lorenz system · Chaotic systems · Rössler system · Synchronization

1 Introduction

Chaos in dynamical systems is very common and has been highly demonstrated. The ordinary differential equation of the chaotic dynamical system is linearised around the required fixed point to entitle application of linear control theory. Although this idea is effective but the approximation region for the linearised model is not exactly defined. Also linearisation may take away the chaotic nature to a certain degree. In 1990, Pecora and Carroll [1] introduced a method to synchronization two identical chaotic systems. After that chaos synchronization has attracted a great recognition from different fields and has been encountered by researchers in the last few decades [2–7]. By synchronization means the trajectory of drive system to govern response system so that trajectory of response system goes along with trajectory of drive system asymptotically. Many methods such as OGY method [8], active control method [9], feedback approach [10], backstepping design [11], time-delay feedback approach

A. K. Singh (✉)
Department of Mathematics, Amity University,
Mumbai 410206, Maharashtra, India
e-mail: ajit.brs@gmail.com

[12], nonlinear control technique [13] and etc. have been studied for picking up chaos control and synchronization.

However, most of the study has based on chaotic systems with certain parameters. But in real application, some or all of the parameters are uncertain. In fact, one can rarely ever attain parameters of chaotic systems in communication theory, so the study on the synchronization of uncertain chaotic systems has some practical application [14–16]. In this regard, Han et al. [17], Yassen [18], Singh et al. [19], Park [20] and Elabbasy et al. [21] investigated the synchronization of uncertain chaotic systems.

Synchronization in low dimensional chaotic systems is designed. Subsequently synchronization of high dimensional chaotic systems has emerged an interesting area in the field of nonlinear dynamics. Therefore, the research on synchronization of time delayed chaotic systems has obtained reasonable recognition. Time delayed systems are naturally connected to systems with memory that convinced for most of biological and engineering systems such as dynamics of optical systems viz. Ikeda system, blood production in patients with leukaemia viz. Mackey–Glass model, population dynamics, laser physics, physiological model, control system, neural networks, etc. [22–26]. Hence, time delay chaotic systems can be considered as a special cases of spatiotemporal systems, which extends synchronization to infinite dimensional systems.

In practical applications of chaos synchronization theory, uncertainties, external disturbances and time delays occur commonly in chaotic synchronization and many more real control systems. There are still many problems whose studied to be worthy of attention in this field. For example, time delay can consider in inaccurate feedback control behaviours, and then result in the instability and non synchronous phenomena of chaotic systems. There is still scope to put some efforts to reduce the conservatism in order to synchronize chaotic systems efficiently and more accurately.

Motivated by the above discussions, author investigates synchronization of chaotic systems subjected to the time delays, uncertainties and external disturbances. This paper also addresses the chaotic attractor of two different uncertain, external disturbance and time delays chaotic systems with non linearity inputs.

2 Mathematical Model

Consider an uncertain and external disturbance chaotic drive system

$$\frac{dX_d(t)}{dt} = (A + \Delta A) X_d(t) + F_d(X_d(t - T)) + D_d(t), \quad (1)$$

and an uncertain and external disturbance chaotic response system

$$\frac{dX_r(t)}{dt} = (B + \Delta B) X_r(t) + F_r(X_r(t - T_1)) + D_r(t) + U(t), \quad (2)$$

where $X_d = [x_d, y_d, \dots, z_d]^T \in \mathbb{R}^n$ and $X_r = [x_r, y_r, \dots, z_r]^T \in \mathbb{R}^n$ represent state vector variables. Matrices $A, B \in \mathbb{R}^{n \times n}$ are constant. Functions $F_d, F_r : \mathbb{R}^n \rightarrow \mathbb{R}^n$ are nonlinear. Parametric uncertainties $\Delta A, \Delta B \in \mathbb{R}^{n \times n}$ are bounded with $\|\Delta A\| \leq \lambda_d$ and $\|\Delta B\| \leq \lambda_r$. External disturbances $D_d(t)$ and $D_r(t)$ are bounded with $\|D_d(t)\| < \mu_d$ and $\|D_r(t)\| < \mu_r$. $\|\cdot\|$ denotes the matrix norm. Control function $U(t) \in \mathbb{R}^n$ is based on the synchronization method. Let the error state vector is defining in the following manner

$$e(t) = X_r(t) - X_d(t),$$

then the error system is obtained as

$$\begin{aligned} \frac{de(t)}{dt} &= (B + \Delta B + \Delta A)e(t) + F(X_d(t), X_r(t)) \\ &+ D_r(t) - D_d(t) + U(t), \end{aligned} \quad (3)$$

where

$$\begin{aligned} F(X_d(t), X_r(t)) &= F_r(X_r(t - T_1)) - F_d(X_d(t - T)) \\ &+ (B + \Delta B - A)X_d(t) - \Delta AX_r(t). \end{aligned}$$

Using active control method the appropriate control function is chosen to stabilize error system (3).

3 Systems Description

3.1 Advanced Lorenz System

The advanced Lorenz system [27] is given by the following set of differential equations

$$\begin{aligned} \frac{dx_d(t)}{dt} &= \alpha(y_d(t) - x_d(t)) \\ \frac{dy_d(t)}{dt} &= -x_d(t)z_d(t) + \beta x_d(t) + \gamma y_d(t) \\ \frac{dz_d(t)}{dt} &= x_d^2(t) - \delta z_d(t) \end{aligned} \quad (4)$$

where $x_d(t), y_d(t)$, and $z_d(t)$ are driving system state variables, α, β, γ and δ are parameters. When the system parameters are set to $\alpha = 20, \beta = 14, \gamma = 10.6, \delta = 2.8$ and initial condition $[x_d(t), y_d(t), z_d(t)]^T = [-19, -12, -6.5]^T$, chaotic attractor of the system (4) is shown in Fig. 1.

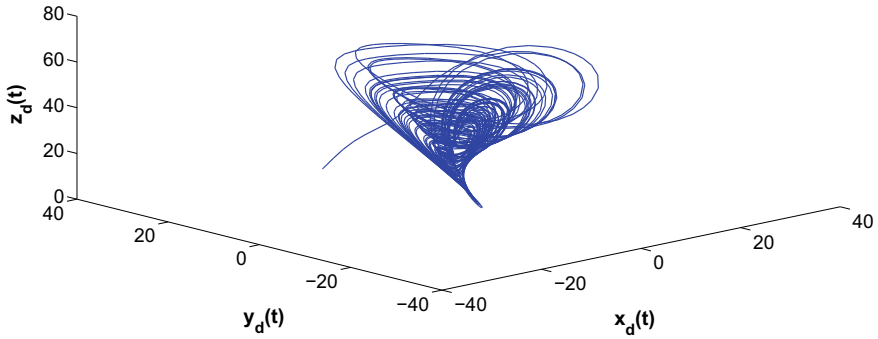


Fig. 1 Chaotic attractor of the advanced Lorenz system

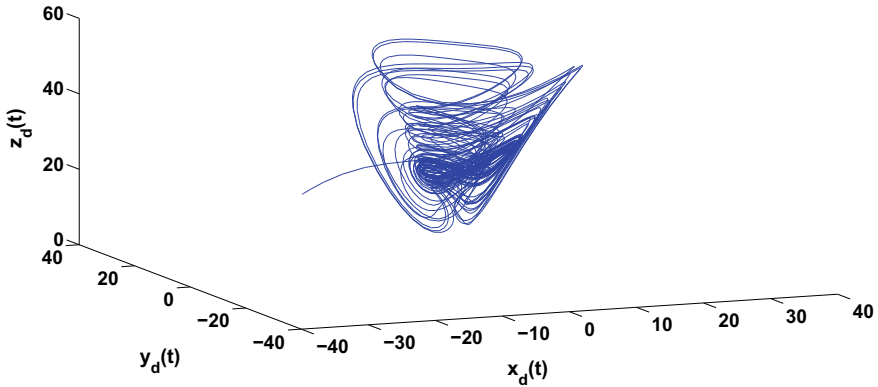


Fig. 2 Phase portrait of the time delay advanced Lorenz system

The time delay advanced Lorenz system [28] is given by

$$\begin{aligned}
 \frac{d x_d(t)}{d t} &= \alpha\left(y_d(t)-x_d(t)\right)+\rho x_d(t-\tau) \\
 \frac{d y_d(t)}{d t} &=-x_d(t) z_d(t)+\beta x_d(t)+\gamma y_d(t) \\
 \frac{d z_d(t)}{d t} &= x_d^2(t)-\delta z_d(t)
 \end{aligned}
 \tag{5}$$

where variables τ and ρ are lag time and control parameter respectively. For appropriate choice of the variables τ and ρ system (5) shows chaotic nature. For $\tau=0.001$, and $\rho=3$, phase portrait of the time delay chaotic system (5) is depicted in Fig. 2.

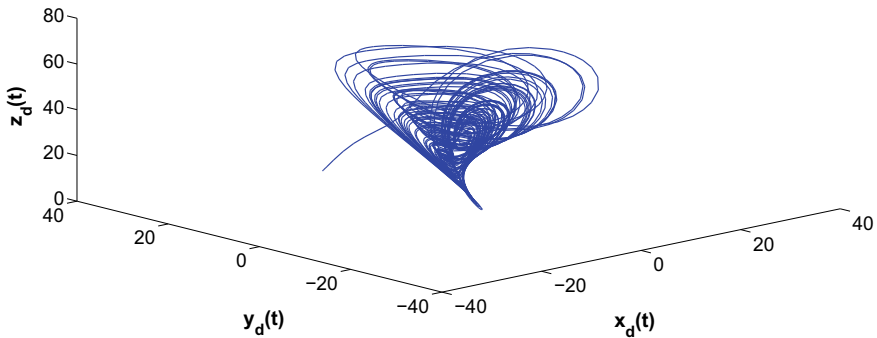


Fig. 3 Phase portrait of the uncertainty and external disturbance time delay advanced Lorenz system

In the presence of uncertainties terms and external disturbances, the time delay advanced Lorenz system (5) is consider as

$$\begin{aligned}
 \frac{d x_d(t)}{d t} &= \alpha\left(y_d(t)-x_d(t)\right)+\rho x_d(t-\tau)+0.12 x_d(t) \\
 &\quad +0.09 z_d(t)+0.5 \sin (10 t) \\
 \frac{d y_d(t)}{d t} &=-x_d(t) z_d(t)+\beta x_d(t)+\gamma y_d(t) \\
 &\quad +0.02 x_d(t)-0.3 \cos (50 t) \\
 \frac{d z_d(t)}{d t} &=x_d^2(t)-\delta z_d(t)+0.11 y_d(t)+0.3 z_d(t) \\
 &\quad +1.5 \sin (20 t)
 \end{aligned} \tag{6}$$

with the uncertainty $\Delta A = \begin{bmatrix} 0.12 & 0 & 0.09 \\ 0.02 & 0 & 0 \\ 0 & 0.11 & 0.3 \end{bmatrix}$ and the external disturbance $D_d(t) =$

$$\begin{bmatrix} 0.5 \sin (10 t) \\ -0.3 \cos (50 t) \\ 1.5 \sin (20 t) \end{bmatrix}. \text{ The phase portrait of the system (6) is shown by Fig. 3.}$$

3.2 Rössler System

The Rössler system [29] is written by the set of differential equations

$$\begin{aligned}
 \frac{d x_r(t)}{d t} &= -y_r(t) - z_r(t) \\
 \frac{d y_r(t)}{d t} &= x_r(t) + \alpha_1 y_r(t) \\
 \frac{d z_r(t)}{d t} &= \beta_1 + x_r(t) z_r(t) - \gamma_1 z_r(t)
 \end{aligned}
 \tag{7}$$

where $x_r(t)$, $y_r(t)$, and $z_r(t)$ are response system state variables, α_1 , β_1 and γ_1 are parameters. When system parameters are taken as $\alpha_1 = 0.2$, $\beta_1 = 0.2$, $\gamma_1 = 5.7$ and initial condition $[x_r(t), y_r(t), z_r(t)]^T = [0.5, 1, 1.5]^T$, chaotic attractor of the system (7) is shown in Fig. 4.

The double time delay Rössler system [30] is described as

$$\begin{aligned}
 \frac{d x_r(t)}{d t} &= -y_r(t) - z_r(t) + \rho_1 x_r(t - \tau_1) + \rho_2 x_r(t - \tau_2) \\
 \frac{d y_r(t)}{d t} &= x_r(t) + \alpha_1 y_r(t) \\
 \frac{d z_r(t)}{d t} &= \beta_1 + x_r(t) z_r(t) - \gamma_1 z_r(t)
 \end{aligned}
 \tag{8}$$

where variables τ_1 and τ_2 are lag time; ρ_1 and ρ_2 control parameter. For appropriate choice of the variables system (8) shows chaotic behaviour. For $\tau_1 = 1.0$, $\tau_2 = 2.0$, $\rho_1 = 0.2$ and $\rho_2 = 0.5$, phase portrait of the double time delay chaotic system (8) is depicted in Fig. 5.

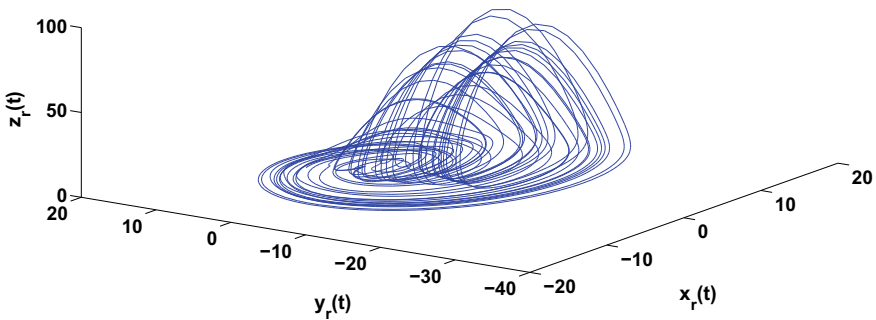


Fig. 4 Chaotic attractor of the Rössler system

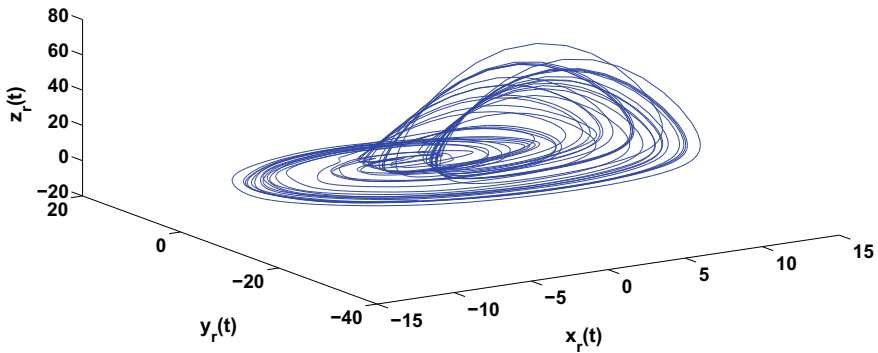


Fig. 5 Phase portrait of the double time delay Rössler system

With uncertain terms and external disturbances, the double time delay Rössler system is described as

$$\begin{aligned}
 \frac{dx_r(t)}{dt} &= -y_r(t) - z_r(t) + \rho_1 x_r(t - \tau_1) + \rho_2 x_r(t - \tau_2) \\
 &\quad + 0.01x_r(t) + 0.05 \sin(30t) \\
 \frac{dy_r(t)}{dt} &= x_r(t) + \alpha_1 y_r(t) + 0.05z_r(t) + 0.4 \cos(20t) \\
 \frac{dz_r(t)}{dt} &= \beta_1 + x_r(t) z_r(t) - \gamma_1 z_r(t) - 0.02y_r(t) \\
 &\quad + 0.1z_r(t) - 0.1 \sin(25t)
 \end{aligned} \tag{9}$$

with the uncertainty $\Delta B = \begin{bmatrix} 0.01 & 0 & 0 \\ 0 & 0 & 0.05 \\ 0 & -0.02 & 0.1 \end{bmatrix}$ and the external disturbance

$D_r(t) = \begin{bmatrix} 0.05 \sin(30t) \\ 0.4 \cos(20t) \\ -0.1 \sin(25t) \end{bmatrix}$. The phase portraits of the system (9) is shown through Fig. 6.

4 Synchronization

Consider the system (5) drives the system (9). Then the response system is written as

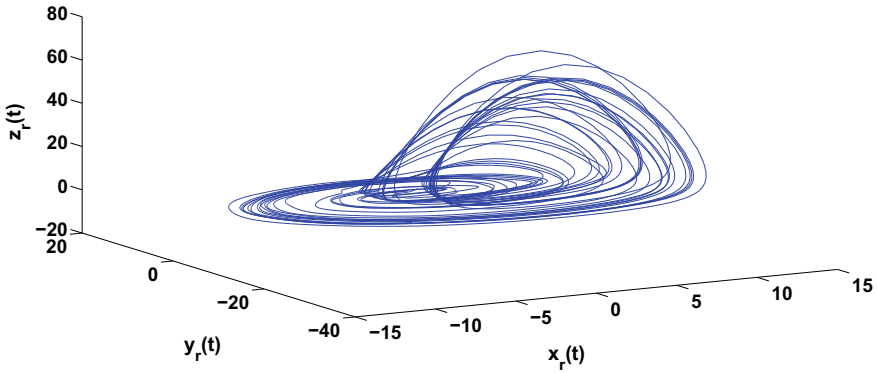


Fig. 6 Phase portrait of the uncertainty and external disturbance double time delay Rössler system

$$\begin{aligned}
 \frac{d x_r(t)}{d t} &= -y_r(t) - z_r(t) + \rho_1 x_r(t - \tau_1) + \rho_2 x_r(t - \tau_2) \\
 &\quad + 0.01 x_r(t) + 0.05 \sin(30t) + U_1(t) \\
 \frac{d y_r(t)}{d t} &= x_r(t) + \alpha_1 y_r(t) + 0.05 z_r(t) + 0.4 \cos(20t) + U_2(t) \quad (10) \\
 \frac{d z_r(t)}{d t} &= \beta_1 + x_r(t) z_r(t) - \gamma_1 z_r(t) - 0.02 y_r(t) \\
 &\quad + 0.1 z_r(t) - 0.1 \sin(25t) + U_3(t).
 \end{aligned}$$

Compare system (1) with system (6); and system (2) with system (10) and defining the active control functions as

$$\begin{aligned}
 U_1(t) &= \rho x_d(t - \tau) - \rho_1 x_r(t - \tau_1) - \rho_2 x_r(t - \tau_2) \\
 &\quad - (0.01 + \alpha) x_d(t) + (1 + \alpha) y_d(t) + z_d(t) \\
 &\quad + 0.12 x_r(t) + 0.09 z_r(t) + 0.5 \sin(10t) \\
 &\quad - 0.05 \sin(30t) + V_1(t) \\
 U_2(t) &= -x_d(t) z_d(t) - (1 - \beta) x_d(t) \\
 &\quad - (\alpha_1 - \gamma) y_d(t) - 0.05 z_d(t) \\
 &\quad + 0.2 x_r(t) - 0.4 \cos(20t) \\
 &\quad - 0.3 \cos(50t) + V_2(t) \\
 U_3(t) &= x_d^2(t) - \beta_1 - x_r(t) z_r(t) + 0.02 y_d(t) \\
 &\quad - (0.1 + \delta + \gamma_1) z_d(t) + 0.11 y_r(t) \\
 &\quad + 0.3 z_r(t) + 1.5 \sin(20t) \\
 &\quad + 0.1 \sin(25t) + V_3(t)
 \end{aligned} \quad (11)$$

and taking the error variables as

$$e_1(t) = x_r(t) - x_d(t), \quad e_2(t) = y_r(t) - y_d(t), \quad e_3(t) = z_r(t) - z_d(t),$$

the error system (3) is reduced to

$$\begin{aligned} \frac{d e_1(t)}{d t} &= 0.13 e_1(t) - e_2(t) - .01 e_3(t) + V_1(t) \\ \frac{d e_2(t)}{d t} &= 0.12 e_1(t) + \alpha_1 e_1(t) + 0.05 e_3(t) + V_2(t) \\ \frac{d e_3(t)}{d t} &= -0.09 e_2(t) + (0.4 - \gamma_1) e_3(t) + V_3(t). \end{aligned} \quad (12)$$

The error system (12) is to be controlled by a new control linear function of error states inputs $V_1(t)$, $V_2(t)$ and $V_3(t)$. Defining the appropriate control inputs $V_i(t)$, in order to stabilize the system (12) such that $\lim_{t \rightarrow \infty} e_i(t) = 0$, $i = 1, 2, 3$. This means that that system (6) can be asymptotically synchronized with system (10). This is achieved by choosing a 3×3 matrix A such that

$$\begin{bmatrix} V_1(t) \\ V_2(t) \\ V_3(t) \end{bmatrix} = A \begin{bmatrix} e_1(t) \\ e_2(t) \\ e_3(t) \end{bmatrix}.$$

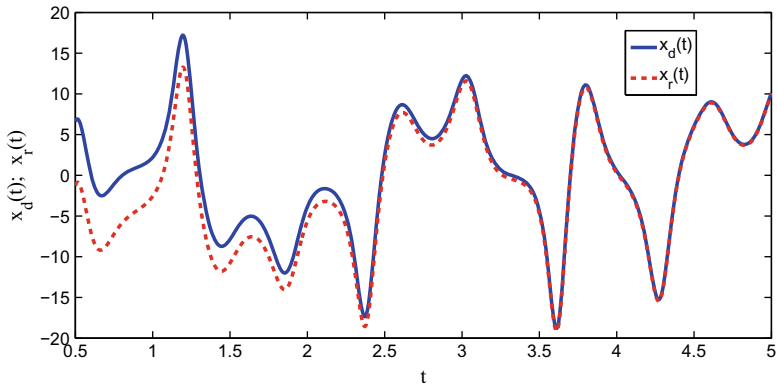
Let the matrix A is chosen in the form

$$A = \begin{bmatrix} -1.13 & 1 & 0.01 \\ -0.12 & \alpha_1 - 1 & -0.05 \\ 0 & -0.09 & \gamma_1 - 1.4 \end{bmatrix}.$$

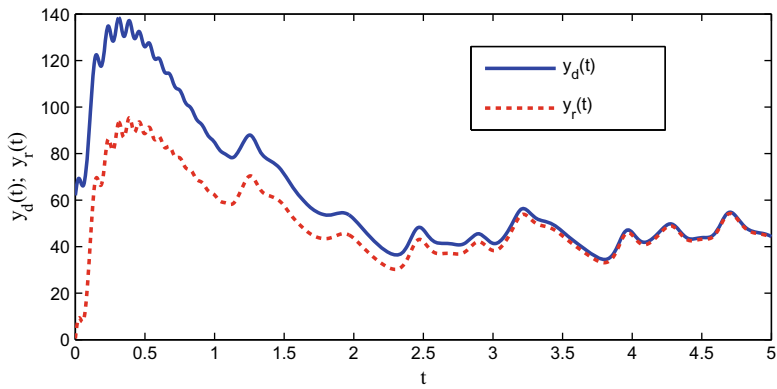
In this particular choice, the closed loop system has the eigen values -1 , -1 and -1 , which leads that the error states $e_i(t) \rightarrow 0$ as $t \rightarrow \infty$, $i = 1, 2, 3$. Thus the synchronization between considered systems (6) and (10) is achieved.

5 Simulation Results

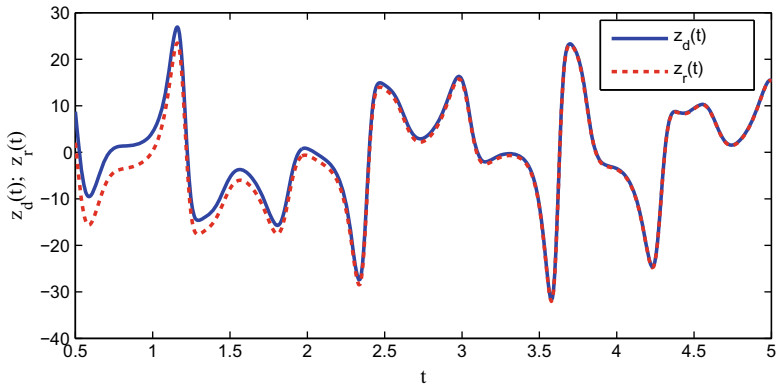
In this section, numerical simulation results are presented to show the effectiveness of considered active control method in synchronization of advanced Lorenz system and Rössler system along with time delay, uncertainties and external disturbances. Taking time step size $t = 0.001$, fourth order Runge-Kutta method is applied to solve the differential equations. Then initial error vector is $[e_d(t), e_r(t), e_3(t)]^T = [19.5, 13, 8]^T$ as parameters are used as previous. The state trajectories of drive system (6) and response system (10) are shown in Fig. 7. It is observed from Fig. 8 that the advanced Lorenz system and Rössler systems are synchronized with error functions converge to zero as time becomes very large.



(a) x_d and x_r



(b) y_d and y_r



(c) z_d and z_r

Fig. 7 State trajectories of the drive and response systems

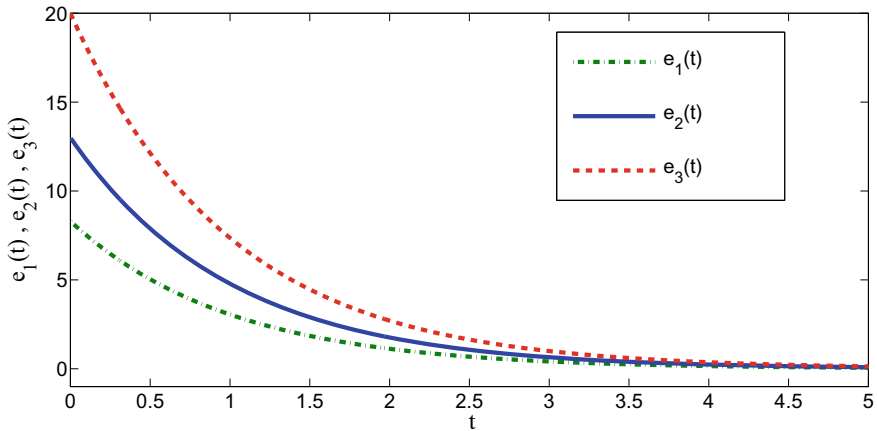


Fig. 8 Error plot

Acknowledgments The author, Dr. A. K. Singh wishes to express his gratitude to Prof. Subir Das of the Department of Mathematical Sciences, Indian Institute of Technology (BHU), Varanasi-221005, India, for his continued assistance.

References

1. Pecora LM, Carroll TL (1990) Synchronization in chaotic systems. *Phys Rev Lett* 64(8):821
2. Ge ZM, Lee CI (2005) Control, anticontrol and synchronization of chaos for an autonomous rotational machine system with time-delay. *Chaos Solitons Fract* 23(5):1855–1864
3. Ge ZM, Lee CI (2005) Anticontrol and synchronization of chaos for an autonomous rotational machine system with a hexagonal centrifugal governor. *J Sound Vib* 282(3–5):635–648
4. Chu YD, Zhang JG, Li XF, Chang YX, Luo GW (2008) Chaos and chaos synchronization for a non-autonomous rotational machine systems. *Nonlinear Anal R World Appl* 9(4):1378–1393
5. Liu H, Jin H, Liao X, Yu C, Xu CZ (2011) Live virtual machine migration via asynchronous replication and state synchronization. *IEEE Trans Parallel Distrib Syst* 22(12):1986–1999
6. Singh AK, Yadav VK, Das S (2017) Dual combination synchronization of the fractional order complex chaotic systems. *J Comput Nonlinear Dyn* 12(1):011017
7. Weng T, Yang H, Gu C, Zhang J, Small M (2019) Synchronization of chaotic systems and their machine-learning models. *Phys Rev E* 99(4):042203
8. Ott E, Grebogi C, Yorke JA (1990) Controlling chaos. *Phys Rev Lett* 64(11):1196
9. Singh AK, Yadav VK, Das S (2017) Synchronization between fractional order complex chaotic systems. *Int J Dyn Control* 5(3):756–770
10. Lü J, Lu J (2003) Controlling uncertain Lü system using linear feedback. *Chaos Solitons Fractals* 17(1):127–133
11. Singh AK, Yadav VK, Das S (2016) Comparative study of synchronization methods of fractional order chaotic systems. *Nonlinear Eng* 5(3):185–192
12. Park JH, Kwon O (2005) LMI optimization approach to stabilization of time-delay chaotic systems. *Chaos Solitons Fractals* 23(2):445–450
13. Singh AK, Yadav VK, Das S (2019) Nonlinear control technique for dual combination synchronization of complex chaotic systems. *J Appl Nonlinear Dyn* 8(2):261–277

14. Chua LO, Itoh M, Kocarev L, Eckert K (1993) Chaos synchronization in Chua's circuit. *J Circuits Syst Comput* 3(01):93–108
15. Chen M, Han Z (2003) Controlling and synchronizing chaotic Genesio system via nonlinear feedback control. *Chaos Solitons Fractals* 17(4):709–716
16. Singh AK, Yadav VK, Das S (2019) Synchronization of time-delay chaotic systems with uncertainties and external disturbances. *Discontin Nonlinearity Complex* 8(1):13–21
17. Han X, Lu JA, Wu X (2004) Adaptive feedback synchronization of Lü system. *Chaos Solitons Fractals* 22(1):221–227
18. Yassen M (2005) Adaptive synchronization of rossler and Lü systems with fully uncertain parameters. *Chaos Solitons Fractals* 23(5):1527–1536
19. Singh AK, Yadav VK, Das S (2017) Synchronization between fractional order complex chaotic systems with uncertainty. *Optik* 133:98–107
20. Park JH (2005) Adaptive synchronization of Rossler system with uncertain parameters. *Chaos Solitons Fractals* 25(2):333–338
21. Elabbasy E, Agiza H, El-Dessoky M (2004) Adaptive synchronization of Lü system with uncertain parameters. *Chaos Solitons Fractals* 21(3):657–667
22. Ikeda K, Daido H, Akimoto O (1980) Optical turbulence: chaotic behavior of transmitted light from a ring cavity. *Phys Rev Lett* 45(9):709
23. Singh AK (2022) Synchronization and secure communication of chaotic systems. In: Iyer B, Ghosh D, Balas VE (eds) *Appl Inf Process Syst*. Springer, Singapore, pp 575–584
24. Mackey MC, Glass L (1977) Oscillation and chaos in physiological control systems. *Science* 197(4300):287–289
25. Yongzhen P, Shuping L, Changguo L (2011) Effect of delay on a predator-prey model with parasitic infection. *Nonlinear Dyn* 63(3):311–321
26. Singh AK (2022) Complex chaotic systems and its complexity. In: Chadli O, Das S, Mohapatra RN, Swaminathan A (eds) *Mathematical analysis and applications*. Springer, Singapore, pp 1–9. https://doi.org/10.1007/978-981-16-8177-6_10
27. Chen G, Lü J (2003) *Dynamics of the Lorenz system family: analysis, control and synchronization*. Science Press, Beijing
28. Xiao-hong Z, Zhi-yong C, Yuan-yuan Z (2009) Synchronization and circuit experiment simulation of chaotic time-delay systems. In: 2009 Pacific-Asia conference on circuits, communications and systems. IEEE, pp 781–784
29. Rössler OE (1976) An equation for continuous chaos. *Phys Lett A* 57(5):397–398
30. Ghosh D, Chowdhury AR, Saha P (2008) Multiple delay Rössler system-bifurcation and chaos control. *Chaos Solitons Fractals* 35(3):472–485

Optimization Techniques

Optimization of Machining Parameters on Vertical Milling Machine for Al-CNT Composites Using Taguchi Design of Experiments



Sachchida Nand, Manvandra Kumar Singh, and C. M. Krishna

Abstract Aluminum is ductile, cheapest, and light material and when alloyed with CNT using casting methods have wide applications in aviation industry and automobile industry due to its increase in strength and decrease in weight. In order to make various components, the machinability of this alloy needs to be tested on CNC machines which are mostly applicable for increasing productivity. In this paper, work piece selected is Al-CNT composite and tool material selected is HSS tool and experiments are performed for different combinations of selected input variables. The objective of this research, on the basis of optimum values of material removal rate (MRR) and tool wear rate (TWR), is to derive an optimum combination of these input variables for maximizing productivity. Input parameters used are cutting speed (N), feed (F), and depth of cut (Dp) and the range of values considered for study are based on various speed ranges used in automobile industry. For data collection, Taguchi (L9 orthogonal array) design of experiments are used and for regression modeling, ANOVA (MINITAB version 18) is used. Regression equations for material removal rate and tool wear rate are presented for prediction purpose.

Keywords Al-CNT composite · Cutting parameters · Productivity · Design of experiments · And vertical milling machine

S. Nand (✉) · M. K. Singh
Department of Mechanical Engineering, Amity School of Engineering and Technology, AUMP,
Gwalior 474005, India

M. K. Singh
e-mail: mksingh@gwa.amity.edu

C. M. Krishna
Department of Mechanical Engineering, Maulana Azad National Institute of Technology, Bhopal,
M.P 462003, India

1 Introduction

In several engineering applications, there is a requirement of very light material with good mechanical properties. Aerospace, automobile, sports equipment, electronic equipment, etc., are some of the applications which need these required properties. The metal matrix composites produced by Aluminum 6061 and CNTs may be appropriate solution for such types of applications. In most of the cases, machining of Al-CNT composite on milling machine poses a challenge if the CNT in the matrix is not distributed uniformly. Hence, it is important to study the such composites' machining characteristics and to understand how the input parameters, such as, depth of cut, feed, and cutting speed are to be selected in order to maximize selected output parameters. In this research paper, CNC high speed vertical milling machine is selected for machining Al-CNT composite and to conduct experiments using Taguchi Design of Experiments in order to decrease the number of experiments and to reduce experimentation time and cost. In addition to reduction of cost, to concentrate mainly on productivity, this can be achieved by taking material removal rate and tool wear rate as output parameters. As material removal rate increases, the manufacturing time and in turn manufacturing cost reduce drastically and hence productivity increases.

Aladdin [1] predicted tool life in the end milling process and obtained first- and the second-order models by using a response surface optimization process that has a leading factor, speed, axial cutting depth, and feed. Alekseev et al. [2] observed that the impact of carbon nanotubes which in form of different weight percentage in the mechanical properties of cast A5 aluminum with CNT's composite. Alojzic et al. [3] studied the key challenges of product customization, shorter lead-time, and growing product diversities to meet new levels of the manufacturing standard from governing to distributed systems for manufacturing industries. Aranke et al. [4] studied tribological behavior of AA 7075 reinforced with MWCNT by pin-on-disc, block-on-ring, abrasive wear tester, etc.

Arunachalam et al. [5] discussed the importance of stir casting in the productions of MMCs. Baskar et al. [6] established different types of algorithms (GA, Hill Climbing algorithm, memetic algorithm, etc.) for milling operations to optimize different machining variables (i.e., genetic algorithm (GA), memetic algorithm, and hill climbing algorithm) and for both single-tool and multi-tool operations by taking the three objective functions, such as (a) less production cost, (b) low production time, and (c) more profit. Bhashara et al. [7] proposed adaptation of a crossover for the single factory that manufactures the components and considered in most of the process planning cases. Brezocnik et al. [8] predicted and established genetic algorithm programming for surface roughness and obtained the prediction accuracy increase by vibrations in the end milling process when the feed rate is most influenced by surface roughness. Choi et al. [9] developed nanostructured composite of Al 2024/CNTs and investigated strengthening characteristics in terms of boundary hardening, edge hardening, and hardening by CNTs. Chandrasekaran et al. [10] reviewed on modeling and optimization using soft computing methods spanning approximately two decades.

Dewangan et al. [11] experimented with the uniform dispersion of CNT in MMC by ultrasonic waves of high intensity. Esawi [12] studied the effect on mechanical properties of CNTs on Al composite prepared by the application of ball milling process and hot extrusion process. Fnides et al. [13] studied cutting force and roughness of surface of components made of hot work steel. The author introduced a mathematical model and identified that the tangential cutting force is very sensitive to the variation of depth of cut and to the variation of cutting forces. Feed rate and flank wear variations are also responsible for surface roughness. Ganesh Babu et al. [14] achieved the machining parameter effects to show if depth of cut increases then cutting force in the direction of tangent is also increased throughout end milling operation on AlSiC metal matrix composite material. Ghani et al. [15] correlated different machining variables of speed, low depth of cut, and low feed rate for improved surface finish and minimum cutting force. Results have shown that axial depths of cut increase when cutting forces also increase.

Pare et al. [16] obtained surface roughness models after optimization using four meta-heuristic techniques and their work admitted that gravitation search algorithm (GSA) proved to be the finest out of these four unconventional optimization techniques for surface roughness and that teacher–learner-based optimization (TLBO) gave better result in terms of number of iterations. They found that non-linear regression equation, better explains the correlation between surface roughness and input parameters. From this literature review, output parameters, such as, tool wear rate, and material removal rate are selected. Similarly, input parameters, such as, cutting speed, depth of cut, and feed rate are selected. A regression modeling is used for establishing relationship between the above variables. These are explained in the subsequent paragraphs.

2 Methodology and Experimentation

In this research, experiment contains three factors each at three levels. So, total number of runs required is 27 without replications. With three replications, for each combination, total number of experiments is 81. But by Taguchi L9 array, nine experiments have been carried in order to make meaningful conclusions with 96% confidence level.

2.1 Work Material

In present study, Al-CNT is used as work piece. It is suitable for manufacturing of automotive and aeronautics industry components. The Al-CNT composite is prepared using stir casting method. The advantage of this method is that the composite is made using controlled conditions and desired consistency can be obtained by selecting

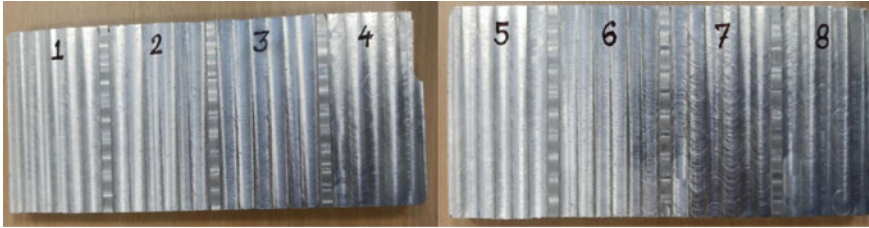


Fig. 1 Work piece after machining

proper speed of stirring the mixture of Al and CNT. Work piece after machining is shown in Fig. 1.

2.2 Selection of Equipment and Tools

The tool selection is done on the basis of five factors, such as the machine being used, the material being used, the quantities of machining parts, the requirements of the customer, and the details of the tool to be used. For measuring the weights of work piece and machine tool before and after machining, a weighing machine is used separately for work piece and the tool. In this paper, a CNC milling machine of computer aided manufacturing laboratory (in MANIT, Bhopal) is used for machining of Al-CNT ($150 \times 70 \times 25$ mm) with selected process parameters and with end mill cutting tool (HSS). The CNC milling machine is having Siemen's code and 20 tool magazine supplied by MTAB MaxMill Plus.

2.3 Process Parameters and Their Different Levels

The input process parameters for milling operation and their several levels are given in Table 1. The output parameters chosen are material removal rate and tool wear rate. They are measured as weight difference during machining divided by the machining time. Greater value of material removal rate and least value of tool wear rate are preferred.

Table 1 Input process parameters and their different levels

Input parameters	Level 1	Level 2	Level 3
Spindle speed (rpm)	2000	3000	4000
Feed rate (mm/min)	100	150	200
Depth of cut (mm)	0.2	0.3	0.4

3 Results and Analysis

The data collected with necessary calculations are shown in Table 2. For the development of linear regression equation using MINITAB software, this data is used. Regression analysis process is used for developing the relationship among variables in order to predict output variables. The linear regression equations developed using MINITAB 18 software, are shown in Eqs. (1 and 2).

$$MRR = - 0.0534 + 0.000028V + 0.000179F + 0.0966D \tag{1}$$

$$TWR = -0.000248 + 0.000000V + 0.000000F + 0.000244D \tag{2}$$

The significance of input factors on MRR and TWR are tested using ANOVA analysis (shown in Tables 3 and 4) and they are found to be significant to 95% confidence limit as evident by the P-value obtained. The coefficients are significant as the F-value is greater than the tabulated F-value. Hence, the above equations can be used for predicting MRR and TWR for given input variables.

Table 2 Experimental data and computed output variables

Exp. no.	V	F	D	MRR	TWR
1	2000	150	0.2	0.049689	3.10881E-05
2	2000	200	0.3	0.061739	6.08696E-05
3	2000	250	0.4	0.089484	0.000129032
4	2500	150	0.3	0.063492	6.34921E-05
5	2500	200	0.4	0.085988	0.000117284
6	2500	250	0.2	0.091714	0.000131429
7	3000	150	0.4	0.1075	0.000177632
8	3000	200	0.2	0.083403	0.000115183
9	3000	250	0.3	0.093094	0.000154696

Table 3 Analysis of variance for MRR

Source	DF	Adj SS	Adj MS	F-value	P-value
Regression	3	0.002195	0.000732	6.92	0.031
V	1	0.001156	0.001156	10.93	0.021
F	1	0.000479	0.000479	4.53	0.087
D	1	0.000560	0.000560	5.29	0.070
Error	5	0.000529	0.000106		
Total	8	0.002724			

Table 4 Analysis of Variance for TWR

Source	DF	Adj SS	Adj MS	F-value	P-value
Regression	3	0.000000	0.000000	9.42	0.017
V	1	0.000000	0.000000	15.58	0.011
F	1	0.000000	0.000000	6.20	0.055
D	1	0.000000	0.000000	6.49	0.051
Error	5	0.000000	0.000000		
Total	8	0.000000			

4 Conclusion

This study indicates that the parameters cutting speed, feed, and depth of cut are the essential factors impacting the MRR and TWR of Al-CNT composites. The regression equations are developed. They can be used successfully for predicting the output variables with a confidence limit of 95%. These results can be used by industrialists for setting their machining conditions for given output variables and researchers for optimizing the machining conditions using various optimization techniques.

References

1. Alauddin M, El Baradie MA (1997) Tool life model for end milling steel (190 BHN). *J Mater Process Technol* 68:50–59
2. Alekseeva AV, Dubova DY, Predtechenskiya MR (2018) Influence of carbon nanotubes on mechanical properties of cast aluminum, grade A5. *Inorgan Mater Appl Res* 9(2):270–278
3. Alojzij S, Peter B, Goran B (1998) A multi-agent approach to process planning and fabrication in distributed manufacturing. *Comput Ind Eng* 35:455–458
4. Aranke O, Gandhi C, Dixit N, Kuppan P (2018) Influence of multiwall carbon nanotubes (MWCNT) on wear and coefficient of friction of aluminium (Al7075) metal matrix composite. *Mater Today Proc* (5):7748–7757
5. Ramanathan A, Krishnan PK, Muraliraja R (2019) A review on the production of metal matrix composites through stir casting–furnace design, properties, challenges, and research opportunities. *J Manufact Process* 42:213–245
6. Baskar N, Asokan P, Saravanan R, Prabhakaran G (2006) Selection of optimal machining parameters for multi-tool milling operations using a memetic algorithm. *J Mater Proc Technol* 174, 239–249
7. Bhashara RSV, Shunmugam MS, Narendran TT (1999) Operation sequencing in CAPP using genetic algorithms. *Int J Prod Res* 37(5):1063–1074
8. Brezocnik M, Kovacic M, Ficko M (2004) Prediction of surface roughness with genetic programming. *J Mater Process Technol* 157:28–36
9. Choi HJ, Min BH, Shin JH, Bae DH (2011) Strengthening in nanostructured 2024 aluminum alloy and its composites containing carbon nanotubes. *Compos Part A* 42:1438–1444
10. Chandrasekaran M, Muralidhar M, Murali KC (2010) U. S. Dixit.: Application of soft computing techniques in machining performance prediction and optimization: a literature review. *Int J Adv Manufact Technol* 46:445–464

11. Dewangan S, Ganguly SK, Banchhor R (2018) Analysis of Al 6061-TiO₂-CNT metal matrix composites produced by stir casting process. *Int J Eng Manag Res* 8:147–152
12. Esawi AMK, Morsi K, Sayed A, Taher M, Lanka S (2010) Effect of carbon nanotube (CNT) content on the mechanical properties of CNT-reinforced aluminium composites. *Compos Sci Technol* 70(16):2237–2241
13. Fnides B, Aouici H, Yallese MA (2008) Cutting forces and surface roughness in hard turning of hot work steel X38CrMoV5-1 using mixed ceramic. *Int J Sci Res* 2(70):73–78
14. Ganeshbabu B, Selladurai V, Shanmugam R (2008) Analytical modeling of cutting forces of end milling operation on aluminum silicon carbide particulate metal matrix composite material using response surface methodology. *ARNP J Eng Appl Sci* 3(2):5–18
15. Ghani JA, Choudhury IA, Hassan HH (2004) Application of Taguchi method in the optimization of end milling parameters. *J Mater Process Technol* 145:84–92
16. Pare V, Agnihotri G, Krishna C (2015) Selection of optimum process parameters in high-speed CNC end-milling of composite materials using meta-heuristic technique- a comparative study. *J Mech Eng* 61(3):176–186

Numerical Study on Domain Independency for Prediction of Vortex Shedding Parameters of a Circular Cylinder



Vidya Chandran, Sheeja Janardhanan, and M. Sekar

Abstract The catastrophes of history make vortex-induced vibration an extensively studied area. The response predictions of offshore and sub-sea structures have gained importance off-late ever since these have been widely used by the petroleum industry. Most of the studies have confined to the comprehension of wake characteristics and the estimation of hydrodynamic loading and shedding parameters of stationary cylinders. Computational fluid dynamics has evolved as one of the effective tools in prediction of response characteristics under vortex shedding and many researchers have studied various aspects of computations that are crucial with reasonable degree of accuracy. This paper addresses the effect of the geometrical shape of fluid domain that encompasses a marine riser during simulations. Four different shapes are analyzed using Reynolds Averaged Navier–Stokes Equation-based commercial solver, ANSYS®. All four domains have the same number of elements, mesh density, and flow Reynolds number (Re). Hydrodynamic force coefficients and frequency of shedding in each case were estimated and compared with previously published numerical and experimental results. It is observed that circular domain is the most efficient in predicting both loading and shedding characteristics with less than 10% deviation as against the theoretical results. Elliptical and square domains failed to capture the vortex shedding phenomenon. The study reveals a significant characteristic of numerical simulations on the modeling and meshing of both near-wall and wake regions.

Keywords Vortex-induced vibration · CF response · IL response

V. Chandran

SCMS School of Engineering and Technology, Ernakulum, Kerala, India

S. Janardhanan

School of Naval Architecture and Ocean Engineering, Indian Maritime University,
Visakhapatnam, Andhra Pradesh, India

M. Sekar (✉)

AAA College of Engineering and Technology, Sivakasi, Tamil Nadu, India

© The Author(s), under exclusive license to Springer Nature Singapore Pte Ltd. 2022

353

M. K. Singh and R. K. Gautam (eds.), *Recent Trends in Design, Materials
and Manufacturing*, Lecture Notes in Mechanical Engineering,

https://doi.org/10.1007/978-981-16-4083-4_28

1 Introduction

When a bluff body encounters a fluid flow at Reynolds Number (Re) above 40, it is observed to oscillate in the direction of fluid flow and also perpendicular to it. This phenomenon is a result of boundary layer separation in the wake of the bluff body owing to adverse pressure gradients. Vortex-induced vibration (VIV) of underwater structures is a much investigated topic from the nineteenth century. Progress in research on this complex phenomenon took pace with the famous Tacoma Narrows Bridge collapse in 1940. A wind of a very normal speed of approximately 20 m/s caused the bridge to undergo torsional vibrations at the rate of 14 vibrations/min [1]. The collapse of this bridge which spanned the Tacoma Narrows strait was primarily due to aero-elastic flutter caused by resonance of the wind frequency and the natural frequency of the structure. The wind frequency may be interpreted as the frequency at which, the air flow across the bridge was shedding vortices in its wake. This incident boosted the research in the field of VIV, which led to the development of many tools for predicting vortex shedding frequency and amplitude. Several analytical, empirical, semi-empirical, experimental, and numerical tools were developed for accurate prediction of VIV of underwater structures [2, 3] anticipating such catastrophes in ocean environment and also understanding the level of fatality when associated with highly explosive petroleum products. Even though experimental approaches are more reliable, they are indeed expensive and demand huge infrastructure. The need for visualization and thereby understanding the inherent physics of such complex fluid structure interaction phenomenon pave way to numerical analysis of flow around bluff bodies using Computational Fluid Dynamics (CFD) tools [4]. The accuracy of prediction using CFD depends on many factors such as the geometry, grid quality, turbulence modeling, etc. Since vortex shedding is a coupled fluid structure interaction phenomenon greatly influenced by the wake of the structure, modeling of the wake flow is as important as that of the near wall flow [5]. Hence, unlike other CFD problems, VIV prediction is highly influenced by the shape of the domain selected for analysis. In this paper, a comparative study of the accuracy of VIV prediction is conducted for four different two-dimensional (2D) domain shapes—circular, elliptical, rectangular, and square domains with a uniform average mesh density and flow parameters are determined.

1.1 Vortex-Induced Vibration

Vortex shedding is a fluid phenomenon occurring at the wake of bodies, especially bluff bodies as a result of boundary layer separation. The separated layer will tend to cause fluid rotation, since the outer layer which is in contact with the free stream, moves faster than the inner layer, in contact with the body surface. This fluid rotation results in the formation of vortices, which are shed at the wake of the body alternatively from either side. The alternate shedding of vortices leads to the development

of different lift forces on each side of the body causing the body to oscillate in the direction perpendicular to the direction of flow, otherwise known as cross flow (CF) direction [6]. If the vortex shedding frequency matches the natural frequency of the body, it will enter into resonant vibration at high amplitudes. This phenomenon is known as lock-in [7]. Boundary layer separation and the resulting vortex shedding also leads to variation of drag force on either side of the body in the direction of flow. As a result, the body oscillates in the direction of flow otherwise known as in-line (IL) direction [8]. It is observed that during lock-in the body oscillates with a frequency equal to that of vortex shedding in CF direction and at twice that of vortex shedding in the IL direction [9].

Hydrodynamic lift and drag forces acting on the body during vortex shedding is given by Eqs. (1 and 2), respectively.

$$F_L = \frac{1}{2} C_L \rho A V^2 \quad (1)$$

$$F_D = \frac{1}{2} C_D \rho A V^2 \quad (2)$$

C_D is the coefficient of drag, ρ is the density of the fluid, A is the projected area of the object, and V is the free stream velocity of the fluid. C_L is the coefficient of lift.

The magnitude of hydrodynamic force coefficients and the shedding frequency strongly depends on the flow Reynolds number, Re . The shedding frequency can be expressed non-dimensionally as Strouhal Number, St as shown in Eq. (3):

$$St = \frac{f_v D}{V} \quad (3)$$

f_v is the shedding frequency. Accurate prediction of these parameters is critical in the design of offshore structures and pipelines to keep them away from the lock-in region, which may lead to severe catastrophes [10].

Studies have proved CFD as an efficient tool to predict the hydrodynamic vortex shedding parameters [11]. Influence of several parameters like grid quality and turbulence model used in the analysis were investigated by several researchers [12, 13]. It was observed that quality of grid not only in the near wall region but also in the wake is much important for predicting this complex fluid–structure interaction phenomenon. In this paper, a comparative study on the accuracy of shedding parameters predicted by four different domain shapes is presented. A comparative study on circular, elliptical, rectangular, and square domains were carried out to ascertain the most appropriate geometrical shape for simulations in this field.

2 Numerical Model

2.1 Meshing

Flow around a 2D cylinder of diameter 0.02 m is analyzed using four different domain shapes to compare values of vortex shedding parameters. For each domain, a structured grid is generated using ANSYS® 18 ICEM CFD platform. The study aims to find the most suitable domain shape for the prediction of vortex shedding characteristics. Figures 1a–d show the computational domains used for the estimation of hydrodynamic loads and shedding frequency of a stationary cylindrical structure. The origin of the Cartesian coordinate system is located at the center of the cylinder. The domain size is fixed ensuring there is no boundary or entrance effect.

Since vortex shedding is a fluid phenomenon for which wake characteristics are important, capturing of wake flow physics is ensured by taking wake length sufficiently large. For each domain, the maximum lateral distance from the cylinder to the boundary, especially in flow direction is taken equal to $30D$ [14], where D is the diameter of the cylinder. The geometric parameters of various domains are represented in Table 1. The geometry has been blocked and a structured mesh was generated for hydrodynamic analysis. A grid independency test has also been conducted at $Re = 1000$ for the selected domain.

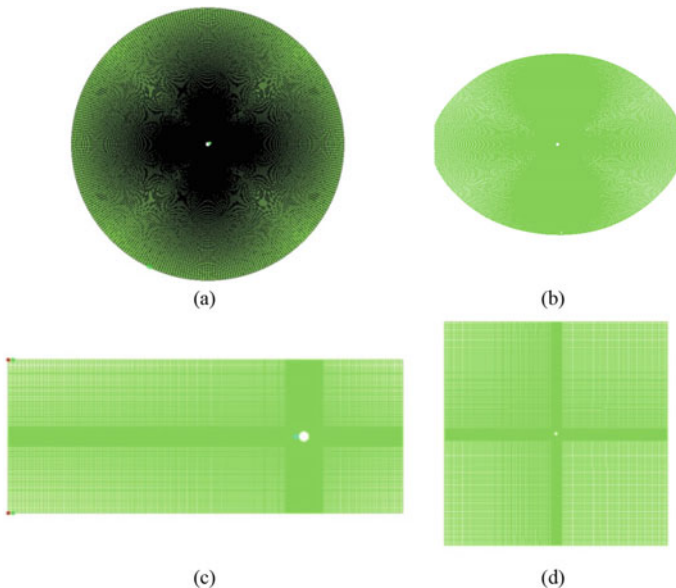


Fig. 1 Various domains used for simulation of flow past 2D cylinder **a** Circular domain, **b** Elliptical domain, **c** Rectangular domain, and **d** Square domain

Table 1 Geometric parameters of various domains

Domain type	Minimum element size	Total no. of Elements	Domain size	Domain area (m ²)
Circular	0.0002	79,000	Diameter, $d = 1.2$ m	1.13
Elliptical	0.0002	79,000	Major axis, $a = 0.8$ m Minor axis, $b = 1.2$ m	0.75
Rectangular	0.0002	79,000	Length, $L = 0.8$ m, Breadth, $B = 0.4$ m	0.32
Square	0.0002	79,000	Side, $S = 1.2$ m	1.44

Vortex shedding is a boundary layer phenomenon. Hence, the accuracy of prediction of the hydrodynamic force coefficients strongly depends on near wall grid elements. The near wall element size for each grid is 2×10^{-4} which is observed to be sufficient to accommodate at least 20 elements within the hydrodynamic boundary layer of the cylinder. For each case, the total number of elements is also controlled and made not more than 80,000. Details of various grids are given in Table 1.

2.2 Flow Analysis

The hydrodynamic analysis of each grid is performed using ANSYS®-18 FLUEN. Flow Re is maintained uniform at $Re = 1000$, which falls in the subcritical range [15]. Fluid consider for the simulation is water—liquid which is available in the fluent materials data base. Density of water (ρ) is 998.2 kg/m^3 and the dynamic viscosity is 0.0001 Pa.s . Details of boundary conditions applied are given in Table 2. Pressure and velocity are coupled using PISO scheme with skewness correction factor unity. Least square cell-based gradient is chosen for spatial discretization. Spatial discretization

Table 2 Details of applied boundary conditions for hydrodynamics flow analysis

	Boundary	Domain type			
		Circular	Elliptical	Rectangular	Square
Boundary conditions	Inlet	Velocity inlet (Specified velocity)	Velocity inlet (specified velocity)	Velocity inlet (specified velocity)	Velocity inlet (specified velocity)
	Outlet	Pressure outlet	Pressure outlet	Pressure outlet	Pressure outlet
	Cylinder wall	No slip	No slip	No slip	No slip
	sidewalls	–	Symmetry boundary condition	Symmetry boundary condition	Symmetry boundary condition

scheme for pressure, momentum, and turbulent kinetic energy is set as second-order upwind. A first-order implicit transient formulation is used for the simulation.

Time step size for the transient simulation is fixed as 0.001 s ensuring the near wall Courant number to be less than unity. Also, for capturing the shedding phenomenon properly, it is ensured that each theoretical time period of shedding (calculated from St Number) consists at least 20 time steps. To account for the increased turbulence, $k-\omega$ SST model has been used. Contours of pressure distribution in the domain are given in Fig. 2 and the time histories of C_L and C_D in Fig. 3. From the contours of pressure distribution, shedding of alternate vortices is evident at current Re . The cylinder is expected to oscillate at the frequency of vortex shedding which is same as that of the frequency of oscillation of lift force or lift coefficient.

Hydrodynamic forces estimated from the flow analysis are expressed in non-dimensional coefficients of lift and drag. Fluent simulation writes the time histories of these coefficients. The time histories of lift and drag coefficient after convergence for time duration of 10–20 s are given in Fig. 3. Hydrodynamic parameters of vortex shedding obtained from the simulation are presented in Table 3. It is observed that there is a significant influence of domain shape on the shedding parameters. It should be noted that the number of elements as well the mesh density in all grids are the same.

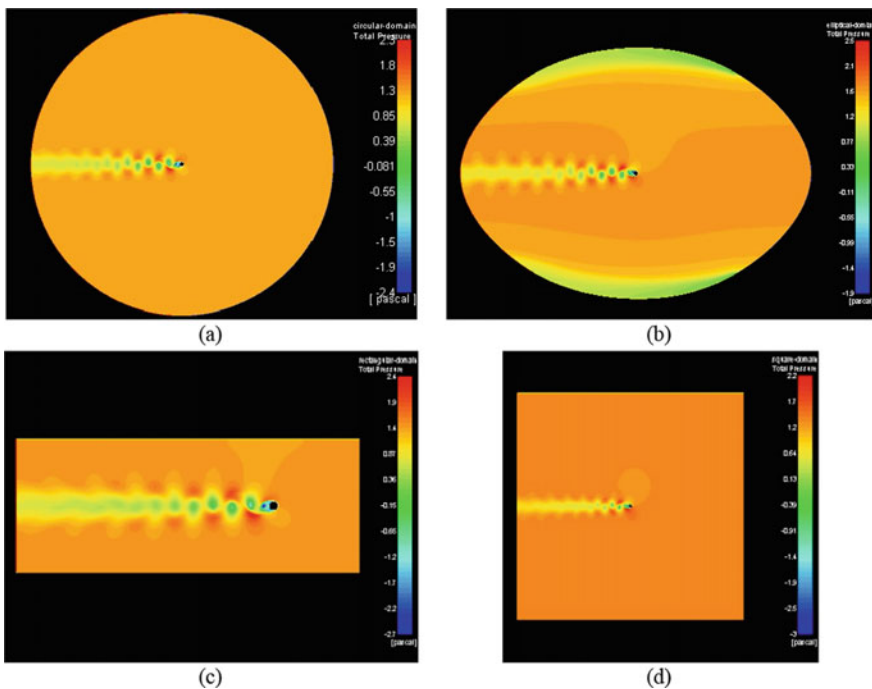


Fig. 2 Total pressure contours from hydrodynamic analysis **a** Circular Domain, **b** Elliptical Domain, **c** Rectangular Domain, and **d** Square Domain

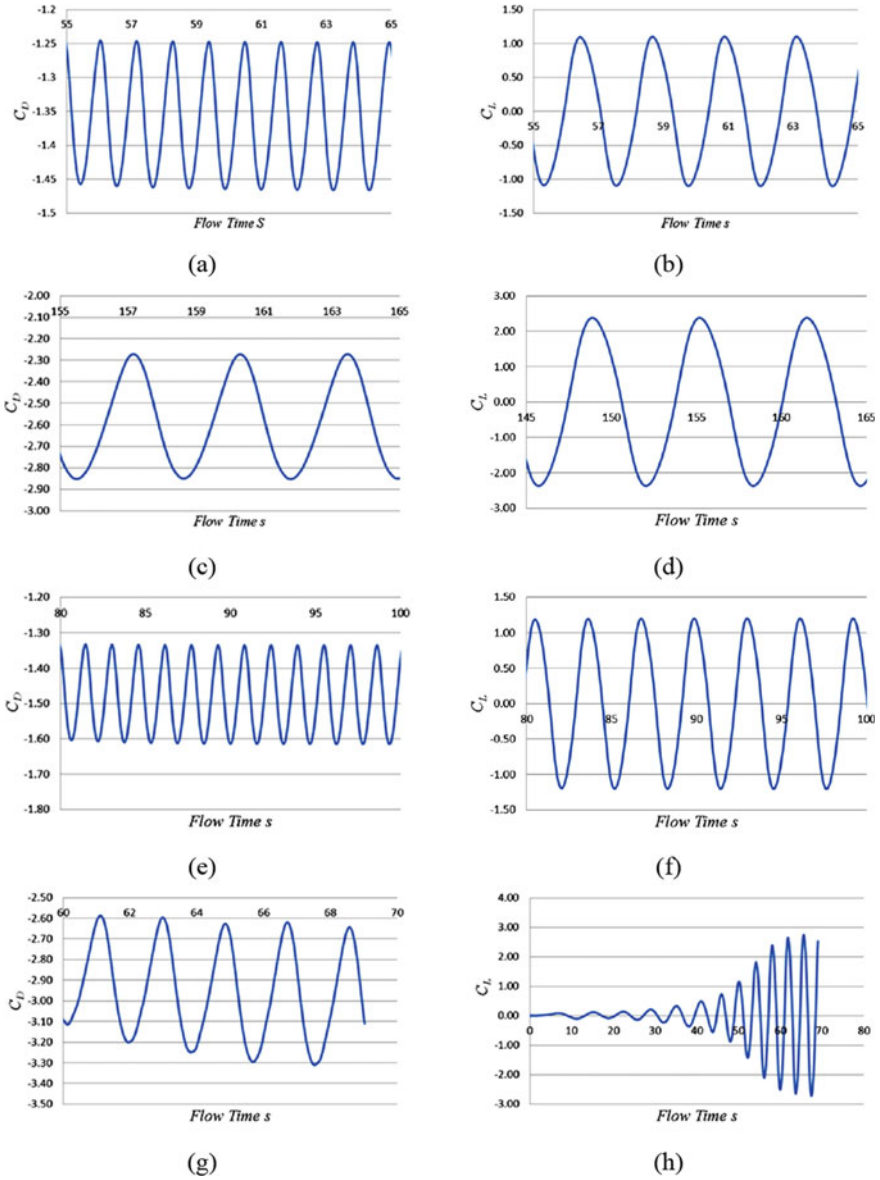


Fig. 3 Time histories of coefficient of drag and lift. **a** C_D for circular domain, **b** C_L for circular domain, **c** C_D for elliptical domain, **d** C_L for elliptical domain, **e** C_D for rectangular domain, **f** C_L for rectangular domain, **g** C_D for square domain, **h** C_L for circular domain

Table 3 Vortex shedding parameters predicted by various domains

Parameters	Domain			
	Circular	Elliptical	Rectangular	Square
Coefficient of Drag, C_D	1.35	2.57	1.47	2.9
Coefficient of Lift, C_L	1.1	2.37	1.2	2.8
Frequency of oscillation of Drag, f_D	0.9	0.31	0.65	0.56
Frequency of oscillation of Lift, f_L	0.45	0.16	0.33	0.3
Frequency of Vortex shedding, f_v	0.45	0.16	0.33	0.3
Strouhal Number, St	0.18	0.06	0.13	0.12

3 Results and Discussions

From the simulations carried out on various domain shapes, it is observed that the drag coefficient is over predicted by elliptical and square domains. With rectangular domain, the value of C_D is 1.47 and, with circular domain, C_D is 1.35. The predicted C_D values at $Re = 1000$ by the circular and rectangular domains are quite close to the experimental and numerical result values shown in Table 4 [16–18]. Circular domain is found to be successful in closely predicting C_D and hence it is compared with the previously published values in Table 4. The compared domains show a similar trend in predicting coefficient of lift C_L of the cylinder as that of C_D with the circular domain giving a more realistic value of 1.1.

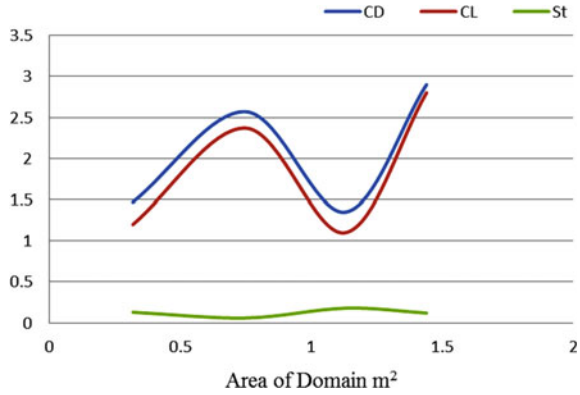
Irrespective of the domain shape, it is observed that drag force oscillates at twice the frequency of lift. This is a proven phenomenon in the physics of vortex shedding behind a circular cylinder [9]. Every domain could successfully replicate this ratio of drag and lift oscillations. Predicted values of shedding frequency indicates that the circular domain is most effective in capturing the vortices. This observation is further strengthened by the value of St predicted. For $Re = 1000$ the theoretical value of St for a circular cylinder is 0.2 [9]. Only the simulation using circular domain satisfies this theory.

A comparative graph of the hydrodynamic force coefficients and non-dimensional shedding frequency is presented in Fig. 4. The rectangular domain occupies the least domain area of 0.32 m². As the number of elements in grid is same for all cases, the rectangular domain is supposed to have the highest mesh density. And hence rectangular domain is expected to give a more realistic and accurate prediction of

Table 4 Drag Coefficient for $Re = 1000$ from various experimental and numerical studies

Source	C_D	Source	St
Experimental [16]	0.9	Experimental [19]	0.202
Numerical [17]	1.15	2D Numerical [20]	0.201
Numerical [18]	1.2	3D Numerical [21]	0.203
Present (Circular domain)	1.35	Present (Circular domain)	0.18

Fig. 4 Variation of shedding parameters with area of the domain



parameters. On contrary, the circular domain which has the second largest area has given good predictions both in terms of hydrodynamic force coefficients as well as shedding frequency. Elliptical domain which is having lesser area than the circular domain has produced erroneous predictions with a Strouhal number value $St = 0.06$. This is due to the influence of side walls as seen from the pressure contours represented in Fig. 2b. Also the convergence seems to be very slow with this type of domain. Square domain is also not efficient in predicting the shedding parameters with over predicted values of force coefficients. This is a strong indication that the accuracy of prediction in case of vortex shedding parameters not only depends on the average mesh density but also is a strong function of the meshing strategy. Grid of the circular domain is more or less uniform in the entire fluid domain thus ensuring effective accounting of the wake physics. Elliptical and circular domains have similar meshing strategy. The poor performance of elliptical domain can be related to blockage effect of curved side boundaries. Rectangular and square domains are meshed with improved mesh density in the wake of the cylinder over a predefined strip of flow in order to capture the shed vortices. But it should be understood from reduced accuracy that the far wake must also be captured to ensure perfect prediction. There is a drop in the value of St , when the far wake mesh density is compromised. This observation indicates that the shedding is influenced not only by the shape and orientation of the bluff body, but also the fluid flow in its vicinity.

4 Conclusions

A strong influence of domain shape on the accuracy with which the VIV parameters are numerically predicted is observed. Circular domain is observed to predict the phenomenon of shedding with most accuracy. The predicted values of hydrodynamic force coefficients and shedding frequencies are within 10% deviation from the theoretical values for the circular domain. Elliptical domain failed to predict both hydrodynamic forces and shedding frequency. A deviation of nearly 90% is

observed comparing the values of force coefficients obtained using circular and elliptical domains. Even though square domain seems to be a modification of rectangular domain an over prediction of 97% is observed for hydrodynamic force coefficients compared to the values given by rectangular domain. Both rectangular and square domains have predicted the shedding frequency with almost same accuracy showing a 35% deviation from theoretical value. Values of St presented are a strong indication of the efficacy of circular domain in effectively capturing the effect of shedding vortices. For a circular cylinder, the theoretical value of St is 0.2. Numerical result from circular domain shows only a 10% deviation. Grid used in the circular domain is unique in the sense that the mesh density is uniform throughout the domain without abrupt transitions at any section. Rectangular domain can be expected to give accurate VIV prediction with a more uniform and finer grid. The following points can be concluded from this work:

- For the same number of elements, circular domain is the most suitable one for VIV prediction.
- Circular domain gives an accurate prediction of both hydrodynamic load and frequency of response which is very much needed for a response analysis.
- For striking a compromise between accuracy and area of the mesh, rectangular domains can be considered as the next judicial option.
- Rectangular domain successfully predicted hydrodynamic force coefficients but the accuracy of frequency prediction is compromised.
- Elliptical and square domains are not suitable for VIV response prediction.

References

1. <https://www.simscale.com/blog/2018/07/tacoma-narrows-bridge-collapse/> accessed on 16 oct 2020
2. Feng CC (1968) The measurement of vortex induced effects in flow past stationary and oscillating circular and d-section cylinders. Doctoral dissertation, University of British Columbia
3. Zhou CY, So RMC, Lam K (1999) Vortex-induced vibrations of an elastic circular cylinder. *J Fluids Struct* 13(2):165–189
4. Saltara F, Neto AA, Lopez JIH (2011) 3D CFD simulation of vortex-induced vibration of cylinder. *Int J Offshore Polar Eng* 21(03):192–197
5. Chandran V, Janardhanan S, Sekar M (2019) Towards reducing computational effort in vortex induced vibration prediction of a cylindrical riser. *Period Tche Quimica* 16(33):853–865
6. Dong S, Karniadakis GE (2005) DNS of flow past a stationary and oscillating cylinder at $Re=10000$. *J Fluids Struct* 20(4):519–531
7. Besem FM, Thomas JP, Kielb RE, Dowell EH (2016) An aeroelastic model for vortex-induced vibrating cylinders subject to frequency lock-in. *J Fluids Struct* 61:42–59
8. Chandran V, Sekar M, Janardhanan S (2019) Influence of frequency ratio on hydroelastic response of a cylinder with degrees of freedom under vortex induced vibration. *Int J Innov Technol Explor Eng* 8:307–312
9. Naudascher E, Rockwell D (1994) *Flow induced vibrations—an engineering guide*. Dover publications, INC, New York

10. Chen W-L, Zhang Q-Q, Li H, Hui H (2015) An experimental investigation on vortex induced vibration of a flexible inclined cable under a shear flow. *J Fluids Struct* 54:297–311
11. Chandran V, Sekar M, Janardhanan S, Menon VG (2018) Numerical study on the influence of mass and stiffness ratios on the vortex induced motion of an elastically mounted cylinder for harnessing power. *Energies* 11:2580
12. Cheung JCK, Melbourne WH (1983) Turbulence effects on some aerodynamic parameters of a circular cylinder at supercritical Reynolds numbers. *J Wind Eng Ind Aerodyn* 14:399–410
13. Kamkar SJ (2011) Mesh adaptation strategies for vortex dominated flows. Ph. D Thesis, Stanford University
14. Anton G (2012) Analysis of vortex-induced vibration of risers. Master's thesis in Applied Mechanics, Chalmers University of Technology, Sweden
15. Narendran K, Murali K, Sundar V (2015) Vortex-induced vibrations of elastically mounted circular cylinder at Re of the O (105). *J Fluids Struct* 54:503–521
16. Anderson JD (2005) Ludwig Prandtl's boundary layer. *Phys Today* 58(12):42–48
17. Braza M, Chassaing PHHM, Minh HH (1986) Numerical study and physical analysis of the pressure and velocity fields in the near wake of a circular cylinder. *J Fluid Mech* 165:79–130
18. Jordan SK, Fromm JE (1972) Laminar flow past a circle in a shear flow. *Phys Fluids* 15(6):972–976
19. Norberg C (2003) Fluctuating lift on a circular cylinder: review and new measurements. *J Fluids Struct* 17(1):57–96
20. Khan NB, Ibrahim Z (2019) Numerical investigation of vortex-induced vibration of an elastically mounted circular cylinder with One-degree of freedom at high Reynolds number using different turbulent models. *Proc Inst Mech Eng Part M J Eng Marit Environ* 233(2):443–453
21. Dong S, Karniadakis GE (2005) DNS of flow past a stationary and oscillating cylinder at $Re = 10000$. *J Fluids Struct* 20(4):519–531

Design and Performance—Analysis of Hybrid Drive Optimized for Torque–Speed Characteristic Requirements of Heavy Vehicles



Kumaran Duraikannu, Yuddhveer Singh Kachhawa, Abhishek Vats, and Sahil Purushotham Kanchan

Abstract Hybrid vehicles are the vehicles driven by the combination of motive powers from the internal combustion engine (ICE) and the electric motor. The project focuses on the development of a hybrid mechanical device for automobiles. The primary objective was to increase the output torque and moderate the operative load on the engine. The coupling designed uses the concept of epicyclic arrangement of four bevel gears for the transmission of motion. The coupling proves to be useful in scenarios where the vehicles are required to stop and move at quick intervals. The power split device was designed with a test vehicle, “TATA LPT 909 EX2.” The motor selection was made on the basis of the engine characteristics and the overall torque requirement of the vehicle during electric mode and hybrid mode of operation. The motor used to aid the IC engine was “Emrax Motor.” Hand calculations and simulations using SolidWorks Motion Analysis were made. The Total Input Power (TIP) is associated with the Total Output Power (TOP) to acquire the torque yield of the hybrid system through the coupling. The analysis of the design was done on ANSYS Workbench with the torque from the motor and the engine to verify the safety of the designs and compute the Factor of Safety (FOS). Proof of concept for the hybrid drive was made with a working prototype using 3D printed parts and tested, which validates the concept of a hybrid drive for desired torque–speed characteristics of a selected vehicle.

Keywords Hybrid · Vehicles · Coupling · Engine · Electric · Torque · Speed · Motor · Performance

K. Duraikannu · Y. S. Kachhawa (✉) · A. Vats · S. P. Kanchan
Department of Mechanical Engineering, SRM Institute of Science and Technology, Chengalpattu
District, Kattankulathur, Tamil Nadu 603203, India
e-mail: yk6385@srmist.edu.in

© The Author(s), under exclusive license to Springer Nature Singapore Pte Ltd. 2022
M. K. Singh and R. K. Gautam (eds.), *Recent Trends in Design, Materials and Manufacturing*, Lecture Notes in Mechanical Engineering,
https://doi.org/10.1007/978-981-16-4083-4_29

365

1 Introduction

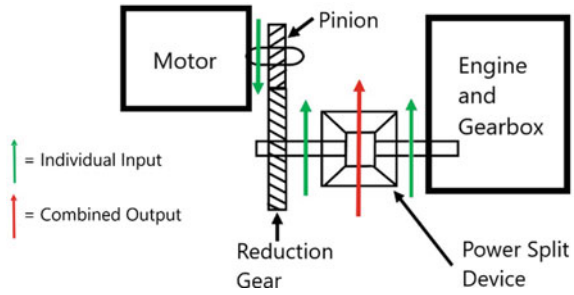
Hybrid Vehicles are highly efficient and environment-friendly vehicles which work on both ICE and electric motors. Extensive work has been done in the field of hybrid vehicles, but many steps can be taken to increase their efficiency and to reduce their cost because in some scenarios complete electric vehicles (EVs) are a long goal. There are different kinds of hybrid vehicles, differentiated by their transmission and according to the type of hybridization available. Each kind of advancement has its upside and downside. Various procedures are utilized to accomplish the hybridization of power trains and to yield the maximum efficiency. Some different techniques are additionally utilized, e.g., regenerative braking which utilizes the possibility of charging of battery for extra life. The most common technique employed in hybrid vehicles is using the gasoline ICE to run a generator which charges the battery to operate the electric motor and drive the vehicle. Hybridization of consumer cars is widely implemented by various companies, but in recent years, the focus has been shifted towards the heavy vehicle sector. There are numerous difficulties which need to be tackled in the heavy vehicle's hybridization such as high-power requirements, high torque requirements, and ruggedness in operation. The aim of this work was to lay a foundation of hybrid vehicles in the heavy vehicle industry. Hybridization of heavy vehicles will ensure a smooth transition from already existing IC engines to electric motors. It will also help to tackle the problems currently at hand while simultaneously working towards the electrification of this sector. This study focuses on developing a gear mechanism which will integrate the power of the propulsion units, i.e., internal combustion engine and electric motor. The main aim was to develop a mechanical coupling device to integrate the power of the existing IC Engine with a high torque motor to improve the running characteristics and thus decrease the load on the engine. To successfully attain our objective of coupling the two independent sources, we used the transmission differential concept to develop our design. We provided two independent inputs to our coupling (which is a differential) to gain a single output [1].

2 Experimental Methods and Performance Measures

2.1 *Parallel Hybrid Coupling*

Parallel hybrid coupling is a device used to couple the two independent sources used to drive a vehicle. This coupling can be used for the addition of torque and can allow the powertrain to receive power when one of the power sources is turned off. The parallel hybrid coupling which we developed was a differential-based PSD which uses the concept of reverse differential action where the input from the two power sources was provided through two different input shafts, and the output was the addition of both the inputs. The differential-based PSD is the core component

Fig. 1 Line diagram for differential-based parallel hybrid coupling



of any PHEV or SPHEV as it directly influences the control strategy of the power systems and the performance of the vehicle. The working of a power split device is explained in the line diagram of the parallel hybrid coupling represented in Fig. 1. The coupling housed bevel gears in epicyclic gear arrangement along with a helical gear pair to provide the necessary reduction and ensure noise-free operation [2].

2.2 Selection of Test Vehicle

For the development of the coupling device, a test vehicle was selected in order to obtain key values for the calculations and design. The test vehicle gave us the torque and power values which were then used to attain the key parameters of the gearbox. This also provides us with a room to improvise on certain aspects of the design. The vehicle selected by us was “TATA LPT 909 EX2.”

Specification of the test vehicle [3]:

Engine specification:

Model: TATA LPT 909 EX2.

Type: 4 Cylinder in-line water-cooled, Turbo-inter-cooled CRDI engine.

Max. Engine output: 93.2 kW (125 BHP) at 2400 RPM.

Max. Torque: 400 Nm at 1300–1600 RPM.

Gearbox specification:

Type: GBS 6F/1R (550-Synchromesh).

No of gears: 6 forward and 1 Reverse,

Gear ratios: 1st gear–6.9, 2nd gear–4.02, 3rd gear–2.39, 4th gear–1.46, 5th gear–1.00, 6th gear–0.84 (Over drive), Reverse gear–6.37.

Rear-axle specifications:

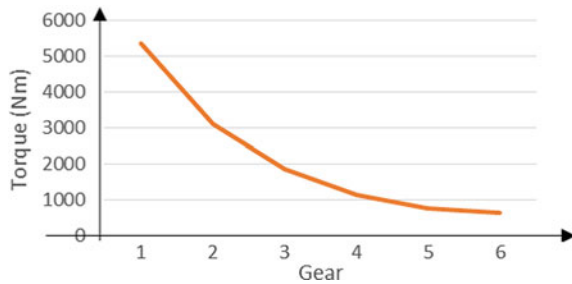
Type: Hypoid gears with a single reduction and a fully floating shaft.

Speed ratio: 3.875:1.

Table 1 Maximum engine output

Gear	Max. RPM	Gear ratio	Torque (Nm) developed on the crankshaft	Final drive	Torque output (Nm) on the wheels	RPM on the wheels	Maximum velocity of the vehicle at each gear (kmph)
1	2400	6.9	400	3.875	5347.5	89.76157	13.988
2		4.02			3115.5	154.0684	24.009
3		2.39			1852.25	259.1443	40.383
4		1.46			1131.5	424.2156	66.107
5		1			775	619.3548	96.517
6		0.84			651	737.3272	114.901

Fig. 2 Variation of engine torque



2.3 Torque and RPM Calculations and Tabulations

The calculations of torque and RPM were made using standard formulas, the performance of the benchmark engine can be premeditated using similar methods, the data was tabulated in Table 1, and a graph was plotted for it as shown in Fig. 2.

2.4 Selection of Driving Electric Motor

Selection of electric motor plays an integral part in designing the entire hybrid system as it the second impelling unit which was installed to enhance the overall output of the benchmark vehicle and therefore, it ought to be comparable to the ICE preinstalled. As in SPHEV, the electrically driven motor used should be capable of impelling the automobile on its own and can also assist the ICE used. The motor shortlisted was EMRAX 348 (Low-Voltage Motor). This a Permanent Magnet Synchronous Combined Cooled (Air + Liquid-cooled). The specification of the motor is tabulated in the below Table 2 showing all the operating parameters [4].

Table 2 Motor Specification

Peak torque	1000 Nm
Continuous torque	500 Nm
RPM range	3200–4000 RPM
Peak power	330 kW at 3200 RPM
Continuous power	200 kW at 3200 RPM
Efficiency	98%
Dry mass	40 kg
Maximal battery voltage	

Table 3 Elemental composition (constituents, in percent)

Carbon	Silicon	Manganese	Chromium	Sulphur	Phosphorous
0.17–0.22	0.15–0.35	1.00–1.40	1.00–1.30	0.35 (max.)	0.35 (max.)

2.5 Material Selection

The standards followed were the Indian Standards or IS. Material which we selected for our gears was IS9175, commonly known as 20MnCr₅. This material is widely used for manufacturing gears in gearbox, differential, axle, etc. 20MnCr₅ can be measured as an industry standard. The industry standard material endures diverse cures to obtain the preferred properties required to make the gears. The elemental composition of the 20MnCr₅ is tabulated in Table 3. The mechanical properties of 20MnCr₅ are Tensile strength: 1000–1300 MPa, Yield stress(min): 700 MPa, Izod impact value: 40 J [5].

3 Results and Discussion

3.1 Design of a Parallel Hybrid Coupling

The design process of the power split device starts with the design calculations [6] of the respective gears. The coupling consists of four bevel gears which act as a differential and help in the addition of torque. SolidWorks 2017 was the software package used to implement the entire designing phase of the gearbox.

Fig. 3 Bevel gear

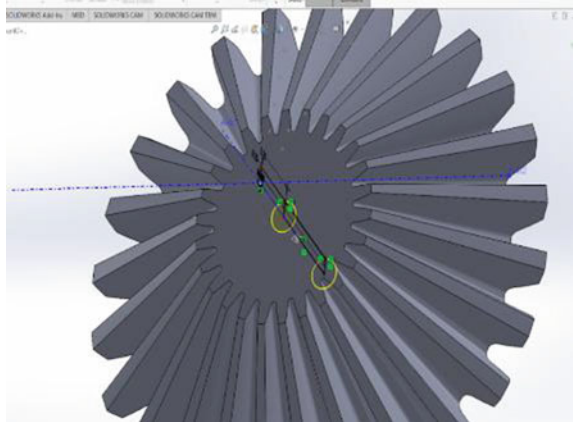
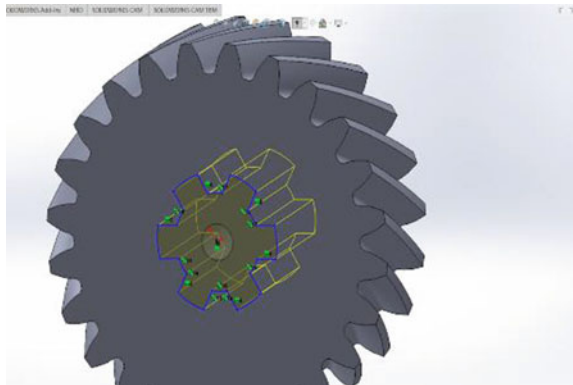


Fig. 4 Helical gear



3.2 Bevel and Helical Gear—Computer-Aided Design

A plane is selected and sketch was drawn with proper dimensions and extruded as shown in Fig. 3 of the bevel gear and Fig. 4 of a helical gear.

3.3 Assembly of the Parallel Hybrid Gearbox

Every part of the assembly was designed and developed using SolidWorks and the assembly, using mates and constraints was also performed. In Fig. 5, we can visualize how the coupling will look after production. The verification of characteristics of PSD was completed by both theoretical calculations and simulation from the software. The verification was done to check whether we satisfy our basic requirement of the problem statement and the behavior of the device under different modes and running condition.

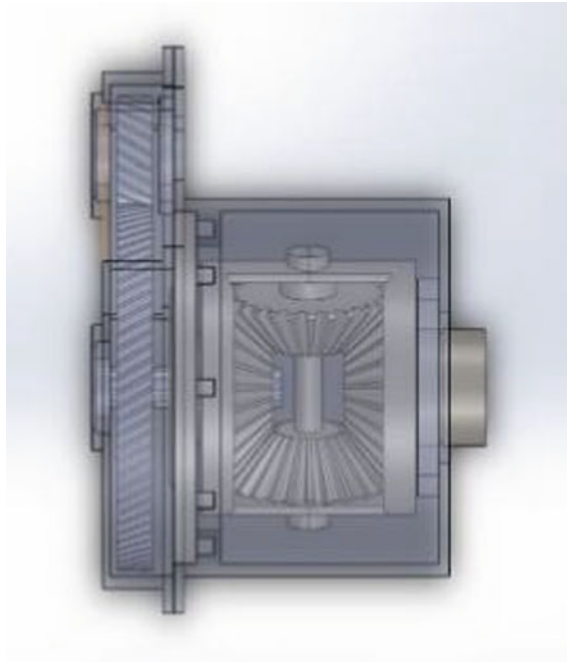


Fig. 5 Assembled CAD of the parallel hybrid gearbox

3.4 Theoretical Verification of Power Split Device

The output RPM of the PSD was calculated from the standard relations. Figure 6 shows the common differential arrangement when both the output shafts are at the same speed. Similarly, we calculated the theoretical speed at all the gears as depicted in Table 4.

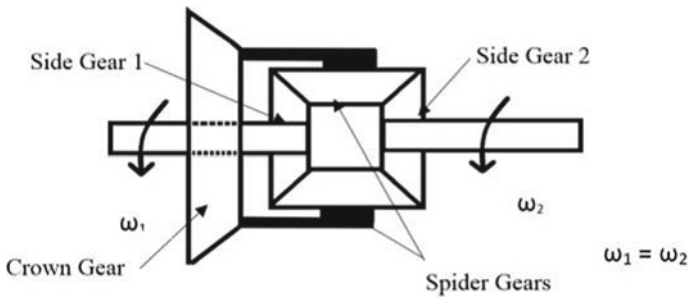


Fig. 6 Differential arrangement when wheels are moving in a straight line

Table 4 Theoretical RPM

Motor RPM	Motor RPM after reduction	Gear	Engine RPM	Gear ratios	Engine RPM after initial reduction	Calculated coupled RPM
3000	923.0769	1	2400	6.9	347.826	635.451
	923.0769	2		4.02	597.014	760.045
	923.0769	3		2.39	1004.184	963.630
	923.0769	4		1.46	1643.835	1283.456
	923.0769	5		1	2400	1661.538
	923.0769	6		0.84	2857.142	1890.11

$$\text{RPM of crown gear} = \frac{\text{RPM}_1 + \text{RPM}_2}{2}$$

3.5 Verification of Power Split Device Through Motion Analysis

With the purpose of performing motion analysis, the gearbox was completely reassembled in a separate assembly file. All the mates and constrains were chosen systematically and in a specific sequence. It was made sure that the assembly was not over-defined nor under-constrained. The gears were rotated with the help of the cursor before starting the motion analysis so as to check and verify all the mates. Once all the mates were defined, contact between parts was defined and the input parameters of the different RPMs were given. The graphs plotted in SolidWorks motion analysis were in the units of degrees/s which was converted to RPM. The motion analysis was conducted for every gear pair in SolidWorks, as shown in Figs. 7 and 8. From the motion analysis we found the hybrid coupled RPM for each and every gear pair which was tabulated in Table 5 and compared with the theoretically calculated coupled RPM.

Similarly, the performance of the benchmarked test vehicle was premeditated for Hybrid Mode using similar methods, and the data was represented in Tables 6 and 7. From the data of Tables 6 and 7, the graph was plotted, as shown in Figs. 9, 10 and 11.

Using the above calculations torque on each and every gear in hybrid mode was calculated and the Tables 8, 9, and 10 were generated having Torque Output of Motor, Torque Output of Engine, and Combined Hybrid Torque [7] and RPM, respectively.

Using the Tables 8, 9 and 10 graphs are plotted as Figs. 11 and 12. The snapshot of ANSYS window during finite element analysis of helical gear is depicted in Figs. 13 and 14.

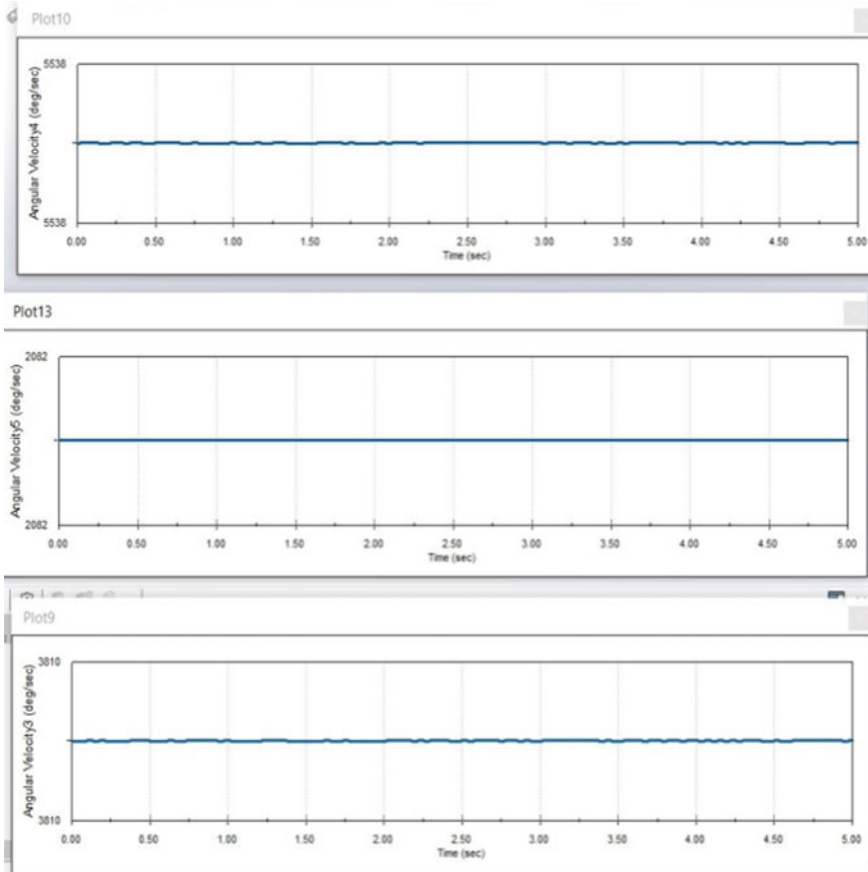


Fig. 7 Motion analysis for first gear

3.6 Prototyping

A 3D printed scaled prototype of the PSD was made for the easy understanding and demonstration of the running conditions of the hybrid coupling. 3D printing belongs to a few of the cheapest and most widely used method for rapid prototyping. Mostly, it melts the material and layers it on top and creates the subsequent layers and creates the 3D model. The prototype was made after the design and analysis phase using the dimensions obtained in the design process. The prototype was manufactured using 3D printer Ultimaker 1. The material used in printing was PLA plastic due to its easy printability in the printer. Pre-requisite data for printing was configured in software CURA as shown in Fig. 15 which can also show the estimated time for completion. The below mentioned Fig. 16 shows the computer-aided design made of a prototype in different orientations.

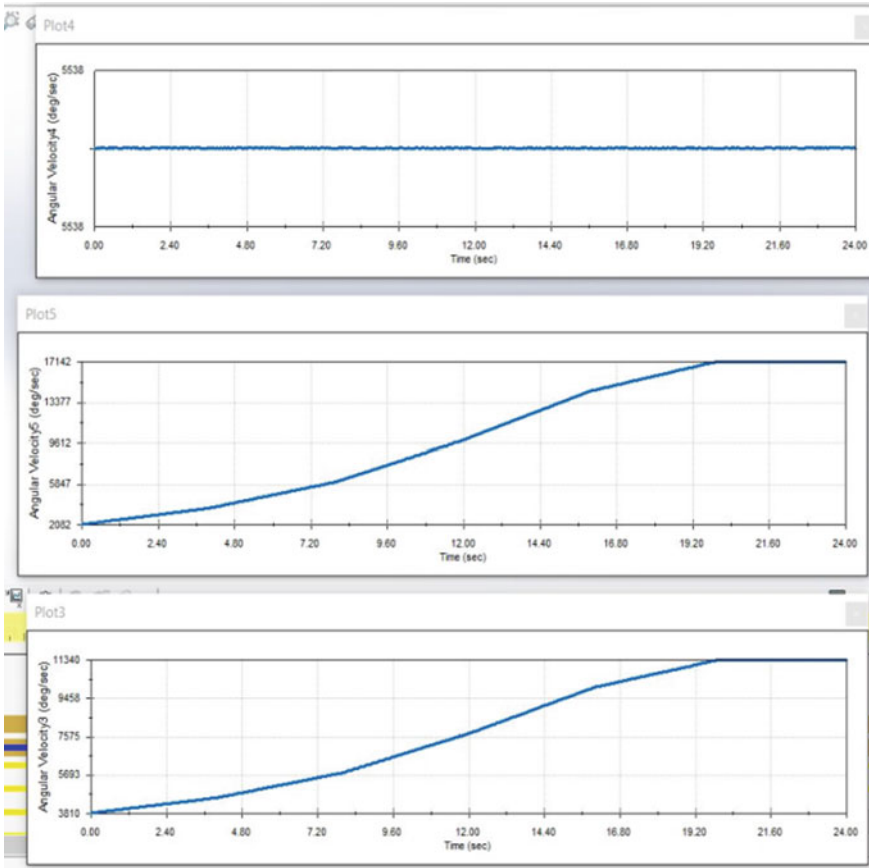


Fig. 8 Motion analysis for hybrid mode

Table 5 Hybrid RPM

Motor RPM	Motor RPM after reduction	Gear	Engine RPM	Gear ratios	Engine RPM after initial reduction	Calculated coupled RPM	Hybrid coupled RPM
3000	923.0769	1	2400	6.9	347.8261	635.4515	635
	923.0769	2		4.02	597.0149	760.0459	760
	923.0769	3		2.39	1004.184	963.6305	963.5
	923.0769	4		1.46	1643.836	1283.456	1283
	923.0769	5		1	2400.000	1661.538	1661.5
	923.0769	6		0.84	2857.143	1890.110	1890

Table 6 Coupled RPM (Motion Analysis)

Engine RPM	Gear ratios	Engine RPM after initial reduction	Coupled RPM (motion analysis)
2400	6.9	347.826	635.451
	4.02	597.014	760.045
	2.39	1004.184	963.630
	1.46	1643.835	1283.456
	1	2400	1661.538
	0.84	2857.142	1890.109

Table 7 Speed of Vehicle

RPM on the differential in only engine mode	RPM on the differential in coupled hybrid mode	Speed of the test vehicle in only engine mode (kmph)	Speed of the test vehicle in coupled hybrid mode (kmph)
89.761	163.987	14.634	26.736
154.068	196.140	25.119	31.978
259.144	248.678	42.250	40.544
424.215	331.214	69.163	54.001
619.354	428.784	100.978	69.908
737.327	487.770	120.212	79.525

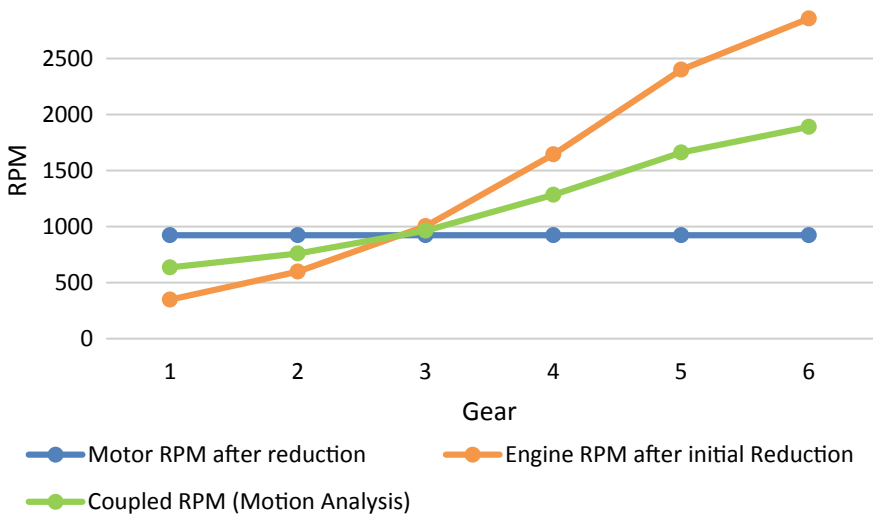


Fig. 9 RPM at different modes

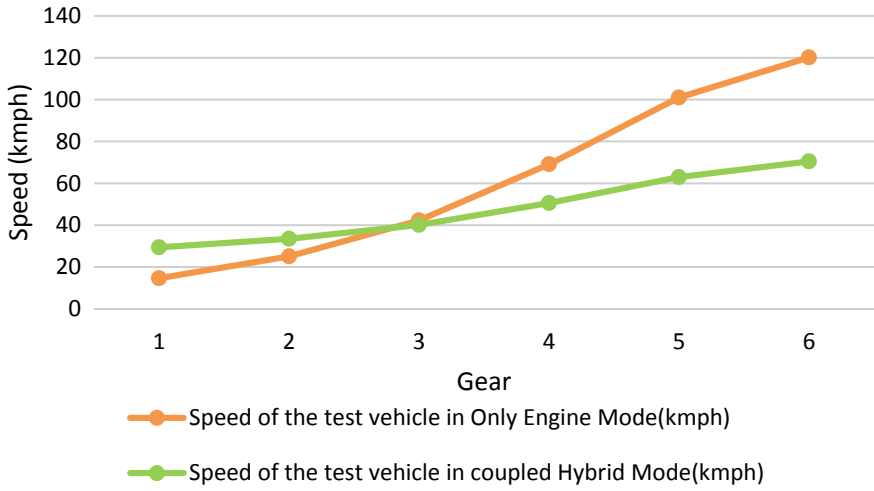


Fig. 10 Velocity benchmarked

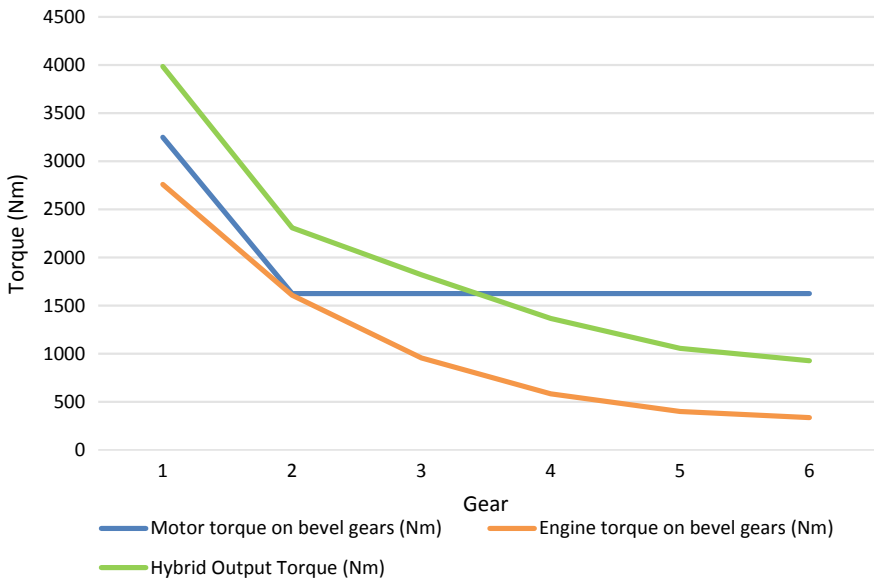


Fig. 11 Torque output in different modes

Table 8 Torque output of motor

Motor torque (Nm)	Motor RPM	Motor reduction	Motor torque on bevel gears (Nm)	Motor RPM on bevel gear
1000	3000	3.25	3250	923.07
500			1625	

Table 9 Torque Output of Engine

Gear	Gear ratio	Engine torque on bevel gears (Nm)	Engine RPM on bevel gears
1	6.9	2760	347.826087
2	4.02	1608	597.0149254
3	2.39	956	1004.1841
4	1.46	584	1643.835616
5	1	400	2400
6	0.84	336	2857.142857

Table 10 Combined Hybrid Torque and RPM

Motor input power (HP)	Engine input power (HP)	Total input power (HP)	Combined hybrid RPM	Hybrid output torque (Nm)	Hybrid output torque at wheels (Nm)
330	93.2	423.2	635.451	3985.364	7721.643
200	93.2	293.2	760.045	2308.495	4472.709
200	93.2	293.2	963.630	1820.783	3527.767
200	93.2	293.2	1283.456	1367.060	2648.679
200	93.2	293.2	1661.538	1055.986	2045.973
200	93.2	293.2	1890.109	928.285	1798.553

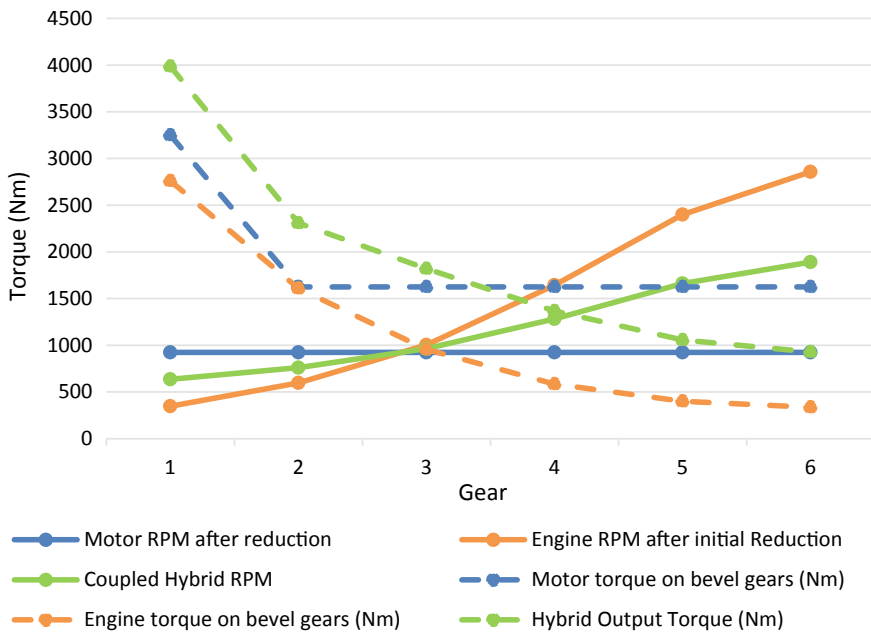


Fig. 12 Torque output and RPM in different modes

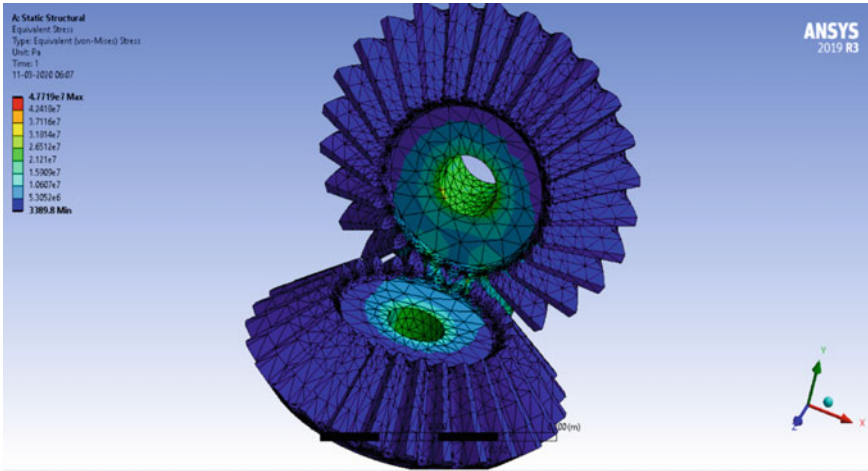


Fig. 13 FEA of bevel gear pair

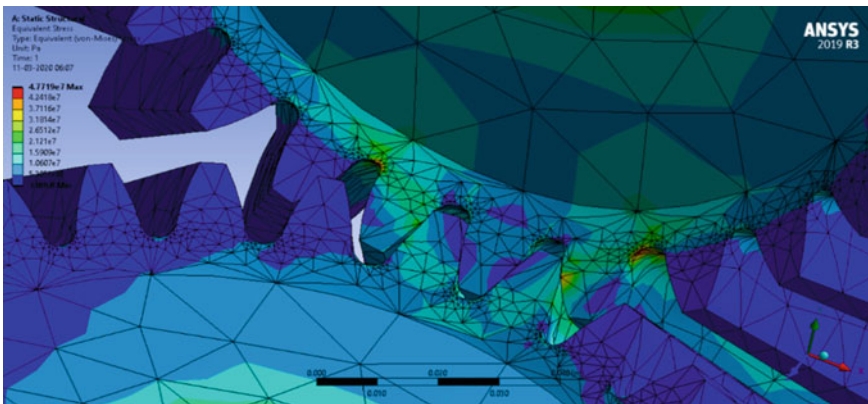


Fig. 14 FEA of bevel gear pair showing maximum stress

The gears were scaled down from their actual size for the ease of printing as the full-scale model requires a huge amount of time to get printed and due to size limitation of the printer it cannot accommodate the print of this large size. A casing was designed for housing the gears and to enclose the prototype. The material used for the printing the prototype was PLA which is prevalent material used in 3D printing. It is conventionally used for 3D printing as it is easily available and can easily be accommodated in different varieties of 3D printers. The fixture for mounting the gearbox and the motors is made using Poly-methyl methacrylate (PMMA) as shown in Fig. 17.

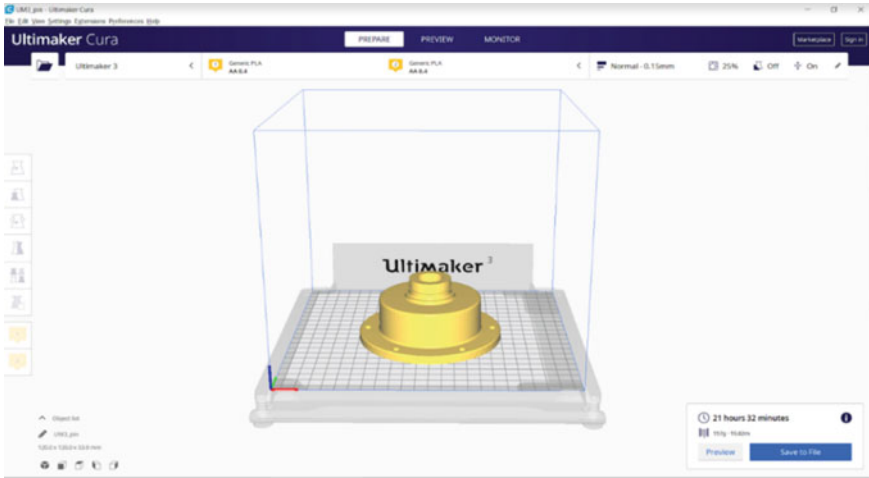


Fig. 15 Software setup for 3D printing (CURA)

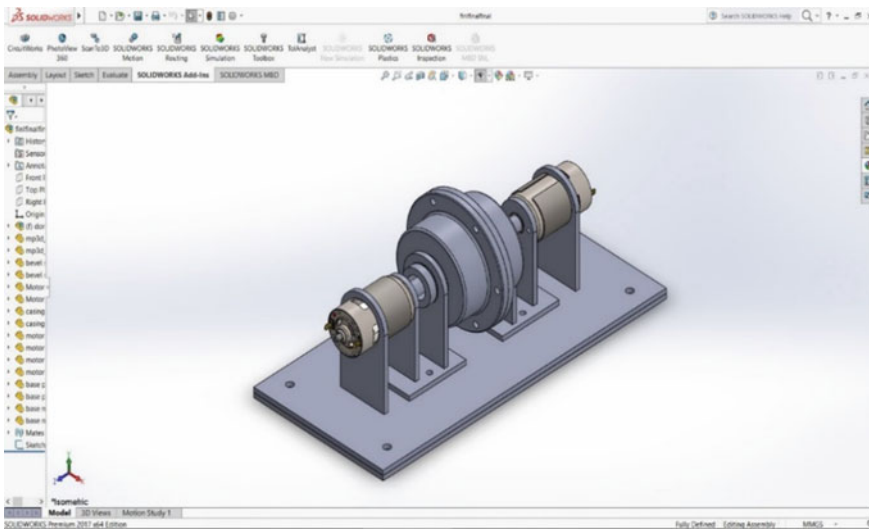


Fig. 16 CAD of prototype isometric view

4 Conclusions

An overall increase in the initial RPM of the test vehicle can be recorded from 347.8 to 635.45 RPM. Thus, we can infer the successful coupling of both the inputs. The RPM initially increases and then decreases as the PSD averages the RPM of both the input drivers. This is because the RPM of the motor remains constant and that

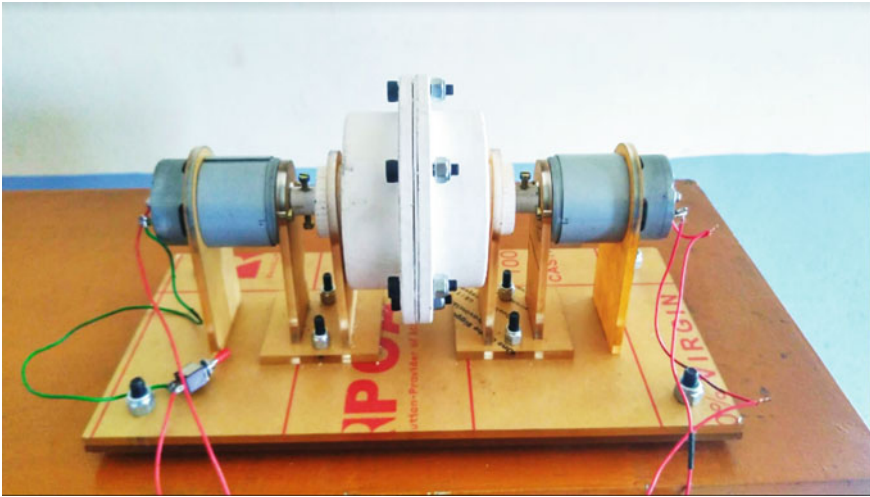


Fig. 17 Proof of concept prototype

of the ICE keeps on increasing. The input speed from the ICE at first gear to the PSD is 347.8 RPM, while that of the EM is 923.1 RPM. The output RPM obtained by providing these inputs simultaneously, is 635.45 RPM. The torque output of the benchmarked vehicle using the ICE at its first gear was 5347.5 Nm on the wheels. Upon installation of the PSD, the output torque increases to 7721.66 Nm on the wheels while maintaining the same final axle reduction. An increase of 44.39% can be seen in the initial starting torque of the vehicle with the installation of the PSD. The output power of the benchmarked vehicle on the ICE alone was 93.2 kW. With the addition of an electric motor, the supplementing peak power of the motor increases the output power to 359.72 kW. The running torque of the motor is 200 kW which makes the running power of the test vehicle 249.22 kW. With the installation of the PSD, the initial high torque requirements of heavy vehicles are met for urban applications. The higher initial torque can thus allow the vehicles to lift the load with greater ease.

References

1. Saša Milojević F, Tomas Skrucany S, Hranislav Milošević T, Darko Stanojević F, Mladen Pantić F, Blaža Stojanović S (2018) Alternative drive systems and environment friendly public passengers transport. *Appl Eng Lett* 3:105–113
2. Vijayaragavan E, Aditya Vatsa F, Adil Hossain S, Agam Dubey TF (2019) Design of torque enhancer for hybrid vehicles using planetary gear. *Int J Rec Technol Eng (IJRTE)* 8(1S2) ISSN: 2277–3878
3. TATA Light Trucks, Products <https://light-trucks.tatamotors.com>
4. Emrax, E-Motors, 348 <https://emrax.com>

5. Bureau of Indian Standards (1986) <https://archive.org/details/gov.in.is.9175.20.1986/page/n5/mode-/2up>
6. Kalaikathir Achagam F (2015) PSG design data book, Kalaikathir Achagam, PSG college of engineering.
7. Epi Inc. (2011) http://www.epieng.com/piston_engine_technology/power_and_torque.html

Handling and Scheduling of Inner-City Lagoon Water Through Numerical Index and Multivariate Statistics



Yogesh Shukla, Nasir Khan, and Sonia Shivhare

Abstract Dynamic study and chief element study are accustomed to learning regarding water that when it is uncovered in the environment, it has various impurities possessing many dangerous things which could be harmful to any living organisms. If impure water is taken by them, it is about to cause severe damage to their fitness. So, to make water drinkable and free from different impurities, some refinement methods have been used in this paper. These particular methods have the necessities of scheduling and manipulation to handle the treatment of water. We have used the multivariate statistical tools for managing huge and difficult figures so as to get improved information about the lagoon water value.

Keywords Dynamic study · Chief element study · Multivariate statistical tools · Raid gravity filter · WQI

1 Introduction

The water when exposed to the atmosphere contains many impurities which are harmful to any living organisms; it is likely to cause serious harm to their health. Hence, in order to make water potable and free from various impurities, purification methods are found out.

In the immediate future, drastic changes in the design of water treatment. The goal of water treatment is the production of accomplishing this goal should be reasonable with respect to capital and operation personal they should be able to cope with the variable is raw water quality, demand those are present use. Water quality criteria based on present-day standards and guides are present to assist in the water system performance goal for any plants. The storm is commonly characterized as the occasional inversion of winds and the related precipitation. In India, such changes in

Y. Shukla (✉)
VIT Bhopal University, Bhopal, MP, India

N. Khan · S. Shivhare
Amity University Madhya Pradesh, Gwalior, MP, India

climatic conditions are experienced multiple times in a year. At the point when dampness-loaded breezes streaming in the southwesterly heading from the Indian Ocean causes precipitation over the Indian sub-landmass from June to September, the wonder is named as South West (SW) Monsoon. Most pieces of the nation get downpour from SW Monsoon.

Besides, the beginning of the storm is once in a while deferred which influences the planting of many downpours sustained harvests. On different events, the storm may start on schedule, yet numerous mid-season breaks happen to prompt crop disappointments, and regularly ranchers need to re-sow their harvests. In such cases, the poor ranchers face huge misfortunes as they lose their time, work, and sources of info, yet in addition, need to contribute again on seeds and contributions for the second time in a similar season with no certification of accomplishment. The downpour nourished ranchers are commonly poor and have little assets; they additionally don't get satisfactory credit from the budgetary establishments.

In this paper, we discussed the commencement of the rainy season on a callous ground [1]. By and large, it is outstanding that the precipitation marvels amid summer rainstorms over the Asian summer storm district are delivered by the southwesterly rainstorm. In any case, the precipitation wonders before the foundation of storm flow every year have not been examined, despite the fact that they may add to the foundation of rainstorm dissemination. In this investigation, the conditions when the irregular precipitation amid the pre-rainstorm period happened in 1998 are uncovered utilizing everyday mean reanalysis information. Tempests of this period are called pre-rainstorm tempests. The present investigation envelops some significant parameters related to pre-rainstorm tempests and attempts to distinguish at least one significant indicator and predicts so that, later on, relapse examination (straightforward or different) should be possible advantageously to consider pre-storm tempests.

The alternating rainfall during the season of pre-monsoon is shown that it is indicated that the rotation in rainfall in the pre-monsoon season is supplemented by the westerly passage. By using the numerical method, we are able to solve and clarify this problem. In this paper, it is not certain whether the precipitation occasions amid the pre-rainstorm period impact the foundation of the storm course. The warmth spending examination over the Indochina Peninsula amid the pre-rainstorm period ought to be done. Moreover, the job of the air-land connection for the rainstorm beginning. In India study on the lake is very limited. After the industrialization and population growth in developing countries, the recent decades are witness of water pollution [2-8]. Around the urban lake, the area population increased day by day and continuously infringed lake areas because of demand for water and land [9]. This process work as waste discarding locations that affected our locality with adverse effects [10].

The lakes in the urban areas are becoming poisonous or more polluted due to the turn loose of sewage from the households and the sediments. As result these immoderate additions, namely nitrates and phosphates vexatious increased in the lake and form anaerobic and pulverize it. Such a bothersome change in water science [11] brings disintegration of lake water quality.

2 Methodology

The system embraced in the present examination comprises of.

- PCC OR Pearson Correlation Coefficient
- Testing OF Persistence
- Logic Prepositional.

2.1 Correlation Coefficient of Pearson

Degree of association between two variables ‘ α ’ and ‘ β ’ measured by Pearson Correlation Coefficient (PCC). PCC mathematically is calculated as

$$\rho_{\alpha\beta} = \frac{\frac{1}{n} \sum_{i=1}^n (\alpha_i - \alpha)(\beta_i - \beta)}{\sqrt{\frac{1}{n} \sum_{i=1}^n (\alpha_i - \bar{\alpha})^2} \sqrt{\frac{1}{n} \sum_{i=1}^n (\beta_i - \bar{\beta})^2}} \tag{1}$$

where

$n \rightarrow$ Observed value total number

$\alpha \rightarrow$ Mean of the variable α

$\beta \rightarrow$ Mean of the variable β .

Following symbols are used in this section: $\rho_{d\Delta\rho}, \rho_{d\Delta T}, \rho_{d\Delta v}, \rho_{d\Delta R/H}, \rho_{v\Delta T}, \rho_{v\Delta P}, \rho_{v\Delta R/H}, \rho_{\Delta R/H\Delta P}, \rho_{\Delta R/H\Delta T}$, and $\rho_{v\Delta R/H}$. Above-mentioned quantities have statistically analyzed and differently measured for every year in April and May.

2.2 Calibrate for Perseverance

Diligence implies the presence of measurable reliance among progressive estimations of a similar variable [12]. Persistence is measured by lag-1 autocorrelation. In the Sect. 3, we are counted as a dichotomous random variable χ for PCCs by using Eq. (1), shown by

$$\begin{aligned} \chi &= 1 \quad \text{if } |p| < 0.5 \\ &= 0 \quad \text{if } |p| > 0.5 \end{aligned} \tag{2}$$

We have to prepare the entries 0 and 1, respectively, and orderly. In the subsequent stage in Eq. (2), the slack 1 autocorrelation coefficient is determined for each succession.

2.3 Propositional Logic

Propositional logic is developed the logic for fining the al possible results between 0 and 1. In this type of logic, a mathematical relationship is required to express the appropriation of the reality of a variable [1]. A capacity called an “enrollment work” is expected to demonstrate the degree to which a variable ‘x’ has the trait ‘F’. Enrollment capacities are characterized on a vast expanse of talk shown by the exploration variable. In the present paper, slack 1 autocorrelations make the essential universes of talk. XI is for April and X2 is for May. The suggestion ‘P’ tried for the present examination is:

“The level of relationship between any pair of parameters is reliably exceptionally high is extremely valid.” Thus, the relationship function is written as

$$\begin{aligned} \mu_x(r) &= 0; && \text{if } r \text{ is less than } 0.5 \\ &= r/0.6; && 0.5 < x < 0.6 \\ &= 1 && \text{if } x > 0.6 \end{aligned}$$

3 Conclusion

From the above study and study of Figs. 1, 2, and 3, the following are found:

- (a) Monsoon water is associated with Pre-Monsoon water is mostly dependent upon post-monsoon water.

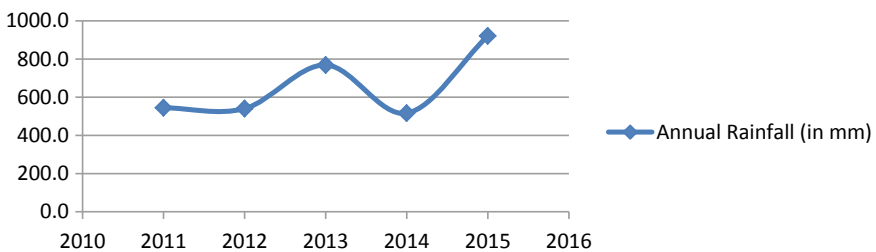


Fig. 1 Rainfall (in mm) (Yearly)

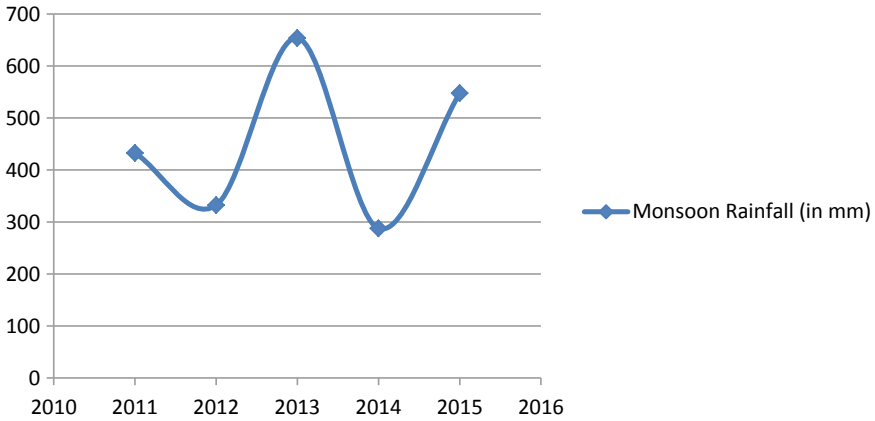


Fig. 2 Monsoon rainfall (in mm)

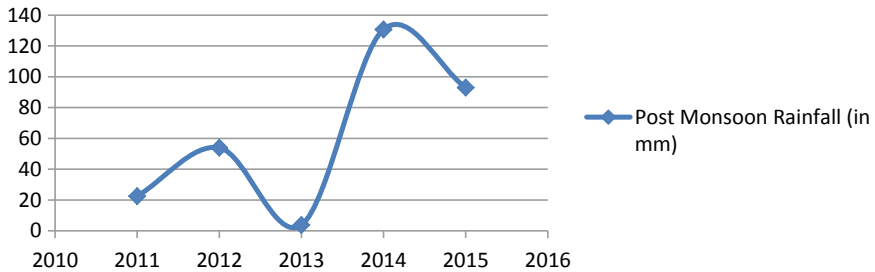


Fig. 3 Post-monsoon rainfall (in mm)

- (b) Maximum Monsoon water with pre-monsoon depends mostly upon the humidity change ratio during the thunderstorm.
- (c) During the pre-monsoon, surface temperature also changed and monsoon is depending highly upon the duration of the post-monsoon water.
- (d) Change in relative humidity during the post-monsoon depend upon the duration of the total monsoon period. In pre-monsoon, humidity change and total monsoon do not depend on each other.
- (e) Degree of association between water quality of pre-monsoon water and post-monsoon water. During the monsoon, variation in air pressure and relative humidity remains almost the same.

After analysis of a sample of monsoon and post-monsoon, we find that some of major features like changes in surface temperature, changes in relative humidity, and degree of association between water qualities. Monsoon water is more impure than post-monsoon water.

Since, we got analyzed result, so new techniques for water purring should be applied on monsoon water rather than post-monsoon water.

References

1. India meteorological department monsoon monograph. New Delhi, IMD (2012)
2. Gautam SK, Maharana C, Sharma D, Singh AK, Tripathi JK, Singh SK Evaluation of ground water quality in the Chota nagpur plateau region of the Subarnarekha river basin, Jharkhand State, India. *Sustain Water Qual Ecol.* <https://doi.org/10.1016/j.swaqe.2015.06.001>
3. Oişte AM (2014) Groundwater quality assessment in urban environment. *Int J Environ Sci Technol* 11(7):2095–2102
4. Singh P, Thakur JK, Kumar S (2013) Delineating groundwater potential zones in a hard- rock terrain using geospatial tool. *Hydrol Sci J* 58:213–223
5. Sharma BR, Rao KV, Vittal KP, Ramakrishna YS, Amarasinghe U (2010) Estimating the potential of rainfed agriculture in India: prospects for water productivity improvements. *Agric Water Manag* 97(1):23–30
6. Singh SK, Srivastava PK, Pandey AC (2013) Fluoride contamination mapping of ground water in Northern India integrated with geochemical indicators and GIS. *Water Sci Technol Water Supply* 13(6):1513–1523
7. Singh SK, Srivastava PK, Pandey AC, Gautama SK (2013) Integrated assessment groundwater influenced by a confluence river system: concurrence with remote sensing and geochemical modeling. *Water Resour Mange* 24:4291–4313. <https://doi.org/10.1007/511269-013-0408-y>
8. Wang B, Lin H (2002) Rainy season of the Asian–Pacific summer monsoon. *J Climate* 15:386–398
9. Thakur JK, Diwakar J, Singh SK (2015) Hydro geochemical evaluation of groundwater of Bhakatpur Municipality Nepal. *Environ Earth Sci.* <https://doi.org/10.1007/512665-0154514-4>
10. Matsumoto J (1997) The seasonal changes in Asian and Australian monsoon regions. *Adv Atmos Sci* 14:231–245
11. Akoto O, Adiyiah J (2007) Chemical analysis of drinking water from some communities in the Brong Ahafo region. *Int J Environ Sci Technol* 4(2):211–214
12. Gadgil S, Kumar KR (2006) The Asian monsoon—agriculture and economy in the Asian monsoon. Wang B (ed) Springer, Praxis, UK, pp 651–683

Multi-objective Optimization and Numerical Analysis of Coil Spring Used in Automobile Suspensions



Anurag Tripathi, K. Rameshkumar, and S. Saravanamurugan

Abstract The present work focuses on optimization of a helical coil compression spring made of ASTM A227 CLASS II and this type of springs are utilized in three wheelers. The main goal is to maximize natural frequency and strain energy absorption of the spring using a multi-objective optimization formulation. The performance of the spring may be enhanced by improving the capacity of strain energy absorption. The stiffness and geometric parameters of the spring has an impact on natural frequency and strain energy. Design parameters of a spring such as wire and mean coil diameter, number of active coils and pitch are optimized in this study. Pareto-optimal solutions are generated using Non-Dominated Sorting Genetic Algorithm-II and the results are verified using numerical approach. Modal and static analyses have been carried out for the selected designs generated by NSGA-II.

Keywords Multi-objective optimization · Coil spring · Pareto-optimal solutions · Numerical model

1 Introduction

Design optimization is one of the most crucial fields of engineering design. Optimization helps to give the better design of product considering various limitations imposed. The design problem is conceived as a mathematical problem consists of objective function, constraints, design variables, and bounds. A set of mathematical equation that fulfills the desired condition is considered as objective function. The objective function needs to be optimized either by maximization or minimization according to the requirements. Constraints are satisfied while finding the optimum values of the design parameters. It is important that design parameters should influence both the objective function and as well as constraints. Optimization problem formulation is broadly classified into single-objective and multi-objective

A. Tripathi · K. Rameshkumar · S. Saravanamurugan (✉)

Department of Mechanical Engineering, Amrita School of Engineering, Amrita Vishwa

Vidyapeetham, Coimbatore, India

e-mail: s_saravana@cb.amrita.edu

© The Author(s), under exclusive license to Springer Nature Singapore Pte Ltd. 2022

389

M. K. Singh and R. K. Gautam (eds.), *Recent Trends in Design, Materials*

and Manufacturing, Lecture Notes in Mechanical Engineering,

https://doi.org/10.1007/978-981-16-4083-4_31

optimization problems. Single-objective optimization problem involves only one objective function subject to design and bound constraints, whereas most of the real-world problems involve multiple objectives subject to design and bound constraints. Considering the difficulty to solve multi-objective optimization problems, many researches considered objective functions separately and obtained solutions using traditional and modern heuristic-based approaches. Traditionally, method such as weighted sum approach, where weights are assigned to objective function is used to solve multi-objective optimization problem and the multiple objectives are formulated as a single-objective optimization problem. These problems were solved using traditional and as well as modern heuristic methods. Off late, researchers have developed methodology to arrive non-dominated solutions considering optimization problems with multiple objectives without considering objectives separately. In this paper, coil spring used in light automobile has been modeled as a multi-objective optimization problem and Pareto-optimal solutions are obtained using heuristic approach.

The spring is one of the important components in an automobile. Varieties of springs are used in automobiles such as helical coil springs and leaf springs. These springs are used as a part of suspension system in the automobiles. Optimizing the spring's wire diameter, coil diameter, and pitch leads to minimization of cost and maximization of comfort of the passengers. In most of the research in optimization area, researchers and industry practitioners solve the multi-objective problem by assigning weights and used traditional methods to arrive solutions to the problem. The spring are optimized for many different objectives like minimizing the mass, volume, stress distribution, space constraints, and maximizing the natural frequency, strain energy, etc. Yokota et al. [1] has developed the optimal weight design problem considering allowable shear stress, wire diameter, mean diameter, and number of active coil of spring as a constraints. They solved the optimization problem using genetic algorithm. Wahl [2] conducted series of test on springs to provide the huge data for the study purpose. Many heuristic techniques like genetic algorithm and particle swarm algorithms were used in their study to find the optimum solution to design variable such as wire diameter, mean coil diameter, number of active turns, and pitch of coil. Ranganathan et al. [3] compared the performance of wave spring with the conventional helical coil spring. The authors chose the two material for the spring design, i.e., Chrome silicon and music wire. Under different static load conditions, springs were tested. Dynamic analysis was also carried out by varying the forces between 3000 and 4000 N. In static and dynamic conditions, deformation and von Mises stresses were estimated for wave spring and coil spring. Saravanamurgan et al. and Ram et al. [4, 5] used numerical optimization technique to optimize tuned spring-damper-mass system. Rameshkumar et al. [6] explored particle swarm optimization technique to optimize continuous function. Geem et al. [7] proposed a new Harmony Search Algorithm (HAS). The proposed algorithm was developed by observing the music rhythm to search for perfect to reach the state of harmony. This harmony became analogous to the optimum solution for the problem. The authors have optimized the design parameters of helical coil spring. The bi-objective functions are considered in their study are minimizing the weight and maximizing the

strain energy of coil spring. Xiao et al. [8] have considered the Particle Swarm Optimization (PSO) algorithm for optimizing the weight of helical coil spring considering the constraints such as maximum axial deflection, shear stress, and critical frequency, space between the coils, spring index, and fatigue. Three design variable was chosen for optimization such as Wire Diameter (d), Mean diameter (D), No. of turns (N). PSO algorithm was used for optimization process in their study. Raja et al. [9] have considered Simulated Annealing (SA) and Cuckoo Search (CS) to get the optimum parameters of helical coil spring formulated as a constrained optimization problem. Optimality criteria considered are maximizing the natural frequency and strain energy of helical coil spring.

Many engineering design problems involve simultaneous solutions of multiple objective functions. Number of extensions of Genetic Algorithms (GA) has been developed by the researchers to obtain Pareto-optimal solutions simultaneously [10–13]. Later Deb et al. [14] proposed a modified and improved algorithm called Non-Dominated Sorting Genetic Algorithm-II (NSGA-II). The important features of NSGA-II include use of elitist principle, explicit diversity preserving mechanism and emphasizing non-dominated solutions. The proposed algorithm takes the advantage of handling the mixed, continuous, and discrete variable. They have considered practical examples to prove the importance and computation capability of their procedure. Taktak et al. [15] have used two-noded FEM model of coil spring each of 6 degree of freedom to make the 3D isotropic helical beam model. In their formulation, they have also considered the shear strain effect, which is based on the resultant force using a hybrid approach. In their modeling approach, the complexity arises due to shape of structure and coupling the behavior of strain. The numerical results are presented for 2D and 3D beam at different load condition. Rahul et al. [16] applied multi-objective optimization technique to optimize helical spring used in three wheelers. Yang et al. [17] have considered the axial load under different dynamic conditions. They have modeled the spring by Euler–Bernoulli curved beam element based on absolute nodal coordinate formulation. The author specially focused when the spring comes in partial or fully contact stresses when the structure experiences an impact load or a load higher than the safe limit. The concept of contact comes into picture which leads to deterioration of spring, uneven damage and leads to failure before the expected life.

Most of the research work is focused on optimizing design parameter of helical coil spring using single-objective formulation. Real-world problems involving multiple objectives were solved by considering objective separately or by assigning weights for the objectives using traditional weighted sum methods. In most cases, problem formulation does not include real-world constraints such as variable load and factor of safety. Use of heuristic approaches to identify non dominated solutions is not well explored for multi-objective formulation of spring problems. In this paper, the open coil spring used in an automobile has been modeled as a bi-objective optimization problem. Two objective functions, namely, maximizing strain energy and natural frequency are considered in this study. The objective functions are subjected to

various realistic constrains. Pareto-optimal solutions are arrived by adopting NSGA-II procedure. The solution obtained by NSGA-II is validated by conducting modal analysis.

2 Objectives and Problem Formulation

The objectives of this study are given as follows:

- To optimize the helical coil spring using multi-objective optimization formulation with an objective of maximizing the strain energy and maximizing natural frequency considering realistic constraints.
- To conduct modal and static analysis of helical spring to validate the non-dominant solutions obtained using the heuristic approach.

2.1 Problem Formulation

In this paper, the helical coil spring is designed for static load conditions. A circular, constant diameter, constant pitch helical open coil spring used in an automobile suspension is considered in this study for optimization. The spring material is ASTM A227 CLASS II material. Design variables, objective function formulations, constraints, and variable bounds are discussed in this section.

Design Variables. The design variables taken into consideration for optimizing the overall design are:

- i. Wire Diameter (d)
- ii. Mean Coil Diameter (D)
- iii. No. of Active Coil (N)
- iv. Pitch of coil (p)

Objective Functions of the Optimization Problem

- a. *Natural Frequency of Coil Spring.* In the design of spring, it is assumed that the load is applied at a very slow rate. But in actual case, the springs works in a nonlinear pattern and experience stress and vibration. The natural frequency of the spring is to be high to improve the dynamics performance of the spring. The natural frequency formula is provided in the Equation-1. The natural frequency needs to be maximized.

$$f = \frac{1}{2} \sqrt{\frac{k}{m}} \quad (1)$$

$$k = \frac{Gd^4}{8D^3N} \quad (2)$$

where k = Stiffness of spring; m = mass of the spring; G = Shear modulus of rigidity; d = Wire diameter; D = Mean coil diameter; and N = No. of active coils

- b. *Strain Energy.* Strain energy has a significant impact on design of spring. The amount of energy stored by the spring to perform useful work is depending on the strain energy value of the spring. The strain energy function is shown in the Equation-3 and it has to be maximized.

$$U = \frac{8F^2d^3N}{GD^4} \tag{3}$$

where F = Force.

Constraint Formulation. The realistic constraints were taken into consideration in the optimum problem formulation. Table 1 depicts the various realistic constraints

Table 1 Details of various constrained imposed on the objective function

S. no	Condition	Expression	Equation no
1	Shear Stress	$\tau = K_s \frac{8FD}{\pi d^3}$	(4)
2	Length Under Loading	$\frac{Fmax}{k} + 1.05(N + 2)d - lmax$	(5)
3	Allowable Deflection under Preload Condition	$\frac{Fp}{k} - \delta_{pm}$	(6)
4	Max Deflection Under Loading,	$\frac{Fp}{k} + \frac{(Fmax-Fp)}{k} + 1.05(N + 2)d - \frac{Fmax}{k} + 1.05(N + 2)d$	(7)
5	Spring Index	$C - \frac{D}{d}$	(8)
6	Coil Diameter	$(D + d) - Dmin$	(9)
7	Wire Diameter	$dmin - d$	(10)
8	Deflection condition for Preload and Max. Load	$\delta_w - \frac{(Fmax-Fp)}{k}$	(11)
9	Buckling Condition	$b_c - \frac{(NP+2d)}{D}$	(12)
10	Soderberg Equation	$\frac{1}{FOS} = \frac{\tau_m}{\tau_y} + \frac{\tau_a}{\tau_e} \left(\frac{2\tau_y}{\tau_e} - 1 \right)$ where; $\tau_m = K_s \frac{8FmD}{\pi d^3}$; $\tau_a = K_w \frac{8FaD}{\pi d^3}$ $K_s = \frac{(4C-1)}{(4C-4)} + \frac{0.615}{C}$ and $K_w = 1 + \frac{1}{2C}$	(13)

Notations: τ = Shear Stress (MPa); F = Force (N); J = Polar Moment of Inertia; A = Area; T = Torque; FOS = Factor of Safety; G = Shear Modulus of Rigidity (MPa); E = Young's Modulus (MPa); k = Stiffness of spring; δ = Deflection (mm); l = Length (mm); τ_m = Mean Stress (MPa); τ_a = Amplitude Stress (MPa); τ_e = Endurance Stress (MPa); τ_y = Yield Stress (MPa); b_c = Buckling (mm); m = Mass of spring.

Table 2 Design parameters

Parameter name	Value
Maximum Force (Fmax)	3200 N
Minimum Force (Fmin, Fp)	1337 N
Constant, A	1983
Constant, n	0.190
Maximum allowable deflection under preload	152.4 mm
Deflection from preload	31.75 mm
Maximum free length	340 mm
Minimum wire diameter	5 mm
Maximum mean diameter	100 mm

Table 3 Bounds for the design variables

Bound	Wire diameter, d (mm)	Mean coil diameter, d, (mm)	No. of active turn, (no.)	Pitch, P, (mm)
Lower bound	11	50	7	33
Upper bound	13	95	12	50

imposed on the objective functions. The parametric values of the design parameters used for optimization is given in Table 2.

Bounds for the Design Variable. Bounds imposed on the design variables are provided in the Table 3.

3 Multi-objective Optimization of Coil Spring

3.1 Non-dominated Sorting Genetic Algorithm-II

Genetic Algorithm (GA) is a heuristic procedure used to find near-optimal or optimal solutions. GA works are based on the Darwin's theory of evolution. John Holland introduced GA in 1960 and it was further developed by Goldberg [18]. Goldberg applied GA to a variety of applications and the technique has become popular. Initially, GAs were developed to solve single-objective optimization problems. Multi-objective optimization problems do not have a unique solution as in the case of single-objective optimization problem. It's not possible to arrive set of non-dominated solutions using the GA. All the non-dominated solutions are optimum for a multi-objective optimization problem. The designer can select any of the non-dominated

solutions based on their requirement. Simple GAs have been extended to solve multi-objective optimization problem to find Pareto-optimal points (non-dominated solutions). Srinivas and Deb [12] modified the generic GA called Non-Dominated Sorting Genetic Algorithm (NSGA) and successfully generated Pareto-optimal points and solved many test functions. Deb et al. [14] modified the NSGA and proposed NSGA-II with efficient constraint handling mechanism. NSGA-II appears to converge to the Pareto-optimal solutions with good spread out of solutions for variety of optimization problems.

3.2 NSGA-II Procedure

The working of NSGA-II is shown in this section. Parameters used for convergence of NSGA-II are provided in Table 4.

Step 1: Set iteration counter, $t = 1$

Step 2: Create the Parent Population, 'PPt' of size 'N' and Children Population, 'CPt' of size 'N'.

Step 3: Build Combined Population CPt of size 2N

Step 4: Identify Non-Dominated Fronts, NDF1, NDF2,...NDFk in 'CPt'

Step 5: Determine the 'CD' (Crowding-Distance) of the sorted solutions in all fronts

Step 6: Create new population (new generation) PPt+1, by choosing first 'N' individuals in 'CPt'

Step 7: Select next-generation Child Population, 'CPt+1' of size 'N' by applying genetic operations on population PPt+1

Step 8: Set iteration $t = t + 1$

Step 9: Go To Step 3 and continue until the iteration counter/Termination criterion reached the set value

Step 10: Report the Non-Dominated Solutions

NSGA II has been implemented in the Matlab platform. Initial experiments were conducted to fine-tune the better convergence of NSGA-II. A population size and maximum iterations of 160 and 5000, respectively, resulted in 55 non-dominated solutions in the Pareto Front. The Pareto front obtained by the NSGA-II is depicted in Fig. 1. Non-dominated solutions are given in Table 5. The state of finding resources in such a way that the selection of one individual out of many does not exacerbate the performance of other individuals is known as Pareto efficiency. All the solutions on Pareto front are optimum solution and the one may take any solution according to the need.

Table 4 NSGA—II Parameters

S. no	Description of the parameter	Parameter value
1	Number of variable	4
2	Population size	160
3	Pareto fraction	0.35
4	Selection function	Tournament selection
5	Constraint tolerance	1e-10
6	Crossover function	Intermediate
7	Crossover fraction	0.8
8	Function tolerance	1e-10
9	Max generation	5000
10	Mutation function	Adaptive feasible

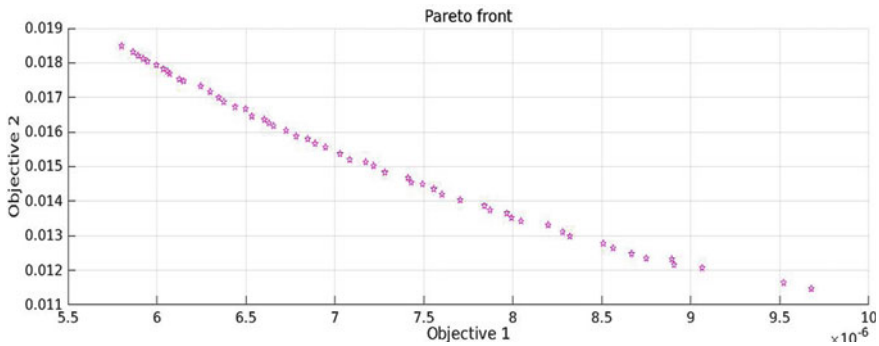


Fig. 1 Pareto front obtained by NSGA-II

4 Numerical Analysis of Coil Spring

The purpose of doing numerical analysis is to validate the solutions obtained by NSGA-II. In this study, Pareto front solutions were taken and numerical analysis is carried out to investigate the behavior of the coil spring. Coil springs were modeled with parameters obtained from the NSGA-II. Modal and static analyses are carried out. Spring parameters chosen from the Pareto front for static analysis is provided in the Table 6. Six random solutions from the top, middle and bottom of the Pareto front, respectively, to carryout numerical studies and validation.

4.1 Modeling of Helical Coil Spring

Material Selection. For light automotive, springs are made of ASTM A227 CLASS II. It has high carbon content (0.45–0.85% of C and 0.6–1.3% of Mn). Modeling

Table 5 Non-dominated solutions

S. no	x (1), d, Wire diameter, mm	x (2), D Coil diameter, mm	x (3), N, No. of active coils, Nos	x (4), P Pitch, mm	Strain energy, U (Joules)	Frequency, F (Hz)
1	12.28980	92.71018	9.55349	33.01601	172.3672384	54.08014295
2	12.00045	84.00318	7.000015	36.01175	103.3442619	87.16116216
3	12.00975	86.20170	7.342827	34.81291	116.7791830	79.06264551
4	12.28076	92.50726	9.353316	33.34446	168.1440620	55.41419843
5	12.26741	91.99897	9.329419	33.57554	165.6840117	56.09812791
6	12.24050	91.56249	8.665767	33.79174	153.0570048	60.75319385
7	12.22128	90.89073	8.350352	33.29396	145.1733972	63.83141946
8	12.07697	87.82284	7.307582	35.39201	120.1859757	76.99304135
9	12.22784	91.29458	9.369842	33.60496	164.7244790	56.53050389
10	12.05015	87.21430	7.100430	35.08694	115.3900761	80.12917900
11	12.02611	86.19179	7.433280	34.53695	117.5352195	78.23553905
12	12.25997	91.59864	8.618187	34.27314	151.4310076	61.13118575
13	12.03668	87.01034	7.051219	35.44209	114.2984079	80.96595279
14	12.15992	89.43980	8.416583	33.99001	142.2640039	65.05271873
15	12.12023	88.36217	7.314013	34.66010	120.7818598	76.27082176
16	12.25747	91.85746	8.843742	33.38578	156.8429212	59.25595687
17	12.01745	84.47850	7.034593	35.44848	105.0315484	85.89557402
18	12.26088	91.72144	8.430105	33.31309	148.6785061	62.31282560
19	12.10621	87.85651	7.822015	33.86558	127.5552213	72.11248158
20	12.24296	91.63464	7.980517	35.29403	141.1736287	65.79484720
21	12.27509	92.15612	9.364363	33.21195	166.7403694	55.73971108
22	12.26108	91.34617	8.834757	33.32986	153.9004163	59.98721139
23	12.27057	92.27068	9.432371	33.10999	168.8269999	55.19021358
24	12.00045	84.00318	7.000015	36.01175	103.3442619	87.16116216
25	12.07598	86.89158	7.655194	34.40769	121.9803639	75.09947339
26	12.27338	91.62192	9.143923	33.17958	160.0897085	57.70705860
27	12.28785	91.98663	7.857442	33.23837	138.5612026	66.54651172
28	12.02182	86.47692	7.021802	34.54030	112.2945599	82.19429732
29	12.28891	92.66895	9.414273	33.09003	169.6777447	54.90914970
30	12.23509	91.26232	8.863783	33.94816	155.2939917	59.77725437
31	12.04785	87.13130	7.715358	34.92665	125.1209867	73.94734614
32	12.15644	89.13748	7.901142	33.42366	132.3532789	69.67524854
33	12.10183	87.78404	8.193275	34.98341	133.4720163	68.97772365
34	12.28950	92.61460	9.038661	33.01718	162.5903552	57.21802301

(continued)

Table 5 (continued)

S. no	x (1), d, Wire diameter, mm	x (2), D Coil diameter, mm	x (3), N, No. of active coils, Nos	x (4), P Pitch, mm	Strain energy, U (Joules)	Frequency, F (Hz)
35	12.28847	92.54425	9.495435	33.13675	170.4750115	54.59058144
36	12.19562	89.70062	8.007421	34.66633	134.9440004	68.13122188
37	12.21659	90.77236	7.761132	34.05228	134.6098017	68.75193661
38	12.14952	89.40192	7.766158	33.69374	131.5528147	70.41662820
39	12.28803	92.67406	9.052525	33.01739	163.2320424	57.05317166
40	12.24834	91.65585	8.343529	33.34100	147.4383935	62.97427431
41	12.28129	91.88729	9.012611	33.06260	158.7560431	58.23831460
42	12.28980	92.71018	9.553490	33.01601	172.3672384	54.08014295
43	12.12104	88.68965	8.227719	34.04351	137.3498317	67.42307301
44	12.15090	89.28007	7.697580	34.01467	129.7998011	71.23433708
45	12.01528	85.32422	7.304492	34.98495	112.4508229	81.13150945
46	12.12180	88.80827	8.966771	33.25738	150.2511145	61.78948205
47	12.14960	89.07263	8.717766	33.80165	146.0427489	63.29776341
48	12.26112	91.83068	9.323925	33.59586	165.0177999	56.30445236
49	12.13020	88.80130	7.604123	34.16495	127.0356396	72.74380663
50	12.16823	89.54147	8.509768	35.14969	143.9361535	64.25075187
51	12.13592	88.51013	8.443374	33.03630	139.4098740	66.06914278
52	12.11360	87.98547	7.682892	35.68225	125.5323436	73.23216785
53	12.01649	85.52132	7.120589	34.96999	110.3365015	82.83088251
54	12.27345	91.95395	8.901185	33.01792	157.5369243	58.83386171
55	12.20710	90.59588	8.720489	33.81339	150.8361853	61.48659265

Table 6 Test cases taken from pareto front for numerical studies

S. no	Wire diameter (d), mm	Mean coil diameter (D), mm	No. of active turns (N), Nos	Pitch (p), mm
Spring 1	12.28	92.71	10	33.01
Spring 2	12.00	84.00	7	36.01
Spring 3	12.21	90.77	8	34.05
Spring 4	12.12	88.68	9	34.04
Spring 5	12.2	90.59	9	33.81
Spring 6	12.01	84.47	7	35.44

Table 7 Material properties of ASTM A227 CLASS II

Properties	Value
Young modulus (GPa)	204
Poisson ratio	0.29
Density (kg/m ³)	7985

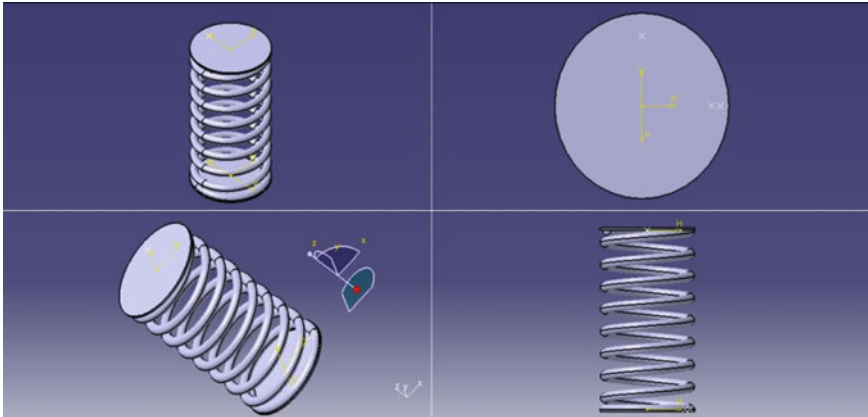


Fig. 2 Model of spring (1) used for static analysis

of coil spring is done using CATIA V5 software. The mechanical Properties of the material are given in Table 7.

Modeling of Helical Coil Spring. Modeling of coil spring has been done using CATIA V5 software. Helical coil spring model 1 is shown in Fig. 2. Similarly, for the other coil springs (Spring 2–Spring 6) CAD models are created for analysis. The fixed boundary conditions on both sides of the spring were considered for modal analysis. Boundary condition for the static analysis was considered as one side fixed and the load is applied from the other end.

5 Modal Analysis

The modal analysis is used to discover the dynamic characteristic of system in the form of mode shapes and frequency. The modal analysis is based on stiffness and mass of the component. In modal analysis, the governing equation of the system is partial differential equation, which is solved by imposing boundary condition. Modal Analysis is done on all the six springs. To find out excitation frequency, the Standard road bump is taken into consideration. The standard used for finding excitation frequency follows IRC 99–1988. The standard road bump according to IRC 99–1988 is shown in Fig. 3. Excitation frequency is computed for different conditions using Eq. (4) is given in Table 4 considering maximum velocity as 16.66 m/s. The

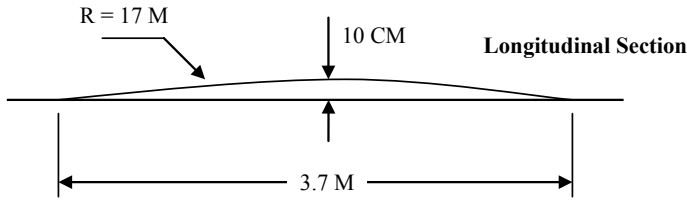


Fig. 3 Standard road bump: IRC 99–1988

excitation frequency is found using the Eq. 14.

$$f = \frac{v}{\lambda} \quad v = \text{Velocity} \left(\frac{m}{s} \right); \lambda = \text{wavelength}(m) \quad (14)$$

For the spring experiencing a compression force between two parallel plates, normally the first mode of vibration (Lowest natural frequency) will experience the vibratory motion in middle portion of spring where the end of spring remains stationary. Second mode of vibration of the spring occurs at a point of $\frac{1}{4}$ and $\frac{3}{4}$ distance from the spring end. Various modes (first five modes of the spring) in bending, compression, twisting, and shearing is depicted in Fig. 4. The mode values of the spring are exhibited in Table 5. For modal analysis, the type of element used for analysis is “C3D10” having number of element as 27,000. From the modal analysis, it is observed that excitation frequency is less than the natural frequency of spring.

6 Static Structural Analysis

6.1 Static Numeric Solution (Shear Stress and Deflection) and Comparing with Analytical Solution

Static load is taken into account to determine the possible fundamental and derived result such as deformation, strain, stress, etc. To perform the FEA analysis, the FEA tool requires following inputs, namely meshed model, fully defined boundary condition, material properties (Modulus of elasticity, Poisson ratio), and applied force. To perform the analysis the ‘.stp’ file is imported to ABAQUS. In static analysis, the force of 3200 N is applied on the spring from one end. Meshing details of the spring is given in the Table 6. The induced shear stress and deformation of spring model 1 which are simulated using the ABAQUS is shown in Figs. 5 and 6, respectively. Similarly, the shear stress and deflections for other springs (spring modes 2–6) are computed. The details of theoretical and numerical values (static analysis) of maximum shear stress and deformation of all the spring models are shown in Table 7. Shear stress in springs, designed with the parameters obtained by the NSGA-II using theoretical and numerical approach has good correlation.

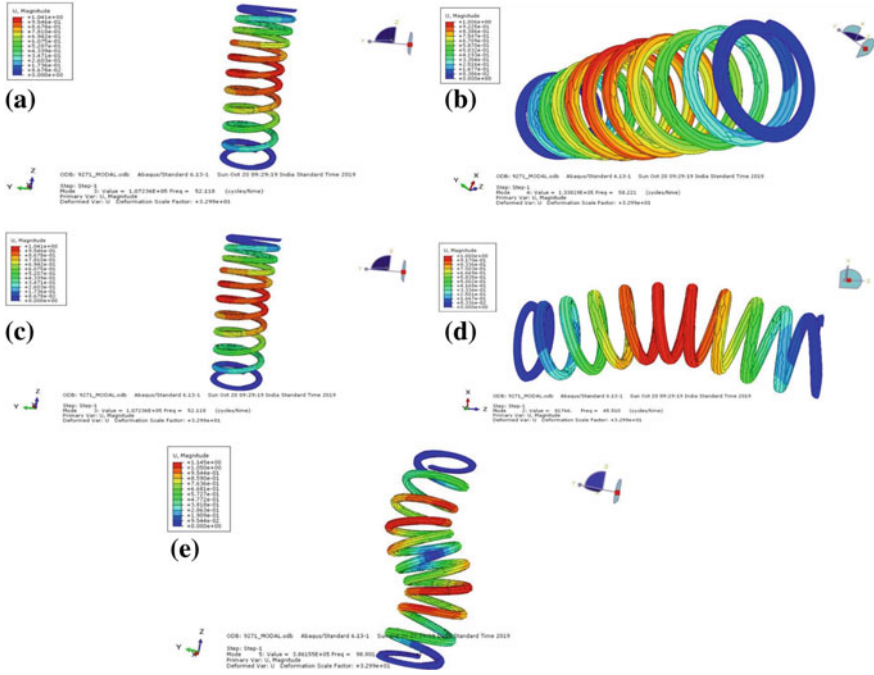


Fig. 4 a Mode 1: Bending about y-axis. b Mode 2: Bending about x-axis. c Mode 3: Compression. d Mode 4: Twisting. e Mode 5: Shearing

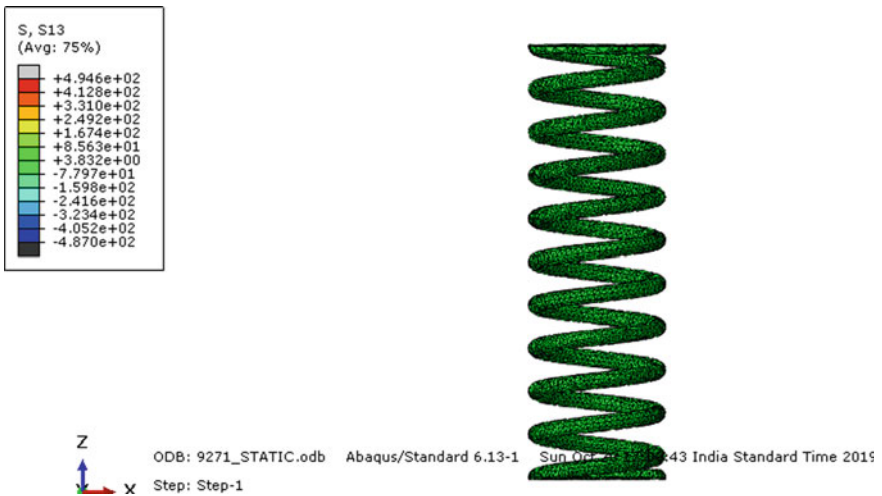


Fig. 5 Shear stress of the spring model 1



Fig. 6 Deflection of the spring model 1

Maximum deviation of 2.10% is observed for the spring model 4. Considering the deformation, the maximum deviation observed is 12.2%.

6.2 Static Numeric Solution (Strain Energy) and Comparing with NSGA-II Solution

From the FEA simulations, strain energy of the spring is also computed and compared with the solutions obtained by the NSGA-II. A typical strain energy plot for the spring model 1 is exhibited in Fig. 7. Details of strain energy for all the spring models are

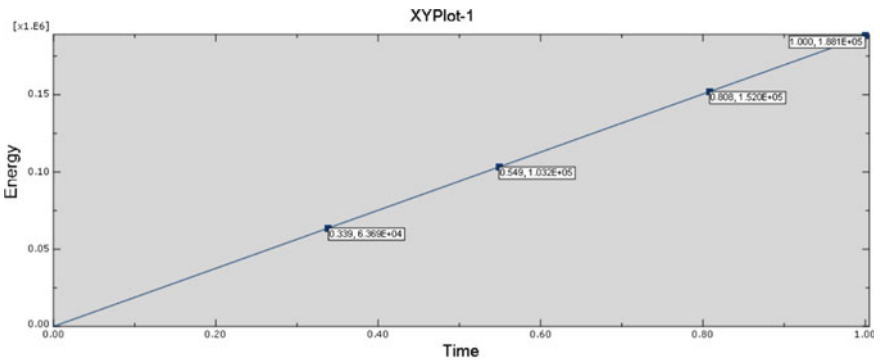


Fig. 7 Strain energy plot for the spring model 1

Table 8 Excitation frequency of springs

S. no	Wavelength (m)	Velocity (m/s)	Excitation frequency (Hz)
1	3.7	2.778	0.750
2	3.7	5.556	1.506
3	3.7	11.11	3.002
4	3.7	16.66	4.502

Table 9 Mode values of the springs

Specimen	Frequency, Hz				
	1st mode Bending about y-axis	2nd mode Bending about x-axis	3rd mode Compression	4th mode Twisting	5th mode Shearing
Spring 1	45.143	45.510	52.118	58.221	98.901
Spring 2	83.071	85.995	91.225	98.807	168.56
Spring 3	64.473	66.226	69.216	76.022	131.10
Spring 4	54.958	55.551	62.618	69.602	118.55
Spring 5	54.213	54.851	60.587	67.438	115.68
Spring 6	83.330	86.610	90.862	98.281	167.96

Table 10 Meshing details of the spring models for static analysis

Spring models	No. of nodes	No. of elements	Element type	Shape	Geometric order
Spring 1	98,244	56,292	C3D10	Tetrahedral	Quadratic
Spring 2	61,615	34,676			
Spring 3	159,796	97,433			
Spring 4	263,462	163,060			
Spring 5	81,000	45,962			
Spring 6	386,440	215,156			

provided in Table 8. It is found that the maximum deviation is 5.53%. It may be inferred that there is close correlation between NSGA-II and Numerical solution.

Table 11 Theoretical and numerical values of shear stress and deflection for all the spring models

Spring Model	Shear stress, MPa		% Deviation	Deformation, mm		% Deviation
	Theoretical	Numerical (FEA)		Theoretical	Numerical (FEA)	
Spring 1	494.40	487.50	1.40	108.03	111.10	2.76
Spring 2	490.40	480.40	2.05	64.60	73.61	12.2
Spring 3	487.8 0	487.30	0.10	86.90	98.60	11.8
Spring 4	488.19	498.70	2.10	93.90	103.40	9.18
Spring 5	487.65	497.20	1.92	97.30	107.0	9.06
Spring 6	481.1 0	478.40	0.62	65.0	68.0	2.62

Table 12 Comparison of strain energy values obtained by numerical method and NSGA-II

Specimen	NSGA-II (Joules)	FEA (Joules)	% Error
Spring 1	180.99	188	3.72
Spring 2	103.34	109.4	5.53
Spring 3	139.04	146.51	5.09
Spring 4	150.24	156.68	4.11
Spring 5	156	162.23	3.84
Spring 6	104.74	106.58	1.72

7 Conclusions

In this paper, a helical coil spring is optimized for having high natural frequency and strain energy absorption. Non-dominated Pareto solutions have been obtained using NSGA-II. In order to validate the solutions obtained from NSGA-II, modal analysis has been performed by selecting extreme solutions. The value of natural frequency is compared with optimum solution arrived using NSGA-II. Moreover, the excitation frequency of the coil spring is found to be less than the natural frequency and hence the design is safe. Strain energy and shear stress of the spring have been compared with the solutions of NSGA-II and existence of close correlation between the solution obtained by NSGA-II and numerical procedure has been observed. The designer may opt for one of the non-dominated solution obtained by NSGA-II. Further studies can be carried out to validate the results using experimental procedure.

References

1. Yokota T, Taguchi T, Gen M (1997) A solution method for optimal weight design problem of helical spring using genetic algorithms. In: Proceedings of the 21st international conference, computers and industrial engineering, pp 71–76
2. Wahl AM (1963) General design consideration for helical compression or extensional springs, mechanical springs, 2nd edn. McGraw-hill, New York
3. Ranganathan S (2019) Modeling and analysis of helical and wave spring behavior for automobile suspension, No. 2019–28–0130.SAE Technical Paper (2019).
4. Sundaram S, Alwarsamy T, Devarajan K (2015) Optimization of damped dynamic vibration absorber to control chatter in metal cutting process. *J Vibr Control* 21(5):949–958
5. Ram HVG, Saravanamurugan S (2019) Regenerative chatter control in turning process using constrained viscoelastic vibration absorber. In: IOP conference series: materials science and engineering, vol 577, No. 1. IOP Publishing
6. Rameshkumar K, Rajendran C, Mohanasundaram KM (2012) A novel particle swarm optimisation algorithm for continuous function optimisation. *Int J Oper Res* 13(1):1–21
7. Geem ZW, Kim JH, Loganathan V (2001) A new heuristic optimization algorithm: harmony search and simulation 76(2):60–68
8. Qimin X, Liwei L, Qili X (2009) The optimal design and simulation of helical spring based on particle swarm algorithm and MATLAB. *Wseas Trans Circuits Syst.* 8(1)
9. Na GRE, Rb S, Sd N (2017) Helical spring design optimization in dynamic environment based on nature inspired algorithms. *Int J Theor Appl Mech* 12(4):709–739
10. Rey Horn J, Nafpliotis N, Goldberg DE (1993) Multiobjective optimization using the niched pareto genetic algorithm, IlliGAL report 93005
11. Fonseca CM, Fleming PJ (1993) Genetic algorithms for multiobjective optimization: formulation discussion and generalization. In: *Icga*, vol 93 (1993), pp 416–423
12. Srinivas N, Deb K (1995) A fast and elitist multi-objective genetic algorithm: Nsga-ii. *Evolut Comput* 2(3):221–248
13. Deb K, Agrawal S, Pratap A, Meyarivan T (2000) A fast elitist non-dominated sorting genetic algorithm for multi-objective optimization: NSGA-II. In: *International conference on parallel problem solving from nature*. Springer, Berlin, pp 849–858
14. Deb K, Pratap A, Agarwal S, Meyarivan TAMT (2002) A fast and elitist multiobjective genetic algorithm: NSGA-II. *IEEE Trans Evolut Comput* 6(2):182–197
15. Taktak M, Dammak F, Abid S, Haddar M (2005) A mixed-hybrid finite element for three-dimensional isotropic helical beam analysis. *Int J Mech Sci* 47(2):209–29 (2005)
16. Rahul MS, Rameshkumar K (2020) Multi-objective optimization and numerical modelling of helical coil spring for automotive application. In: *Materials today: proceedings*
17. Yang CJ (2014) Modeling and dynamics analysis of helical spring under compression using a curved beam element with consideration on contact between its coils. *Meccanica* 49(4):907–917
18. Goldberg DE (2002) The design of innovation: lessons from and for competent genetic algorithms by David E. Goldberg, vol. 7. Springer Science & Business Media (2002)

Mechatronics and Robotics

Replicating the Natural Limb Structure of a Mammal-Type Quadruped on a Highly Compact 12-DoF Robot to Deduce a Relation Between Limb Structure and Canine Gait Efficiency



Divyaansh Singh and Apurv Verma

Abstract The environment provides us with the versatile types of gait cycles, bipedal walking displayed by humans, Quadrupedal gait, which is shown by most mammals, Pentapedal sequences considered for kangaroos. Gait is the output of multiple limb movements created by numerous processes of muscle extension and retraction. In recent years, quadruped robots have gained significant attention due to their biomimetic capabilities, maneuverability, and versatility. However, in mobile robotics, moving on uneven terrains still poses an issue. Even after the improvements in wheeled robots, there are certain limitations that only the legged robots would prove advantageous to, with their feral manner of gait. This paper focuses on the mammal-type quadrupedal robot structure with the inclining research towards understanding the gait cycles and optimized designs of the quadrupeds. To understand how a naturally achieved locomotion is dependent on the structure. This paper provides the close propinquity of actual manufactured mechanical design to the naturally present quadruped while balancing its CoG and getting a better grip on versatile surfaces.

Keywords Centre of gravity · Coxa · Degrees of freedom · Femur · Tibia · Quadruped gait

1 Introduction

Quadrupedal robots are known for their multi-limb, multi-degree of freedom feature, and discrete motion trajectory. They are more maneuverable and adaptable in a non-structural environment and have better flexibility, stability, and tolerance to fault than a wheeled or crawler robot. In recent years, locomotion has been the hot spot for robotics. The significant advantage of the quadrupedal movement is not only to provide better stability but also a full range of joint motion, increased speed,

D. Singh (✉) · A. Verma

Department of Mechanical Engineering, SRM Institute of Science and Technology,
Kattankulathur, Chennai, India

e-mail: da6202@srmist.edu.in

better load capacity, less mechanical redundancy, and less complexity than bipedal. Therefore, the development of quadruped robots has always been highly valued, and it is of great theoretical and practical value to carry out relevant theoretical and technical research in-depth.

The two major categories of Quadrupeds based on leg structures are mammal-type and sprawling-type. The mammal-type robot structure helps for faster walking capability, reduced torque requirements, and increased balance in its static position, and this structure is also adjustable to walk in narrow regions as it has smaller footplates. The anatomy of the leg of a quadrupedal being is concise and consists of three major parts, namely—coxa (hip joint), femur (thigh bone), and tibia (bone below knee joint). They have a low CoG, and, as a result, if it topples over, the damage to the body is considered minimal. It is this low CoG that helps the robot to climb steep planes; with the bending of their forelimb knees, the CoG is shifted towards the front, helping it to work in different terrains. This feature plays a vital role if the robot is used for carrying objects.

2 Experiment

2.1 Mechanical Design

The model of the quadruped robot was designed majorly in SolidWorks, as shown in Fig. 1. A 12-degrees-of-freedom robot that closely resembles the actual quadruped structure of the majority of mammals. It is designed to verify its proximity to the naturally available quadruped leg design and how does this structure affect the locomotion. The design is scaled to a very small size for testing and research purposes. Table 1 shows the dimensions of the quadruped robot. After fabricating the proto-

Fig. 1 Solid works model of the quadruped

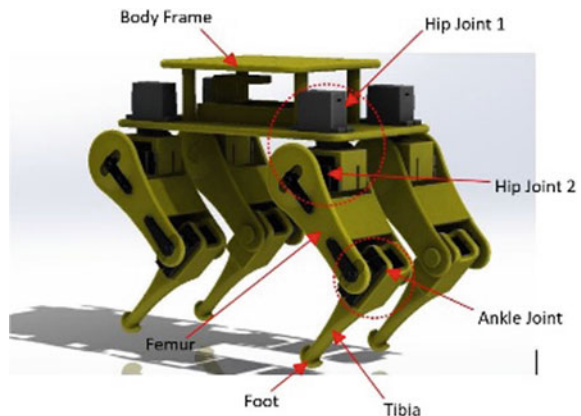
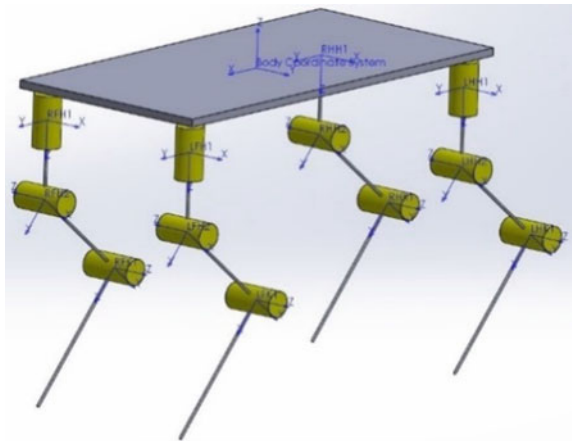


Table 1 Quadruped specifications

S. no	Properties	Value
1	Length	161.48 mm
2	Height (legs extended)	184.89 mm
3	Width	108.75 mm
4	Total leg length	141.94 mm
5	Femur	60 mm
6	Tibia	80.34 mm
7	Degrees of freedom	12

Fig. 2 12-Dof Leg configuration



type of the quadruped, the length of the femur and tibia are 60 mm and 80.34 mm, respectively.

Figure 2 shows the joint configuration of the robot. LUFL, RUFL, LLFL, RLFL, LUHL, RUHL, LLHL, RLHL represent the Left Upper Fore limb, Right Upper Fore Limb, Left Lower Fore Limb, Right Lower Fore limb, Left Upper Hind Limb, Right Upper Hind Limb, Left Lower Hind Limb, Right Lower Hind Limb. Each leg consists of 2-DoF for hip joints designated as H and 1-Dof Knee joint identified as K.

To make the body of the quadruped lightweight as well as to increase weight carrying capacity up to its optimum capability, the parts of the quadruped are 3D printed using Polylactic Acid (PLA) with the infill of 90%, a layer height of 0.2 mm with 2 outer walls (Figs. 3, 4, 5, 6, 7 and 8).

The major parts of the mechanical design are:

- (1) **Femur**—The femur or the thigh bone is the connection of the legs to the body. It is the femur that supports the part below the knee. The femur is an integral part of any quadruped cycle, as it determines the length of every step taken. In this model, the femur is directly below the coxa, which is more closely related to the naturally seen quadrupeds and also gives it better stability during the

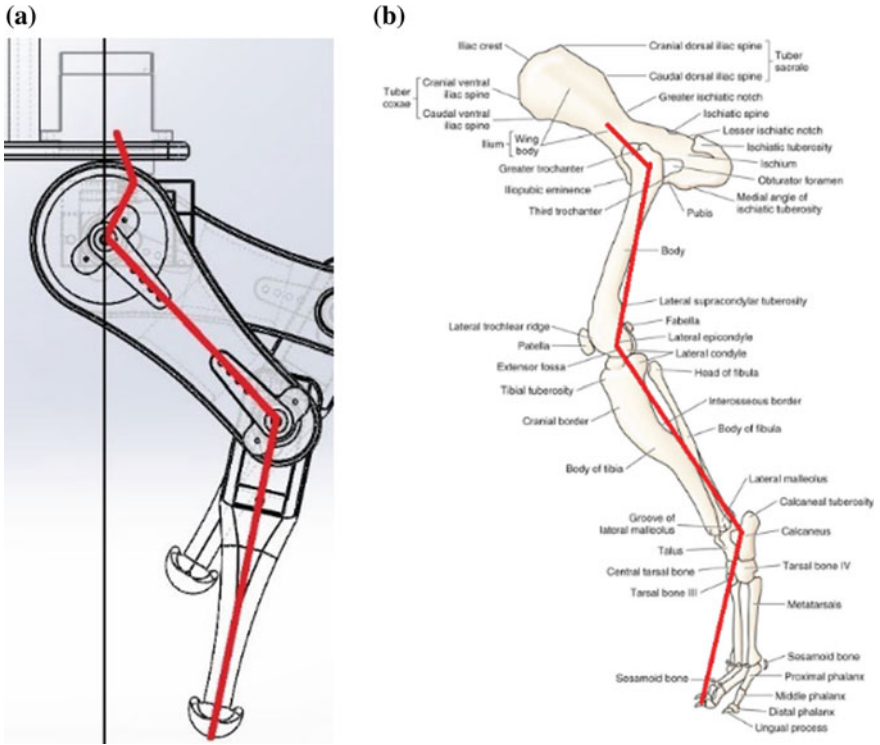


Fig. 3 Comparison of **a** Quadruped robot and **b** Actual dog limb structure with respect to the central axis connecting the joints

Fig. 4 Mechanical model of the femur

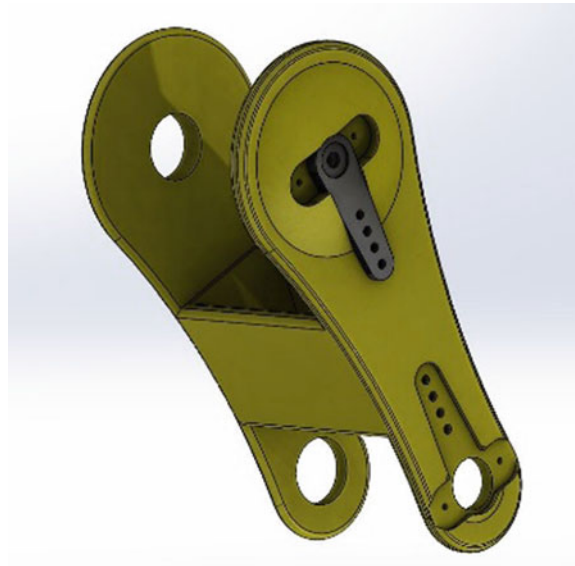


Fig. 5 Mechanical model of the tibia



gallops and sprinting, compared to the quadrupeds where the legs are away from the body. Here, the femur is not provided with any servos but acts as a connection to the hip and stifle joint to resemble the actual flexor surface of quadrupeds.

- (2) **Tibia**—The tibia or the bone below the knee, this part is responsible for the connection to the femur and creating contact with the ground. It is assembled with one servo motor for the 1-DoF stifle joint. It is this part of the quadruped which generates the suspension and maintains stability. In the model, the tibia is connected directly below the femur, creating one continuous link.
- (3) **Body Frame**—The body frame was developed considering the length of the coxa, femur (thigh bone), and tibia (bone below the knee). There is a snap-fit slot provided for the Li-po battery, for its easy insertion and removal. For increased control over the CoG of the quadruped robot, an extra slot on the top is provided, which can be used for the application of multiple boards and sensors. Hence, it would not disturb the overall setup maintaining the CoG inside the convex hull of the quadruped robot. With this setup, proper distribution of weight is achieved, and hence balancing of the robot even with 3-leg ground

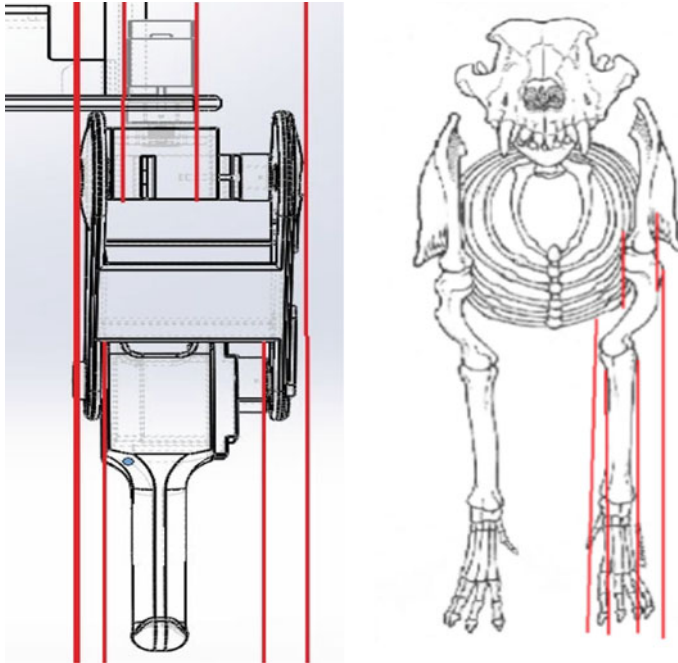


Fig. 6 Structural similarity between robot and natural quadruped chain created from coxa to tibia

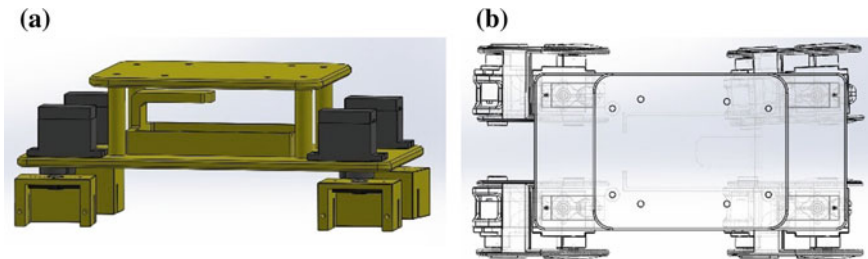


Fig. 7 Mechanical model of the body frame **a** side view **b** top view

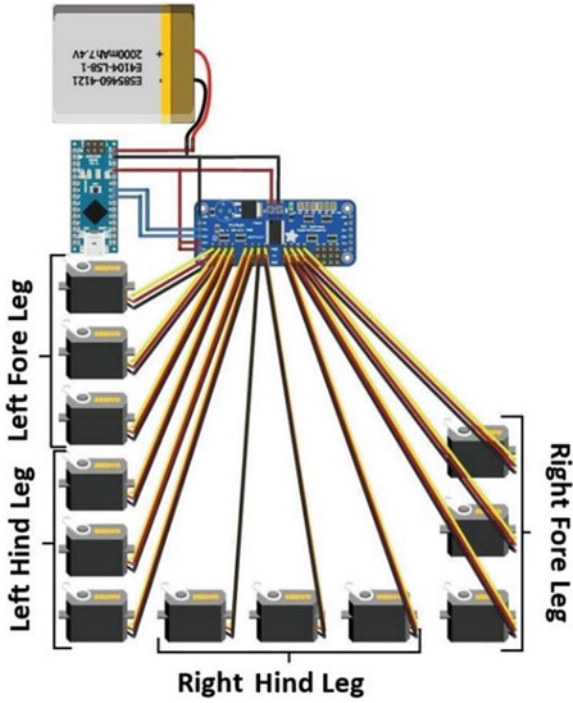
contact becomes effortless. The increased CoG balance makes this setup more comfortable for different locomotion types of the quadrupedal robot like the Walk, Trot, and Gallop.

- (4) **Foot**—The foot, being the end part of the tibia, is in direct contact with the ground. The footplates are made semicircular to have a point contact with the ground for any quadruped orientation. This increases the length of stroke and versatile methods of foot placements, reducing the robot being toppled. The footplates are also equipped with a silicone rubber grip to reduce the slippage on smooth planar surfaces. It is also responsible for absorbing shocks at the

Fig. 8 Mechanical model of the foot without the attached grip



Fig. 9 Control circuit



heel strike, providing a stable platform for the body, and acting as a rigid lever for propulsion.

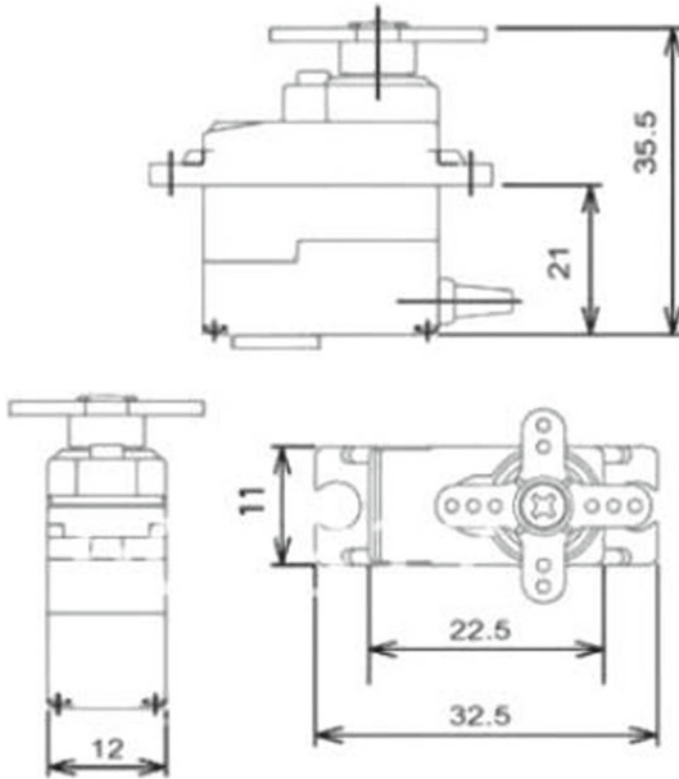
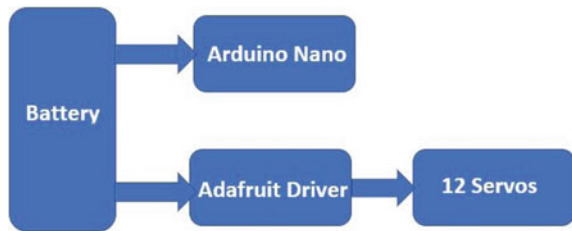


Fig. 10 MG90S servo dimensioning

Fig. 11 Power Action Flow



2.2 Electronic System

The quadruped electronic control becomes complex to some degree when 12 DoF is to be controlled on such small hardware. The primary electronic components used are as follows (Figs. 9, 10 and 11):

- (1) **Microcontroller**—Arduino nano is a small Atmel ATmega 328 based development board. It has 14 Digital Input/Output Pins, of which 6 provide Pulse

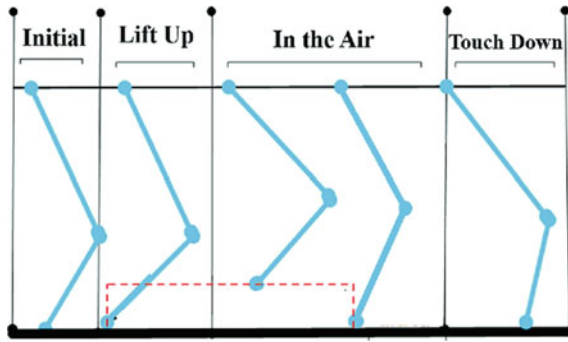


Fig. 12 Individual leg cycle while walking

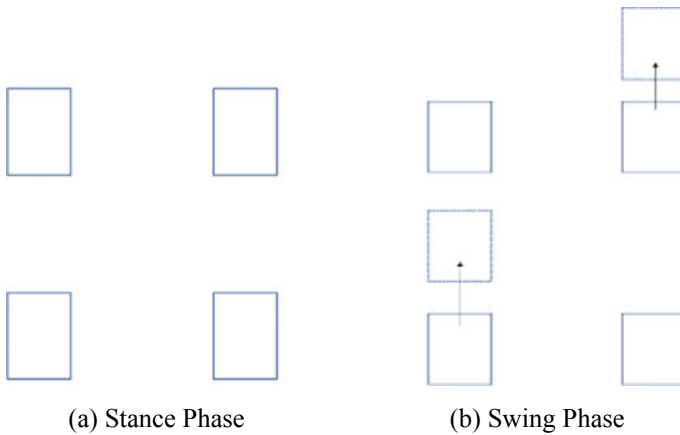


Fig. 13 Foot Placements

Width Modulation output. It also has 8 analog input pins with 32 Kb of the flash memory, of which the bootloader uses 2 KB. It has SRAM of 2 Kb and EEPROM of 1 Kb. Additional to these features, it also has an oscillator on board, which runs at 16 MHz. The board measures just at 0.70" × 1.70", is this small we chose this board and also because it communicates using I2C protocol, which is used to control the Servos via the Adafruit PCA9685 board.

- (2) **Servo Controller**—The Adafruit PCA9685 is a 16-channel servo driver. It can communicate with the Arduino nano via its analog pins using the I2C protocol. It can drive 16 servos at once and can be extended to drive more servos possible for the head and neck. The board is 5 V safe and has reverse polarity protection. The boards have 16 output ports. Each port has 3 pins PWM at the top, V + in the middle, and GND at the bottom. Each PWM channel runs independently of one another, but they all run at the same frequency.

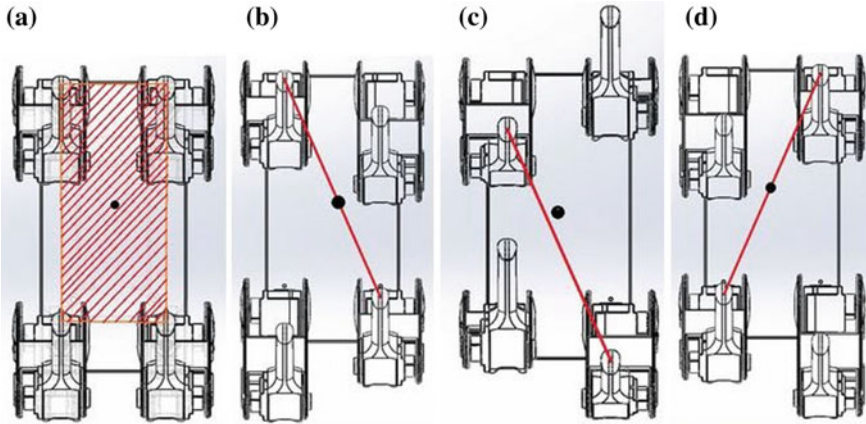


Fig. 14 COM stability while walking **a** COM at the center of convex hull at initial stage **b** COM on the contact line while diagonal legs lift **c** COM is pushed towards the front for forward motion **d** COM restored within the contact line while the other diagonal legs lift

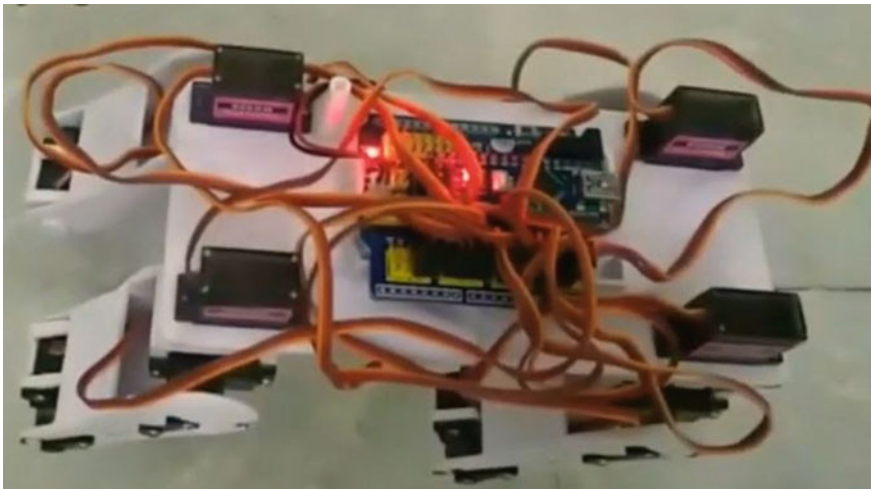


Fig. 15 Testing Gait cycle on the fabricated model

- (3) **Servo Motors**—The quadruped robot uses MG90S micro servo motors for all its actuations, being a 12-DoF robot consisting of 12 MG90S. These motors are taken into consideration because of their lightweight and high torque capacity. In this quadruped, we only require the position control without the feedback this motor was chosen. The motor has a stall torque of 1.8 kg*cm at 4.8 V and 2.2 kg*cm at 6 V with a rotational angle up to 180°. This motor consists of 3 pins- Red wire powers the motor with + 5 V, Brown wire connects to GND,

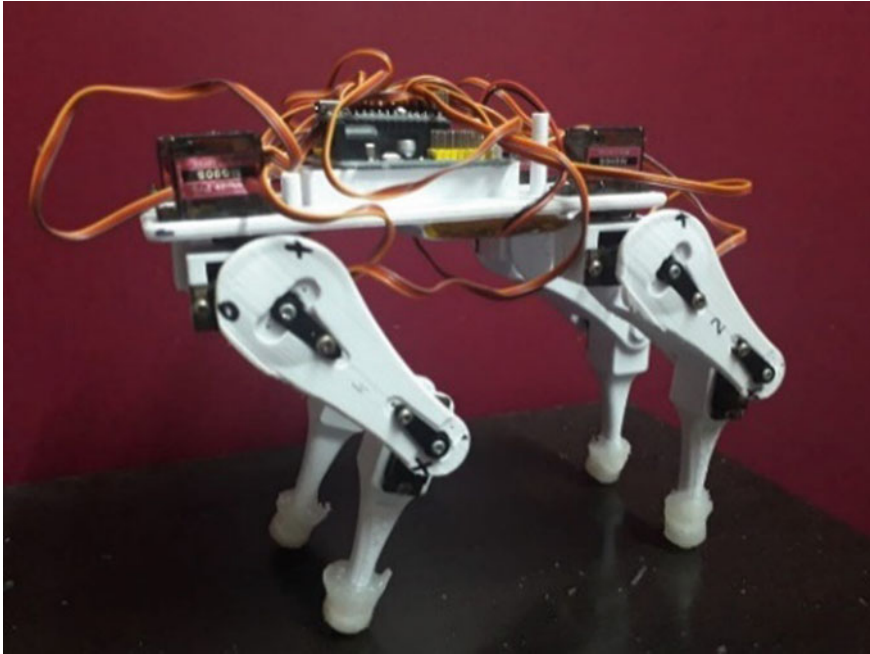


Fig. 16 Fabricated model of the quadrupedal robot

and the last Orange wire—PWM signal is given through this wire to drive the motor.

2.3 Motion Planning

The Gait of the Quadrupedal Robot is divided into two phases, namely-Stance Phase, and Swing Phase. The synchronicity between the two phases is essential so that the required acceleration center of mass also aids in the motion of the Quadrupedal Robot (Figs. 12, 13 and 14).

While going from Stance Phase to Swing Phase, the knee joints and hip joints between RUFL and RLFL, and LUHL and LLHL (configuration can be considered on the diagonally opposite sides) rotates and center of mass of the Quadruped shifts upward (swing phase), after placing the right front foot and left hind foot forward, the center of mass shifts slightly downward coming back to its original coordinates on the Quadruped. The Quadruped has come back to the Stance Phase. The same takes place with the remaining knee joints. The knee joints and hip joints between LUFL and RLFL, and RUHL and RLHL rotates and center of mass of the Quadruped shifts towards upward (Swing Phase) and after placing the left front foot and right hind foot forward, the center of mass shifts downward coming back to its original

coordinates on the Quadruped. The Quadruped has come back to the Stance Phase again. This repeated cycle of changes between Stance and Swing Phases develops the cyclic exchange of gravitational potential energy and kinetic energy of the center of mass of the Quadrupedal Robot.

3 Results and Discussion

The study displayed results of efficient gait achieved when the legs of the quadruped were in-line with the body, as natural mammals like dogs have. This structure increases the stability and efficiency while walking and lets it perform various other canine gaits like gallop, amble, pace, trot, canter with ease. Studying the prototype even on a compact scale, the results received very extremely close to the original walking pattern of the dogs. With proper weight distribution throughout the body and the appropriate similarity with naturally available structure, using even the default or open-source codes for the quadruped gait, the robot could quickly adapt (Figs. 15 and 16).

4 Conclusion

This paper's primary objective is to try deriving the relationship between the natural design of the quadrupeds and their efficient gait. The quadruped robot's design has helped to understand why the naturally available quadrupeds have such efficiency, compared to the mechanical quadrupeds with legs present outside the main body. The design of the quadrupedal robot was optimized and fabricated. With such an uncomplex and small design of just 184.89 mm, a highly efficient gait was obtained. This research can be further developed for large-scale models to establish the stride to greater accuracy. One, out of many iterations, the design problem of the mammal-type quadruped robot was solved, and the natural gait was nearly obtained while balancing its CoG and getting a better grip on the versatile surfaces; also, this was done while taking into account of the anatomy of quadrupedal beings.

References

1. Zhou L, Qian H, Xu Y, Liu W (2017) Gait design and comparison study of a quadruped robot. In: 2017 IEEE international conference on information and automation (ICIA), Macau, pp 80–85. <https://doi.org/10.1109/ICInfA.2017.8078886>
2. Liu D, Sun M, Qian D (2018) Structural design and gait simulation of bionic quadruped robot. In: 2018 international conference on advanced mechatronic systems (ICAMechS), Zhengzhou, pp 16–20. <https://doi.org/10.1109/ICAMechS.2018.8507037>

3. Reitmaier S, Schmidt H (2020) Review article on spine kinematics of quadrupeds and bipeds during walking. *J Biomech* 102:109631. <https://doi.org/10.1016/j.jbiomech.2020.109631>
4. Du W, Fnadi M, Benamar F (2020) Rolling based locomotion on rough terrain for a wheeled quadruped using centroidal dynamics. *Mech. Mach. Theory* 153:103984. <https://doi.org/10.1016/j.mechmachtheory.2020.103984>
5. Carlisle LD, Memili E, Linford RL, Slater KA, Nicodemus MC (2019) Relationship between gait mechanics and the speed of the trot in the Weimaraner dog breed. *Top Companion Anim Med* 35:26–30. <https://doi.org/10.1053/j.tcam.2019.03.003>
6. DeCamp CE (1997) Kinetic and kinematic gait analysis and the assessment of lameness in the dog. *Veterin Clin North Am: Small Animal Pract* 27(4):825–840. [https://doi.org/10.1016/s0195-5616\(97\)50082-9](https://doi.org/10.1016/s0195-5616(97)50082-9)
7. McLaughlin RM (2001) Kinetic and kinematic gait analysis in dogs. *Veterin Clin North Am: Small Animal Pract* 31(1):193–201. [https://doi.org/10.1016/s0195-5616\(01\)50045-5](https://doi.org/10.1016/s0195-5616(01)50045-5)
8. Zhong Y, Wang R, Feng H, Chen Y (2019) Analysis and research of quadruped robot's legs: a comprehensive review. *Int J Adv Robot Syst*
9. Feng H, Wang R (2008) Construction of central pattern generator for quadruped locomotion control. In: 2008 IEEE/ASME international conference on advanced intelligent mechatronics, Xi'an, China, pp 979–984. <https://doi.org/10.1109/AIM.2008.4601794>
10. Xu K, Zi P, Ding X (2019) Gait analysis of quadruped robot using the equivalent mechanism concept based on metamorphosis. *Chin J Mech Eng* 32:8. <https://doi.org/10.1186/s10033-019-0321-2>
11. Bhatti Z, Waqas A, Mahesar A, Karbasi M (2017) Gait analysis and biomechanics of quadruped motion for procedural animation and robotic simulation 10(7)
12. Griffin T, Main R, Farley C (2004) Biomechanics of quadrupedal walking: How do four-legged animals achieve inverted pendulum-like movements? *J Exper Biol* 207. <https://doi.org/10.1242/jeb.01177>
13. Iida F, Gomez G, Pfeifer R (2005) Exploiting body dynamics for controlling a running quadruped robot. In: ICAR '05. proceedings., 12th international conference on advanced robotics, 2005, Seattle, pp 229–235. <https://doi.org/10.1109/ICAR.2005.1507417>
14. Ho T, Choi S, Lee S (2007) Development of a biomimetic quadruped robot. *J Bionic Eng* 4:193–199. [https://doi.org/10.1016/S1672-6529\(07\)60032-8](https://doi.org/10.1016/S1672-6529(07)60032-8)
15. Zhang X, Zheng H, Xu G, Cheng Z, Zhao L (2005) A biological inspired quadruped robot: structure and control. 2005 IEEE international conference on robotics and biomimetics - ROBIO, Hong Kong, pp 387–392. <https://doi.org/10.1109/ROBIO.2005.246298>

Automation in Robotics with Artificial Intelligence



Yogini Borole  and C. G. Dethé

Abstract This document provides an introduction to man-made brain power, robots, and experimental streams that look at the financial and physiological consequences of this and other related innovations. We present a preliminary assessment of man-made knowledge and expertise to work on financial matters with writing managers and integrate existing methods adopted by investigators here. We look at the understanding of non-counterfeit fraud, mechanical autonomy, and the use of system sequences and robust systems, striving for the most remarkable commitment to these points by authoritative and technical analysts, as well as photographs of future experiments.

Keywords Robots · Artificial intelligence · Structural strategy · Humanoid robot's introduction · Automation

1 Introduction

Man-made knowledge with robots with common roots above (middle) extensive past of connection with logical argument. The introduction of AI and Mechanical technology took place at the same time, and initially there was no clear distinction between the two controls. The explanation is that the concept of "intelligent machine" often promotes robots and robots. One could argue that there is only one in every unusual robot machine, and absolutely Artificial Intelligence is even more concerned with the expert (for example, experts who can be compared to a bodily mechanism). Instead, the vast majority of special difficulties in addition to arrangements desired to set up robots are not controlled by man-made research. The logical distinction between the camps can be seen in the 70's, when Robotics was found to be more focused on mechanical operation, and Artificial Intelligence used robots to show that

Y. Borole (✉)
Savitribai Phule Pune University, Pune, India

G H Raisoni College of Engineering and Management, Pune 412207, India

C. G. Dethé
UGC-Staff College, Nagpur 440022, India

machines could work similarly in normal conditions. Subsequently, the challenges posed by the construction of mechanical capabilities in unrestricted environments have led Artificial Intelligence scientists to justify Robotics as a popular test site for AI. Alternatively, experimenting with Robotics has encouraged the development of advanced robots. This situation changed during that time, when robots began to overflow and AI and Robotics research centers were apparently prone to conditions that could not be controlled in the same way. Specifically, the robots competition I has begun: they have certainly played an important task of reconstructing the complex communication between Computer-based intelligence and Robotics, which these days is one of the most inspiring developments in social setting testing beyond that, at the Europe market.

In summary, the point among the effort of Artificial Astute and Robotics is quite extremely difficult to build; however, the issues that need to be taken into account altogether to shape brainy automata are clearly recognized by the experimental network, and robotic construction is also considered an example of an AI framework [21]. Following the heading of the article we will refer to this experimental group as Artificial Intelligence Robotic. We close this short presentation by a repudiation explanation: the ideas included in the article of Artificial Intelligence research that automata usage as a popular prototypical for a brainier driver, no attempt to give a complete view. Over the ages, automation analysts consume too addressed approximately of the issues controlled by the current paper, however, the perspective on robotics research regarding Artificial Intelligence might not be correctly replicated herein article. This paper is structured as following. In the succeeding unit we look at main logical challenges within area. At the same time, we look at organizations and relations with a variety of topics that are often associated with this, and with a different order. Afterword, we present some of the app features created for testing.

2 Temptations

Herein section we break down the ongoing work that can be portrayed as Artificial Intelligence Robotics, by organizing it into two key problems in the arrangement of robots: Discovery plus Recognition.

2.1 *Discovery*

Although there are currently complete approvals for the basic design of a private specialist / automaton, the topic of in what way this system can be done has been the subject of a long discussion yet to be considered. Specialists and, apparently, robots, often bring a variety of gadgets to find and make devices. The continuity of sensing components to the actuators is adjusted by a limited different component as well as the demonstration of the communication among these components defines

the manufacturing of the cause. A primary, completely dedicated vision, [11, 16] world buildings and activities. Comprehension details are specified to model the world, the facilitator produces the tasks to be performed, in addition, the execution module works by implementing these programs. The action-cycle of the system cycle is performed more than once. The problem is that structure a high-quality prototypical and producing preparations is a tedious process and, after all, these structures have shown that there is a lack of professionals deployed in different universities. Responsive designs focus on the critical function of a robot, for example, translating a path or sensor, and, suggesting a rapid interaction between development and response. Creeks implant design [4] are done with skill levels that contain a category of activity-focused practices. Each level is bound to accomplish a particular task, (e.g., siege, rolling, etc.) and cognitive knowledge is clearly defined by that task. Responsive structures, while properly caring for natural elements, do not allow the majority of builders to think of broader areas of understanding (not identified by specific behaviors), and to distinguish complex situations. Indeed, the use of high-quality language is a must, as it may require the creation of a global model, and in this way reasoning is often integrated into the framework of a working system. Lack of ideas about frameworks for production and achievement of goals. The above thinking has encouraged a renewed effort to join the robot-based concept as an intelligent expert, with its responsive functionality. So far another test field has been added in recent years: Deep Thinking. The name was first introduced by a series of experiments at the University of Toronto conducted by author [20]. The latest concept of intelligent automata, adopted, of the EU model, certainly serves the original purpose of incorporating thoughtful operators into real robots, but more so it takes a broader perception, by observing at the view / work series from a larger perspective, in bio-enlivened structures, such as in the work of consent and age of acts of love (see next section). Psychological Mechanical technology aims to plan and adopt real experts (in some portable robots) that can perform complex tasks in real situations, and as a result are unique, flying, and completely unknown, lacking humanoid help. Intelligent automata can be controlled at a critical level, by providing them with a picture of the domain and collaborating the promises that will be made as goals to be achieved.

The descriptive feature of the mind-blowing automaton is the proximity of intelligent abilities to think of information derived from nature and the functions be able to execute. The scheme and adoption of mental automata have tended to the other, which can be expressed in two circles: work speculation and framework.

2.2 *Success*

Although there is now a universal consensus on the important construction of the independent automaton / robot, the subject of how this framework can be made depends on the long discussion has not been considered. Specialists and, apparently, robots, often bring a variety of gadgets to find and make devices. The progression

of sensing elements info to actuators is handled by a limited unusual components and the display of interactions between these components defines operators as manufacturing. The first structures fully committed [11, 16] consider the robot to be an operator that incorporates high environmental representation and potential functions. Comprehension details are specified to model the world, the facilitator produces the tasks to be performed, in addition, the execution module works by implementing these programs. The cycle of process planning is done consistently. The problem is that constructing a complex prototypical and producing orderliness is a tedious exercise and, as a result, these structures have shown a shortage of professionals planted in dynamic areas. The types of receiver models focus on the critical function of the robot, for example, to understand a track or sensor, in addition, to suggest a quick interaction between the intensity and the response.

River use design [4] is created by skill levels that contain a set of practices assigned to tasks. Each level is responsible for performing a specific task, (for example, obstruction, displacement, etc.) and cognitive knowledge is specially defined for that task. The models you embrace, while rightly obsessed with natural elements, do not allow a large part of fashion to think in terms of wide-ranging (unknown) behaviors, and to see composite circumstances. Trendy fact, the usage of high-level representative linguistic is absurd, as this one may need the creation of a global model, and in this way reasoning is often collected in the framework of a working system. Lack of organizational ideas about efficiency and objectives.

The above thinking has encouraged renewed efforts to integrate the robot-based concept as an intelligent expert, with its receptive functionality. So far another field of experimentation has emerged in recent ages: Reasoning Robotic. The term was first presented by a series of experiments at the York *University* conducted by author [14]. The latest concept of intelligent robots, adopted, of the EU model, certainly serves the original purpose of incorporating thoughtful operators into the real robots, but more so it takes a broader perspective, through observing at the understanding / work cycle from a broader perspective, to bio-enlivened structures, such as adoption and age enthusiastic (see next section). Intellectual Advanced mechanics aims to plan and adopt real experts (for a variety of robots) that can accomplish complex deployments in real, and powerful, stable and completely unknown environments, without human assistance. Intelligent automata can be organized at an important stage, by provided that them with a worldview and communication of tasks to be performed as targets to be achieved. An outstanding manifestation of a mental robot is the proximity of mental thinking skills to data obtained from the world and the functions it can perform. System and mental recognition space-based robots, which can be ordered in two circles: work ideas and frame construction.

2.3 *Guessing Work*

Various job specs have been created to address operator details. They are defined by the power of clarity, the ability to speak in complex situations, by permitted

paymasters, and by the use of strategic philosophy. A few formalities have been tested by the author [12, 20]: The proposed procedures address a few aspects of job exposure including discovery, diligence, nondeterminism, and simultaneous. Also, they are also extended with a possible display, exposure of period. In any case, an important portion of the task passed on to the speculation of the work is separated from the applications of real robots, with special cases [3, 5, 7, 10]. The most popular way to deal with the display of work on robots relies on dynamic, expanding techniques selected by the automaton, depending on the operating location [21]. Moreover, this method does not ensure exposure to the presentation of structures that define a dynamic framework, while focusing on the task selection tool.

Models: There are many highlights that are thought to be important in the construction of professional models and every proposal shows a response that captures a few outstanding ones. Ways to deal with projects that are trying to combine symbolic and responsive thinking are presented in the model in [1, 18] as it is assumed to be Hybrid Architectures. We can often highlight the expertise of classified insecticides with two levels: the level of negotiation, where the critical status of the provider is maintained and the choice of what works to be done, and the level that can be used, when world conditions are guaranteed. The comparative method of information summarizes Creeks' thoughts [17, 24]. The robotics is a actual technology that works closely with the earth and that robots work not only with the robot controller, but also with the way the robot interacts with its body and the earth. A distinct commitment to the adoption of robotic models stems from evolving experiments, in which developmental machines are a field of experimentation aimed at creating robots with transformational cycles created by natural elements [16]. The, e.g., is, neurofluffy frames have been effectively utilized in the plan of robotic models.

Typically, construction work is carried out in a unique setting for robotic programming situations, including certain selected control languages. A large part of this work is very concerned with the construction of viewing points and will not be allowed here.

2.4 Framework Designs

Robot surveillance is an undeniable test field in AI and Mechanical technology. The current default frames are restricted to standard viewing frames. Real fact, automata need to use additional types of sensing elements, e.g., laser run locator, finder, etc. to prevent powerful visual challenges in addition to, unstable situations. An automated automotive operator needs to manage rich and uncluttered environments that are compatible and interactive, with a variety of operators (either robots or humans, etc.). In order to run smoothly and efficiently, a robot must have the option to understand the concept of comprehension. From AI perspective, including high-level age, descriptive demonstration of the physical world. The growth of such displays requires both established, information-driven cycles that symbolize knowledgeable structures from the dream framework, and high-frequency cycles where complex, figurative data

is used to determine and continue to understand the scene. In order to achieve this, the robot must be endowed with the ability to think, to comprehend, compile, follow, and consider the performance of engaging and professional objects. The richness of the earth's motion is transmitted to the sensory input sensors. As it turned out, the imaginary modes of the robotic thinking frame should be bound to the sensory components. On the other hand, the robotic vision network approached rendering of scene scenes primarily for 2D / 3D hobby writing and recovery travel limits, obviously between chaos and obstacles, regulates the movement of the automaton. This method is identified as the visible performance of the robot frame [9]. On the other hand, a team of AI people has developed rich and descriptive methods of interpreting the image and depicting cycles, times, tasks, and as a rule, of dynamic conditions, as shown in the previous article. Be that as it may, robotic vision testing and AI information development have developed independently and focused on a variety of problems. From a single point of view, robotic vision analysts have widely accepted that the issue of visual displays is closed with 2D / 3D redesign of affecting sections and their navigation factors. Instead, a group of Artificial Intelligence people for the most part did not deal with the problem of obtaining the disclosure of information from the senses. Since the first paper of author citing [19], some suggestions have been made in this field of experimentation. The basis for attempts to guide a successful conceptual framework for dynamic perception of a dynamic forum has been tested over time [15] by adopting the flexible Horn interim metrics to provide a moderate practice that speaks to the scheme and initiates information about dynamic scenes. This official use is intervening the exposure of the area of temporary statistics enhanced by camcorders and the framework of the critical age range of flawed language text. The corresponding framework [6] depends on the level of expression: subconscious mind, perception, and level of signals. Specifically, the basic assumption that will be in the middle of the road.

The level of exposure does not fall between the two categories of exposure mentioned earlier. So to fill this hole, the concept of calculated space is accepted, to be shown where data is displayed about the measurement area. The space used moves as an intermediate display between the subconscious data (e.g., non-theoretically ordered), and appropriately compiled information. Some of the most important indigenous (Find, Track, Rediscover) that symbolize the binding of images to relevant information as such and such an independent matter of a particular will have been raised and discussed [8]. In order to obtain a consistent record of robotics comprehension that connects visual data to high-level displays, as proposed by the concept of addiction perception [23]. In this theory, the development of robotics is to discover and clarify visual information as shown by the basic theory that shows the interaction of robots with nature.

3 Connection with Other Areas of Artificial Intelligence

As of now shown, AI Robotic testing meets various sub-AI areas. In fact, an automated expert can be considered a focus on the foundation of a good Introductory Information System, and as a result in all aspects of AI to some degree related to Robotics. Below, we take a look at the organizations associated with some of the AI research points remembered for this integration. AI learning methods are used in many subjects from the robotic system. Depending on the previously accepted structure, both work and recognition can be supported by learning methods. In addition, a number of mechanisms involving the preparation step are sought after the emergence of mechanized learning approaches to dealing with hereditary systems, as well as, neural systems.

From a career perspective, approaching learning can be used for important work skills, transparent movements, but in addition to learning useful habits, geographical diversity, and opposition learning, among other things. Clearly, the learning cycle has to deal with the difficulty of tests with real robots. All factors considered, in a few test settings (e.g., Robo Cup), learning and variability of critical skill, for example, mobility, vision correction, have been shown to be more compelling than manipulation of boundaries by hand.

3.1 *The Edutainment*

Toy robots promise that they will be used for both research and training purposes, on the grounds that they are low cost and very attractive to low students. Indeed, however, at the moment, accessible readable units seem to offer much reduced power, toy robots are an exciting business market. Therefore, the design of smart toys automata is an interesting open door for Artificial Intelligence scientists. Contribution in Aibo automata [25] illustrates this possibility: the success of many experimental missions in the creation not only in Robo Cup contests, but in addition to indicating supplementary aspects of Artificial Intelligence and Automation study.

3.2 *Multiexpert Framework*

The Multi-Robot Framework can be measured as a multi-expert framework, but the mechanisms for achieving integration and participation in framework are frequently unsuitable to manage the risks and shortcomings of standard Robots models. Different robots can achieve stronger and more compelling performance by accomplishing integrated elements that do not work on single robots. The interaction of different and different robots has an uncommon power to be used in complex spaces

that may require the use of canny and a combination of different forces. The structure, design, and, experimentation of robots are grouped into groups that represent a combination of logical and special difficulties.

3.3 Ordinary Language Analysis

It is a visible attribute of leading and local technicians the ability to interact with individuals in a common language; as a result, common language management techniques find an interesting application space for automata (Robo Care business). Artificial Intelligence Estimation and Automatic Consultation Integration with AI Logics and Automated Reasoning is essential for Cognitive Robotic activity, but we try not to extend it here, as argued in the earlier post. Developmental Calculation and Chromosomal Software design Developmental Robotic is another way of viewing robots as autonomous living creatures that build their abilities closely in this environment without human intervention. Improving efficiency technology uses techniques from calculation development.

4 Interaction with Different Orders

4.1. Mechanical technology is a collaborative arena to create an operational automaton, a couple of responsibilities from various controls are required such as material science, electrical structure, electronic planning, mechanical structure, programming, AI, and so on. It is along these lines irksome in like manner to have an average establishment of expressions, documentations, and techniques. In this respect, the undertakings to portray a normal way of thinking of expressions for a mechanical innovation discipline [22] are significant. In particular, Artificial Intelligence Robotics works together with a couple of investigation disciplines outside AI. Mechanical Robotics Many contact centers may be found between Artificial Intelligence, Robotics, and Manufacturing Robotics. In early days there were not good and cut capabilities between the two fields, as of now referred to. Today, research in Industrial Robotics is masterminded toward the ensured and clever control of mechanical regulators what's more, in the field of organization progressed mechanics. The ways of thinking in Industrial Robotics are grounded in Automatic Control Theory [2]. The association between the robot and the earth is normally shown by techniques for a couple of kinds of information structures. Furthermore, frameworks are regularly established on numerical methodologies and progression speculation. PC Vision Robot Vision is unequivocal with respect to PC vision, since Robot Vision is intrinsically unique, as in the robot may successfully find its information sources and it can similarly go to the best view position to help the visual information. Also, Robot Vision should be acted in nonstop, considering the way that the robot ought to rapidly react to visual upgrades. All things considered, the robot can't quantify for a long

time a comparable picture because the normal conditions may move, so the robot needs to oversee assessed, anyway at the last possible second information.

A couple of assessment focuses and conversations in this field have strong associations with AI and Robotics, for example, if a Processor Visualization scheme may be established on the interior depiction of the earth or it must be essentially responsive.

4.2. Electromechanical system incorporates capacities after electric powered planning, electronic structure, motorized planning. These abilities are painstakingly connected to Artificial Intelligence and Automation: the investigation field of electric powered planning anxieties engines as well as actuators, though automatic planning basically anxieties sheets for automaton control, for information attainment and overall for the hardware that makes the automaton working.

Motorized structure stresses clearly the motorized contraction of the actual automaton. Opinion is, electromechanical system, Artificial Intelligence and Automation have fitted dealings: electromechanical system mostly bases on the automaton hardware at all stages, while Artificial Intelligence and Automation manage the item that marks the automaton usable likewise, self-administering.

4.3. Embedded Systems: The AI writing computer programs is inserted in the substantial machine. Therefore, the robot programming structure necessities to work continuously in command to assurance that the robot adequately adjusts to the developing condition; it should be defended with easy debasement in solicitation to confirm that the automaton may work similarly in circumstance of harms; the hardware game plan of the automaton should be small control proposed to overhaul the series, etc. Beginning here of view, a couple of the ordinary troubles of embedded structures are moreover challenges for cutting edge mechanics systems.

4.4. Human–Robot Interface: The field of Human–Robot Interface is related to the collaboration modalities between the customer and the robot. This field may be apportioned into two subfields: the scholarly Human–Robot Interface also, the actual HRI [13]. Scholarly HRI examines the movement of information between the customer and the robot and it is essentially based on collaboration modalities, which may length from abstract interfaces to voice additionally, signals. The interface may be practically watchful as in the robot may be constrained by a fixed plan of requests or it may unravel a series printed in typical linguistic before a course of action of signs executed by the manager. The interface may in like manner be adaptable as in the robot may conform to the director through a proper planning stage. Actual Human–Robot Interface rather concerns the arrangement of naturally safe robots. The guideline thought is to intervene pleasing segments among motors and moving bits of the robot in order to hinder hurts if there ought to emerge an event of impact, besides, without execution setback. Thusly, this investigation is immovably related to the investigation of Artificial Intelligence and Automation, while actual research is more associated by investigation in Mechanical Automation.

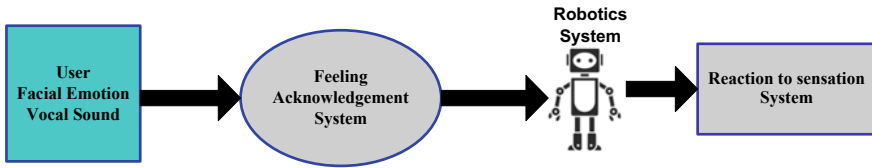


Fig. 1 Generalized diagram for the multimodal signals for emotion recognition for human–robot interaction

5 Results and Discussion

Computerized reasoning was firmly connected with the investigation of human brain science. Brain science had two driving grade schools: behaviorism and intellectual. Behaviorism: Refused the hypothesis of the psychological cycles, and demanded examining the came about activity or the upgrade carefully objective. The delegates of this hypothesis have been diminishing with time. Intellectual brain science: The cerebrum is a data preparing gadget. Man-made reasoning additionally bolsters this thought, and the main picture delineates the data handling model of the cerebrum.

5.1 *Man-Made Intelligence Emotion Recognition and Psychology*

What we need to form into the AI is passionate comprehension and cognizance. The essential rundown is that feelings are communicated in a wide assortment of ways, which makes it hard to dependably surmise how somebody feels from a straightforward arrangement of facial developments. The ongoing examination shows that feelings are communicated in an extensive blend of ways making it inconceivably hard to depend on translations deduced on how somebody feels from facial developments. There is a few passionate acknowledgment of AI calculations. The standard enthusiastic acknowledgment calculations deducing sentiments of individual’s dependent on facial examination. In any case, the relationship between’s sure outward appearances and feelings are frequently basically imperfect. Figure 1 shows the generalized diagram for the multimodal signals for emotion recognition for human–robot interaction.

5.2 *Artificial Intelligence Emotion, Cognitive Robotics, and Psychology*

Scientists from fields as differing as software engineering, brain science, neuroscience, arithmetic, neuroscience, kinematics, and psychological science are drawing

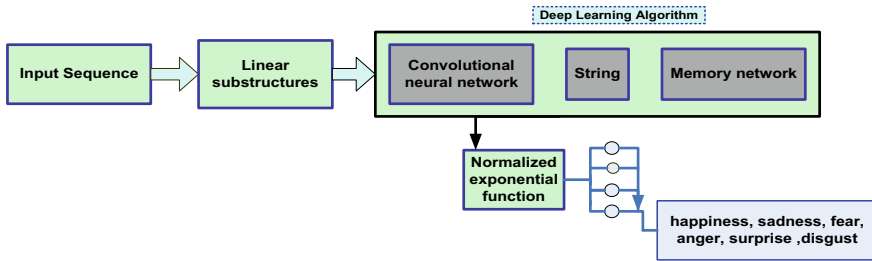


Fig. 2 The generalized model which can be used for emotion recognition

nearer to making PCs and robots that can reason, learn, and perceive feeling. A hypothesis of brain is fundamental for the improvement of sympathy; fundamental for the advancement of compassion; amygdala harm is related with shortfalls in principle of brain advancement. They may at long last understand a fantasy that is as old as the golem of Jewish legends and as current as blockbuster sci-fi: robots that comprehend human feelings, and that can adjust to new conditions and unforeseen circumstances. Figure 2 shows the generalized model which can be used for emotion recognition.

6 Conclusion

Computerized reasoning and advanced mechanics have encountered emotional increments in execution, what’s more, this has prompted more noteworthy subsidizing for computerized reasoning and in an ongoing increment in scholastic exploration around the results of these advances for firms, laborers, and economies. In this briefing, we characterize the key ideas, survey the current writing, recognize suggestions for authoritative plan, and portray open doors for authoritative and methodology scholars. We contend that AI calculations for feeling acknowledgment and mechanical feeling discernment measures will be of basic significance in the early improvement of sympathetic man-made reasoning what’s more, robot brain science when responsiveness to normal control practices will depend partially on the capacity to perceive the enthusiastic, and on the capacity to perceive the passionate conditions of human and different robots. Further, the capacity to perceive torment, sufferings, dread, outrage in other individuals and robots may require the more developed hypothesis of psyche during the formative stage that is basic for discovering that others are aware, feeling life forms: an ability that is required by the robots to treat others operators appropriately. There is a need to heighten research on human–robot collaboration, more prominent spotlight on checking robots and feeling investigation to beat the mental obstructions that should be conquered to accomplish more resistance and higher acknowledgment of robots.

References

1. Arkin RC (1995). Just what is a robot architecture anyway Turing equivalency versus organizing principles. In: AAI spring symposium on lessons learned from implemented software architectures for physical agents
2. Bicchi A, Tonietti G (2004) Fast and soft arm tactics: Dealing with the safety-performance tradeoff in robot arms design and control. *IEEE Robot Autom Mag* 11(2)
3. Bonarini A, Matteucci M, Restelli M (2003) Filling the gap among coordination, planning, and reaction using a fuzzy cognitive model. In: *RoboCup 2003: Robot Soccer World Cup VII*, vol 003. Springer, Berlin, pp 662–669
4. Brooks RA (1986). A robust layered control system for a mobile robot. *IEEE J Robot Autom* 2(1)
5. Castelpietra C, Guidotti A, Iocchi L, Nardi D, Rosati R (2002) Design and implementation of cognitive soccerbots. In: *RoboCup 2001: Robot Soccer World Cup V*. Springer, Berlin, pp 312–318
6. Chella A, Frixione M, Gaglio S (2000) Understanding dynamic scenes. *Artificial Intell* 123:89–132
7. Chella A, Gaglio S, Pirrone R (2001) Conceptual representations of actions for autonomous robots. *Robot Auton Syst* 34:251–263
8. Coradeschi S, Saffiotti A (2003) An introduction to the anchoring problem. *Robot Auton Syst* 43(2–3):85–96
9. Corke PI (1996) *Visual control of robots: high-performance visual servoing*. Wiley, New York
10. De Giacomo D, Iocchi L, Nardi D, Rosati R (1999) A theory and implementation of cognitive mobile robots. *J Logic Comput.* 5(9):759–785
11. Fikes R, Nilsson N (1971) STRIPS: a new approach to the application of theorem proving to problem solving. *Artificial Intell* 2
12. Finzi A, Pirri F (2001) Combining probabilities, failures and safety in robot control. In: *Proceedings of IJCAI-01*, pp 1331–1336
13. Hallam J, Bruyninckx H (2006) An ontology of robotics science. In: Christensen HI (ed) *European robotics symposium 2006*. Springer, Berlin, pp 1–14
14. Lesperance Y, Levesque HJ, Lin F, Marcu D, Reiter R, Scherl RB (1994) A logical approach to high-level robot programming. In: *AAAI Fall symposium on control of the physical world by intelligent systems*
15. Nagel HH (2004) Steps toward a Cognitive Vision System. *AI Mag* 25(2):31–50
16. Nilsson NJ (1984). *Shakey the robot*. Technical Report 323, SRI international, Menlo Park
17. Pfeifer R, Scheier C (1999) *Understanding intelligence*. MIT Press, Cambridge
18. Piaggio M (1998) *Classifying robot software architecture*. AI*IA Notizie, 4
19. Reiter R, Mackworth A (1989) A logical framework for depiction and image interpretation. *Artif Intell* 41:125–155
20. Reiter R (2001) *Knowledge in action: logical foundations for describing and implementing dynamical systems*. MIT Press, Cambridge
21. Russell SJ, Norvig P (2003) *Artificial intelligence: a modern approach*. Pearson Education
22. Sciavicco L, Siciliano B (2000) *Modelling and control of robot manipulators*, 2nd edn. Springer, Berlin
23. Shanahan M (2005) Perception as abduction: turning sensor data into meaningful representation. *Cognit Sci* 29:103–134
24. Steels L (1991) Towards a theory of emergent functionality. In: Meyer JA, Wilson SW (eds) *From animals to animals I*. MIT Press, Cambridge
25. Veloso M, Uther W, Fujita M, Asada M, Kitano H (1998) Playing soccer with legged robots. In: *Proceedings of IROS-98, intelligent robots and systems conference*, Victoria, Canada. (October 1998)

Modeling and Path Planning of a Grocery Robot



R. Venkatesh , B. Satish Kumar , K. Umamaheswara Rao ,
and K. Dileep

Abstract This paper deals with a grocery robot which mimics work done by salesperson or customer and eases the shopping process. Due to corona outbreak it is very difficult for the customer to put their lives in the risk for going to retail stores where there is a high risk of spread of corona virus through mass gatherings. So, an automated grocery robot is proposed, through which the customer can procure his requirement in the grocery stores with the help of this grocery robot. The robot is fetched with customer data through the excel sheet from the storekeeper. Based on this data the robot is going to pick the groceries in the list and returns the goods/items to the customer. The grocery robot is enabled with artificial intelligence technology (A* Algorithm) for searching the optimal path to reach the item in the racks. The deep learning concept is used for object detection for picking the right item for the customer. This complete task is accomplished with the help of python programming for both object detection and path finding process for the robot. The grocery robot is modeled with the help of solid works software.

Keywords Path planning · Solidworks · A* algorithm · Object recognition · Deep learning

1 Introduction

Liang et al. [1] depicted that robot picking of articles in distribution centers and stores. Items are frequently stacked or adjusted in explicit manner. A particular picking methodology is regularly connected to explicit course of action designs. Based on this a technique is proposed wherein gatherings of normally organized articles are identified from a picture, and the game plan example of each gathering is recognized.

R. Venkatesh (✉) · B. Satish Kumar · K. Umamaheswara Rao · K. Dileep
Koneru Lakshmaiah Education Foundation, Guntur, AP, India

Asaoka et al. [2] illustrated that online business satisfaction stockrooms, manual thing picking is a work serious and repetitive errand. Along these lines, computerization picking of things can improve efficiency and spare expense for web-based business organizations. It exhibits a computerized robot picking arrangement that meets the necessities of robotizing the picking of things from racks. Investigations were directed utilizing a model of the proposed framework. The test outcomes show the framework is equipped for picking a few consistently molded and sporadically formed things from the canisters of the rack. It can possibly be utilized in genuine online business satisfaction distribution.

Niranjan et al. [3] explained that the CMU-RI Nav-Lab bunch has grown such a framework has a primary sensor as laser scanner. This framework worked effectively and efficiently on indoor and open-air stages with a few types and arrangements of 2D and 3D laser scanners. The applications fluctuate from crash notice frameworks, individual characterizations, watching human tracks, and contributing to a dynamic organizer. A few of these frameworks were assessed in live field tests and demonstrated to be strong and solid.

Saxena et al. [4] illustrated that the mechanical arm where the ability of a human being to carry out a responsibility is restricted not by his psychological control yet by his physical quality. In a situation where human association cannot be conceivable to be specific where the robots can be employable. An automated arm is been designed where it is constrained by the collaboration with the human hand utilizing flex sensor, Arduino Uno, RF module (Wi-Fi Module), and servo engine.

Mertz et al. [5] getting a handle on a formerly obscure entity, one for which a 3D model is not accessible, is a difficult issue. Further, even whenever given a model, despite everything one needs to choose where to handle the item. This paper presents a learning calculation that neither requires nor attempts to manufacture, a 3D model of the article.

Robot is a machine intended to execute at least one errand consequently with more exact speed and accuracy. With the advent of industrial revolution 4.0, technologies like artificial intelligence and machine learning had improved the efficiency of robots. The main theme of robots in the workspace is to reduce the fatigue on the human labor. Robots also increase speed, the speed of performing various tasks in more efficient manner. Because of Covid-19 pandemic, to ease the shopping process the grocery stores of larger settings, i.e., Wal-Mart, Reliance market, Best price, etc. where there is more possibility of spread of Covid-19 infection grocery robots were employed. This grocery robot is equipped with a camera having high resolution. This camera is mounted on the robot manipulator in such a way it captures the pictures of the grocery items and captured images were stored in the memory allotted in Raspberry Pi controller. The camera employed in the grocery robot is capable of taking pictures of the items with high speed and the construction of robot is made in such a way that the camera won't get any damage while picking and placing the grocery items into the basket. With many completion of arm-tooling options available, pick and place robots can be revamped to fit unequivocal age requirements. Moving immense, little, generous, or hard-to-manage things can be a basic task to robotize in the modern

grocery stores. Consistency is likewise an advantage of utilizing a pick and place framework [6, 7].

Shopping for food is a standard action that individuals everywhere throughout the world perform all the time. Outbreak of corona virus made the people panic to get into grocery stores for their daily requirements [8, 9]. Be that as it may, markets and general stores remain to a great extent unavailable to individuals with visual debilitations. Hence there requires an intelligent bot which mimics what customers do in grocery stores. In any case, their activities are altogether organized by a focal PC. This is on the grounds that our apply autonomy investigates group faces a momentous test: to create keen and summed up mechanical arrangements and frameworks fit for picking the 50,000 unique things accessible on grocery stores securely and dependably. While people can rapidly learn and build up all way of systems for getting a handle on different things dependent on what they plan to do with them, robots should be encouraged these procedures and that is the reason computer-based intelligence assumes such a significant job as well.

This new arrangement is theoretically basic in its structure and when contrasts it with the size of the errand it has been worked for. The robot pick station comprises a suction cup on the finish of an explained arm [10]. The arm is furnished with a pipe racing to an air blower, which is equipped for lifting things paying little respect to their deformability and shape, as long as they are inside the weight limitation and the suction cup can make a water/air proof seal with the thing's surface (i.e., it has a large enough surface accessible and isn't permeable). All together for this procedure to run easily, the calculation controlling the robot expected to have a comprehension of where the cases were found and of the ideal handle purposes of the things inside the box. This may sound straight forward yet building up the robot's comprehension of its surroundings is exceptionally testing. Deep learning technique is been employed for object recognition such that the appropriate item is been picked up by the grocery robot. The computer vision employs this deep learning technology; thousands of images were been tested and trained for using tensor flow algorithm from the object recognition process.

2 Algorithm

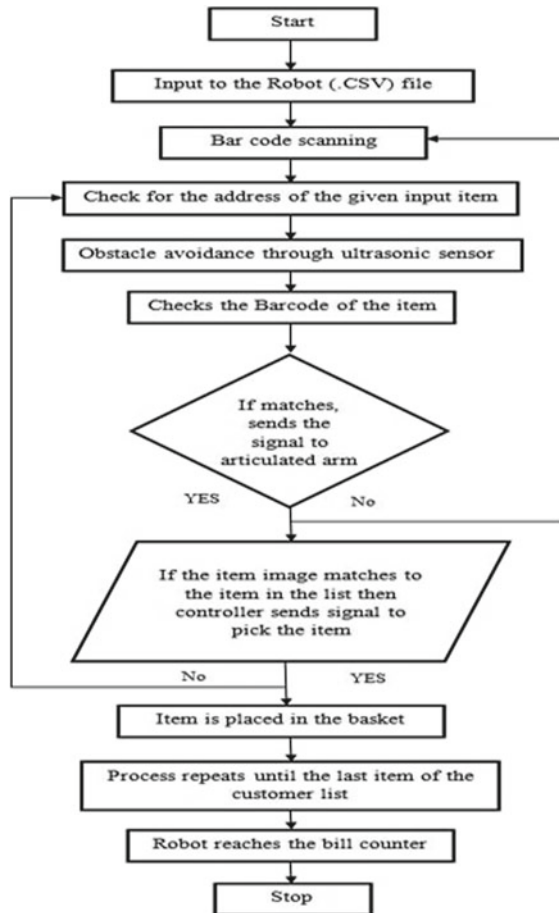
See (Fig. 1).

3 Methodology

For making the automatic robot for picking the item in the grocery stores the following methodology is employed.

The customer data is been fetched to grocery robot through the blue tooth technology. Raspberry pi controller acts as a transceiver and receives the customer data

Fig. 1 Algorithm of grocery robot



[11]. This data is been extracted and is analyzed using Natural Language Processing (NLP) technology. Raspberry pi controller controls the robot while planning, moving, picking, and placing of item in the basket. A barcode scanner is the device used to read barcodes of the item. Bar code scanners are mainly used in inventory management, checks whether that item is available in the store of larger warehouses. In this paper the grocery robot is employed with vacuum gripper to pick the items and place them properly in the basket without any damage to the item. Robot is employed with an adaptable vacuum cup [12]. Compacted air is blown into the suction cup to discharge the item. The benefit of the suction cup is that if there is any power failure it will not let the item to tumble down (Fig. 2).

The ultrasonic proximity sensor is used to detect whether the gripper or the end effector has approached the item to pick desired item [13]. With the help of ultrasonic sensor, robot identifies the obstacles over its path. The image recognition sensor detects the item to match the items in the customer list.

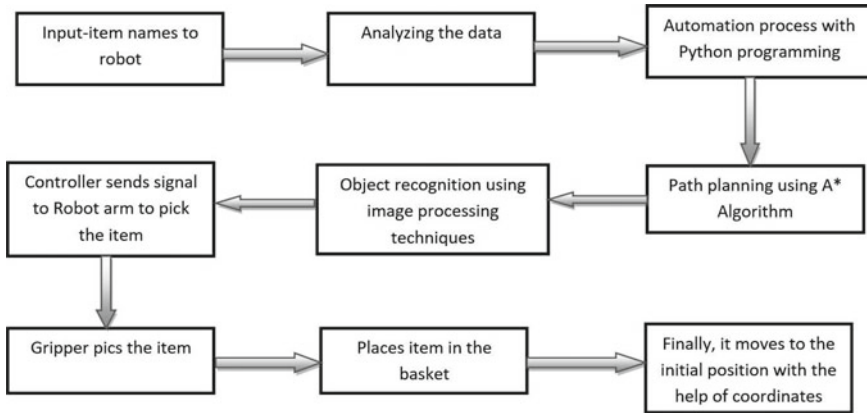


Fig. 2 Flow chart of processes in grocery robot for picking and placing grocery items

An actuator is a device which takes input data from sensors and acts accordingly by the control signals given from the controller unit. The electric actuator utilizes an electric motor to generate the required torque for the work to be done. Electric actuator is employed in the construction of grocery robot model as they work without noise and are quite suitable for the indoor applications which is of low cost when compared to the other actuators. Servomotor is used as actuator for the grocery robot, for its feedback and exact position control, speed; servomotor is best suitable for picking and placing of grocery items in the basket. Its ruggedness and durability made it the best actuator for grocery robot [14]. The maintenance cost and size of the electric actuator is very less when compared to the other actuators. The response time of electric actuators is very high when compared to the other actuators.

A robot’s workspace is the total volume swept out by the end effector as the manipulator executes all possible motions [15]. The shape of the workspace depicts the application for which each design can be used (Fig. 3).

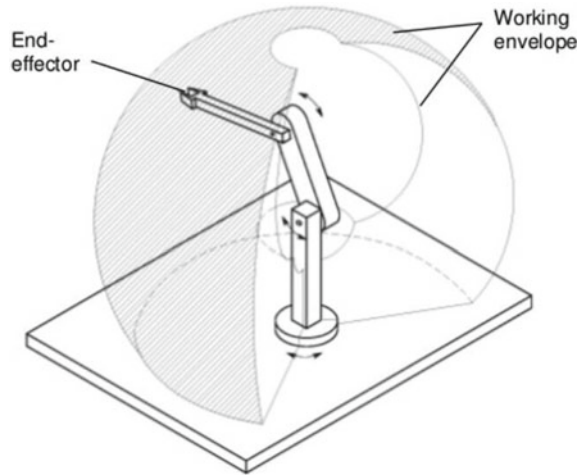
Path making plans generates a geometric path, from an initial to very last factor passing through pre-described via points [16], either in the joint area or the open area within the robotic, while the trajectory planning algorithms take a given geometric course and endow it with the records [17].

Factors to be considered for path planning of grocery robot:

1. The route length ought to be shortest.
2. The suitable path is the only in which the robotic can pass in the shortest time.
3. The route needs to be as far as feasible from the boundaries.
4. The direction must be gentle without sharp turns.
5. The direction must consider the movement constraints.

In this grocery robot, A* algorithm is been employed. A* search finishes searching process to calculate the most effective sequence of node transitions. In addition to this step A* defines one to locate bounded area within which further route planning operations can take place.

Fig. 3 Workspace of grocery robot



3.1 Tangent Graph-Based Making Plans

This limits the set of trajectories to contingents among boundaries and obstacle barriers from which the minimal distance course being discovered in widespread. The hassle of shortest course planning in known surroundings for unicycle like cell robots with a difficult constraint at the robot's angular velocity became solved. It became assumed that the surroundings include some of probably nonconvex barriers with a constraint on the curvatures of their limitations, together with a consistent target that should be reached by means of the robot. It has been proved that the shortest path consists of edges of the so-called tangent graph.

Not only the above examples but additionally one of the simplest and earliest algorithms used within the oldest strategies in robots for the handiest paths, this is Dijkstra's set of rules [18]. Starting from the initial vertex in which the course must begin, the set of rules marks all the straight neighbors of the first vertex by the price to get close by. It in that case proceeds from the vertex with the least cost to all its adjoining vertices and marks them with the value to get to them thru itself if this cost is decreased [19].

A* is the computationally expensive while both the search space is big, e.g., Due to a nice grain decision essential for the mission, or the size of the hunt problems are high, e.g., while making plans for a robot with more than one degree of the liberty. A greater latest advance known as Rapidly exploring Random Trees (RRT) addresses this trouble by the usage of a randomized method that goals on the rapidly exploring a greater area of the quest space with iterative alteration [20]. RRT can be used for route-making plans via retaining the fee to start on every introduced point and biasing the choice of points to sometimes failing close to the aim [21].

Important Steps in A* Algorithm. The first step in route-making plans is choosing a map representation that is appropriate to the application. Secondly lessen the robotic

workspace to some extent, which permits planning in the configuration area. This lets in the application of usual shortest direction locating algorithms, which have packages in a large variety of domain names, not limited to robots.

3.2 Modeling of Grocery Robot

Grocery robot is modeled with the help of Solidworks modeling software. All the individual components of grocery robot were designed initially and were assembled properly at the later stages using this software. The detailed view of Modeling of grocery robot is given below. Figure 4 represents the complete working model of the grocery robot. Figure 5 depicts how the robot is capable of picking the items in the store with the help of Vacuum grippers. Through this vacuum cum grippers, items are been carefully picked from the racks and are placed without any damage into the baskets attached to the grocery robot. Items in the bottom racks are picked up by the robot with the help of servo motors, where servomotors were having the advantage of absolute positional feedback which tracks and locates the item accurately. This action is been modeled and shown in Fig. 6. Figure 7 shows how the item picked up by the grocery robot and carefully places the item into the basket. A special type of gripper is made such that it can hold various types of items without any miscarriage; this is modeled and shown in Fig. 8

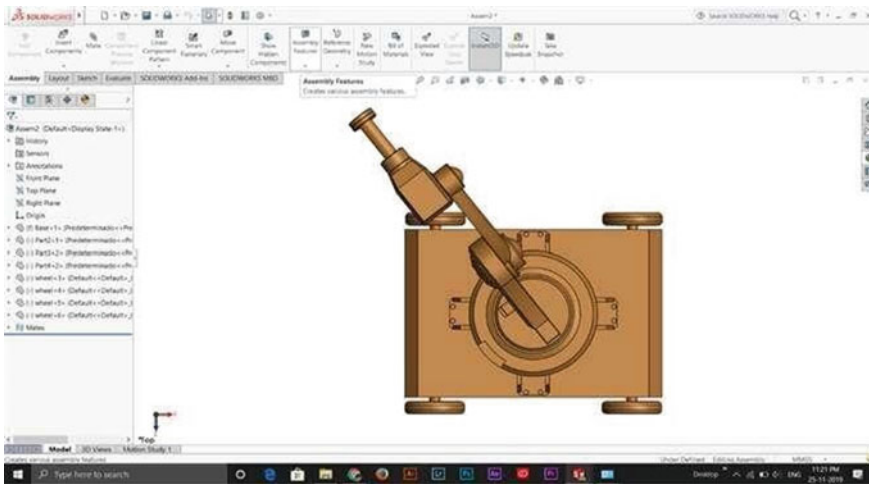


Fig. 4 Working model of grocery robot

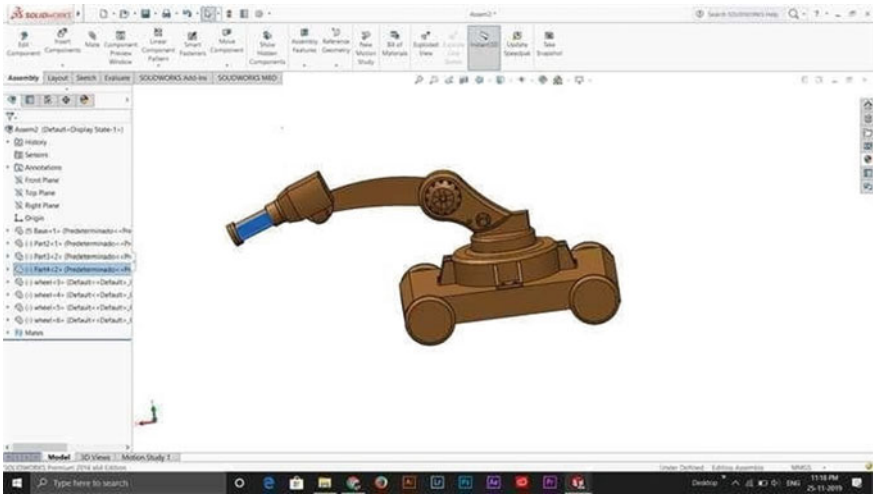


Fig. 5 Picking of grocery item using vacuum gripper

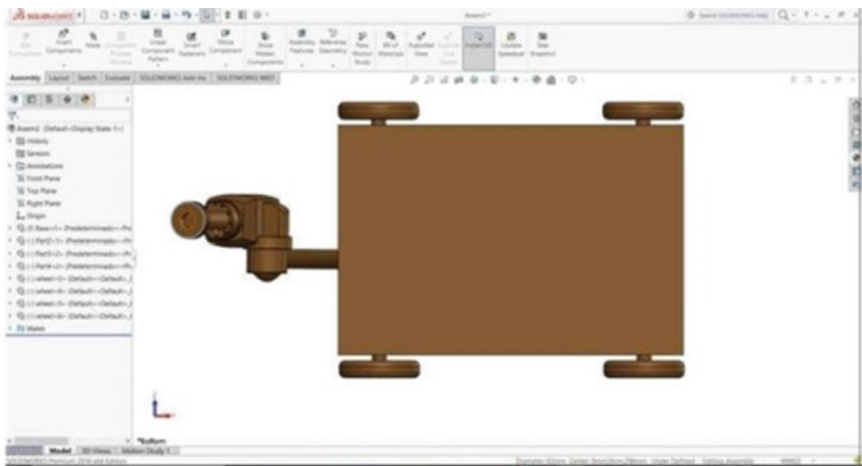


Fig. 6 Picking of grocery items in lower racks

3.3 Image Processing

A picture is described as a 2-dimensional function, $f(x, y)$, where x and y are spatial coordinates [22], and the amplitude of f at any pair of coordinates (x, y) is called the depth of that picture at that factor. We call it a digital image when x, y and amplitude values of are 'f' finite. In different words, a picture can be described by means of a 2-dimensional array especially arranged in rows and columns. A picture can be represented in different words by means of a 2-dimensional array especially arranged

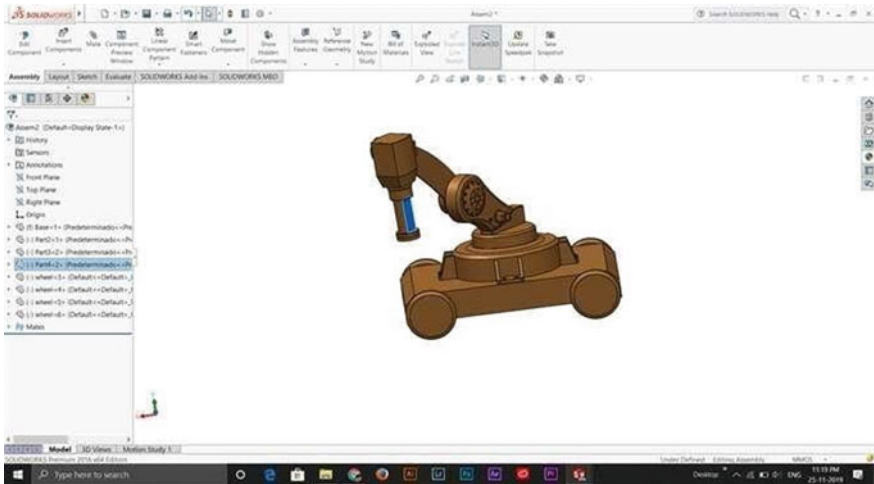


Fig. 7 Placing grocery item in the basket

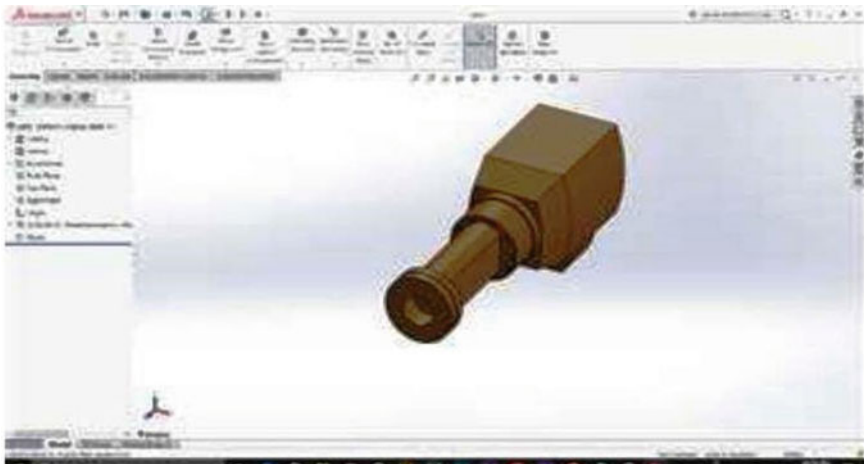


Fig. 8 Solid works model of gripper of grocery robot

in rows and columns. Digital Image consists of a finite wide range of elements, each of which in a specified fee has a specified area. These factors are called image factors, image components, and pixels. A pixel denotes the elements of a digital image (Fig. 9).

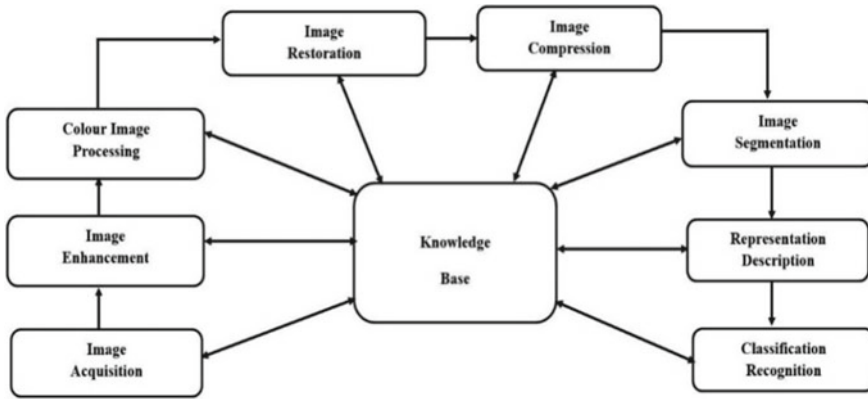


Fig. 9 Block diagram of steps involved in image recognition

3.4 Steps Involved in Setting the Object Detection Process

1. Installation Anaconda app, CUDA, and cuDNN libraries.
2. Setting up Tensor Flow Directory and Anaconda Virtual Environment.
3. From TensorFlow's model zoo download the Faster-RCNN-Inception-V2-COCO model.
4. Set up new Anaconda virtual surroundings.
5. Configuration of Pythonpath environment variable.
6. Compilation of Protobufs and runningsetup.Py.
7. Testing of TensorFlow setup.
8. Generate Training Data.
9. Create Label Map and Configure Training.
 - (a) Label map
 - (b) Configure training set data
10. Run the Training.
11. Use the Newly Trained Object Detection Classifier.

4 Results

See (Figs. 10, 11 and 12).



Fig. 10 Dataset in knowledge base

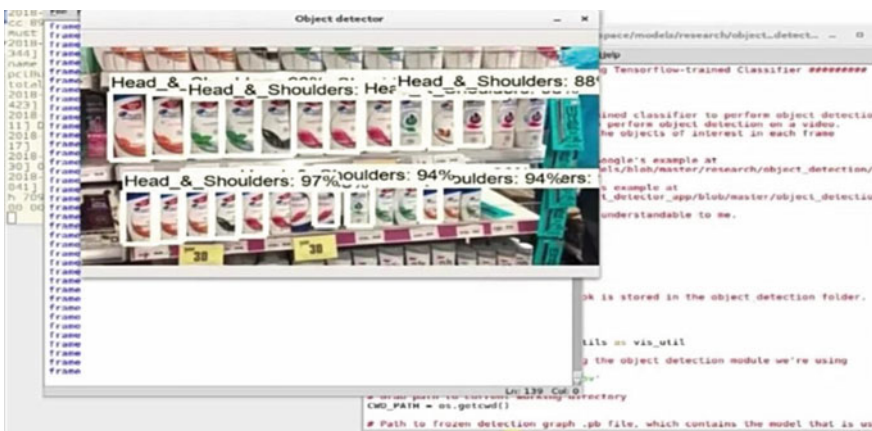


Fig. 11 Object identification with accuracy

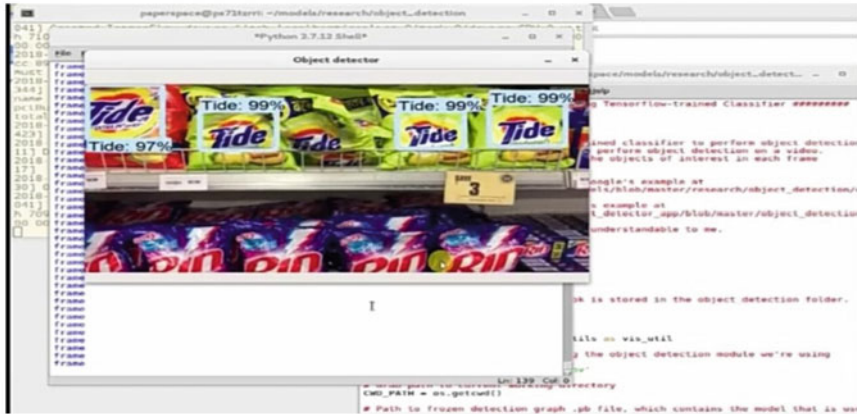


Fig. 12 Grocery item recognition with accuracy

5 Conclusion

With this paper a grocery robot is been modeled which is used to reduce to contain the spread of Covid-19 virus for the customers and along saves the time of customers. This grocery robot reduces the fatigue on the customers and eases their shopping process. The flexibility of the robotic arm while picking and placing the grocery item in the basket leaves the shopping process in efficient manner. The accuracy of object detection is been done with the help of deep learning technology. Computer vision is the concept behind object recognition and identification, i.e., trained Tensor flow model. Deep learning involves numerous numbers of image sets in its knowledge base, the item captured using camera will be compared with the trained and tested image sets in the knowledge base. With the advanced deep learning concepts like Karas, the speed and efficiency of grocery robot will be increased in the near future.

References

1. Liang C, Chee KJ, Zou Y, Zhu H, Causo A, Vidas S, Teng T, Chen IM, Low KH, Cheah CC (2015) Automated robot picking system for e-commerce fulfillment warehouse application. In: The 14th IFToMM world congress. (October)
2. Asaoka T, Nagata K, Nishi T, Mizuuchi I (2018) Detection of object arrangement patterns using images for robot picking. *Robomech J* 5(1):23
3. Niranjana L, Suhas A, Sreekanth B (2018) Design and implementation of robotic arm using proteus design tool and arduino-uno. *Indian J Sci Res* 17(2):126–131
4. Saxena A, Driemeyer J, Ng AY (2008) Robotic grasping of novel objects using vision. *Int J Robot Res* 27(2):157–173
5. Mertz C, Navarro-Serment LE, MacLachlan R, Rybski P, Steinfeld A, Suppe A, Urmson C, Vandapel N, Hebert M, Thorpe C, Duggins D (2013) Moving object detection with laser scanners. *J. Field Robot.* 30(1):17–43

6. Nabat V, de la O RODRIGUEZ M, Company O, Krut S, Pierrot F (2005) Par4: very high speed parallel robot for pick-and-place. In 2005 IEEE/RSJ international conference on intelligent robots and systems. IEEE, pp 553–558. (August)
7. Bancroft D, Kietzmann M, Agennix AG (2003) Pick and place robot system. U.S. Patent 6,658,324.
8. Grashuis J, Skevas T, Segovia MS (2020) Grocery Shopping Preferences during the COVID-19 Pandemic. *Sustainability* 12(13):5369
9. Donthu N, Gustafsson A (2020) Effects of COVID-19 on business and research. *J Bus Res* 117:284
10. Mantriota G (2007) Optimal grasp of vacuum grippers with multiple suction cups. *Mech Mach Theory* 42(1):18–33
11. Vanitha M, Selvalakshmi M, Selvarasu R (2016) Monitoring and controlling of mobile robot via internet through raspberry Pi board. In 2016 second international conference on science technology engineering and management (ICONSTEM). IEEE, pp 462–466. (March)
12. Chen FY (1982) Gripping mechanisms for industrial robots: an overview. *Mech Mach Theory* 17(5):299–311
13. Massa DP (1999) Choosing an ultrasonic sensor for proximity or distance measurement part 1: acoustic considerations. *Sensors* 16(2):3
14. Huang T, Mei J, Li Z, Zhao X, Chetwynd DG (2005) A method for estimating servomotor parameters of a parallel robot for rapid pick-and-place operations.
15. Tsai YC, Soni AH (1985) Workspace synthesis of 3R, 4R, 5R and 6R robots. *Mech Mach Theory* 20(6):555–563
16. Muthuswamy S, Manoochchri S (1992) Optimal path planning for robot manipulators
17. Udupa SM (1977) Collision detection and avoidance in computer controlled manipulators. Doctoral dissertation, California Institute of Technology
18. Deng Y, Chen Y, Zhang Y, Mahadevan S (2012) Fuzzy Dijkstra algorithm for shortest path problem under uncertain environment. *Appl Soft Comput* 12(3):1231–1237
19. Broumi S, Bakal A, Talea M, Smarandache F, Vladareanu L (2016) Applying Dijkstra algorithm for solving neutrosophic shortest path problem. In 2016 international conference on advanced mechatronic systems (ICAMEchS). IEEE, pp 412–416. (November)
20. Cheng P, LaValle SM (2002) Resolution complete rapidly-exploring random trees. In Proceedings 2002 IEEE international conference on robotics and automation (cat. no. 02CH37292), vol 1. IEEE, pp 267–272. (May)
21. Kothari M, Postlethwaite I (2013) A probabilistically robust path planning algorithm for UAVs using rapidly-exploring random trees. *J Intell Rob Syst* 71(2):231–253
22. Berryman JG (1985) Measurement of spatial correlation functions using image processing techniques. *J Appl Phys* 57(7):2374–2384

Mechatronic System for an Automated Dynamics Staircase for Walking Difficulty People to Travel in Public Road Transportation Vehicles



Mrunal Swaroop Peravali, Gadudasu Babu Rao, Praveen Kumar Bannaravuri, Mona Sahu, Dasariraju Lakshmi Deepak, Sumanth Ratna Kandavalli, Kumara swamy Pulisheru, and Srinivasa Rao Gorrepati

Abstract The present research work was carried out on the issues faced by the elderly citizens and walking difficulty people, while boarding and de-boarding the buses that fly in rural areas as well as urban areas in India. The buses mostly having fixed steps and high road clearance of 600–700 mm. An attempt was made to solve this problem by the design and development of an automated step system. Here an algorithm was developed to keep the safety of the people and tested the functioning of the system by coding a program to carry out the necessary functions and calculate the essential values for the process to take place. Based on the action performed by the passenger, the staircase can come down, pick them up and wait till they pass the clearance area and get back to its initial position keeping the safety of the persons in mind. This automated system can be significantly allowing the passengers to board and de-board the buses easily independently without any help from people interfering in between.

Keywords Staircase · Microcontroller · Sensors · Elder citizens and Public transport

M. S. Peravali · G. B. Rao (✉) · P. K. Bannaravuri · M. Sahu · D. L. Deepak · S. R. Kandavalli
Department of Mechanical Engineering, Karunya Institute of Technology and Sciences,
Coimbatore 641114, Tamil Nadu, India

K. Pulisheru
Department of Mechanical Engineering, National Institute of Technology, Imphal 795004,
Manipur, India

S. R. Gorrepati
Department of Mechanical Engineering, Amity University, Noida 201313, Uttar Pradesh, India

1 Introduction

In the present decay the several modes of transportations available, the most commonly used would be the public transport vehicles. These Public transport vehicles that are existing in countries might seem to be convenient to the huge majority of population but the truth is far from the image in the people’s mind. Transportation is an extremely important factor for those who are physical-disabilities and senior citizens. People with such special needs have consistently described how transportation barriers bring up hurdles in their lives. The low floor buses in cities like Delhi, Mumbai, and Bangalore are initiatives to make transportation smooth but are only moderately solving the problems of physically disabled people as shown in Fig. 1. Though there were a lot of improvements in the public transport scenario, implementation for the mass or rural areas and especially the physically disabled are not properly addressed [1–6].

Commute plays a very important role in our daily lives. Not only does it help us with our day-to-day activity but also plays a key role in connecting the people and engaging for a healthy and constructive lifestyle. But this isn’t always true when it comes to the elderly or physically disabled people. Boarding and alighting steps into the bus is often a really hard and painful task for many. In a world of 7.8 billion people



Fig. 1 Difficulties faced by physically challenged people in boarding the Bus

in 2020, there are at least 703 million people, who are older than 65 and are expected to reach 1.5 billion by the year 2050 [7]. According to world population prospects 2019 provided by the United Nations Department of Economic and Social Affairs, in the last 2 decades the percentage of people aged above 50 in Indian population increased by 5.9%, i.e., 13.40 in 2000 and 19.40 in 2020. With increase in the quality of life increases the life expectancy increases too. A report released by the United Nations Population Fund and Help Age India suggests that the number of elderly persons is expected to grow to 173 million by 2026. This rapidly aging population and biological changes to older adults' bodies mean that orthopedic problems are increasingly common. From the figures of Centers for disease control and prevention (CDC) at least 1 out of 3 elderly people suffer from osteoarthritis which is the most commonly found in most of the adults. It is clear that a strong correlation between age and disability. About 15% of the world's population has a disability. The report according to world health organization (WHO) on disability clearly states that the worldwide estimate for disability is on the rise due to population ageing and the fatly spread of chronic diseases, as well as improvements in the methodologies used to measure disability [8].

About the 1/3rd of older people have a disability and in a few nations as many as 2/3rd of disabled people are also elderly; 80% of the world's 500 million disabled people live in developing countries; disability linked with poverty closely [9]. These barriers in the movement greatly restrict the extent to which people with disabilities can participate in the day-to-day activities. In most of the modern nations, maintenance of transport is often a hurdle because of many reasons such as the geographic constraints, and the weather conditions. So, to overcome this issue, most of the buses are the high-floor buses and have a good ground clearance but can't be steps that are not "accessible" to everyone. Excessive bus-to-platform gaps often make boarding and alighting more difficult for all passengers and especially for children, elderly or frail persons, blind persons, and passengers using wheel chairs. This uncurbed gap often requires passengers to watch the gap while they board and alight, causing delay and also creating an increase in the risk of injuries. To overcome these issues, the researchers all over the world came up with different ideas to solve this problem. Some of them are discussed here:

1. **Shaped Staircase Lift for Personal Use and Transport of Goods:** This is a lift which uses a step-shaped shaft for uplifting and lowering a person or goods on a platform over one or more steps. The lift is suitable for use by persons with or without a wheelchair. This is especially suited for domestic purposes and used for the lifting the person in wheelchair and without. This can't be implemented on a vehicle, as it is difficult to attach and detach the mechanism when needed [10].
2. **Low Floor Buses:** A low floor bus is a sort of bus which was without steps between the bottom and therefore the floor of the bus at one or more entrances. It generally refers to a bus that's accessible from a particular minimum height of step from ground level which makes it accessible to the general public, mainly

the aged and other people with disabilities, including those in wheelchairs and walkers.

3. **Kneeling Buses:** Kneeling buses are another innovative design made to assist the elderly and therefore the disabled. This system has an air-adjustable suspension. The kneeling bus, this name is taken from the kneeling-like manner during which it lowers itself at the stop. This feature allows the driving force to truly lower the bus to the curb to form entering and exiting the bus much easier. By depressing the button inside, the compressor and suspension then revisit to initial and operating height.
4. **Need of the Automated Stairs:** Low floor and Kneeling buses can provide a help to the elderly and disabled peoples, but it also comes with a few disadvantages. Most potential one existence that these buses aren't mostly suited to the rural roads and the hilly roads due to bad road conditions and low ground clearance. As optimum ground clearance has to be considered for a comfortable ride, high-floor buses are suited for most of the roads in rural India, and thus modification has to be made to these steps to make them reachable for elderly and physically challenged communities. Thus, automating the steps to get the stairs closer to the ground level and then carry them back to the top is the most suitable way to ease the effort in climbing the steps [11].

2 Design of the Mechanism and Electronic Controller

The mechanism of dynamics steps conceptual design and the electronic controller for operating the dynamics step were discussed in the following sections.

2.1 Conceptual Design of the Mechanism

SolidWorks is a solid modeler and utilizes a parametric feature-based approach which was initially developed by PTC (Creo/Pro-Engineer) to create models and assemblies. The whole staircase system consists of three movable steps and a fixed step whereas the specially designed steps have sliders in them for the steps to move up and down directions (only vertical movement) in a comfortably manner as shown in Fig. 2. The steps have a movement restrictor in them to restrict the motion in the steps from falling down by providing sensors. The steps are actuated by two linear actuators, arranged at either side of the base step and powered by a 24 V DC motor. The total stroke length of the actuator is 1800 mm and each step is divided equally according to the total stroke length of the actuator.

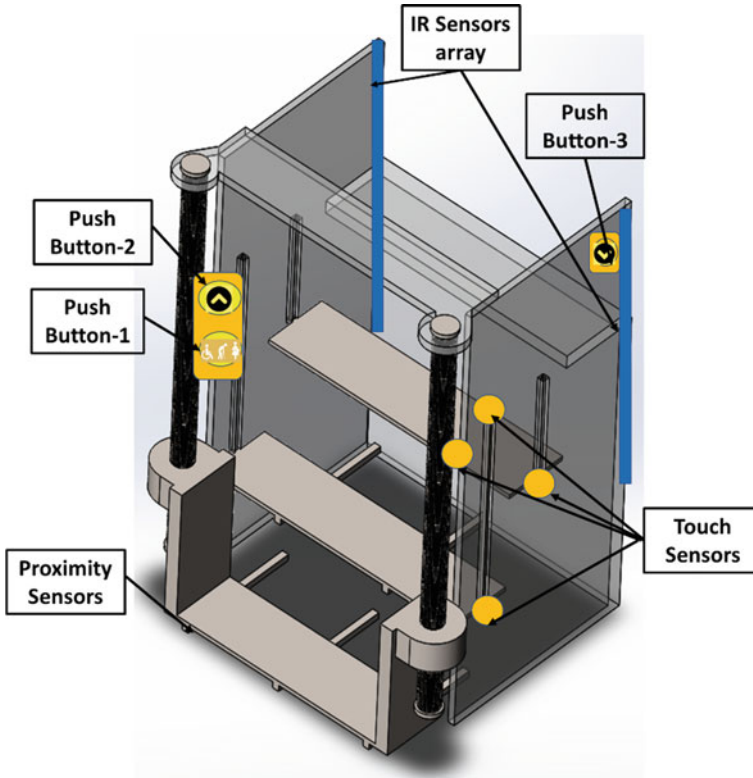


Fig. 2 CAD modeling of an automated dynamic steps and its components

2.2 Development of Electronic Controller

The block diagram of the electronic controller is shown in Fig. 3. Hardware of the electronics controller consisting of Arduino Uno, HC-SR04 Ultrasonic Sensor, IR Sensors, L293D Motor driver, Pushbuttons, Stepper Motors, Limit switches, and the Software used is Arduino IDE. IDE is used to code the microcontroller.

The electronic circuit for the controller as shown in Fig. 4 and each component's working description are discussed below. Figures 5, 6 and 7 shows the elderly people's boarding, lifting, and de-boarding of the bus. Arduino UNO-this is an opensource online platform which supports Atmega328P. This board is the brain of the entire automated system, and all the extra components are attached to this as peripherals. It has 20 I/O pins of which 14 are digital and 6 are analog pins. It also has 6 digital PWM (Pulse Width Modulation) pins. It comes with a reset button, an USB Connector, a power jack, and a 16 MHz quartz oscillator. Ultrasonic sensors-the distance between the object and the sensor is measured using an ultrasonic sensor. An ultrasonic sensor measures the distance by emitting sound waves at a specific frequency and receiving

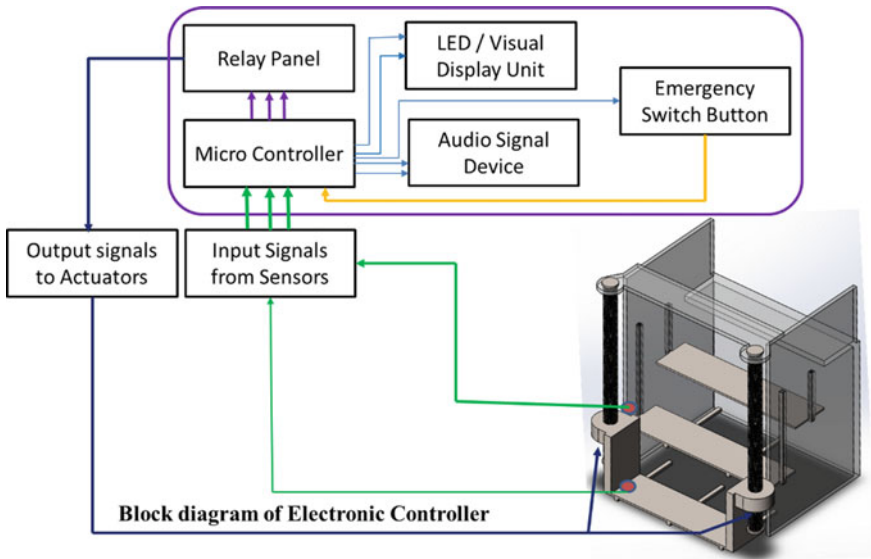


Fig. 3 Block diagram of an automated dynamic steps

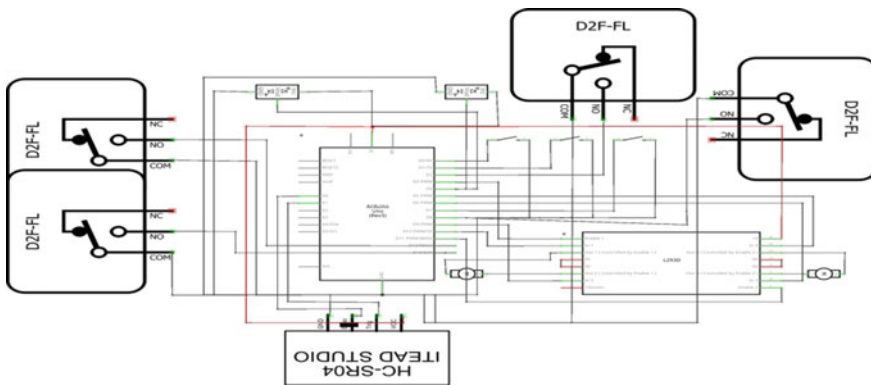


Fig. 4 Circuit diagram of an automated dynamic steps built in fritzing

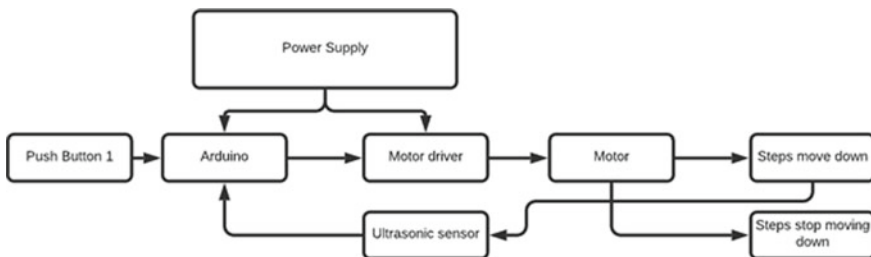


Fig. 5 Flow chart for boarding the bus by elderly or disable persons

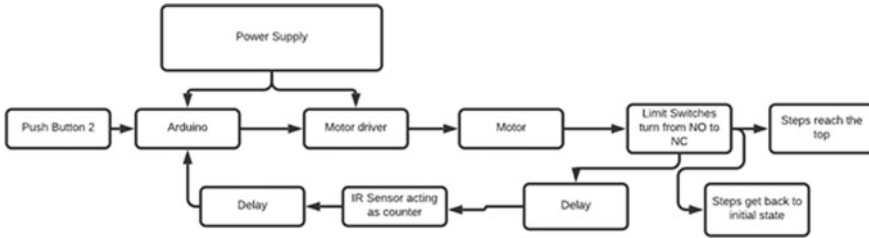


Fig. 6 Flow chart for lifting the elderly or disable persons till the floor level of the bus

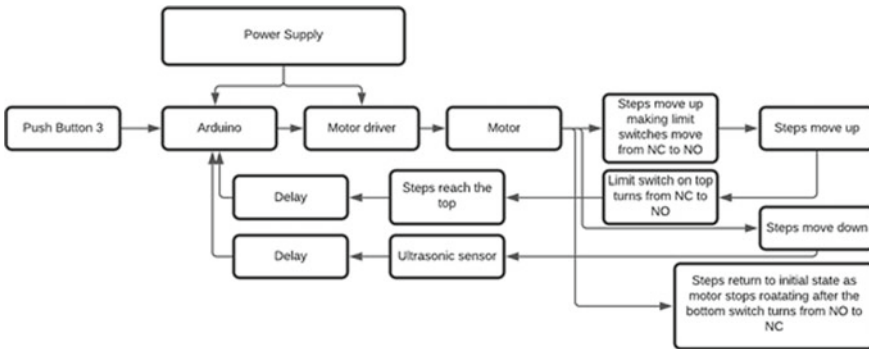


Fig. 7 Flow chart for de-boarding the bus by elderly or disable persons

them after reflection from the surface. Thus, the distance is measured. An Ultrasonic sensor is a proximity sensor, which can record the distance using acoustic waves. It measures distance by sending out sound waves with a specific frequency and then calculates the time taken for the waves to bounce back after hitting the surface. In this way the distance between the object and the sensor is measured. Stepper Motor-stepper motors are direct current motors that move in distinct steps. They have multiple coils that are organized in groups, which are called phases. Energizing each phase in an order, rotate the motor one step at a time. The precise positioning and controlling can be achieved by employing a controller. Stepper motors are available in many different sizes and styles and electrical characteristics. Stepper motors are the motor of choice for several precision motion control applications.

L293D Motor Driver: H-Bridges are used to control motor speed and direction by controlling the Pulse Width Modulation (PWM) and polarity. Pulse Width Modulation is also a method of controlling the duration of an electronic pulse. The longer pulses make the wheel turn faster whereas the shorter the pulses make them slower. The polarity makes the actuator move in different directions, when thus changing the direction of motor rotations. Here it is used to control the direction of motor rotation. This rotation enables the power screw to rotate, thus causing the actuation of the steps up and down. IR Sensor-infrared radiation can be detected by using electronic device which is an active infrared sensor. It both emits and detects infrared

radiation. It contains two parts: a light emitting diode (LED) and a receiver. When an object comes on the brink of the sensor, the infrared from the LED reflects off of the thing and is detected by the receiver. Active IR sensors are commonly used in obstacle detection systems or as counters. Here it is used as a counter trigger which triggers a counter whenever a person crosses by. Pushbuttons: A Pushbutton switch is a simple switch mechanism which simply turns on and turns off. Here these pushbuttons provide the input to get the start or end of each process and used three pushbuttons, to start the activity associated with each. Limit Switches: A type of electromechanical switch that is operated by the motion of a moving item. It contains an actuator and a few mechanical contacts. When an object comes into contact with the actuator, the device either makes or breaks an electrical connection. It is used for controlling machinery as part of a control system as a safety interlock, or to count objects passing a point. There are two positions in this NO (Normally Open) and NC (Normally closed). All the Switches are placed in NO position. The limit switches are placed in between the steps which allow the microcontroller to govern the position and to get the trigger.

3 Simulation Results

3.1 Working Principle of the Mechanism

A differently abled person/elderly comes near the steps, pushbutton-1 (with identification mark of disability or elderly), upon sensing the input from the pushbutton-1, the microcontroller gives a sign to turn the motor clockwise, which transfers the steps down until it reaches just a few centimeters above the ground. The non-contact type proximity sensor (Ultrasonic sensor) which is located at the bottommost of the initial step may send a signal to the controller when it is just a few cm away from the ground which in turn sends a command to the controller to stop the motor from further rotations. Once the passenger steps on the first step then he can press another pushbutton-2 (having an upward arrow symbol). The signal from this pushbutton-2 ensures the controller to send commands to electrical actuators to rotate in the reverse direction, i.e., anti-clockwise direction. So, the initial step along with the passenger starts moving upward.

When the first step reaches the level of the second step the ribs of the first step can line up with the second step, and the interaction type switch (Limit switch) located at the slot ensures proper alignment and moves up along with the second step. As the first step keeps on moving up and reaches the level of the third step, then the ribs of the second step align with the third step, then the contact type switch located at the slot ensures proper alignment and moves up along with the third step.

Finally, when the first step reaches the level of the fourth step or floor level of the vehicle, then the contact type switch located at the slot ensures proper alignment of all the steps to floor level. This trigger from the limit switch sends a command to

the controller which makes the actuator stop. An audio or visual signal is passed to the passenger to walk on the floor into the bus and move toward the assigned seat. When the passenger crosses the steps zone, the array of IR sensors located in the rods ensures that the passenger safely crosses the steps zone. Once the IR signal is received from the sensor controller then starts the actuator again making it rotate in a clockwise direction. This makes the steps move down.

When the step comes to the level of the third step, the contact type switch ensures that the third step is settled properly. As it moves down the contact switches get triggered and the position is aligned. Once the first step reaches its initial position the limit switch is triggered, sending the command to stop the motor from further rotations. This ensures that the first step is in normal position, where other people can board or alight the vehicle.

When the differently abled passenger wants to alight the vehicle, then he/she presses the pushbutton located on the rod (downward direction) and waits for a few seconds until all the steps form a level equal to the floor of the vehicle. An audio or visual signal so that others can be cautioned. Once the person boards the step, after a slight delay the steps start to move down (Fig. 8).

During this process, all the limit switches that were in NC condition change to NO condition. When the last limit switch is triggered, the ultrasonic sensor gets activated. When the distance between the ground and stairs reaches the initialized value, the actuator stops allowing the passenger to de-board. A few seconds delay is deployed, following which an audio or visual signal so that others may be cautioned and then actuators get activated. When the initial position is reached, the actuators stop. The simulation of the electronics controller is shown in Figs. 9, 10 and 11, respectively.

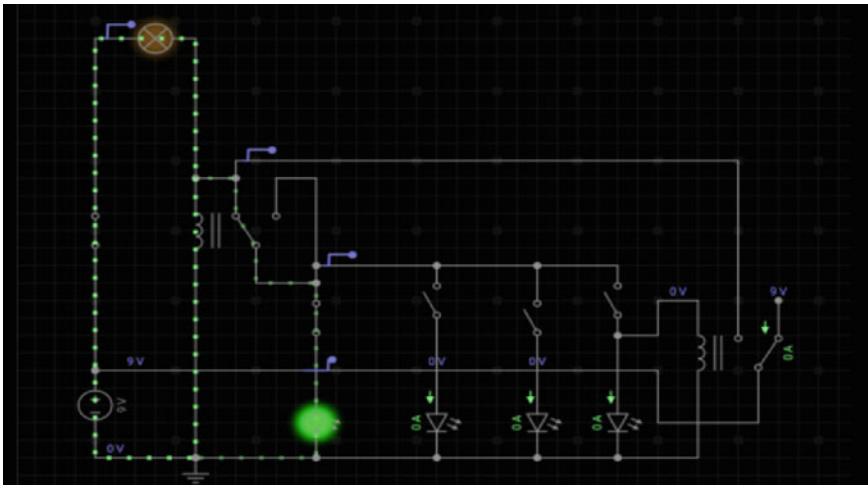


Fig. 8 While boarding the bus by elderly or disable persons

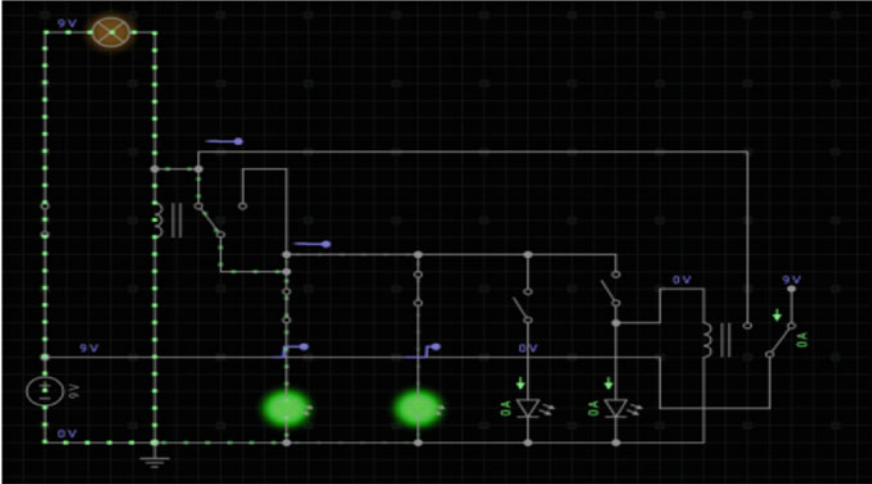


Fig. 9 While traveling upward direction along with elderly or disable persons

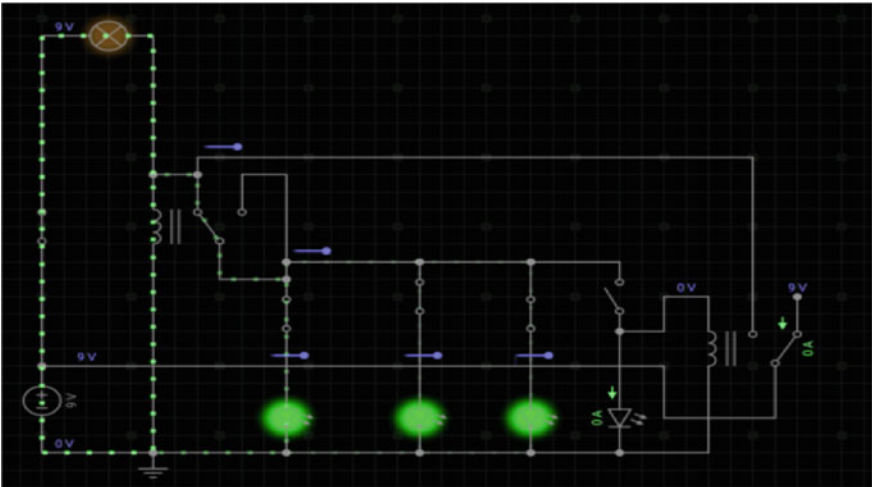


Fig. 10 After reaching the top step or bus-floor level

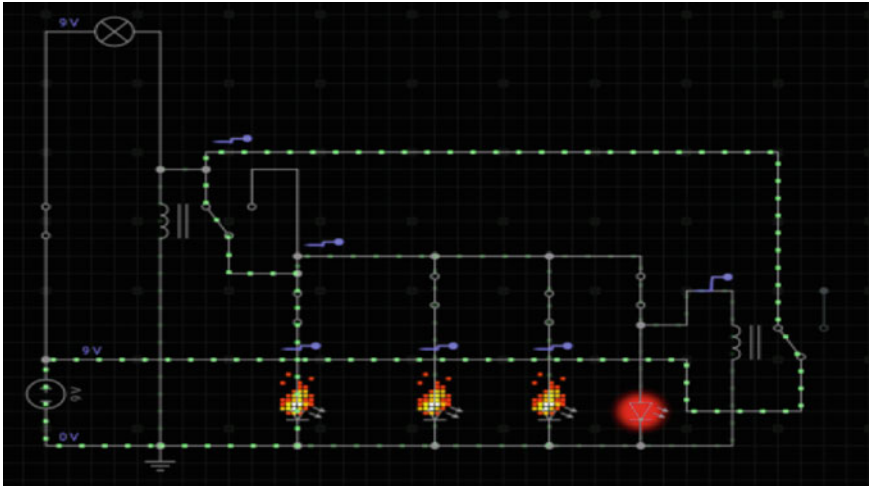


Fig. 11 While de-boarding or returning to initial position of steps

4 Conclusion

An automated staircase modeling was designed in the solidworks and verified the working of the mechanism. Flow chart and its algorithm were prepared for writing the Arduino coding by keeping the safety of the elderly or physically challenged people and tested the functioning of the system by coding a program to carry out the required functions by an electronics controller. Based on the action performed by the passenger or an assistant, the staircase comes down to reach the ground level, picks up the person till it reaches the top floor of the bus. After reaching the top step, the controller waits till they pass the clearance area and get back to its initial position by considering the safety of the persons. This automated system can be greatly allowing the elderly or disabled passengers can board and de-board the public transport easily without any assistance from other people interfering in between. The mechatronic system is successfully designed for an automated staircase system and simulated the functioning of the controller.


References

1. Schroeder S, Schroeder S (2009) Step shaped stair case lift for personal use and transport of goods. US Patent No: 7,484,595
2. Nimz FE, Czech EA, Winamac RW, Goodrich L, Kevin L (1989) Stair climbing aid. US Patent No: 4,844,199
3. Crawford W (1993) Rotary bus lift with power towable platform. US Patent No: 5,180,275
4. Ronald IW (1994) Stair climbing support. US Patent No: 5,355,904

5. en.wikipedia.org/wiki/Bangalore_Metropolitan_Transport_Corporation
en.wikipedia.org/wiki/Low-floor_bus
6. <https://www.thehindubusinessline.com/opinion/working-towards-a-disabled-friendly-india/article25040700.ece>
7. Elderly in India Profile and programmes 2016. Central Statistics Office Ministry of Statistics and Programme Implementation Government of India. http://mospi.nic.in/sites/default/files/publication_reports/ElderlyinIndia_2016.pdf
8. https://www.who.int/disabilities/world_report/2011/report/en/
9. Porter G, Tewodros A, Gorman M (2018) Mobility, transport and older people's well-being in Sub-Saharan Africa: review and prospect. In: Curl A., Musselwhite C (eds) Geographies of transport and ageing. Palgrave Macmillan, Cham. https://doi.org/10.1007/978-3-319-76360-6_4
10. Patil DS, Yadav UN, George S et al (2020) Developing an evidence-informed framework for safe and accessible urban mobility infrastructures for older adults in low- and middle-income countries: a protocol for realist synthesis. *Syst Rev* 9:196. <https://doi.org/10.1186/s13643-020-01456-w>
11. AbsarAlam M, Faisal A (2013) Urban transport systems and congestion: a case study of indian cities. Publisher: United Nations, pp 33–43

Design and Development of Mechatronic System for an Automated Ergonomic Keyboard Tray



Mona Sahu , Gadudasu Babu Rao, Wilson M. Kumar, S. J. Vijay, Achshah Phebe Chrysolin, Ajith Purushothaman Madan, Samuel Jebish, and Joseph J. John

Abstract In various fields of work, with the high percentage of time spent on working on computers, repetitive and prolonged use of computer keyboard and mouse in the incorrect position may lead to muscle aches and discomfort. This research was aimed to design and fabricate an automated ergonomic keyboard tray which will automatically adjust the height of the keyboard tray with the height of the armrest of the computer chair as per ergonomic guidelines for each user. This design can provide neutral posture while working on the keyboard, hence reducing the possibility for the development of pain in the shoulders, arms, and wrists. This research concluded that the automated ergonomic keyboard tray can maintain close to neutral posture for the computer users while working on the keyboard and eventually reducing pain in the upper arm, forearm, and wrist.

Keywords Computer keyboard · Microcontroller · Neutral posture · Risk factor · And pain

1 Introduction

The usages of computers at work and home have become quite common all around the globe. The dependence on computers is continuously increasing. Many individuals in offices are found to spend the majority of their time working on a computer. These individuals and those having a history of musculoskeletal infirmity are most likely to develop repetitive stress injuries. The key risk factor which leads to repetitive stress injuries is lack of proper ergonomic position while typing on the keyboard affecting the wrists, hands, and forearms. If computer users continue for prolonged days type on a keyboard in awkward positions can cause fatigue in related muscles leading to swelling of tendons and joints and additionally cause nerve damage. Carpal tunnel syndrome is the most predominant form of repetitive stress injury. The compression

M. Sahu (✉) · G. B. Rao · W. M. Kumar · S. J. Vijay · A. P. Chrysolin · A. P. Madan · S. Jebish · J. J. John

Department of Mechanical Engineering, Karunya Institute of Technology and Sciences, Coimbatore, TamilNadu 641114, India

of nerves in the wrist causes carpal tunnel syndrome leading to numbness in the hands and the fingers [1]. This injury may even need surgery resulting in pain, distress, loss of worktime and ultimately reducing productivity.

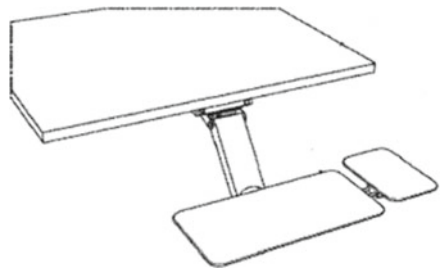
The implementation of ergonomic improvements can reduce the risk factors causing discomfort, can lead to fewer injuries, increase productivity and sustainability of employees, reduce workers compensation claims, and increase job satisfaction of employees. Office ergonomics deals with sitting with neutral postures, designing, or arranging workplaces, products, and systems to fit the people who utilize them and to minimize the risk of injury or harm.

Based on the review conducted by Rajesh Raghunathan et al. [2], it is found that various types of computer keyboard trays and wrist rests are developed by the industry to give support to the keyboard and the wrists of a user to maintain a proper ergonomic typing position. The main aim of the designers of these keyboard trays is to maintain close to neutral posture of the users while typing. Based on the several guidelines like OSHA, ISO, ANSI, etc., while placing the hands on the keyboard, the neck and shoulders should be relaxed, upper arms on their sides, elbows close to 90 degrees or greater, and wrists straight [3, 4]. Normally, when placing the keyboard on the desk surface, the arms get elevated and not parallel to the floor which leads to pain in upper arms, shoulders, and upper back. Instead, the keyboard can be placed on an height adjustable keyboard tray or users may raise the height of the chair and use a footstool. It is also suggested to keep the keyboard legs folded up or slightly away from the user to maintain negative angle.

Some of the existing computer keyboard trays are fitted under the work surface [4]. These trays can be retracted to an extended position, i.e., outside the front edge of the work surface and closer to the user. Many such trays also have an additional feature to tilt the keyboard tray and adjust the angle of the keyboard based on their comfort. Some of these keyboard trays have rigid material with sharp edges and unintended contact with hard surfaces can cause injury to the users working on the keyboard for long period of time [4]. Most of the keyboard trays have very less space provided to place the mouse and this can further more cause repetitive stress injury.

According to the invention done by John Failing [5], the adjustable keyboard tray and mouse pad (Fig. 1) can be vertically adjusted for height adjustment and horizontal motion is given to bring the keyboard from rest position to user's position and swivel movement for adjusting the typing angle. Mouse tray can also be adjusted for height

Fig. 1 Adjustable keyboard tray and mouse pad [5]



and angle. This articulated keyboard tray can be positioned at an angle relative to horizontal, and the mouse pad can also be positioned in horizontal position [5].

In another invention, the height of the articulated keyboard by Kenneth A. Patriarco [6] can be manually adjusted. The front to back motion can be adjusted by slider rail mechanism. Mouse tray also can be elevated and lowered. The height adjustable desks with ultraviolet light irradiation of keyboard tray [7] consist of a height adjustable table, with telescopic movement. Ultraviolet light unit may be manually activated using a power switch. Ultraviolet light unit may be automatically controlled when connected with motion sensor or via a timer mechanism that activates the UV light unit for a regularly scheduled irradiation session [7]. Adjustable workstations are one of the main approaches used to fit the workstations to a wide range of users and also to decrease extended sitting time [8].

According to studies done by Workineh [9], changing the work positions helps permit the different parts of the body to rest before pain is developed. This helps the user to work without pain, for longer periods of time, improving the overall productivity. Another study done by Workineh [10], concluded that working on a computer in different working positions gives each user a different degree of comfort. This showed that a particular posture gives more comfort for certain parts of the body than other postures. It was also observed in this study that a particular position of the user was more suitable for only some kind of tasks and not all the computer tasks [10].

Various researchers found that one of the independent risk factors for pain among computer users was the lack of physical activity during work. Hence, certain researchers have examined the possibility to increase physical activity during computer work by using sit-stand workstations and dynamic workstations [11]. It was observed that standard office tasks (typing, reading, cognitive tasks, etc.) performance were hardly affected while working on sit-stand and dynamic workstations. Nevertheless, mouse pointing and clicking which involves fine motor actions of the hands were affected by the movements at a dynamic and standing workstation [12]. It was concluded that the overall performance deteriorated on dynamic workstations [11].

Hence, it is found that repetitive stress injuries affect an individual's wrist, hands, and forearms. To reduce this pain in the forearm, upper arm, wrist, it is essential to maintain non-neutral posture of the forearm, upper arm, and wrist. Therefore, the objective of this research was to adjust the keyboard tray automatically to the height of the armrest of the chair. This in turn will enable the user to maintain a proper ergonomic typing position.

2 Design of the Keyboard and Electronic Controller

2.1 Modeling of Automated Keyboard Tray

The keyboard tray was designed similar to the usual keyboard stand available in the market using three different links. Three mechanisms are involved in the design,

namely, slider mechanism, revolute mechanism, and tilt mechanism. The slider mechanism is utilized for the linear movement (toward and away from the user) of the keyboard tray. The revolute mechanism is to move the keyboard up and down. The tilt mechanism is designed to adjust the keyboard tray parallel to the table. An existing keyboard tray available in the market was dismantled and the frame was utilized as the frame for the automated keyboard tray. The entire mechanism was fixed on a standard table.

The computer-aided design of the automated keyboard tray is shown in Fig. 2. As shown in Fig. 2, the slider is guided by 8 mm dia. stainless steel rod of length 500 mm. The stainless steel rods are fixed in place by L-clamps which are attached to the table. A slider slides over the stainless steel rods by means of linear bearings. A stepper motor (NEMA 17) was used to control the sliding motion of the slider. The rotary motion of the stepper motor shaft was converted to linear movement via belt drive. A belt of 6 mm width and 857.1 mm length was used. The stepper motor was controlled by Arduino UNO. The isometric view of the slider mechanism is shown in Fig. 3 and the name of the components in the isometric is given in Table 1.

The revolute mechanism which consisted of the stepper motor was fixed to the slider plate. The isometric view revolute mechanism is shown in Fig. 4. The shaft of the stepper motor was attached to the worm gear which was used to convert the revolving motion of the stepper motor to linear motion to enable the height adjustment of the keyboard tray. The height of the keyboard tray was adjusted with reference to the height of the armrest of the chair. When the revolute mechanism starts working, the tray also tilts down and doesn't remain parallel to the arm rest and thus causes discrepancy in the positioning. Thus, to avoid this, a gyro sensor along with a stepper

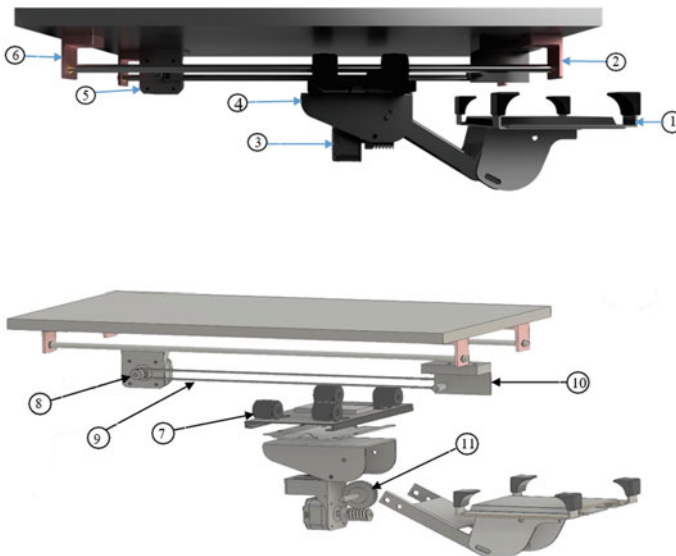


Fig. 2 CAD model of automated keyboard tray

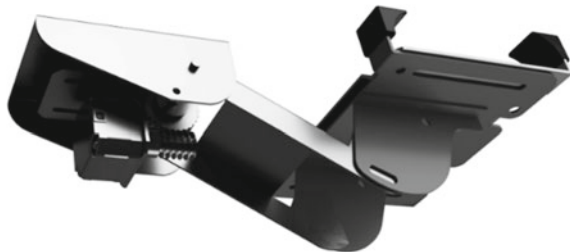


Fig. 3 Isometric view of slider mechanism

Table 1 Components name list of the automated keyboard tray

S. no	Component name	Specification
1	Keyboard frame	–
2	Stainless steel rod	8 mm dia., 500 mm length
3	NEMA 17 stepper motor	Torque 4.8 kg-cm
4	Slider plate	105 * 210 mm
5	Stepper motor mount	NEMA 17
6	L clamp	30 * 33 mm
7	Linear bearings	8 mm ID, 10 mm OD
8	Timing belt pulley	Pulley Teeth number: 16 Pulley Pitch: 2 mm Pulley Bore: 5 mm
9	Timing belt	857 mm
10	Pulley holder	120 * 50
11	Worm gear	Worm gear outer diameter: 18 mm Worm gear no. of teeth: 5 Worm wheel outer diameter: 39 mm Worm wheel no. of teeth: 25

Fig. 4 Isometric view of revolute mechanism



motor setup was fitted below the tray so that after recording the base position of the tray, in case the revolute motion starts, the tray aligns itself parallel to the arm rest of the chair.

The various ranges for all three mechanisms were considered. The linear movement of the keyboard tray was taken as 400 mm from the rest position toward the

Table 2 The selection of the range of movement of three mechanisms

Movement	Range	Remarks
Linear	400 mm	From the rest position
Revolute	0–140 mm	The armrest height for 5th–95th is considered
Tilt	–10 to + 20°	The keyboard tray will be parallel to the table using gyro sensor

user. For the revolute movement, the armrest of the chair was taken as the reference. The book “Indian Anthropometric Dimensions” by Debkumar Chakrabarti [13] was referred to select the range of movement of the two mechanisms, i.e., linear and revolute motion of the keyboard. The ranges were considered from 5th percentile female to 95th percentile male. For tilt movement, the keyboard must be maintained parallel to the table. Table 2 shows the selection of the range of movement for the three mechanisms.

2.2 Development of Electronic Controller

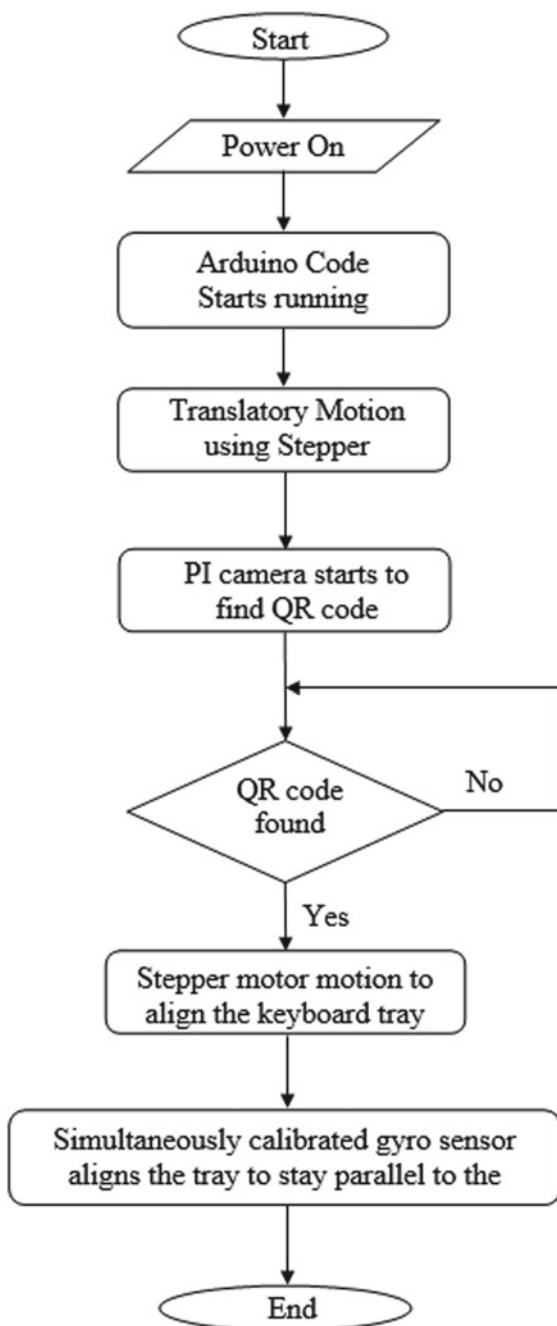
The program logic for the control of the 3 mechanisms was designed. The flow chart illustrating the algorithm is given in Fig. 5.

An Arduino UNO microcontroller (ATMEGA 328) was used. The code was tested prior to being compiled into the final program. The DRV8825/A4988 motor driver was used to control the stepper motor for the movement of the slider mechanism. The motor driver was affixed to the microcontroller to run the stepper motor. Another stepper motor was used for the revolute motion. The rotary motion of the stepper motor was enhanced by the meshing of two gears.

At first the signal was given to the stepper motor to move the slider 400 mm from the home position toward the user. After which, the Pi camera detects the QR code in the real-time environment. The stepper motor of the revolute motion was programmed to operate till the tray was in line with the QR code which was placed on the armrest. Simultaneously with the revolute motion provided by the revolute stepper motor, the gyroscope stepper motor was programmed to keep the keyboard tray parallel to the ground using an MPU-6050 accelerometer and gyro sensor which was calibrated to achieve the desired position as stated above. All the mechanisms work in equilibrium and the desired outcome were achieved.

The circuit diagrams for linear movement, revolute movement, and tilt movement of keyboard tray are shown in Figs. 6, 7, and 8, respectively.

Fig. 5 Flow chart of the algorithm



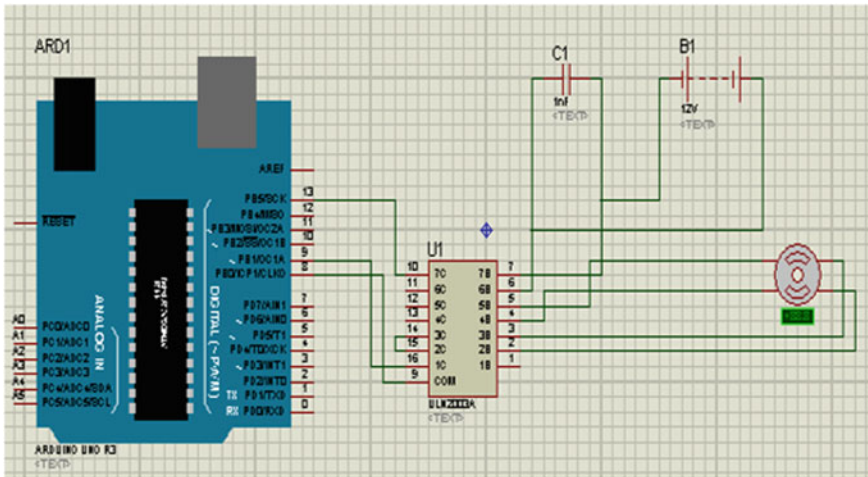


Fig. 6 Circuit diagram for linear movement of keyboard tray

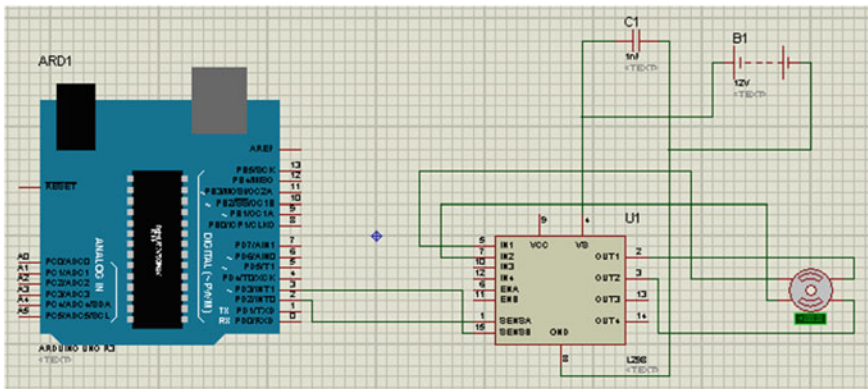


Fig. 7 Circuit diagram for revolute movement of keyboard tray

3 Simulation Results

3.1 Working Principle of the Mechanism

The detailed working principle of the automated keyboard tray is given in this section. At first, the user sits on the adjustable chair and adjusts the seat height as well as the armrest height according to his/her convenience or according to ergonomic principles of seating. Thereafter, the user switches ON the automated keyboard tray. The slider stepper motor starts rotating as per the requirement to move the slider 400 mm front. The rotary motion of the stepper motor is converted into translatory motion using

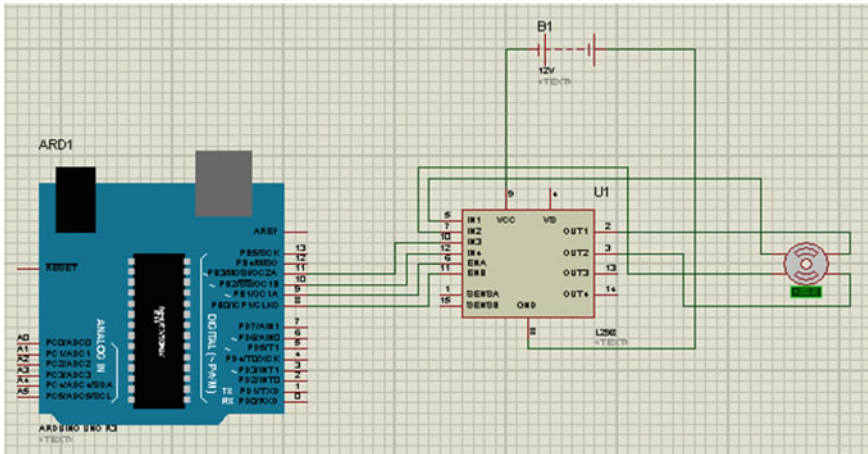


Fig. 8 Circuit diagram for tilt movement of keyboard tray

the belt drive mechanism. This will bring the keyboard from the home position, i.e., under the table to just outside the table edge.

After the linear motion, the revolute movement is incorporated to move the keyboard up and down. The stepper motor used for this revolute motion will receive the input from the processed output of the Pi camera module. Using OpenCV module, the Pi camera attached to the Raspberry Pi starts detecting the QR code in the real-time environment and sends back signals through the Raspberry Pi processor and thus after processing the received signals, the pins in the Arduino board connected with the Pi via I2C communication is triggered such as to send the processed signals for the stepper motor alignment with respect to the desired position of the keyboard tray. Simultaneously, gyroscope stepper motor is fixed below the keyboard tray to keep the keyboard tray parallel to the floor. For this independent mechanism, L298N motor driver was used as well as MPU-6050 3-axis accelerometer and gyro sensor was used.

Once the work on PC is completed by the user and the QR code is out of sight, the entire tray retracts back to its home position and it is turned OFF. The fabricated prototype is shown in Fig. 9.



Fig. 9 Fabrication of an automated tray mechanism

4 Conclusion

The design and fabrication of the three different mechanisms and one feedback mechanism of automated keyboard tray were successfully completed. The fabrication of the slider mechanism was completed, and the circuit was designed and built. The code for the 400 mm linear movement of keyboard tray was tested. It was found that the keyboard tray exactly moves 400 mm from the home position to the required position with respect to the table edge. The fabrication of the revolute mechanism which moves from home position, i.e., 0 mm to a height of 140 mm was completed. The code for the revolute movement of the keyboard tray was tested.

It was found that the stepper motor motion required to keep the keyboard tray in line with the QR code works with existing constraints of 0–140 mm works as desired. Based on the testing of the mechanism the camera successfully detects the QR code. The fabrication of the tilt mechanism was completed and the electronic circuit was designed and built. The code for the calibration of the gyro sensor as well as its working with the stepper motor was tested. It was found that the keyboard tray exactly moves as per the stepper motor motion fixed below the tray such as to always keep it parallel to the ground. The fabrication of the feedback mechanism was completed, and the I2C communication established works as desired.

The three different mechanisms and one feedback mechanism of the automated keyboard tray are designed and built. From the results, it can be concluded that the algorithm for the automated keyboard tray can be incorporated to build an automated adjustment system which will adjust the keyboard to the height of the armrest. Hence, by using this type of automated system, it can maintain close to neutral posture for the computer users while working on keyboard and eventually reduce pain in upper arm, forearm, and wrist.

References

1. You D, Smith AH, Rempel D (2014) Meta-analysis: association between wrist posture and carpal tunnel syndrome among workers. *Saf Health Work* 5(1):27–31
2. Rajesh R, Srinath R (2006) Review of recent developments in ergonomic design and digital human models. *Ind Eng Manag* 5(2), 1–7
3. Woo EHC, White P, Lai CWK (2015) Ergonomics standards and guidelines for computer workstation design and the impact on users' health—a review. *Ergonomics* 59(3):1–13
4. Muñoz LM (2016) Evaluating the ergonomics in interaction with computers. *J Ergon* 6(2)
5. Swanton JF (2018) Adjustable keyboard tray and mouse pad. Patent No: US 9, 968, 186 B2
6. Patriarco KA (2014) Articulating keyboard and mouse platform system. Patent No: US 8,864,091 B1
7. Herring JB, Gilbreath SM (2017) Height adjustable desks with ultraviolet light irradiation of keyboard tray. Patent No: US 2017/0071332 A1
8. Leavy J, Jancey J (2016) Stand by me: qualitative insights into the ease of use of adjustable workstations. *AIMS Publ Health* 3(3):643–648
9. Workineh SA, Yamaura H (2015) Multi-position ergonomic computer workstation design to increase comfort of computer work. *Int J Ind Ergon* 53:1–9
10. Workineh SA, Yamaura H (2015) Effects of multiple working positions on user comfort: a study on multi-position ergonomic computer workstation. *Proc Manufact* 3:4792–4799
11. Commissaris DACM, Könemann R, Hiemstra-van Mastrigt S, Burford, E-M, Botter J, Douwes M, Ellegast RP (2014) Effects of a standing and three dynamic workstations on computer task performance and cognitive function tests. *Appl Ergon* 45(6):1570–1578
12. Koren K, Pišot R, Šimunič B (2016) Active workstation allows office workers to work efficiently while sitting and exercising moderately. *Appl Ergon* 54:83–89
13. Chakrabati D (1997) Indian anthropometric dimensions for ergonomic design practice, 1st edn. National Institute of Design, Ahmedabad 380 007, India

Product Design and Development

Comparative Study of the Rear and Rear Side Impact on a Roll Cage Using FEM



Santosh Kumar Kurre, Jitendra Yadav, and Shubham Thakur

Abstract Nowadays, the expectations of the customers from the car manufacturers are increasing day by day. Everybody demands a car, which ensures safety and security in case of misfortunes. For testing the crashworthiness of the car structures, manufacturers use various test methodologies such as quasi-static testing, impact testing, and crushing modes and mechanisms. The present study deals with the dynamic analysis, which is carried out on the roll cage for its impact testing of the rear and rear side impact. For simulating the transient dynamic analysis of the roll cage by simulation. The model analysis shows that maximum deflection and the maximum velocity for rear impact were found 22.3 mm and 42.5 mm/s, respectively, at nodes 3, 27, 29. Whereas in case of the rear side impact maximum deflection and maximum velocity are 3.5 mm and 1.8 mm/s, respectively, at node 36.

Keywords FEM · Rear impact · Roll cage · Rear side impact

1 Introduction

Today occupant safety is one of the pioneer concerns for the car manufacturers. There is several new standards are set up in different crash conditions for the safety of the occupants, such as angle impacts, rear impacts, frontal head-on collision, side impacts, to improve the traffic ability [1], and rollover. The front impact is very dangerous, and fatal for the occupant in all over the world as given by Honnagangaiah [2]. In ATVs, the driver and occupants are susceptible to harm due to lack of protection and proclivity for ejection at the time of a crash [3]. The AVT dynamics caters its

S. K. Kurre (✉) · J. Yadav · S. Thakur
University of Petroleum and Energy Studies, Dehradun 248007, India
e-mail: skurre@ddn.upes.ac.in

J. Yadav
e-mail: jyadav@ddn.upes.ac.in

S. Thakur
e-mail: 500069394@stu.upes.ac.in

impact on soil properties, energy efficiency, vehicle traction, and harvesting but safety is one of the prime concerns [4]. The design of the automobile mid-rail is done to carry the load/absorb the energy of frontal impact/crash. However, low fuel consumption, lightweight, and the higher rigidity of the vehicle are expected from the modern vehicle. Therefore, steel usages are being replaced composite material. Thus it will provide two benefits one is to enhance fuel utilization and the second one is to increase the safety of vehicle and occupants. In this research, an effort is made to replace the steel rails with the carbon fiber, and glass fiber composite materials. The parametric evaluation of the rail is conducted to determine the maximum possible energy absorbing. The rail of carbon/epoxy composite material with appropriate orientation and thickness can absorb more energy than the steel rails. Composite rail in the vehicle sustains more load and saves the occupant.

Kader et al. [5] worked on speed bump and automotive suspension analysis. They designed a model car and optimized the speed for the speed bump. They used to simulation model firstly, spring single mass and damping and second spring and double mass damper. For model B tire was considered the second mass. Both models were examined for three cosine waves model and discrete representation of bump in the Swarthmore Campus. Roots et al. [6] modeled an Automotive Chassis using Msc /Nastran. In comparison to the initial configuration by appropriate design, they reported 500% increase in torsional stiffness. The difficulty of roll cage design was evaluated non-linear finite element analysis using Msc/Nastran. A full-scale chassis design was used to analyze the roll cage/ frame. The results were found in an acceptable 10% of the test results despite the simplifying assumptions. Traditionally automotive manufacturers believe on experience and expertise to design and develop the chassis. The finite Element Analysis is one of the best tools to check the suitability of designs. Silcock et al. [7] have proposed a novel method that composite tube can be used potentially in automotive crash structures. They applied the axial load on tubes to crush the tube under a quasi-static condition with repeating load. They found that specific energy absorption averages to 85 kJ/kg. Vehicle dynamics is significant to vehicle safety and stability [8–10]. The impact and severity of the collision analysis on an off-road vehicle to improve the roll cage strength is the prime concern of this paper. The dynamics have been captured by analyzing the impact from the rear and side rear of the vehicle using ANSYS.

2 Methodology

Simulation by the software ANSYS 10.0 has been performed to implement Transient Dynamic Analysis of Roll cage model. Transient dynamic analysis (sometimes called Time-History analysis) is one of the techniques used to determine the dynamics of a structure (Roll cage) under the action of any general time-dependent loads and deflections. The time-varying deflections, stresses, and forces developed in the chassis of the roll cage are determined by the above-mentioned technique. It allows all types of linearity and nonlinearities. It is easy to use because it provides the liberty

of choosing master degrees of freedom or mode shapes in reduced transient dynamic analysis and mode of superposition methods, respectively.

The effect on the on-vehicle from the rear is dangerous for back seat occupants. So the rear impact and rear side impact are analyzed in this paper. There are 80 nodes which are generated to complete the analysis. The steel material is used to design the roll cage.

3 Rear Impact

In this case, a vehicle coming at a speed of 40 km/h, strikes to the roll cage at its rear portion. The purpose of this analysis is to ensure the strength and stability of the roll cage in the case where a vehicle strikes to it from the rear. Table 1 shows the total impact load on the nodes for rear impact. The velocity of striking vehicle = 40 km/h.

Relative deflection is the deflection in UZ direction (means deflection in vertical upward or downward direction) at each node of the roll cage concerning time in the global coordinate system. This deflection is due to the impact of the vehicle. The relative deflections of all nodes on the roll cage and the relative velocities of all nodes on the roll cage are shown in Figs. 1, 2, 3, 4 and 5.

From the comparison of deflection time plots for different nodes, it is found that the maximum deflection occurs at nodes 3, 27, and 29 of the magnitude 22.3 mm and maximum velocity also occurs at the same node of the magnitude of 42.5 mm/s. The nodal solution view for the rear is shown in Fig. 6.

Table 1 The total impact load on the nodes for rear impact

Time (s)	Force on each node (N)	Node of application	Total impact load (N)
1.1	175	1, 2, 26, 27	700
1.2	350	1, 2, 26, 27	1400
1.3	525	1, 2, 26, 27	2100
1.4	700	1, 2, 26, 27	2800
1.5	875	1, 2, 26, 27	3500
1.6	1050	1, 2, 26, 27	4200
1.7	1225	1, 2, 26, 27	4900
1.8	1400	1, 2, 26, 27	5600
1.9	1575	1, 2, 26, 27	6300
2	1750	1, 2, 26, 27	7000

RDMAX_27 = 22.3 MM

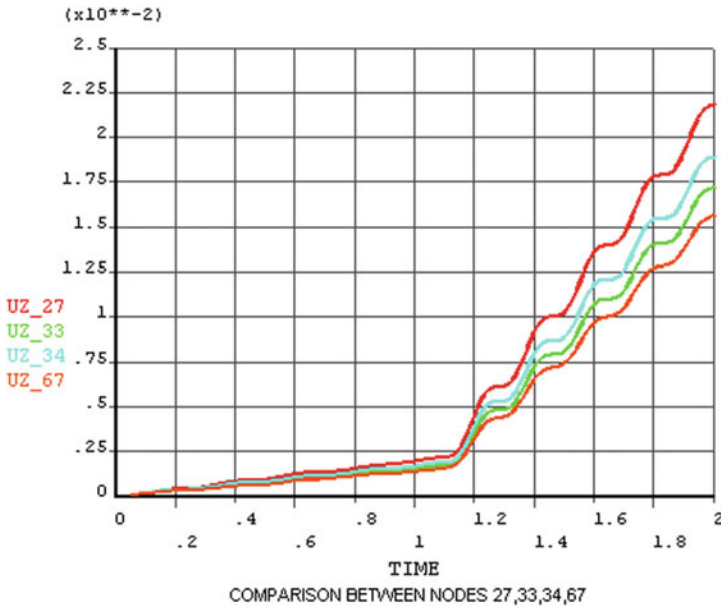


Fig. 1 Rear impact relative deflection versus time for nodes 27, 33, 34, 67

4 Side Impact at the Rear Part

In this case, a vehicle coming at a speed of 40 km/h, strikes to the roll cage at its side portion of the rear part. The purpose of this analysis is to ensure the strength and stability of the roll cage in a case where a vehicle strikes to it from the rear. Table 2 shows the total impact load on the nodes for rear side impact at a velocity of striking vehicle = 40 km/h.

Relative deflection is the deflection in UY direction (means deflection in horizontal forward or backward direction) at each node of the roll cage concerning time in the global coordinate system. This deflection is due to the impact of the vehicle. The relative deflections of all nodes on the roll cage and the relative velocities of all nodes on the roll cage are shown in Figs. 7, 8 and 9. The nodal solution of the roll cage of the rear side impact is shown in Fig. 10.

From the comparison of deflection time plots for different nodes, it is found that the maximum deflection occurs at node 36 of the magnitude 3.5 mm and maximum velocity also occurs at the same node of the magnitude of 1.85 mm/s. The nodal solution view for the rear side impact is shown in Fig. 10.

RDMAX_29 = 22.3 MM

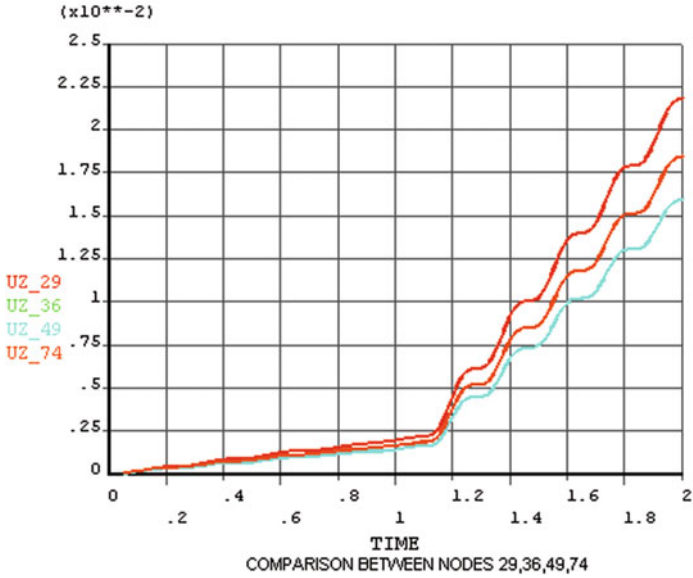


Fig. 2 Rear impact relative deflection versus time for nodes 29, 36, 49, 74

RDMAX_3 = 22.3 MM

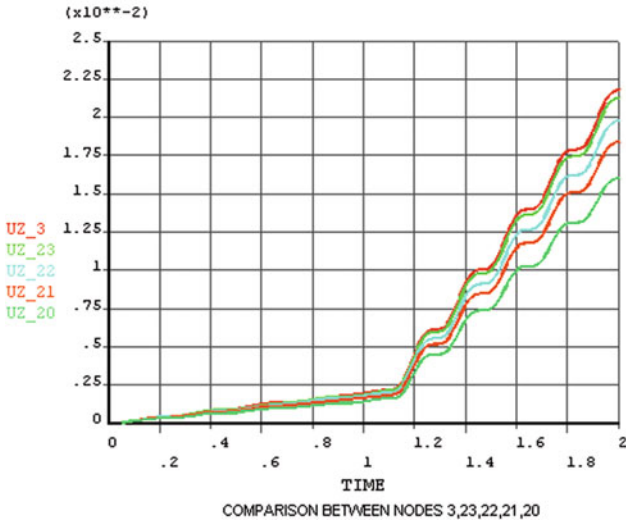


Fig. 3 Rear impact relative deflection versus Time for nodes 3, 23, 22, 21, 20

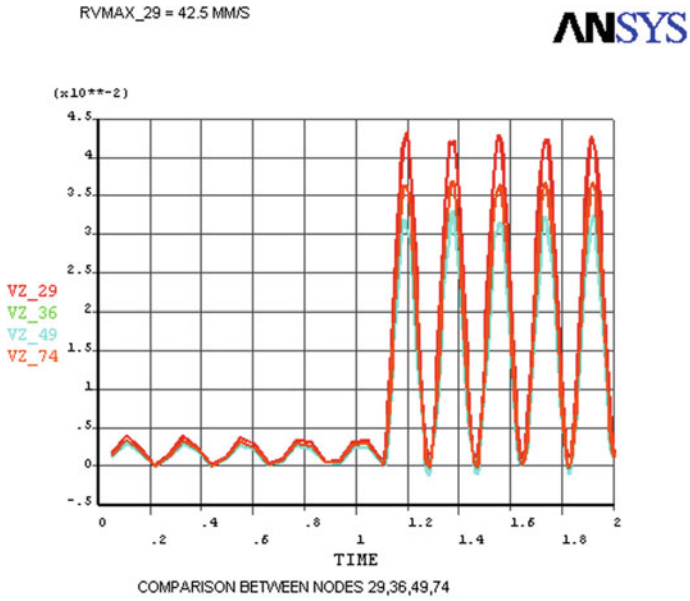


Fig. 4 Rear impact relative velocity versus time for nodes 29, 36, 49, 74

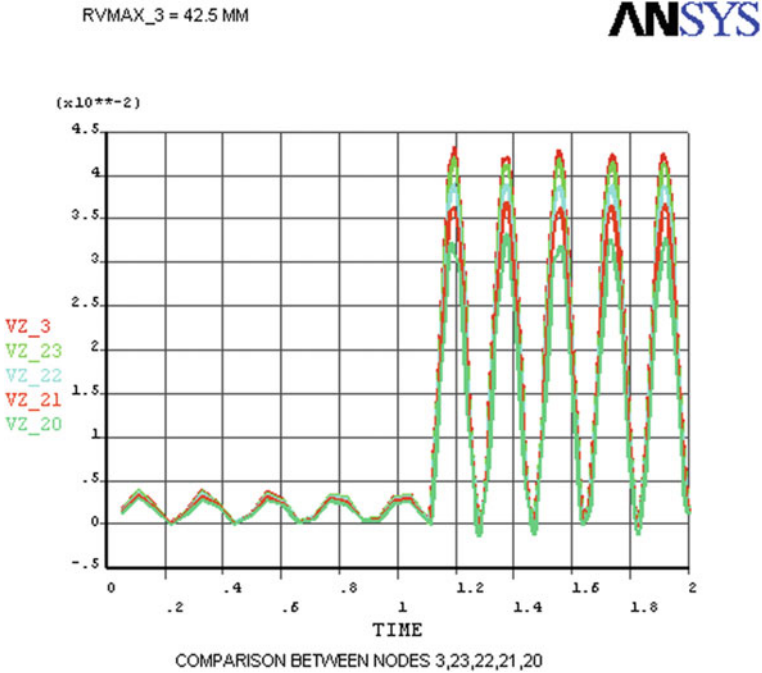


Fig. 5 Rear impact relative velocity versus time for nodes 3, 23, 22, 21, 20

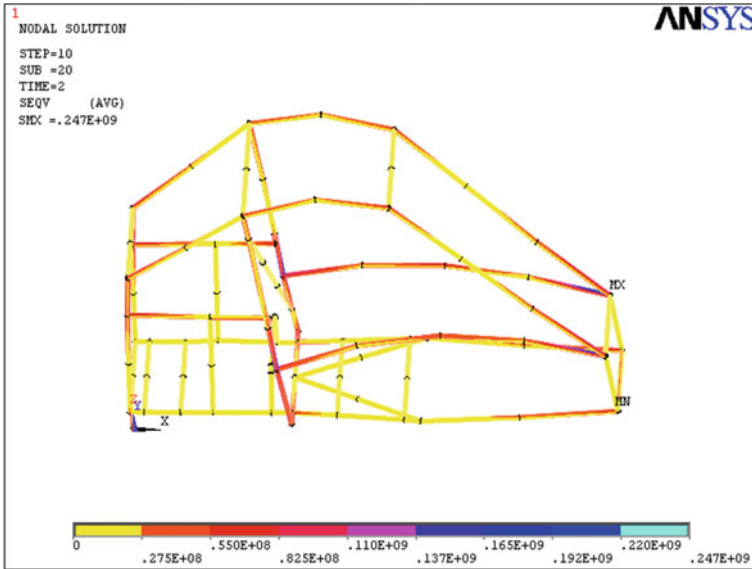


Fig. 6 Nodal solution for rear impact

Table 2 The total impact load on the nodes for rear side impact

Time (s)	Force on each node (N)	Node of application	Total impact load (N)
1.1	140	2, 6, 27, 29, 36	700
1.2	280	2, 6, 27, 29, 36	1400
1.3	420	2, 6, 27, 29, 36	2100
1.4	560	2, 6, 27, 29, 36	2800
1.5	700	2, 6, 27, 29, 36	3500
1.6	840	2, 6, 27, 29, 36	4200
1.7	980	2, 6, 27, 29, 36	4900
1.8	1120	2, 6, 27, 29, 36	5600
1.9	1260	2, 6, 27, 29, 36	6300
2	1400	2, 6, 27, 29, 36	7000

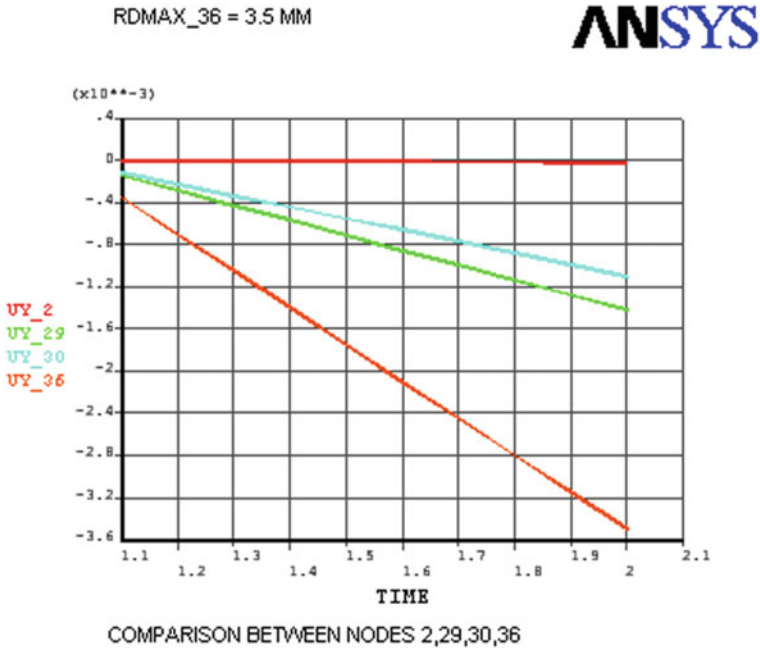


Fig. 7 Rear side impact relative deflection versus time for nodes 2, 29, 30, 36

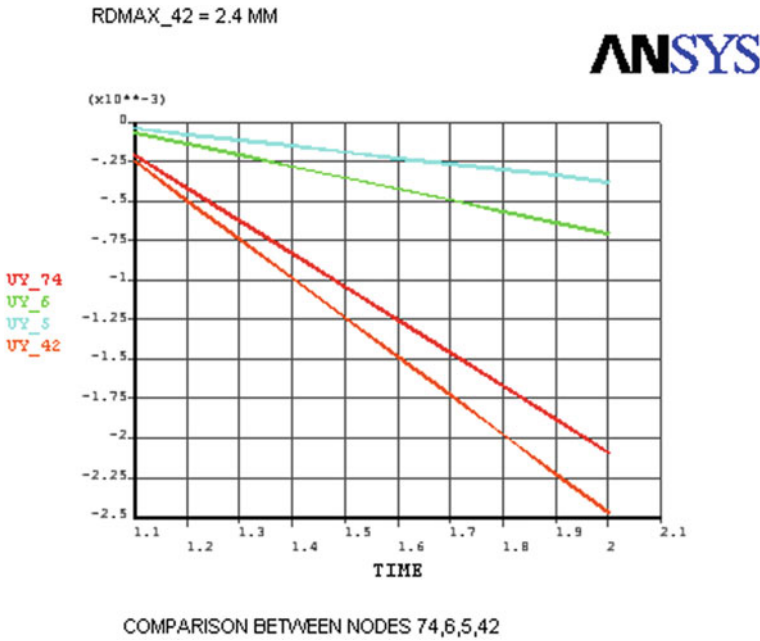


Fig. 8 Rear side impact relative deflection versus time for nodes 74, 6, 5, 42

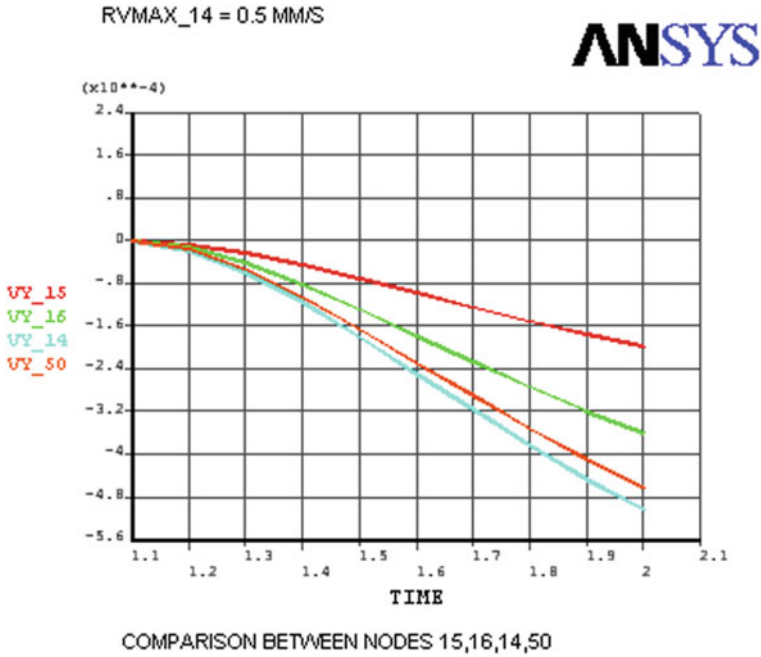


Fig. 9 Rear side impact relative velocity versus time for nodes 14, 15, 16, 50



Fig. 10 Nodal solution for rear side impact

5 Conclusion

The finite element method is used to analyze the impact on the roll cage using ANSYS software. The stability and strength of the roll cage were observed. The model analysis shows that maximum deflection and the maximum velocity for rear impact were found 22.3 mm and 42.5 mm/s, respectively, at nodes 3, 27, 29. Whereas in case of the rear side impact maximum deflection and maximum velocity are 3.5 mm and 1.8 mm/s, respectively, at node 36. The impact from the rear is more dangerous than the rear side impact at the given condition of speed 40 km/hr. Therefore, it is essential to make the roll cage stiffer in case of rear impact than that in case of rear side impact.

References

1. Xie X, Gao F, Huang C, Zeng W (2017) Design and development of a new transformable wheel used in amphibious all-terrain vehicles (A-ATV). *J Terramechanics* 69:45–61
2. Honnagangaiah KN (2006) Design and evaluation of composite car-front subframe rails in a sedan and its corresponding occupant crash injury response (2006)
3. Russo BJ, Smaglik EJ (2015) Analysis of factors affecting injury severity for riders or occupants of all-terrain vehicles and golf carts involved in police-reported crashes. *Accid Anal Prev* 133:105289. Accessed 2019
4. Gray JP, Vantsevich V (2015) V: Multi-vehicle convoy mobility in severe terrain conditions: factor impact analysis, estimation and control strategy. *J Terramechanics* 61:43–61
5. Kader A, Dobos A, Cullinan M (2004) Speed bump and automotive suspension analysis. <http://www.sccs.Swart.edu/users/06/adem/engin/e12/lab4/>. Accessed Aug 2007
6. Roots M, Brown J, Anderson N, Wanke T, Gadola M (1995) The contribution of passenger safety measures to the structural performance in sports racing cars. UK Cranf Univ
7. Silcock MD, Garschke C, Hall W, Fox BL (2005) A novel method of tube manufacture for vehicle crashworthiness utilising the QUICKSTEP™ process. In: SAMPE Europe 2005: proceedings of the 26th international SAMPE Europe conference: nanotechnology assists leadership and success of the composite technology, pp 239–244
8. Genta G (1997) *Motor vehicle dynamics: modeling and simulation*. World Scientific
9. Fischer MP, Kamla T, Wieser A, Waras H, Premstaller R (2001) Coupled multi-body and FE analysis to simulate engine induced chassis vibrations
10. Kelly SG (1996) *Schaum's outline of theory and problems of mechanical vibrations*. McGraw-Hill

Design and Analysis of a Structure to Support Two Star Sensors



S. Rai Rajakumar, X. Ajay Vasanth, I. Kantharaj, and R. Srinivasan

Abstract Composite materials such as carbon fiber reinforced plastics or CFRP for short are finding their way into a variety of uses mainly for space applications. Backed by favorable mechanical properties and high strength-to-weight ratio. Engineers are expanding the use of such composites into day-to-day applications. Apart from composite materials, sandwich structures are also a frequently used material for space applications. The core of these sandwich structures generally honeycomb in nature shows immense shear strength properties but are however weak to concentrated are often used together. This project highlights the use of CFRP skins and aluminum honeycomb-based sandwich structures to design a structure two-star sensor and verify the design by conducting a free vibrations as well as static analysis.

Keywords Honeycomb · CFRP · Sandwich · Two-star sensor · Free vibrations

1 Introduction

The term remote sensing has in the recent past has gained a lot of popularity wherein the data is acquired without any physical contact with the medium. They can be further classified into active and passive remote sensing. In active remote sensing the data is performed from the emission of signals from satellite and then the acquisition of data is carried. In the latter data is acquired by emission of radiation from planetary bodies. These are usually performed by employing a star sensor. Star sensor belongs to the category of smart cameras that takes pictures every ten seconds and the acquired picture will be compared with a catalogue of stars. The on-board computer will be used to identify the orientation of satellite from the above data and the thrusters will be fired is required for changing its path. Reduction of mass has been a major

S. R. Rajakumar · X. A. Vasanth (✉) · I. Kantharaj
Department of Mechanical Engineering, Karunya Institute of Technology and Sciences,
Coimbatore 641114, India

R. Srinivasan
Department of Mechanical Engineering, Sri Krishna College of Technology, Coimbatore 641042,
India

© The Author(s), under exclusive license to Springer Nature Singapore Pte Ltd. 2022
M. K. Singh and R. K. Gautam (eds.), *Recent Trends in Design, Materials
and Manufacturing*, Lecture Notes in Mechanical Engineering,
https://doi.org/10.1007/978-981-16-4083-4_38

485

concern in the design of aircraft and space industries, where every extra kilogram of structural payload will increase the cost to a great deal. A satellite or spacecraft in general consists of two-star sensors mounted on individual support structures. The main objective of this research was to replace two-star structures with a single structure thereby enabling it to carry an additional component. The revised support has to be analyzed for free vibration and quasi-static conditions. The position of the sensors was of concern as the field view should not get affected by the revised structure. The weight of a single two-star sensor will be 6.5 kg and since it was suggested to use a single support it was very important that the modified single support does not increase the weight as they don't do any good in that case.

This made the researchers to look at more efficient structures, due to which, honeycomb structures were proposed as an alternate by Aero Research Limited in 1938 [1]. The main criteria were to use the Honeycomb between two skins, as a shear web. Though it was referred to as a better alternate, adhesive technology was not fully developed to bond skins on to honeycomb, directly. Only after the development of epoxy resin, bonding of aluminum skins with aluminum honeycomb was made possible. Though different configurations of honeycomb structures and different bonding material were put to use, the best combination of both was a tedious process as they depend on the application.

The initial works were carried out to evaluate the effect of failure and material property degradation [2]. A three-dimensional progressive damage model (PDM) was fabricated in this work, where stress analysis, failure analysis, and material property degradation were carried. The combination of failure criteria along with degradation rules influenced in the prediction of failure load. Xu and Qui [3] analyzed natural frequency of composite sandwich beam with lattice like truss structure by using Euler–Bernoulli theory. The composite employed was carbon fiber reinforced composite in a hardened beam and the stacking sequence was 0/45/0/-45/0. It was proposed that natural frequency increased with the increase of core or face thickness, but it was pointed though there was an initial increase it gradually decreased with truss radius and angle increases. Full filling and half filling voids in honeycomb were considered and the better efficient structure was studied [4]. It was observed that foams, visco-elastic and particulate filling in honeycomb voids has improved its damping properties. It was also stated that partial occupation of voids results in minimal density and more damping efficiency, about 60% of improvement was found in damping as energy provides energy dissipation. Investigations on the nonlinear vibrations of composite sandwich plates made of carbon fiber reinforcements and having pyramidal truss core were carried out[5]. It was stated that strut radius and angle of inclination affected the resonance frequency band of sandwich plate. It was also found that the layer number and core height not only had an influence on the resonance frequency band, but also affected the response amplitude significantly. There were several other studies where free vibrations of sandwich plates were carried out[6]. Classic laminated plate theory was used to calculate the natural frequencies of sandwich plate having pyramidal core [7]. From the observation it was stated that traits of variation in natural frequencies and ratios of sandwich plates with different cores were similar.

2 Design Constraints

In order for star sensor to be supported, there were various constraints had to be considered in the designing phase. With respect to space structures, stiffness-based design has to be adopted. The modified structure had to possess a frequency so that it could cope with the frequency that exists during the take off. The proposed design needed to act as a single interface for both star sensors instead of two different structures, and also to be free of any skewed surface to ease the manufacturing process. And the most important was the field of view of star sensor should not be changed but movement along the baffle axis of star sensor was allowable.

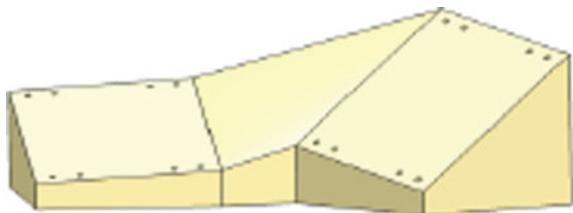
Apart from the reasons mentioned above it is mandatory that mass should be reduced to the maximum extent possible to conserve the amount of fuel. For any space exploration it was desired to keep pay load at its maximum. This can be achieved only by reducing or removing the unwanted mass in the structure. The initial brackets had a mass of 1.1 kg and hence if the modified structure is lower than the value, the main objective will be fulfilled.

3 Conceptual Design of Modified Structure

The models created were looked not only from the perspective of reducing the mass but also from the manufacturing perspective.

The first conceptual model developed is shown in Fig. 1. Though it seemed to serve the purpose it was found that the presence of skewed surface in the middle section developed a stress. Apart from that it required more stiffening which will cause an increase in weight and it also the manufacture would be a tedious process. The second conceptual model (Fig. 2) was too large in volume and thus the weight increased. The presence of skewed surface, small cuts, and non-symmetric geometry made it very difficult to introduce sandwich structure. The next conceptual model (Fig. 3) had projections on its sides which was metallic thereby increasing the weight. The final conceptual model (Fig. 4) met all the desired constraints. It had a larger surface where composites or sandwich structure could be used. Lugs and angles were introduced to increase the stiffness of the body and this conceptual model was used for analysis.

Fig. 1 Model one



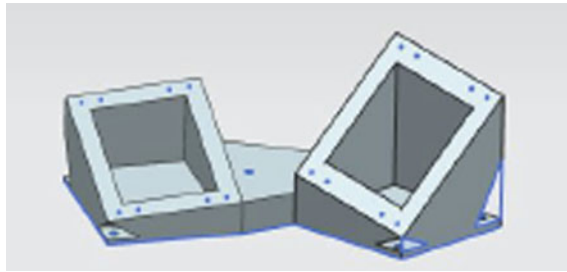


Fig. 2 Model two

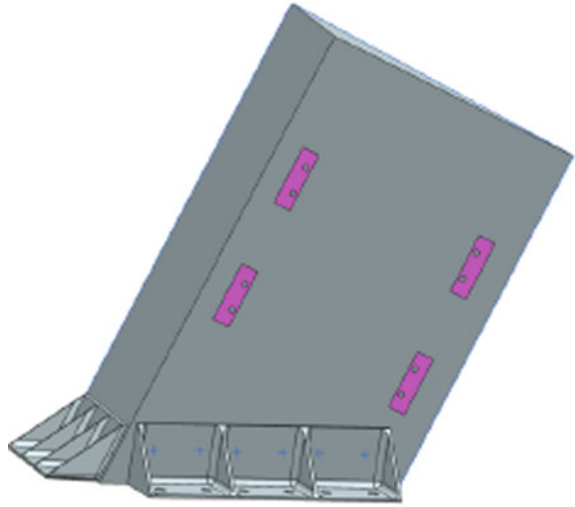


Fig. 3 Model three

4 Computational Analysis

For performing computation analysis NASTRAN was used and the elements were used according to the requirements. CONM-2 a lumped mass system, where point elements were created and associated with 0-D property was used. Multi-point constraints (MPC) were used to join bolting points of the star sensor with 0-D element (Fig. 6). The required material properties were given as per Table 1. Aluminum being an isotropic material was created by using create isotropic option under material

Fig. 4 Final mode



selection. However, aluminum core being a hexagonal structure whose properties vary orthogonally, 2D orthotropic option under material selection was used (Figs. 5 and 6).

The whole base was constrained and all nodes along the perimeter of the base were fixed. Hoffman failure criteria were used to check the efficiency of the design, whether it could withstand the load. Configurations with varying skin thickness and core thickness were suggested during the computational analysis to find the optimum combination. Angle thickness (horizontal and vertical) was maintained as a constant throughout the computational analysis (Table 2).

Table 1 Material properties

Material	Young's modulus (N/m^2)	Poisson's ratio	Shear Modulus (N/m^2)	Density (kg/m^3)
Aluminum face sheet	$7.2 * 10^{10}$	0.33	$27 * 10^9$	2800
Aluminum core	$1 * 10^4$	0.33	$G_{lw} = 1 * 10^4$ $G_{lt} = 1.85 * 10^8$ $G_{wt} = 0.89 * 10^8$	32
CFRP BD	$14.7 * 10^{10}$	0.003	$G_{lt} = 4 * 10^9$	1660

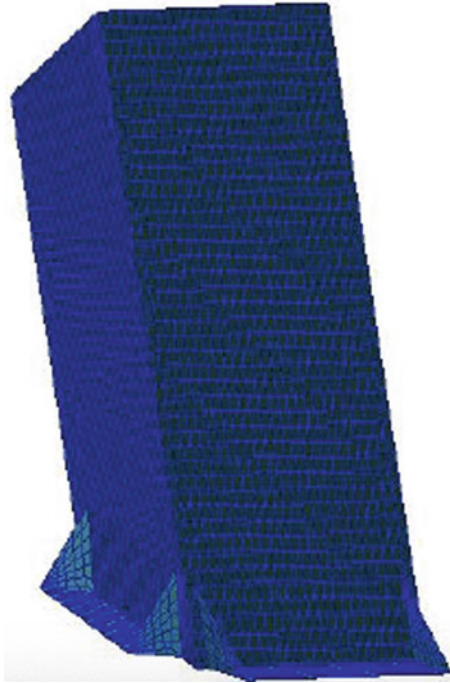


Fig. 5 Meshed structure

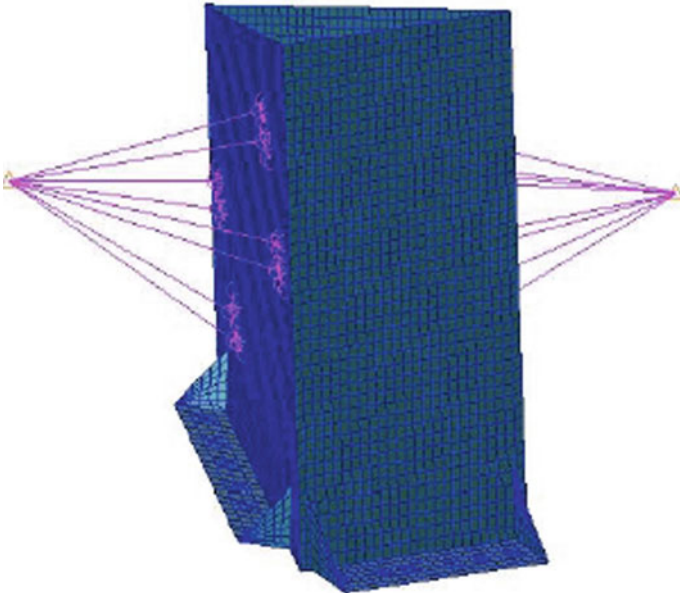


Fig. 6 Applied MPC

Table 2 Parameters varied during computational analysis

Parameters	Varied values
Skin thickness	10 mm, 15 mm
Core thickness	15 mm, 20 mm, 25 mm

5 Results and Discussion

Static analysis was performed out on the modified structure, an inertial load of 20 g was applied in x-, y-, and z-axes, respectively, (Table 3). Failure indices were found by Hoffman criteria.

From Table 3, it can be observed that the failure indices were high in the z-direction. Free vibration test was also performed on the modified structure and its corresponding frequency. From this it can be observed that the highest frequency was present when the skin thickness was 15 mm and core thickness was 20 mm. The main reason for the increase in frequency was due to the increased thickness in both the parameters that resulted in a slight increase in mass. The increase in mass as specified above is infinitely small compared to the conventional structure where a mount is present to support one sensor camera (Table 4).

Table 3 Direction of load and its failure indices

Direction of load	Failure indices
X axis (20 g, 0, 0)	$3.29 * 10^{-2}$
Y axis (0, 20 g, 0)	$6.28 * 10^{-2}$
Z axis (0, 0, 20 g)	$7.35 * 10^{-2}$

Table 4 Free vibration frequency

S. No	Skin thickness		Core thickness (mm)	Angle thickness		Frequency (Hz)
	No. of layers	Thickness per ply (mm)		Horizontal	Vertical	
1	10		15	4	2	105
2	10		20	4	2	110
3	10		25	4	2	115
4	15		15	4	2	108
5	15		20	4	2	116

6 Conclusion


The conventional two-star sensor was modified and a new structure was proposed as an alternate to the existing one. The metallic support of the structures was eliminated by using composite sandwich material. Using Hoffmann criteria it was found that the highest failure indices were present in the z-axis. The vibration frequency was found to increase as skin thickness and angle thickness increased. Though increasing the thickness further may prove to be useful, constraints in manufacturing and the limitation of mass will be prove to be a hindrance. Although the conclusion of this computation work states that there will be increased performance a better understanding and conclusion about the same can be arrived only after the real-time experimentation or real-time simulation work.

References

1. Budd EG (1938) Double-walled sheet metal structure and method of making. US2108795A. (22 Feb 1938)
2. Dano M-L, Kamal E, Gendron G (2007) Analysis of bolted joints in composite laminates: Strains and bearing stiffness predictions. *Compos Struct* 79(4):562–570
3. Xu M, Qiu Z (2013) Free vibration analysis and optimization of composite lattice truss core sandwich beams with interval parameters. *Compos Struct* 106:85–95
4. Boucher M-A, Smith CW, Scarpa F, Rajasekaran R, Evans KE (2013) Effective topologies for vibration damping inserts in honeycomb structures. *Compos Struct* 106:1–14
5. Chen J, Zhang W, Sun M, Yao M, Liu J (2016) Parametric study on nonlinear vibration of composite truss core sandwich plate with internal resonance. *J Mech Sci Technol* 30(9):4133–4142
6. Chen JE, Zhang W, Sun M, Yao MH, Liu J (2018) Free vibration analysis of composite sandwich plates with different truss cores. *Mech Adv Mater Struct* 25(9):701–713
7. Guo Z, Liu C, Li F (2017) Vibration analysis of sandwich plates with lattice truss core. *Mech Adv Mater Struct* 0(0):1–6

Designing and Fabrication of a Device for Automation of the Film Transfer Process in Floating Film Transfer Method



Nitesh Kumar, Gopal Ji , and Manvandra Kumar Singh

Abstract Corrosion of metals is a big problem for the scientists. Corrosion is dangerous for both economy and human lives. There are various methods to save the corrosion losses; however, coating of metals with protective films is one of the most effective methods. For effective corrosion protection, thin and compact film is highly desirable. Floating film transfer method (FFTM) is a unique technique for thin film preparation. FFTM is capable of producing ultrathin films with high quality at economical price, which is its greatest strength. However, some improvements can be done for better accuracy and easiness of the process. FFTM comprises two basic processes: 1, film formation; and 2, film transfer over any required substrate. In this work, we have designed and fabricated a small device to automate the film transfer process in FFTM. The different parts of the device have been designed with simulation software and printed by 3D printing machine. Some additional parts are also used for ensuring smooth functioning of the device. After device fabrication, the utility of the device in FFTM is also illustrated through experiments. The results indicate that the device is serving the purpose for what it is built for.

Keywords FFTM · Corrosion · Thin film · Automation · Device fabrication

1 Introduction

Corrosion of metals not only affects their aesthetic appearance but also destroys their functional properties [1, 2]. This can lead to dangerous situation involving investment and human lives. Hence, corrosion losses must be prevented. There are many methods

N. Kumar · G. Ji (✉)

Department of Mechatronics, Centre for advanced studies, Dr. APJAKTU Lucknow, Lucknow, UP 226031, India

e-mail: gopalji@cas.res.in

M. K. Singh

Department of Mechanical Engineering, Amity School of Engineering and Technology, Amity University, Gwalior, Madhya Pradesh 474005, India

e-mail: mksingh@gwa.amity.edu

© The Author(s), under exclusive license to Springer Nature Singapore Pte Ltd. 2022

493

M. K. Singh and R. K. Gautam (eds.), *Recent Trends in Design, Materials*

and Manufacturing, Lecture Notes in Mechanical Engineering,

https://doi.org/10.1007/978-981-16-4083-4_39

that are used for corrosion prevention. Coating of metals with protective layer is one of the most powerful methods for corrosion prevention [3, 4]. However, coating protection highly depends on film quality. For effective corrosion protection, thin and compact film of protective material is preferred [5]. There are many methods for thin film production; however, cost and instrumentation are big problems in use of them. FFTM is a unique method of producing thin film with high quality at the economic price [6, 7], which successfully overcomes the restriction of cost and instrumentation of complex processes.

FFTM comprises two simple processes: first is film formation and second is film transfer [8]. Film formation is based on surface energy gradient. For film formation, two solutions are selected. Out of which, one should be hydrophilic and other should be hydrophobic (volatile). The material that is to be casted as film is dissolved in volatile solution. Then, one drop of that solution (volatile solvent material) is casted over hydrophilic solution. Due to difference in surface energies, the film is formed and spread over hydrophilic solution. A schematic of the process is shown in Fig. 1. γ_1 is surface energy of hydrophilic solution, γ_2 is surface energy of hydrophobic solution and γ_{12} is interfacial surface energy. S is spreading coefficient, which is

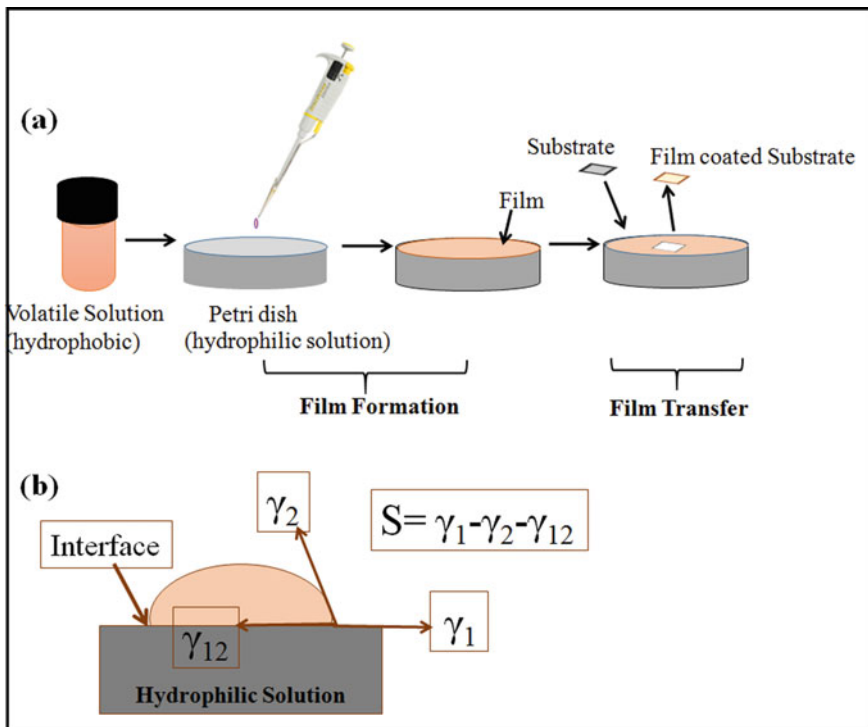


Fig. 1 a A schematic illustration of floating film transfer method and b Basics of film formation process

very important parameter. The film will be formed only if S is greater than zero. Once the film is formed, it can be transferred to any substrate via manual stamping in conventional FFTM.

In this work, a device is designed and fabricated for the automation of film transfer process in FFTM. Some components of the device are purchased, and some are designed and printed by 3D printing machine. After device fabrication, the experiments are done to show its usefulness. The results of the experiments strongly indicate that device is working and can add improvement in FFTM.

2 Experimental Details

2.1 Device Fabrication

Different parts of the device like rack, pinion and casing (Fig. 2) were printed by 3D machine (MakerBot, Replicator+). The 3D printing details are: material, poly lactic acid (PLA); bed temperature, 210 °C; nozzle, 0.4 mm; pattern, honeycomb; and infill density, 75%. The 3D design and technical parameters of the components are given in Table 1.

Some of the components like 8 bit microcontroller (Arduino Uno R3), potentiometer and servo motor (Futaba S 3003) were purchased from the local electronics market and used directly in the device. The proposed design of the device is given in Fig. 3.

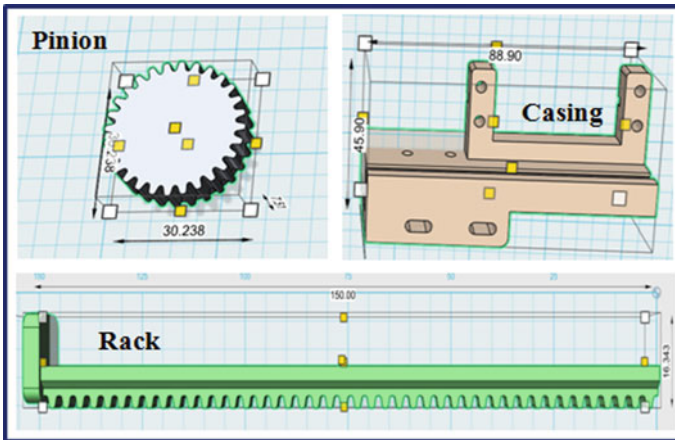
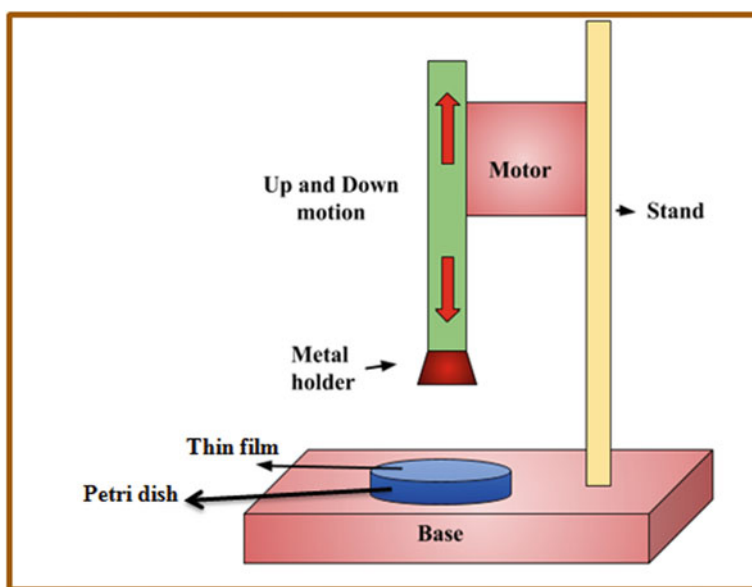


Fig. 2 Autodesk123D software image of the rack, pinion and casing of the device

Table 1 Design parameters of the rack, pinion and casing of the device

Parameters	Values	Parameters	Values	Parameters	Values
Length	150 mm	Diameter	30.23 mm	Length of the casing	88.90 mm
Width	3.81 mm	Angle	35.5°	Distance between post	40.50 mm
Loop Length	10.276 mm	Number of teeth	28	Width	39.25 m
Angle	22.6°	Distance between teeth	1.03 mm		
Distance between teeth	1.368 mm	Width	5.58 mm		
Number of teeth	44	Loop length	13.982 mm		
Rack		Pinion		Casing	

**Fig. 3** Proposed design of the device

2.2 Film Formation and Transfer

In our work, water is taken as hydrophilic solution (high surface energy) and acetone is selected as hydrophobic solvent (low surface energy). For demonstration purpose, camphor is used to form the film. An amount equal to 250 mg of camphor was dissolved in 20 mL of acetone. A 100 μL of thus prepared solution was cast on water

filled (up to 3/4th height) petri dish (Fig. 1). The floating film was formed on the top of water within seconds.

As in convention FFTM, the film transfer is done via manual stamping. In this work, the film transfer process was done by the fabricated device. A glass slide was hold between grippers provided in the device and moved toward petri dish by potentiometer. As soon as glass slide touched the film, the device was stopped. Afterwards, reverse motion was started and glass slide coated with camphor film started to go up. Thus film was transferred over glass slide. The whole process is discussed in results in detail.

3 Results and Discussion

This section is divided into two sections for discussing results obtained in this work. First part is related with the fabrication, and second part is about improvement of film transfer process in FFTM.

3.1 3-D Printed Components and Fabricated Device

The 3D components were printed as per their design parameters and are shown in Fig. 4.

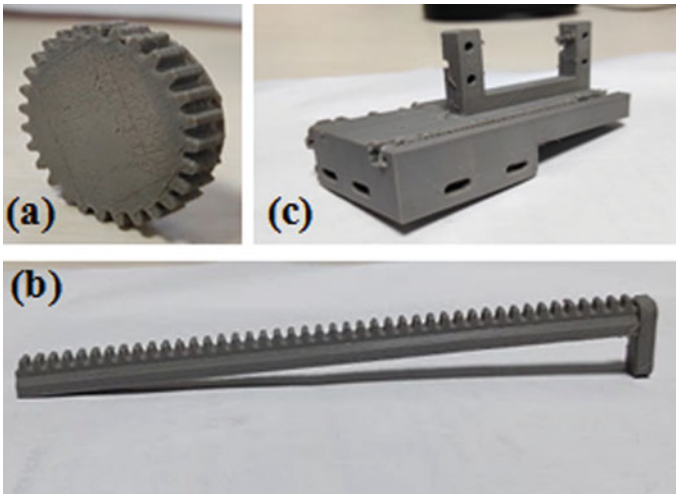


Fig. 4 3D printed **a** pinion, **b** rack and **c** casing of the device

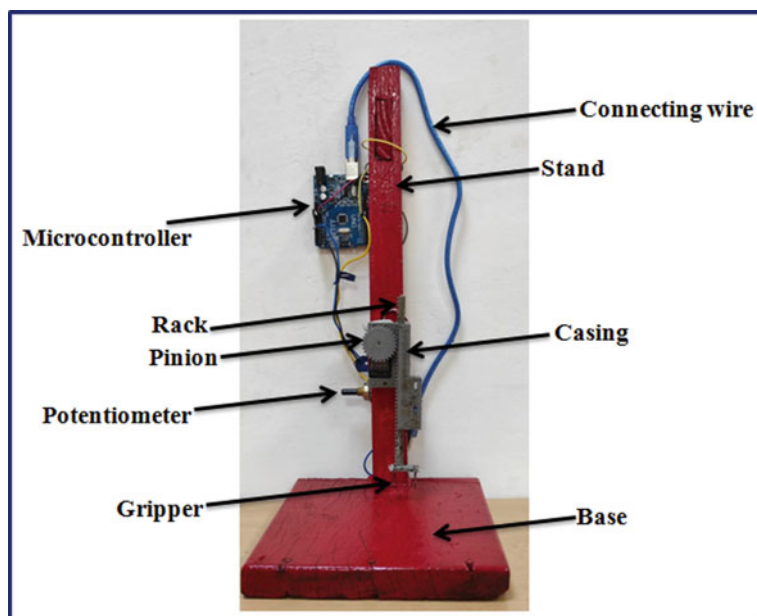


Fig. 5 Photographic image of fabricated device

Apart from these printed parts, some parts like wooden base, Arduino Uno R3, potentiometer, iron wires for gripping and wires for connection were purchased from the local market. All these parts were assembled to fabricate the device. The fabricated device is shown in Fig. 5.

This fabricated device was used for the improvement of film transfer process in FFTM.

3.2 Film Formation and Transfer

The film formation was performed by FFTM. For forming a film, few drops of the camphor-acetone solution were cast on the water substrate. A film of camphor is formed on the top of water substrate within few seconds. The mechanism of film formation is already explained and given in Fig. 1b. The surface energies of water and acetone are 72 mN m^{-1} and 25.2 mN m^{-1} , respectively [8]. The interfacial surface energy of water-acetone at room temperature is 30.8 mN m^{-1} . In this case, S will be equal to 16 mN m^{-1} that is clearly greater than zero. Hence, film is formed.

After the film formation, the transfer of the film over glass slide was done with the help of the fabricated device. The glass slide was gripped mechanically with the help of iron wires. Then, the device was made to move towards water surface through potentiometer of this device. The potentiometer was attached with Arduino



Fig. 6 Photographic images captured during film formation and transfer process

Uno and accordingly programmed for up and down movement of the rack. As soon as glass slide touched the film formed over water substrate, the potentiometer was stopped, did wait for few seconds and then moved in opposite direction. Thus, the rack gently touched the film and film is transferred over glass slide. The whole process is explained through Fig. 6. Thus, it was clear that the fabricated device was extremely helpful in film transfer process.

4 Conclusion

The problem of corrosion can be eliminated by coating of protective material on metals. For this, thin and compact film is required, which is the guaranteed output of FFTM. In conventional FFTM, the film transfer is manual. So, we have tried to automate this process in this work. The present work is focused on fabrication of a device for automation of the film transfer in floating film transfer method. The device is designed and successfully fabricated with 3D printed parts and purchased parts. After fabrication, the device is successfully used for automated film transfer. Hence, it is clear that the fabricated device is working well. This can speed up the FFTM and its accuracy. In the near future, we are also planning to prepare polymer films coated metal substrates using this device and to test them against corrosion.

Acknowledgements Nitesh wants to thank Dr. A.V. Ullas, Dr Piyush Jaisawal (Both from CAS Lucknow) and faculties of Mechatronics Department in CAS Lucknow.

Conflict of Interests Authors have no conflict of interests.

Availability of Data and Material Data will be available on request.

Authors Contribution Nitesh has performed all the experiments under supervision of Dr. Gopal Ji. Dr. Manvendra Kuamr Singh has helped in writing of the manuscript.

References

1. Srivastava M, Tiwari P, Srivastava SK, Kumar A, Ji G, Prakash R (2018) Low cost aqueous extract of *Pisum Sativum* peels for inhibition of mild steel corrosion. *J Mol Liq* 254:357–368
2. Ji G, Anjum S, Sundaram S, Prakash R (2015) *Musa Paradisica* peel extract as green corrosion inhibitor for mild steel in HCl solution. *Corros Sci* 90:107–117
3. Pandey RK, Yadav SK, Upadhyay C, Prakash R, Mishra H (2015) Surface plasmon coupled metal enhanced spectral and charge transport properties of poly(3,3'-dialkylquarterthiophene) Langmuir Schaefer films. *Nanoscale* 7:6083–6092
4. Pandey RK, Upadhyay C, Prakash R (2017) Self-assembly of solution-processable polyindole via langmuir-blodgett technique: an insight to layer-dependent charge transport and electronic parameters. *Chem Select* 2:6009–6015
5. Mishra R, Nirala NR, Pandey RK, Ojha RP, Prakash R (2017) Homogenous dispersion of MoS₂ nanosheets in polyindole matrix at air-water interface assisted by Langmuir technique. *Langmuir* 33:13572–13580
6. Soeda J, Matsui H, Okamoto T, Osaka I, Takimiya K, Takeya J (2014) Highly oriented polymer semiconductor films compressed at the surface of ionic liquids for high performance polymeric organic field-effect transistors. *Adv Mater* 26:6430–6435
7. Pandey RK, Singh AK, Prakash R (2014) Directed self-assembly of poly(3,3'-dialkyl quarter thiophene) polymer thin film: effect of annealing temperature. *J Phys Chem C* 118:22943–22951
8. Pandey RK, Mishra R, Ji G, Prakash R (2019) Corrosion prevention of commercial alloys by air-water interface grown, edge on oriented, ultrathin squaraine film. *Sci Rep* 9:1–12

Filter Design for Radar Signal Analysis Using Field Programmable Gate Array



Anil Kumar Sahu, Abhishek Singh, and Harish Kumar Shakya

Abstract Today's RADAR applications such as in the military and surveillance require the real-time processing of signals and with higher accuracy and resolution. Analysis of data from high-speed RADAR is a significant problem. The Von-Neumann processors commonly used for signal processing are limited in time-sensitive applications due to their serial instruction streams. The FPGA architectures are popular choice for the realization of high-speed designs, which are time critical in nature. Here, FPGA Virtex-6 is used as the core for implementation. When radar signals travel long distances, their strength decreases and noise starts to occur, which makes the analysis of data from such signals difficult. To reduce noise, we use the AD9652 and design an FIR BPF filter. This paper introduces the architecture, characteristics and the fundamentals of digital filters and provides an efficient way of FPGA-based implementation of the filter design for RADAR signals. MATLAB tool has been involved to calculate the filter coefficient, and design a filter in the VHDL language and inspect the output in Chipscope using the Xilinx ISE tool. We received +12 dB gain in signal-to-noise ratio of Radar system.

Keywords RADAR · FPGA · DSP · Signal processing · FIR · Xilinx · MATLAB

A. K. Sahu (✉)
Bharat Institute of Engineering and Technology, Hyderabad, India

A. Singh
Variable Energy Cyclotron Centre, Kolkata, India
e-mail: singhabhishek@vecc.gov.in

H. K. Shakya
Amity University Gwalior, Gwalior, Madhya Pradesh, India
e-mail: hkshakya@gwa.amity.edu

1 Introduction

It is well known that the echoes received from the RADAR target get affected by the interference from environmental noise by the spreading from the air particles and other RF signals, which share a common transmitted RF spectrum [1]. Thus, it is most important to clean up the received signal by improving its signal-to-noise ratio. Most common method is to implement a matched filter circuit whose main function is to give optimal signal-to-noise ratio at the output for a given noise signal [2]. In a matched filter design by knowing the received pulse shape, it is possible to realize a matched filter such that its impulse response matches the transmitted pulse shape [3]. In this way, the received pulse echoes experience very low noise, and all the pulses will be accurately identified by the threshold detection process [4].

RADAR signal processing is done to reinforce the received noisy signal submerged in the noise and interference from a wide bandwidth. The pulse RADAR signals are of wider bandwidth compared to the CW RADAR signals, so the noise is added over a larger spectrum in the received signal [5]. In this work, the received RF pulsed signal is down converted to the lower spectrum of IF frequency and is then filtered by a digitally implemented bandpass filter [6]. The filter implemented on FPGAs is tuned to the received signal bandwidth, so that the superfluous noise can be filtered out easily and thus improve the SNR (signal-to-noise) of the pulse received. The IF signal is then captured inside the FPGA using a high sample rate digitizer [7] and then passed through a band-pass digital filter whose pass band should match [8] the pulse train bandwidth. This method is unique from the matched filter implementation in which the input signal determines the impulse response of the filter [9]. Since, this is not the optimum filter design approach like in a matched filter response, some of the noise will always be present in the output signal [10]. So the standard optimum SNR at the output will not be achievable as in the container of matched filter response [11].

2 Methodology

2.1 Architecture

The system architecture is drawn in Fig. 1. It represents the receiver part of the RADAR system. The echo signal returning to the assortment of the RF signal will be converted into a relatively low IF signal with the help of super heterodyne and a local oscillator. The super-heterodyne type receiver provides excellent sensitivity and very little conversion loss in detection. Figure 2 shows the experimental block system design for RADAR Signal Analysis.

This generated IF signal is then delivered to the AD9652, an analog-to-digital converter (ADC), whose output is usually in the format of offset binary. The AD9652 will be configured using some registers of the AD9652 to convert its output to a

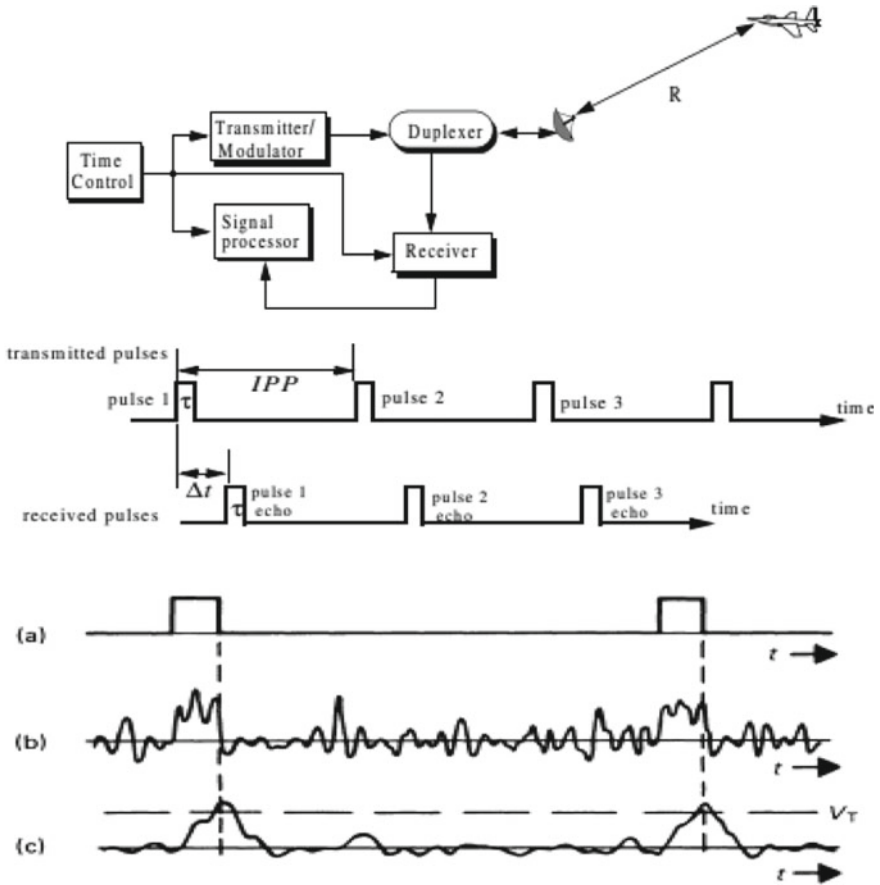


Fig. 1 RADAR Block Diagram with a Transmitter Pulse and b Receiver Pulse with noise and c Received pulse without noise

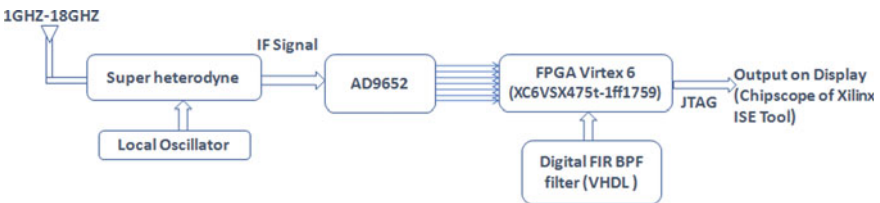


Fig. 2 Experimental blocks for RADAR signal analysis

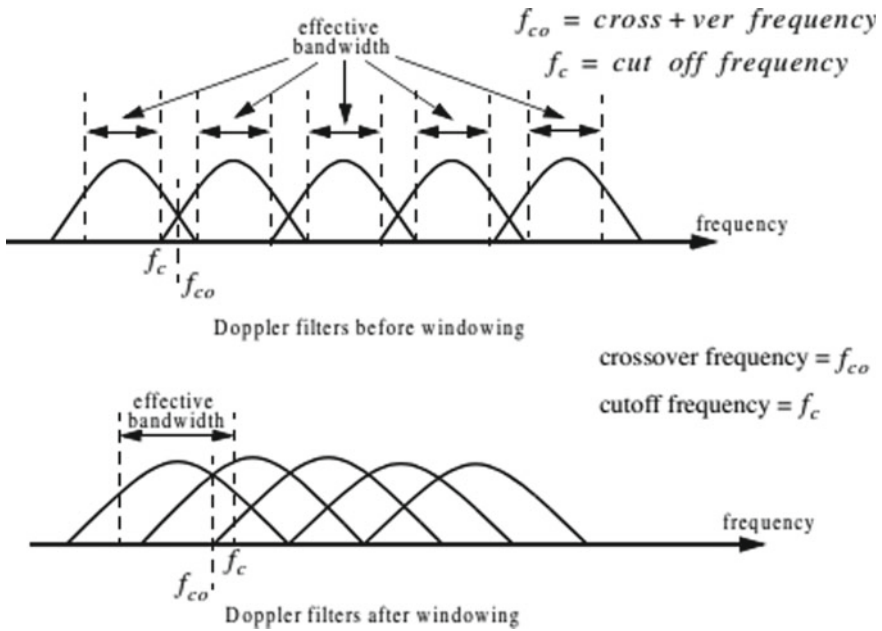


Fig. 3 Windowing for Doppler Filter

complement of two in a data format acceptable by the FPGA. The FPGA handles incoming data, and the BPL filter is preloaded with filter coefficients of any number of four different filters initially generated in the MATLAB FDA tool. The resulting waveform can be tracked into the system with an Ethernet cable after all necessary processing and noise reduction in the signal.

The Doppler channel stride goes like the entryway ride. Be that as it may, for this situation, the Doppler channel range is extended (wide) because of burden capacities. Holding up capacities are normally used to diminish side projection levels. Figure 3 shows windowing for Doppler channel. Since from the objective Doppler recurrence can fall any place between two Doppler channels, the sign there is a misfortune. This is appeared in Fig. 3, where because of the bundle, the hybrid recurrence is littler than the channel cutoff recurrence, which regularly compares to the 3 dB power point.

2.2 A Filtering of Signals

Signal separating implies the preparing of signals by adjusting their conduct in the recurrence space, for the most part to dismiss lower and higher recurrence meddling signals.

To reduce noise content in RADAR signal, we reduce the bandwidth of the receiver using a bandpass filter and a digital FIR filter to improve SNR of RADAR signal.

The signal-to-noise (SNR) ratio at the input of the BPF filter can be expressed as the signal power to the mean value of thermal noise power as follows:

$$\text{Signal to Noise Ratio} = \text{Signal power/Noise power} = S/kBwT \tag{1}$$

where, k is the Boltzmann’s constant = $1.38 \times 10^{-23} \text{ JK}^{-1}$, T = temperature in Kelvin and Bw the bandwidth of the system in Hz.

The structure of a FIR BPF channel depends on boundaries: the data transmission, or cut-off recurrence, the length, N and examining recurrence determined utilizing equation given as indicated follows:

$$2f_c - b/m > f_s > 2f_c + B/m + 1 \tag{2}$$

The FIR filter equation is given as follows:

$$y[n] = b_0x[n] + b_1x[n - 1] + \dots + b_Nx[n - N] \\ = \sum_{i=0}^N b_i \cdot x[n - i], \tag{3}$$

whereas, x[n] represent input signal; y[n] called the output signal for N is the filter order; bi is the value of the impulse response at the i’th instant for $0 < = i < = N$ of an th-order FIR filter.

The AD9652 is a double, 16-piece ADC, with inspecting velocities of up to 310 MSPS, underpins fast sign preparing with extraordinary powerful range over a wide information recurrence run (up to 465 MHz). It underpins input clock frequencies of up to 1.24 GHz. Two registers of AD9652 utilized are appeared in Table 1.

Table 1 Registers of AD9652

Register	Register name	8 bit Data	Function
0X08	Power modes	Bit 0–0 Bit 1–0 Remaining bits zero	Power control in normal operation
0X14	Output mode	Bit 0–0 Bit 1–1 Remaining bits zero	Configure the outputs and the format the data into two’s complement

3 Results and Discussion

3.1 *FPGA Virtex 6 (XC6VSX475T-1FF1759) Utility Target Device*

Results can be verified by one family of FPGA Virtex 6 SXT, which has high signal processing capability. Figure 4 shows FPGA and MATLAB interface. It has in-built error correction and detection, DSP481E slices that consist of accumulator, multiplier (which performs AND, OR logic functions and Barrel Shifting), supports Ethernet MAC up to 25,000 mbps and operates at 1.2–2.5 V.

Figure 5 shows input signal with noise, and Fig. 6 represents input signal passed through 10 MHz filter, Fig. 7 shows input signal passed through 5 MHz filter. Figure 8: input signal passed through 2.5 MHz filter respectively.

When the input signal is applied to FIR BPF filter of 2.5 MHz, the signal to noise ratio increases by +12 db. Hence, the noise reduces to large extent compared to the one without filter. All these outputs are observed in Chipscope of Xilinx ISE tool, and the resultant RTL schematic is also observed in Xilinx ISE Tool as shown in



Fig. 4 FPGA and MATLAB interface

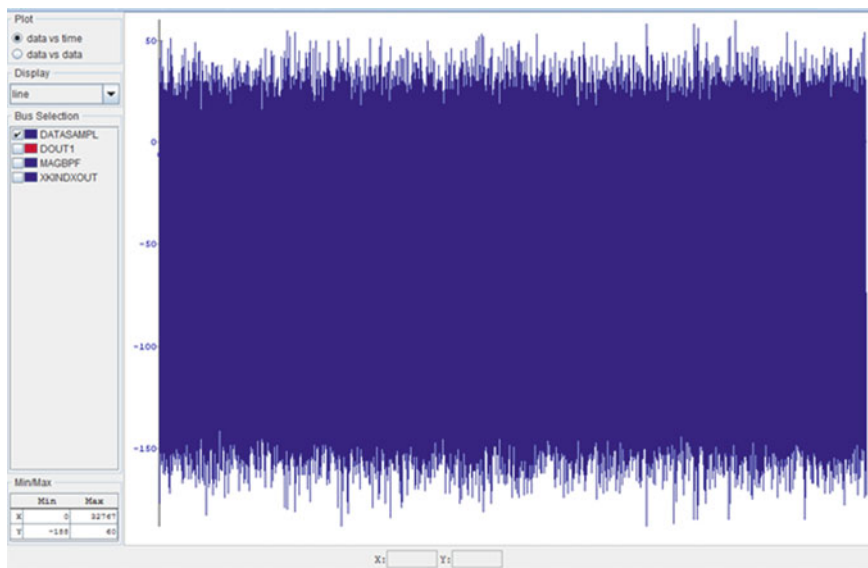


Fig. 5 Input signal with noise

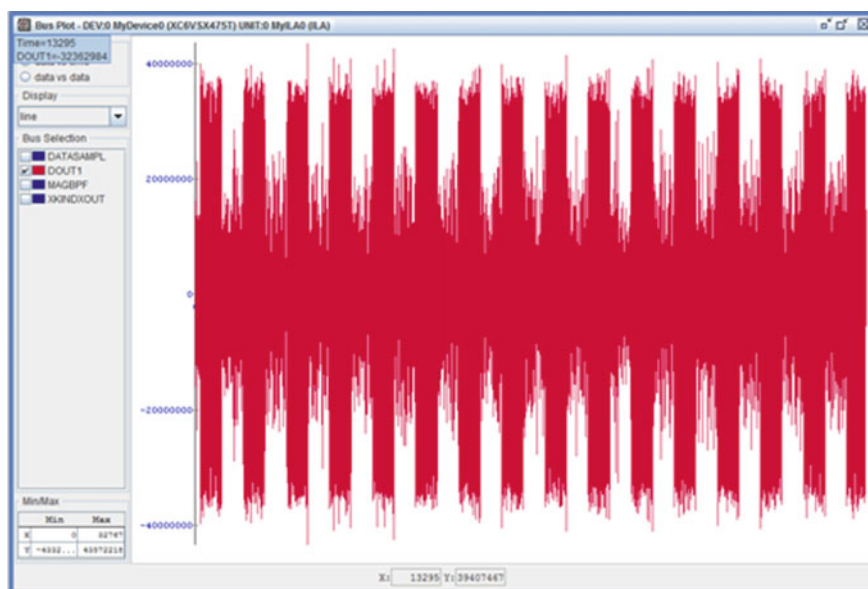


Fig. 6 Input signal passed through 10 MHz filter

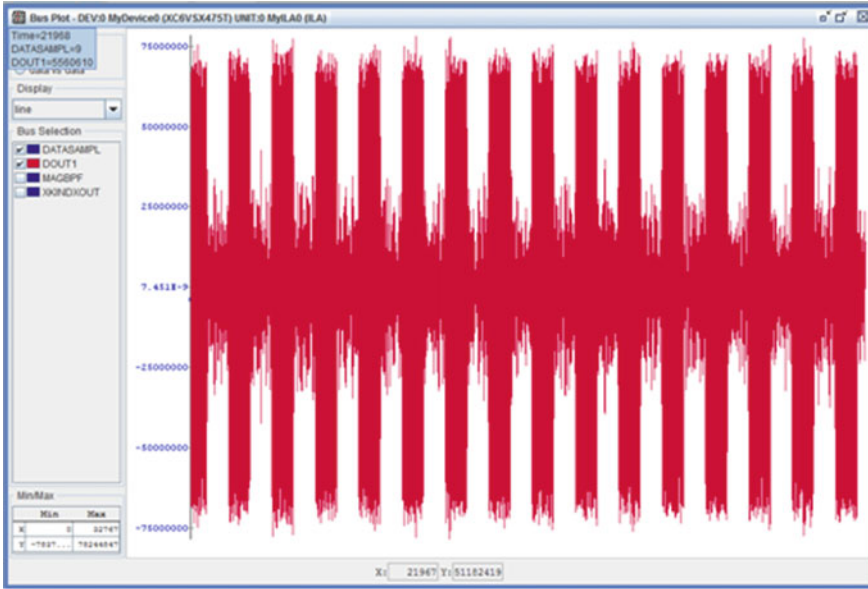


Fig. 7 Input signal passed through 5 MHz filter

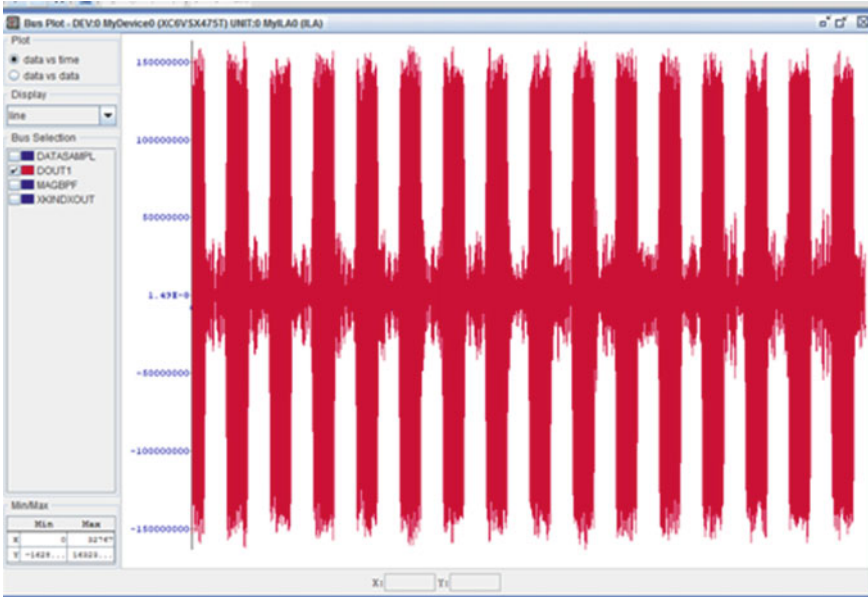


Fig. 8 Input signal passed through 2.5 MHz filter

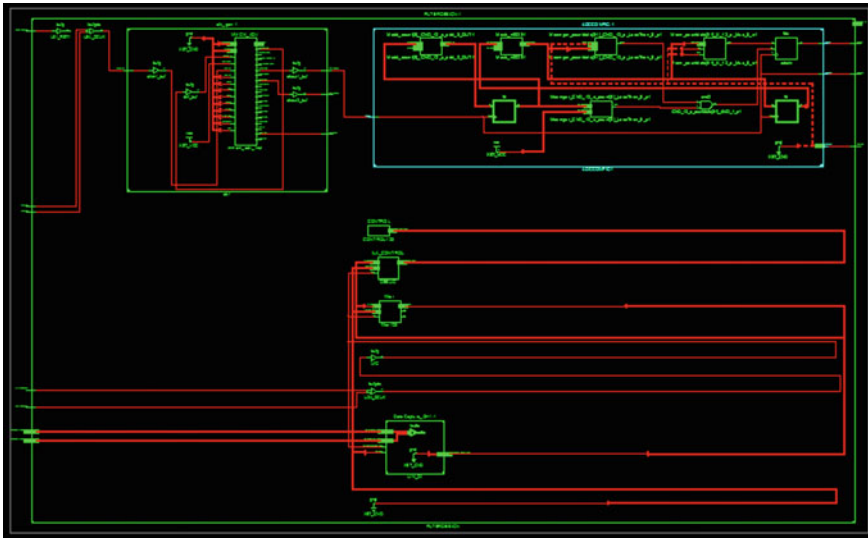


Fig. 9 RTL Schematic view of BPF FIR filter

Table 2 Performance comparison with previous works

Reference number	FPGA used	ADC	Signal strength (IN dBm)	RADAR pulse frequency	Sampling frequency (MHz)	Gain in dB
Zhang et al. [1]	EPIK30TC144	AD9057	0	10 kHz	5.12	+6 dB
This work	XC6VSX475T-1FF1759	Ad9652	-53	160 MHz	210	+12 dB

Fig. 9. Table 2 gives the detailed comparison of previous work with our proposed works. In these works, +6 dB more gain has been received.

4 Conclusion

It has been concluded from the above results that the RADAR receiver has achieved high performance by detecting a weak signal and strengthening the signal by improving the SNR by designing a FIR BPF and AD9652. In this work filter has been analyzed for high speed data rate by using FPGA Virtex 6 (XC6VSX475T-1FF1759) and observe the results in Chipscope using Xilinx ISE 14.7 Tool. Digital filters are implemented in a flexible way where the coefficients can be programmed and changed when required to implement filters of specific requirements on user selection. We have received +12 dB gain.

References

1. Zhang, S Y, Zhang L, Gong Y (2019) An FPGA-based pulse integration system to improve the SNR of radar echo Chengchang. *Int. J. Circ. Syst. Signal Process.* 13 (2019). ISSN: 1998-4464
2. Lakshmaiah MV, Pakardin G, Thimmaiah P (2014) *Int J Sci Eng Res* 5(8). ISSN 2229-5518
3. Aye MM, Thandar Aung T (2016) Digital filters for RADAR signal processing. *Int Res J Eng Technol (IRJET)* 03. e-ISSN: 2395-0056 p-ISSN: 2395-0072
4. Ashwini R, Venkataratnam Ponnu (2017) Design of digital FIR filter for RADAR application. *Int J Innov Res Sci Eng Technol* 6(9). ISSN: 2319-8753
5. Raffo A, Costanzo S, Di Massa G (2017) Software defined doppler radar as a contactless multipurpose microwave sensor for vibrations monitoring. *Sensors* 17(115). [CrossRef] [PubMed]
6. Ding L, Ali M, Patole S, Dabak A (2016) Vibration parameter estimation using FMCW radar. In *Proceedings of the IEEE international conference on acoustics, speech and signal processing (ICASSP)*, Shanghai, China, 20–25 Mar 2016
7. Nieh CM, Huang TY, Lin J (2014) Antenna radiation pattern effects on a short-range vibration-detection radar system. In: *Proceedings of the 2014 international symposium on antennas and propagation conference proceedings*, Kaohsiung, Taiwan, 2–5 Dec 2014
8. Xiong Y, Peng Z, Xing G, Zhang W, Meng G (2018) Accurate and robust displacement measurement for FMCW radar vibration monitoring. *IEEE Sens J* 18:1131–1139
9. Sahu Anil K, Sahu Arvind K (2019) Low transconductance OTA based active comb filter for biomedical applications. In: Luhach A, Singh D, Hsiung PA, Hawari K, Lingras P, Singh P (eds) *Advanced informatics for computing research. ICAICR 2018. Communications in computer and information science*, vol 956. Springer, Singapore. https://doi.org/10.1007/978-981-13-3143-5_12
10. Sahu AK, Chandra VK, Sinha GR, Misra NK (2020) Efficient CTDSM based on GM-C quantiser and improved dynamic element matching. *IET Circuits Devices Syst* 14(5):680–685
11. Misra NK, Wairya S, Singh VK (2014) Preternatural low-power reversible decoder design in 90 nm technology node. *Int J Sci Eng Res* 5(6):969–978. ISSN: 2229-5518

A Greener Framework for Start-Up Involving Order Management



R. Akaash, S. Aswin, M. Jayashuriya, Enoch Somana,
and S. P. Anbuudayasankar 

Abstract Start-ups begin small with the goal of becoming a larger corporation. Success in the start-up field comes through a strong idea, sufficient funding, a great cooperative work ethic and a clear vision. Companies nowadays focus on growth and market expansion, but leave behind sustainability as a long-term goal, this is due to a lack of awareness of measures to reduce the environmental impact of emerging markets. The study's goal is to demonstrate how to create a long-term framework for starting a business. A scenario-based case study is performed involving an order management startup in a primetime location with a multi-pronged, efficient approach towards delivery of orders whilst being an employee-friendly, eco-friendly, pro-technology environment. An in-depth framework for order management is provided. Pick-up and delivery route optimization are performed using Multi Integer Linear Programming (MILP) in MS-Excel for two different scenarios with respective constraints and other details. Finally, the inferred details on how the optimization has reduced distance traveled thereby reducing fuel consumption are discussed. The paper gives a pedagogy on how a startup with the necessary attributes can be sustainable and successful at the same time.

Keywords Start-up · MILP · Optimization · Sustainable · Framework · Order management · Shortest distance

1 Introduction

As the world is trying to weather one storm after another, it is of utmost importance that we start to act upon the wishes of our mother. Apart from the significant economic benefits, going green encourages renewable energy consumption, which gives time and nurtures the depleted natural resources. Humans being at the top of the chain are more accountable than any other being, the steps towards a sustainable and renewable

R. Akaash · S. Aswin · M. Jayashuriya · E. Somana · S. P. Anbuudayasankar (✉)
Department of Mechanical Engineering, Amrita School of Engineering, Amrita Vishwa
Vidhyapeetham, Coimbatore 641112, India
e-mail: sp_anbu@cb.amrita.edu

© The Author(s), under exclusive license to Springer Nature Singapore Pte Ltd. 2022
M. K. Singh and R. K. Gautam (eds.), *Recent Trends in Design, Materials
and Manufacturing*, Lecture Notes in Mechanical Engineering,
https://doi.org/10.1007/978-981-16-4083-4_41

511

future can range from a drop to an ocean. People as a whole must strive to make the world better for our future generations. An entrepreneur is a starter or initiator who creates something new, like an initiative, a business, or a company. The entrepreneur might not be the idea creator, but he or she is the one that decides to make that idea a reality, to achieve and be part of this reality an entrepreneur must understand the ever-fleeting and ever-developing market whilst coping up and satisfying customer needs [1]. An entrepreneur who can inculcate a new aspect of customer needs without depending on personal experiences is deemed to be successful [2]. Entrepreneurship is an ideology or a mindset of walking against the odds and making things happen. Key values of Entrepreneurship are: Ability to take risk, Innovation, Vision, Open-mindedness, Flexibility, and Intuition. More often start-ups fail because of deviation of the team from these values.

A start-up is any company founded by an entrepreneur to solve real-world problems, develop products, provides services using technology or other resources giving rise to a Scalable Economic Model. Start-ups start small with the goal of becoming a large corporation. A start-up can be formed by a team of as little as one member. Success of a start-up often revolves around having a strong idea, co-operative team, sufficient funding, and a long-term vision. Start-up business ventures are also affected by the advisers who work with them. Start-ups that do not have co-operative role-players are affected due to the lack of decisive decision-making thereby causing a wide range of problems during the buildup process [3]. Start-ups have high growth potential, hence investors come forward to fund their ideas.

Start-up sphere in India is booming. The Department for the Promotion of Industry and Internal Trade (DPIIT) has acknowledged over 27,916 start-ups, as of February 1, 2020. Bangalore also known as Silicon Valley of India is known for its start-ups [4]. With government initiatives like Start-up India and Make in India supporting their growth, start-ups in India have better chances of being a success.

India being a developing country has immense scope for start-ups. Intriguingly, India has undergone a metamorphosis to become a juggernaut developer of start-ups owing to its rising economy, per-capita income, and the overall purchase power parity of its citizens. The steering ideas have a drizzling start but an outburst growth. Some interesting trends to be noted include the shifting of the start-up boom outside the top-tier cities; evolution of new ideas; emergence of new B2B start-ups, and greater inflow of investment from around the World. All these indicators point to a maturing of the start-up ecosystem and an entrepreneurial story that will gain pace in the future.

Technology growth has been tremendous within the past decade, so has been people's desire to get things done easily. With start-ups providing services for an easy lifestyle, people can now focus on other things leaving the tedious work for the service-providing companies. The business model of these companies works on the nature of people to desire an ease in lifestyle. One of the main aspects of a laid-back lifestyle is the customer getting whatever they need at their doorstep. For this to occur efficiently, the delivery companies have to deliver the products in the fastest possible manner, in the least possible time. A pivotal aspect for this to work is a delivery management network with proper and highly coordinated dispelling and organization of transferors through a group of junctions that require delivery

[5]. There are numerous such companies in the space of logistics, FMCG, food and beverages, professional services.

In general, companies provide services and make life easy, but many do not emphasize sustainability, leaving behind enormous amounts of carbon footprints. The problem lies in the lack of awareness of measures to reduce environmental impact. In order to give an elaborate elucidation on how emerging organizations could minimize the detrimental effects on environment, this case study of a service start-up is enkindled. The purport of this study is to demonstrate a sustainable framework for creating an order management-related start-up that includes conceptual summarization, a high level of quantification emphasis, and consideration of the constraints of a developing market [6].

2 Establishing a Start-Up

Logistics, generally, is the term associated with the enterprises that happen within the limits of a corporation. To build a successful corporation, its roots must be strong and deep and the root from which every corporation grows is a start-up. A start-up that is coming up the ladder cannot have a “passing the buck” approach, as it is not the hallmark of a sustainable business model [7]. So, an efficient start-up with the right pieces leads to a successful corporation. The start-up that is considered here, functions in the day-to-day order delivery management market. This market, in general, is highly competitive and heavily thronged, hence maintaining an edge over the competition is the need of the hour. This start-up tackles the competition with a multi-pronged fork, it operates using zone-based location division. Base of the company is order centric. With an initial work on order management and temporary base set in Chennai,

Tamil Nadu, India as listed below which is further elaborated in Fig. 1, the day-to-day operations are managed.

- a. W1—Velachery
- b. W2—Besant Nagar—Adyar
- c. W3—Neelankarai
- d. W4—Mylapore
- e. W5—Vadapalani

Being in a prime-time area is another added advantage. As mentioned above, the current base of operation is a temporary one, after careful consideration of the volume and quality of orders, the company might choose to expand with the same base of operation or relocate to a better market.

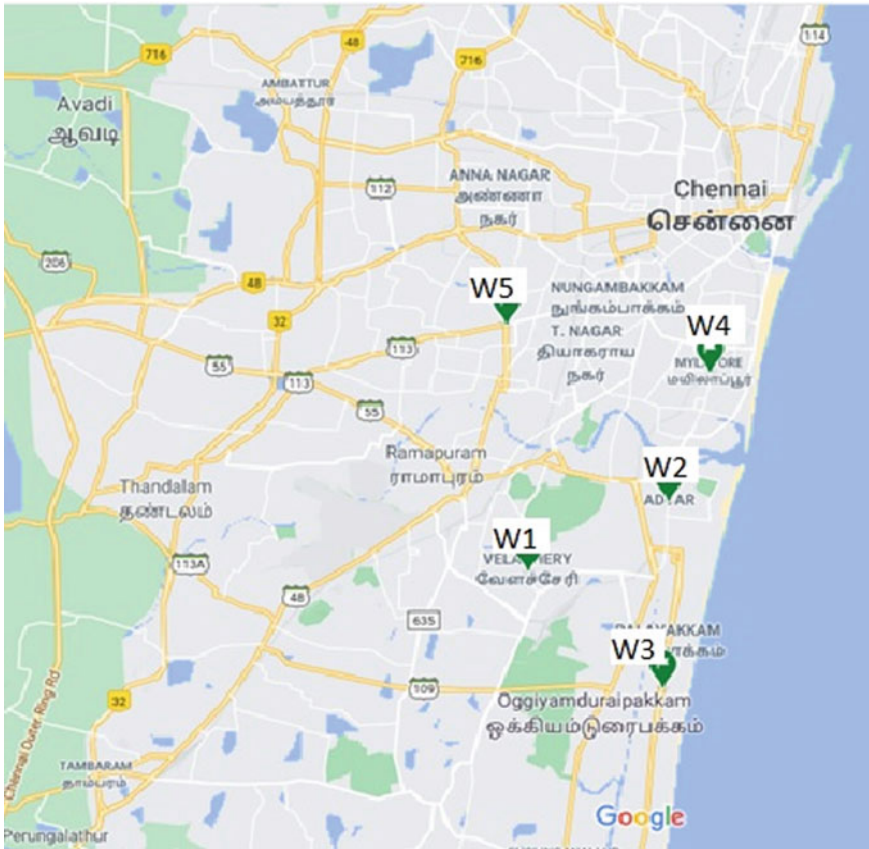


Fig. 1 Location of Warehouses across Chennai, India [18]

2.1 Maintaining the Edge Over Competition

The company employs a multipronged approach to beat the heat of the market; this involves efficient order management. Order tracking happens with the help of a real-time analysis. Once the order received is pertained to be pharmaceutical or medical in nature, it is immediately scanned in reference to the prescription. Scanning of such packages can be performed via a built-in scanner in the app. In order to avoid delay in delivery of packages, GPS is used for real-time tracking. Affiliation with local businesses as trusted partners will result in the elevation of the company’s stature, will provide a more holistic approach, will also dispense extensive resources and an array of product lines at subsidized rates. The company being a deep-rooted endowment will tolerate no compromise in “on-time delivery”. All these attributes will not only benefit the start-up but will also ennoble the entire market. Customer satisfaction will be another top priority as it acts as the major fuel for the company’s further expansion.

2.2 Employee Management

Employees are paid on a credit-based system wherein credits are awarded based on how many deliveries they complete in a month. Employee work hours are flexible, they can work either part-time or full time, and compensation will be provided during peak and heavy order hours. Best performing transferors are identified through an efficiency rating system provided by the customer (this is based on the satisfaction of the customer) and are provided bonuses.

2.3 Transportation

Green Vehicle Routing Problem (GVRP) is given importance in the current market as happens to be the perfect amalgamation of both environmental sustainability and the economic standpoint in harmony [8]. It promotes a symbiotic relationship between the start-up and its surrounding market by optimizing delivery routes, which, in turn, reduces fuel consumption and environmental degradation whilst keeping in mind the economical aspect of carrying out the operation [9]. The entire fleet of vehicles is categorized into either rental or vehicles owned by the company. All the bikes owned by the company are Compressed Natural Gas (CNG) powered, which is not the case for the rented ones. The employees are provided with “CNG Fuel Cards”, which is the product of a joint venture between the start-up and a government-aided bank. The same card is used for refueling both rental and owned delivery vehicles. For the cards assigned to the owned vehicles, after the fuel amount is debited, a specific number of green credits are added proportionally to the quantity of CNG consumed. This is done to promote and create awareness to use green fuel sources, which, in turn, results in a cut back in the levels of carbon emission throughout the network thereby leading to a sustainable supply chain [10].

2.4 Marketing Strategies

As a brand new start-up, it is pivotal to have a competitive market strategy in order to create a niche in this fleeting market. The following are the strategies that are put into work towards developing a brand name.

- Free service for three orders of the day, picked via lucky draw.
- Promo code will be provided for an order within 10 kms, this code can be used for the next order provided it happens within the next 5 days.
- For orders above ₹2500, the next order has no delivery charges.
- Regular customers will be given access to a redeemable wallet through which they can participate in a cashless transaction.

- For orders above ₹1000, along with their package, the customers are provided with a sampling, encouraging them to participate in our greener environment initiative.

2.5 Framework for Order Management System

Planning is the parent of any successful operation. Likewise, for the start-up to be successful and to create its own niche, it must collectively follow a meticulously laid out framework. For a company starting its stride in the order management market, it is necessary to inculcate an efficient transfer of information and goods. The entire network of pickup and delivery junctions must be latticed [11]. The following framework, Fig. 2, gives an overview of transfer of information in a delivery management start-up.

The four pillars of converting an order into a successful delivery include acquisitions, carrying out the task, dispatching and fulfilling customer needs [12]. The chain starts when the order is received from the customer through the application through which the delivery address of the order is obtained and verified. Using the Order Management System, the product details are obtained and are cross-referenced to find a suitable product pickup address. Following this, details of the transferor in the vicinity of the pickup address are obtained [13]. Using Google Maps, the shortest route for pickup and delivery is calculated, simultaneously the information about the product is intimated to the pickup store through pre-defined suppliers. The key here is to identify the balance between cost, punctuality, and the advancement in route optimization for the delivery vehicles of the company [14].

The transferors are given GPS access to guide them to the delivery address, all the while optimizing their routes in accordance with traffic and other delays. Finally, once the product is delivered to the concerned location, a delivery confirmation is sent both to the customer and the overseeing authority, invoice and other details regarding the transaction are uploaded to the database. After this, the status of the transferor is updated, and he/she is ready for the next pickup delivery.

3 Methodology

Linear programming gives the highest or the lowest values to the linear objective function, which is subjected to one or more limitations. Mixed Integer Programming (MIP) goes a step ahead and gives one more constraint, which states at minimum one of the values must be an integer [15].

The three main excerpts that define vehicle routing are decisions, objectives, and constraints. In general, networks are strongly based on design and strategical optimization [16]. MILP concerns with predicaments where some values are limited to integers while others can be non-integer values. Here the programming outputs

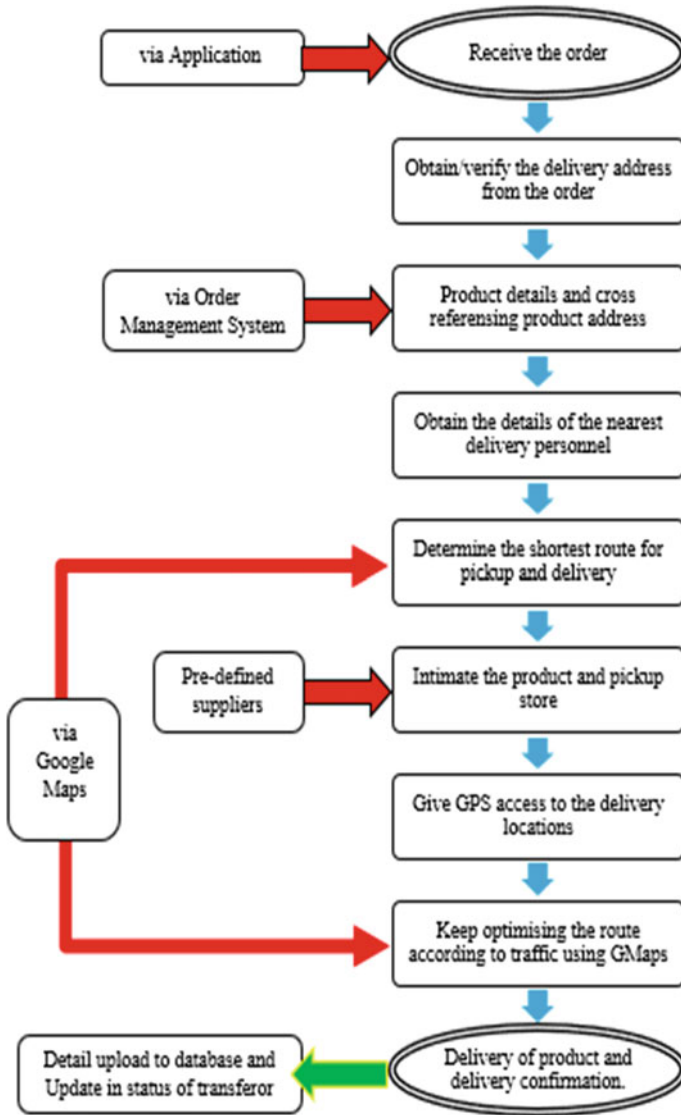


Fig. 2 Order management framework

are being restricted to be either 0 or 1. The optimization problem is created as an extensive MILP predicament with binary values for selection and load assignment of impedimenta.

4 Scenarios

To apply the theoretical concepts of linear programming and route optimization into a real-time situation and understand the changes, they bring upon to the original results, a couple of scenarios are considered. This is to provide a fourth wall perspective to the existing order management framework. It is of utmost importance to consider scenarios in areas that are networkable. This will result in a comprehensive calculation process making it more applicable for future estimations.

4.1 Scenario 1

Here, a scenario where an order is received from D1 (Alandur). The nearest warehouse to this area is situated in W1 (Velachery). Hence, W1 becomes the base of operation in this case. The pick-up stores (P1 = Apollo Pharmacy, P2 = Spencer's Hyperstore, P3 = A.P Broilers, P4 = Pet Universe) are first notified about the required package. The start-up has taken in contracts with these stores that are in the vicinity of the warehouse. This collaboration is to ensure that the ordered items are available at discounts and that the delivery of the products is at the earliest. This also ensures the amount of fuel consumed is minimal and the customers value the delivery system. The details regarding these locations and their respective distances are listed in Table 1.

As discussed above, the orders were received from areas in and around W1 (initial constrain). The data were inputted in excel along with order locations. Then the respective distances were obtained through Google maps and were noted. The inputted data are processed through the solver. The first step of data processing includes fixing the objective function to reduce the separation distance (distance between the two places). This is followed by where the variable cells are fixed as order values. Finally, cell references are added and constraints are fixed as the order column values (excluding similar permutations).

4.2 Scenario 2 at a Glimpse

Here, the first order is obtained from D1 (Marudeeswar Nagar). So, the nearest warehouse of W2 (Besant Nagar—Adyar) is chosen. The product order of meat, pastry, and pet items (P2, P3, P1, respectively) is confirmed, and the transferor is sent to complete the order. Before the order is completed, the order management system updates another customer nearby who needs pastry, groceries, and medicine (P3, P4, P5, respectively). Delivery locations on the picked course are updated along with newly obtained ones, which will all be delivered based on the order acquired

Table 1 Shortest distance calculation using MILP—Scenario 1

Location	Velachery	Pet shop	Grocery	Meat	Pharmacy	Alandur	Assigned location after optimization	Order of delivery	Distance of travel
1	Velachery	0	2	0.1	0.7	0.5	Velachery	1	0.5
2	Pet shop	2	0	1.3	1	1.5	Pharmacy	5	0.6
3	Grocery	0.1	1.3	0	0.7	0.6	Grocery	3	0.7
4	Meat	0.7	1	0.7	0	2.5	Meat	4	1
5	Pharmacy	0.5	1.5	0.6	2.5	0	Pet shop	2	1.6
6	Alandur	3.8	1.6	4	4.5	2.3	Alandur	6	
1	Check Velachery	1	1					Total Distance (km)	4.4



Fig. 3 a Geographical locations of warehouse and pickup areas for scenario 1 [18], b dynamic locator of transferor for scenario 1

through route optimization [17]. The transferor order is then updated with the second delivery point being D2 (Thiruvannamur). At this juncture, the transferor can deliver the goods under two different scenarios. Details regarding these locations are marked in Fig. 3.

Scenario 2.1

The orders were received from areas in and around W2 (initial constrain) and have to be delivered to D1 (Marudeeswarar Nagar) and D2 (Thiruvannamur), deliver to D2 being the final constraint. The data were inputted in excel along with order locations. Following this, the respective distances were obtained through Google Maps and were noted. The details regarding these locations and their respective distances are listed in Table 2. The inputted data were processed through the solver. The first step of data processing being, setting the objective function to cut down the separation distance, then by changing the variable cells into the values of the order column. Then adding cell reference and constraints, the constraints being again the values of the order column (similar permutations excluded). In this scenario, the transferor completes the delivery in a systematic fashion. Details regarding these locations are marked in Fig. 4.

Scenario 2.2

The orders were received from areas in and around W2 (initial constrain) and have to be delivered to D1 (Marudeeswarar Nagar) and D2 (Thiruvannamur) deliver to D1 and D2 being the ultimate and penultimate constraints. The data were inputted in excel along with order locations. Similar to what was performed in Scenario 2.1, the respective distances were obtained through Google Maps and were noted. The details regarding these locations and their respective distances are listed in Table 3.

Table 2 Shortest distance calculation using MILP—Scenario 2.1

Location	Adyar-Besant Nagar	Pet shop	Grocery	Meat	Pharmacy	Pastry	Marudeeswarar Nagar	Thiruvannamur	Assigned location after optimization	Order of delivery	Distance of travel
1 Adyar-Besant Nagar	0	0.2	2.4	1.4	1.9	1.5	2.5	3.5	Adyar-Besant Nagar	1	0.2
2 Pet shop	0.2	0	2.5	1.7	2.3	2	2.8	3.7	Pet shop	2	1.7
3 Grocery	2.4	2.5	0	1	0.3	1.1	0.3	2.5	Meat	4	0.3
4 Meat	1.4	1.7	1	0	0.6	0.3	0.9	2.6	Pastry	6	0.8
5 Pharmacy	1.9	2.3	0.3	0.6	0	1.2	1	2.2	Marudeeswarar Nagar	7	0.3
6 Pastry	1.5	2	1.1	0.3	1.2	0	0.8	2.1	Grocery	3	0.3
7 Marudeeswarar Nagar	2.5	2.8	0.3	0.9	1	0.8	0	2.4	Pharmacy	5	2.2
8 Thiruv-anmayur	3.5	3.7	2.5	2.6	2.2	2.1	2.4	0	Thiruvannamur	8	
1 Check Adyar		1	1							Total distance (km)	5.8



Fig. 4 a Geographical locations of warehouses and pickup areas for scenario 2.1 [18]. b Dynamic locator of transferor for scenario 2.1

The inputted data were processed through the solver. The first step of data processing being, setting the objective function to cut down the separation distance, then by changing the variable cells into the values of the order column. Then adding cell reference and constraints, the constraints being again the values of the order column (similar permutations excluded). In this scenario, the transferor picks up all the orders and delivers them accordingly. Details regarding these locations are marked in Fig. 5.

5 Results and Discussion

From the above research, a framework for setting up an order management firm with a sustainable ideology was established. The idea of sustainability revolves around reducing carbon emissions by minimizing the traveling distance by Operations research models. The following Table 4 gives a comparison between optimized and unoptimized distances.

MILP is used for reducing the distance traveled by the employees. After reviewing both the scenarios, it is evidently seen that the distance to be traveled achieved by MILP is significantly lesser than the distance to be traveled without optimization. Through a quantitative analysis of MILP, it is found that the travel distance reduces by almost 50%, which also implies 50% reduction in fuel consumed. The case study shows three different scenarios of travel, and all the scenarios show a reduction in travel distance when MILP methodology is implemented.

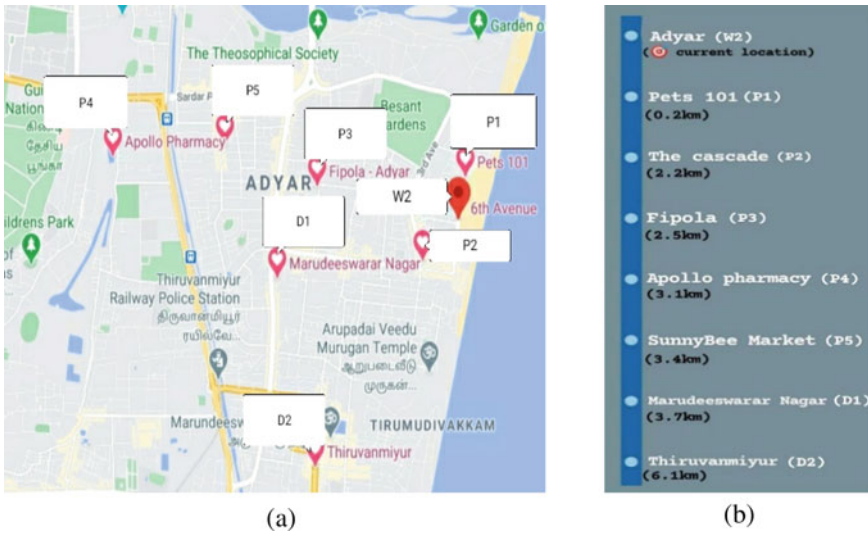


Fig. 5 a Geographical locations of warehouses and pickup areas for scenario 2.2 [18]. b Dynamic locator of transferor for scenario 2.2

Table 4 Comparison of distances without and with optimization

Scenario	Distance without optimization (km)	Distance with optimization (km)
1	10.9	4.4
2.1	10.3	5.8
2.2	13.7	6.1

6 Conclusion

This paper involves the premise of establishing a start-up in the order management and delivery market. It gives a detailed overview of the tribulations of such an organization. The exegesis provides the details on current, day-to-day marketing strategies employed to capture market shares along with providing a framework for order management, all the while keeping in mind the environmental and sustainability aspect of developing such an enterprise. A brief and concise methodology is imparted on how the pickup and delivery route location could be optimized, to reduce fuel consumption. Two different scenarios of order pickup and delivery are analyzed, the difference between the distance of the route taken by a particular transferor before and after optimization is evidently highlighted and inferred. Alternate methods to create sustainable order management companies are suggested and discussed.

Measures must be taken to reform current events and reduce carbon footprint. Humans as residents of the top chain are starting to be accountable by identifying alternate and clean fuel sources and inculcating it in our delivery system. Delivery

start-ups have commenced to use Gobar gas and CNG instead of pumping their vehicles with crude. What is being done might not be big, but it has definitely brought up an anomaly in the commercial corporate world. The changes must begin at the grass-root level to produce stronger ripples.

If people start doing what is right by them instead of doing what they want the world would be a better place for all. Here is to our small step, which will potentially be a big leap for a sustainable mankind. The future of route optimization and thereby reducing the fuel consumption looks immensely promising. What this paper has outlined is just the tip of the iceberg. The scenarios that are considered were solved using Microsoft Excel software, and it reduced the fuel consumption by a considerable amount. So, with a dedicated laboratory environment and a crew, this route optimization program can be stimulated for a larger number of nodes, which will cover longer distances with denser networks, simultaneously, achieving mind-boggling optimization levels. This kind of research can result in a bug free, error free, route optimization application that can be put into use not only just by delivering management conglomerates but also by the common man.

References

1. Taskin Gumus A, Fuat Guneri A, Keles S (2009) Supply chain network design using an integrated neuro-fuzzy and MILP approach: a comparative design study. *Exp Syst Appl* 36(10):12570–12577
2. Tengoh Robertson K (2013) A business survival framework for african immigrant-owned businesses in the Cape Town Metropolitan Area of South Africa. *Art Mediterranean J Soc Sci* 4(13):247–260
3. Schick H, Marxen S, Freimann J (2002) Sustainability issues for start-up entrepreneurs. Greener Management International, University of Kassel, Germany
4. Inc42.com. <https://inc42.com/features/30-startups-to-watch-the-startups-that-caught-our-eye-in-february-2020/>. Accessed 18 Sept 2020
5. Anbuudayasankar SP, Ganesh K, Mohandas K (2008) Mixed-integer linear programming for vehicle routing problem with simultaneous delivery and pick-up with maximum route-length. *Int J Appl Manage Technol* 6(1):31–52
6. Anwer Arshi T, Venkoba R, Sardar I, Swapnil M (2020) SECURE—a new business model framework for measuring start-up performance. *J Entrepr Emerg Econ* (2020) (In Press). <https://doi.org/10.1108/JEEE-02-2020-0043>
7. Anbuudayasankar SP, Ganesh K, Lenny Koh SC, Mohandas K (2009) Clustering-based heuristic for the workload balancing problem in enterprise logistics. *Int J Value Chain Manage* 3(3):302–315
8. Sruthi A, Anbuudayasankar SP, Jeyakumar G (Dec 2019) Energy efficient green vehicle routing problem. *Int J Inform Syst Supply Chain Manage* 12(4):27–41
9. Bergset F (2015) Green start-ups – a new typology for sustainable entrepreneurship and innovation research. *Journal of Innovation Management (JIM)* 3(3):118–144
10. Anbuudayasankar SP, Ganesh K, Lenny Koh SC, Mohandas K (2010) Unified heuristics to solve routing problem of reverse logistics in sustainable supply chain. *Int J Syst Sci* 41(3):337–351
11. Tajik N, Tavakkoli-Moghaddam R, Vandana B, Meysam Mousavi S (2014) A robust optimization approach for pollution routing problem with pickup and delivery under uncertainty. *J Manuf Syst* 33(2):277–286

12. Dachyar M, Zufri L (2016) Improving order management system in pump industry. *ARPN J Eng Appl Sci* 11(7):4917–4923f
13. Ganesh K, Narendran TT, Anbuudayasankar SP (2014) Evolving cost-effective routing of vehicles for blood bank logistics. *Int J Logist Syst Manage* 17(4):381–415
14. Liu J, Wei Liu Y-L (2014) Express company's vehicle routing optimization by multiple-dynamic saving algorithm. *J Indus Eng and Manage* 7(2):390–400
15. Mixed Integer Programming, Chapter 482, NCSS Statistical Software module [online], https://ncss-wpengine.netdna-ssl.com/wp-content/themes/ncss/pdf/Procedures/NCSS/Mixed_Integer_Programming.pdf, last accessed 2020/09/27.
16. Yokoyama R, Hasegawa Y, Ito K (2002) A MILP decomposition approach to large scale optimization in structural design of energy supply systems. *Energy Convers Manage* 43(6):771–790
17. Zhang Y, Chen XD (2014) An optimization model for the vehicle routing problem in multi-product frozen food delivery. *J Appl Res Technol (JART)* 12(2):239–250
18. Google Maps. <https://www.google.com/maps/place/Chennai,+Tamil+Nadu/@13.0474878,80.0689252,11z/data=!4m5!3m4!1s0x3a5265ea4f7d3361:0x6e61a70b6863d433!8m2!3d13.0826802!4d80.2707184>. Accessed 25 Sept 2020

Tribology

Prediction of Brake Pad Wear Using Various Machine Learning Algorithms



John Jeyaraj Steffan, Immanuel Johnraja Jebadurai ,
Lazarus Godson Asirvatham , Stephen Manova , and Jeffrey Pon Larkins

Abstract The present study deals with the prediction of brake pad wear using four different algorithms, namely, Regression tree, Linear Regression, Support Vector Regression and Support Vector Machine. The experimental data obtained from the pin on disc wear tester are considered for the analysis. The effect of frictional force, load and RPM on the amount of wear is predicted using four different algorithms. Initially, the amount of wear is predicted by varying the frictional force from 3.5 to 11 N with constant rpm of 200, 300 and 400, and further, the amount of wear is also predicted by varying the rpm from 600 to 1300 with constant frictional force of 20 N. The results showed that an average percentage deviation of 3.65, 1.37, 1.5, 1.52% is observed for the former and a percentage deviation of 2.15, 0.42, 0.75 and 0.75% for the latter for Regression tree, Linear Regression, Support Vector Machine and Support Vector Regression algorithms, respectively, when compared with that of the experimental results. It is also observed that the linear regression algorithm showed a minimum root mean square error (RMSE) value of 0.002088 and 0.03549 for both analyses, respectively. Based on the obtained results, a mathematical model is also developed to predict the amount of wear as a function of frictional force, load and rpm. It is also found that the developed model agrees well with the published literature with a deviation of ± 1.12 and $\pm 0.40\%$ for both the analyses, respectively. Hence, it is suggested that the proposed model is useful in predicting the actual life of brake pad for various heavy commercial vehicles.

J. J. Steffan · I. J. Jebadurai

Department of Computer Science Engineering, Karunya Institute of Technology and Sciences,
Tamil Nadu, Coimbatore 641114, India

e-mail: steffanjohn@karunya.edu.in

L. G. Asirvatham (✉) · S. Manova

Department of Mechanical Engineering, Karunya Institute of Technology and Sciences, Tamil
Nadu, Coimbatore 641 114, India

e-mail: godson@karunya.edu

S. Manova

e-mail: manovas@karunya.edu.in

J. P. Larkins

IMARTICUS Learning Institute, Tamil Nadu, Chennai 600 029, India

© The Author(s), under exclusive license to Springer Nature Singapore Pte Ltd. 2022

529

M. K. Singh and R. K. Gautam (eds.), *Recent Trends in Design, Materials
and Manufacturing*, Lecture Notes in Mechanical Engineering,

https://doi.org/10.1007/978-981-16-4083-4_42

Keywords Brake pad wear · Prediction · Algorithm · Machine learning · Regression

1 Introduction

Automobile industry is considered as one of the world's largest economic sectors by revenue and contributes about 7.5% of India's Gross Domestic Product (GDP). Particularly, the production rate of commercial vehicles such as Sports Utility Vehicles (SUVs) and Multi Utility Vehicles (MUVs) has increased by 30% in the year 2019. The combination of flexible seating arrangements, space requirements and high power in a compact frame makes these commercial vehicles more attractive from end-user's perspective. Despite having good quality parts in these commercial vehicles, every individual component has its own fatigue limit. Particularly, in the braking system, the components such as brake pads, brake disc and brake fluid have a particular limit up to which they can be used. As the brake pads and the brake disc are under continuous wear, it is considered to be a major threat to the end users as the brake pad wear leads to brake failure.

The performance of the braking system for these modern commercial vehicles depends mainly on emergency braking ability and its operational safety. To ensure good braking ability, Antilock Braking System (ABS) is being employed, which increases the stability and steerability of the vehicles. The main objective of ABS is to attain the maximum braking power by avoiding wheel slip. Due to this high braking power, the wear rate in the brake pads also increases and it leads to brake failure. Even though many research works have been carried out to improve the life of brake pads, the prediction of wear rate without doing real-time experiments is still a great challenge. Thus, the prediction of wear rate, thereby to know the life of brake pads is considered to be of great interest in today's automobile industry. Very few works have been done to predict the wear rate by considering the stopping distance and temperature as input parameters. Various machine learning techniques such as Artificial Neural Networks (ANN), Linear Regression etc., are used in the existing works to predict the wear rate of the brake pads. However, the study on brake pad wear monitoring using frictional force and RPM as input parameters remains undone in the open literatures. Thus, the present work deals with the prediction of brake pad life by considering its wear rate based on frictional force, load and RPM, thereby proposing an efficient algorithm for brake pad wear monitoring. Some of the most productive works that deal with prediction and improvement of braking performance are listed as follows.

Rohilla et al. [1] compared the performance of ABS without controllers and with controllers such as P, PI, PD, PID and observed that the performance of the braking system is improved by all controllers, but PID controller gives the best result by significantly reducing the stopping distance and minimizing the stopping time. Quantitatively, the stopping distance for ABS without controller is 56.3364 m at a stopping time of 3.3284 s and with PID controller is 42.6188 m at a stopping time of 2.9514 s.

Xiao et al. [2] simulated a model to enhance the performance of ABS using fuzzy controller for different road conditions. It was stated that higher adhesion coefficient between wheel and the surface results in a smaller change in slip ratio. In addition, the fuzzy controller can effectively improve the braking performance thereby maintaining the optimum slip rate of 0.2. Zhang et al. [3] studied the performance of ABS in three axle rigid truck. Model of the truck was built in ADAMS/Car software, and Matlab/Simulink was used for the logic threshold control Antilock Braking System. The simulation was carried out in three arrangements, which included six sensors and six solenoid valves, six sensors and four valves, four sensors and four valves. The simulation results obtained using logic threshold control are found to be effective as it reduces the stopping distance and maintains the adhesion coefficient above 0.75 with ABS. The authors have also stated that the arrangements with six sensors six valves and six sensors four valves have an advantage in longitudinal braking performance and the one with four sensors four valves has better lateral performance. Aparow et al. [4] proposed a simulation work for developing a ABS using vehicle longitudinal model (VLM). A 5 degree of Freedom (5-DOF) VLM was built. Several handling tests such as sudden acceleration and sudden braking tests have been performed to authenticate the vehicle model. This model has been used to design a PID controller for controlling the longitudinal slip and reducing the stopping distance. Two control loops have been used based on cascade control system. The primary or outer loop controller is used to control the vehicle model's brake torque, and the secondary or inner loop controller is used to control the hydraulic model of the brake. A performance comparison has been done with P, PI, PD and PID controllers. It has been stated that the use of PID controller in ABS shows lower maximum overshoot of 0.25–0.3, shorter settling time of 3 s and less significant steady state errors. Chetan et al. [5] have suggested a method of using a machine learning algorithm to calculate the brake pad wear based on the stopping distance. Parameters such as vehicle speed, braking force and load on the vehicle are assumed to be constant for all the trials. Multivariate linear regression was used to identify the relationship between stopping distance and the brake pad thickness. As the plot was parabolic, a second-order curve was fit to the data. The author formulated this relationship such that the brake pad wear can be determined by giving the stopping distance to the model. It was also stated that the parameters that were assumed to be constant, will not be constant in real-life applications and higher-level machine learning algorithms can be used to relate the two parameters. Kareem et al. [6] developed an Artificial Neural Network (ANN) for predicting wear and temperature in a pin-disc contact. It was stated that any change in the load, speed and temperature can have a significant effect on the wear rate of the material. Experiments and predictions were carried out with steel and aluminum pads to determine the effect of pressure and rotational speeds on wear and temperature rise. An ANN model with five neurons in the input layer, eight and seven neurons in the first and second hidden layers, respectively, and three neurons in the output layer was developed to predict the wear and final temperature of the pad and disc. Szczypinski et al. [7] have done a research work focused on the estimation of coefficient of friction of brake pad and disc during braking of a vehicle with respect to the external conditions. The vehicle used for testing is a B segment vehicle. The

desired velocity can be achieved by driving those rotary drums by electrical motors and after the desired velocity is attained, the drums are detached from the motors by clutches and the braking is started. The tests are conducted under dry and wet conditions of the brake disc, with acting ABS and without ABS. Based on the measured data, ANN model was built with the aim of estimating the coefficient of friction on the basis of different operating conditions. The input parameters are brake caliper pressure and wheel slip during braking. In the cases of with and without ABS, the use of ANN facilitates the estimation of mean values of braking coefficients during braking under various conditions. The author also suggests that the application of the neural network can increase the precision of the control algorithms of active safety systems like ABS. Gailis et al. [8] performed a statistical analysis to determine the vehicle brake pad wear. It was stated that the dynamics of wear of brake pads differ from front to rear axle and also inner and outer pads. Wear data are collected from all four wheels with respect to mileage, and it is plotted. Using a data analysis software, the regression equation is generated. The authors have proposed a relation between the mileage and brake pad wear and also state that the observed variance does not allow for acceptable prediction of brake pad wear using linear regression model.

The authors carefully reviewed the above-mentioned literatures, and it was observed that most of the experimental works were carried out to enhance the real-time braking performance by incorporating PID controller in an ABS model. With improvement in the braking performance, there is an increase in wear rate, which reduces the life of brake pads. Thus, predicting the wear rate of brake pads before employing it in real-time application is found to be essential. Very few research works were focused on predicting the life of brake pads by considering the stopping distance and temperature. However, no work has been carried out till date to predict the life of brake pads by considering the RPM, frictional force and braking load as input parameters. Therefore, the present work deals with prediction of brake pad wear and wear rate monitoring by considering the parameters such as load, frictional force and rpm using various machine learning algorithms thereby proposing an efficient algorithm with a mathematical model.

2 Proposed Method

2.1 Experimentation

The pin-on disc experimental setup is used for various applications. Depending on the applications, the data are obtained by setting various conditions. The conditions required for this test are an RPM range of 200–1400, frictional force in the range of 3–12 N and load in the range of 10–30 N. The data are to be obtained using two different conditions. The first condition is maintaining a constant RPM and varying the frictional force and load. While the second is, maintaining a constant frictional force and varying the RPM [9]. By using various machine learning algorithms, the



Fig. 1 Pin on disc experimental setup

amount of wear can be predicted based on the test data. The pin on disc experimental setup to measure the amount of wear is shown in Fig. 1.

2.2 Algorithms Used

Linear Regression. This algorithm is used to predict the value of a dependent variable based on multiple independent variables. It can be formulated as:

$$Y = b_0 + b_1x_1 + b_2x_2 + b_3x_3 + \dots + b_nx_n \tag{1}$$

Here, y is a single independent variable, which depends on multiple independent variables $x_1, x_2, x_3, \dots, x_n$ [10].

For this application, four mathematical relations could be obtained based on the four different sets of data. For constant RPM, the equation is as follows:

$$Y = \beta_0 + \beta_1X_1 + \beta_2X_2 \tag{2}$$

where, Y is the amount of wear of the brake pads in microns, X_1 and X_2 are load and frictional force, respectively. This equation is similar for the dataset of 200, 300 and 400 RPM except for the coefficients $\beta_0, \beta_1, \beta_2$, which varies for each of the dataset.

Likewise, for constant frictional force, the equation is as follows:

$$Y = \beta_0 + \beta_1 X_1 \quad (3)$$

where, Y is the amount of wear of the brake pads in microns and X_1 is the RPM.

Regression Tree. A decision tree used for regression is called a Regression Tree. The tree contains decision nodes, which represent the value of the input variable and, leaf nodes that represent the decision. The decision node that corresponds to the best predictor will be the topmost node and is known as the root node. The decision tree divides the data into smaller nodes called buckets or sub-nodes. This is repeatedly done during the training process until only identical nodes are left. This is done based on the reduction of variance and information gain (which says the amount of information in an event) [11].

Reduction of Variance

$$\text{Variance} = \Sigma(X - \mu)^2 / N \quad (4)$$

where, X is the sample, μ is the mean and N is the number of samples.

Reduction of variance is done in four steps:

1. The variance of each child node is calculated individually for each split.
2. The weighted average variance of all child nodes in each split is calculated.
3. Split with the lowest variance is selected.
4. Steps 1–3 are repeatedly performed until homogenous nodes are obtained.

Information Gain

$$\text{Information Gain} = 1 - \text{Entropy} \quad (5)$$

Entropy determines a node's purity. A node has a higher purity if the entropy value is low. Homogenous node has zero entropy. From the above equation, it can be inferred that the information gain is higher for nodes that are pure.

The number of buckets is decided by the algorithm itself

$$\text{Entropy} = - \sum_{i=1}^n p_i \log_2 p_i \quad (6)$$

where, p is the percentage of each class in the node.

Splitting using Information Gain is done in four steps:

1. The entropy of each child node is calculated individually for each node.
2. The weighted average entropy of all child nodes in each split is calculated.
3. The split with the highest information gain is selected.
4. Steps 1–3 are performed until homogenous nodes are obtained [12].

Support Vector Regression (SVR). SVR algorithm uses the concept of Support Vector Machine (SVM) for predicting a continuous variable. The linear regression model reduces the error between predicted and observed value, while SVR automatically fits in best line with threshold error value. SVR classifies all the prediction lines into two types. The prediction lines, which do not pass between the error boundaries, are not considered, as the threshold (ϵ) value is lesser than the difference of predicted value and observed value. However, the lines passing the error boundary are significant for predicting the value of a future point. Basically, SVR performs high dimension linear regression [13].

SVR model is built as follows:

1. Collecting the training dataset, $\tau = \{X, Y\}$
2. Choosing a kernel (it converts from lower to higher dimensional data)
3. Forming the correlation matrix, \hat{K}

$$K_{ij} = \exp\left(\sum_k \theta_k |x_k^i x_k^j|\right) + \epsilon \delta_{ij}$$

4. Training the machine approximately or exactly, to get the contraction coefficient using $\hat{K} \vec{a} = \vec{y}$.

Where, \vec{y} is the vector of values corresponding to the training data and \vec{a} vector of unknowns that have to be solved.

$$\Rightarrow \vec{a} = \hat{K}^{-1} \vec{y}$$

5. The elements of the coefficient matrix are estimated as follows:

$$K_i = \exp\left(\sum_k \theta_k |x_k^i - x_k^*|^2\right)$$

Support Vector Machine (SVM). Kernel-based SVM is a basic SVM algorithm that uses kernel functions, which apply some complex mathematical operations on lower dimensional data points and convert them into higher dimensional space. There are different types of kernels such as Gaussian RBF Kernel, polynomial kernel, sigmoidal kernel, linear kernel, etc. For the analysis of this given data, linear kernel is used. SVM is using linear kernel functions similar to Support Vector Regression [14].

3 Results and Discussions

3.1 Frictional Force Versus Experimental Wear at Different RPM(s) and RPM Versus Experimental Wear at Constant Frictional Force

Figure 2a shows the relation between frictional force and wear, and it can be observed that, at a constant RPM, the increase in frictional force causes an increase in the amount of wear. The mathematical relation between coefficient of friction (μ), frictional force (F) and normal load (N) is important to explain the concept of increase in wear rate with an increase in frictional force.

$$\mu = F/N \Rightarrow N \times \mu = F \tag{7}$$

From the above equation, it can be inferred that normal load is proportional to frictional force. During the braking action, the brake pads apply a normal load on the brake disc. Al-samarai et al. [9] stated that an increase in normal load increases the frictional force between the brake pads and the brake disc, and this causes an increase in temperature due to the tillage effect caused by the frictional force at the contact surface. This results in adhesion and leads to an increase in the amount of wear. Therefore, the amount of wear observed is a result of the action of frictional force and load applied at a constant RPM. In Fig. 2a, it is observed that, at a constant RPM of 200, the amount of wear varies from 0.0879 to 0.2268 μm with the frictional force varying from 3.5 to 10.5 N, respectively, also at a constant RPM of 300, the amount of wear varies from 0.0879 to 0.2049 μm with the frictional force varying

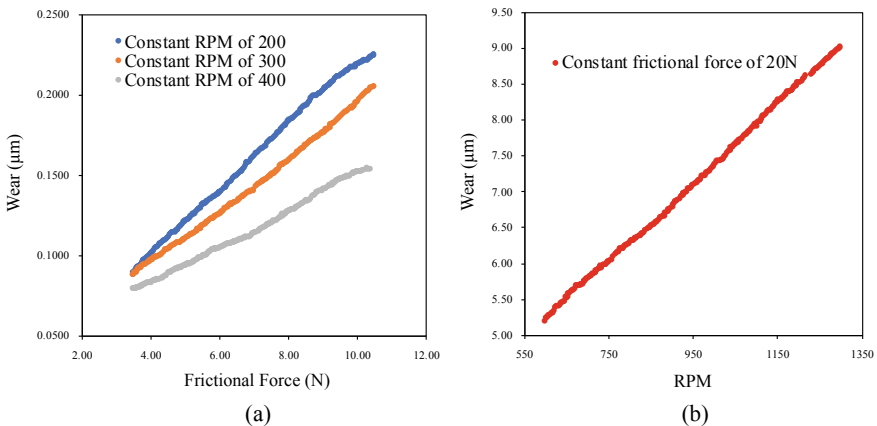


Fig. 2 a Frictional force versus experimental wear at 200, 300 and 400 RPM, b RPM versus experimental wear at a constant frictional force of 20 N

from 3.5 N to 10.5 N, respectively, and at a constant RPM of 400, the amount of wear varies from 0.0789 to 0.1531 μm with the frictional force varying from 3.5 N to 10.5 N respectively. Figure 2a also shows another trend in which, at any given value of frictional force, the amount of wear is greater for lower RPM of 200 and smaller for higher RPM of 400, provided, the amount of wear is increasing throughout. There is an increase of 11.37% at 200 RPM with respect to 300 RPM, an increase of 20.9% at 300 RPM with respect to 400 RPM and an increase of 29.27% at 200 RPM with respect to 400 RPM. Chowdhury et al. [15] stated that this trend is because of change in the shear rate, which affects the mechanical properties of the surfaces in contact. When the shear rate is higher, strength of the materials is greater, and this results in lower actual area of contact and lower frictional force. Figure 2b shows the relation between RPM and wear, and it is being observed that the amount of wear increases with increase in RPM at a constant frictional force. At a constant frictional force of 20 N, the amount of wear varies from 5.1951 to 9.014 μm with the RPM varying from 600 to 1300, respectively. This is because the length of rubbing increases as the sliding speed increases, and, this, in turn, generates frictional heat, which decreases the strength of the materials. These data are used to train the prediction model. Prediction algorithms namely Linear Regression, Regression Tree, SVM and SVR have been used to fit a curve over the data represented in Fig. 2a and b.

3.2 Prediction of Wear at 200 RPM Using Various Prediction Algorithms

Figure 3 shows the predictions of the four different algorithms used for predicting the amount of wear with respect to frictional force and load at a constant RPM of 200. Amongst the set of algorithms used, it is observed that linear regression algorithm makes the best prediction with the least RMSE value of 0.003059 and a residual standard error of <0.1. The very low RMSE value and very low residual standard error (standard deviation of the residuals) show that the prediction results are accurate with an R-square value of 99.51%. Based on Eq. (2), the mathematical model can be written as:

$$Y = \beta_0 + \beta_1 X_1 + \beta_2 X_2 \tag{8}$$

The values of $\beta_0, \beta_1, \beta_2$ are obtained by performing multiple linear regression algorithm. By substituting the values, respectively, the above equation can be written as:

$$Y = 0.02366 - 0.03140 \times \text{Load} + 0.10917 \times \text{FF} \tag{9}$$

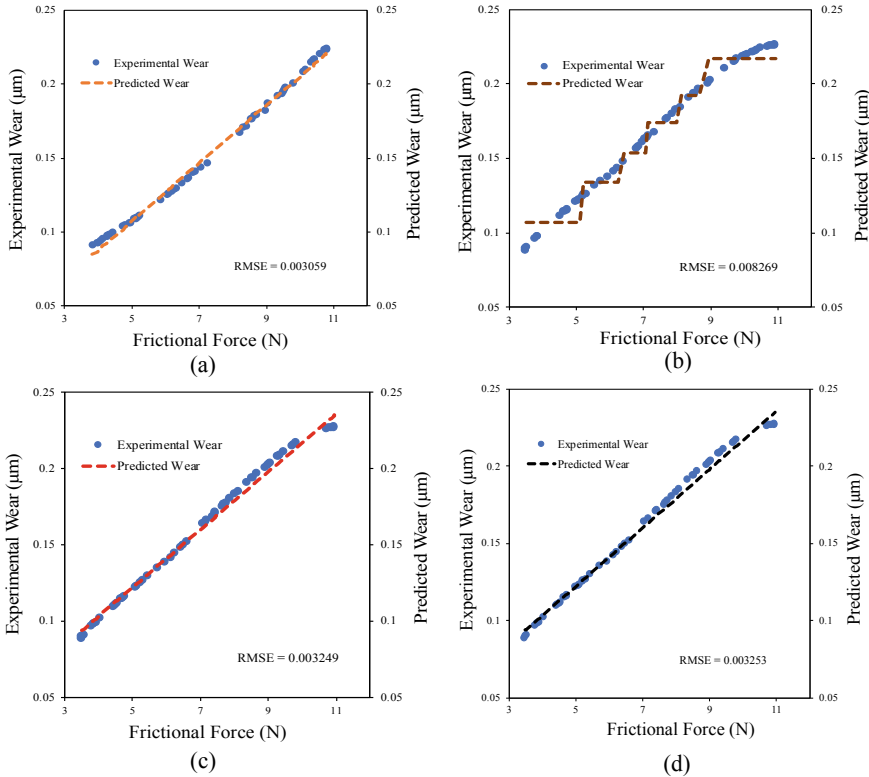


Fig. 3 **a** Prediction using Linear Regression, **b** Prediction using Regression Tree, **c** Prediction using SVM, **d** Prediction using SVR at 200 RPM

3.3 Prediction of Wear at 300 RPM Using Various Prediction Algorithms

Figure 4 shows the predictions of the four different algorithms used for predicting the amount of wear with respect to frictional force and load at a constant RPM of 300. It is observed that linear regression algorithm shows the best prediction result with the least RMSE value of 0.001776 and a minimum residual standard error of <0.1 when compared to the other algorithms used. The very low RMSE value and very low residual standard error (standard deviation of the residuals) show that the prediction results are accurate with an R-square value of 99.72%. Based on Eq. (2), the mathematical model can be written as:

$$Y = \beta_0 + \beta_1 X_1 + \beta_2 X_2 \tag{10}$$

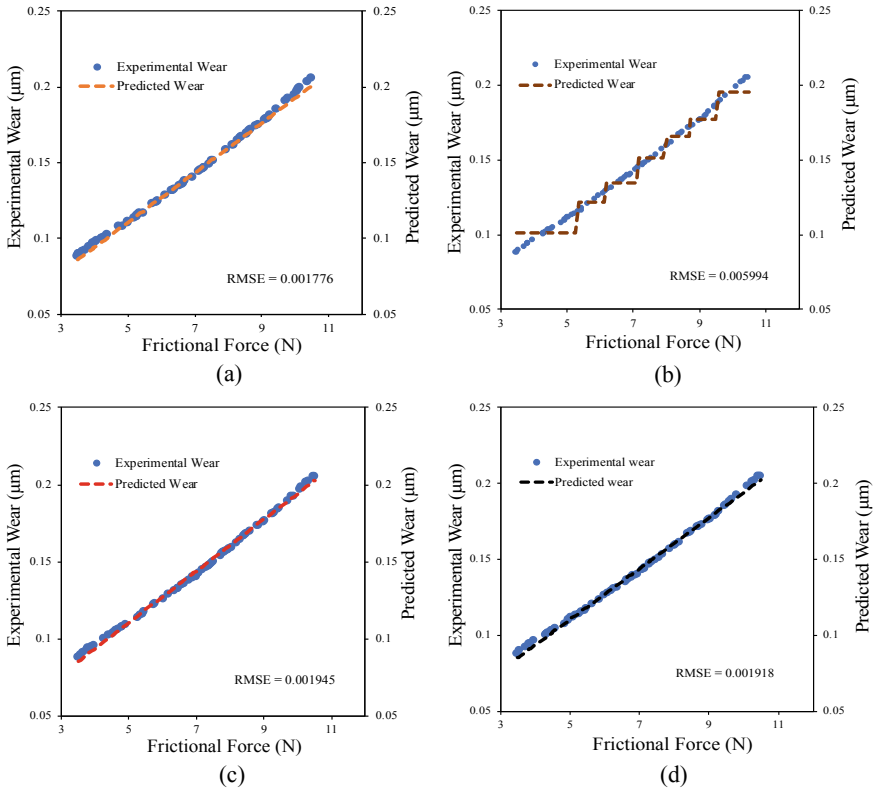


Fig. 4 *a* Prediction using Linear Regression, *b* Prediction using Regression Tree, *c* Prediction using SVM, *d* Prediction using SVR at 300 RPM

The values of $\beta_0, \beta_1, \beta_2$ are obtained by performing multiple linear regression algorithm. By substituting the values respectively, the above equation can be written as:

$$Y = 0.028208 + 0.006492 \times \text{Load} - 0.002117 \times \text{FF} \tag{11}$$

3.4 Prediction of Wear at 400 RPM Using Various Prediction Algorithms

Figure 5 shows the predictions of the four different algorithms used for predicting the amount of wear with respect to frictional force and load at a constant RPM of 400. It is observed that, when compared to the other algorithms used, linear regression algorithm makes the prediction with the least RMSE value of 0.001430 and a very

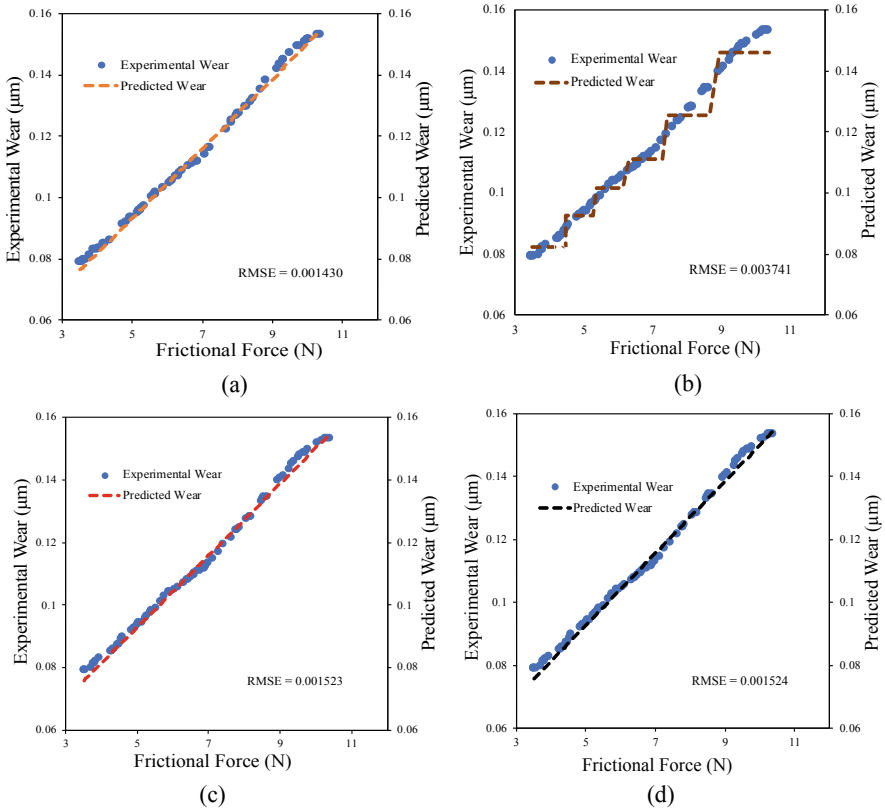


Fig. 5 **a** Prediction using Linear Regression, **b** Prediction using Regression Tree, **c** Prediction using SVM, **d** Prediction using SVR at 400 RPM

low residual standard error of <0.1. The very low RMSE value and very low residual standard error (standard deviation of the residuals) show that the prediction results are accurate with an R-square value of 99.56%. Based on Eq. (2), the mathematical model can be written as:

$$Y = \beta_0 + \beta_1 X_1 + \beta_2 X_2 \tag{12}$$

The values of $\beta_0, \beta_1, \beta_2$ are obtained by performing multiple linear regression algorithm. By substituting the values, respectively, the above equation can be written as,

$$Y = 0.03615 + 0.01632 \times \text{Load} - 0.03522 \times \text{FF} \tag{13}$$

3.5 Prediction of Wear at a Frictional Force of 20 N Using Various Prediction Algorithms

Figure 6 shows the predictions of the four different algorithms used for predicting the amount of wear with respect to RPM at a constant frictional force of 20 N. It is observed that, when compared to the other algorithms used, linear regression algorithm makes the prediction with the least RMSE value of 0.03549 and a very low residual standard error of <0.1. The very low RMSE value and very low residual standard error (standard deviation of the residuals) show that the prediction results are accurate with an R-square value of 99.9%. Based on Eq. (3), the mathematical model can be written as,

$$Y = \beta_0 + \beta_1 X_1 \tag{14}$$

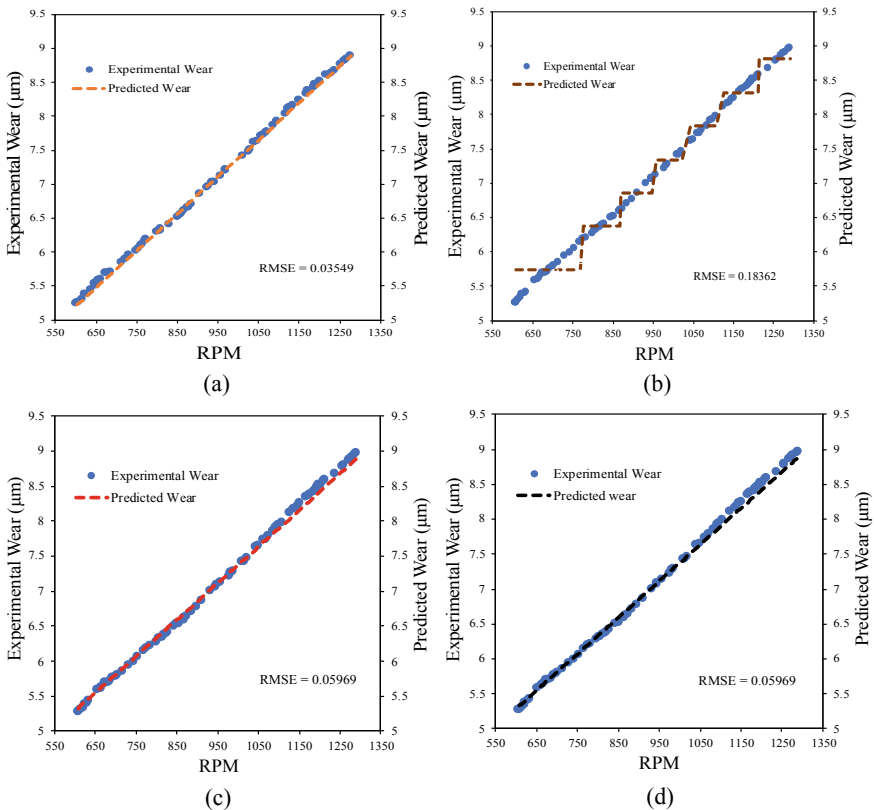


Fig. 6 a Prediction using Linear Regression, b Prediction using Regression Tree, c Prediction using SVM, d Prediction using SVR at a constant frictional force of 20 N

The values of β_0 , β_1 are obtained by performing multiple linear regression algorithm. By substituting the values, respectively, the above equation can be written as,

$$Y = 1.93947 + 0.00544 \times \text{RPM} \quad (15)$$

From the results, it is observed that the prediction of linear regression algorithm gives the best result for all the cases. This is because of the linear relationship between the response variable, which is the amount of wear for both the conditions (constant RPM and constant frictional force), and the predictor variables, which are frictional force and load for one condition and RPM for the other condition, respectively. Also contributing to this are the absence of correlation between the error terms (autocorrelation) and the absence of correlation between the independent variables (multicollinearity).

4 Conclusion

The experimental data from the pin-on-disc setup are used for prediction of brake pad wear. Based on the results, the following conclusions are drawn:

1. Initially, the amount of wear is predicted by varying the frictional force from 3.5 to 11 N with constant rpm of 200, 300 and 400, and further, the amount of wear is also predicted by varying the rpm from 600 to 1300 with constant frictional force of 20 N.
2. Prediction has been done using four different machine learning algorithms, namely, linear regression, regression tree, support vector regression and support vector machine.
3. Linear regression algorithm shows the least RMSE value of 0.002088 and 0.03549 for both the conditions such as constant RPM and constant frictional force, respectively. This results in high accuracy because of the linear relationship between the response variable and the predictor variables along with the absence of autocorrelation and multicollinearity.

The proposed mathematical model can be used to determine the life of the brake pads for various commercial vehicles.

References

1. Rohilla P, Jitender A, Dhingra A (2016) Design and analysis of controller for antilock braking system in Matlab/simulation. *Int J Eng Res Technol* 2(9):583–589
2. Xiao L, Hongqin L, Jianzhen W (2016) Modeling and simulation of anti-lock braking system based on fuzzy control. *Int Adv Res J Sci Eng Technol* 3(10):110–113

3. Zhang XQ, Yang B, Yang C, Xu GN (2012) Research on ABS of multi-axle truck based on ADAMS/Car and Matlab/Simulink. *Procedia Eng* 37:120–124
4. Ahmad F, Hudha K, Jamaluddin H, Bahru J (2012) Modelling and PID control of antilock braking system with wheel slip reduction to improve braking performance. *Int J Veh Saf* 6(3):265–296
5. Harlapur CC (2019) Brake pad wear detection using machine learning. *Int J Adv Res Ideas Innov Technol* 5(2):498–550
6. Hassan AKF, Mohammed S (2016) Artificial neural network model for estimation of wear and temperature in pin-disc contact. *Univ J Mech Eng* 4(2):39–49
7. Szczypinski-Sala W, Dobaj K (2018) The estimation of friction coefficient of brake pad-disc during braking process in different operating conditions. In: *IOP conference series material science and engineering*, vol 421, no 2
8. Gailis M (2012) On prediction of motor vehicle brake pad wearout. *Eng Rural Dev* 1–7
9. Silicon A, Alloy C, Al-samarai RA, Ahmad KR (2012) Effect of load and sliding speed on wear and friction of aluminium–silicon casting alloy. *Int J Sci Res Publ* 2(3):3–6
10. <https://www.aionlinecourse.com/tutorial/machine-learning/multiple-linear-regression>
11. <https://www.analyticsvidhya.com/blog/2020/06/4-ways-split-decision-tree/>
12. <https://www.aionlinecourse.com/tutorial/machine-learning/decision-tree-intuition>
13. <https://www.aionlinecourse.com/tutorial/machine-learning/support-vector-regression>
14. <https://www.analyticsvidhya.com/blog/2017/09/understaing-support-vector-machine-example-code>
15. Chowdhury MA, Khalil MK, Nuruzzaman DM, Rahaman ML (2011) The effect of sliding speed and normal load on friction and wear property of aluminum. *Int J Mech Mechatron Eng* 11(1):53–57

Abrasive Wear Behavior of Bio-Fiber-Reinforced Epoxy Composites with Taguchi Approach



Tanusree Bera , Lopamundra Mohapatra, Ved Prakash, and S. K. Acharya

Abstract In this paper, the wood apple shell/epoxy composites were fabricated by hand lay-up technique. The wood apple shell particulates vary from 5, 10, 15, and 20 wt.%. The abrasive wear tests have been carried out using a pin-on-disc wear tester. In this study, the design of experiments has been applied to evaluate the abrasive wear rate of the composites. The experiments were conducted using the L16 (44) orthogonal array. Analysis of variance (ANOVA) was used to analyze the various impacts of the process variables on the abrasive wear rate. The wt.% of wood apple shell, load, sliding velocity, and speed are the control variables. The results concluded that the load has a maximum impact on the abrasive wear rate.

Keywords Wood apple shell · Pin-on-disc wear tester · Taguchi method · Analysis of variance (ANOVA) · Abrasive wear rate

1 Introduction

Synthetic fibers are mostly used in various fields due to their high stiffness and strength properties. But now a day, the applications of synthetic fibers are decreasing due to non-biodegradability and expensive in nature. In today's world, biodegradability becomes an important factor to reduce environmental pollution and to maintain the balance in the ecosystem. This problem motivates the researchers to move from the synthetic fiber to natural fiber in their research work. The easily availability of

T. Bera (✉) · V. Prakash · S. K. Acharya
Department of Mechanical Engineering, National Institute of Technology Rourkela, Rourkela,
India

S. K. Acharya
e-mail: skacharya@nitrkl.ac

L. Mohapatra
Department of Mechanical Engineering, Indian Institute of Technology Kharagpur, Kharagpur,
India

inexpensive natural fiber and with the ease of manufacturing process multiplies the use of natural fiber as filler or reinforcement in the polymer composites industries.

Wood apple is a natural fiber, considered a sacred tree in India. It has a scientific name of *Aegle marmelos*. It is also known as Bengal quince, golden apple, Japanese bitter orange, stone apple or wood apple. It also presents as a natural species in South Asia, Srilanka, Thailand, and Malaysia like countries. Wood apple shell has composed of 39.54% cellulose, 26.06% hemicellulose, 30.86% lignin, and other carbonaceous compounds [1].

Abrasive wear is very common in many industries. It is a type of wear that leads to faster loss of materials than other forms of wear such as adhesive wear. It involved the penetration of harder abrasive particles on the soft materials and caused damaged or loss of material due to plastic deformation. To study the wear behavior of the materials, a lot of experimental tests have to perform on the materials. It took a lot of time and cost. In order to get an optimum result with less experimental test time and cost, design of experiments (DOEs) technique is used in the study.

Extensive work has been carried out on the implementation of the Taguchi method on composites. Mishra and Biswas [2] found that the sliding wear has the maximum impact both on the wear rate and coefficient of friction. Mishra et al. [3] applied Taguchi's L16 orthogonal array to assess erosion behavior of ZA-27/silicon carbide metal matrix composites. It has been observed that the impingement velocity and filler addition influence more on the wear rate. Patnaik et al. [4] worked on design of the experiments' method to calculate the optimum parameter of the erosion of polyester (E-glass and SiC particles) composites. Experimental results revealed that the size of Erodent, percentage of SiC, impingement velocity, and impact angle, are significant to minimize the erosion rate. Mishra and Biswas [5] developed jute fiber reinforced epoxy composites. The authors found that the sliding velocity has the significant parameter to minimize the wear rate and friction coefficient. Patnaik et al. [6] conclude that the sliding velocity has the maximum contribution to the wear behavior. Mohanta and Acharya [7] used the design-of-experiments (DOE) method to calculate the erosive wear rate of composites. It has been observed that the impingement velocity is the most important parameter to minimize the erosive wear of the composites.

In this study, an attempt has been made to prepare a wood apple shell/epoxy composite and to calculate the abrasive wear rate of the wood apple shell/epoxy composites with various process parameters include weight fraction of the wood apple shell, load, sliding velocity, and speed. An optimization technique Taguchi's L16 array was used for conducting experiments.

2 Experimental Details

2.1 Fiber Preparation

The wood apple shell fiber used in this present study is collected from the Rourkela, Odisha, India. It washes properly with the help of distilled water in order to remove dirt and impurities that are adhering to the surface of the shell. The wood shell is broken into large pieces and properly removes the inner core (seeds and flesh). The outer shell washed several times with distilled water. The outer cover shell is allowed to dry properly under the Sun for 7–8 days until all moisture is removed. The dried wood shells are crushed into small pieces in a crusher; these small pieces are converted into particulate form using a ball milling machine. The collected powder was sieved and segregated into a size of 212 microns. The complete procedure of fiber preparation is shown in Fig. 1.

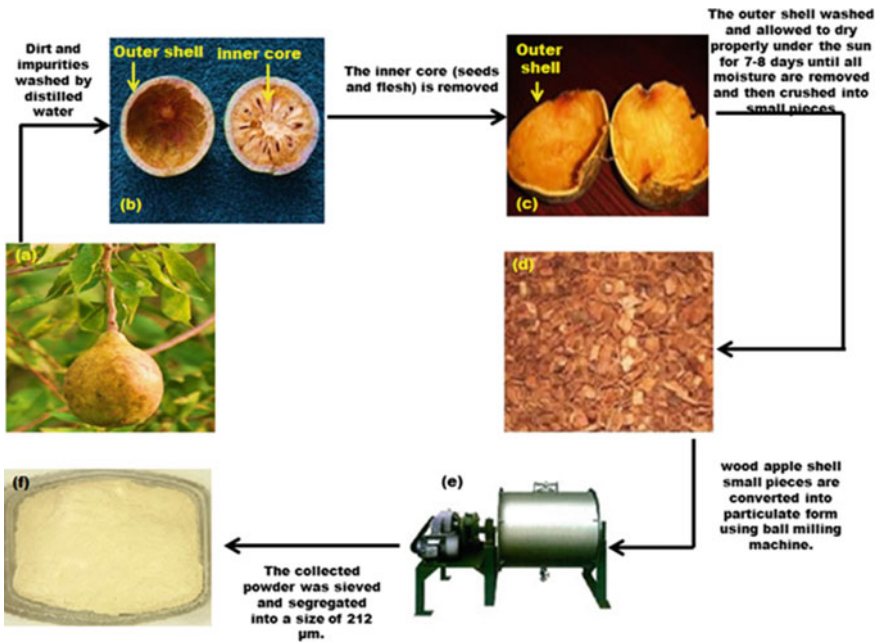


Fig. 1 The complete procedure of fiber preparation

2.2 Fabrication of Composites

The composites are prepared with wood apple shell particulates as filler in polymer matrix composites with various percentages with a step of 5 wt.%. The epoxy resin used in this project is Araldite LY556, which is belonged to epoxide family with common name Bis-Phenol-A-Diglycidyl-Ether and supplied by CIBA GUGYE India Limited. It has a density of 1.16 gm/cc. A designed and fabricated steel mold is utilized for making cylindrical specimen of length 30 mm and diameter of 10 mm. The calculated amount of wood apple shell particulates and epoxy resin with hardener (10:1) mixture is poured in the mold cavity (Fig. 2a) after that both halves of the mold cavity are properly aligned and fixed (Fig. 2b). The specimens are allowed to be inside the mold cavity for 1 day at room temperature. After 1 day, the specimens are taken out from the mold cavity (Fig. 2c) and machined to calculate the size for wear testing.

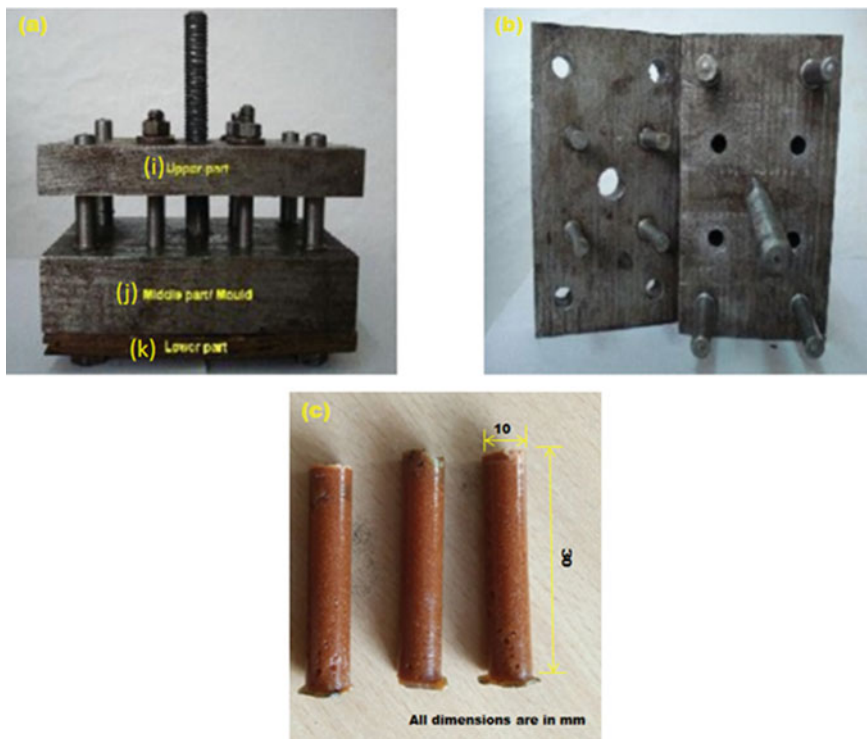


Fig. 2 a Steel mold for composite preparation (i) upper part of the mold (j) middle part of the mold (k) lower part of the mold b two halves of the mold c composite pin samples

2.3 Abrasive Wear Test

The abrasive wear test is carried out with the specimens under dry conditions at ambient temperature with pin-on-disc-wear tester, which is similar to the one used by Bera et al. [8].

3 Results and Discussion

3.1 Effect of Load on Wear Rate

Figure 3 shows the variation of wear rate with various loads. It is seen that for all loads, the wear rate is high at the initial period and gradually lowers as the load increases for the rest of the test period. This is because, at the initial stage of the experiment, the abrasive paper is fresh but as the specimen slides against the abrasive paper; the sharp edges of the abrasive particles get damaged, and it becomes smooth. The accumulation of wear debris on the interstitial spaces between the abrading particles also reduces the wear rate.

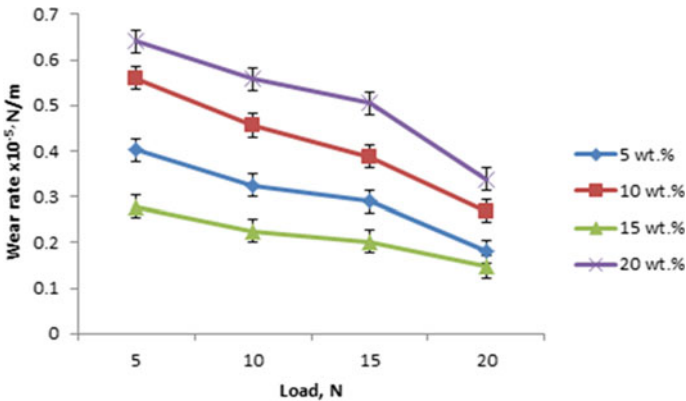


Fig. 3 Effect of load on wear rate at a sliding velocity of 2.0944 m/s

4 Experimental Design and Optimization

4.1 The Taguchi Approach

A Taguchi approach is a powerful tool used widely in industries to improve the quality of the manufactured products. This method is commonly used in analyzing engineering data. This is also known as a robust design, which helps in reduction of the number of tests with the implementation of orthogonal arrays. This design lessens the effects of various factors that are difficult to control. It gives an easy, powerful and standardized approach to select the best factors during the fabrication process.

Many researchers [2–7] have studied the abrasive wear behavior of polymer composites with various parameters; they found that the parameters, like volume fraction, load, sliding velocity, speed, etc. largely influence the abrasive wear rate of the composites. In this study, the effect of the same parameters is studied using L16 (44) orthogonal design. The controlling parameters of the tests are presented in Table 1. The conventional experimental design requires 256 runs for four parameters with four levels whereas Taguchi’s design reduces it to only 16 runs, which greatly reduces the experimental time and cost. The investigational observations are further converted into signal-to-noise (S/N) ratios. There are three types of S/N ratios, namely, the smaller-the-better, the higher-the-better, and the nominal-the-best. The S/N ratios for each level of the test parameters depend on the type of performance characteristics. In this study, the goal is to minimize the abrasive wear rate. Therefore, the smaller-the-better quality characteristic is used, which is shown in Eq. 1.

Smaller the better characteristic (minimize):

$$S/N_s = -10\log\left[\frac{1}{n} \sum_{i=1}^n y_i^2\right] \tag{1}$$

where y_i is the data and n is the experimental observation number.

Table 1 Levels of the control factors used in the abrasive wear tests

Control factor	Level 1	Level 2	Level 3	Level 4	Units
A: wt.% of wood apple	5	10	15	20	wt.%
B: Load	5	10	15	20	N
C: Sliding velocity	0.5235	1.0472	1.5708	2.0944	m/s
D: Speed	100	200	300	400	RPM

Table 2 S/N ratio for abrasive wear rate

Experiment number	A: wt.% of wood apple (%)	B: Load (N)	C: Sliding Velocity (m/s)	D: Speed (RPM)	Abrasive wear rate (N/m)	S/N ratio (dB)
1	5	5	0.5235	100	0.0000010	120.446
2	5	10	1.0472	200	0.0000012	118.416
3	5	15	1.5708	300	0.0000043	107.391
4	5	20	2.0944	400	0.0000045	106.878
5	10	5	1.0472	300	0.0000012	118.786
6	10	10	0.5235	400	0.0000022	113.152
7	10	15	2.0944	100	0.0000022	105.547
8	10	20	1.5708	200	0.0000053	103.073
9	15	5	1.5708	400	0.0000070	101.809
10	15	10	2.0944	300	0.0000081	140.762
11	15	15	0.5235	200	0.0000001	113.893
12	15	20	1.0472	100	0.0000020	111.119
13	20	5	2.0944	200	0.0000028	120.491
14	20	10	1.5708	100	0.0000009	117.266
15	20	15	1.0472	400	0.0000014	109.683
16	20	20	0.5235	300	0.0000033	102.793

5 Analysis and Evaluation of Experimental Results

5.1 Analysis of the S/N Ratio

Table 2 shows the abrasive wear rate of wood apple shell epoxy composites under various test conditions. The average value of S/N ratio for abrasive wear rate is found to be 113.219 dB. The analysis of the effect of each control factor (wt.% of wood apple shell, load, sliding velocity, and speed) on the abrasive wear rate is performed with Minitab 18, statically software specially used for experimental data analyzing applications. Figure 4 shows the effects of each factor that influences the wear rate of the composites. The S/N ratio response is given in Table 3. Optimal abrasive variables of the control factors for minimizing the abrasive wear rate can clearly find out from Fig. 4. The optimum level for each control factor is determined with the highest S/N ratio in the levels of that control factor. Hence, the levels and S/N ratios for the abrasive wear rate value are specified as factor A (level 3, S/N = 116.9), factor B (level 1, S/N = 115.4), factor C (level 4, S/N = 118.4), factor D (level 3, S/N = 117.4). The optimum abrasive wear rate is obtained with a 15 wt.% of wood apple shell (A3), at 10 N load (B2), with a sliding velocity of 2.0944 m/s (C4) and at a speed of 300 RPM (D3) (Fig. 4).

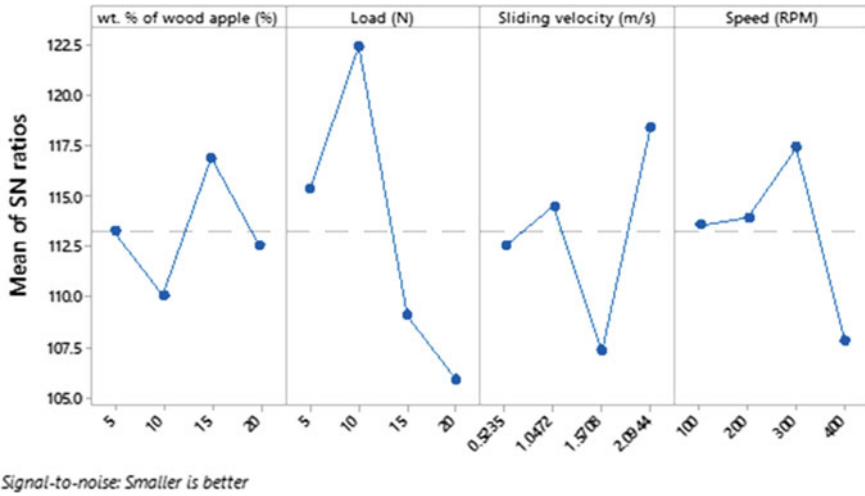


Fig. 4 Effect of process parameters on the average S/N ratio for abrasive wear rate

Table 3 Response Table for S/N ratio for abrasive wear rate factor

Level	A wt.% of wood apple (%)	B Load (N)	C Sliding velocity (m/s)	D Speed (RPM)
1	113.3	115.4	112.6	113.6
2	110.1	112.4	114.5	114.0
3	116.9	109.1	107.4	117.4
4	112.6	106.0	118.4	107.9
Delta	6.8	16.4	11.0	9.6
Rank	4	1	2	3

6 ANOVA Method

ANOVA is an analytical technique that is performed on the experimental test data to regulate the independent interconnections of the entire control factors. In this study, ANOVA is used to analyze the effects of weight fraction of wood apple shell, load, sliding velocity, and speed on the abrasive wear rate. The ANOVA results for the abrasive wear rate are shown in Table 4. This analysis is carried out for a level of confidence at 5% significance. The importance of the control factors in ANOVA is evaluated by comparing the P values of each control parameter. The last column of Table 4 shows the contribution of each parameter on the performance output. According to Table 4, the contributions of the A, B, C, and D factors on the abrasive wear rate are found to be 0.950, 0.393, 0.559, and 0.794, respectively. Hence, the load (B) shows the lowest p-values (0.393), which shows that the effect of the load (B) on the abrasive wear rate of the wood apple shell polymer composites is highly significant.

Table 4 Results of ANOVA for abrasive wear rate

Source	DF	Adj SS	Adj MS	F-value	P-Value
A	3	0.000000	0.000000	0.11	0.950
B	3	0.000000	0.000000	1.40	0.393
C	3	0.000000	0.000000	0.83	0.559
D	3	0.000000	0.000000	0.35	0.794
Error	3	0.000000	0.000000		
Total	15	0.000000			

7 SEM Morphology of Worn Surfaces

Figure 5 shows the surface morphology of the worn-out samples of wood apple shell/epoxy composites. At 5 N load, the surface damage of the composite is very less. As we increase the load, the surface damage increased. At 20 N load, the craters and surface damage both occur on the composites. This indicates that higher load leads to debonding of epoxy and fiber particulates, hence, create higher depth of

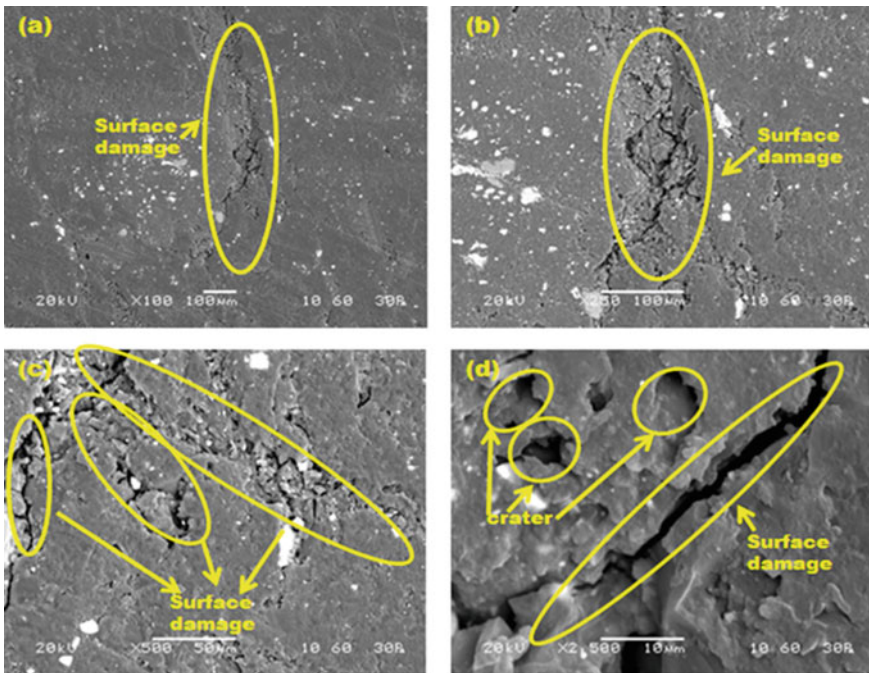


Fig. 5 SEM morphology of worn samples after abrasive wear test **a** 5 N, **b** 10 N, **c** 15 N, **d** 20 N of load

surface damage and deep craters on the surface of the composites [5, 6]. The SEM morphology of the worn surfaces revealed the abrasive wear mechanism.

8 Conclusions

The following conclusions are drawn from this study:

- According to the results of statistical and experimental, it revealed that the 15 wt.% of wood apple shell gives better abrasive wear resistance.
- The optimum levels of the process parameters for minimizing the abrasive wear rate using signal-to-noise ratio are determined. The optimal conditions for abrasive wear rate are observed at A3B2C4D3 (i.e., wood apple shell = 15 wt.%, load = 10 N, sliding velocity = 2.0944 m/s, and speed = 300 RPM).
- The most dominating control factor in the statistical analyses for minimization of abrasive wear rate is the load.
- The SEM morphology of the worn surfaces revealed the abrasive wear mechanism.

Acknowledgements We are thankful to the authorities of NIT Rourkela, India, for providing the facility for carrying out this research work.

References

1. Lawrence JR, Swerhone GDW, Leppard GG, Araki T, Zhang X, West MM, Hitchcock AP (2003) *Appl Environ Microbiol* 69:5543–5554
2. Mishra V, Biswas S (2015) *J Ind Text* 44:781–797
3. Mishra SK, Biswas S, Satapathy A (2014) *Mater Des* 55:958–965
4. Patnaik A, Satapathy A, Mahapatra SS, Dash RR (2008) *J Reinf Plast Compos* 27:1093–1111
5. Joshi AG, Kumar MP, Basavarajappa S (2014) *Proc Mater Sci* 5:863–872
6. Mishra V, Biswas S (2016) *Polym Compos* 37:270–278
7. Patnaik A, Satapathy A, Dwivedy M, Biswas S (2010) *J Compos Mater* 44:559–574
8. Mohanta N, Acharya SK (2015) *J Polym Eng* 35:391–399

Effect of Surface-Treated Calcium-Copper-Titanate as a Lubricant Additive in Cottonseed Oil on Tribo Performance in Sliding Contacts



Rajeev Nayan Gupta, A. P. Harsha, and Tej Pratap

Abstract The present work exhibits the tribological study of environment benign cottonseed oil, with and without blending of nanoparticles as a lubricant additive, using four-ball test rig. The present investigation focused on the close contact sliding conditions, because of the major possibilities of material loss between the dynamically mating surfaces. Surface-treated calcium-copper-titanate, $\text{CaCu}_3\text{Ti}_4\text{O}_{12}$ (CCTO, <90 nm) nanoparticles, as an additive, in different concentrations (i.e. from 0.1 to 1.0%w/v) have been used in the base cottonseed oil to formulate the nanolubricant. CCTO nanoparticles have been treated with sodium dodecyl sulfate to alter the surface characteristics of the nanoadditive and form S-CCTO, to avoid nanoparticle agglomeration. The nanoparticle's dose was optimized on the basis of minimum wear scar diameter (WSD) in antiwear test. The test nanolubricants were prepared by vigorous stirring and ultrasonication for stable and uniform suspension of the nanoparticles in cottonseed oil. The weld load property of the nanolubricants has been tested by extreme pressure property test (ASTM D2783). Worn surfaces have been characterized by using scanning electron microscope for analyzing the wear scar morphology, while for surface roughness studies, atomic force microscope has been used. The obtained test result shows that the small additive concentration improves the tribological properties significantly. It was observed that 0.25%w/v concentration exhibits maximum reduction in the WSD (i.e. 34.4%) in antiwear test, whereas in extreme pressure test, the maximum weld load was observed at 1.0%w/v.

R. N. Gupta (✉)

Department of Mechanical Engineering, National Institute of Technology, Silchar 788010, Assam, India

e-mail: rajeev@mech.nits.ac.in

A. P. Harsha

Department of Mechanical Engineering, Indian Institute of Technology (BHU), Varanasi 221005, Uttar Pradesh, India

T. Pratap

Department of Mechanical Engineering, Motilal Nehru National Institute of Technology Allahabad, Prayagraj 211004, Uttar Pradesh, India

© The Author(s), under exclusive license to Springer Nature Singapore Pte Ltd. 2022

555

M. K. Singh and R. K. Gautam (eds.), *Recent Trends in Design, Materials*

and Manufacturing, Lecture Notes in Mechanical Engineering,

https://doi.org/10.1007/978-981-16-4083-4_44

Keywords Cottonseed oil · Antiwear · Antifriction · Extreme-pressure · Nanoparticle

1 Introduction

Wear and friction are the primary causes of failure of any mechanical components in relative motion. These parameters are also responsible for huge loss of material and energy. These failure aspects can be suppressed significantly by the use of appropriate lubricant between the surfaces in dynamic contact. Globally, around 85% applied lubricants in industrial and commercial purposes are mineral and synthetic oils to improve the tribological properties. However, these oils are non-degradable, toxic and left hazardous impact on the environment. Therefore, considering environment health and limited petroleum base stock, researchers are focused in exploring vegetable-based biolubricants as renewable source to use for tribological contact situations [1]. Vegetable-based oils are comprehensively biodegradable, non-toxic, good lubricity and environment friendly. Vegetable-based oils have also capability to improve the tribological properties but inferior thermos-oxidation stability, which limits its widespread use. These limitations can be reduced up to a certain level either by using different types of additives or by self-modification of the fatty acid structure of the base oils. Many researches are exploring to formulate the additives to improve the tribological properties especially in boundary lubrication regime [2]. These additives act as antioxidant, viscosity modifier, antiwear agent etc. and range from organic particles, compounds to nanoparticles having different shapes [3]. From the last two decades, the researchers have attention on nanoparticles as an oil additive in terms of improvement in tribological properties. These nanoparticles could be metals, ceramics, nanosheet, magnetic nanoflakes etc. [4–6]. Friction and wear reduction of nanoparticles depend on compatibility with base oil along with shape, size, and physiochemical nature [7]. The nanolubricants have improved tribological properties in the nanoparticle size range of 2–150 nm [8]. In the present study, surface modified CCTO nanoparticles used with different concentrations in base cottonseed oil and the effect on tribological performance have been evaluated. The hypothetical mechanisms for improvement in tribological properties have also been reported.

2 Experimental Details

2.1 Materials

Cottonseed oil having viscosity $0.063 \text{ N}\cdot\text{s}/\text{m}^2$ at $30 \text{ }^\circ\text{C}$, refractive index 1.378 and saponification value 156 was acquired from Hi-Media industries, India and used without further purification. CCTO nanoparticle has been synthesized via sol-gel

method reported by Gupta and Harsha (2017) and modified with sodium dodecyl sulfate (SDS) to alter the surface property of the CCTO nanoparticles [9].

2.2 Surface Treatment of CCTO Nanoparticles

Due to higher density and solid nature of nanoparticle than base oil, the chance to settle down of nanoparticle is more in base oil. Also, nanoparticles have high surface energy, which may cause the agglomeration of the nanoparticles to stabilize itself. Therefore, to make the proper suspension and avoid agglomeration of the nanoparticles for prolong time inside the cottonseed oil, the nanoparticle surfaces have been treated with SDS. Three neck glass round flask, magnetic stirrer, glass condensation systems were used for chemical treatment. CCTO to SDS was used in weight ratio of 1:5, for the surface capping. Initially, the measured amount of SDS blended in ethanol, under control heating and mixing at 70 °C and 1000 rpm, respectively. IKA-HS4 magnetic stirrer-cum-hot plate was used for the said purpose. Further, the calculated amount of CCTO nanoparticles was mixed thoroughly in as prepared SDS solution for 24 h. After the complete chemical reaction, the chemically treated nanoparticles were separated using filter paper. These filtered nanoparticles were further washed with hot ethanol and dried. At last, the treated nanoparticles were thoroughly smashed in pestle and mortar, to get the surface-treated nanoparticles and named as S-CCTO.

2.3 Tribological Testing and Characterization

Four ball tester (Manufacturer DUCOM Industries Pvt. Ltd., India) was used to study the antiwear (based on scar size on worn surface) and extreme pressure properties (for weld load characteristics) as per the ASTM D4172 and D2783 standards, respectively [10, 11]. The experimental setup is presented in Fig. 1. Four new and fresh AISI 52,100 steel balls (each 12.7 mm diameter) were used all the tests. Out of four balls, one ball was fixed in rotating spindle with the help of ball collet. Other three balls were positioned in the lower stationary ball-pot. The top ball was pressed against the three lower stationary balls and load applied either as per ASTM D4172 or D2783, depending upon the type of tribo test. For antiwear test, the operating condition was: load 392 N, time 3600 s, spindle speed 1200 r.p.m., and lubricant temperature at 75 + 2 °C. Friction variation was recorded automatically during the test.

For extreme pressure test, a series of load was applied until all four balls get welded together. These tests were performed at room temperature for the test duration of 10 s. Prior to the tribological tests, each ball and ball pot assembly wiped thoroughly with acetone to remove any residue on the surfaces, if any. Every tribo test was performed at least three times for reproductive results.

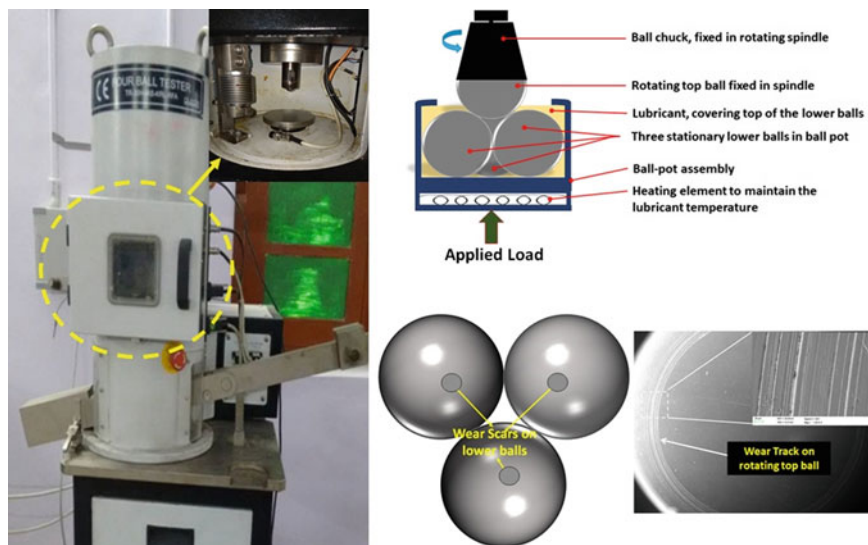


Fig. 1 Experimental setup

SDS-treated CCTO nanoparticles (S-CCTO) have been analyzed using Fourier transform infrared technique (FTIR; model TENSOR 27 by Bruker optics) to confirm the surface treatment. Scanning Electron Microscope (SEM, model Zeiss EVO 18 Research) has been used to characterize the morphology of worn surfaces. Atomic force microscope (AFM, model BT 02,218, Nanosurf easyscan 2 basic AFM, Switzerland) has been used for the evaluation of worn surfaces.

3 Experimental Details

3.1 FTIR of SDS-Treated CCTO Nanoparticles

The FTIR spectra of CCTO nanoparticles, SDS, and S-CCTO nanoparticles have been depicted in Fig. 2.

FTIR spectrum of S-CCTO follows the same trend as CCTO nanoparticles, which is the good agreement that no such structural change in treated nanoparticles as compared with original nanoparticles during the reaction of surface treatment. However, the spectrum of the SDS powder shows distinct trend. The variation of the S-CCTO pattern exhibits that few absorption band of SDS were also present in S-CCTO, which completely absent in original CCTO particles. The stretching absorption bands produced at 1064 , 1272 , and 2870 cm^{-1} show medium C-O stretching, strong C-O stretching, and medium C-H stretching, respectively. However, the absorption band at 893 cm^{-1} represents strong C-H bending. It clearly confirms that the as-synthesized

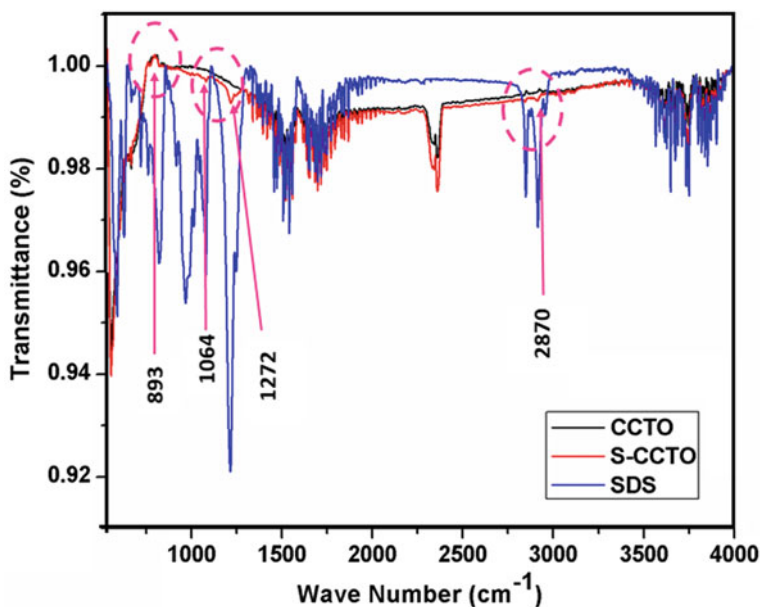


Fig. 2 FTIR spectra of SDS, CCTO and S-CCTO

CCTO nanoparticles were modified successfully with the surface treatment by SDS and S-CCTO formed.

3.2 Tribological Property

Antiwear Characteristics. Antiwear characteristics of the worn surfaces with different set of nanolubricants have been analyzed with SEM micrographs and depicted in Fig. 3. Abbreviations CO, 0.1CC, 0.25CC, 0.5CC and 1.0CC represent base cottonseed oil, cottonseed oil with concentration of 0.1, 0.25, 0.5 and 1.0%w/v of S-CCTO, respectively.

It observed that maximum scar size was obtained with raw cottonseed oil, i.e. 760 μm (approximately). However, a significant improvement in wear scar was observed with the addition of small quantity of S-CCTO nanoparticle additive. Initially, decreasing then increasing trend of WSD observed with an increase in S-CCTO concentration in cottonseed oil. Although 0.1%w/v concentration reduced the WSD; however; 0.25%w/v concentration considered as optimum due to minimum WSD. The variation in wear scar diameter, coefficient of friction (COF), and roughness are enumerated in Table 1. It shows minimum WSD was 498.1 μm with nearly 34.4% reduction in WSD as compared with the base cottonseed oil. Also, with further

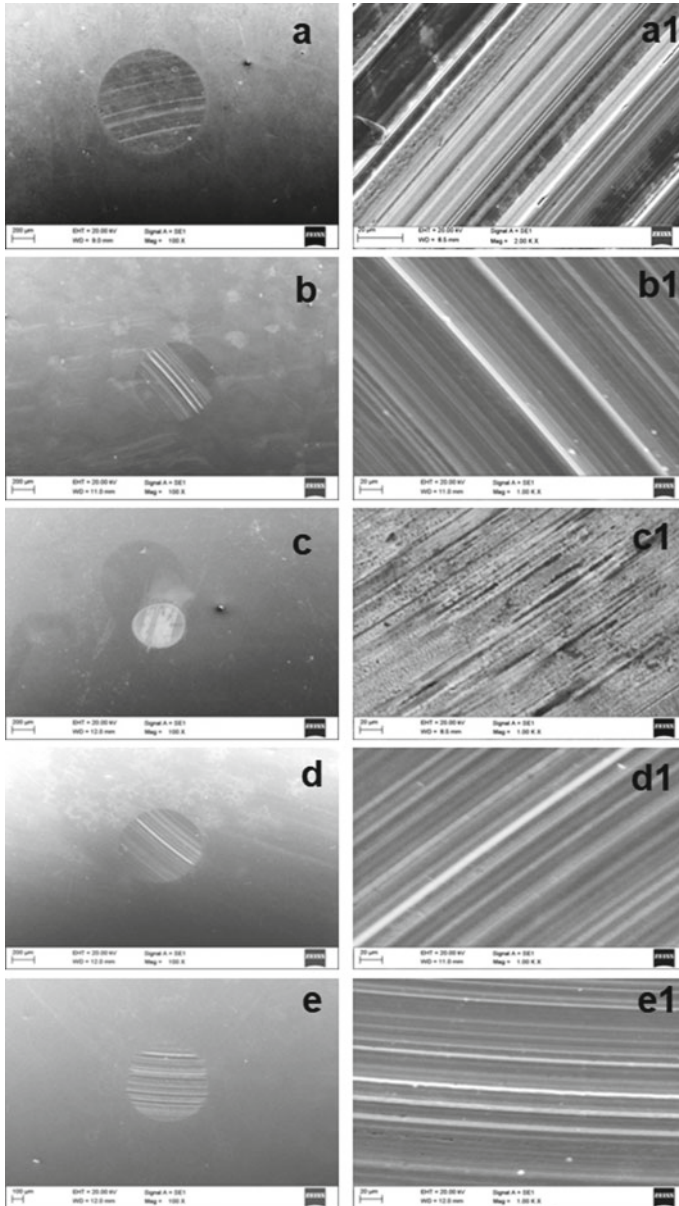


Fig. 3 SEM images of wear scar for different nanolubricant compositions at 100× and 1000× magnification; **a** CO, **b** 0.1CC, **c** 0.25CC, **d** 0.5CC, and **e** 1.0CC

Table 1 Summary of WSD, roughness, and coefficient of friction

	CO	0.1CC	0.25CC	0.5CC	1.0CC
WSD(μm)	760	691.2	498.1	611.5	721.3
Line roughness, R_q (nm)	870.2	513.1	112.9	221.1	361.4
Surface roughness, S_q (nm)	853.9	526.4	102.2	163.5	302.7
COF	0.085	0.061	0.052	0.060	0.068

increase in concentration from 0.25%w/v WSD start to increase again. Surface roughness images of the worn surfaces for different nanolubricant compositions have been depicted in Fig. 4. It exhibits good agreement with the variation in WSD variation. The minimum roughness, i.e. R_q 112.9 and S_q 102.2 nm, was noticed with 0.25%w/v dose, while the corresponding roughness noticed maximum with raw cottonseed oil alone as 870.2 and 853.9 nm, respectively.

The reasons for this improvement might be; first, the rolling sliding action of nanoparticles, which act as nanobearing between mating surfaces or simultaneous filling of rough surface valley and formation of tribo-film just over nanoparticle and second, decrease in real area of contact between contacting surfaces. It directly reflects the enhanced antiwear property.

Antifriction Characteristics. The variation in coefficient of friction is depicted in Fig. 5, and corresponding average COF is enumerated in Table 1. Approximately

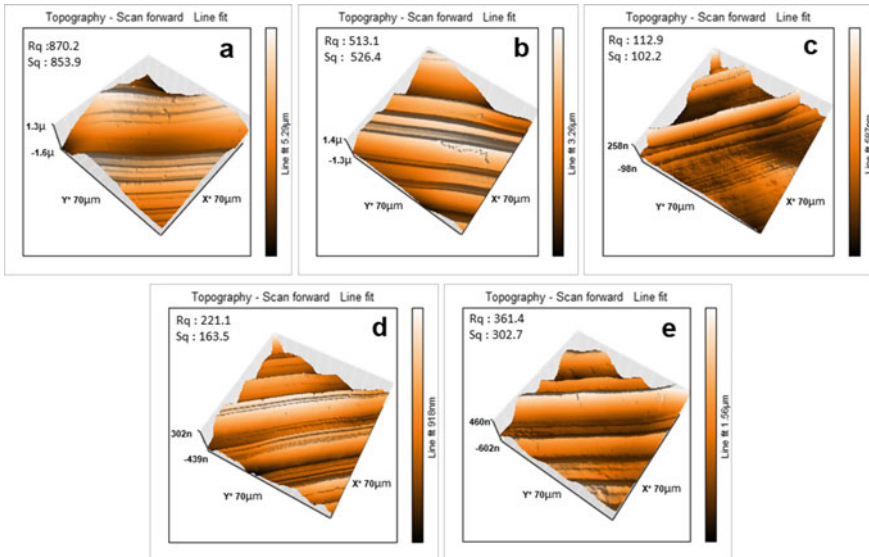


Fig. 4 AFM images of surface roughness of wear scar for different nanolubricant compositions; **a** CO, **b** 0.1CC, **c** 0.25CC, **d** 0.5CC, and **e** 1.0CC

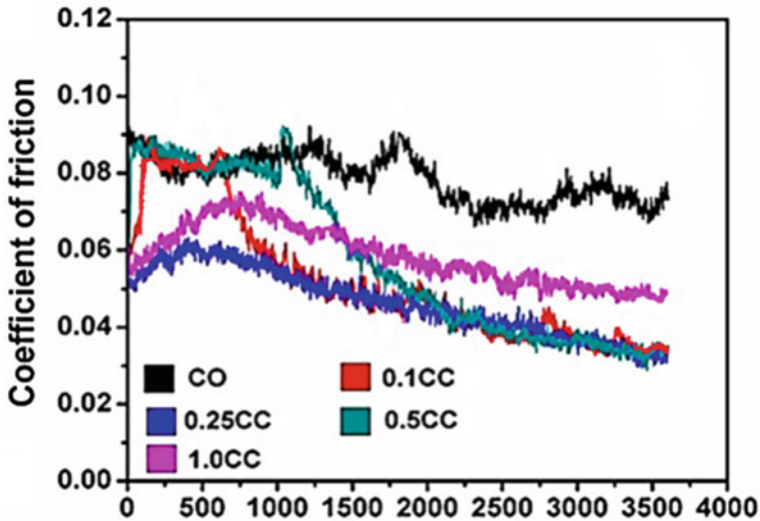


Fig. 5 Friction coefficient behavior for different nanolubricant compositions [load 392 N, speed 1200 rpm, temperature 75 °C and time 3600 s]

up to 500 s, all the nanolubricants show increasing trend, thereafter continuously decreasing behavior. It may be due to the wear-in period during initial run time.

Maximum average COF was noticed as 0.085 with raw cottonseed oil. A small amount of nanoadditives in the base oil reduces COF value substantially. The lowest average COF was recorded with 0.25CC, as 0.052. And, with an increase the concentration beyond this limit COF started to increase again. It shows good agreement with WSD variation. Therefore, 0.25CC can be considered as the optimum condition for both antiwear and antifricition characterization.

Extreme pressure Characteristic. The improvement in weld load capacity for various nanolubricant compositions was obtained only with 1.0CC (i.e. cottonseed with 1.0%w/v S-CCTO). It shows the maximum weld load capacity of 200 kgf for 1.0CC only. However, other compositions along with cottonseed oil alone have shown the same weld load capacity of 160 kgf. It can be speculated that due to higher load and high rotation of 1760 rpm (As per the ASTM standard), the tribo-film formed at the interface was not sufficient to survive with cottonseed oil lubrication. Even with the low concentrations, most of the nanoparticles escape from the interface, which shows the same weld behavior as raw cottonseed oil. On the contrary, at the highest concentration of 1.0%w/v, the optimum number of particles might be present at the interface to separate the asperities. It reflects the improved extreme pressure property.

4 Conclusions

The summary of the present work concluded pointwise as follows:

- The surface treatment of the CCTO nanoparticles was done successfully with sodium dodecyl sulfate to form S-CCTO and avoid agglomeration.
- Optimum concentration of S-CCTO has been observed as 0.25%w/v in cottonseed oil for antiwear and antifriction study. A maximum of 34.4% reduction in WSD has been observed with 0.25%w/v concentration with respect to base cottonseed oil. And, maximum improvement in roughness was around 87%.
- The most effective extreme pressure results were obtained with 1.0%w/v concentration of S-CCTO in cottonseed oil. Weld load capacity was maximum for S-CCTO concentration of 1.0%w/v, whereas other composition shows similar potential as base cottonseed oil.

References

1. Nagendramma P, Kaul S (2012) Development of ecofriendly/biodegradable lubricants: an overview. *Renew Sustain Energy Rev* 16:764–774
2. Nehme G, Mourhatch R, Aswath PB (2010) Effect of contact load and lubricant volume on the properties of tribofilms formed under boundary lubrication in a fully formulated oil under extreme load conditions. *Wear* 268:1129–1147
3. Fuyan Z, Bai Z, Ying F, Zhao D, Yan C (2012) Tribological properties of serpentine, $\text{La}(\text{OH})_3$ and their composite particles as lubricant additives. *Wear* 288(1):72–77
4. Kotia A, Ghosh GK, Srivastava I, Deval P, Ghosh SK (2019) Mechanism for improvement of friction/wear by using Al_2O_3 and SiO_2 /Gear oil nanolubricants. *J Alloy Compd* 782:592–599
5. Qu M, Yao Y, He J, Ma X, Feng J, Liu S, Hou L, Liu X (2017) Tribological study of polytetrafluoroethylene lubricant additives filled with Cu microparticles or SiO_2 nanoparticles. *Tribol Int* 110:57–65
6. Cho DH, Kim JS, Kwon SH, Lee C, Lee YZ (2013) Evaluation of hexagonal boron nitride nano-sheets as lubricant additive in water. *Wear* 302:981–986
7. Zhao J, Chen G, He Y, Li S, Duan Z, Li Y, Luo J (2019) A novel route to the synthesis of an $\text{Fe}_3\text{O}_4/\text{h-BN}$ 2D nanocomposite as a lubricant additive. *RSC Adv* 9:6583–6588
8. Zhang BS, Xu BS, Xu Y, Gao F, Shi PJ, Wu YX (2011) Cu nanoparticles effect on the tribological properties of hydrosilicate powders as lubricant additive for steel-steel contact. *Tribol Int* 44:878–886
9. Gupta RN, Harsha AP (2017) Synthesis, characterization, and tribological studies of calcium–copper–titanate nanoparticles as a biolubricant additive. *Trans ASME, J Tribol* 139(2):021801-1–021801-11
10. ASTM D4172, Reapproved 2010, “Standard test method for wear preventive characteristics of Lubricating fluid (four-ball method)”, ASTM International, 100 Barr Harbor Drive, PO Box C700, West Conshohocken, PA 19428-2959, United States
11. ASTM D2783, Reapproved 2009, “Standard test method for measurement of extreme-pressure properties of lubricating fluids (Four Ball Tester)”, ASTM International, 100 Barr Harbor Drive, PO Box C700, West Conshohocken, PA 19428-2959, United States